UNDERSTANDING DISK SUBSTRUCTURES WITH 3D SELF-CONSISTENT THERMODYNAMICS

By

Shangjia Zhang (张尚嘉)

Bachelor of Science – Astronomy and Astrophysics
Bachelor of Science – Physics
University of Michigan, Ann Arbor
2018

A dissertation submitted in partial fulfillment
of the requirements for the

Doctor of Philosophy – Astronomy

Department of Physics and Astronomy
College of Sciences
The Graduate College

University of Nevada, Las Vegas
May 2024

UNLV | GRADUATE COLLEGE

Dissertation Approval

The Graduate College
The University of Nevada, Las Vegas

March 28, 2024

This dissertation prepared by

Shangjia Zhang

entitled

Understanding Disk Substructures with 3D Self-Consistent Thermodynamics

is approved in partial fulfillment of the requirements for the degree of

Doctor of Philosophy – Astronomy
Department of Physics and Astronomy

Zhaohuan Zhu, Ph.D.
Examination Committee Chair

Rebecca Martin, Ph.D.
Examination Committee Member

Daniel Proga, Ph.D.
Examination Committee Member

Amei Amei, Ph.D.
Graduate College Faculty Representative

Alyssa Crittenden, Ph.D.
Vice Provost for Graduate Education & Dean of the Graduate College

ABSTRACT

Protoplanetary disks are birthplaces of planets. The past decade witnessed a great advancement in disk observations by Atacama Large Millimeter Array (ALMA) and extreme adaptive optics (ExAOs). Hundreds of disks have been observed at high angular resolutions and revealed rich substructures (e.g., gaps/rings) at midplane and atmosphere, at least part of which are perturbed by planets. Deep understanding of disk physics has a great potential to unveil more young planets from substructures and distinguish those that are not caused by planets. I worked on constraining young planet populations using planet-disk interaction simulations and substructures and self-consistent treatment of thermal structures of protoplanetary disks. I developed the tool to infer planet mass by fitting the relationship between the gap width, planet mass, disk viscosity, grain size, and gas surface density using planet-disk interactions simulations. Then I used substructures found in DSHARP (Disk Substructures at High Angular Resolution Project) to infer a population of young planets at 10-100 au with 10-100 Earth masses, which is at a different regime from detected mature exoplanets. To improve the tool, I used an additional set of simulations to demonstrate the effectiveness of deep learning in obtaining planet and disk properties. To improve the statistics, I subsequently used a more uniformly selected Taurus sample to infer the planet occurrence rates considering selection and detection biases. However, these results are based on isothermal simulations commonly adopted in the field. Dust and thermal structures in disks can affect these interpretations. By changing the disk cooling rate, I found a certain regime that planet-launched spirals can be damped, leading to narrower and shallower gaps. Focusing on the rings, I showed

that the concentration of large grains at the ring can lead to a drop of temperature, which changes the shape of the ring and may even lead to more rings. Radiation hydrodynamic simulations can capture the thermal structure in a time-dependent manner, improving self-consistency. I used rad-hydro to study a hydrodynamic instability, vertical shear instability (VSI) that operates in the outer disk. VSI can lead to kinematic and morphological substructures that can be misinterpreted as planet origin. I found that when considering realistic temperatures, the kinematics change significantly compared to previous isothermal simulations, resulting in entirely different observational signatures. The cool midplane becomes quiescent whereas the atmosphere becomes turbulent. The classical radially narrow, vertically extended circulation pattern disappears and becomes more isotropic turbulence. These are consistent with existing ALMA observations and can be tested for the ongoing ALMA large program exoALMA. Zonal flows and substructures can develop depending on the disk inner cavity size. A strong shear flow occurs at the boundary between the cool midplane and superheated atmosphere, leading to layered accretion.

ACKNOWLEDGEMENTS

I owe the completion of this dissertation to the invaluable support of numerous individuals.

First and foremost, I extend my deepest gratitude to my advisor, Zhaohuan Zhu, whose unwavering support has been the bedrock of my PhD journey. His boundless enthusiasm for science and wealth of ideas have been constant wellsprings of inspiration. Zhaohuan's ability to unravel complex subjects in a clear and intuitive manner has been truly invaluable. Moreover, he adeptly guided me in using state-of-the-art simulations to complement cutting-edge observations. Despite our institution's lesser-known status, his global network of connections significantly enriched my academic and professional development.

I also want to express my heartfelt appreciation to Lee Hartmann and Nuria Calvet for their pivotal role in bringing me to Las Vegas and their enduring support throughout my academic and personal pursuits.

My sincere thanks extend to my collaborators (listed in the following chapters), whose dedication and insights have greatly enriched my work. Special gratitude is owed to the DSHARP team, lead by Sean Andrews, for setting a high standard and providing a strong foundation for my PhD journey. Additionally, I am indebted to Akimasa Kataoka and Takahiro Ueda for their invaluable guidance on ALMA dust polarization, especially during challenging times. A special acknowledgment is reserved for Yan-Fei Jiang, whose powerful radiation hydro code was indispensable in realizing the culmination of my dissertation. His remarkable responsiveness, deep understanding, and concise solutions were invaluable assets throughout.

My deepest gratitude also goes to my friends and colleagues in Las Vegas and around the world, whose support has enriched both my academic and personal life. I am particularly thankful to those who were part of the small astro group at UNLV when I just arrived. I want to thank Chao-Chin Yang, who always helped me solve detailed problems that puzzled me for a long time. He even extended beyond research to various aspects of daily life, including the daunting task of finding an apartment. I also wish to thank Charlie Abod, Shunke Ai, Hans Baehr, Chen Cheng, Xiao Hu, Chenliang Huang, Min Li, Jiawei Luo, Ian Rabago, David Rice, Jeremey Smallwood, and others who make the department active and meaningful.

I want to thank faculty members at UNLV, my committee members Rebecca Martin, Daniel Proga, Amei Amei, and previous committee member Shichun Huang for their care about my project. I also want to thank Bing Zhang for always being there and asking constructive questions during my preparation talks. I thank Mingon Kang for his encouragement to turn the machine learning class project he taught into a publication.

In the challenging year of the pandemic, I spent an entire year in Beijing. I am grateful to Xiaofeng Wang, Ziping Zhang, and Xin Li for generously providing me with a desk at Beijing Planetarium. Additionally, I extend my thanks to Xue-Ning Bai, Chris Ormel, and Pinghui Huang for hosting me at Tsinghua University, enabling scientific discussions despite being on the other side of the Pacific.

Finally, but most importantly, I dedicate this dissertation to my family. I thank my parents, Lin Gu and Qing Zhang, for instilling in me a love for science since childhood. When I was a child, stargazing together with them shaped my journey and fueled my passion for exploration. To my wife, Muze Huang, who has always stood by me, supporting me through every endeavor. Together, we've explored what the desert has to offer and embraced the wonders of nature. And to

our expecting baby, whose arrival fills us with anticipation and joy, this dissertation is a testament to the love and dedication of our family.

TABLE OF CONTENTS

LIST OF TABLES

LIST OF FIGURES

CHAPTER 1 Introduction

Over the past few decades, the discovery of more than five thousand planets orbiting other stars (exoplanets) has offered new perspectives on our place in the universe. Many of these exoplanets are exotic, possessing different masses, orbits, and compositions compared to our Solar System planets. This plethora of planetary diversity raises fundamental questions in astronomy and planetary science: How do planets form and evolve? Is our solar system unique? To address these questions, a direct approach is to search for young planets in their formation sites – protoplanetary disks.

Stars and planets form almost simultaneously. Perturbations in dense molecular clouds lead to instability and collapse, resulting in the formation of protostars. Due to the conservation of angular momentum, not all material falls onto the star; instead, a disk forms around the protostar. For the first 0.1 to 1 million years, the protoplanetary disk is surrounded by an envelope, where material accretes onto the disk. Since stars form in clusters along filamentary structures, disks can also interact with each other. On the other hand, the disk launches winds and jets that push away the envelope. When the disk mass exceeds that of the envelope, the disk enters the Class II phase, making it easier to observe. Throughout this evolutionary track, stars move away from each other so that disk interactions become less frequent. Meanwhile, infall from the envelope diminishes, making the disk more isolated, even though late infall and radiation from massive stars remain influential in disk evolution (Ginski et al. 2021). At this stage, the disk can persist longer, typically from 1 to 10 million years, while material continues to accrete onto the star and planets, asteroids,

and comets form within the disk, hence its designation as a protoplanetary disk. Eventually, the gaseous disk dissipates, forming debris disks analogous to our Solar System's asteroid belt and Kuiper Belt. Understanding when and how planets form in protoplanetary disks can elucidate the diversity observed in exoplanetary systems and provide insights into the formation process of our own solar system. Understanding how dust and gas transport in the disk will help us comprehend how materials, including water, are transported within the disk and ultimately delivered to Earth.

1.1 Observational Background

The past decade witnessed advancements in disk observations by ALMA (The Atacama Large Millimeter/submillimeter Array) and ExAOs (Extreme Adaptive Optics). Recent efforts have allowed us to see details in each of the disk evolution phases, even at the early Class 0/I stages, thanks to programs such as the ALMA eDisk (Ohashi et al. 2023). Nevertheless, we still accumulate the most information at the Class II disk phase, where the envelopes have dissipated and the disk becomes more optically thin so that we can almost see through the midplane (Bae et al. 2023).

At this stage, hundreds of disks have been observed at high angular resolutions and revealed rich substructures (e.g., gaps/rings) at multiple layers (Bae et al. 2023; Pinte et al. 2023; Benisty et al. 2023). ALMA dust continuum probes the planet-forming midplane, sensitive to mm-sized particles. ALMA molecular lines probe disk upper layers, where 3D disk kinematics are unraveled from channel maps (Pinte et al. 2023). Since molecular lines are observed at different velocity channels (or frequencies), substructures are not only observed in the continuum or frequency integrated images, but also velocity maps. The most powerful tracers are various CO isotopologues, which trace multiple disk τ= 1 depending on the abundance. While different line tracers are sen-

sitive to the local or global physical and chemical condition, they provide tight constraint on disk physical and chemical condition (Öberg et al. 2023). Near infrared scattered light images reveal the disk scattering surface probing smaller micron-sized particles (Benisty et al. 2023). Additionally, near-IR scattered light and ALMA dust polarization observations provide insight on dust properties (e.g., Kataoka et al. 2015; Tazaki et al. 2023).

These substructures can be loosely divided into several categories (Figure 1.1). They are **rings/cavity** ("transition" disk with bright ring, depleted cavity), **rings/gaps** (concentric, axisymmetric pattern of enhancing and depleting intensity), **arcs** (non-axisymmetric substructure, a partial ring extends only a certain azimuthal angle) and **spirals** (ranging from m=2 to asymmetrical spirals). Individual disks can also have features with multiple morphological types (e.g., rings&spirals in IM Lup, Elias 27, and rings&arc in HD 143006). The morphological types between mm dust continuum and scattered-light observations can also be different (e.g., HD 135344B, rings&arc in dust continuum and spirals in scattered-light image) (Andrews 2020; Bae et al. 2023).

Some of these substructures must be due to planetary perturbations, supported by recent discoveries of young planets PDS 70b/c (Keppler et al. 2018a; Haffert et al. 2019a; Isella et al. 2019a). However, detecting embedded planets in disks is still challenging. Deeper understanding of disk physics holds great potential to unveil more young planets from substructures and distinguish non-planetary origins even with current technology.

1.2 Theoretical Background

The theory of planet-disk interaction, proposed by Lin & Papaloizou (1979) and Goldreich & Tremaine (1980), predates the observation of substructures. In this framework, a planet or any

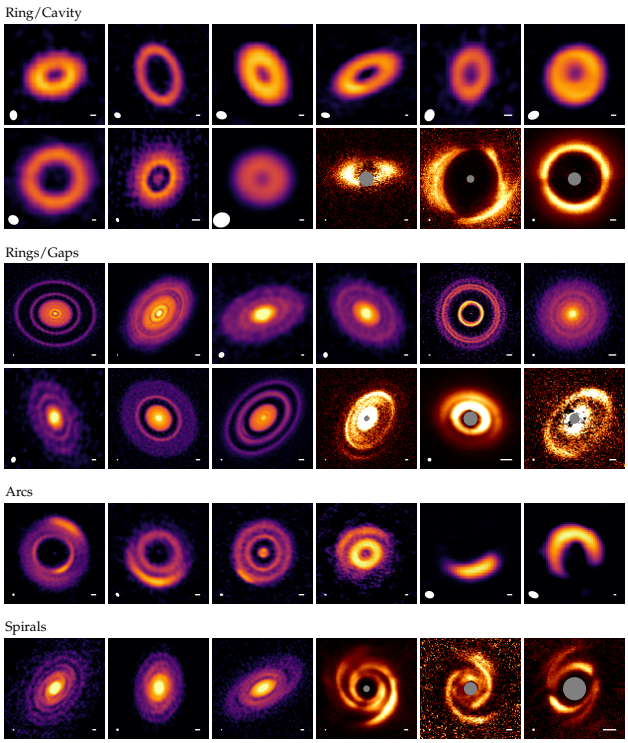

Figure 1.1: A gallery of disk substructure morphologies; the color maps for mm continuum are purplish and infrared scattered light are yellowish (see Figure 11 in Andrews 2020 and references therein).

perturber within a rotating disk can induce spirals, exerting torque on the disk. As the spiral wave steepens into a shock, a gap may form (Rafikov 2002), trapping dust particles at the gap edge and leading to substructures in the dust continuum (Pinilla et al. 2012; Zhu et al. 2011). So far, planets have been successfully invoked to explain nearly all observed substructures. These substructures can be attributed to populations of protoplanets (Zhang et al. 2018b; **?**), with localized perturbations in kinematics providing strong evidence for the formation of giant planets (Teague et al. 2018c; Pinte et al. 2018a). Substructures in scattered light images may also originate from young planets (Asensio-Torres et al. 2021; Benisty et al. 2023). However, direct detection of young planets remains rare, partly due to detection limits.

On the other hand, more than 20 mechanisms other than planets could potentially lead to substructures. This non-exhaustive list includes disk dispersal via MHD-driven winds (Takahashi & Muto 2018) or photoevaporative flows (Ercolano & Pascucci 2017), zonal flows in MHD disks (Johansen et al. 2009a), mass pileup at the boundary between magnetically active and dead zones (Flock et al. 2015), spontaneous ring formation due to reduced accretion by concentrated dust (Dullemond & Penzlin 2018; Hu et al. 2019), and condensation fronts at icelines (Zhang et al. 2015a). Advancements in understanding the physics of disks and the development of these theories with robust observational predictive power are essential for competing with the planet scenario. Ultimately, such advancements will enable us to determine with more certainty whether a specific substructure is due to a planet or an alternative mechanism.

To that end, a natural first step is to treat disk thermal structure self-consistently. In the outer region of protoplanetary disk, the heating comes from the central star and the cooling comes from the dust radiative cooling. In a classical picture, stellar irradiation, which peaks at optical to UV wavelengths, is optically thick to the disk and primarily heats the disk's surface (referred to as the

$\tau_* = 1$ surface). Then the reprocessed photons at longer wavelengths can penetrate deeper and heat up the midplane, since the opacity is lower at longer wavelengths. This stellar-irradiated or passive disk model results in a superheated upper layer and cooler midplane (Chiang & Goldreich 1997), corroborated by recent ALMA observations (Law et al. 2022; 2023; 2024). However, most current simulations assume a constant vertical temperature. This simplification might be justifiable for modeling midplane thin dust layers for ALMA observations, but fails for kinematic and scattered light data probing higher layers. Temperature differences can alter instabilities (Zhang et al., in review) and planet-induced kinematics (Bollati et al. 2021).

Another common assumption in disk hydrodynamic simulations is locally isothermal equation of state, meaning that the disk temperature is preset at any given location and does not evolve with time. In reality, the gas can heat and cool in the disk. The cooling time can vary drastically from inner disk to the outer disk and from midplane to the atmosphere (Hubeny 1990). A simple but efficient way to simulate the finite cooling time is the prescription of orbital cooling or beta cooling (Gammie 2001). The method relaxes the energy of the gas to a background state by an amount proportional to the prescribed timescale at every time-step. Considering the finite cooling time, the planet-launched spiral can dampen depending on local cooling time, resulting in a narrower and shallower gap (Miranda & Rafikov 2020b; Zhang & Zhu 2020). Various hydrodynamic instabilities are also sensitive to the cooling time (Lesur et al. 2022).

Therefore, to disambiguate the origins of substructures, pinpoint planet locations, and constrain planet masses, a comprehensive understanding of disk thermodynamics is essential. As the spiral arm propagates to a higher altitude with a higher temperature, it will have a wider opening angle. The spirals that are due to buoyancy resonance are also highly dependent on thermodynamics (Bae et al. 2021). The complex 3D geometry often leads to shadowing, which changes heating and

cooling rates. The accreting planet can also cast shadows, affecting the dynamics by changing the pressure gradient (Montesinos et al. 2021). The gap can have different temperatures, affecting dynamics (Zhang et al. 2021b). These phenomenon are difficult to capture in simulations with preset temperature and cooling structures. Thus, the full coupling between the radiation transport and hydrodynamics becomes necessary.

Seminal radiation hydrodynamic (rad-hydro) studies with self-consistent thermal structures (without planets: e.g., Flock et al. 2020; with planets: e.g., Szulágyi et al. 2022) improved our understanding but had limitations. The radiation transport method they adopted (flux-limited diffusion, or FLD) is valid only in optically thick regions, and cannot capture shadowing and beam crossing. In protoplanetary disks, both optically thin and thick regions coexist, with beam crossing and shadowing. Additionally, small vertical extents adopted in past work (e.g., Flock et al. 2020) lead to conclusions similar to pure-hydro simulations. It is time to overcome these shortcomings with the help of the state-of-the-art Athena++ (Stone et al. 2020) implicit radiation module (Jiang 2022), which incorporates angle-dependent radiative transfer equations to model the radiation transport. It can capture both optically thin and thick regimes and treat shadowing and beam crossing accurately.

In the following chapters, I begin with simple locally isothermal disk models and progressively incorporate more realistic physics in subsequent chapters. In Chapters 2 and 3 I use planet-disk interaction simulations to match substructures identified in high angular resolution ALMA observations to infer young planet populations. In Chapter 4, I introduce a machine learning technique aimed at inferring planet mass and disk properties. Chapter 5 explores the effects of disk self-gravity and cooling on gap formation induced by planets. Chapter 6 focuses on the self-consistent modeling of the thermal structure of rings within protoplanetary disks. Chapter 7 investigates the

impact of considering dust grain porosity on the inference of disk and dust properties from ALMA continuum and polarization observations. Finally, Chapter 8 employs radiation-hydrodynamic simulations to examine stellar irradiated disks and predict observational signatures concerning disk kinematics and morphology.

CHAPTER 2 The Disk Substructures at High Angular Resolution Project (DSHARP): VII. The Planet-Disk Interactions Interpretation

Shangjia Zhang,[1] Zhaohuan Zhu ,[2] Jane Huang,[3] Viviana V. Guzmán,[4,5] Sean M. Andrews,[3] Tilman Birnstiel,[6] Cornelis P. Dullemond,[7] John M. Carpenter,[4] Andrea Isella,[8] Laura M. Pérez,[9] Myriam Benisty,[10,11] David J. Wilner,[3] Clément Baruteau,[12] Xue-Ning Bai,[13] and Luca Ricci[14]

[1]Department of Physics and Astronomy, University of Nevada, Las Vegas, 4505 S. Maryland Pkwy, Las Vegas, NV, 89154, USA

[2]Department of Physics and Astronomy, University of Nevada, Las Vegas, 4505 S. Maryland Pkwy, Las Vegas, NV, 89154, USA

[3]Harvard-Smithsonian Center for Astrophysics, 60 Garden Street, Cambridge, MA 02138, USA

[4]Joint ALMA Observatory, Avenida Alonso de Córdova 3107, Vitacura, Santiago, Chile

[5]Instituto de Astrofísica, Pontificia Universidad Católica de Chile, Av. Vicuña Mackenna 4860, 7820436 Macul, Santiago, Chile

[6]University Observatory, Faculty of Physics, Ludwig-Maximilians-Universität München, Scheinerstr. 1, 81679 Munich, Germany

[7]Zentrum für Astronomie, Heidelberg University, Albert Ueberle Str. 2, 69120 Heidelberg, Germany

[8]Department of Physics and Astronomy, Rice University, 6100 Main Street, Houston, TX 77005, USA

[9]Departamento de Astronomía, Universidad de Chile, Camino El Observatorio 1515, Las Condes, Santiago, Chile

[10]Unidad Mixta Internacional Franco-Chilena de Astronomía (CNRS, UMI 3386), Departamento de Astronomía, Universidad de Chile, Camino El Observatorio 1515, Las Condes, Santiago, Chile

[11]Univ. Grenoble Alpes, CNRS, IPAG, 38000 Grenoble, France

[12]CNRS / Institut de Recherche en Astrophysique et Planétologie, 14 avenue Edouard Belin, 31400 Toulouse, France

[13]Institute for Advanced Study and Tsinghua Center for Astrophysics, Tsinghua University, Beijing 100084, China

[14]Department of Physics and Astronomy, California State University Northridge, 18111 Nordhoff Street, Northridge, CA 91130, USA

2.1 Abstract

The Disk Substructures at High Angular Resolution Project (DSHARP) provides a large sample of protoplanetary disks having substructures which could be induced by young forming planets. To explore the properties of planets that may be responsible for these substructures, we systematically carry out a grid of 2-D hydrodynamical simulations including both gas and dust components. We present the resulting gas structures, including the relationship between the planet mass and 1) the gaseous gap depth/width, and 2) the sub/super-Keplerian motion across the gap. We then compute dust continuum intensity maps at the frequency of the DSHARP observations. We provide the relationship between the planet mass and 1) the depth/width of the gaps at millimeter intensity maps, 2) the gap edge ellipticity and asymmetry, and 3) the position of secondary gaps induced by

the planet. With these relationships, we lay out the procedure to constrain the planet mass using gap properties, and study the potential planets in the DSHARP disks. We highlight the excellent agreement between observations and simulations for AS 209 and the detectability of the young Solar System analog. Finally, under the assumption that the detected gaps are induced by young planets, we characterize the young planet population in the planet mass-semimajor axis diagram. We find that the occurrence rate for $> 5\,M_J$ planets beyond 5-10 au is consistent with direct imaging constraints. Disk substructures allow us probe a wide-orbit planet population (Neptune to Jupiter mass planets beyond 10 au) that is not accessible to other planet searching techniques.

2.2 Introduction

Discoveries over the past few decades show that planets are common. The demographics of exoplanets have put constraints on planet formation theory (e.g. review by Johansen et al. 2014; Raymond et al. 2014; Chabrier et al. 2014). Unfortunately, most discovered exoplanets are billions of years old and have therefore been subject to significant orbital dynamical alteration after their formation (e.g., review by Davies et al. 2014). To test planet formation theory, it is crucial to constrain the young planet population right after they are born in protoplanetary disks. However, the planet search techniques that have discovered thousands of exoplanets around mature stars are not efficient at finding planets around young stars ($<$10 Myrs old) mainly due to their stellar variablity and the presence of the protoplanetary disks. Fewer than 10 young planet candidates in systems $<$10 Myrs have been detected so far (e.g. CI Tau b, Johns-Krull et al. 2016; V 830 Tau b, Donati et al. 2016; Tap 26 b, Yu et al. 2017; PDS 70 b, Keppler et al. 2018a; LkCa 15 b, Sallum et al. 2015).

On the other hand, recent high resolution imaging at near-IR wavelengths (with the new adaptive optics systems on 10-meter class telescopes) and interferometry at radio wavelengths (especially the ALMA and the VLA) can directly probe the protoplanetary disks down to au-scales, and a variety of disk features (such as gaps, rings, spirals, and large-scale asymmetries) have been revealed (e.g.Casassus et al. 2013; van der Marel et al. 2013; ALMA Partnership et al. 2015a; Andrews et al. 2016a; Garufi et al. 2017). Despite that there are other possibilities for producing these features, they may be induced by young planets in these disks, and we can use these features to probe the unseen young planet population.

Planet-disk interactions have been studied over the past three decades with both analytical approaches (Goldreich & Tremaine 1980; Tanaka et al. 2002) and numerical simulations (Kley & Nelson 2012; Baruteau et al. 2014). While the earlier work focused on planet migration and gap opening, more recently efforts have been dedicated to studying observable disk features induced by planets (Wolf & D'Angelo 2005; Dodson-Robinson & Salyk 2011; Zhu et al. 2011; Gonzalez et al. 2012; Pinilla et al. 2012; Ataiee et al. 2013; Bae et al. 2016; Kanagawa et al. 2016a; Rosotti et al. 2016a; Isella & Turner 2018), including the observational signatures in near-IR scattered light images (e.g. Dong et al. 2015a; Zhu et al. 2015a; Fung & Dong 2015), (sub-)mm dust thermal continuum images (Dipierro et al. 2015a; Picogna & Kley 2015; Dong & Fung 2017; Dong et al. 2018a), and (sub-)mm molecular line channel maps that trace the gas kinematics at the gap edges or around the planet (Perez et al. 2015a; Pinte et al. 2018b; Teague et al. 2018a).

Among all these indirect methods for probing young planets at various wavelengths, only dust thermal emission at (sub-)mm wavelengths allows us to probe low mass planets, since a small change in the gas surface density due to the low mass planet can cause dramatic changes in the dust surface density (Paardekooper & Mellema 2006; Zhu et al. 2014a). However, this also means

that hydrodynamical simulations with both gas and dust components are needed to study the expected disk features at (sub-)mm wavelengths. Such simulations are more complicated due to the uncertainties about the dust size distribution in protoplanetary disks. Previously, hydrodynamical simulations have been carried out to explain features in individual sources (e.g. Jin et al. 2016; Dipierro et al. 2018; Fedele et al. 2018). With many disk features revealed by DSHARP (Andrews et al. 2018a), a systematic study of how the dust features relate to the planet properties is desirable. By conducting an extensive series of disk models spanning a substantial range in disk and planet properties, we can enable a broad exploration of parameter space which can then be used to rapidly infer young planet populations from the observations, and we will also be more confident that we are not missing possible parameter space for each potential planet.

In this work, we carry out a grid of hydrodynamical simulations including both gas and dust components. Then, assuming different dust size distributions, we generate intensity maps at the observation wavelength of DSHARP. In §5.4, we describe our methods. The results are presented in §8.4. The derived young planet properties for the DSHARP disks are given in §2.5. After a short discussion in §8.5, we conclude the paper in §7.8.

2.3 Method

We carry out 2-D hydrodynamical planet-disk simulations using the modified version of the grid-based code FARGO (Masset 2000) called Dusty FARGO-ADSG (Baruteau & Masset 2008a;b; Baruteau & Zhu 2016). The gas component is simulated using finite difference methods (Stone & Norman 1992), while the dust component is modelled as Lagrangian particles. To allow our simulations to be as scale-free as possible, we do not include disk self-gravity, radiative cooling,

or dust feedback. These simplifications are sui for most disks observed in DSHARP. Most of the features in these disks lie beyond 10 au where the irradiation from the central star dominates the disk heating such that the disk is nearly vertically isothermal close to the midplane (D'Alessio et al. 1998). Although the dust dynamical feedback to the gas is important when a significant amount of dust accumulates at gap edges or within vortices (Fu et al. 2014; Crnkovic-Rubsamen et al. 2015), simulations that have dust particles but do not include dust feedback to the gas (so-called "passive dust" models) serve as reference models and allow us to scale our simulations freely to disks with different dust-to-gas mass ratios and dust size distributions. As shown in §2.5, passive dust models are also adequate in most of our cases (especially when the dust couples with the gas relatively well). Simulations with dust feedback will be presented in Yang & Zhu (2018).

2.3.1 Setup: Gas and Dust

We adopt polar coordinates (r, θ) centered on the star and fix the planet on a circular orbit at $r = 1$. Since the star is wobbling around the center of mass due to the perturbation by the planet, indirect forces are applied to this non-inertial coordinate frame.

We initialize the gas surface density as

$$\Sigma_g(r) = \Sigma_{g,0}(r/r_0)^{-1}\,, \tag{2.1}$$

where r_0 is also the position of the planet and we set $r_0 = r_p = 1$. For studying gaps of individual sources in §2.5, we scale $\Sigma_{g,0}$ to be consistent with the DSHARP observations. We assume locally isothermal equation of state, and the temperature at radius r follows $T(r) = T_0(r/r_0)^{-1/2}$. T is related to the disk scale height h as $h/r = c_s/v_\phi$ where $c_s^2 = RT/\mu = P/\Sigma$ and $\mu = 2.35$. With our

setup, h/r changes as $r^{1/4}$. In the rest of the text, when we give a value of h/r, we are referring to h/r at r_0.

Our numerical grid extends from 0.1 r_0 to 10 r_0 in the radial direction and 0 to 2π in the θ direction. For low viscosity cases (α = 10^{-4} and 10^{-3}), there are 750 grid points in the radial direction and 1024 grid points in the θ direction. This is equivalent to 16 grid points per scale height at r_0 if $h/r = 0.1$. For high viscosity cases (α=0.01), less resolution is needed so there are 375 and 512 grid points in the radial and θ direction. For simulations to fit AS 209 in §2.5.1, the resolution is 1500 and 2048 grid points in the radial and θ direction to capture additional gaps at the inner disk. We use the evanescent boundary condition, which relaxes the fluid variables to the initial state at $r < 0.12 r_0$ and $r > 8 r_0$. A smoothing length of 0.6 disk scale height at r_0 is used to smooth the planet's potential (Müller et al. 2012).

We assume that the dust surface density is 1/100 of the gas surface density initially. The open boundary condition is applied for dust particles, so that the dust-to-gas mass ratio for the whole disk can change with time.

The dust particles experience both gravitational forces and aerodynamic drag forces. The particles are pushed at every timestep with the orbital integrator. When the particle's stopping time is smaller than the numerical timestep, we use the short friction time approximation to push the particle. Since we are interested in disk regions beyond 10s of au, the disk density is low enough that the molecular mean-free path is larger than the size of dust particles. In this case, the drag force experienced by the particles is in the Epstein regime. The Stokes number *St* for particles

(also called particles' dimensionless stopping time) is

$$St = t_{stop}\Omega = \frac{\pi s \rho_p}{2\Sigma_{gas}} = 1.57 \times 10^{-3} \frac{\rho_p}{1\mathrm{g\,cm^{-3}}} \frac{s}{1\mathrm{mm}} \frac{100\mathrm{g\,cm^{-2}}}{\Sigma_g}. \quad (2.2)$$

where ρ_p is the density of the dust particle, s is the radius of the dust particle, and Σ_g is the gas surface density. We assume ρ_p=1 g cm^{-3} in our simulations. We use 200,000 and 100,000 particles for high and low resolution runs, respectively. Each particle is a super particle representing a group of real dust particles having the same size. The super particles in our simulations have Stokes numbers ranging from 1.57×10^{-5} to 1.57, or physical radii ranging from 1 μm to 10 cm if $\Sigma_{g,0}$=10 g cm^{-2} and $\rho_p = 1\mathrm{g\,cm^{-3}}$. We distribute super particles uniformly in $log(s)$ space, which means that we have the same number of super particles per decade in size. Since dust-to-gas back reaction is not included, we can scale the dust size distribution in our simulations to any desired distribution.

During the simulation, we keep the size of the super-particle the same no matter where it drifts to. Thus, the super-particle's Stokes number changes when this particle drifts in the disk, because the particle's Stokes number also depends on the local disk surface density (Equation 6.13). More specifically, during the simulation, the Stokes number of the every particle varies as being inverse proportional to the local gas surface density.

Turbulent diffusion for dust particles is included as random kicks to the particles (Charnoz et al. 2011; Fuente et al. 2017). The diffusion coefficient is related to the α parameter as in Youdin & Lithwick (2007) through the so-called Schmidt number Sc. In this work, Sc is defined as the ratio between the angular momentum transport coefficient (ν) and the gas diffusion coefficient (D_g). We set $Sc = 1$ which serves as a good first order approximation, although that Sc can take on different

values and its value can differ between the radial and vertical directions (Zhu et al. 2015b; Yang et al. 2018),

2.3.2 Grid of Models

To explore the full parameter space, we choose three values for $(h/r)_{r_0}$ $(0.05, 0.07, 0.1)$, five values for the planet-star mass ratio (q$\equiv M_p/M_*$ = 3.3×10^{-5}, 10^{-4}, 3.3×10^{-4}, 10^{-3}, 3.3×10^{-3} M_*, or roughly M_p = 11 $M_\oplus$, 33 $M_\oplus$, 0.35 M_J, 1 M_J, 3.5 M_J if $M_* = M_\odot$), and three values for the disk turbulent viscosity coefficient ($\alpha = 0.01, 0.001, 0.0001$). Thus, we have 45 simulations in total. We label each simulation in the following manner: `h5am3p1` means h/r=0.05, $\alpha = 10^{-3}$ (`m3` in `h5am3p1` means minus 3), $M_p/M_* = 3.3 \times 10^{-5} M_*$ (`p1` refers to the lowest planet mass case). We also run some additional simulations for individual sources (e.g. AS 209, Elias 24) which will be presented in §2.5.1 and Guzmán et al. (2018).

This parameter space represents typical disk conditions. Protoplanetary disks normally have h/r between 0.05 and 0.1 at $r > 10$ au (D'Alessio et al. 1998). While a moderate $\alpha \sim 10^{-2}$ is preferred to explain the disk accretion (Hartmann et al. 1998), recent works suggest that a low turbulence level ($\alpha < 10^{-2}$) is needed to explain molecular line widths in TW Hya (Flaherty et al. 2018a) and dust settling in HL Tau (Pinte et al. 2016a). When α is smaller than 10^{-4}, the viscous timescale over the disk scale height at the planet position (H_p^2/ν) is longer than $10^4/\Omega_p$ or 1.6 million years at 100 au, so that the viscosity will not affect the disk evolution significantly. In §2.5.1, we carry out several simulations with different α values to extend the parameter space for some sources in the DSHARP sample. As shown below, when the planet mass is less than 11 $M_\oplus$, the disk features are not detectable with ALMA. When the planet mass is larger than 3.5 M_J, the

disk features have strong asymmetries, and we should be able to detect the planet directly though direct imaging techniques.

We run the simulations for 1000 planetary orbits (1000 T_p), which is equivalent to 1 Myr for a planet at 100 au or 0.1 Myr for a planet at 20 au. These timescales are comparable to the disk ages of the DSHARP sources.

2.3.3 Calculating mm Continuum Intensity Maps

For each simulation, we calculate the mm continuum intensity maps assuming different disk surface densities and dust size distributions. Since dust-to-gas feedback is neglected, we can freely scale the initial disk surface density and dust size distribution in simulations to match realistic disks.

Both the disk surface density and dust size distribution have large impacts on the mm intensity maps. If the dust thermal continuum is mainly from micron sized particles and the disk surface density is high, these dust particles have small Stokes numbers (Equation 6.13). Consequently, they couple to the gas almost perfectly and the gaps revealed in mm are very similar to the gaps in the gas. If the mm emission is dominated by mm sized particles and the disk surface density is low, the dust particles can have Stokes numbers close to 1 and they drift very fast in the disk. In this case, they can be trapped at the gap edges, producing deep and wide gaps. To explore how different dust size distributions can affect the mm intensity maps, we choose two very different dust size distributions to generate intensity maps. For the distribution referred to as DSD1, we assume $n(s) \propto s^{-3.5}$ with a maximum grain size of 0.1 mm in the initial condition ($p = -3.5$ and s_{max}=0.1 mm. This is motivated by recent (sub-)mm polarization measurements (Kataoka et al.

2017; Hull et al. 2018a), which indicate that the maximum grain size in a variety of disks is around 0.1 mm. In the other case referred to as DSD2, we assume $n(s) \propto s^{-2.5}$ with the maximum grain size of 1 cm ($p = -2.5$ and s_{max}=1 cm). This shallower dust size distribution is expected from dust growth models (Birnstiel et al. 2012) and consistent with SED constraints (D'Alessio et al. 2001) and the spectral index at mm/cm wavelengths (Ricci et al. 2010b;a; Pérez et al. 2015). Both cases assume a minimum grain size of 0.005 μm. We find that the minimum grain size has no effect on the dust intensity maps since most dust mass is in larger particles. Coincidentally, these two size distributions lead to the same opacity at 1.27 mm (1.27 mm is the closest wavelength to 1.25 mm in the table of Birnstiel et al. 2018) in the initial condition (the absorption opacity for the s_{max} =0.1 mm case is 0.43 $\mathrm{cm^2\,g^{-1}}$, while for the s_{max} =1 cm case it is 0.46 $\mathrm{cm^2\,g^{-1}}$ based on Birnstiel et al. 2018). More discussion on how to generalize our results to disks with other dust size distributions can be found in §2.4.2.

For each simulation, we scale the simulation to different disk surface densities. Then for each surface density, we calculate the 1.27 mm intensity maps using DSD1 or DSD2 dust size distributions. For the $s_{max} = 0.1$ mm dust size distribution (DSD1), we calculate the 1.27 mm intensity maps for disks with $\Sigma_{g,0}$ = 0.1 $\mathrm{g\,cm^{-2}}$, 0.3 $\mathrm{g\,cm^{-2}}$, 1 $\mathrm{g\,cm^{-2}}$, 3 $\mathrm{g\,cm^{-2}}$, 10 $\mathrm{g\,cm^{-2}}$, 30 $\mathrm{g\,cm^{-2}}$, and 100 $\mathrm{g\,cm^{-2}}$ (seven groups of models). The maximum-size particle in these disks (0.1 mm), which dominates the total dust mass, corresponds to St= 1.57×10^{-1}, 5.23×10^{-2}, 1.57×10^{-2}, 5.23×10^{-3}, 1.57×10^{-3}, 5.23×10^{-4}, and 1.57×10^{-4} at $r = r_p$. For the s_{max} =1 cm cases (DSD2), we vary $\Sigma_{g,0}$ as 1 $\mathrm{g\,cm^{-2}}$, 3 $\mathrm{g\,cm^{-2}}$, 10 $\mathrm{g\,cm^{-2}}$, 30 $\mathrm{g\,cm^{-2}}$, and 100 $\mathrm{g\,cm^{-2}}$ (five groups of models), and the corresponding St for 1 cm particles at $r = r_p$ is 1.57, 5.23×10^{-1}, 1.57×10^{-1}, 5.23×10^{-2}, and 1.57×10^{-2}. For each given surface density above, we only select particles with Stokes numbers smaller than the corresponding St in our simulations and use the distribution of these particles

to calculate the 1.27 mm intensity maps. For the s_{max} =1 cm dust distribution (DSD2), we do not have $\Sigma_{g,0}$ = 0.1 g cm^{-2}, 0.3 g cm^{-2} cases since 1 cm particles in these disks have Stokes numbers larger than the largest Stokes number (1.57) in our simulations.

Here, we lay out the detailed steps to scale each simulation to the disks that have surface densities of $\Sigma_{g,0}$ listed above, and then calculate the mm intensity maps for these disks.

1) First, given a $\Sigma_{g,0}$, we find the relationship between the particle size in this disk and the Stokes number of super-particles in simulations. For each particle in the simulation, we use its Stokes number in the initial condition to calculate the corresponding particle size s (Equation 6.13 with known Σ_g). The Stokes number of test particles at $r = r_p$ in the initial condition ranges from St_{min} = 1.57 $\times$ 10^{-5} to St_{max} = 1.57, or in terms of grain size, $s_{min}^{code} = St_{min} \times 2\Sigma_{gas}/(\pi\rho_p)$ and $s_{max}^{code} = St_{max} \times 2\Sigma_{gas}/(\pi\rho_p)$ from Equation 6.13. For instance, a 1 μm particle in a disk with Σ_g = 10 g cm^{-2} at the planet position corresponds to the particle with St = 1.57 $\times$ 10^{-5} at $r = r_p$ in the initial setup of the simulation. For dust grains with $St < St_{min}$ = 1.57 $\times$ 10^{-5}, we use the gas surface density $\Sigma_g(r, \theta)$ in our simulations to represent the dust, assuming small dust grains are well coupled with the gas.

2) Then, with a given $\Sigma_{g,0}$, we use the assumed particle size distributions (DSD1 and DSD2) in the initial condition to calculate the mass weight for each super-particle in the simulation. Note that during the simulation, the resulting dust size distribution at each radius is different from the initial dust size distribution since particles drift in the disk. As mentioned above, we divide the dust component in the disk into two parts: (a) the small dust particles ($s < s_{min}^{code}$) represented by the gas component in the simulation and (b) large dust particles ($s \geq s_{min}^{code}$) represented by the super-particles in the simulation. We calculate the initial mass fractions of the dust contributed by

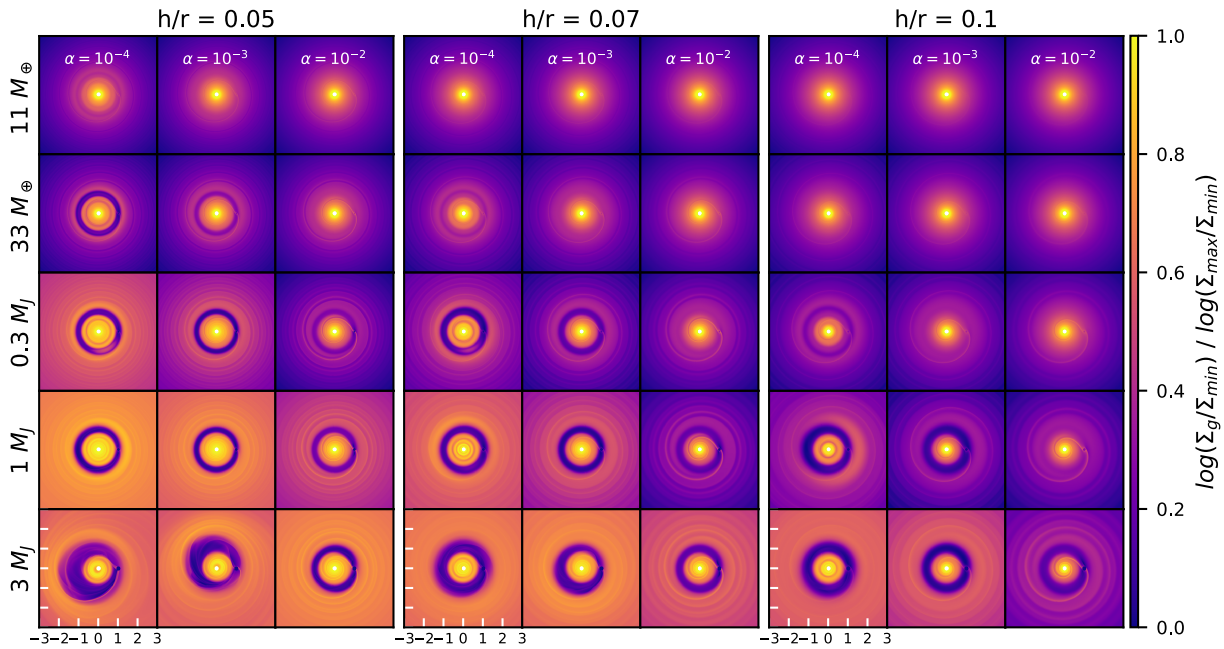

Figure 2.1: The 2-D gas surface density in log scale for h/r=0.05, 0.07 and 0.1 from left to right panel blocks. In each block, the models for $\alpha = 10^{-4}, 10^{-3}, 10^{-2}$ are shown from left to right. The planet mass increases from top to bottom, namely M_p = 11 $M_\oplus$, 33 $M_\oplus$, 0.3 M_J, 1 M_J and 3 M_J, if M_* = $M_\odot$. In each panel, the star is located at the center, and the plotting region is 3 × 3 in units of r_p, where r_p is the distance between the star and the planet. The planet is located at (x,y) = (1,0) and orbits counterclockwise around the star. Σ_{max} and Σ_{min} are chosen to highlight the structures in each panel.

part (a) and (b). The mass fraction of small particles (part a) with respect to the total dust mass is

$$f_{sd} = \int_{min\{s_{min}, s_{min}^{code}\}}^{min\{s_{max}, s_{min}^{code}\}} s^{3+p} ds \Big/ \int_{s_{min}}^{s_{max}} s^{3+p} ds \,, \tag{2.3}$$

and the mass fraction of large particles using dust super-particles (part b) is

$$f_{ld} = 1 - f_{sd} \,. \tag{2.4}$$

We want to explore two dust size distributions $n(s) \propto s^{-3.5}$ and $s^{-2.5}$, given the minimum and maximum dust size s_{min} and s_{max}. However, the super-particles in our setup have a different

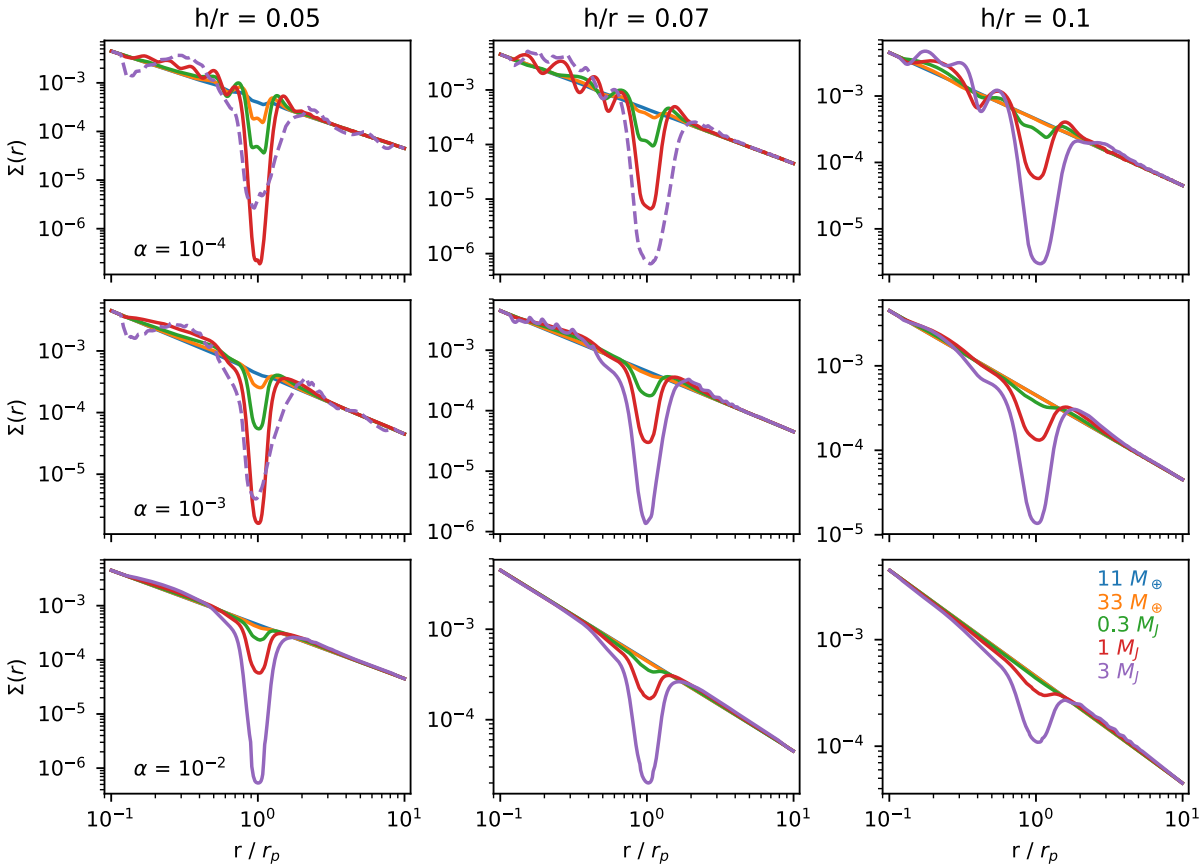

Figure 2.2: The azimuthally-averaged gas surface density for models of h/r=0.05, 0.07 and 0.1 are shown from left to right. Disks with $\alpha = 10^{-4}, 10^{-3}, 10^{-2}$ are shown from top to bottom. Blue, yellow, green, red and purple curves represent the gas surface density for planet mass M_p = 11 $M_\oplus$, 33 $M_\oplus$, 0.3 M_J, 1 M_J and 3 M_J respectively, if $M_* = M_\odot$. The dashed curves show the cases with visible asymmetry at the gap edge in Figure 2.1.

distribution. The number of super-particles $N(s)$ follows a uniform distribution in the $log(s)$ space, $\int N(s)ds \propto dlog(s)$. Thus for dust in part (b), if $f_{ld} > 0$, we give each particle (having size s) a mass weight to scale them into the desired distribution:

$$w_i(s) = \frac{M_{tot}}{N_{part}} \frac{s^{3+p} / \int_{max\{s_{min}, s_{min}^{code}\}}^{s_{max}} s^{3+p} ds}{s^{-1} / \int_{s_{min}^{code}}^{s_{max}^{code}} s^{-1} ds}, \tag{2.5}$$

where M_{tot} is the total dust mass in the disk and N_{part} is the total number of super-particles in the simulation.

3) Next, we assign the opacity for each particle to derive the total optical depth. DSHARP opacities are produced by Birnstiel et al. (2018), which contains a table of absorption and scattering opacities for a given wavelength and grain size, $\kappa(\lambda, s)$. For part (b) dust component, we assign each particle a DSHARP absorption opacity $\kappa_{abs,i}(s_i)$ at 1.27 mm based on the particle's size, where s_i is the s value in the table that is the closest to this particle size. If the particle size is smaller than the minimum size in the opacity table, we take the opacity for the minimum sized particle in the table, namely using a constant extrapolation, since the opacity is already independent of the particle size at the lower size end of the opacity table. We bin all super-particles in each numerical grid cell to derive the total optical depth through the disk for particles in part (b):

$$\tau_{ld} = f_{ld} \frac{\sum_i w_i(s) \kappa_{abs,i}(s)}{A_{cell}}, \tag{2.6}$$

where the sum is adding all particles in the cell, and A_{cell} is the surface area of the grid cell. The optical depth contributed by part (a) is simply

$$\tau_{sd} = f_{sd} \kappa_{ma} \Sigma_g / 100 \tag{2.7}$$

where

$$\kappa_{ma} = \int_{min\{s_{min}, s_{min}^{code}\}}^{min\{s_{max}, s_{min}^{code}\}} \kappa_{abs}(s) s^{3+p} ds \tag{2.8}$$

is the mass-averaged opacity of the small dust within the range of dust sizes in part (a). The final optical depth for each grid cell at (r, θ) is the sum of both components,

$$\tau(r, \theta) = \tau_{sd}(r, \theta) + \tau_{ld}(r, \theta). \tag{2.9}$$

Note that we do not consider dust and gas within one Hill radius r_H around the planet for our analysis since our simulations are not able to resolve the circumplanetary region. Thus, we impose the optical depth there to be the minimum optical depth within the annulus (r_0 - r_H) < r < (r_0 + r_H).

4) Then, we calculate the brightness temperature or intensity for each grid cell as

$$T_b(r,\theta) = T_d(r)(1-e^{-\tau(r,\theta)}), \tag{2.10}$$

and we assume that the midplane dust temperature follows the assumed disk temperature. Thus,

$$T_d(r) = T_d(r_0)\left(\frac{r}{r_0}\right)^{-0.5}. \tag{2.11}$$

Because we seek to derive a scale-free intensity for different systems, the Rayleigh-Jeans approximation is made here. For the young solar system and the HR 8799 calculations in §2.6.1, and the detailed modeling of AS 209 and Elias 24 in §2.5.1 and §2.5.1, we use the full Planck function at ν = 240 GHz to derive more accurate intensities.

The normalized brightness temperature ($T_b(r,\theta)/T_d(r_0)$) is adequate for the gap width and depth calculation in §2.4.2. But for individual sources, we would like to calculate the absolute brightness temperature. Then, we need to multiply the normalized brightness temperature by the disk temperature at r_0 ($T_d(r_0)$). We estimate $T_d(r_0)$ using

$$T_d(r_0) = \left(\frac{\phi L_*}{8\pi r_0^2 \sigma_{SB}}\right)^{1/4} \tag{2.12}$$

where L_* is the stellar luminosity and ϕ is a constant of 0.02 coming from an estimate from Figure 3

in D'Alessio et al. (2001). This disk mid-plane temperature is the same as Equation 5 in Dullemond et al. (2018), and more details can be found there. We calculate $T_d(r)$ for each DSHARP source using the stellar properties (L_*) listed in Andrews et al. (2018a). Knowing $T_d(r)$, we can simply derive h/r at the gap position using $h/r = c_s/v_\phi$ (the M_* that is used to calculate v_ϕ is also given in Andrews et al. (2018a).).

5) Finally, we convolve these intensity maps with two different Gaussian beams. The beam size is $\sigma = 0.06 r_p$ and $\sigma = 0.025 r_p$ respectively. For a protoplanetary disk 140 pc away, this is equivalent to FWHM (Full Width Half Maximum) beam size of 0.1" and 0.043" if $r_p = 100$ au, or 0.05" and 0.021" if $r_p = 50$ au.

2.4 Simulation Results

2.4.1 Gas

We will first present results for the gas component in the simulations, including gaseous gap profiles (§2.4.1) and the sub/super Keplerian gas motion at the gap edges (§2.4.1).

Density

Figure 2.1 shows the two-dimensional gas density maps for all the simulations at 1000 planetary orbits. The left, middle, and right panel blocks show simulations with h/r=0.05, 0.07, and 0.1. Within each panel block, $\alpha = 10^{-4}$, 10^{-3}, and 10^{-2} cases are shown from left to right. Some large-scale azimuthal structures are evident in the figure. First, low α disks exhibit noticeable horseshoe material within the gap. Since the planet is at (x=1, y=0) and orbiting around the star in the counterclockwise direction, most horseshoe material is trapped behind the planet (around the

L5 point). This is consistent with the shape of the horseshoe streamlines around a non-migrating planet in a viscous disk (Masset 2002). Second, the gap edge becomes more eccentric and off-centered for smaller h/r, smaller α and larger planet mass cases (especially for $M_p \geq 3\ M_J$). Such an eccentric gap edge for the $M_p \geq 3\ M_J$ planet is consistent with previous studies (Lubow 1991a;b; Kley & Dirksen 2006; Teyssandier & Ogilvie 2017). Third, large-scale vortices can be seen at the gap edges for some of the $\alpha = 10^{-4}$ cases. Although they are not very apparent in the gas surface density maps, they can trap dust particles azimuthally, causing a large azimuthal contrast in the dust continuum images (as shown in §2.4.2).

The azimuthally averaged gas surface density profiles for all the models are shown in Figure 2.2. Several noticeable trends in this figure are:

1) When the planet mass increases, the gap depth normally increases. However, when the gap is very eccentric (e.g. `h5am4p5`, `h5am3p5`), the azimuthally averaged gas surface density at the gap is actually higher than the cases with lower mass planets. This is because azimuthal averaging over an elliptical gap smears out the gap density profile.

2) With the same planet mass, gaps in $h/r = 0.1$ cases are shallower but wider than the $h/r = 0.05$ cases. This is consistent with previous studies (Fung et al. 2014a; Kanagawa et al. 2015a; 2016a).

3) For a given planet mass and h/r, the gaps are shallower and smoother with increasing α. With $\alpha = 0.01$ and 10^{-3}, the gap edge is smooth, and there is only a single gap at $r/r_p \sim 1$. With $\alpha = 10^{-4}$, there are clearly two shoulders at two edges of the gap, and the material in the horseshoe region still remains in some cases. Especially, for low mass planets in $\alpha = 10^{-4}$ disks, the gap at $r/r_p \sim 1$ appears to split into two adjacent gaps. This is consistent with non-linear wave steepening theory (Goodman & Rafikov 2001; Muto et al. 2010; Dong et al. 2011a; Duffell &

MacFadyen 2012; Zhu et al. 2013) which suggests that the waves launched by a low mass planet in an inviscid disk need to propagate for some distance to shock and open gaps, leaving the horseshoe region untouched.

5) For $\alpha = 10^{-4}$ cases, we see secondary gaps at $r/r_p \sim 0.6$ in h/r=0.05 disks, $r/r_p \sim 0.5$ in $h/r = 0.07$ disks, and $r/r_p \sim 0.4$ in $h/r = 0.1$ disks. For some cases, we can even see tertiary gaps at smaller radii. These are consistent with simulations by Bae et al. (2017a); Dong et al. (2017a) and these gaps are due to the formation of shocks from the secondary and tertiary spirals (Bae & Zhu 2018a;c).

Kinematics Across the Gap

Recent works by Teague et al. (2018a) and Pinte et al. (2018b) have shown that, using molecular lines, ALMA can detect the velocity deviation from Keplerian rotation in protoplanetary disks. Such deviations are caused by the radial pressure gradient at the gaseous gap edges,

$$\frac{v_\phi^2}{r} = \frac{v_K^2}{r} + \frac{1}{\rho_{gas}} \frac{\partial P}{\partial r}. \tag{2.13}$$

In our 2-D simulations, v_K is simply $\sqrt{GM_*/r}$ and P is Σc_s^2. Equation 8.7 suggests that the deviation from the Keplerian motion is

$$\frac{\Delta v_\phi}{v_K} \sim \frac{r}{2\rho_{gas} v_K^2} \frac{\partial P}{\partial r},$$

where $\Delta v_\phi = v_\phi - v_K$. In a smooth disk where $\partial P/\partial r \sim P/r$, this deviation is very small, on the order of $(h/r)^2$ or $\leq$1% in a typical protoplanetary disk. But if the gaseous disk has a sharp pressure transition (e.g. at gap edges), the deviation from the Keplerian rotation can be significantly larger. In Figure 2.3, we plot the azimuthally averaged $\delta v_{rot} \equiv (v_\phi - v_K)/v_K$ and Σ in run `h5am4p4`.

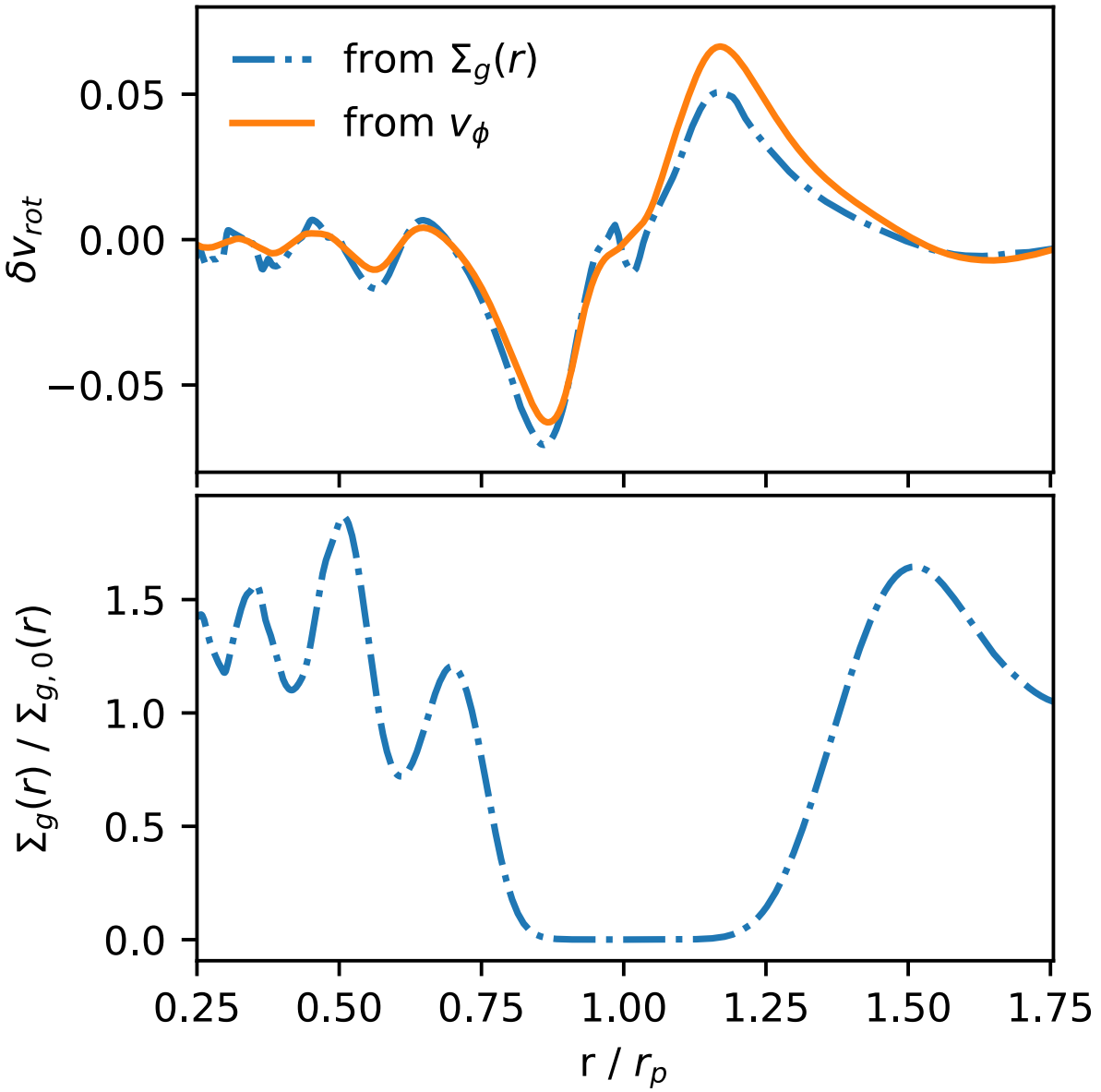

Figure 2.3: The deviation from the Keplerian velocity δv_{rot} (the upper panel) and the normalized disk surface density (the disk density over the initial disk density, the lower panel) across the gap for model `h5am4p4`. In the upper panel, the directly measured δv_{rot} is plotted as the orange curve, while the δv_{rot} derived from the radial force balance is plotted as the blue curve.

The directly measured δv_{rot} is plotted as the orange curve in the upper panel, while the calculated δv_{rot} using the disk surface density profile (presented in the lower panel) and Equation 8.7 is plotted as the blue curve in the upper panel. We can see that Equation 8.7 reproduces the measured

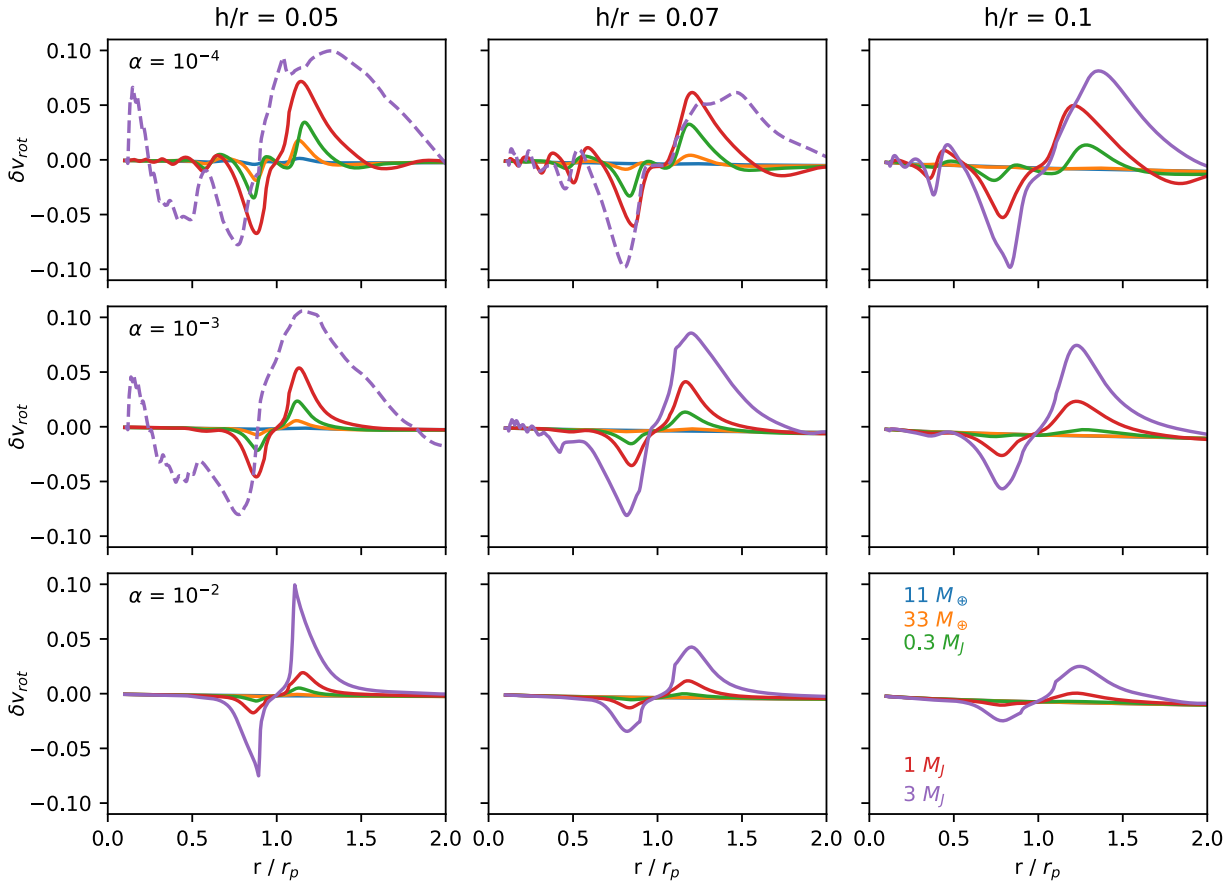

Figure 2.4: The deviation from the Keplerian velocity for all runs, where δv_{rot} = (v_ϕ - v_K) / v_K. The layout is the same as Figure 2.2.

azimuthal velocity very well, confirming that the sub/super Keplerian motion is due to the radial pressure gradient.

Figure 2.4 shows δv_{rot} for all our cases. As expected, when the gap is deeper due to either smaller α, smaller h/r, or a more massive planet, the amplitude of δv_{rot} is larger. However, when the gap becomes very eccentric and off centered (e.g. `h5am4p5`, `h5am3p5`), the azimuthally averaged δv_{rot} shows a much wider outer bump, indicating an eccentric outer disk. We label these cases as dashed curves in Figure 2.4 and unfilled markers in panel a of Figure 2.5. Another interesting feature shown in Figure 2.4 is that the presence of the gap edge vortices in $\alpha = 10^{-4}$

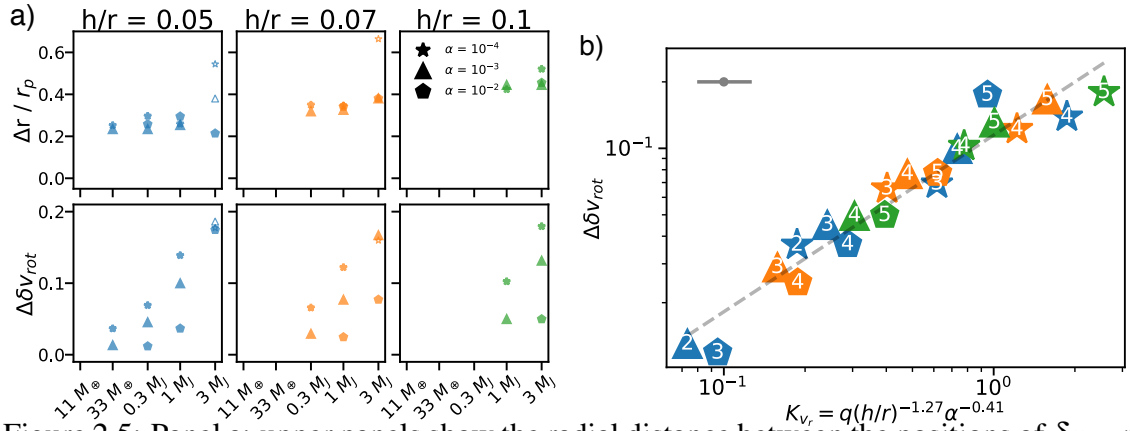

Figure 2.5: Panel a: upper panels show the radial distance between the positions of δv_{rot} maximum and minimum peaks (Δr). Bottom panels show the difference between δv_{rot} at its maximum and minimum values ($\Delta\delta v_{rot}$). The star, triangle and pentagon markers represent models with $\alpha = 10^{-4}$, 10^{-3} and 10^{-2}, respectively. The unfilled markers are eccentric cases the same as in Figure 2.2 and 2.4 shown in dashed lines. Panel b: the fitting formula (Equation 2.16) with all measured $\Delta\delta v_{rot}$ in panel A. The numbers inside the symbols represent cases with different planet masses in ascending order (e.g., "1" stands for 11 $M_\oplus$). The error-bar is shown at the upper-left corner.

cases does not affect the azimuthally averaged δv_{rot} very much. They look similar to the larger α cases without vortices. We interpret this as: if the vortex is strong with fast rotation, it has a smaller aspect ratio so that it is physically small (Lyra & Lin 2013) and contributes little to the azimuthally averaged gas velocity profile; and if the vortex is weak, although it has a wider azimuthal extent its rotation is small compared with the background shear so again it contributes little to the global velocity profile.

The radial distance and amplitude of the sub/super Keplerian peaks are plotted in panel a of Figure 2.5. $\Delta\delta v_{rot}$ is the difference between the maximum δv_{rot} (at $r > r_p$) and the minimum δv_{rot} (at $r < r_p$) from Figure 2.4. Note that these velocity peaks are not peaks (or rings) at mm intensity images that will be presented in §2.4.2. We first notice that the distance between these peaks in $\Delta r/r$ is roughly 4.4 times h/r, which is not sensitive to either the planet mass or α (upper panel a). Thus, we can use the distance of these sub/super-Keplerian peaks to roughly estimate the disk

temperature. On the other hand, the amplitude of the sub/super Keplerian peaks depends on all of these parameters (lower panel a). With increasing planet mass, the amplitude increases until the gap edge becomes eccentric. For the same mass planet in the same h/r disk, the amplitude decreases with increasing α. For the same mass planet in the same α disk, the amplitude decreases with increasing h/r.

Thus, using gas kinematics, we can first use the distance between the peaks to estimate h/r, and then we can use the amplitude together with the estimated h/r and assumed α value to derive the planet mass.

Following Kanagawa et al. (2015a; 2016a), we seek simple power laws to fit various observable quantities throughout the paper so that the fittings can be easily used by the community. Here, we try to find the best fit for $\Delta\delta v_{rot}$. We define a K_{v_r} parameter that is proportional to q and has power law dependence on h/r and α,

$$K_{v_r} = q(h/r)^{ph}\alpha^{pa}\,. \tag{2.14}$$

We try to find the best fitting parameters ph and pa. If ph=0 or pa=0, it means that the fitting does not depend on the disk h/r or α, respectively. First, we assign values to ph and pa, and we can make the log $\Delta\delta v_{rot}$ - log K_{v_r} plot for all the data points. Then, we do a linear-regression fitting for these data points using

$$\Delta\delta v_{rot} = AK_{v_r}^{B}\,. \tag{2.15}$$

The coefficients in the fitting (A and B) are thus determined. The sum of the square difference of the vertical distance between the data points and the fitting is σ. Finally, we vary ph and pa and follow the same fitting procedure until the minimum σ is achieved. The resulting ph and pa are the best degeneracy parameters, and A and B are the best fitting parameters. For $\Delta\delta v_{rot}$, the fitting

formula is:

$$K_{v_r} = q(h/r)^{-1.27}\alpha^{-0.41}$$

with

$$\Delta\delta v_{rot} = 0.11K_{v_r}^{0.80}. \tag{2.16}$$

Thus, the sub/super Keplerian motion is most sensitive to h/r, followed by q and α. The fitting formula is shown in panel b of Figure 2.5 together with all measured $\Delta\delta v_{rot}$. The uncertainty in K_{v_r} is estimated by measuring the horizontal offset between each data point and the fitting line. From the distribution of the offset, the left side error is estimated by the 15.9 percentile of the distribution and the right side error is 84.1 percentile of the distribution. The uncertainty in $log_{10}(K_{v_r})$ is $^{+0.103}_{-0.099}$, which is about a factor of 1.25 of K_{v_r}.

2.4.2 Dust Thermal Emission

After exploring the gaseous gaps, we study the gaps in mm dust continuum maps in §2.4.2. We detail our method to fit the gap width and depth in §2.4.2.

Axisymmetric and Non-axisymmetric Features

As discussed in §2.3.3, we have 45 simulations with different h/r, α, and M_p. For each simulation, we generate seven continuum maps for seven $\Sigma_{g,0}$ with the DSD1 dust size distribution and five continuum maps for five $\Sigma_{g,0}$ with the DSD2 dust size distribution. Thus, we produce 45×12 mm maps.

The mm intensity maps for a $\Sigma_{g,0} = 3\,\mathrm{g\,cm^{-2}}$ disk with DSD1 and DSD2 dust size distributions are presented in Figures 2.6 and 2.7, respectively. We want to emphasize that, if the opacity is a

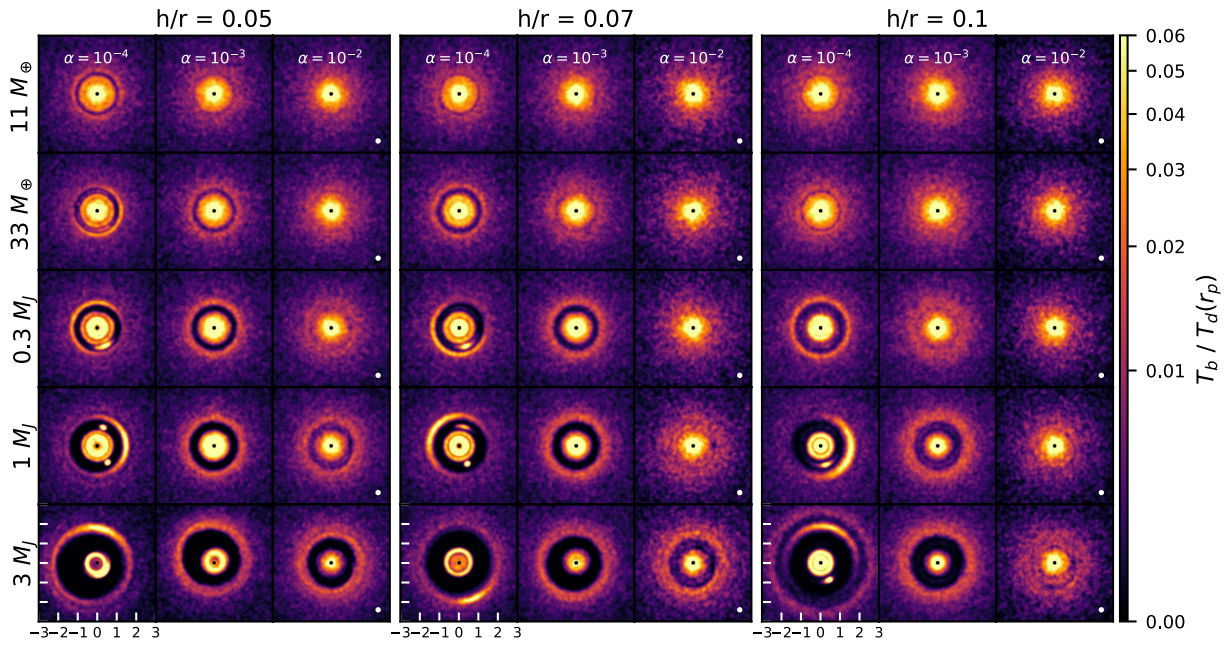

Figure 2.6: The dust continuum emission maps for cases with h/r=0.05 (left panels), h/r=0.07 (middle panels) and h/r=0.1 (right panels) at 1.27 mm. The initial gas surface density at the planet position $\Sigma_{g,0}$ is 3 g cm^{-2}. The initial dust size distribution is assumed to follow $n(s) \propto s^{-3.5}$ with the maximum grain size of 0.1 mm (DSD1). The layout is the same as Figure 2.1. The images are convolved with a Gaussian kernel with σ of 0.06 r_p (or FWHM of 0.14 r_p), which is shown in the bottom right of the panels.

constant with the maximum dust size (which roughly stands when the maximum dust size, s_{max}, is not significantly larger than the wavelength of observation), there is a degeneracy in the relative intensity maps between different Σ_g and s_{max} because only the Stokes number matters for the gas dynamics. For example, the shapes of intensity maps for the $\Sigma_{g,0} = 3\,\mathrm{g\,cm^{-2}}$ and $s_{max} = 0.1\,\mathrm{mm}$ cases are very similar to the $\Sigma_{g,0} = 300\,\mathrm{g\,cm^{-2}}$ and $s_{max} = 1\,\mathrm{cm}$ cases, since they have the same Stokes number. Thus, Figure 2.6 should be regarded as the dust well-coupled limit, while Figure 2.7 should be regarded as the dust fast-drifting limit.

Regarding the gaps and rings, there are several noticeable trends:

1) By comparing these two figures, we can see that the rings are more pronounced when particles with larger Stokes numbers are present in the disk. For the well-coupled case (Figure 2.6), the

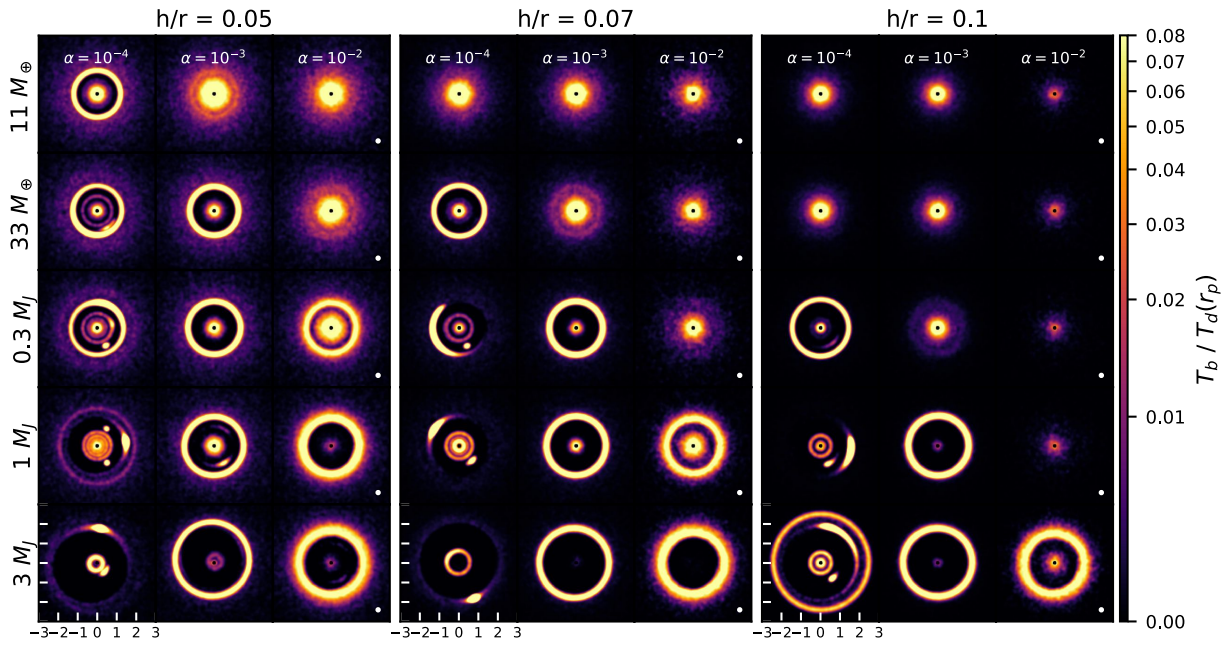

Figure 2.7: Similar to Figure 2.6, except that the initial dust size distribution is assumed to follow $n(s) \propto s^{-2.5}$ with the maximum grain size of 1 cm (DSD2).

gap edge is smoothly connecting to the outer disk and the outer disk is extended. However, for the fast-drift particle cases (Figure 2.7), there is a clear dichotomy: either the disk does not show the gap or the gap edge becomes a narrow ring. This is because the gap edge acts as a dust trap so that a small gaseous feature can cause significant pileup for fast-drifting particles.

2) The marginal gap opening cases are in panels that are along the diagonal line in Figures 2.6 and 2.7, which are similar to the trend for the gaseous gaps in Figure 2.1.

3) The narrow gap edge of the the fast-drifting particle cases (Figure 2.7) becomes wider with a higher α due to turbulent diffusion. Thus, if we know the particles' Stokes number at the gap edge, we can use the thickness of the ring to constrain the disk turbulence, as shown in Dullemond et al. (2018).

Besides axisymmetric structures, there are also several non-axisymmetric features to notice:

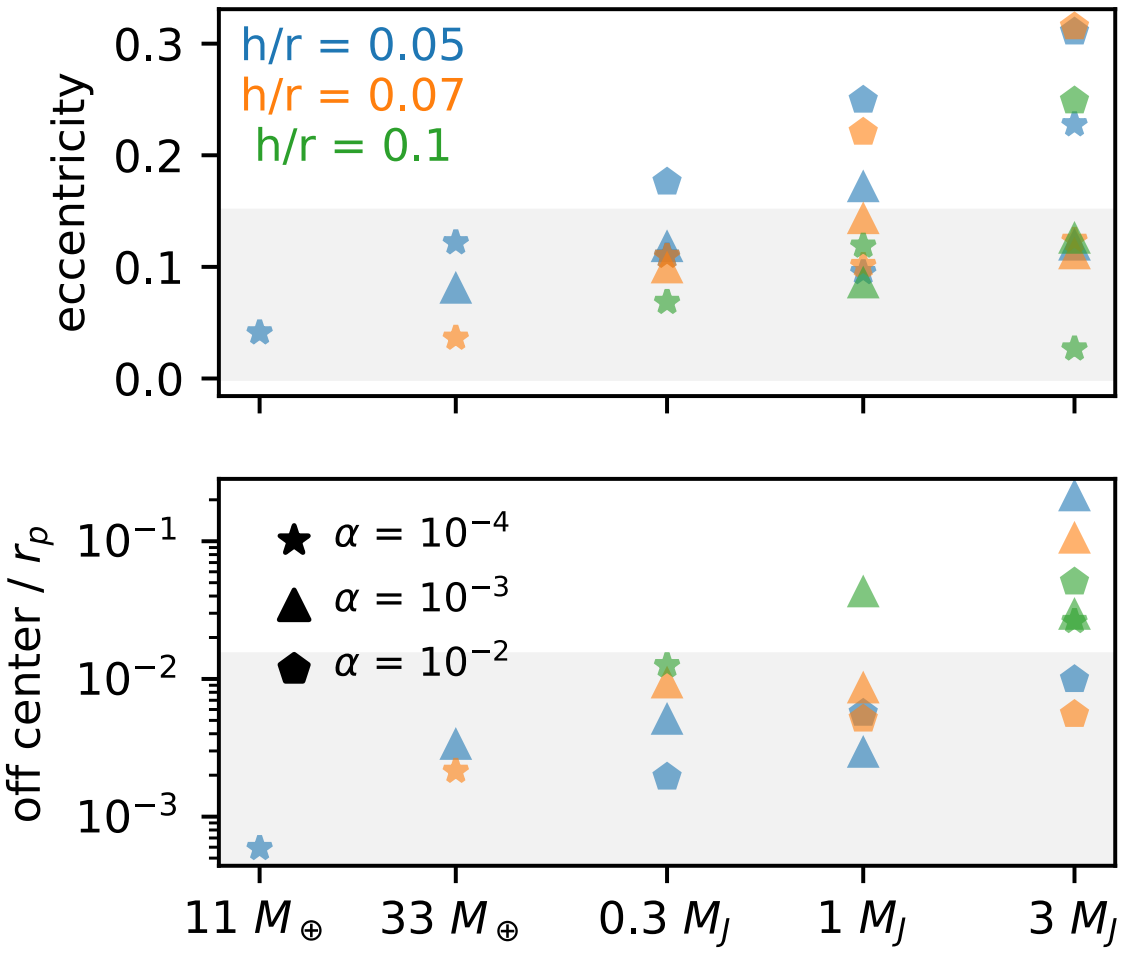

Figure 2.8: Eccentricity (upper panels) and distance between the ellipse center and the central star (lower panels) for intensity images from $\Sigma_{g,0} = 3\ \mathrm{g\,cm^{-2}}$ (Figure 2.6 and 2.7).

1) The gaps in the lower left panels (`h5am4p5`, `h5am3p5`) are clearly eccentric and off-centered. We may be able to use the ellipticity of the gap edges to infer the planet properties. Thus, for every mm intensity map, we find the local maximum in each azimuthal angle and use linear fitting method to measure the gap eccentricity and the distance between the center of the ellipse and the star. We find that, even in mm images generated from disks having dramatically different Stokes numbers, the gap eccentricity and off-centered distance are quite similar. However,

the lower planet mass cases for the DSD1 have mild dust trapped rings thus having lower SNR, while the higher mass cases for the DSD2 have strong asymmetry, thus leading to half of the rings with the low SNR. Thus, we combine the fitting results for both DSD1 and DSD2 at $\Sigma_{g,0}$ = 3 g cm^{-2}, and pick up the smaller values for eccentricity and the off-centered distance (Figure 2.8). We also test several cases with the ring-fitting method described in §3.1 in Huang et al. (2018c) (a MCMC fitting of the offset Δx, Δy, the semi-major axis, the aspect ratio and the position angle) and find that the derived eccentricity and the distance from the central star are very similar to those derived here. Clearly, both eccentricity and off-centered distance increase with the planet mass, which is consistent with gas only simulations in Kley & Dirksen (2006); Ataiee et al. (2013); Teyssandier & Ogilvie (2017); Ragusa et al. (2018). These quantities do not quite depend on h/r and α except a weak trend that gaps in larger α disks have higher eccentricities. Unfortunately, due to the limited number of super-particles in the simulations, the Poisson noise in the intensity maps prevents us from measuring the eccentricity very accurately. The adopted Gaussian convolution kernel to reduce the Poisson noise has a σ_c of 0.06 r_p. If the major-axis and the minor-axis have an error of σ_c/2, the uncertainty of the eccentricity is $\Delta e = \left(1-(1-0.03/2)^2\right)^{\frac{1}{2}} = 0.17$. Thus, any measured eccentricity smaller than 0.15 is consistent with zero eccentricity. For the same reason, any off-centered distance smaller than half of the pixel size (0.015) is consistent with zero. We mark these uncertainties as the light grey area in Figure 2.8. On the other hand, if the eccentricity and the off-centered distance is above these limits, our results suggest that the eccentric gap edge may be a signature of a massive planet in disks. Eccentric and off-centered gap edges have been measured in HL Tau (ALMA Partnership et al. 2015a) and HD 163296 (Isella et al. 2016), which may suggest that these gaps are induced by planets.

2) For the lowest viscosity cases ($\alpha = 10^{-4}$), particle concentration within vortices can be seen

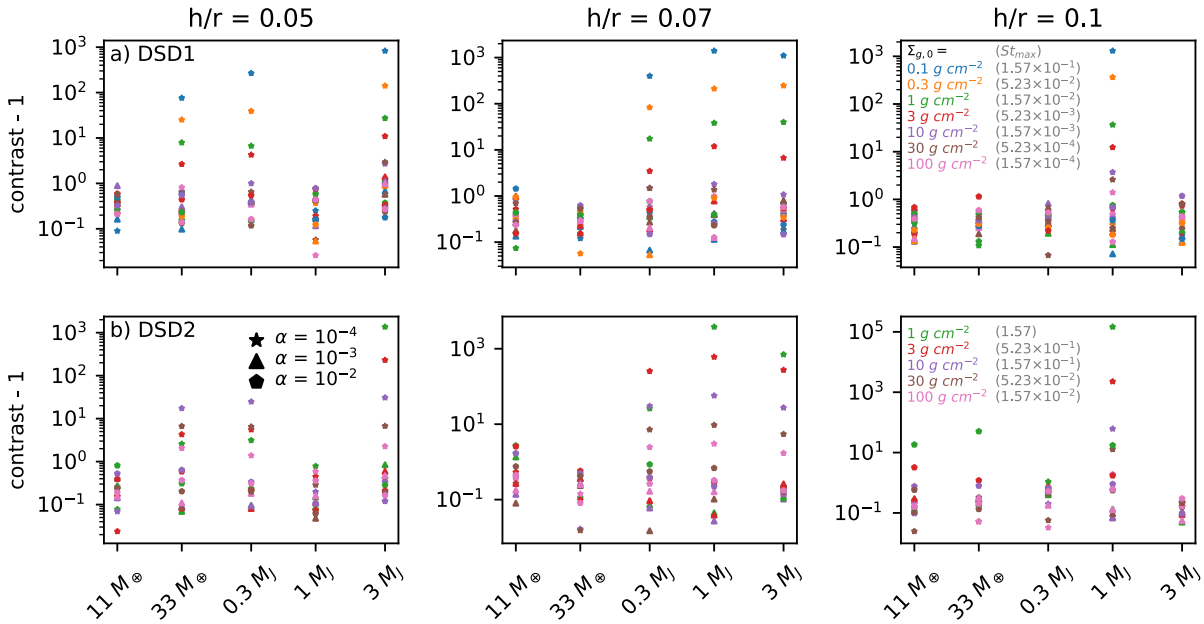

Figure 2.9: The contrast at the outer gap edge for every model. The upper panels use DSD1 dust size distribution while the lower panels use DSD2 dust size distribution. Contrast is the intensity of the brightest part of the ring over the intensity at $\Delta\theta = 180^\circ$ opposite location on the ring.

at the gap edge. Even a 33 $M_\oplus$ planet can induce particle-concentrating vortices. Interestingly, the vortex sometimes is inside the gap edge, e.g. $h/r = 0.05$, $M_p = 1M_J$ case and $h/r = 0.1$, $M_p = 3M_J$ case. This is probably because large particles are trapped at the gap edges, while small particles move in and get trapped into the vortex. For the majority of cases, the vortices that cause significant asymmetry in mm intensity maps are at the gap edge where $dP/dr = 0$. To characterize such large-scale asymmetries, Figure 2.9 shows the contrast at the gap edge, which is the ratio between the intensity of the brightest part of the ring over the intensity 180 degree opposites on the previously fitted ellipse. The figure shows that the case with a smaller gas surface density tends to show a higher contrast. We note that the contrast is very large in some cases. A 33 $M_\oplus$ planet can lead to a factor of 100 contrast at the gap edge for a $h/r = 0.05$ disk with $St = 0.16$ particles. Thus, a low mass planet may also explain some of the extreme asymmetric systems: e.g. IRS 48

(van der Marel et al. 2013) and HD 142527 (Casassus et al. 2013).

3) The dust concentration at L5 or both L4/L5 is seen in some $\alpha = 10^{-4}$ cases, consistent with previous simulations (Lyra et al. 2009). These features are more apparent than those in the gas (Figure 2.1). As pointed out by Ricci et al. (2018), such features may be observable. On the other hand, we want to emphasize that the dust concentration at Lagrangian points is not in a steady state, and the amount of dust at those points decreases with time. Thus, in this paper, we will not use these feature to constrain the planet properties.

Fitting Gaps/Rings

To derive the relationship between the gap profiles and the planet mass, we azimuthally average the mm intensity maps as shown in Figure 2.10. The solid curves are for models with $s_{max} = 0.1$ mm (DSD1), while the dashed curves are for models with $s_{max} = 1$ cm (DSD2).

We try to find the relationship between the planet mass and the gap properties (such as the gap width Δ and depth δ), using the dust intensity profiles in Figure 2.10. Previous works such as Kanagawa et al. 2016a; 2015a; Dong & Fung 2017 studied the relationship between the planet mass and the gaseous gap width and depth. However, mm observations are probing dust with sizes up to mm/cm and these dust can drift in the gaseous disk. Thus, studying only the gaseous gap profiles is not sufficient for explaining mm observations and carrying out a similar study but directly for dust continuum maps is needed. We seek to first find a relationship between disk and planet properties (α, h/r, and M_p) using the fitting of the azimuthally averaged gas surface density profile, and characterize those three parameters using a single parameter K (for the depth-K relation) or K' (for the width-K' relation). Then, we fit the azimutally averaged dust intensity profile for our grid of models and find their depth-K and width-K' relations. Overall, our fitting follows Kanagawa et al.

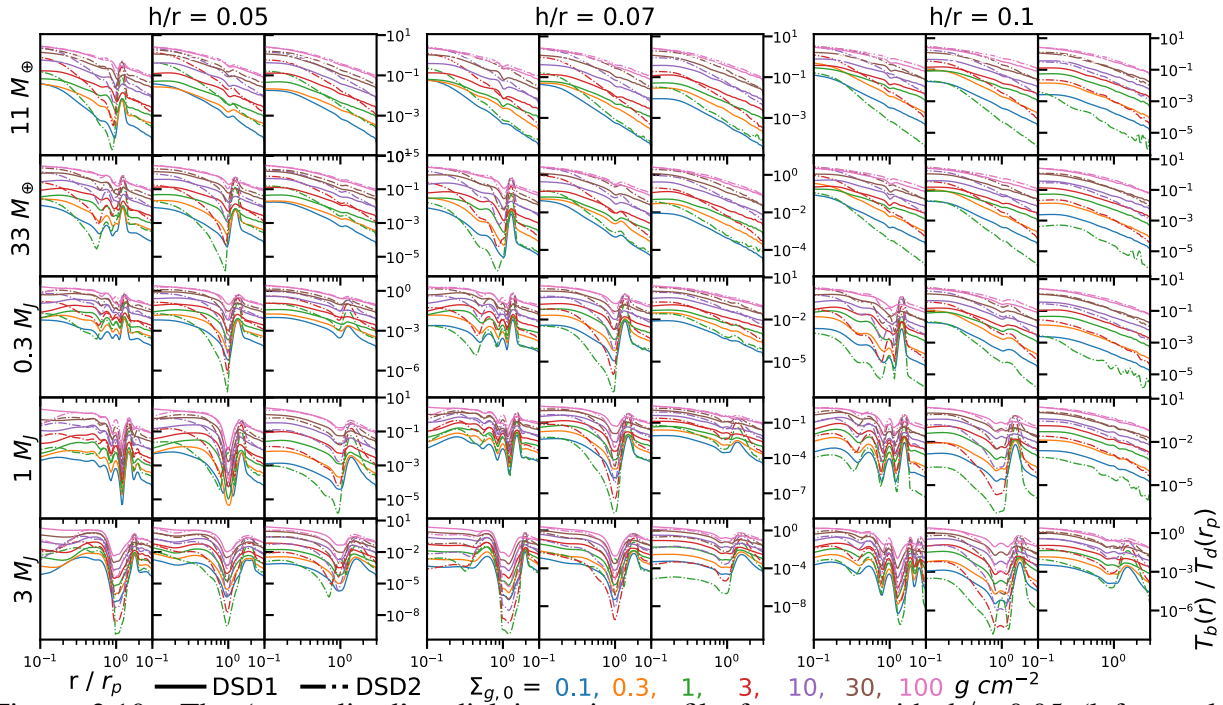

Figure 2.10: The 'normalized' radial intensity profile for cases with h/r=0.05 (left panels) h/r=0.07 (middle panels), and h/r=0.1 (right panels). From left to right in each panel block, $\alpha = 10^{-4}, 10^{-3}, 10^{-2}$ in disks. From top to bottom, the planet mass increases (the layout is similar to Figure 2.1, 2.6 and 2.7.). The solid curves are calculated with the DSD1 dust size distribution, while the dot-dashed curves are calculated with the DSD2 dust size distribution. The seven colors of lines denote different initial gas surface densities ($\Sigma_{g,0}$). The profiles are smoothed with a Gaussian kernel with σ =0.06 r_p.

(2016a) and Kanagawa et al. (2015a) but extend those relationships to dust particles with different sizes.

The detailed steps are the following:

(1) We measure the gap depth (δ) for both gas surface density profiles (Figure 2.2) and mm intensity profiles (Figure 2.10). From the outer disk to the inner disk, we first find the outer peak (the first local maximum, which corresponds to where dust piles up due to the dust trapping) and mark this point as r_{peak}, and then find the bottom of the gap (local minimum) inside r_{peak} and mark it as r_{gap}. r_{gap} is not necessarily r_p. As demonstrated in Figure 2.11, the gap can have the

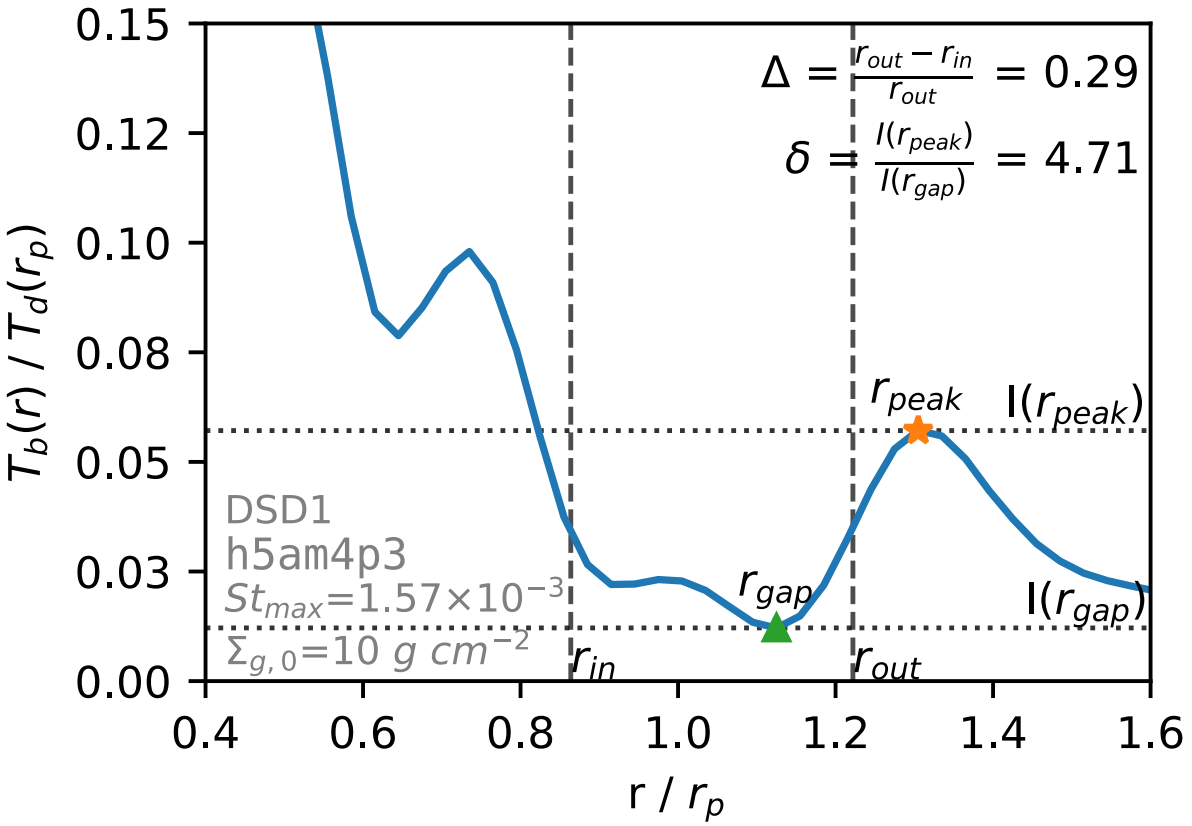

Figure 2.11: An example of our definition of the gap depth (δ) and width (Δ). r_{peak} (marked by a star) and r_{gap} (marked by a triangle) are first found and are used to calculate I_{edge}, which is the average between $I(r_{peak})$ and $I(r_{gap})$. r_{out} and r_{in} are positions where the intensity equals I_{edge}. The gap width (Δ) is (r_{out}-r_{in})/r_{out}. The depth (δ) is $I(r_{peak})/I(r_{gap})$. (This example is taken from model `h5am4p3` with $\Sigma_{g,0}$ = 10 g cm^{-2} and DSD1.)

deepest point further out than r_p. This is because some gaps have significant horseshoe material in between. In some extreme cases with very shallow gaps, only the outer portion of the gap that is outside the horseshoe region is visible (e.g. the top middle panel in Figure 2.10). We define the gap depth δ as

$$\delta_\Sigma = \Sigma(r_{peak})/\Sigma(r_{gap})\,, \tag{2.17}$$

for the gas surface density profiles, and

$$\delta_I = I_{mm}(r_{peak})/I_{mm}(r_{gap})\,, \tag{2.18}$$

for the dust mm intensity profiles.

(2) Measuring the gap width (Δ) for these profiles. To calculate the width, we first define the edge quantities as the average between the peak and gap surface densities (for gas) or the mm intensities (for intensity maps):

$$\Sigma_{edge} = \frac{\Sigma(r_{peak}) + \Sigma(r_{gap})}{2}\,, \tag{2.19}$$

and

$$I_{edge} = \frac{I_{mm}(r_{peak}) + I_{mm}(r_{gap})}{2}\,. \tag{2.20}$$

Then, we find one edge r_{in} at the inner disk and the other r_{out} at the outer disk, where $\Sigma(r_{in}) = \Sigma(r_{out}) = \Sigma_{edge}$ for the gas surface density or $I(r_{in}) = I(r_{out}) = I_{edge}$ for the dust intensity (Figure 2.11). Thus, we define the gap width Δ for either the gas surface density or the dust intensity as

$$\Delta = (r_{out} - r_{in})/r_{out}\,. \tag{2.21}$$

Figure 2.12 shows Δ for all $\Sigma_{g,0}$ cases with DSD1 (panel a) and DSD2 (panel b) dust distributions. If there is some horseshoe material around r=r_p separating the main gap into two gaps, the horizontal Σ_{edge} or I_{edge} line will cross through the horseshoe and we treat two individual gaps as a single one (i.e., the r_{in} is taken to be the r_{in} of the inner gap and r_{out} is taken to be the r_{out} of the

outer gap), but the individual gaps on either side of the horseshoe region are also plotted in Figure 2.12 as fainter makers and they are connected to the main gap width using dotted lines.

Note that our definition of gap width is more convenient to use than that in Kanagawa et al. (2016a), because the width here is normalized by r_{out} instead of r_p as in Kanagawa et al. (2016a). In actual observations, we do not have the knowledge of the planet position r_p within the gap. Another difference between our defined gap width and the one used in Kanagawa et al. (2016a) is that we use $(\Sigma(r_{peak})+\Sigma(r_{gap}))/2$ to define Σ_{edge} while Kanagawa et al. (2016a) use $\Sigma_0/2$ to define the gap edge. Our definition enables us to study shallow gaps that are shallower than $\Sigma_0/2$.

(3) Fitting the width (Δ)-K' relation. We first use the width Δ measured from the gas surface density profiles to find the optimal degeneracy parameter K' following the same procedure as in Equation 2.14. Similarly, a least squares fitting was done to minimize the sum of the square difference of the vertical distance between the points and the linear-regression line log(Δ) vs. log(K'). With this procedure, we derive that the optimal K' is

$$\frac{K'}{0.014} = \frac{q}{0.001}\left(\frac{h/r}{0.07}\right)^{-0.18}\left(\frac{\alpha}{10^{-3}}\right)^{-0.31}. \tag{2.22}$$

With this definition of K', the best fitting relationships ($\Delta = AK'^{B}$) are found for each initial gas densities with two dust size distributions DSD1 and DSD2. The resulting A and B for these fits are listed in Table 1 in Zhang et al. (2018b). Note that our definition of K' is equivalent to the square root of K' defined in Kanagawa et al. (2016a). Compared with the fitting formula for the gas surface density in Kanagawa et al. (2016a), our K' is less sensitive to h/r and the gaseous gap width is less sensitive to q. We confirm that this is largely due to our different definition of the gap width (compared with their definition, our normalized gap width is smaller for wide gaps and

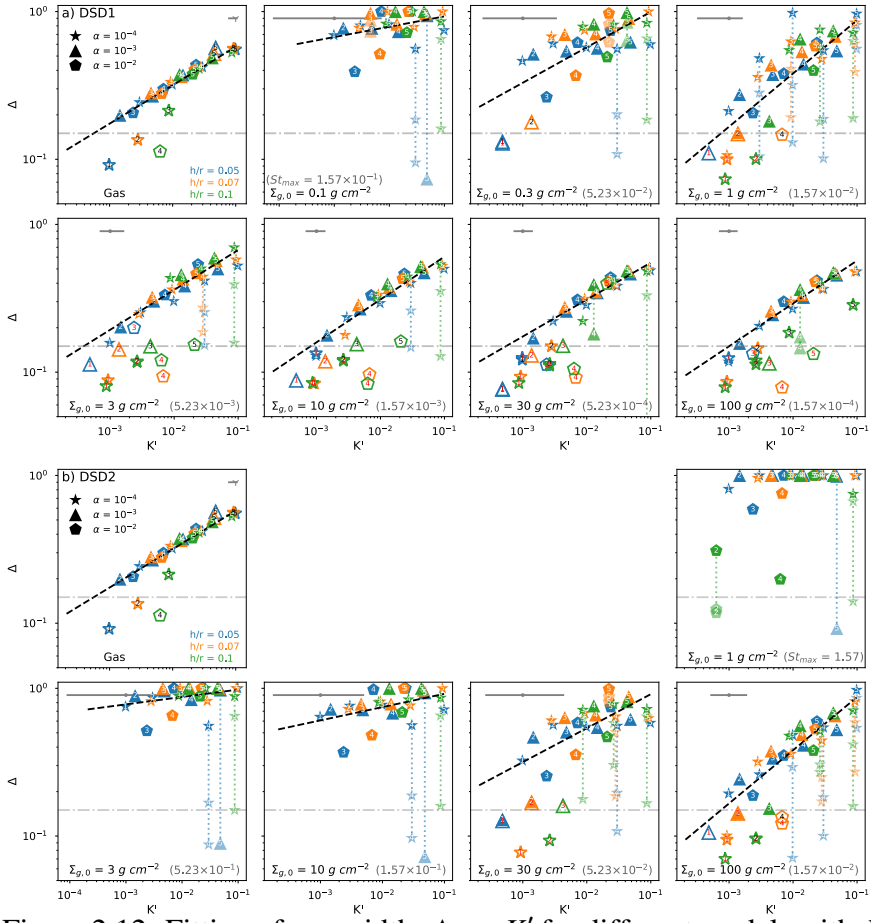

Figure 2.12: Fitting of gap widths Δ vs. K' for different models with dust size distribution $\{s_{max},\ p\}$ = $\{0.1\ mm, -3.5\}$ (panel a) and $\{s_{max},\ p\}$ = $\{1\ cm, -2.5\}$ (panel b). The first panel is the fitting of the gas surface density, which is used to calibrate the index above h/r and α. The best fit is $K' = q(h/r)^{-0.18}\alpha^{-0.31}$. The stars, triangles, and pentagons represent models of α = 10^{-4}, 10^{-3}, and 10^{-2}, respectively. Models for h/r = 0.05, 0.07 and 0.1 are in blue, orange, and green respectively. The label 1, 2, 3, 4 and 5 within symbols represent the planet mass from 10 $M_\oplus$ to 3 M_J increasingly. The rest of panels are fits of gaps in dust intensity profiles. From left to right and top to bottom, they are models scaled to the initial gas density $\Sigma_{g,0}$ = 0.1 g cm^{-2}, 0.3 g cm^{-2}, 1 g cm^{-2}, 3 g cm^{-2}, 10 g cm^{-2}, 30 g cm^{-2}, 100 g cm^{-2}. The best fits using Equation 2.22 are plotted as the dashed lines and the constants A and B are shown in Table 1 in Zhang et al. (2018b). We neglect outliers (shown in unfilled markers) when fitting the line. The outliers either have very shallow gaps, or have double gaps (horseshoe in between), thus have widths smaller than their counterparts. For cases which clearly show that the major gap is split into two by the horseshoe region, the widths of the two individual gaps around the horseshoe are also presented and they are connected to the main gap width with the vertical dotted line. The open symbols with red numbers in them are derived from images which are convolved with a smaller beam of $\sigma = 0.025 r_p$. The grey errorbar on top of each plot shows the uncertainty of the fitting. See tables in Zhang et al. (2018b)

larger for shallow gaps that are normally narrow.).

Figure 2.12 shows the fits for all the cases with DSD1 (panel a) and DSD2 (panel b) dust size distributions. We can see that uncertainties of these fittings become large when $\Delta \lesssim 0.15$. Thus, our fitting procedure does not involve widths that are smaller than 0.15. For these narrow gaps whose widths are smaller than 0.15 (labeled as the open symbols with back numbers in them), their gap profiles start to be affected by the smoothing kernel with $\sigma = 0.06 r_p$. Thus in Figure 2.12, we also plot the widths measured from the profiles that are convolved with a σ = 0.025 r_p kernel. These widths are plotted as open symbols with red numbers in them.

(4) Fitting the depth (δ)-K relation. We adopt the same procedure to fit the depth-K as the width-K' aforementioned. Since no-gap is equivalent to δ=1, we try to find the optimal degeneracy parameter K by a least squares fitting for log(δ - 1) vs. log(K),

$$\delta - 1 = CK^D, \tag{2.23}$$

for various K. The optimal K is fitted to be

$$\frac{K}{24} = \frac{q}{0.001}\left(\frac{h/r}{0.07}\right)^{-2.81}\left(\frac{\alpha}{10^{-3}}\right)^{-0.38}. \tag{2.24}$$

After K is fixed, we use Equation 2.23 to fit the relationship between δ - 1 and K for the dust intensity profiles from different $\Sigma_{g,0}$ with DSD1 and DSD2. C and D are found using linear regression. The resulting C and D in different $\Sigma_{g,0}$ cases with either DSD1 or DSD2 are listed in Table 2 in Zhang et al. (2018b). Figure 2.13 show δ - 1 for all $\Sigma_{g,0}$ cases with DSD1 and DSD2. The best fits are also plotted for each panel. Note that open symbols are not involved in the fitting

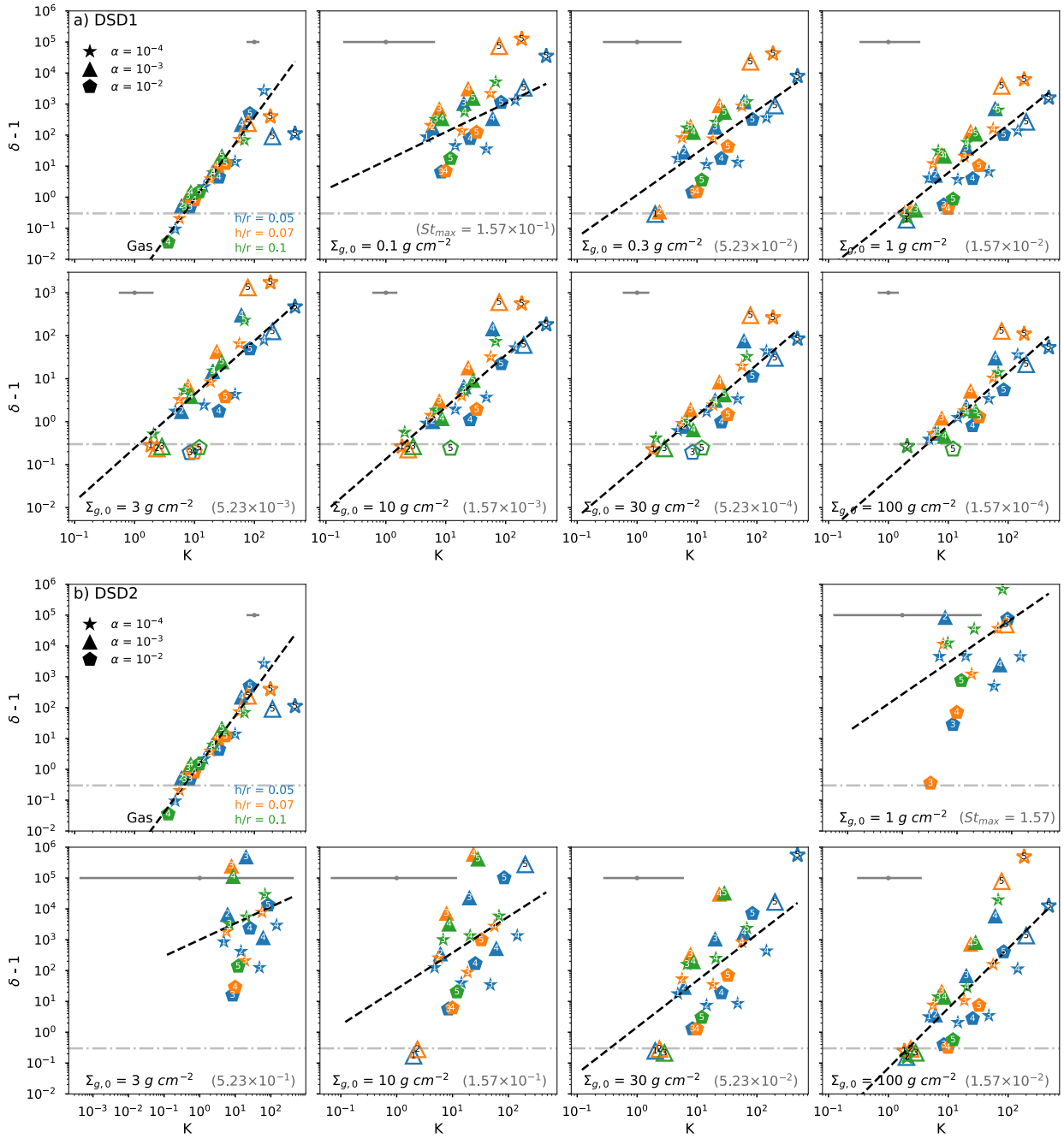

Figure 2.13: Similar to Figure 2.12 but for fits of the gap depths minus one (δ - 1) vs. K. The panel a) adopts the dust size distribution of DSD1 $\{s_{max},\ p\} = \{0.1\ mm, -3.5\}$ while the panel b) adopts DSD2 $\{s_{max},\ p\} = \{1\ cm, -2.5\}$. The best-fit parameters are listed in Table 2 in Zhang et al. (2018b).

since these gaps are eccentric and their depths do not follow the trend for other gaps. Clearly, with the Stokes number increasing, the fitting becomes worse. This is expected since particles with

larger Stokes numbers drift faster and the gap profile becomes more irregular.

(5) The uncertainty of the fittings. We apply the same measure to calculate the uncertainty of the gap width/depth fitting as that of $\Delta\delta v_{rot}$-K_{v_r} relation mentioned in §2.4.1. That is, we measure the horizontal offset (in $log_{10}(K')$ or $log_{10}(K)$) between each point and the fitting line at each sets of dust configurations and also the gas surface density. From the distribution of the offset, the left side error is estimated by the 15.9 percentile of the distribution and the right side error is 84.1 percentile of the distribution. These uncertainties are summarized in Table 1 in Zhang et al. (2018b) and 2 in Zhang et al. (2018b) and marked in grey color at the top of each panel in Figure 2.12 and 2.13. For widths that are larger than 0.15, the uncertainties for the fittings are less than a factor of two for K' (or q) when $St \lesssim 5 \times 10^{-3}$ and around a factor of three for K' (or q) when $5 \times 10^{-3} < St \lesssim 5 \times 10^{-2}$. When $St \gtrsim 10^{-1}$, particles drift to the central star quickly and most of the gaps only have a single ring left at the outer disk so that $\Delta \sim 1$ and the uncertainties for K' at a given Δ is very large. For these cases, we cannot use the gap width to estimate the planet mass.

Finally, we summarize all the fits for the width and depth in Figure 2.14. In the Appendix, we provide gap depth δ and width Δ of our whole grid of models. In spite of the dramatically different dust size distributions between DSD1 and DSD2, the fits for DSD1 are quite close to fits for DSD2 as long as the Stokes number for the maximum-size particles is the same (e.g. red solid and dot-dashed lines). This is reasonable since only the Stokes number matters for the dust dynamics, and DSD1 have a similar opacity as DSD2. For 1 mm observations, the opacity is roughly a constant when $s_{max} \lesssim 1$ cm (the opacity is slightly higher when $s_{max} \sim 1$mm, see Birnstiel et al. 2018). Thus, different disks with different surface densities ($\Sigma_{g,0}$) and different dust size distributions have the same intensity profiles as long as their Stokes numbers for maximum-size particles (where most of the dust mass is) are the same and $s_{max} \lesssim 1$ cm. Thus, our derived relationships can be used

in other disks with different surface densities and dust size distributions as long as the Stokes number of the maximum-size particles is in our simulated range (1.57×10^{-4} to 1.57). For disks with Stokes number smaller than 1.57×10^{-4}, their gap profiles should be similar to the disks with St=1.57×10^{-4} since dust is well coupled to the gas.

Secondary Gaps/Rings

Previous simulations have shown that a planet can introduce many gaps/rings in disks having very low viscosities (Zhu et al. 2014a; Dong et al. 2017a; Bae et al. 2017a). These gaps can be grouped into two categories: 1) two gaps adjacent to the planet that are separated by the horseshoe material (e.g. two troughs at 0.9 r_p and 1.1 r_p in Figure 2.11, also mentioned in §2.4.1), and 2) secondary shallower gaps much further away into the inner and outer disks (e.g. the gap at 0.6 r_p in Figure 2.11). The two gaps in the first category form because: a) the spiral waves, especially excited by low mass planets, need to propagate in the radial direction for some distance to steepen into spiral shocks and induce gaps (Goodman & Rafikov 2001), b) the horseshoe material has a slow relative motion with respect to the spiral shocks thus this material takes a long time to be depleted. Eventually, these two gaps may merge into one single main gap, which is studied in §2.4.2. The gaps in the second category are induced by additional spiral arms from wave interference (Bae & Zhu 2018a). Instead of disappearing, these gaps will become deeper with time in inviscid disks. Thus, they are useful to constrain the planet and disk properties (Bae & Zhu 2018c).

We label the positions of all these additional gaps and rings in Figure 2.15. We find that the positions of these rings and gaps in dust intensity radial profiles are similar to those in gas surface density profiles. Thus, we plot the positions based on the gas density profiles. It turns out that only disks with $\alpha \leq 10^{-4}$ can form noticeable multiple gaps. Thus, if we find a system with multiple

gaps induced by a single planet (e.g. AS 209 in the next section), the disk viscosity has to be small. From Figure 2.15, we can see that distance between the secondary gap and the main gap mainly depends on the disk scale height (h).

For the secondary gap at $\sim 0.5-0.7$, following our fitting procedure before, we find that the position of the secondary gap (r_{IG2}) and r_p is best fitted with

$$1-\frac{r_{IG2}}{r_p} = 2.3\, q^{0.02}(h/r)^{0.58}\alpha^{-0.01}\,. \tag{2.25}$$

This clearly shows that the position of the secondary gap is almost solely determined by the disk scale height. Thus, if the secondary gap is present, we can use its position to estimate the disk scale height (h/r). The fitting is given in Figure 2.16. The $\alpha = 10^{-5}$ cases are the AS 209 cases which will be discussed in the next section. We caution that the fitting has some scatter. Within each h/r group in Figure 2.16, the r_{IG2}/r_p depends on the planet mass. But this dependence seems to be different for different h/r groups, so that the fitting using all h/r suggests a weak dependence on the planet mass. We also note that our fit is different from the recent fit by Dong et al. (2018b) which has a $q^{-0.2}(h/r)^{1.3}$ dependence (note that their planet mass is normalized by the thermal mass). The difference may be due to: 1) The disks in Dong et al. (2018b) are thinner, where their main set of simulations uses h/r=0.03, 2) Dong et al. (2018b) fit the gap positions at different times for different simulations while we fit the gap positions at the same time in the simulations.

2.5 Planet Properties

With all the relationships derived in previous sections regarding the planet mass and gap profiles, we can now put them together to constrain the mass of potential planets in the DSHARP

disks. We use the measured radial intensity profiles from Figure 2 in Huang et al. (2018c). These profiles are derived by deprojecting the observed images to the face-on view and then averaging the intensity in the azimuthal direction. Details regarding generating the radial intensity profiles are given in Huang et al. (2018c). By using these intensity profiles, we can derive the planet mass following the flowchart given in Figure 2.17.

First, for each source, we plot the observed radial intensity profile and identify gaps that have $\Delta \geq 0.15$. As shown in Figure 2.12, $\Delta \lesssim 0.15$ have large scatter and are sensitive to the size of the convolution beam. By examining the surface density profiles in detail, we find that such narrow gaps are also very shallow and they are actually the outer one of the double gaps around the horseshoe region. Since these gaps are very shallow, the inner one does not cause enough disk surface density change to be identified as a gap. Thus, for narrow gaps with $\Delta \lesssim 0.15$, we do not use the fitting formula to derive the planet mass. Instead, we try to directly match the gap Δ with data points in Figure 2.12 by eye to get a rough planet mass estimate. For these narrow gaps, the size of the convolution beam matters. Thus, if the gap is at 10s of au, we use the widths derived in images with the $\sigma = 0.06 r_p$ beam, and if the gap is at $\sim$100 au we use the widths derived in images with the $\sigma = 0.025 r_p$ beam.

Second, we estimate the gas surface density, using the observed mm flux at the outer disk and/or some other constraints. We integrate the observed intensity from 1.1 r_{gap} to 2 r_{gap} where r_{gap} is the gap center. Using T_d derived by Equation 5.37 and the dust opacity of 0.43 $\mathrm{cm^2\,g^{-1}}$ (§2.3.3), we calculate the averaged dust surface density (Σ_d) from 1.1 to 2 r_{gap}. We have done the same exercise for all our simulations, and Figure 2.18 shows the relationship between $\Sigma_{g,0}$ and the averaged Σ_d at the outer disk for the simulations. Figure 2.18 indicates that, with a smaller gas surface density or larger particles (higher Stokes numbers), the ratio between Σ_d and $\Sigma_{g,0}$ increases

because particles with larger Stokes numbers are more easily trapped at the gap edges. We can then use Figure 2.18 to estimate $\Sigma_{g,0}$ based on the derived Σ_d from the observation, the estimated h/r, and the assumed α and planet mass. After we derive the planet mass, we will go back to this step to see if the derived planet mass is consistent with our assumed mass. Otherwise, we iterate these processes again with the new assumed planet mass. On the other hand, this estimate is prone to large errors. If we have more ways to estimate the gas surface density, such as using molecular tracers or constraints from the gravitational instability, we should adopt these constraints.

Third, with known $\Sigma_{g,0}$ and the assumed dust size distribution, we can calculate St_{max} and use the Δ-K' relationship (§2.4.2 and Table 1 in Zhang et al. (2018b)) to derive the K' parameter. Given the sensitivity limits of ALMA, we decide not to use the gap depth (δ) to estimate the K parameter. For example, two gaps with different depths, one being a factor of 10^5 deep and the other being a factor of 10^3 deep, can look similar if the S/N of the observation is 100.

Next, we need to constrain the disk scale height and the disk α parameter to break the degeneracy of K' in order to derive q. For each major gap, if there is a shallower gap at $r/r_p \sim$0.5-0.7, the shallower gap may be the secondary gap induced by the planet. The distance between the secondary gap and r_p is very sensitive to h (§2.4.2 and Equation 2.25). Thus, the presence of the secondary gap at the right radii not only makes the planet gap-opening scenario more plausible but also gives constraints on the disk scale height. If there is no secondary gap, we may need to use radiative transfer calculations or Equation 5.37 to estimate the disk temperature. The existence of the secondary gap also implies that the disk viscosity parameter $\alpha \lesssim 10^{-4}$. Without the presence of the secondary gap, the α parameter can then be constrained by the symmetry of the disk structures. If the rings/gaps are highly axisymmetric, α is likely to be larger than 10^{-4}.

Finally, we can use Equation 2.22 to calculate q and thus the planet mass. With M_p derived,

we can go back to Step 2 to estimate a more accurate gas surface density. We can also do a consistency check with the derived M_p. For example, we can check if the sub/super-Keplerian motion at the gap edge could be detected (§2.4.1, Equation 2.16), if the planet should produce large-scale asymmetries (e.g. eccentricity, vortices §2.4.2, Figure 2.8), and if the gap depth is consistent with observations (Table 2 in Zhang et al. (2018b)).

Following this procedure (Figure 2.17), we identify potential planets in the DSHARP disks (as summarized in Table 3 in Zhang et al. (2018b)) using the intensity profiles from Huang et al. (2018c). All the gaps with $\Delta \geq 0.15$ in the DSHARP sample have been carefully measured for their widths and then we use the fitting formula to estimate the planet mass based on their widths. These are shown in the upper part of Table 3 in Zhang et al. (2018b). Since each fitting line with a Stokes number comes with an uncertainty in K' (See §2.4.2, and Table 1 in Zhang et al. (2018b)), the uncertainties of the planet mass with the given α and h/r are also included in the table. For shallow gaps with $\Delta \leq 0.15$, our fitting formulae fail to fit the gap widths from the simulations and the gap width is also sensitive to the convolution beam size (Figure 2.12). Thus, we only choose those that look similar to shallow gaps in our grid of numerical simulations and compare them directly with simulations. Thus, only a subset of the shallow gaps in DSHARP sample have been fitted. They are shown in the lower part of Table 3 in Zhang et al. (2018b). Since we compare these shallow gaps with the simulations by eye, proper error estimate can not be provided. Thus, they are considered not robust and complete, and will not be included in the statistical study later. This also means that our statistical study may miss low mass planets. In the next section, we will comment on each case in detail.

Table 3 in Zhang et al. (2018b) gives the gap positions, measured gap widths, outer disk dust surface densities and estimated h/r. Using the dust-to-gas mass ratio (Figure 2.18) in simulations

with different dust size distributions (DSD1 and DSD2), the gas surface densities are also provided. If the gas surface density is above the gravitational instability (GI) limit with $Q = 1$, we use the GI limit as the gas surface density. Then with St_{max} calculated for DSD1 and DSD2, we derive K' for DSD1 and DSD2 using $\Delta - K'$ relationships. To break the degeneracy in K' to derive q, we need to know the disk viscosity. Thus, for either DSD1 or DSD2, we provide three possible planet masses with the disk α=10^{-2}, 10^{-3}, and 10^{-4}. These three masses are labeled as $M_{p,am2}$, $M_{p,am3}$, and $M_{p,am4}$, which are listed in Table 3 in Zhang et al. (2018b). The inferred planet mass is roughly twice as high if α is 10 times larger. This is because $K' = q(h/r)^{-0.18}\alpha^{-0.31}$, so that $q \propto \alpha^{0.31}$ with a given K' and h/r. As shown in Table 3 in Zhang et al. (2018b), many gaps (especially having low $\Sigma_{g,0}$) cannot be fit using DSD2 dust size distribution. This is because the Stokes number for dust in DSD2 is very large, so that particles in the inner disk quickly drift to the central star forming a cavity with a single ring at the gap edge. This is consistent with the conclusion in Dullemond et al. (2018) that large particles (cm-sized) are not preferred in the DSHARP disks.

As can be seen from Equation 6.13 and Table 3 in Zhang et al. (2018b), the Stokes number estimated from DSD1 and DSD2 can differ by three orders of magnitude. DSD1 with s_{max} = 0.1 mm and DSD2 with s_{max} = 1 cm can be seen as two extreme cases. Dust with $s_{max} < 0.1$ mm should have similar profiles as DSD1 since 0.1 mm particles already couple with the gas well in the sample. Dust with s_{max} = 1 cm already drifts very fast and we can hardly find a mass solution for most of our disks. To cover a more comprehensive parameter space, we add a new set of planet masses estimated assuming s_{max} = 1 mm ("1 mm" hereafter). The estimated initial gas density $\Sigma_{g,0}$ are used between the values of DSD1 and DSD2. Holding $\Sigma_{g,0}$ constant, St_{max} for "1 mm" is 10 times larger than that of the DSD1 or 10 times smaller for DSD2. Thus, the Stokes number of the "1 mm" models are in between those two extremes. The gap width-K' relation of the "1

mm" models are taken from the corresponding St_{max} fits in DSD1. The justification is that only the Stokes number matters regarding the gap width, as discussed at the end of §2.4.2 and demonstrated in Figure 2.14. The estimated $\Sigma_{g,0}$, St_{max}, three planet masses given $\alpha = 10^{-4}, 10^{-3}, 10^{-2}$ and their uncertainties are all given in Table 3 in Zhang et al. (2018b) in the order of DSD1, "1 mm" and DSD2 (ascending s_{max}). Among the nine planet masses estimated for each source, we prefer $M_{p,am3}$ with DSD1 size distribution. The main reason that $\alpha = 10^{-3}$ is preferred is that most rings of the DSHARP sample do not show significant asymmetry, indicating that $\alpha \gtrsim 10^{-3}$. On the other hand, if the gaps are shallow, low mass planets in $\alpha = 10^{-4}$ disks can also produce axisymmetric gaps/rings.

2.5.1 Comments on Individual Sources

AS 209

AS 209 is a system with many gaps. Fedele et al. (2018) found two gaps at 62 au and 103 au and they proposed that a 0.7 M_{Saturn} planet at ∼103 au can explain both gaps. Huang et al. (2018c) and Guzmán et al. (2018) identified many gaps in this system including dark annuli at 9, 24, 35, 61, 90, 105 and 137 au. Following our procedure (Figure 2.17), we first derive the K' parameter for the main gap at ∼100 au. The narrow width of the gap suggests that it is a sub-Jupiter mass planet. Then we find that the gap at r = 61 au is shallower than the main gap, and it is at 0.5-0.7 r_p. Thus, we treat it as a secondary gap induced by the planet. The distance between the secondary and primary gaps suggests that $h/r \sim 0.05 - 0.06$ (Equation 2.25 and Figure 2.16). This h/r is slightly smaller than the simple estimate with Equation 5.37, but the faint emission at the near-IR scattered light image (Avenhaus et al. 2018a) may support that the disk is indeed thin (another

possibility is that the disk is significantly less flared.). With this h/r and K', we derive that the 100 au planet has a mass of $q = 3 \times 10^{-4}$ in a $\alpha = 10^{-4}$ disk or $q = 10^{-4}$ in a $\alpha = 10^{-5}$ disk. Motivated by the smaller gaps at 24 and 35 au from the DSHARP data (Guzmán et al. 2018), we carry out several additional simulations extending the range of α to 10^{-5}. Since a smaller α is used, we double the numerical resolution for all simulations that are constructed for AS 209. Surprisingly, the $q = 10^{-4}$ planet in a $\alpha = 10^{-5}$ and $h/r = 0.05$ disk can explain all 5 gaps at 24, 35, 62, 90 and 105 au (Figure 2.19). Although we assume that there is another planet at 9 au to explain the 9 au gap, it is possible that the 9 au gap is also produced by the main planet at 99 au, considering that our simulation domain does not extend to 9 au. We want to emphasize that our simulation with one planet at 99 au not only matches the primary gap around 100 au, but also matches the position and amplitude of secondary (61 au), tertiary (35 au) and even the fourth (24 au) inner gaps. This makes AS 209 the most plausible case that there is indeed a planet within the 100 au gap.

Although the above model reproduces the positions and intensities of gaps and rings very well, its synthetic image (the upper middle panel in Figure 2.19) shows a noticeable horseshoe region and some degree of asymmetry in the rings. Such asymmetry disappears when $\alpha \gtrsim 10^{-3}$. On the other hand, the presence of the tertiary and the forth inner gaps requires a small α. Thus, we carry out a simulation with a radially varying α ($\alpha = 3 \times 10^{-4}(r/r_p)^2$). This model reproduces the 2-D intensity maps better, as shown in the right panels of Figure 2.19 and also presented in Guzmán et al. (2018). Such a radially varying α disk has also been suggested to explain HD 163296 (Liu et al. 2018). If these models are correct, they suggest that α in protoplanetary disks is not a constant throughout, supporting the idea that different accretion mechanisms are operating at different disk regions (Turner et al. 2014).

Dullemond et al. (2018) constrained that the α/St for the ring at 74 au has a range roughly

between 0.03 and 0.7 from the limits of pressure bump width argument (See Table 3 therein). Such constraint is derived using the particle trapping model and does not depend on the origin of the ring. In our $\alpha = 10^{-5}$ model, $\alpha/St_{max} \approx 0.003$ and in our α varying model, $\alpha/St_{max} \approx 0.02$. The actual characteristic St can be smaller, considering that the St_{max} here is the maximum Stokes number at the position of the planet in the initial condition (t_0). Since for both models $n(s) \propto s^{-3.5}$, 50% of the dust mass in t_0 at r_p have $St \leq 0.25\ St_{max}$. Adopting these values, their $\alpha/St \approx 0.012$ and 0.08, respectively. Thus, the $\alpha = 10^{-5}$ model is off the lower limit of α/St by a factor of 3, whereas the α varying model is safely above the lower limit. Considering that the turbulent diffusion with the small α ($\alpha = 10^{-5}$) in our simulations may have not reached to a steady state, we conclude that these models are consistent with Dullemond et al. (2018).

Elias 24

Elias 24 (Cieza et al. 2017) is another system that looks very similar to our planet-disk interaction simulations. It has a deep gap at 57 au, a narrow ring at 77 au, and an extended outer disk (Huang et al. 2018c). The narrowness of the ring is suggestive of particle trapping at the gap edge. Dipierro et al. (2018) estimated that there is a 0.7 M_J mass planet at 57 au, while Cieza et al. (2017) suggested that the mass of the 57 au planet is 1-8 M_J. Our estimate is roughly consistent with these previous estimates. The planet mass is $\sim 0.8\ M_J$ with $\alpha = 10^{-3}$ and DSD1. On the other hand, the clear signature of dust pile-up at the outer gap edge may indicate that dust is larger than 0.1 mm as used in DSD1. If dust particles in Elias 24 are larger than 0.1 mm, the planet mass can be lower than our estimates. Based on our grid of simulations, we run an additional simulation with $\alpha = 5 \times 10^{-4}$, $h/r = 0.07$ and $M_p = 0.16\ M_J (q = 0.2\ M_J/M_*)$. We put the single planet at the 57 au gap and the result is shown in Figure 2.20. The dust distribution is $n(s) \propto s^{-3.5}$, s_{max}=

2 mm, and initial gas surface density $\Sigma_{g,0} = 15$ g cm^{-2}, hence $St_{max} = 2.09 \times 10^{-2}$. Dullemond et al. (2018) estimated that the α/St is between 0.077 to 0.66 at the 77 au bright ring. Our estimated $\alpha/St_{max} = 2.39 \times 10^{-2}$ is roughly consistent with their lower limit considering that 50% of the dust mass has $\alpha/St > 0.096$ under the dust size distribution $p = -3.5$.

Elias 27

The spiral arms detected in Elias 27 (Pérez et al. 2016) suggest that the disk may be undergoing gravitational instability or there is a massive companion at the outer disk (Meru et al. 2017). Besides the spirals, there is a shallow annular gap at 70 au (Huang et al. 2018d). If we follow our procedure to fit this gap, the planet mass is 0.06 M_J using $\alpha = 10^{-3}$ and DSD1. Such a low mass planet can not induce the large-scale spirals as observed (Zhu et al. 2015a). On the other hand, detecting this shallow gap means that if there are massive companions in the system within 200 au (e.g. with masses larger than 0.06 M_J), we should be able to see the induced gaps at the mm continuum images. The lack of deep gaps suggests that there are no massive companions in this disk within 200 au. The spirals must be induced by a massive companion outside 200 au or by some other mechanisms (e.g. GI).

GW Lup

GW Lup has two narrow gaps at 74 and 103 au. The former gap is barely above $\Delta = 0.15$ and the latter is extremely narrow with $\Delta \lesssim 0.15$. We decide to only fit the 74 au gap since the 103 au gap is too shallow to fit with any of our models. To produce the 74 au gap, the planet mass must be very small (~ 0.03 M_J or 10 $M_\oplus$). If both 74 and 103 au gaps are part of a wide gap separated by the horseshoe region, the planet will be at $\sim$ 85 au with $M_{p,am3}$ = 0.36 M_J or $M_{p,am4}$ = 0.18

M_J. The K parameter (Equation 2.14) is thus ~ 11 and the gaseous gap depth δ is ~ 2, which is roughly consistent with the observations (Huang et al. 2018c). Thus, this more massive planet solution remains a possibility.

HD 142666

HD 142666 has several shallow dark annuli at 16, 36, and 55 au (Huang et al. 2018c). The outer two dark annuli (36 and 55 au) as identified in Huang et al. (2018c) have widths of 0.05 and 0.04 by our definition, less than the minimum width measured in our models. Thus, we do not fit those two gaps either. We only fit the 16 au gap, and it suggests that $M_{p,am3}$ is 0.3 M_J with DSD1 and 0.2 M_J with DSD2.

HD 143006

HD 143006 has two wide gaps at r = 22 au and r = 51 au (Pérez et al. 2018). The gap at r = 22 au has the widest relative width (Δ) in all DSHARP disks, which also leads to the highest inferred planet mass with $M_{p,am4} = 10\,M_J$ and $M_{p,am3} = 20\,M_J$. Both submm continuum observations (Pérez et al. 2018) and the near-IR scattered light observations (Benisty et al. 2018) have suggested that the inner disk inside 10 au is misaligned with the outer disk. If such misalignment is caused by a planet on an inclined orbit, the planet mass needs to be larger than 2 M_J in an $\alpha = 10^{-3}$ disk (Zhu 2018), which is consistent with the high planet mass derived from fitting the gap profile here. With such a massive planet predicted, HD 143006 is a prime target to look for exoplanets with direct imaging techniques.

The outer gap at 51 au can be explained by a sub-Jovian planet in the disk. The 51 au gap also has an interesting arc feature at the outer edge, which implies that the disk viscosity may be low

($\alpha \lesssim 10^{-4}$) and $M_{p,am4}$ are preferred in this system.

Note that such high inferred planet-stellar mass ratio at 22 au exceeds the largest q ($3\,M_J/M_*$) in our grid of simulations. This brings more uncertainties to the estimated planet mass. Nevertheless, we believe that our extrapolation of Equation 2.22 to $q = 0.01$ is justifiable since the dust is well coupled to the gas due to the small Stokes number under DSD1, and the previous study with a grid of much higher q (Fung et al. 2014a) showed that the relation between gaseous gap properties and the planet mass can extend to q=0.01.

HD 163296

HD 163296 is another system with multiple gaps. The DSHARP observations (Huang et al. 2018c; Isella et al. 2018) reveal 4 gaps at 10 au, 48 au, 86 au and 145 au. Based on the gap widths, we estimate that the planets at 10 au, 48 au, and 86 au have masses of 0.71, 2.18, 0.14 M_J in an $\alpha = 10^{-3}$ disk with DSD1 dust. If the disk $\alpha = 10^{-4}$, the planet masses are 0.35, 1.07, 0.07 M_J with DSD1 dust. Except the 10 au gap, the rest gaps have been revealed by previous ALMA observations (Isella et al. 2016). Isella et al. (2016) estimated that the 48 au planet has a mass between 0.5 and 2 M_J and the 86 au planet has a mass between 0.05 and 0.3 M_J, which are roughly consistent with our estimate. Our derived gas surface density ($\Sigma_{g,0}$) of 3-30 g cm^{-2} at 48 au and 86 au is also consistent with $\sim$ 10 g cm^{-2} derived in Isella et al. (2016). Teague et al. (2018a) studied the deviation from the Keplerian velocity profile as measured from CO line emission and inferred that the planet at 86 au has a mass around M_J, which is larger than our derived $M_{p,am2}$ by a factor of 3. However, the planet mass assuming $\alpha = 10^{-2}$ and 1 mm sized particles including 1σ error can reach to $\sim 0.6\,M_J$. Considering that the uncertainty is a factor of two in Teague et al. and also the uncertainties in our adopted gas density, dust size distribution and disk viscosity, these results

are still consistent. Liu et al. (2018) has adopted a disk with an increasing α from 10^{-4} at 48 au to 10^{-2} at 86 au, and estimated that planets at 48 au and 86 au have masses of 0.46 and 0.46 M_J (their same values were purely a coincidence). This is consistent with our estimate if we adopt the same α values.

An asymmetric structure is discovered at the outer edge of the 48 au gap (Isella et al. 2018), implying that the disk viscosity $\alpha \lesssim 10^{-4}$. Thus, the $M_{p,am4}$ may be more representative for the 48 au gap.

SR 4

SR 4 has a wide single gap at 11 au. We estimate its mass $M_{p,am3}$ = 2.16 M_J with DSD1 and 0.77 M_J with DSD2. The gap is also quite deep, consistent with the presence of a Jovian mass planet. Thus, SR 4 may be an interesting source to follow up to study its gas kinematics or detect the potential planet with direct imaging observations.

DoAr 25, Elias 20, IM Lup, RU Lup, Sz 114 and Sz 129

These six systems have shallow gaps with $\Delta < 0.15$. Thus, we compare the observed gap widths directly with those derived in numerical simulations (Figure 2.12). The inferred planet mass is less than 0.1 M_J for all these gaps. The smallest planet is 0.02 M_J or 6.4 $M_\oplus$. Note also that IM Lup features intricate spiral arms inside the gap fit at 117 au (Huang et al. 2018d).

On the other hand, DoAr 25, Elias 20, and RU Lup have adjacent double gaps, similar to GW Lup. If we treat these double gaps as one main gap which is separated by the horseshoe material, we can derive the planet mass under this scenario. To explain both the 98 and 125 au gaps in DoAr 25 using a single planet, the planet is at 111 au with $M_{p,am3} = 0.73\,M_J$ or $M_{p,am4} = 0.36\,M_J$.

To explain the 25 and 33 au gaps in Elias 20, the planet is at 29 au with $M_{p,am3} = 0.57 M_J$ or $M_{p,am4} = 0.28 M_J$. To explain the 21 and 29 au gaps in RU Lup, the planet is at 24 au with $M_{p,am3} = 1.18 M_J$ or $M_{p,am4} = 0.58 M_J$. To make the gaps as shallow as possible, we assume DSD1 dust distribution here. Even so, the corresponding gap depth δ is larger than 2 with these planet masses. By comparing with the intensity profiles in Huang et al. (2018c), DoAr 25 has gaps that could be deep enough, while the gaps in both Elias 20 and RU Lup are too shallow and this scenario seems unlikely.

2.5.2 Young Planet Population

Now, we can put these potential young planets in the exoplanet mass-semimajor axis diagram (Figure 8.4). Considering most of these systems do not show asymmetric structures, we pick the planet mass that is derived using $\alpha = 10^{-3}$ and DSD1. The mass errorbar is chosen as the minimum and maximum planet mass among all the nine masses that have constrained values in Table 3 in Zhang et al. (2018b) (columns 11 to 13), adding up the additional uncertainty due to the fitting from the column 14 of the table. Thus, this is a comprehensive estimate of the error covering different disk α (from 10^{-4} to 10^{-2}), particle sizes (s_{max} from 0.1 mm to 1 cm), and the errors of the fitting. The planet masses that are from very narrow gaps in the lower part of Table 3 in Zhang et al. (2018b) (the ones with brackets) are labeled with light circles, and we do not count them in the statistical study below since the narrowness of the gaps leads to large uncertainties in the mass estimate. Bae et al. (2018) has collected young planets from previous disk observations in the literature (most are Herbig Ae/Be stars). Here, we only consider the DSHARP sample (Andrews et al. 2018a). Although this sample is more homogeneous with similar observation requirements, it

is still slightly biased towards bright disks and thus high accretion rate disks around more massive stars.

Since the DSHARP observations have resolutions of $\sim$ 3-5 au and most disks only extend to 200 au in the dust continuum images, the planet population we can probe lies between 5 and 200 au. The probed mass limit is around the Neptune mass in the outer disk and a little bit higher (a factor of $\sim$2) in the inner disk ($<$10 au, with a larger beam size). If there are planet-induced gaps in the disk, we should always detect them at almost all the viewing angles unless the disk is very edge on. Thus, the probability that we are missing gap-induced planets due to the observational bias is small. Under this circumstance, we can simply estimate the planet occurrence rate through dividing the number of planets by the total number of disks observed. Although DSHARP observes 20 disks, 2 are certainly in multiple star systems (Kurtovic et al. 2018). Since we only focus on single star systems here, the total number of disks is 18.

Since the gaps in protoplanetary disks may not be due to young planets, our derived planet occurrence rates should be considered as the upper limits. On the other hand, we may miss planets at the mass detection limit ($\sim$Neptune mass), as evidenced by that we do not include those planets that are fitted by eye and have no error estimates. Thus, the planet occurrence rates for Neptune mass planets may be higher than our estimates.

By comparing with exoplanets discovered with other methods, we find that:

First, we only have one planet that is more massive than 5 M_J. Thus, the occurrence rate for $>$5 M_J planets beyond 5-10 au is 1/18 or 6%. Wide-orbit giant planets are very rare. This is consistent with the direct imaging constraints that the occurrence rate for 5-20 M_J planets at $>$5-10 au is 1-10% (Meshkat et al. 2017a; Vigan et al. 2017a; Bowler & Nielsen 2018a).

Second, using disk features, we may be probing a planet population that is not accessible by

other planet searching techniques. These are Neptune to Jupiter mass planets beyond 10 au. Young planetary systems may harbor Uranus and Neptune mass planets beyond 10 au similar to our Solar System. The occurrence rate for $0.2\ M_J \lesssim M_p \lesssim 5\ M_J$ planets beyond 5-10 au is 8/18 or 44%, and the occurrence rate for all the planets more massive than Neptune and less than 5 M_J beyond 5-10 au is 10/18 or 56%. These rates are comparable to the 31% giant planet ($> 0.1\ M_J$) occurrence rates (Clanton & Gaudi 2014) within 10^4 days (<9 au for solar mass stars). If we consider that our derived planets spread from 5 au to 200 au, the occurrence rate per decade of semi-major axis is 27% and 35%, respectively. This rate is comparable to the occurrence rate (20%) for giant planets ($> 0.1\ M_J$) with period between 10^3 and 10^4 days. Thus, giant planet distribution may be flat beyond several au to $\sim$ 100 au.

Finally, the planet's mass distribution is almost flat from Neptune to Jupiter mass. We have $\sim$ 5 planets with $0.03\ M_J \lesssim M_p \lesssim 0.3\ M_J$, and 6 planets with $0.3\ M_J \lesssim M_p \lesssim 3\ M_J$.

We bin the planet masses in decade in part due to the number of sources available and in part because of the uncertainties of the mass range for each planet (see Figure 8.4). The uncertainties for most of the planet masses are around a factor of 10. We want to emphasize that the derived planet mass has larger uncertainties due to the unknown disk α and dust size distribution. On the other hand, as long as all these disks have similar α values among each other, the derived planet mass will systematically shift up and down with the same fraction (e.g. decreasing the α value by a factor of 10 will decreasing the planet mass by a factor of two for all the planets).

2.6.1 Our Solar System and HR 8799 Analogs in Taurus

Exoplanetary systems are very diverse with systems having multiple low-mass planets within 1 au (as probed by the *Kepler* spacecraft) or systems having multiple giant planets beyond 10s of au (e.g. HR 8799). Our solar system has both terrestrial and giant planets. Are any of the DSHARP sources analogous to our Solar System when it was young? Is DSHARP capable of detecting young Solar System analog or HR 8799 analog?

To answer these questions, we embed planets in our Solar System and HR 8799 into a protoplanetary disk having a minimum mass solar nebulae surface density

$$\Sigma_g = 1700 \left(\frac{r}{au}\right)^{-1.5} \mathrm{g\,cm^{-2}}. \tag{2.26}$$

To maximize our chances to detect disk features, we use DSD2 dust size distribution (s_{max}=1 cm). The initial dust-to-gas mass ratio is 1/100. We run simulations with both $\alpha = 10^{-2}$ and 10^{-4} to explore the parameter space slightly. The mass of the HR 8799 central star is 1.47 $M_\odot$, and the four giant planets in HR 8799 are chosen as 7 M_J at 14.5 au, 7 M_J at 24 au, 7 M_J at 38 au, and 5 M_J at 68 au Marois et al. (2010). The inner and outer boundary of these simulations are 0.1 r_0 and 10 r_0, where r_0 = 10 au for two young solar system runs and r_0 = 20 au for two HR 8799 runs. The $\alpha = 10^{-4}$ run for the solar system has 1500 and 2048 grid points in the radial and θ direction, whereas the three other models have 750 and 1024 grids in the radial and θ direction. The Solar System simulation runs for $\sim$ 500 orbits at 10 au (due to the higher resolution and computational cost) and the HR 8799 simulation runs for $\sim$ 1000 orbits at 20 au. The mm intensity images are

calculated using the temperature structure from Equation 5.37 with luminosities at 1 Myr found from D'Antona & Mazzitelli (1994) given current masses. Before making the ALMA synthetic images, the dust emission for the young solar system and HR 8799 runs are convolved with a 2-D Gaussian FWHM 1.4 au and 2.8 au, respectively.

Then, we use the `CASA simobserve` task to generate synthetic observations with sensitivities and angular resolutions comparable to those of the DSHARP observations, which are shown in Figure 2.22. The angular resolutions in FWHM are equivalent to ~ 5 au in distance and are marked in the lower left corners in the figure. Each set of synthetic observations consist of 12 minutes of on-source integration time with the Cycle 5 C43-5 antenna configuration, 35 minutes on source in the C43-8 configuration, and 35 minutes on-source in the C43-9 configuration. A precipitable water vapor level of 1.0 mm is adopted throughout. The resulting synthetic visibilities are imaged in the same manner as the DSHARP sources, as described in Andrews et al. (2018a). Clearly the DSHARP observational setup is capable of detecting both our Solar System analogs and HR 8799 analogs at a distance of 140 pc away.

The four giant planets induce a wide gap in the HR 8799 analog. When the disk viscosity is high ($\alpha = 10^{-2}$), the disk has an annular ring with an inner cavity, similar to transitional disks (Espaillat et al. 2014). When the disk viscosity is low ($\alpha = 10^{-4}$), we see bright arcs. We also see bright sources at the inner disk, which are vortices at the gap edge between the adjacent pair of planets and the horseshoe region of the planets. In actual observations, we may misinterpret them as planets or circumplanetary disks. One way to distinguish these possibilities is studying if the bright sources are spatially resolved (Zhu et al. 2018). Either the planet or circumplanetary disks should be smaller than the planet's Hill radius. If the structures within the gap are spatially resolved, it is likely that they are not from the planets or the circumplanetary disks.

For the Solar System analog, when the disk viscosity is high ($\alpha = 0.01$), we can only observe the gap induced by Jupiter. When the viscosity is low ($\alpha = 10^{-4}$), the common gap induced by Jupiter and Saturn can be seen. Gap edge vortices and horseshoe regions can also be seen in this case. From the synthetic observations, we can barely see the disk features induced by Uranus and Neptune. Even by examining the radial intensity profiles, we can only see an extremely shallow dimple at the Neptune position. Thus, Uranus and Neptune in our Solar System analogs are not detectable with DSHARP. The reason we have Neptune mass planet candidates in Table 3 in Zhang et al. (2018b) and Figure 8.4 is because either the planet is further away or the central stellar mass is lower (so that q is larger and gaps are deeper).

2.6.2 Caveats

Although we seek to explain gaps with young planets, we want to point out that there are many other possible mechanisms to produce gaps and rings, such as ice lines (Zhang et al. 2015a; Okuzumi et al. 2016a), the dead zone transition (Pinilla et al. 2016), MHD zonal flows (Flock et al. 2015; Ruge et al. 2016), the secular gravitational instability (Takahashi & Inutsuka 2014), disk winds (Bai 2017; Suriano et al. 2018) and so on. On the other hand, quantitative predictions from these mechanisms are desired for the future so that we can test various ideas and understand the nature of these gaps and rings.

Another major caveat in this work is that we fit the gap profiles at 1000 planetary orbits. The gap depth and width *do* change with time (Rosotti et al. 2016a). To get a rigorous comparison between simulations and observations, we need to know when planets formed in the disk and how planets grew in time (Hammer et al. 2017), which we have little knowledge about. We can only

assume that the gap opening timescale is similar to the disk lifetime. Although 1000 orbits at $\sim$ 100 au is close to the disk lifetime, it is only 10% of the disk lifetime for a planet at 20 au. A study similar to this work but also including the gap's change with time is needed in future. On the other hand, we can do some analytical estimates on the relationship between the gap width and time. First, we do not expect that the gap profile can change dramatically over several thousand orbits if the disk has a large α (e.g. $\alpha > 10^{-3}$) and small particles (e.g. $St < 10^{-3}$). This is because, in these disks, the viscous timescale over the gap width is much shorter than 1000 planetary orbits and the gas disk has already reached the steady state. Small particles couple with the gas relatively well and their drift timescale is much longer than several thousand orbits. Dust turbulent diffusion with the large α can further smooth out dust features (Zhu et al. 2012a). Second, for particles which are marginally coupled to the gas ($St \gtrsim 10^{-2}$), they drift fast in the disk and we expect that the gap width will increase with time. As long as the gas profile is fixed (e.g. $\alpha \sim 10^{-3}$), particles will drift twice further away from the planet over twice amount of time. On the other hand, particles with twice St will drift twice further way from the planet over the same amount of time. Thus, we expect that the gap width is proportional to $St \times t$ for fast drifting particles. We have done a test for disks at different orbits and with fast drifting dusts having different Stokes numbers using the Elias 24 simulation above. We find that if the gas profile is about the same, the time t and the Stokes number St indeed play the same role in widening the gap: the gap width at $2t$ is similar to the gap width at t from particles with $2St$. However, we have not explored the full parameter space, and the results may change with some other disk parameters. Especially, if α is small, the dramatic change in the gas profile with time will complicate the issue and break the degeneracy between St and t. A detailed study requires adding the time dimension in the parameter space and is beyond the scope of this paper.

Dust evolution and feedback to the gas is ignored in our study so that we can scale the simulations. In reality, particles are trapped at the gap edges which will promote its growth. When a significant amount of dust is trapped at the gap edge, the dust-to-gas feedback can affect the gap depth and width (Yang & Zhu in prep.) or even trigger streaming instability (Youdin & Goodman 2005). A proper study with all these effects considered is difficult for 2-D numerical simulations. But it can be incorporated into 1-D dust evolutionary models.

We want to emphasize that, as shown in §4, it is straightforward to derive the planet mass assuming other dust size distributions besides DSD1 and DSD2. As shown in Figure 2.14, only the maximum Stokes number affects the gap profiles. Thus, we can calculate the Stokes number for any given dust size distribution, and then use the fits to derive the planet mass.

2.7 Conclusion

DSHARP provides a homogeneous sample of young protoplanetary disks showing a variety of substructures, e.g. rings, gaps, spirals, and small scale asymmetry (Andrews et al. 2018a). If these substructures are induced by forming young planets, they are revealing a hidden young planet population which has not been probed by direct planet searching techniques.

To explore the potential planet population that is responsible to observed features in the DSHARP disks, we carry out two-dimensional hydrodynamical simulations including dust particles to study the relationships between the gap properties and the planet mass. We systematically study a grid of 45 gas models (as in §2.3.2), with three values of α (10^{-4}, 10^{-3}, 10^{-2}), three values of h/r (0.05, 0.07, 0.10), and five values of planet mass (from $10M_{\oplus}$ to $3M_J$). For each model, we scale the dust distribution in the simulation to disks with different surface densities and different dust size

distributions. Two different dust size distributions motivated by (sub-)mm polarization measurements (DSD1: s_{max}=0.1 mm, p=-3.5) and (sub-mm) dust thermal continuum observations (DSD2: s_{max}=1 cm, p=-2.5) are considered. Overall, for each model, we generate 12 millimeter images including 7 images using the DSD1 dust size distribution and 5 images using the DSD2 dust size distribution.

- First, we study the gas structure in these 45 simulations. Overall, the gap becomes deeper with higher q, smaller h/r, and lower α. But when $q \gtrsim 3M_J$ in a low α disk, the gap edge becomes eccentric and the gap depth starts to decrease. These are all consistent with previous studies.

- We study the sub/super-Keplerian motion at the gap edges. We confirm that the deviation from the Keplerian motion is due to the gas radial pressure gradient. The distance between the sub/super-Keplerian motion peaks is roughly 4.4 times h, with a weak dependence on α and q. The amplitude of the sub/super-Keplerian motion peaks is fitted with Equation 2.16, which shows a strong dependence on h/r.

- Then, we study the mm intensity maps for all our simulations. The gap edge becomes more eccentric and off-centered with the increasing planet mass. The eccentricity and off-centered distance are provided (Figure 2.8). Large eccentricity and off-centered distance may be indications of planets in disks.

- Particle trapping in gap edge vortices and the horseshoe region are apparent in mm intensity maps for disks with $\alpha = 10^{-4}$, leading to large-scale asymmetries in the images. For some parameters, even a $33M_\oplus$ planet can lead to a factor of 100 contrast between different az-

imuthal parts of the disk. In some cases, the vortex shows up at smaller radii than the gap edge (similar to the arc structure in HD 163296).

- We derive several empirical relationships between the width/depth of the gaps in mm intensity maps and the planet/disk properties. All the fits for the width and depth are given in Table 1 in Zhang et al. (2018b) and 2 in Zhang et al. (2018b) and shown in Figure 2.14. We show that different disks with different surface densities and different dust size distributions have the same gap shape as long as their Stokes numbers for the maximum-size particles (where most of the dust mass is) are the same. Thus, our derived relationships can be used in other disks with different surface densities and dust size distributions.

- A single planet can open multiple gaps. The position of the secondary gap is fitted with Equation 2.25. We find that the position of the secondary gap is almost solely determined by the disk scale height. Thus, if the secondary gap is present, we can use its position to estimate the disk scale height (h/r).

- With all these relationships, we lay out the procedure to constrain the planet mass using gap properties (the flowchart is presented in Figure 2.17).

- Applying these steps, we identify potential planets in the DSHARP disks. We provide planet masses that are derived using three different values of α and three dust size distributions.

- We comment on the potential planets in each disk. Particularly, for AS 209, we point out that our simulation matches not only the primary gap, but also the position and amplitude of the secondary (61 au), tertiary (35 au) and even the fourth (24 au) inner gaps. This makes AS 209 the most plausible case that there is indeed a planet within the 100 au gap (also in

Guzmán et al. (2018)). The best fit model also suggests that the disk α increases with radii in AS 209, which may have implications for studying disk accretion theory.

- We make synthetic observations for HR 8799 and Solar System analogs to show that DSHARP is capable of detecting giant planets in these systems.

- We plot these potential young planets in the exoplanet mass-semimajor axis diagram (Figure 8.4). We find that the occurrence rate for $> 5\ M_J$ planets beyond 5-10 au is $\sim 6\%$, consistent with direction imaging constraints. Using disk features, we can probe a planet population which is not accessible by other planet searching techniques. These are Neptune to Jupiter mass planets beyond 10 au. The occurrence rate is $\sim 50\%$, suggesting a flat distribution beyond several au and planets with Neptune mass and above are common. On the other hand, we caution that there are large uncertainties for both the origin of these gaps and the inferred planet mass.

Appendix

The fitted gap widths and depths for all the models are listed in Table 4 in Zhang et al. (2018b) and Table 5 in Zhang et al. (2018b). Column (4) shows the gap widths/depths of the gas; Column (5-11) show the gap widths/depths of the dust emission with increasing initial gas surface density $\Sigma_{g,0}$ (decreasing Stokes number St_{max}) under dust size distribution DSD1; similarly Column (12-16) show the gap widths/depths of the dust under DSD2. All widths/depths shown in Table 4 in Zhang et al. (2018b) and 5 in Zhang et al. (2018b) are derived from the images with a Gaussian convolution $\sigma = 0.06\ r_p$ (the larger kernel), except for the bottom of Table 4 in Zhang et al. (2018b) (below the horizontal line and above the double horizontal lines) where widths are derived using σ

= 0.025 r_p (the smaller kernel). These widths with a smaller beam are listed only if the gap widths $\Delta < 0.15$ using the larger kernel (σ = 0.06 r_p). Rows below the double lines show the individual widths of the gaps whose common gap is separated into two due to the horseshoe. The value on top the bar shows the width of the inner gap (Δ_1), whereas the value under the bar shows the width of the outer gap (Δ_2).

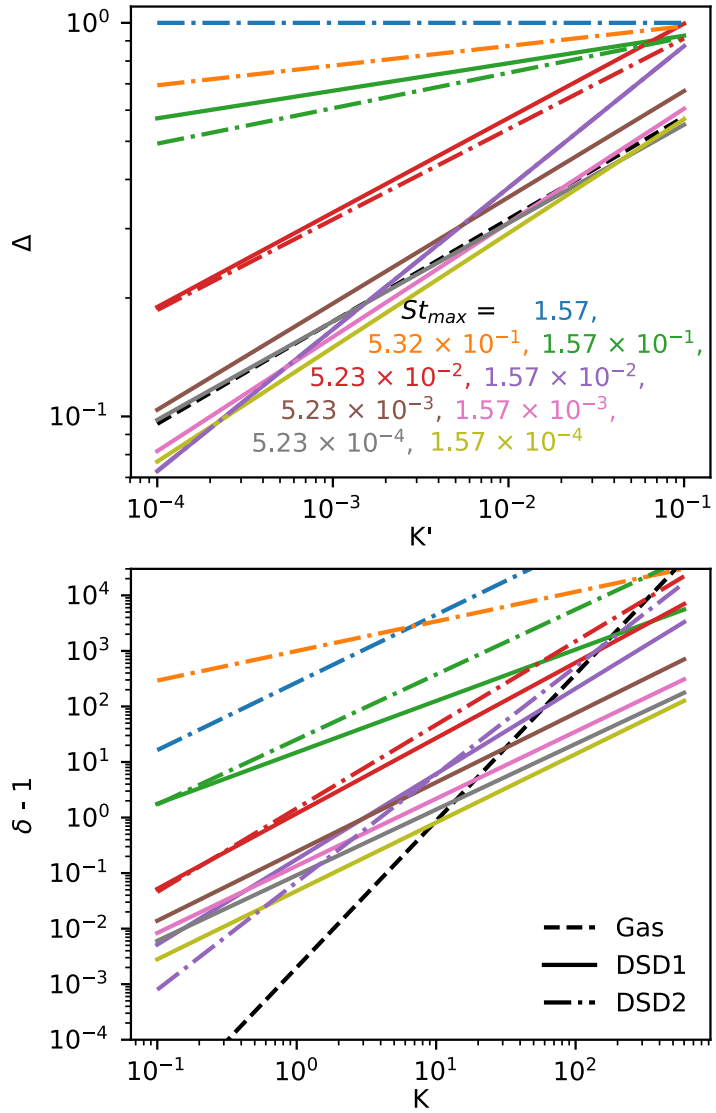

Figure 2.14: Upper panel: Δ-K'. Lower panel: (δ-1) - K. The fits for the gas surface density are shown as the black dashed lines. The fits for the dust continuum intensity are shown as the solid lines for DSD1 ($\{s_{max},\ p\}$ = $\{0.1\ mm, -3.5\}$), and the dashed-dotted lines for DSD2 ($\{1\ cm, -2.5\}$). Maximum Stokes numbers (St_{max}) under $\Sigma_{g,0}$ (DSD1, DSD2) are 1.57 (–, 1 g cm^{-2}), 5.32 × 10^{-1} (–, 3 g cm^{-2}), 1.57 × 10^{-1} (10 g cm^{-2}, 0.1 g cm^{-2}), 5.23 × 10^{-2} (30 g cm^{-2}, 0.3 g cm^{-2}), 1.57 × 10^{-2} (100 g cm^{-2}, 1 g cm^{-2}), 5.23 × 10^{-3} (3 g cm^{-2}), 1.57 × 10^{-3} (10 g cm^{-2}, –), 5.23 × 10^{-4} (30 g cm^{-2}, –), 1.57 × 10^{-4} (100 g cm^{-2}, –).

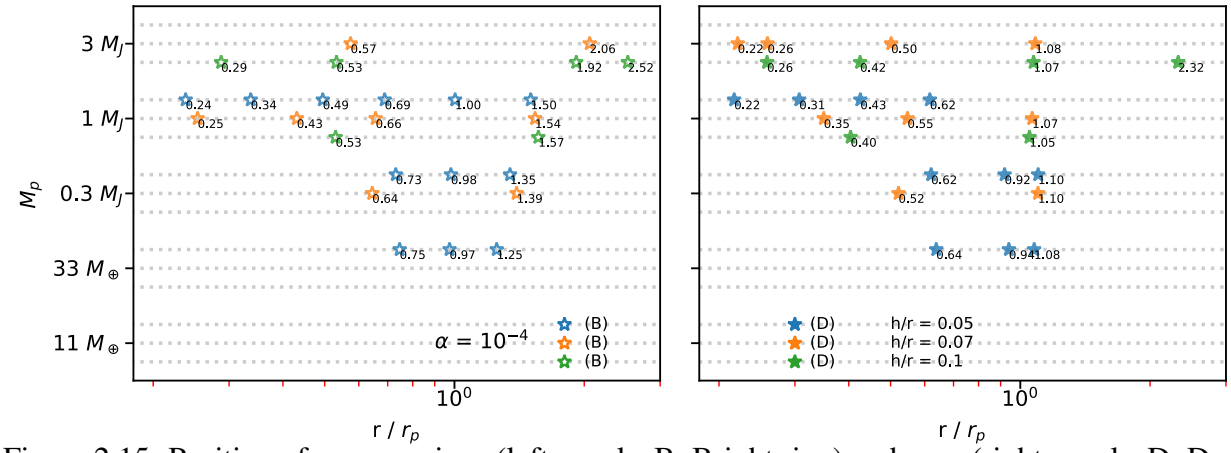

Figure 2.15: Position of gaseous rings (left panels, B: Bright ring) and gaps (right panels, D: Dark annulus) for simulations having $\alpha = 10^{-4}$. Note that, in the right panel, two cases with h/r=0.05 have two minima around $r = r_p$ because the horseshoe region splits the primary gap into two smaller gaps.

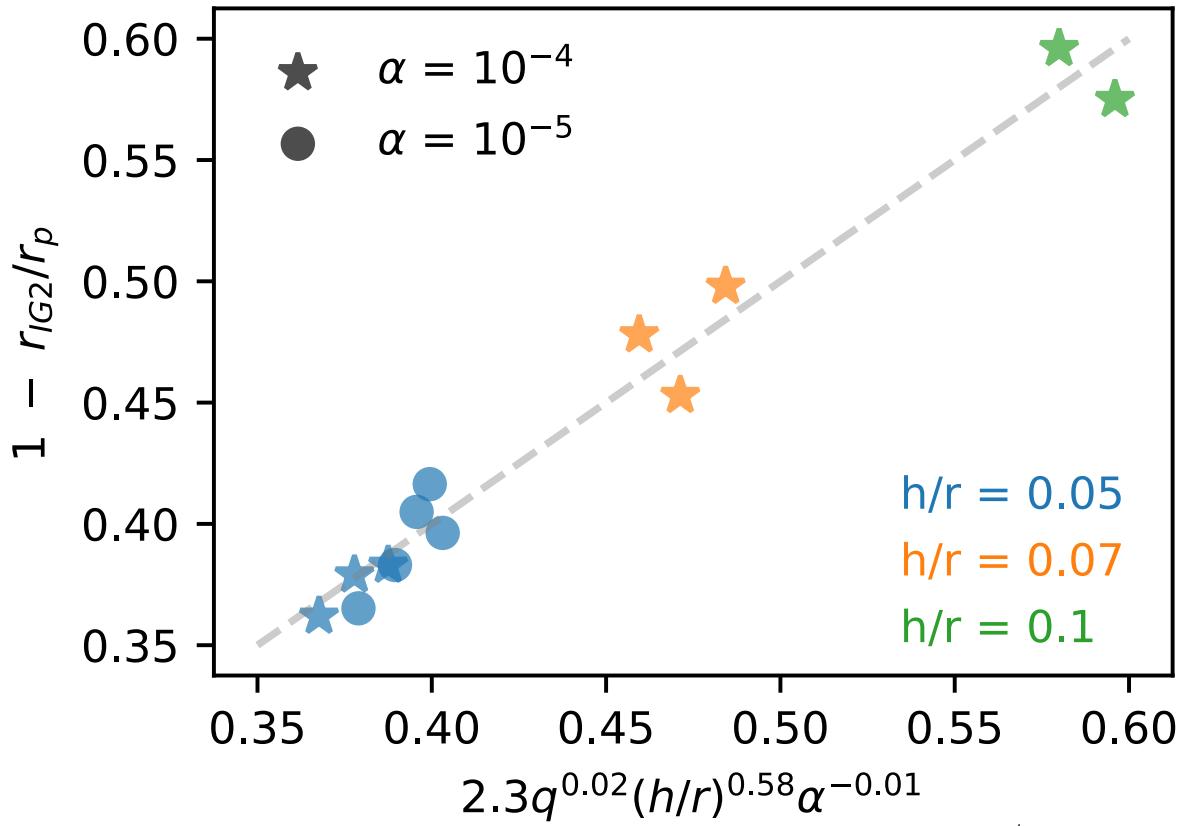

Figure 2.16: The fit of the position of secondary gaps as a function of q, h/r and α.

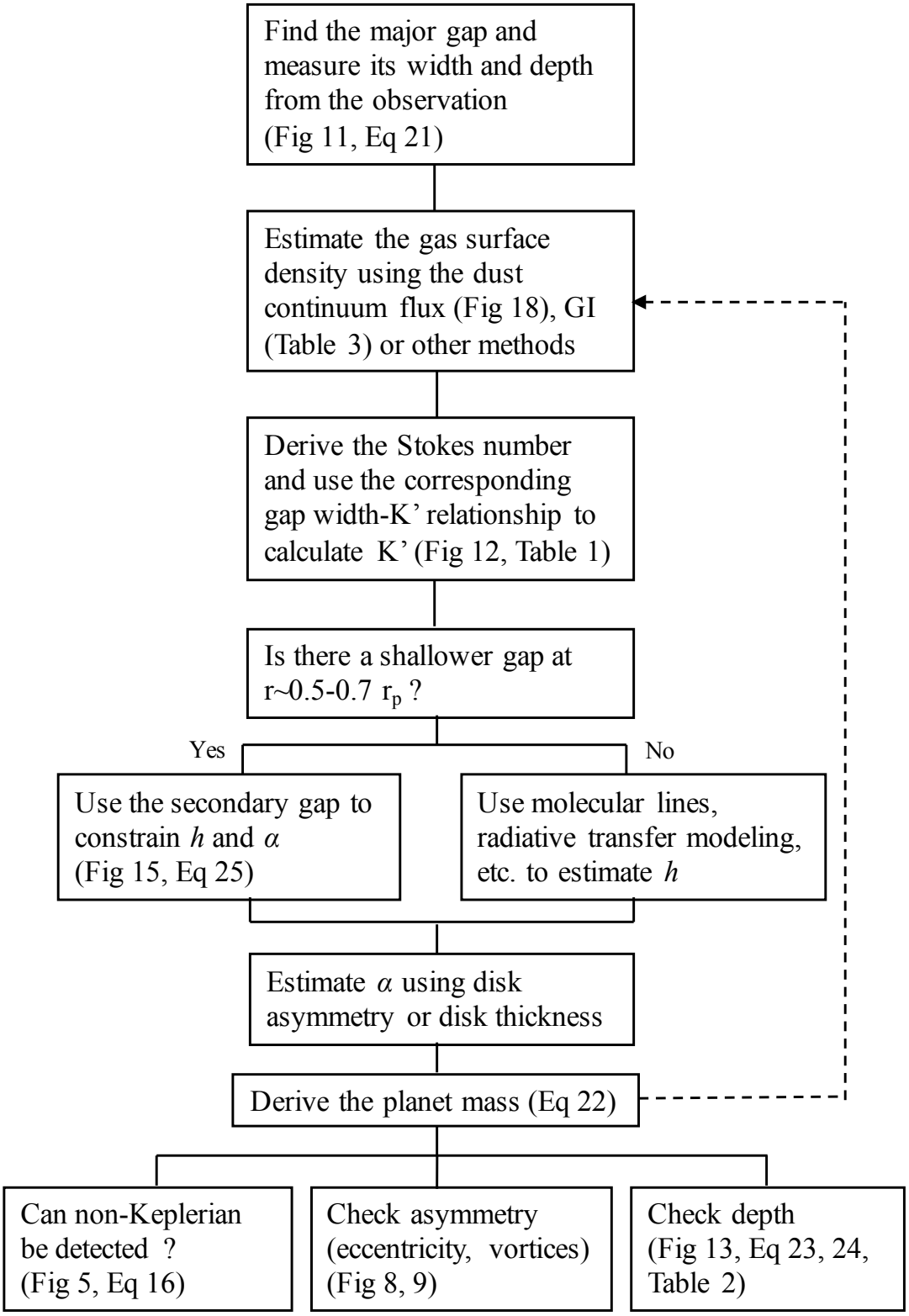

Figure 2.17: The flow chart to derive the planet mass.

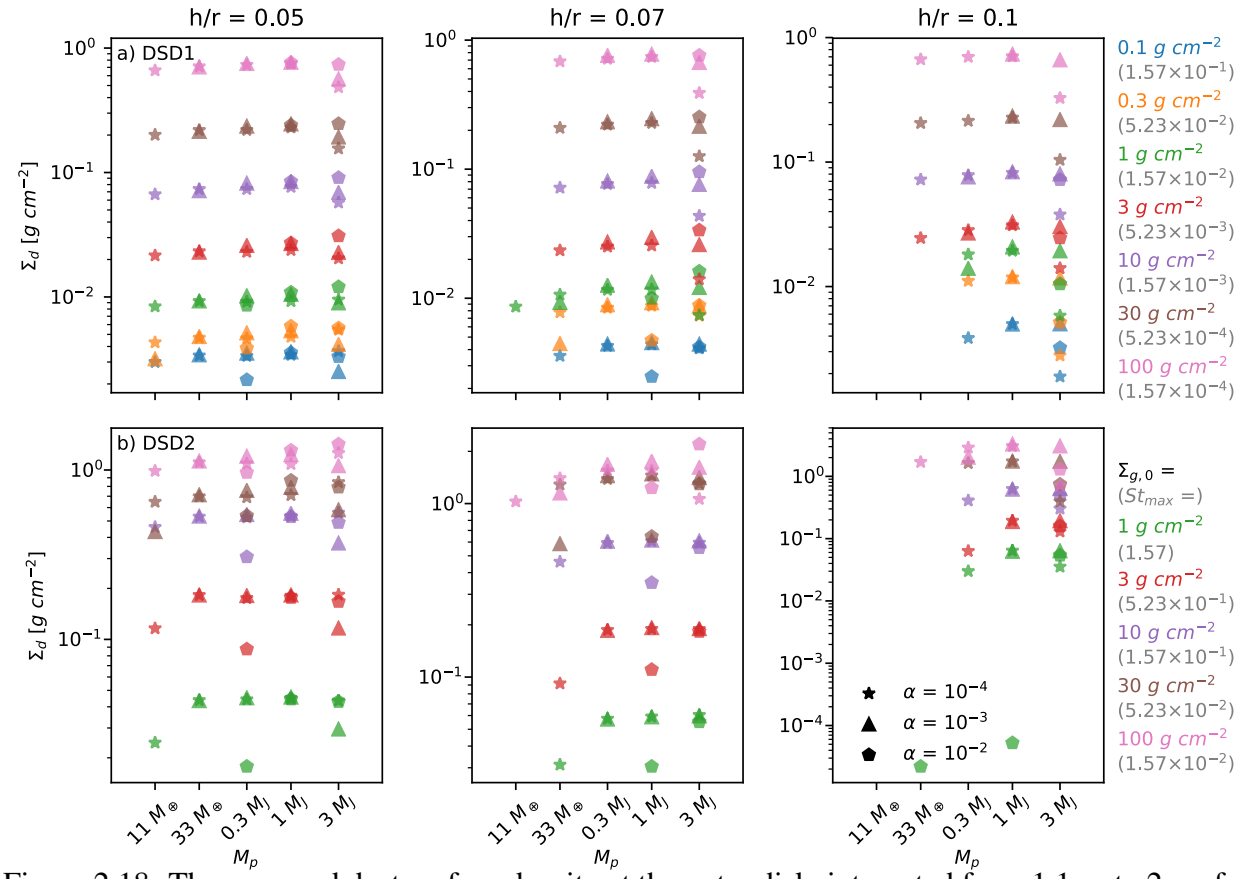

Figure 2.18: The averaged dust surface density at the outer disk, integrated from 1.1 r_p to 2 r_p, for all the models with DSD1 (upper panels) and DSD2 (lower panels).

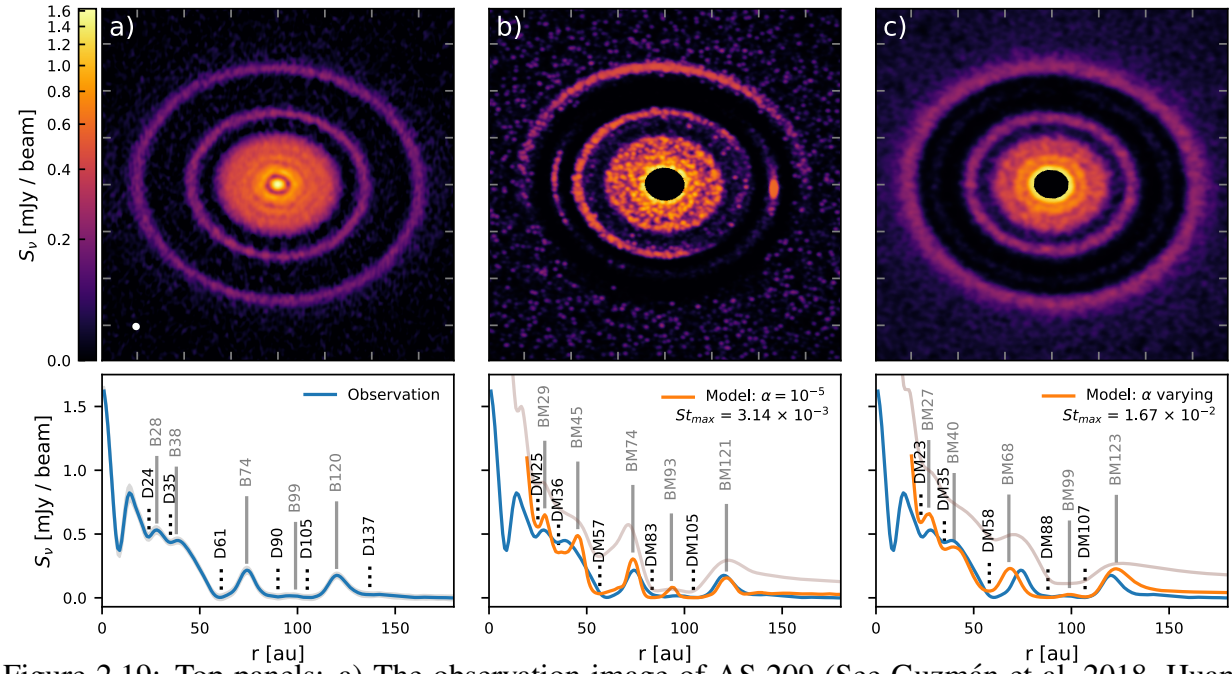

Figure 2.19: Top panels: a) The observation image of AS 209 (See Guzmán et al. 2018, Huang et al. 2018c). The distance between two ticks on the axes is 40 au. b) The synthetic image from the simulation with a single planet ($M_p/M_* = 0.1\ M_J/M_\odot$) at 99 au in a $\alpha = 10^{-5}$, $\Sigma_{g,0} = 15$ g cm^{-2}, $s_{max} = 0.3$ mm and $p = -3.5$ disk at 2000 orbits ($\sim$ 2Myrs). c) The synthetic image from the simulation with a single planet ($M_p/M_* = 0.1\ M_J/M_\odot$) at 99 au in a varying α, $\Sigma_{g,0} = 6.4$ g cm^{-2}, n(s) $\propto s^{-3.5}$, $s_{max} = 0.68$ mm disk at 1350 orbits ($\sim$ 1.35 Myrs). Bottom panels: the azimuthally-averaged intensity profiles. Panel a) is the profile from the observation, and b) and c) are the profiles from the simulations above. The "DM" and "BM" stand for Dark annulus and Bright ring in the Model, respectively; the digits coming after mark the position in au. The gas density profiles of two models are overplotted on the bottom panels in grey color in arbitrary unit.

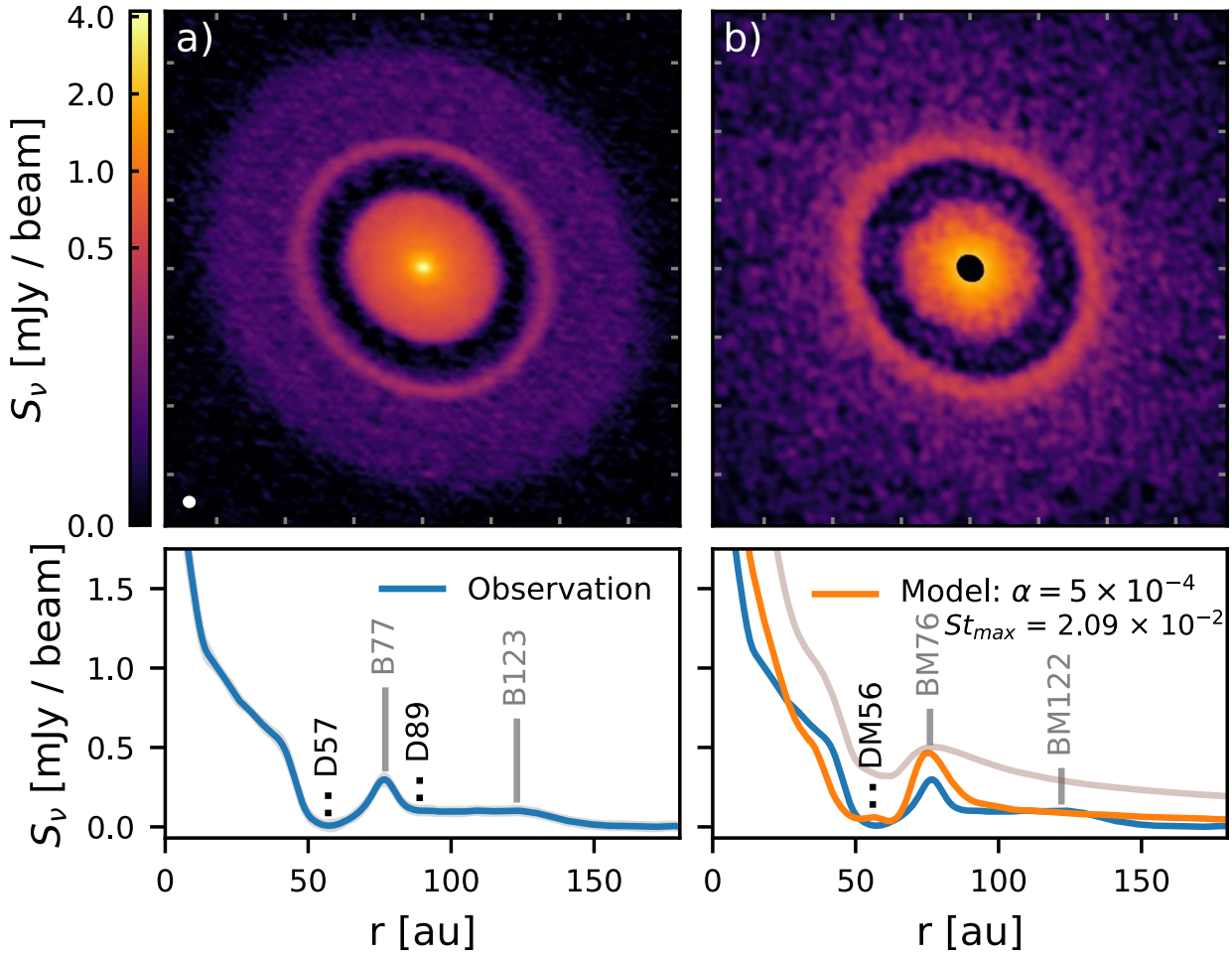

Figure 2.20: The comparison between the observation and the simulation of Elias 24. Top panels: a) Observation images of the Elias 24 (Andrews et al. 2018a) and b) our simulation with a single planet at 57 au. The model image is produced at 1000 planetary orbits, effectively 0.43 Myrs at 57 au. The distance between two ticks on the axes is 40 au. Lower panels: a) The radial profile of Elias 24 (Huang et al. 2018c), b) the radial profile of our simulation. The gas density profile in arbitrary unit is overplotted in grey color. The bright rings and dark annulus are marked the same way as in Figure 2.19.

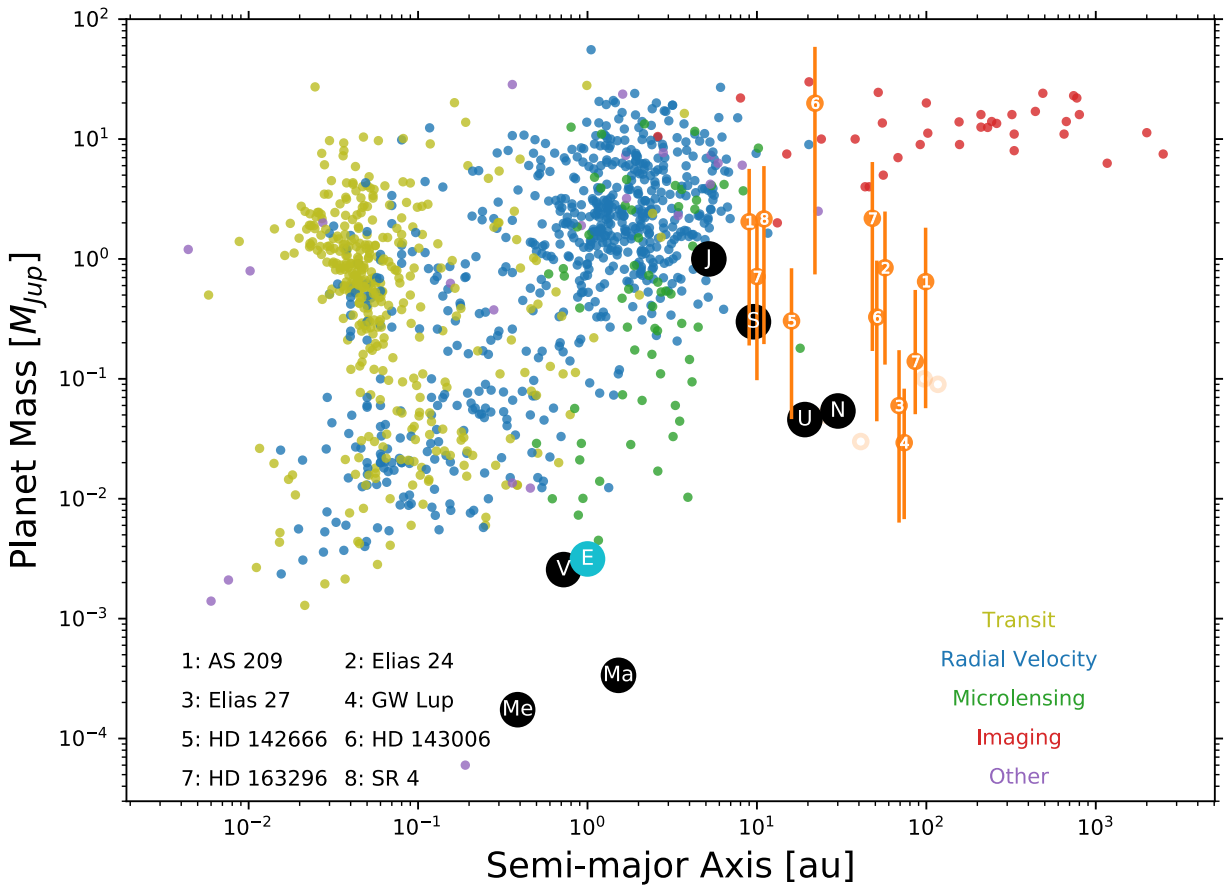

Figure 2.21: Planet mass vs. Planet semi-major axis. Orange circles with errorbars are 12 inferred planets from 8 disks listed in Table 3 in Zhang et al. (2018b) using the mass $M_{p,am3}$, DSD1. The other inferred planet masses with the assumption of $\alpha = 10^{-2}$ and 10^{-4} (DSD1, "1 mm" or DSD2) are listed in Table 3 in Zhang et al. (2018b) as $M_{p,am2}$ and $M_{p,am4}$. We can see that ALMA is sensitive to planets which are not detectable using traditional methods. Young planetary systems may harbor Uranus and Neptune mass planets beyond 10 au similar to our Solar System. For reference, small dots with different colors are exoplanets confirmed as of August, 2018 (https://exoplanetarchive.ipac.caltech.edu). Black circles with white labels are solar system planets, expect that the planet Earth is marked in light blue. Light orange open circles are planets inferred from shallow gaps (also $M_{p,am3}$, DSD1). They are not included in the statistics because we lack the knowledge of their uncertainties.

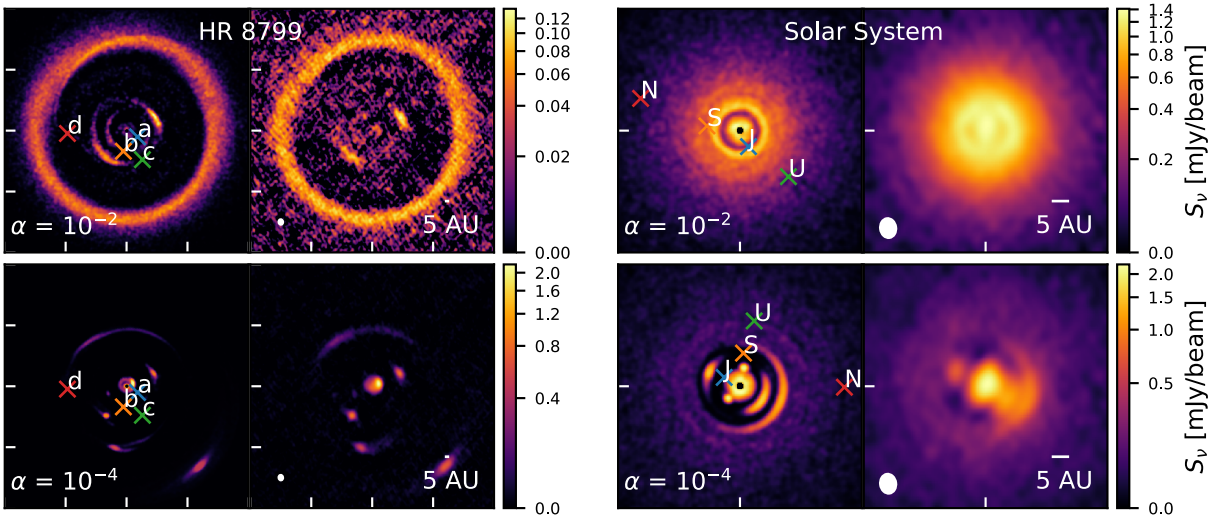

Figure 2.22: Simulation images (the left panel in each panel block) and synthetic observations (the right panel in each panel block, using the same configuration as the ALMA DSHARP observation) of HR 8799 and Solar System at a distance of 140 pc. The top panels adopt $\alpha = 10^{-2}$, while the bottom panels adopt $\alpha = 10^{-4}$. The field of view for HR 8799 images are 2" while that for Solar System is 0.5". The distance between two ticks in HR 8799 is 0.5".

CHAPTER 3 Substructures in Compact Disks of the Taurus Star-forming Region

Shangjia Zhang,[1,2], Matt Kalscheur,[3], Feng Long,[4,5], Ke Zhang,[3], Deryl E. Long,[6], Edwin A. Bergin,[7], Zhaohuan Zhu,[1,2], and Leon Trapman[3]

[1]Department of Physics and Astronomy, University of Nevada, Las Vegas, 4505 S. Maryland Pkwy, Las Vegas, NV, 89154, USA

[2]Nevada Center for Astrophysics, University of Nevada, Las Vegas, Las Vegas, NV 89154, USA

[3]Department of Astronomy, University of Wisconsin-Madison, Madison, WI 53706, USA

[4]Harvard-Smithsonian Center for Astrophysics, Cambridge, MA 02138, USA

[5]Lunar and Planetary Laboratory, University of Arizona, Tucson, AZ 85721, USA

[6]Department of Astronomy, University of Virginia, Charlottesville, VA 22904, USA

[7]Department of Astronomy, University of Michigan, Ann Arbor, MI 48109, USA

3.1 Abstract

Observations of substructure in protoplanetary disks have largely been limited to the brightest and largest disks, excluding the abundant population of compact disks which are likely sites of planet formation. Here, we reanalyze ∼0.1", 1.33 mm ALMA continuum observations of 12 compact protoplanetary disks in the Taurus star-forming region. By fitting visibilities directly, we identify substructures in 6 of the 12 compact disks. We then compare the substructures identified

in the full Taurus sample of 24 disks in single star systems and the ALMA DSHARP survey, differentiating between compact ($R_{\rm eff,90\%} < 50$ au) and extended ($R_{\rm eff,90\%} \geq 50$ au) disk sources. We find that substructures are detected at nearly all radii in both small and large disks. Tentatively, we find fewer wide gaps in intermediate-sized disks with $R_{\rm eff,90\%}$ between 30 and 90 au. We perform a series of planet-disk interaction simulations to constrain the sensitivity of our visibility-fitting approach. Under an assumption of planet-disk interaction, we use the gap widths and common disk parameters to calculate potential planet masses within the Taurus sample. We find that the young planet occurrence rate peaks near Neptune masses, similar to the DSHARP sample. For 0.01 $M_J/M_\odot \lesssim M_p/M_* \lesssim$ 0.1 $M_J/M_\odot$, the rate is 17.4±8.3%; for 0.1 $M_J/M_\odot \lesssim M_p/M_* \lesssim 1$ $M_J/M_\odot$, it is 27.8±8.3%. Both of them are consistent with microlensing surveys. For gas giants more massive than 5 M_J, the occurrence rate is 4.2±4.2%, consistent with direct imaging surveys.

3.2 Introduction

One of the most exciting discoveries in recent years is the prevalence of small-scale substructure (e.g., gaps, rings and spirals) in submillimeter/millimeter continuum emission (e.g., ALMA Partnership et al. 2015b; Zhang et al. 2016; Andrews et al. 2016b; Long et al. 2018a; Huang et al. 2018b; Cieza et al. 2021a) and scattered light observations (e.g., van Boekel et al. 2017; Avenhaus et al. 2018b; Garufi et al. 2018a) of protoplanetary disks. Substructures in disks represent a likely solution to the long-standing problems of rapid radial drift (see Whipple 1972; Weidenschilling 1997; Takeuchi & Lin 2002) and planetesimal formation (see Takeuchi & Lin 2005) inherent to the standard assumption of a smooth gas disk.

A number of physical mechanisms have been proposed to explain such substructures: MHD or

photoevaporative winds (e.g., Alexander et al. 2014; Suzuki et al. 2016b), zonal flows tied to concentrations of magnetic flux (e.g., Johansen et al. 2009b; Bai & Stone 2014; Suriano et al. 2017), a global gravitational instability driven by envelope infall that could produce large-amplitude spiral density waves (Lesur et al. 2015) or gaps and rings (e.g., Kuznetsova et al. 2022), changes in dust properties at condensation fronts (Zhang et al. 2015b; Okuzumi et al. 2016b; Pinilla et al. 2017a), and embedded planets (e.g., Dong et al. 2015b; Zhang et al. 2018c).

However, despite the ubiquity of substructures seen in recent observations and the number of proprosed mechanisms for their generation, studies have been mostly limited to large and bright disks most readily observable at current spatial resolutions (e.g., Huang et al. 2018b; Cieza et al. 2021a). The majority of nearby protoplanetary disks are both fainter and more compact (Ansdell et al. 2016a; Pascucci et al. 2016b; Cieza et al. 2019a; Williams et al. 2019). If substructure is essential to the planetesimal formation problem, and compact disks are likely sites of planet formation, we expect substructures to be a common component of compact disks as well. If they are due to planets, we can infer planet masses and make a more direct comparison to the planet population within the Solar System than is possible when planet masses are inferred from the inner region of extended disks.

In this paper, we aim to provide one of the first statistical results of substructures in compact disks by using the model-fitting approach employed in Zhang et al. (2016) and Long et al. (2020a) to revisit the subsample of smooth, compact disks observed by Long et al. (2019) in high-resolution ALMA imaging of 32 protoplanetary disks in the Taurus Molecular Cloud. In Section 3.3, we briefly describe target selection and observations of the Taurus sample. In Section 3.4, we outline our model-fitting approach, describe how substructures are characterized, and present the results of substructures identified in the subsample of compact disks that were previously classified as

smooth. We compare the frequency, location and properties of substructures found in compact and extended disks within the full Taurus sample, and the ALMA DSHARP survey of nearby disks in Ophiuchus, Lupus and Upper Sco (see Andrews et al. 2018b). In Section 3.5, we use the planet-disk interaction models of Zhang et al. (2018c) and simulated visibilities from a representative compact and extended disks to ascertain the sensitivity of our substructure detection technique to planets of various masses and separations. In Section 3.6, we then calculate potential planet masses by gap widths using the method in Zhang et al. (2018c) and present them on the planet-mass-semi-major-axis diagrams. In Section 3.7, we calculate occurrence rates and compare them to both potential planets in the DSHARP sample and the results of microlensing, direct imaging and radial velocity surveys. We summarize our findings in Section 3.8.

3.3 Observations

Observations of the full 32 disk sample were conducted as part of ALMA Cycle 4 program 2016.1.01164.S (PI: Herczeg). The goal of this observing program was to obtain a minimally-biased, high spatial resolution ($\sim$0.1") sample of the full range of disk types around solar-mass stars in the Taurus star-forming region. Disks around stars of spectral type later than M3 (to ensure sufficient S/N), known binaries with separations less than 0.5", stars with high extinction ($A_V >$ 3 mag), and disks with existing high-resolution ALMA observations were excluded from target selection. The most significant bias of the sample selection comes from the avoidance of existing high resolution observations. Since the existing high resolution observations are biased towards bright and large disks, the Taurus sample can be biased against them. The selected targets sampled a considerable range of disk millimeter brightness, though the exclusion of close binaries naturally

avoided some faint disks. Additional details on target selection, and a table of host star properties, are provided in Long et al. (2019).

Continuum emission from the selected disks were observed in late August and early September of 2017. Spectral windows at 218 and 233 GHz, both with identical 1.875 GHz bandwidths, were used. Average observing frequency was 225.5 GHz, corresponding to a wavelength of 1.33 mm. On-source integration times were between 4 and 10 minutes per target (see Table 2 of Long et al. 2019 for a complete observing log). The C40-7 antenna configuration of ALMA Cycle 4, with baselines of 21 - 3697 meters (15 – 2780 kλ), was used to carry out the observations.

The data were reduced using the Common Astronomy Software Applications (CASA) package (McMullin et al. 2007a), versions 4.7.2 and 5.1.1. Following the standard ALMA pipeline, phase adjustments were made based on the water vapor radiometer measurements. Bandpass, flux and gain calibrations were then applied for each measurement set. From the calibrated visibilities, continuum images were created with the CASA task *tclean* to perform phase and amplitude self-calibrations on targets with S/N $\gtrsim$ 30 (see Long et al. 2018a for greater detail). Data visibilities were then extracted from the self-calibrated measurement sets and final continuum images were produced with Briggs weighting in *tclean*. The typical beam size of the final continuum images was 0.14" x 0.11" and typical RMS noise was 50 μJy beam^{-1}.

3.4 Modeling and Results

Of the 32 observed disks, 12 showed evidence of substructure following the approach of Long et al. (2018a). They determined the major axis of each disk by fitting an elliptical Gaussian profile to the continuum image with CASA task *imfit*. The radial intensity profile along the major axis was

then inspected for evidence of substructure (e.g., inner cavities, extended emission at large radii, resolved rings or emission bumps) not able to be fit with a single smooth central component. Model intensity profiles were produced by combining a central Gaussian profile (or exponentially tapered power law) with additional Gaussian rings inspired by peaks (if any) in the radial profiles. Best-fit models (including the disk properties of position angle, inclination and phase center offsets) were obtained by comparing model and data visibilities, wherein model visibilities were created by a Fourier transform of the model intensity profile and matched to data visibilities with the Markov chain Monte Carlo method to compute the optimal value of free parameters. Total flux and disk radius were then estimated from the best-fit models.

We adopt here the computed disk properties (see Table 3.3 in the Appendix), but use an alternative model-fitting approach directly in the visibility domain to reexamine the subsample of 12 smooth disks around single stars for evidence of small-scale substructure not visible from the continuum images. We do not consider the 8 smooth Taurus disks in multiple star systems as they are not compatible with our fitting routine. The Taurus sample has 24 disks in single star systems. To produce a homogeneous sample for comparison between compact and extended disks (see the definition in Section 3.4.4), we also apply our fitting routine on 12 disks with substructures already found in Long et al. (2018a).

3.4.1 Model-fitting Approach

In the model-fitting approach employed here (see Pearson 1999 for a full treatment), data visibilities are reproduced via a parametric model of the source intensity distribution. Crucially, radial intensity profiles are created by fitting directly in the visibility domain. In the original approach

(Long et al. 2019), intensity profiles are retrieved from the continuum images and visibility fitting is used to optimize model profiles. By starting in the visibility domain, we utilize the full complement of spatial frequency information within the data and can recover smaller scale substructure than can be seen directly in CLEANed continuum images (Zhang et al. 2016).

Visibilities are deprojected using the inclination and position angles given in Table 3.3. For circularly symmetric disk emission, the deprojected visibilities and radial brightness distribution are related by a Hankel transform (Pearson 1999):

$$u' = (u\cos\phi - v\sin\phi) \times \cos i \tag{3.1}$$

$$v' = u\sin\phi + v\cos\phi \tag{3.2}$$

$$V(\rho) = 2\pi \int_0^\infty I_\nu(\theta)\theta J_0(2\pi\rho\theta)d\theta \tag{3.3}$$

where i and ϕ are the disk inclination and position angle, $\rho = \sqrt{u'^2 + v'^2}$ is the deprojected uv-distance in units of λ, θ is the radial angular scale from the center of the disk, and J_0 is a Bessel function of the first kind.

We model $I(\theta)$, the disk intensity distribution, with a parametric function (Equation 3.4) developed by Zhang et al. (2016). This parametric function is characterized by a series of Gaussian functions, each modulated by a sinusoidal function with a spatial frequency of ρ_i. The number of Gaussian functions is determined by the number of distinctive peaks in the disk visibility profile. A peak in visibility indicates that some particular spatial frequency contributes more than others.

Variables $\{a_0, \sigma_0, a_i, \sigma_i, \rho_i\}$ are free parameters. As such,

$$I(\theta) = \frac{a_0}{\sqrt{2\pi}\sigma_0} \exp\left(-\frac{\theta^2}{2\sigma_0^2}\right) + \sum_i \cos(2\pi\theta\rho_i) \times \frac{a_i}{\sqrt{2\pi}\sigma_i} \exp\left(-\frac{\theta^2}{2\sigma_i^2}\right). \tag{3.4}$$

We perform model-fitting with the MPFIT routine (Markwardt 2009). This routine iteratively searches for optimal values of the free parameters using the Levenberg-Marquardt technique. We provide initial guesses for the amplitudes $\{a_i\}$, widths $\{\sigma_i\}$ and central locations $\{\rho_i\}$ of the identified peaks in each visibility profile. The central location of the first peak is invariably set to zero, and we avoid attempting to fit additional Gaussians to the noisy region seen at baselines beyond $\sim$1650 kλ. For GK Tau, HO Tau, HP Tau, HQ Tau, and V836 Tau, the visibilities are very noisy beyond $\sim$1000 kλ, and no clear bump can be identified to justify additional Gaussian components, so only one Gaussian components are used. Additionally, the number of Gaussians used in a fitting can be justified by the chi-square values. In Appendix Figure 3.13, we demonstrate that two-Gaussian component models of DO Tau and DQ Tau reduce the chi-square values by an order of magnitude compared to that of one-Gaussian models. The best-fit model visibilities for the 12 compact disks in our sample are shown in columns one and three of Figure 3.1. The model-derived radial intensity profiles are shown in columns two and four. The best-fit parameters and chi-square values are listed in Appendix Table in (Zhang et al. 2023a). The reanalyses of 12 disks in Long et al. (2018a) are shown in Appendix Figure 3.15 and Table 3.4. We quantify and report the labeled features of the radial intensity profiles in the next two subsections.

3.4.2 Substructure Characterization

We identify substructures in our model radial intensity profiles by searching for local minima and maxima along the curve. Local minima, or dips, in the curve are interpreted as gaps and labeled with the prefix D. Local maxima, or bumps, are interpreted as rings and labeled with the prefix B. The number following each prefix identifies the radial location of the gap or ring (e.g., B12 refers to a ring identified at or near 12 au). This convention follows from the literature (e.g., ALMA Partnership et al. 2015b; Huang et al. 2018b).

Shallow features in the radial intensity profiles not immediately identifiable as gaps or rings, but which deviate from a smooth profile, are characterized as "plateaus" according to the criteria established in Huang et al. (2018b). Inner and outer edges are identified by visual inspection and the deviation is deemed worthy of inclusion if $\frac{1}{I_v(r)}\frac{dI_v(r)}{dr}$, the slope of the radial intensity divided by the radial intensity, exceeds -0.05 (i.e., if the radial decrease of the intensity is small). The inner and outer edges of plateau features are also labeled with the prefixes D and B, respectively.

We measure the widths and depths of gaps and rings following the approach of Huang et al. (2018b). The gap outer edge, and the ring inner edge, are defined as the radius at which model intensities most closely match $I_{mean} = 0.5(I_d + I_b)$. The gap inner edge is the radius interior to gap center with an intensity value closest to I_{mean}, and the ring outer edge the radius exterior to ring center with an intensity value closest to I_{mean}. Widths are then a simple subtraction of inner and outer edges. Gap depths are estimated by $\frac{I_d}{I_b}$, a ratio of the intensities at gap and ring centers. Widths of the plateau features are measured singly as we identify not gaps and rings, but an inner and outer plateau edge. Plateau depths are estimated by fitting a spline function to data on either side of the deviation and measuring how much it varies from the fit.

3.4.3 Model-fitting Results

Substructures are identified in 6 of the 12 compact disks (see left-hand columns of Figure 3.1), and labeled following the convention outlined in the previous subsection. The properties of these substructures are listed in Table 3.1. We note similarities to the recent results of Jennings et al. (2022b).[1] All 6 disks with substructure show at least one gap-ring pair (or plateau) interior to 45 au. BP Tau and DO Tau show evidence of plateau features between 23 and 32 au and 5 and 26 au, respectively. The midpoints of these features (27 and 15 au) could correspond to gap center in future high-resolution data. No gaps are detected interior to 9 au, but the lack of emission in the core of BP Tau hints at substructure. In general, the dearth of structure in the inner disks might be expected given the resolution of our observations ($\sim$15 au at the typical distance to the Taurus region) and the high optical thickness of many disk cores (Ansdell et al. 2018; Huang et al. 2018b). In the case of GI Tau, we note that the bump in its visibility profile occurs in the relatively noisy region beyond 1500 kλ and the two reported features may be an artifact of an overaggressive fit. It is otherwise one of the faintest disks in our 12-disk sample. Feature locations tend to cluster near the middle of disk continuum emission, but this could be a consequence of the aforementioned resolution and optical depth constraints at disk center, and the faintness of disk emission at extended radii. No preferred radial location for substructure features is otherwise obvious.

[1] They use the non-parametric Frankenstein code (Jennings et al. 2020) to directly fit the visibilities from all 24 Taurus disks in single star systems. Of the subsample of 12 compact disks that we reanalyze in this paper, they claim substructure detections in BP Tau and DR Tau consistent with what we identify here. They also note tentative signs of substructure in DO Tau and V409 Tau. We report different results for GI Tau and Haro 6-13, but this could be due to an overaggressive fit of the long baseline data from GI Tau and the shallowness of the feature in Haro 6-13. In general, their published visibility and radial profiles are similar to what we produce here, especially at the shorter baselines.

Disk	Feature	r_0 (au)	Width (au)	Depth ($\frac{I_d}{I_b}$)
BP Tau	B12	11.5	11.4	-
	D23	22.5	9.33	0.985
	B32	31.8	-	-
	D46	45.9	8.17	$\star$
	B57	57.1	8.38	-
DO Tau	D5	5.00	20.6	0.853
	B26	25.6	-	-
DR Tau	D18	18.2	1.71	0.996
	B20	20.2	1.83	-
	D36	36.2	4.71	0.932
	B42	41.7	5.05	-
GI Tau	D9	9.47	5.31	0.462
	B16	15.8	6.75	-
	D29	28.6	2.31	0.875
	B32	31.7	3.22	-
Haro 6-13	D16	16.1	3.06	0.965
	B20	19.9	3.58	-
V409 Tau	D19	19.3	6.59	0.850
	B27	27.2	7.86	-

Table 3.1: Characteristics of Identified Substructures. **Notes:** r_0 represents the radial distance from disk center. No depth measurement is provided for D46 of BP Tau as the intensity at gap center is suspiciously low and the gap-ring pair itself may be an artifact of fitting noisy data at long baselines (see Jennings et al. 2022b for a discussion).

With the exception of the standalone ring at 12 au in BP Tau, all non-plateau features have widths of 1 to 8 au (see Table 3.1). There is no clear correlation between feature location and width, but all features outside of 15 au (equivalent to the resolution limit) have width to radial location ratios between 0.08 and 0.43. This is roughly consistent with what has been observed in other samples (e.g., Huang et al. 2018b). All but a single gap have listed depths greater than or equal to 0.85 (i.e., intensity contrasts between adjacent gaps and rings of 15% or less). On average, these are shallower than the gaps reported in Long et al. (2018a) and Huang et al. (2018b), which could explain why they were overlooked. As implicated before, the gap-ring pair of GI Tau which

shows an intensity contrast in excess of 15% may be the result of a tenuous fit. The wide (and noisy) bump at long baselines within its deprojected visibility profile could instead be fit with a sharp power law (see Figure 11 of Long et al. 2019).

No robust features are detected in the other six disks of the sample (see right-hand columns of Figure 3.1). While these smooth disks are on average both fainter and more compact than those with substructure, they do begin to occupy the same parameter space, which begs the question of what else could separate these two populations. Any hidden substructure, especially in the outer disks, might be hard to identify given their meager total disk fluxes (see Long et al. 2019). It's notable that the brightest of these six smooth disks, DQ Tau, has a deviation from a smooth curve visible around 15 au, but this deviation does not meet the -0.05 slope criteria established previously for plateau features.

In Appendix Figure 3.15, we also present the radial profiles of 12 disks with previously identified substructures in Long et al. (2018a) using our fitting routine. Since these disks generally have more features in the visibility planes, their radial profiles can have very deep gaps below the sensitivity limit of any state-of-the-art observations. Thus, we make a cutoff at 10^{12} mJy/Sr, the sensitivity limit for the DSHARP observations (Andrews et al. 2018b). Emissions below this value is taken as this cutoff value. Their corresponding substructures are listed in Table 3.4 in the Appendix. Overall, we find these profiles are similar to those in Long et al. (2018a), but with more substructures in the inner disks. With our routine, some of the gaps at the outer disks disappear due to the weak emissions. More details can be found in the Appendix.

3.4.4 Comparison of Compact and Extended Disks

We compare our results of the 24 Taurus disks (Long et al. 2018a) and the 18 disks in the DSHARP sample (Andrews et al. 2018b; Huang et al. 2018b). We do not include substructures identified in the relatively small number of additional disks observed at (generally) lower spatial resolutions (see Table 5 of Huang et al. 2018b for a partial listing).

We classify disks with $R_{\rm eff,90\%}$ (the radius which encloses 90% of total disk continuum flux) less than 50 au as compact and disks with $R_{\rm eff,90\%}$ greater than or equal to 50 au as extended. This cutoff is motivated by the finding in Long et al. (2019) that all Taurus disks with $R_{\rm eff,95\%} \geq 55$ au show detectable substructure, and similar cutoff choices in the literature (e.g., van der Marel & Mulders 2021; Jennings et al. 2022b). The average effective radius of our 14 (2 in Long et al. 2018a, and 12 in Long et al. 2019) compact disks is ~ 33 au.

Substructures are detected in 12 of 18 compact disks, and all 24 extended disks (following the results of Long et al. 2018a and Huang et al. 2018b), in single star systems.[2] Our detection of substructure in six compact Taurus disks at least doubles the number of compact disks with claimed detections in the literature (e.g., González-Ruilova et al. 2020; Kurtovic et al. 2021), and allows for a more robust initial comparison of substructure in small and large disks.

We present the disk luminosity-radius relationships for the DSHARP and full Taurus samples in Figure 3.2. We scale luminosities as $F_\nu(d/140)^2$ to a standard distance of 140 pc, with F_ν denoting

[2]Smooth compact disks: *HO Tau, HP Tau, DQ Tau, V836 Tau, GK Tau and HQ Tau*

Compact disks with substructure: *WSB 52, DoAr 33, SR 4, HD 142666, FT Tau, IP Tau, DO Tau, V409 Tau, DR Tau, Haro 6-13, BP Tau and GI Tau*

Extended disks: *GW Lup, DoAr 25, Sz 114, IM Lup, Sz 129, HD 143006, Elias 24, RU Lup, WaOph 6, AS 209, HD 163296, MY Lup, Elias 20, Elias 27, UZ Tau, DS Tau, MWC 480, RY Tau, GO Tau, IQ Tau, DN Tau, CI Tau, DL Tau and CIDA 9*

the total flux from the disk at $\sim$1.3 mm. Scaled luminosities and effective radii from the samples generally follow the scaling relationship observed by Andrews et al. (2018c) in their large sample of nearby protoplanetary disks, with the caveat that those observations were taken at a wavelength of 870 μm. Our six disks with identified substructure begin to occupy the same parameter space probed by Long et al. (2020a) in their analysis of the compact GQ Lup disk. While our six disks without identified substructure are on average $\sim$50% fainter and $\sim$30% more compact than their non-smooth counterparts, three of them (DQ Tau, HO Tau and V836 Tau) occupy positions on the luminosity-size plot where substructures have been detected in similar disks. The discrepancy then is mainly driven by just three extra faint and/or compact disks: HP Tau, GK Tau and HQ Tau. We again note that the emission profile of DQ Tau (as seen in Figure 3.1) does present a deviation from a smooth profile that was very nearly classified as a plateau feature following the classification of Section 3.4.2. Additional disk substructures very likely exist, but do not lend themselves to easy detection because they are too narrow to be resolved, or are present in the extreme inner or outer disk.

We do not apply our model-fitting approach to the sample of eight smooth disks in multiple star systems from Long et al. (2019), but their sizes and luminosities broadly overlap those of the six smooth disks in single star systems. No substructures are detected in disks with $R_{\rm eff,90\%}$ less than 23 au or continuum luminosities below 12 mJy. This underlines the need for better spatial resolution observations of the faintest and most compact disks, with the caveat that those disks may simply be void of substructure.

We display the incidence and location of gaps and rings among the compact and extended samples in the histograms of Figure 3.3. The locations of the gaps and rings in 12 extended disks studied by Long et al. (2018a) are updated with results of our visibility fitting (listed Table 3.4).

Gap locations peak between 15 and 20 au in the compact case and taper off out to $\sim$55 au. The detection of gaps (and rings) past 50 au is possible because emission extends beyond the effective radius threshold of 90% that we use in our determination of a compact disk. Ring locations peak near 20 au and follow much the same trajectory as the gaps.

Considering the extended case, gap locations peak near 40 au and exhibit a slow decline out to $\sim$145 au. Ring incidence peaks near 30 au, and declines in a similar trend. In general, substructure is identified out to large relative separations in both compact and extended disks and does not strongly cluster around any one location. Furthermore, what we describe as a peak is likely an exaggeration of the true distribution given the increased difficulty of detecting features near disk center (high optical depths, smaller characteristic sizes) and in the faint outer regions, and also the rarity of very large disks. The apparent decline is also a function of plotting so many disks together. Some disks have smaller effective radii than others in the same category (compact or extended) and cannot therefore have substructure at the most distant separations plotted (Huang et al. 2018b). This is highlighted by the fact that every disk with identified substructure in our sample has at least one feature near, at or beyond its calculated effective radius. Such a finding is perhaps not surprising if we invoke substructure as a necessary condition to stop the fast radial drift of disk solids predicted under the assumption of a smooth gas disk (e.g., Whipple 1972; Weidenschilling 1997). Ultimately, substructure may be a common occurrence at all radii in both compact and extended disks.

We compare gap widths and depths for compact and extended disks in the combined plots of Figure 3.4. We exclude the four inner disk cavities of Long et al. (2018a) without defined gap locations, and all plateau features identified in the DSHARP sample and this paper. The widths and depths of these plateau features are either not calculated, or calculated differently than the

other features. This leaves 11 gaps in the compact disks and 48 gaps in the extended disks for analysis.

All the gaps in compact disks span widths of less than 10 au, values near the resolution limits of the observations. Huang et al. (2018b) note that beam effects near the resolution limit will generally deflate the measurement of gap widths, and we might therefore expect that our reported widths are an underestimate. Still, gap widths much larger than 10 au would begin to exceed the effective radii of the smallest disks and would be a counterintuitive result in a compact disk. Gap widths in the extended case are more varied, with several exceeding 20 au, but the majority are smaller than 15 au. In both cases, narrow widths cluster in the inner 50 to 60 au. No obvious correlation of gap width and location otherwise exists.

The story is much the same with gap depths. The majority of gaps are shallow, with gap-ring intensity variations below 30%, especially interior to 60 au. It is tempting to link wider and deeper gaps at large radii in the extended disks to a more massive planet population (more massive planets carve out larger gaps under the assumption of planet-disk interaction), but this relationship largely disappears after correcting gap width to gap location (Figure 3.5), a better indicator of planet mass (Kanagawa et al. 2016b; Zhang et al. 2018c). It is worth mentioning that gap widths are on average smaller when the gaps are between 20-50 au, except two very large ones. Wide gaps are more clustered between 10-20 au and 50-80 au. Since planet masses are inferred from the gap width, the paucity of giant planets between 30-50 au can be found in all following planet population figures. We extend this discussion in Section 3.6.1. We also note that the uncertainties are larger in the inner disk where low-mass planets with shallow gaps are especially difficult to study.

3.5 Planet-Disk Interactions: Detection Limit

Planet-disk interactions are proposed as one of the major causes of observed disk substructure (e.g. Rice et al. 2006; Zhu et al. 2012b), and we expect that gap location should coincide with orbital location of the embedded planet. Additionally, more massive planets will form steeper pressure gradients within the disk and create larger gap openings than are created by less massive planets (Fung et al. 2014b; Kanagawa et al. 2015b; Rosotti et al. 2016b; Zhang et al. 2018c).

In order to characterize the sensitivity of our model-fitting approach for detecting substructure induced by young planets, we combine a series of planet simulations with a sample compact disk.

3.5.1 Use of Planet-Disk Interaction Models

We adopt dust surface brightness distributions from the planet-disk interaction models of Zhang et al. (2018c). These 2D simulations include both gas and dust components, and were originally used to explore possible planet properties inferred from substructures identified in the sample of DSHARP disks (see Huang et al. 2018b) under the planet-disk interaction hypothesis. At the radius of the planet, we select a disk aspect ratio (h/r) of 0.05, the $a_{\rm max}$ = 0.1 mm (DSD1) dust size distribution, and a disk surface density of 30 g cm^{-2} (see Section 2 of Zhang et al. 2018c for more detail on these parameters). We vary planet mass, distance to host star and the disk viscosity condition (specifics to follow). Total disk continuum flux at 1.33 mm is set at 50 mJy, a medium value in our sample of Taurus disks. The mass of the host star is fixed at 1 $M_{\odot}$. The disks are assumed to be face-on.

To produce simulated visibilities, the 2D model FITS images are used as inputs to the Python

package *vis_sample*[3] for fast Fourier transform and resampling of the visibility points at the same uv coordinates as the observations of the Haro 6-13 disk. We choose Haro 6-13 to generate our models on the basis of its baseline coverage being typical of our Taurus sample. The simulated visibilities are then deprojected and analyzed as per the same model-fitting approach outlined in Section 3.4.1.

We generate 90 model disks by varying planet mass between five values (11 $M_\oplus$, 33 $M_\oplus$, 0.35 M_J, 1 M_J and 3.5 M_J), planet distance to host star from 5 to 30 au in increments of 5 au, and the disk viscosity condition (α) between 10^{-4}, 10^{-3} and 10^{-2}. More information can be found in Zhang et al. (2018c). We vary the planet-star distance between 5 and 30 au in consideration of where ice and gas giant planets lie within our own solar system, and resolution constraints of our disk observations. We also place a 11 $M_\oplus$ planet at 50 au, as it is a typical radius for potential planets in extended disks (shown in Figure 3.3). We use different values of the disk viscosity condition because this value is not well constrained by existing observations of disk phenomena (e.g., Pinte et al. 2016b; Rafikov 2017; Flaherty et al. 2018b; Trapman et al. 2020), especially for compact disks. We do not vary the disk aspect ratio, but note that higher values will open gaps that are shallower and wider than in the 0.05 case (Zhang et al. 2018c). Our goal is to simulate "average" conditions at the radii of our embedded planets.

Deprojected visibility profiles for three planet-star distances of the M_p = 0.35 M_J and α = 10^{-3} case are shown in the left-hand column of Figure 3.6. From the deprojected profiles, we produce a best-fit visibility model and use it to derive a radial intensity profile for each disk. Best-fit models for these three median cases are produced with multiple Gaussians initiating the MPFIT routine. As planet mass increases, the tendency is for more and larger bumps in the visibility

[3]https://github.com/AstroChem/vis_sample

profile, necessitating more Gaussians to initiate the fitting routine.

In order to classify gap-ring pairs near the locations of our inserted planets as detections or not, we borrow the $\frac{1}{I_\nu(r)}\frac{dI_\nu(r)}{dr}$ test employed previously to identify plateau features. However, we now demand that the slope exceeds 0 instead of -0.05 (i.e., there must be a radial increase of intensity within the bounds of the gap-ring pair), since we want to focus on gaps and rings, but not plateaus. Gaps and rings are easier to infer planet masses from.

3.5.2 Results from the Simulations

We show the results from the model disks for each viscosity condition in the heat maps of Figure 3.7. We assume planets within the detection zone have 100% percent possibility of detection and 0% out of the detection zone. For the $\alpha = 10^{-2}$ case, our model-fitting approach detects Jupiter-mass planets at separations of 15 au or greater from their host stars. Sensitivity improves to 10 au for a multiple Jupiter-mass planet. This mass-radius regime lies at the lower end of what is currently detectable with direct imaging techniques (e.g., Macintosh et al. 2015; Nielsen et al. 2019), and the upper end of what is detectable with the radial velocity technique.[4] Sensitivity extends down to Uranus- and Neptune-mass planets at separations of 20 to 30 au for the low viscosity condition ($\alpha = 10^{-4}$). This is roughly consistent with the semi-major axes of Uranus and Neptune (19 and 30 au, respectively) in our own solar system, and suggests that such planets are detectable in existing observations of protoplanetary disks by model fitting directly in the visibility domain

[4]See NASA Exoplanet Archive for an up-to-date mass-period plot. We note that direct imaging techniques are insensitive to planets close to their host stars because of insufficient contrast. Meanwhile, planets at far separations do not create sufficient wobble in their host stars to be detected by the radial velocity technique. Their long periods also present a challenge to relatively short duration observations.

(assuming proper disk conditions). It also overlaps many of the planet masses and separations that we detect in the medium viscosity case ($\alpha = 10^{-3}$), indicating that the sensitivity of this approach is broadly similar under conditions of low and medium disk viscosity. Moreover, this mass-radius parameter space is not covered by existing exoplanet detection techniques and reinforces the analysis of disk substructure, under the planet-disk interaction hypothesis, as a complement to mature exoplanet surveys for gaining a better understanding of planetary system architectures (Andrews 2020).

For planets simulated at 5 au, model fitting was very sensitive to the number of Gaussians employed in the fitting routine and produced non-physical peaks and valleys in many of the derived radial intensity profiles. This confused our detection test and we ultimately decided to exclude planet simulations at 5 au from consideration. Defaulting to a single Gaussian fit invariably produced radial intensity plots without obvious substructure. Higher resolution observations could help uncover such planets in future model-fitting campaigns.

In general terms, model fitting is most sensitive to massive planets at large relative separations. Detection is aided by conditions of low or medium disk viscosity. Although not shown here, we also recover the gaps carved by a 11 $M_\oplus$ planet at 50 au for $\alpha = 10^{-3}$ and 10^{-4}. Since the 11 $M_\oplus$ planet is marginally detectable, we expect that Super-Earths below that mass may be difficult to be detected with the existing observations.

3.6 Young Planet Population

The Taurus survey (Long et al. 2018a; 2019) is an ideal sample to study the potential young planet population since it samples a full range of disk types around solar-mass stars with spectral

type earlier than M3. The young planet population inferred is less biased than the DSHARP (Andrews et al. 2018b) and ODISEA (Cieza et al. 2021a) surveys, where bright and large disks were preferentially selected. In this section we derive a population of young planet masses using the gap width in the Taurus sample.

Gap Width and Planet Mass. We use the gap width normalized by the gap outer edge[5] (Δ) to infer potential young planet masses, as it is less prone to variation due to sensitivity than the gap depth (e.g., Kanagawa et al. 2016b; Zhang et al. 2018c; Lodato et al. 2019a; Auddy & Lin 2020a). Generally speaking, the gap width is positively correlated with the planet mass. However, this relation can be complicated by the disk's gas and dust components. A stronger gas viscosity α makes the gap narrower. The dust-gas coupling is determined by the Stokes number, St, which is proportional to the dust size, a_{max} over the gas surface density. The coupling is stronger when St $\ll 1$, and the gap is narrower; whereas when St ~ 1, the dust drifts the fastest in the gas, so the gap can be much wider. Zhang et al. (2018c) measure this empirical relation between gap width and planet mass, under different viscosities and St. Then with the assumption of the disk parameters, we can infer the planet mass from the gap width.

3.6.1 Planet Population

In Figure 3.8, we place potential planets derived from the Taurus survey on a planet mass-semi-major axis diagram, along with Solar System planets and confirmed exoplanets (from the NASA Exoplanet Archive (2022) as of April 12), in the same way as Figure 20 in Zhang et al. (2018c). They are derived using the gap width, local dust surface density and an assumption of maximum

[5]We will just use "gap width" hereafter.

grain size ($a_{\rm max}$) and disk viscosity (α) (Zhang et al. 2018c; 2022). We plot the masses assuming $a_{\rm max} = 0.1$ mm and $\alpha = 10^{-3}$. We have to assume these disk parameters since we do not have strong constraints on these parameters. Different assumptions of maximum grain size and disk viscosity would result in systematically different planet masses (an increase of disk viscosity, the dominant uncertainty, by a factor of ten would result in a planet calculated to be twice as massive). We also assume the planet is at the gap location. To be consistent with our injection-recovery study in Section 3.5 (Figure 3.7), we exclude any planet below the detection limit. We also remove the planet for DL Tau at 66 au, since it can be the secondary gap carved by a single planet at 95 au, similar to the case in AS 209 (Guzmán et al. 2018; Zhang et al. 2018c). The complete mass estimation can be found in Table in the Appendix of Zhang et al. (2023a), where we include all possible planets including those are excluded in the figure. We note that GO Tau D12 and FT Tau D26 are on the boundary of detection and non-detection zones. We choose to exclude them for the planet population and occurrence studies. Each disk is labeled with an alphabet representing its size in ascending order (a - e are compact disks and f - m are extended disks, where GI Tau being the smallest). The error bar accounts for the uncertainties in the fitting and a range of viscosities (α from 10^{-4} to 10^{-2}). We also include the potential young planet population uncovered by the DSHARP survey using the same method with more transparent circles, also separated into compact and extended disks, but without alphabetical labels and error bars. We only include gaps with width ratios (Δ) > 0.12 in the figure since the uncertainties are too large to infer planet masses from the narrow gaps. However, we still list their tentative properties in the table. Plateaus (e.g., D5 in DO Tau) do not have a local minimum, so the method in Zhang et al. (2018c) cannot be applied, and they are not listed in the table, in line with Figures 3.4 and 3.5. We also do not estimate the planet masses in the inner cavities of the transition disks in the Taurus sample, as their masses can vary

throughout a large range or may even host multiple planets (e.g., there are at least two planets in PDS 70 (Keppler et al. 2018b; Müller et al. 2018a; Wagner et al. 2018a; Haffert et al. 2019a; Isella et al. 2019b; Christiaens et al. 2019a; Wang et al. 2020a; Hashimoto et al. 2020a)). Compared to Zhang et al. (2018c), we add the following gaps to the DSHARP sample: D25 of Elias 20, D29 of RU Lup, D98 of DoAr 25, and D117 of IM Lup, as their gap widths are also > 0.12. Their masses are inferred using the fitting method, instead of by direct comparison with simulations. Exoplanets detected by various methods are represented by scatter points of different colors. The distribution of planets from the Taurus survey is similar to the distribution from the DSHARP survey.

Interestingly, the giant planets ($> 0.1\ M_J$) between 20-50 au are fewer compared to smaller and larger separations. As planet masses are inferred from gap widths, this echoes our finding in Figure 3.4, where wide gaps are rarer between 20-50 au. Since the definition of the gap width (Δ) used to calculate planet mass is slightly different from the one in Figure 3.4 (normalized by the outer gap edge instead of the gap location), we remake the gap width-gap location plot in Figure 3.9's top panel. It is similar to Figure 3.8 and also to Figure 3.4 except the x-axis is shown in log-scale. We mark the region with fewer wide gaps in ellipse and question mark. Additionally, this dearth of wide gaps is even more evident if we use the effective radius $R_{\rm eff,90\%}$ as the x-axis (bottom panel of Figure 3.9). For $R_{\rm eff,90\%}$ between 30-90 au, most of the gap widths are below 0.2.

More disk surveys of high angular resolution observations are needed to test out whether this void of wide gaps for intermediate sized disks (or gaps with intermediate separations) are statistically significant. If they are, it indicates that gaps at the inner and outer disks may be affected by different physical processes (e.g. different planet formation or evolution mechanisms).

In Figure 3.10, we expand on the analysis by counting potential planets in mass-location bins

among compact and extended disks in the Taurus survey.[6] The y-axes are the planet-star mass ratios in units of Jupiter mass over solar mass. We choose to present the planet-star mass ratio instead of the absolute planet mass since it directly reflects the observable, gap width. Another advantage of using the mass ratio is that we can directly compare our results with those from microlensing surveys. The gap locations are binned with edges at 8, 16, 32, 64, and 128 au, uniformly on a logarithmic scale. The planet masses are binned from 10^{-2} M_J to 100 M_J, with each bin spanning one decade in mass. The choice of bin sizes is arbitrary but able to cover all potential planets. The lower-left hatched region is the detection limit of our observations and model-fitting approach as summarized in Figure 3.7.

In panels (a) and (b), we count the number of planets in the cell (indicated in the lower-left corner of each cell) and divide by the total number of the compact or extended disks in the Taurus subsample of 24 disks in single star systems. If the count is zero, the cell is empty. Both categories have most of their planets at the disk's outer edges (20 to 30 au for the compact disks and 30 to 80 au for the extended disks). Since the planet location is assumed to be at the gap center, the planet location distribution is essentially the gap incidence distribution in Figure 3.3 with shallow gaps ($\Delta < 0.12$) or low-mass planets below the detection limit removed. The most populated cell among compact disks is ([0.1, 1] M_J, [16, 32] au); the most populated cell among extended disks is ([0.01, 0.1] M_J, [32, 64] au).

3.7 Young Planet Occurrence

With the young planet population, we calculate the planet occurrence rates on the planet-mass-semi-major-axis diagram. These occurrence rates are tentative due to the small sample sizes and

[6]For simplicity, we use M_p to represent M_p/M_* when we discuss Figures 3.10 and 3.11.

several possible biases that are difficult to quantify. Still, they can be improved by future surveys with larger sample size and more homogeneous sample selections. We also include the DSHARP sample for comparison, but their biases are even larger. We introduce two kinds of occurrence rates with different assumptions in Section 3.7.1, and list possible biases that affect the results in Section 3.7.2. For the large differences in biases between Taurus and DSHARP samples, we calculate their occurrence rates separately. Then we present results and compare them with current exoplanet statistics in Sections 3.7.3 and 3.7.4.

An earlier work by van der Marel & Mulders (2021) calculated the occurrence rates of structured disks under different stellar masses using all known Class II disk surveys. With the assumption that all extended disks are structured and that all disks with substructures are due to giant planets, they found that current exoplanet demographics can account for all of the disk substructures. While van der Marel & Mulders (2021) had a much larger disk sample size, the purpose of our exercise is to directly calculate the planet occurrence rates on the planet-mass-semi-major-axis diagram as exoplanet statistics, with planet masses ranging from sub-Neptunes to giant planets, and semi-major axis ranging from 8 au to 128 au.

3.7.1 Two Types of Occurrence Rates

In Figure 3.11, we use two different ways to correct for the bias and derive the planet occurrence rates for the Taurus and DSHARP samples (a version showing absolute planet masses is in the Appendix Figure 3.14.).

We first use a simple way to calculate the occurrence rates (panels a and c), that is $n_{pl,cell}/n_{tot}$, where $n_{pl,cell}$ is the number of planets in a cell, and n_{tot} is the total number of disks in a sample.

This is based on the assumptions that (a) all planets form in the dusty disk; (b) whenever they are massive enough, they open gaps; (c) each gap detected corresponds to a planet in a disk; and (d) all planets have been detected. We denote this occurrence as "simple occurrence".

The second kind of occurrence rate is the weighted planet occurrence rate (panels b and d).

$$f_{cell} = \sum_{j=1}^{n_{pl,cell}} \frac{1}{n_{*,j}}, \tag{3.5}$$

where $n_{*,j}$ is the number of disks with radii larger than the radius of the gap and with radii of the inner cavity smaller than the radius of the gap, and j goes over every potential planet in a cell. We use $R_{\mathrm{eff},90\%}$ as the disk radius (if we use $R_{\mathrm{eff},68\%}$ some substructures in the outer disk will be larger than the disk radius itself). We use the innermost ring's location as the cavity size. One assumption of the weighted rate (a) is that there are planets in the outer disk outside of the dusty disk (e.g., kinematic planets, Disk Dynamics Collaboration et al. 2020, or planets below the sensitivity limit, Ilee et al. 2022). Since we cannot detect them, we need to account for these missing planets. Similarly, we also assume planets can be within the cavity where our gap width fitting method cannot be used. The second assumption is that (b) the planet's spatial distribution is independent of the disk size distribution and the cavity size distribution. Each detected planet will be corrected by (i.e., divided by) the fraction of disks larger than the planet location, and the fraction of disks with cavity sizes smaller than the planet location. We denote this occurrence as "weighted occurrence", which is typically larger than the simple occurrence.

We focus on the planet occurrence only at the Class II disk stage. In both types of occurrence rates, we assume that all stars should experience Class II disk stage. We also assume that the sample selection among the Taurus star-forming region is uniform among Class II disks.

3.7.2 Possible Sources of Biases

The young planet population is deduced with the assumption that all substructures are due to the planet. In this sense, these occurrence rates can be treated as upper limits, as other mechanisms can also possibly explain these substructures. Between two types of occurrences, simple occurrence is less than the weighted occurrence since it neglects planets in the disk's inner cavity and regions beyond the detected dusty disk.

Detection Bias

For the Taurus sample, we correct the observation completeness using the test results from Figure 3.7, assuming $\alpha = 10^{-3}$. As Figure 3.7 shows, disk viscosity, planet mass, and planet location can affect the detectability. Other than these factors, disk inclination, observation configuration, stellar luminosity, disk scale height, disk gas and dust surface density, and dust size also affect the detectability. The probability of detection is likely to be around 100% for wide separation, high mass planets, and lower closer to the detection zone boundary. This means the biases of our results are higher for close separation, low mass planets. Ideally, similar to the radial velocity (RV) (Mayor et al. 2011) and transit surveys (Howard et al. 2012), we could perform an injection-recovery study by varying all possible disk parameters and planet masses for a particular disk and use the specific ALMA observation configuration to simulate the synthetic observations. Then we do the parametric fitting for the suite of models to retrieve radial profiles. Finally, we calculate the possibility of the detection and factor that into the occurrence rate. We choose not to include this analysis in the current work due to our small sample size already teeming with large uncertainties. This process can be considered when we have a larger sample in the future.

For the DSHARP sample, we do not perform the parametric fitting since the DSHARP disks have much higher angular resolutions. We use the radial profiles from Andrews et al. (2018b); Huang et al. (2018b) produced through standard `tclean` task. These radial profiles have similar resolutions to those derived from our parametric fitting among Taurus disks. As indicated by Jennings et al. (2022a), using super-resolution fitting barely increase the prominent substructures among this sample.

Selection Bias

The Taurus sample's disks are around stars of spectral type earlier than M3 (Long et al. 2019). It excluded known binaries with separations between 0".1 and 0".5. It also excluded sources with high extinction or faint optical/near-IR emissions to avoid edge-on disks and embedded objects. These selections led to the missing of some low-mass disks. However, many of these low-mass disks are around close binaries. For them, the small size of the disk is due to tidal truncation. It is still possible that some of the low-mass disks are Class II disks around single stars. Unfortunately, it is difficult to quantify what fraction of the low-mass disks should have been counted as Class II disks around single stars. Since we do not make any correction for this fraction, we implicitly assume all the disks excluded are not Class II disks around single stars. The other possible large bias is that this sample selection excluded disks with existing high-resolution data, and these disks are most likely large and bright. This bias is also difficult to quantify. Although the Taurus sample is much more uniform than the DSHARP sample, it still biases towards disks with intermediate sizes and fluxes.

Quantifying the biases in the DSHARP sample is even more difficult. As the survey aimed to obtain as many substructures as possible (Andrews et al. 2018b), bright full disks were selected and

transition disks were avoided. The sample is also a combination of disks from several star-forming regions, so one would need to consider biases in each star-forming region's database on SED and mm dust continuum emissions that come into the sample selection.

The stellar masses in our samples range from 0.3 $M_\odot$ to 2 $M_\odot$ for Taurus and DSHARP samples. While the stellar mass is quite uniformly spaced within the mass range at least for the Taurus sample, the large span of the masses and the small number of disks can lead to large uncertainties if the occurrence rate is strongly dependent on the stellar mass. We note that the RV studies (Mayor et al. 2011; Fernandes et al. 2019; Fulton et al. 2021) and the *Kepler* survey (Thompson et al. 2018) have much more controlled sample selection so the biases can be formally corrected. For example, the *Kepler* sample has stellar mass centered on 1.0 $M_\odot$ with a standard deviation of 0.3 $M_\odot$ (Huber et al. 2017).

Other Assumption

The calculated occurrence rates are the occurrence rates of young planets in systems with protoplanetary disks (Class II systems). We can also translate these occurrence rates to the lower limit of the young planet occurrence rates in the whole star forming region (including Class III disks) by multiplying the rates with the disk fraction F (e.g., Mulders et al. 2021). This approach intrinsically assumes that stars without disks do not have planets, which is why it is a lower limit. F is strongly dependent on the age of the star-forming region. For example, Ribas et al. (2014) (Table 4 therein) provide these fractions from mid-infrared observations between 22-24 μm in several star-forming regions (F=58% for Taurus; 43% for Lupus; 51% for Ophiuchus; 22% for Upper Sco).

3.7.3 Occurrence Rate

With all the caveats in mind, we can discuss the results. Aside from the occurrence rate in each grid, Figure 3.11 also shows the marginalized occurrence rates along gap locations and planet masses on the sides of the histogram. The simple occurrence rate for the Taurus sample peaks at region between 30-50 au, whereas the occurrene rates increases all the way beyond 100 au for the DSHARP sample. This can be due to the larger disk sizes in DSHARP sample. The planet occurrence rate decreases with increasing planet masses. The Taurus sample has a peak between 0.1-1 M_J, whereas the DSHARP sample has the largest occurrence rate between 0.01-0.1 M_J. This difference can be due to the higher detection limit for the Taurus sample. It can also due to the fact that stellar masses in the Taurus sample are on average lower than those in the DSHARP sample (see Table 1 in Long et al. 2019 and Table 1 in Andrews et al. 2018b). Lower mass stars can have thicker disks (due to lower gravity), and thus have higher minimum gap-opening planet masses at a given location (Sinclair et al. 2020). When adopting the weighted occurrence rate, the difference between two samples are smaller. Both of them have higher planet occurrence rates at the larger radii, and at or below a fraction of M_J. Owning to the small samples, the differences between two samples are not significant. By performing the two-sample Kolmogorov-Smirnov (KS) test using the `ks_2samp` task in the PYTHON SCIPY package (Jones et al. 2001–), we confirm that the marginalized occurrence distributions are indistinguishable between Taurus and DSHARP samples for both location and mass distributions (p = 0.77 for simple occurrence and p = 1.0 for weighted occurrence). That both samples' occurrence rates peak at a planet-star mass ratio near the Neptune-Sun mass ratio is consistent with results from microlensing surveys (Suzuki et al. 2016a).

Tentatively, we can also compare the Taurus and DSHARP planet occurrence rates with direct imaging, microlensing and radial velocity (RV) surveys. We report the occurrence rates binned either in planet masses or planet-star mass ratios depending on what is used in the previous literature.

To estimate the uncertainty of the rates, we assume the number of planets within a given range follows a binomial distribution (Howard et al. 2012). They are drawn from an effective total number of stars (i.e., $n_{*,eff,cell} = n_{pl,cell}/f_{cell}$). For the simple occurrence rate, $n_{*,eff,cell}$ is just the total number of disks in a survey. For the weighted occurrence rate, it is the effective (average) number of disks, which is less than or equal to the total number of disks. The quoted $\pm 1\sigma$ are at the 15.9 and 84.1 percentile levels in the cumulative distribution function.

Direct Imaging

The occurrence rate for wide orbit ($>$ 10 au) giant planets ($\sim$5 to 13 M_J) from the direct imaging method is believed to be around 1% (Bowler & Nielsen 2018b), with some studies suggesting it could be as high as 5 to 10% (Meshkat et al. 2017b; Nielsen et al. 2019). Here both samples have one planet as such, which give occurrence rates of 4 to 6% (the simple and weighted occurrence rates are 4.2$\pm$4.2% and 5.0$\pm$5.0% for the Taurus sample, and 5.6$\pm$5.6% and 5.6$\pm$5.6% for the DSHARP sample, respectively), consistent with the direct imaging surveys.

Microlensing

Most of our parameter space (orbits $>$ 20 au and planet masses between sub-Neptune to Jupiter mass) is unique to the disk and cannot yet be probed by other detection methods, but substructures at $\sim$10 au start to overlap with planet locations from microlensing surveys. We compare

our occurrence rates per decade in planet-star mass ratio (q) and separation with values from the microlensing survey of Suzuki et al. (2016a). First, we count our planets from all locations. Since these disk substructure locations span a little more than a decade (from 8 to 128 au), we divide our marginalized values (in Figure 3.11) by 1.2 to be consistent with their definition. The simple and weighted occurrence rates for the Taurus and DSHARP samples are summarized in Table 3.2. Suzuki et al. (2016a) find the peak of the occurrence rate at $q = 1.7\times10^{-4}$ (or 0.18 $M_J/M_\odot$, 3.3 $M_{Nep}/M_\odot$) to be 61^{+21}_{-16}%. It is similar to our highest weighted occurrence values for both samples, but we do not have enough resolution to compare at a specific narrow mass bin. Their median occurrence rate between 0.01 and 0.1 $M_J/M_\odot$ is around 20%, which is consistent with our simple occurrence rates in both samples. Their median occurrence rate between 0.1 and 1 $M_J/M_\odot$ is also around 20%. Our simple occurrence rates are also consistent with the result, whereas the weighted occurrence rates are much higher. To compare with the parameter space that overlaps microlensing surveys, we also calculate the occurrence rates between 8 and 16 au, normalized as per logarithmic radius. For planet mass ratios from 0.1 to 1 $M_J/M_\odot$, occurrence rates are 41.5±27.7% for simple occurrence (48.2±31.6% for weighted occurrence) for the Taurus sample and 36.9±18.5% for simple occurrence (38.0±19.5% for weighted occurrence) for the DSHARP sample. These are higher than the microlensing results, but consistent within 1σ. For planet mass ratios from 1 to 10 $M_J/M_\odot$, rates are 13.8±13.8% for simple occurrence (17.5±17.5% for weighted occurrence) for the Taurus sample and 36.9±18.5% for simple occurrence (38.0±19.5% for weighted occurrence) for the DSHARP sample, higher than those in the microlensing survey.

Poleski et al. (2021) calculate the occurrence rate for ice giants (planets with orbits from 5 to 15 au and mass ratios from 0.01 to 3.3 $M_J/M_\odot$) to be $1.4^{+0.9}_{-0.6}$ per microlensing star, 2.4σ higher than what was found in Suzuki et al. (2016a). Our occurrence rates estimated from substructures

Mass Ratio ($M_J/M_\odot$)	Survey	Simple Occurrence	Weighted Occurrence
[0.01, 0.1)	Taurus	17.4±8.3%	40.7±20.0%
[0.01, 0.1)	DSHARP	27.8±11.1%	$57.9^{+22.2}_{-11.1}$%
[0.1, 1)	Taurus	27.8±8.3%	52.4±15.4%
[0.1, 1)	DSHARP	23.1±11.1%	37.7±18.2%
[1, 10)	Taurus	10.4±8.3%	$22.1^{+9.1}_{-18.2}$%
[1, 10)	DSHARP	18.5±11.1%	22.0±13.3%
[10, 100)	Taurus	3.5±3.5%	4.2±4.2%
[10, 100)	DSHARP	4.6±4.6%	4.6±4.6%

Table 3.2: Planet Occurrence Rates for Taurus and DSHARP Sample.

beyond 8 au are lower. The simple (and weighted) occurrences are 12.5±8.3% (15.0±10.0%) for the Taurus survey and 16.7±11.1% ($17.3^{+5.9}_{-11.8}$%) for the DSHARP survey, much lower than what is found in Poleski et al. (2021). On the other hand, Neptune-mass planets within 15 au might still be hidden under the detection limits.

Radial Velocity (RV)

Fernandes et al. (2019) indicate that the occurrence rate of giant planets (masses between 0.1 to 20 M_J and 0.1 to 100 au from their host stars) is 26.6%, using a fitting with a broken power law and a turnover at the snowline on existing data within several astronomical units. Fulton et al. (2021) corroborate the broken power-law with 2σ significance but found a shallower decline beyond the snowline. Fernandes et al. (2019) infer that the disk substructure occurrence rate is much higher than that, so only part of the substructure can be due to planets. We calculate the simple and weighted occurrences to be 50±8.3% and 94.4±7.7% for the Taurus survey and 55.6±11.1% and $79.7^{+15.4}_{-7.7}$% for the DSHARP survey. These are higher than the extrapolated value in Fernandes et al. (2019). However, the simple occurrence for the Taurus sample is still consistent with their

value within 3σ. As such, the hypothesis that all gaps are due to planets cannot be ruled out solely based on their extrapolated occurrence rate. Other than non-planet origins for disk gaps, the slight discrepancy can be explained if the decrease in occurrence rate beyond snowlines cannot be extrapolated, or that these samples are somehow biased toward higher substructure occurrence rates. Perhaps it is also possible that the young planet population is very different from the mature population, as young planets will continue to grow and migrate (Nayakshin et al. 2022). To compare directly with current exoplanet statistics, these samples could be used as an initial condition for population synthesis studies to evolve them to a mature stage (Wang et al. 2022).

3.7.4 Occurrence for Different Stellar Types

The dependency between planet occurrence and stellar mass can also be tested using planets inferred from disk gaps. In Figure 3.12, we separate the Taurus (top panels) and DSHARP (bottom panels) samples into three stellar mass regimes: M dwarfs (0.1 $M_\odot < M_* \leq 0.5\ M_\odot$), Sun-like stars (0.5 $M_\odot < M_* \leq 1\ M_\odot$) and massive stars ($M_* > 1\ M_\odot$). The y-axis is the absolute planet mass in Jupiter mass. We only calculate the simple occurrence rates, which are the number of planets in a cell divided by the number of disks within the given mass range (marked as n_{disks}). There are five transition disks in the Taurus survey that could also affect the occurrence rates. However, since their masses, locations and numbers are all uncertain, we only mark them using arrows in the figure and choose not to include them in the calculations of the occurrence rates. The upper limit of the planet location is taken as the outer ring of the cavity, whereas the lower limit of their planet masses is set at 1 M_J. With our calculated occurrence rates, we can compare the Taurus and DSHARP samples to trends found in exoplanet surveys.

While the stellar mass dependence from *Kepler* is mainly for sub-Neptunes within 1 au, we can test out their trends for our samples on much larger separations. From the *Kepler* survey, sub-Neptune exoplanets are more common around low-mass stars (Howard et al. 2012; Mulders 2018). Their occurrence rate around M stars is a factor of 2 to 4 higher than their occurrence rate around FGK stars (Mulders et al. 2015; Gaidos et al. 2016). Our results show that the occurrence rates for sub-Neptune planets around M dwarfs, Sun-like stars and massive stars are 14.3%$\pm$14.3%, 27.3$\pm$9.1% and 16.7$\pm$16.7% for the Taurus sample, and 50.0$\pm$25.0%, 22.2$\pm$11.1% and 0% for the DSHARP sample. For the DSHARP survey, the factor of $\sim$2 higher occurrence rates around M dwarfs relative to Sun-like stars is consistent with the *Kepler* survey. However, we need higher resolution observations of compact disks to study sub-Neptune planets in the inner disks.

Giant planets occur more frequently around high-mass stars (Johnson et al. 2010), but the dependence is weaker and less statistically significant than the dependence with metallicity (Mulders 2018). A caveat is that the dependence of giant planets with stellar mass includes many planet below a Jupiter mass (Ghezzi et al. 2018; Fulton et al. 2021). The occurrence rates of planets $>$ 1 M_J among the three mass regimes are 0%, 27.3$\pm$9.1% and 16.7%$\pm$16.7% for the Taurus sample, and 0%, 22.2$\pm$11.1% and 40.0$\pm$20.0% for the DSHARP sample. Direct imaging surveys constrain the occurrence rate of planets $>$ 1 M_J and $>$ 10 au separation to be $5.7\%^{+3.8}_{-2.8}$ for FGK stars (Vigan et al. 2017b; 2021). The values calculated here are much higher. Nielsen et al. (2019) find the occurrence rate for $M_* > 1.5$ $M_\odot$ to be $24^{+13}_{-10}\%$, while Vigan et al. (2021) find $23.0^{+13.5}_{-9.7}\%$ for BA stars. Our values are consistent with these results within 1σ. Perhaps the most relevant result comes from the NaCo-ISPY large program, where young planets were searched around 45 young stars surrounded by protoplanetary disks (Cugno et al. 2023). Most of the stars in the survey have $M_* > M_\odot$. The occurrence rates for semis-major axis between 20-500 au, and $T_{\rm eff}$ between 600-

3000 K are $21.2^{+24.3}_{-13.6}$%, $14.8^{+17.5}_{-9.6}$%, $10.8^{+12.6}_{-7.0}$% for R_p = 2, 3, 5 R_J. While the masses of these young planets are difficult to constrain, our occurrence rates are roughly consistent with these values if both populations have similar planet masses.

3.8 Summary

We reanalyze 1.33 mm ALMA continuum observations of 12 compact disks in the Taurus star-forming region, initially classified as smooth and featureless in the analysis of Long et al. (2019). We also reanalyze 12 disks with substructures found Long et al. (2018a). Our approach is to fit their deprojected visibility profiles directly, which is more sensitive to small-scale disk substructure. We compare the incidence and characteristics of substructure in the populations of compact and extended disks within the Taurus sample of 24 disks in single star systems and the high-resolution DSHARP survey. We then test the sensitivity of these observations and our fitting approach by analyzing mock observations of substructures created by planet-disk interaction simulations. We conclude by calculating potential planet masses and occurrence rates and comparing them to the results of mature exoplanet surveys. Our main findings are as follows:

1. We detect substructure in the continuum emission of 6 out of 12 compact disks in our sample. This at least doubles the number of compact disks ($R_{\rm eff,90\%} < 50$ au) with known substructure. Detected substructures are generally shallow and narrow, with widths on order of 5 au. On average, the 6 smooth disks are both fainter and more compact than the six disks with identified substructure.

2. No substructures are detected in compact disks with $R_{\rm eff,90\%}$ below 23 au or continuum luminosities below 12 mJy. Assuming such disks are not universally featureless, this highlights

the need for better spatial resolution observations of the most compact disks.

3. Combining our work with the results from Long et al. (2018a) and the DSHARP survey (Huang et al. 2018b), we find that substructure is present in two-thirds of compact disks ($R_{\mathrm{eff,90\%}} < 50$ au). Our statistics indicate that the occurrence of substructure peaks near 20 au for compact disks and 40 au for extended disks, but this could be an artifact of biases against substructure detection near disk center and in faint outer regions. Substructure is otherwise present out to large relative radii. There may be no preferred location for substructure in either compact or extended disks.

4. In the Taurus and DSHARP samples, gap widths and depths are greater in extended disks than in compact disks, but this discrepancy largely disappears after normalizing gap width to gap location.

5. Tentatively, we find that fewer wide gaps are located between 20-50 au or found within disks with $R_{\mathrm{eff,90\%}}$ between 30-90 au. If all of the gaps are created by planets, this means that fewer giant planets exist at intermediate separations or in intermediate sized disks.

6. Given the case of low or medium disk viscosity ($\alpha \leq 10^{-3}$), our fitting approach detects Neptune-mass planets at separations of 20 to 30 au. This mass-radius parameter space is not probed by existing exoplanet detection techniques, and suggests that substructure analysis could be used to improve our understanding of system architectures under the planet-disk interaction hypothesis.

7. With our newly detected substructures, we infer more potential planets within compact disks and obtain a more complete view of the young planet population.

8. We calculate planet occurrence rates for both the Taurus and DSHARP surveys using simple and weighted methods. Occurrence rates in both samples roughly increase with separation from the host star, and decrease with planet mass. Planet occurrence is highest for Neptune-mass planets, and in the outer disks. The values from both samples are consisent within 1σ in each bin.

9. In a large parameter space, our calculated occurrence rates for the Taurus sample broadly agree with microlensing and direct imaging surveys. For 0.01 $M_J/M_\odot \lesssim M_p/M_* \lesssim$ 0.1 $M_J/M_\odot$, the rate is 17.4±8.3%, consistent with microlensing surveys. For 0.1 $M_J/M_\odot \lesssim M_p/M_* \lesssim 1$ $M_J/M_\odot$, it is 27.8±8.3%, higher than the results from microlensing surveys but consistent within 1σ. For gas giants more massive than 5 M_J, the occurrence rate is 4.2±4.2%, which is consistent with direct imaging surveys.

3.9 Appendix

Table 3.3 shows the derived disk parameters from Long et al. (2019) that were used in this work. For example, distance is used to scale to a standard luminosity, disk flux is used to make parameter space comparisons, effective radius is fundamental in the determination of compact and extended disks, and inclination and position angle are used in visibility deprojections. Table **??** shows the best-fit parameters in Equation 3.4 and chi-square values for these 12 compact disks. Figure 3.13 demonstrates that two-Gaussian component models of DO Tau and DQ Tau reduce the chi-square values by an order of magnitude compared to that of one-Gaussian models. Thus, we adopt two-Gaussian models for these two disks. The table in the Appendix of Zhang et al. (2023a) shows the planet masses inferred from all Taurus gaps, including those narrow and/or tentative

gaps excluded from the figures. Figure 3.14 is a recreation of Figure 3.11, but with absolute planet masses on the y-axis instead of the planet-star mass ratio.

Figure 3.15 shows the reanalysis of 12 disks with substructures found in Long et al. (2018a), along with the substructures listed in Table 3.4. Among these 12 disks, DL Tau and FT Tau have the most gaps and rings within extended and compact disks, respectively. DL Tau has 7 gaps and 7 rings. We note that the spacing of the gaps resembles that of AS 209. Since one planet is possible to carve out multiple gaps with characteristic spacing when α is low (Zhu et al. 2014b; Bae et al. 2017b; Dong et al. 2017b; 2018c; Bae & Zhu 2018b;d; Zhang et al. 2018c; Miranda & Rafikov 2019a), a planet at 95 au may also explain the secondary gap at 66 au, or even at 47 au (Zhang et al. 2018c). Thus, we only use one planet to explain the ring at 95 au and the gap at 66 au in the planet population and occurrence rate calculation. FT Tau has 2 gaps and 2 rings, implying that compact disks might also be highly substructured if we observe them with a higher resolution.

Name	Distance (pc)	F_ν (mJy)	$R_{\rm eff,90\%}$ (au)	Inclination (deg)	PA (deg)
BP Tau	129	$45.15^{+0.19}_{-0.14}$	37.49	$38.2^{+0.5}_{-0.5}$	$151.1^{+1.0}_{-1.0}$
DO Tau	139	$123.76^{+0.17}_{-0.27}$	33.43	$27.6^{+0.3}_{-0.3}$	$170.0^{+0.9}_{-0.9}$
DQ Tau	197	$69.27^{+0.15}_{-0.19}$	37.02	$16.1^{+1.2}_{-1.2}$	$20.3^{+4.3}_{-4.3}$
DR Tau	195	$127.18^{+0.20}_{-0.22}$	48.42	$5.4^{+2.1}_{-2.6}$	$3.4^{+8.2}_{-8.0}$
GI Tau	130	$17.69^{+0.25}_{-0.07}$	23.43	$43.8^{+1.1}_{-1.1}$	$143.7^{+1.9}_{-1.6}$
GK Tau	129	$5.15^{+0.19}_{-0.11}$	11.61	$40.2^{+5.9}_{-6.2}$	$119.9^{+8.9}_{-9.1}$
Haro 6-13	130	$137.10^{+0.24}_{-0.21}$	32.42	$41.1^{+0.3}_{-0.3}$	$154.2^{+0.3}_{-0.3}$
HO Tau	161	$17.72^{+0.20}_{-0.17}$	41.39	$55.0^{+0.8}_{-0.8}$	$116.3^{+1.0}_{-1.0}$
HP Tau	177	$49.33^{+0.16}_{-0.15}$	22.00	$18.3^{+1.2}_{-1.4}$	$56.5^{+4.6}_{-4.3}$
HQ Tau	158	$3.98^{+0.08}_{-0.17}$	31.09	$53.8^{+3.2}_{-3.2}$	$179.1^{+3.2}_{-3.4}$
V409 Tau	131	$20.22^{+0.12}_{-0.18}$	38.84	$69.3^{+0.3}_{-0.3}$	$44.8^{+0.5}_{-0.5}$
V836 Tau	169	$26.24^{+0.16}_{-0.12}$	31.58	$43.1^{+0.8}_{-0.8}$	$117.6^{+1.3}_{-1.3}$

Table 3.3: Compact Disk Model Parameters. This table is a recreation of Tables 1 and 3 from Long et al. (2019), with new effective radii calculated from the model intensity profiles produced in this work. Distance estimates are from Gaia DR2 parallax data (Gaia Collaboration et al. 2016; 2018). Distances and effective radii are shown without uncertainties as those uncertainties are very small (1% or less).

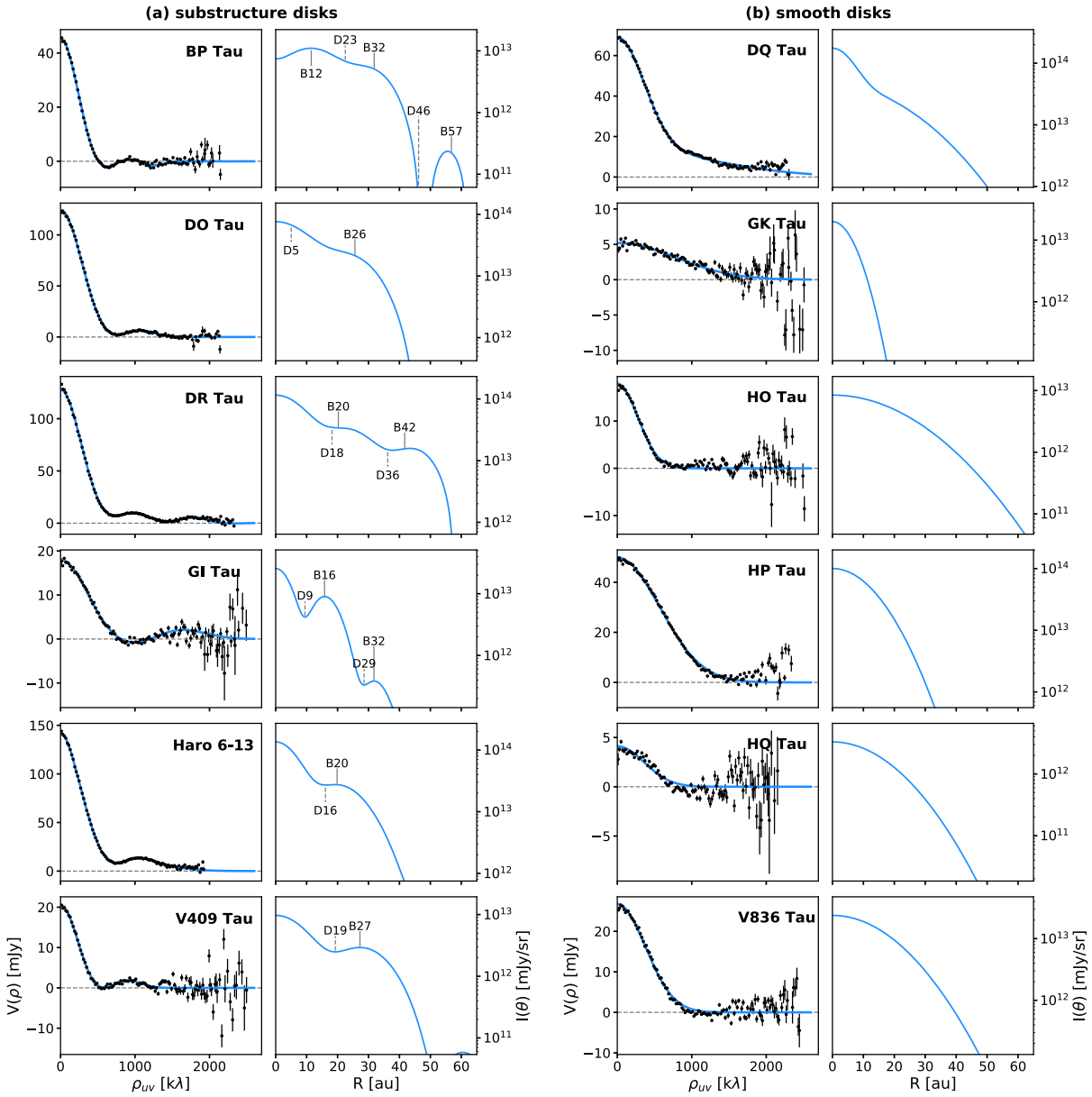

Figure 3.1: Deprojected visibility and radial intensity profiles for the six disks with identified substructure (a) and the six smooth disks (b) following our fitting approach. Overlaid in blue on the visibility curves are our best-fit models, which are used to derive the adjacent radial intensity profiles. Dashed black lines on the radial intensity curves of panel (a) mark gaps, and solid gray lines mark rings.

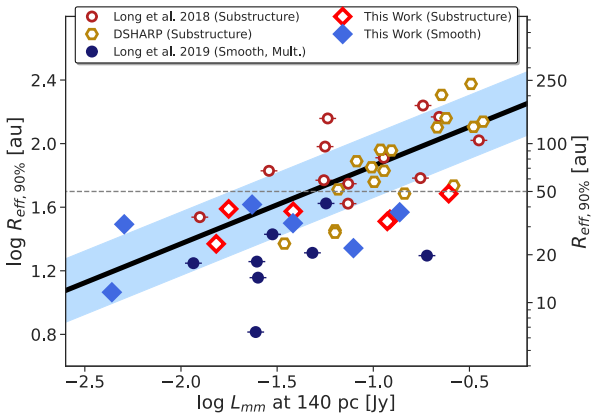

Figure 3.2: Disk continuum luminosity-size relationship for the DSHARP and full Taurus samples. The dark blue circles represent the subsample of eight smooth disks in multiple star systems from Long et al. (2019). Our chosen cutoff of 50 au effective radius for compact and extended sources is marked by a dashed gray line. The solid black line denotes the millimeter scaling relation (scaled to $R_{\rm eff,90\%}$) observed by Andrews et al. (2018c) in their sample of 105 nearby protoplanetary disks. The light blue shading represents the 68% confidence interval (plus an additional scatter term) of that relation.

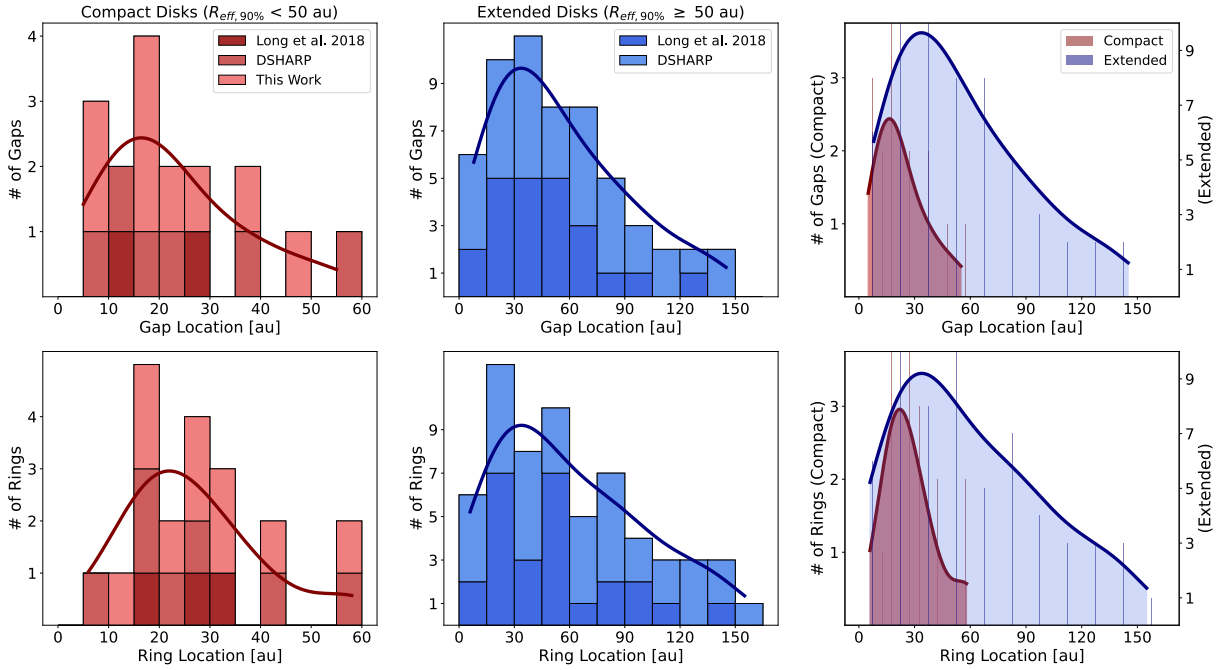

Figure 3.3: Incidence of gaps and rings in 5 au radial location bins for the compact case (left-hand panels), and 15 au bins for the extended case (middle panels). Probability density functions (PDFs) of substructure locations (scaled to match the underlying histograms) are overlaid in red and blue, respectively. These PDFs are plotted together in the right-hand panels for a more direct comparison of gap and ring locations in compact and extended disks.

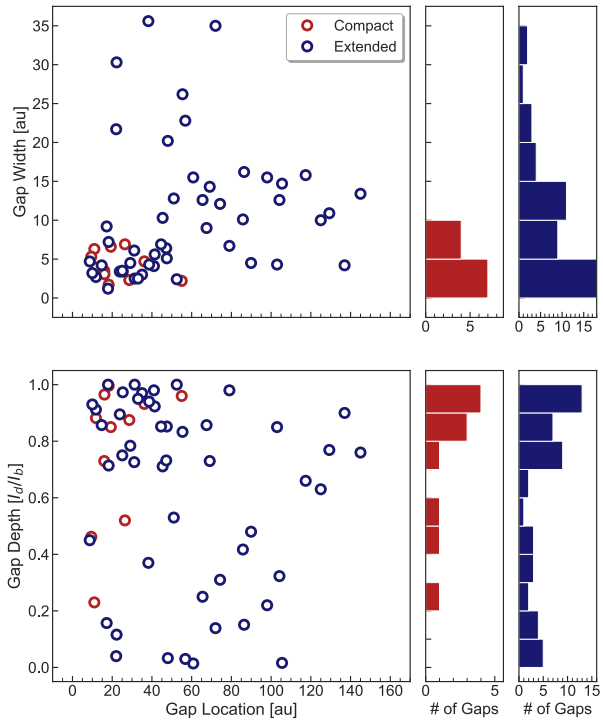

Figure 3.4: Comparison of gap widths (top panels) and gap depths (bottom panels) for gap-ring pairs in the compact and extended disks of Long et al. (2018a), Huang et al. (2018b) and this paper. Gap depths are as described in Section 3.4.2, with values near unity representing shallow features and values near zero representing deep features.

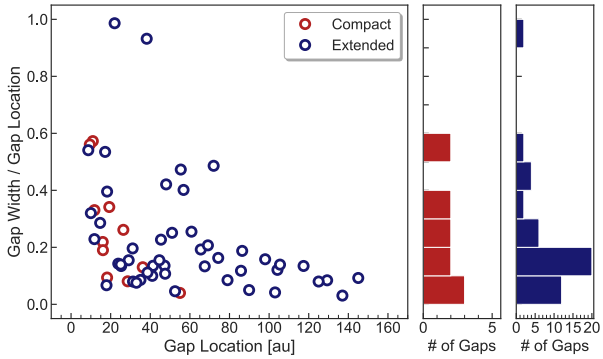

Figure 3.5: Normalization of gap width to gap location for compact and extended disks. This ratio is a better indicator of potential planet mass than absolute gap width and depth alone.

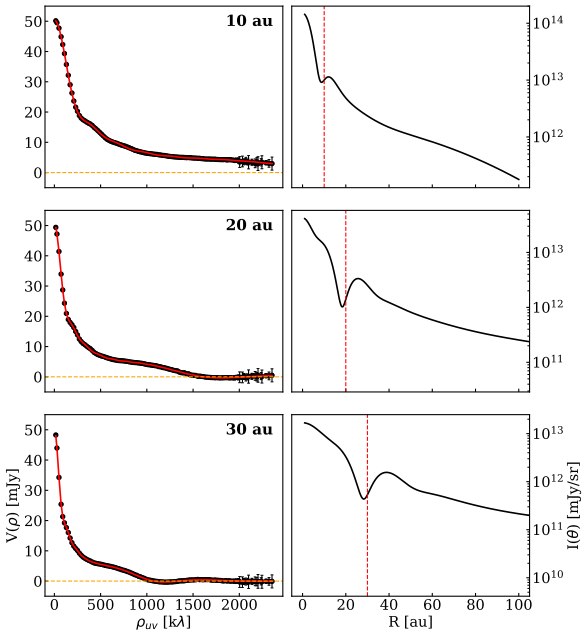

Figure 3.6: Deprojected visibility and radial intensity profiles for an approximately Saturn-mass ($M_p \approx 1.2\ M_{Saturn}$) planet injected at 10, 20 and 30 au under the $\alpha = 10^{-3}$ medium viscosity regime. Our best-fit model of the visibility profile is overlaid in red in the left-hand column, and the location of each inserted planet is marked by a red dashed line on the adjacent radial intensity curves. The orange dashed lines represent the zero point of the visibilities.

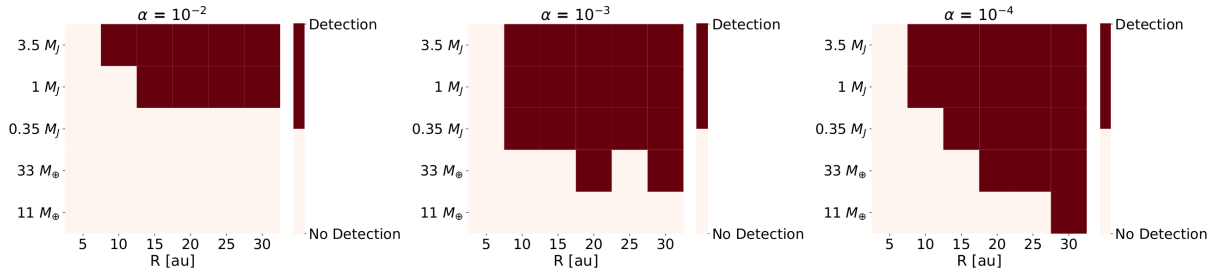

Figure 3.7: Detections and non-detections of simulated planets from 5 - 30 au under three different disk viscosity conditions: $\alpha = 10^{-2}$ (left), $\alpha = 10^{-3}$ (middle) and $\alpha = 10^{-4}$ (right).

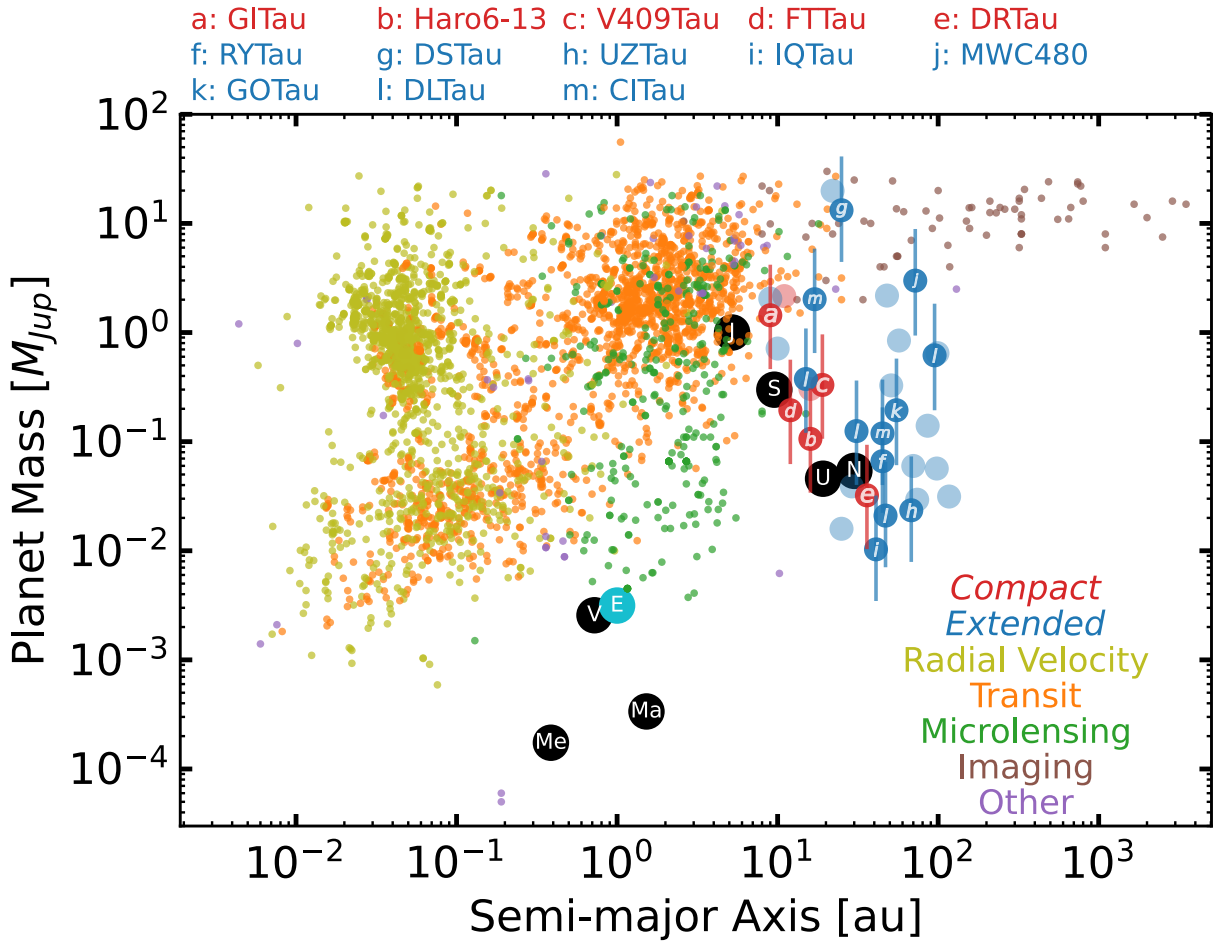

Figure 3.8: Potential young planets in the Taurus sample with detected exoplanets on the planet mass-semi-major axis diagram. The planet mass is calculated as the mass assuming $a_{\max} = 0.1$ mm and $\alpha = 10^{-3}$ (see Table in the Appendix of Zhang et al. (2023a)). The semi-major axis is equivalent to the gap location. Compact disks are in red and extended disks are in blue. The number inside the circle indicates the disk in which the planet resides. The error bar encompasses the uncertainties in the fitting and the disk viscosity. Exoplanets detected by various methods are marked with different colors.

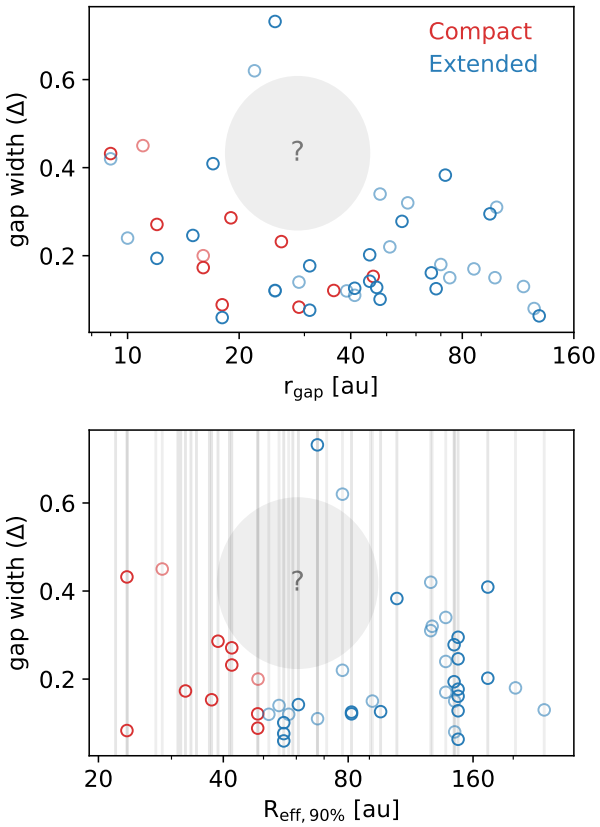

Figure 3.9: The gap width vs. gap location (top panel) and gap width vs. effective disk radius (bottom panel) for Taurus and DSHARP samples. Gaps in compact disks are in red and extended disks in blue. The gaps in the DSHARP sample are marked in more transparent colors. For the bottom panel, each vertical line represents a disk radius. Points threaded by the same vertical line belong to the same disk. The intermediate regions with fewer wide gaps are marked by ellipses and question marks.

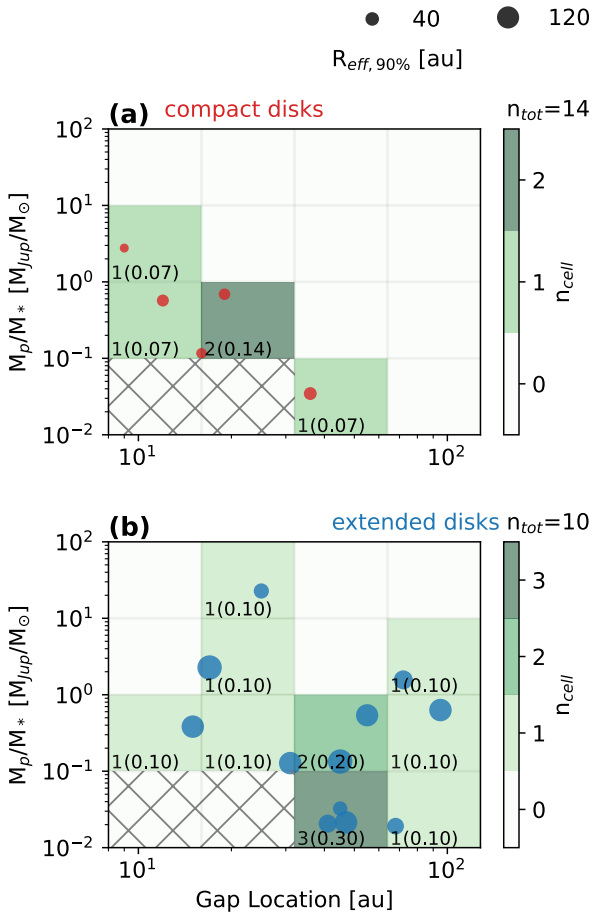

Figure 3.10: Counts of potential young planets in the Taurus sample in each cell of a planet mass-gap location diagram, separated by compact (top panel) and extended (bottom panel) disks. The counts are indicated in the lower-left corner of each cell. The counts over the total number of compact or extended disks are listed in the parentheses. The hatched region is the detection limit. The y-axis is the planet-star mass ratio in units of Jupiter mass over solar mass. The disk size is proportional to the marker size, as indicated by the legend in the top right corner.

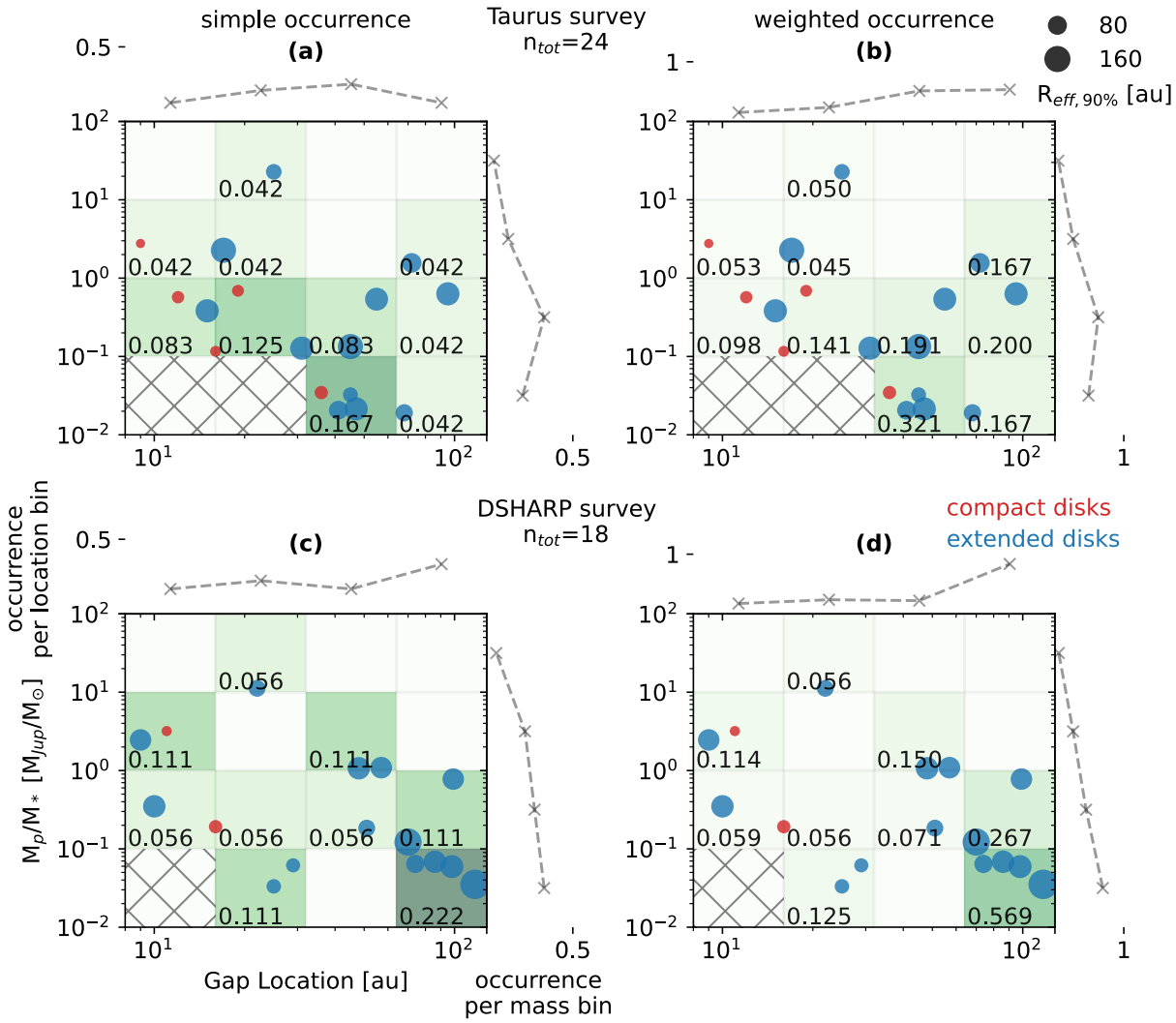

Figure 3.11: The simple (left) and weighted (right) occurrence rates of the potential young planets in the Taurus (top) and DSHARP (bottom) samples. The fraction of planets relative to the total number of disks in the sample (or relative to the fraction of disks larger than the planet location and inner cavity's radius smaller than the planet location in the weighted case) is indicated in the lower left corner of each cell. The marginalized occurrence rates are indicated on the top and right of each histogram. Red circles are compact disks and blue circles are extended disks.

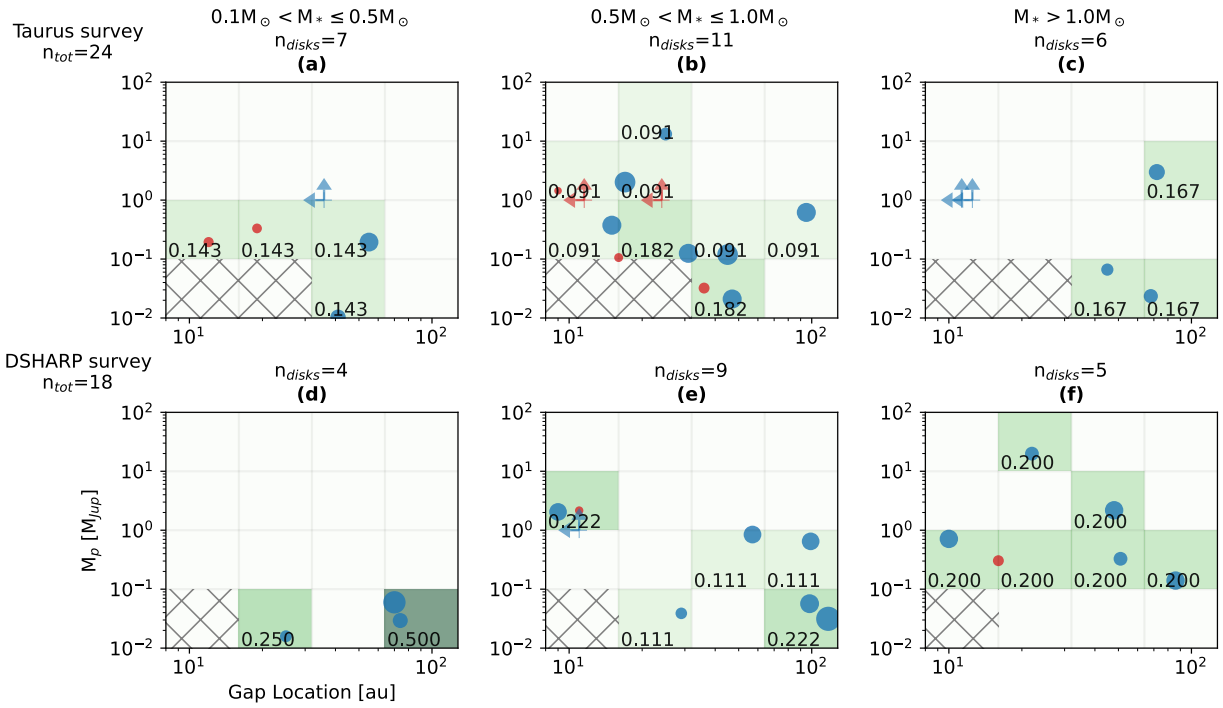

Figure 3.12: The simple occurrence rates of the potential young planets in the Taurus and DSHARP samples separated by three different stellar mass bins, with boundaries at 0.5 and 1 $M_\odot$. The layout for each diagram is similar to Figure 3.11, but the y-axis represents the absolute planet mass. The number of disks that have host stellar masses within a certain range is marked at the top of each diagram. The arrows are five potential giant planets in the transition disks in the Taurus survey. We use the ring location outside the cavity as the upper limit of the planet location and one Jupiter mass as the lower limit of the planet mass, since the planet locations and masses are both uncertain. Given these uncertainties, and the fact that multiple planets can exist in a cavity, these potential giant planets are not included in the occurrence rates.

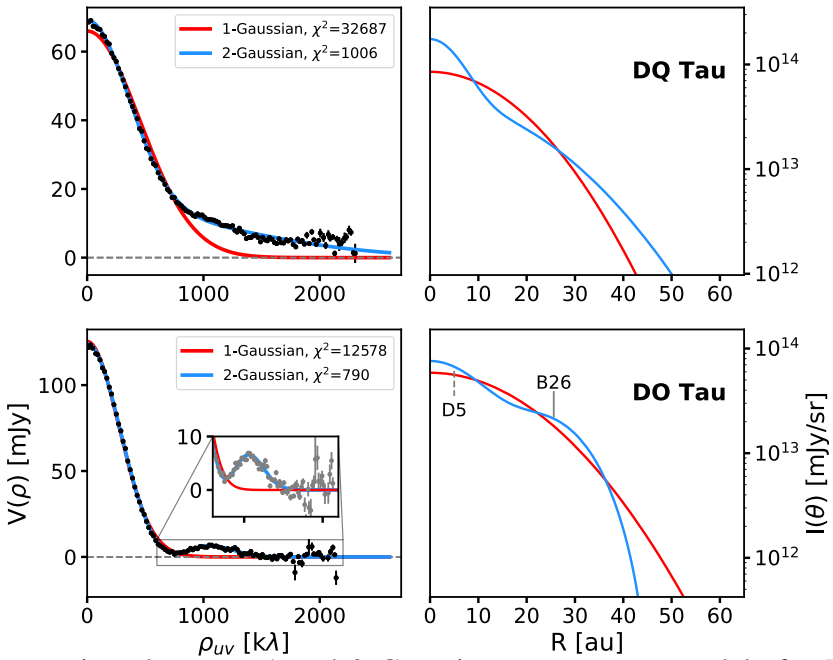

Figure 3.13: Comparison between 1 and 2 Gaussian-components models for DQ Tau and DO Tau disks. It shows that the 1-Gaussian models largely under-reproduce the visibilities beyond 1000 kλ, while the 2-Gaussian models reproduce the data at longer baselines much better.

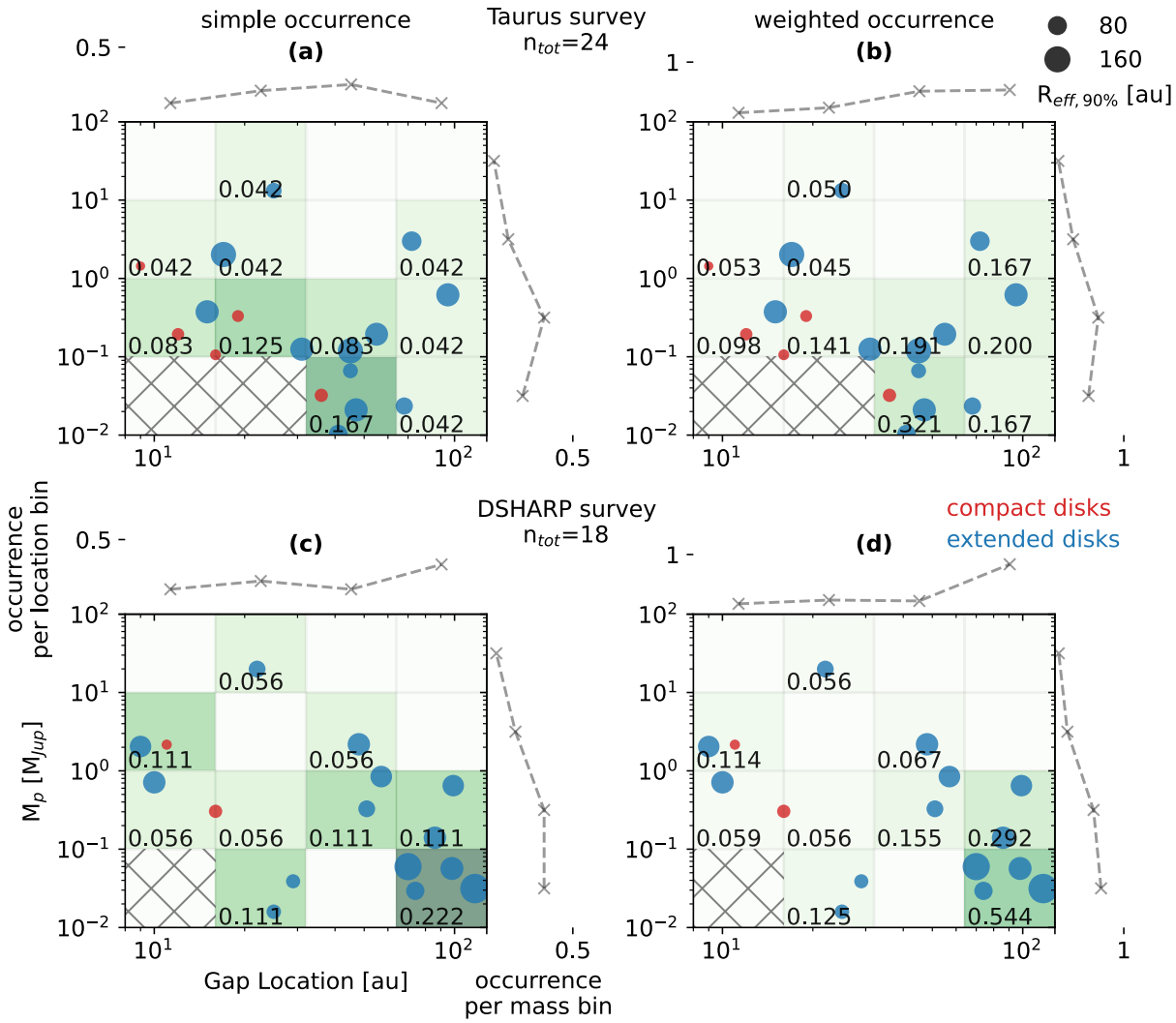

Figure 3.14: Same as Figure 3.11, but the y-axes are planet masses rather than planet-star mass ratios.

Disk	Feature	r_0 (au)	Width (au)	Depth ($\frac{I_d}{I_b}$)
CI Tau	D17	17.2	9.2	0.157
	B29	28.9	14.4	-
	D45	45.4	10.3	0.711
	B60	59.5	16.9	-
CIDA 9A	B17	16.8	1.4	-
	D22	22.2	30.3	0.116
	B36	35.9	12.1	-
	D53	52.5	2.41	1.000
	B55	55	2.44	-
DL Tau	D15	14.7	4.2	0.857
	B20	19.7	4.8	-
	D31	31.1	6.1	0.726
	B38	38	7	-
	D47	47.2	6.4	0.732
	B54	53.9	5.9	-
	D66	65.5	12.6	0.250
	B76	75.8	7.9	-
	D86	85.8	10.1	0.417
	B95	95	7.5	-
	D104	104.2	12.6	0.323
	B116	115.5	11	-
	D129	129.3	10.9	0.769
	B140	140	8.1	-
DN Tau	D18	17.9	1.2	1.000
	B19	19.3	1.2	-
	D31	31.3	2.5	1.000
	B34	34.1	2.5	-
	D48	47.5	5.1	0.852
	B53	53.4	5.5	-
DS Tau	D18	18.2	7.2	0.714
	B25	25.2	5.2	-
	D38	38.2	35.6	0.370
	B55	55.1	12.9	-

Table 3.4: Characteristics of Identified Substructures (Taurus Disks in Long et al. (2018a)).

Disk	Feature	r_0 (au)	Width (au)	Depth ($\frac{I_d}{I_b}$)
FT Tau	D12	11.8	3.9	0.882
	B16	16.4	4.4	-
	D26	26.4	6.9	0.520
	B34	34.1	8.0	-
GO Tau	D12	11.8	2.7	0.912
	B15	15.3	3.8	-
	D55	55.4	26.2	0.833
	B73	72.5	6.6	-
IP Tau	B27	26.6	12.5	-
IQ Tau	D41	41.4	5.6	0.923
	B48	47.7	5.7	-
MWC 480	D72	72	35	0.139
	B98	97.6	13.7	-
RY Tau	B14	14.2	17.6	-
	D45	44.6	6.9	0.852
	B53	52.6	7.5	-
UZ Tau E	B11	11.3	10.2	-
	D25	25.3	3.4	0.973
	B29	29.4	3.9	-
	D68	67.5	9	0.857
	B78	77.9	9.5	-

Table 3.5: (continued) Characteristics of Identified Substructures (Taurus Disks in Long et al. (2018a))

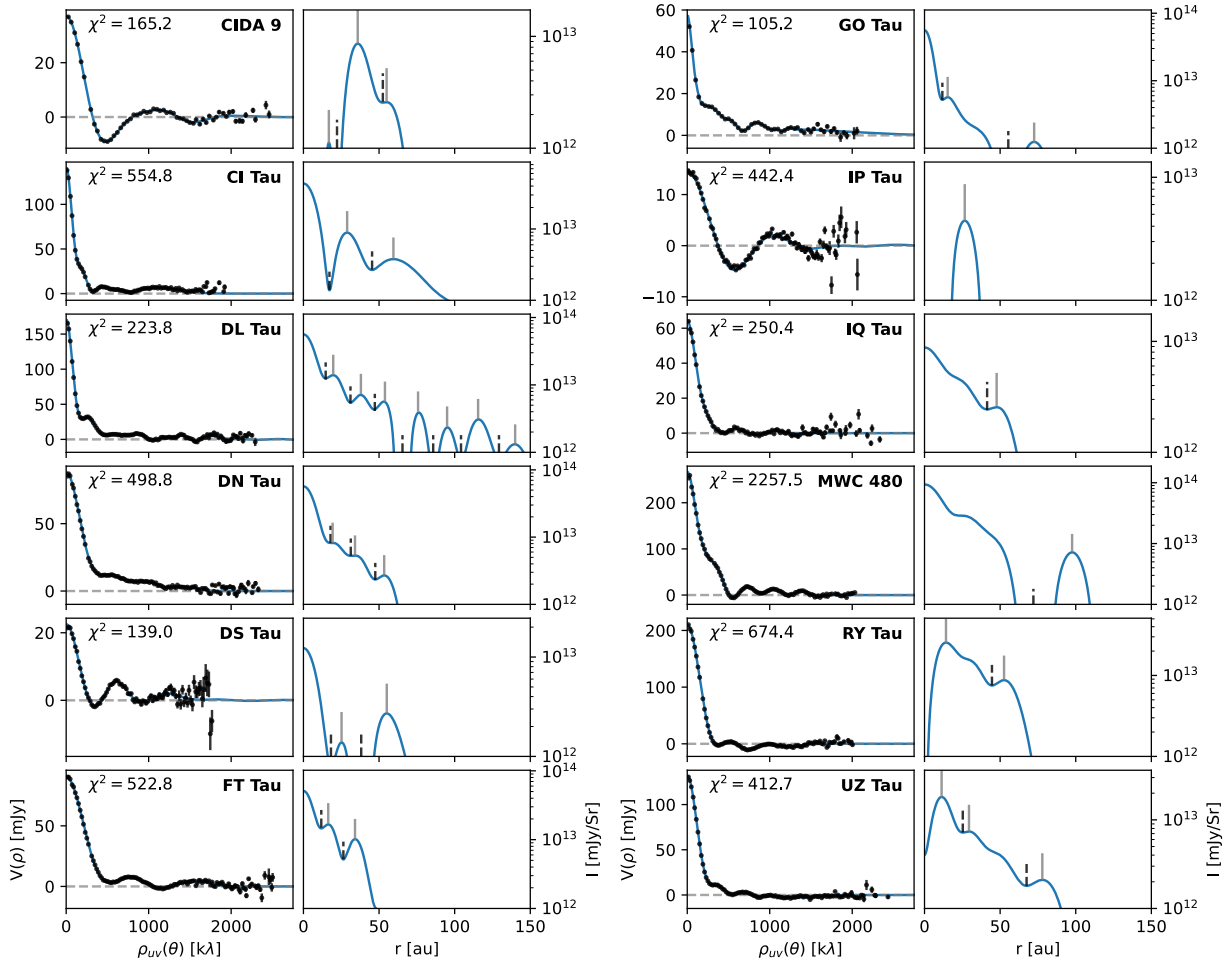

Figure 3.15: Deprojected visibility and radial intensity profiles for the 12 disks with identified substructures in (Long et al. 2018a) following our fitting approach. Overlaid in blue on the visibility curves are our best-fit models, which are used to derive the adjacent radial intensity profiles. The χ^2 score of the fitting is marked on each panel. Dashed black lines on the radial intensity curves of panel (a) mark gaps, and solid gray lines mark rings. These feature names can be found in Table 3.4.

CHAPTER 4 PGNets: Planet Mass Prediction Using Convolutional Neural Networks For Radio Continuum Observations of Protoplanetary Disks

Shangjia Zhang[1], Zhaohuan Zhu[1], Mingon Kang[2]

[1]Department of Physics and Astronomy, University of Nevada, Las Vegas, 4505 S. Maryland Pkwy, Las Vegas, NV, 89154, USA

[2]Department of Computer Science, University of Nevada, Las Vegas, 4505 S. Maryland Pkwy, Las Vegas, NV, 89154, USA

4.1 Abstract

We developed Convolutional Neural Networks (CNNs) to rapidly and directly infer the planet mass from radio dust continuum images. Substructures induced by young planets in protoplanetary disks can be used to infer the potential young planets' properties. Hydrodynamical simulations have been used to study the relationships between the planet's properties and these disk features. However, these attempts either fine-tuned numerical simulations to fit one protoplanetary disk at a time, which was time-consuming, or azimuthally averaged simulation results to derive some linear relationships between the gap width/depth and the planet mass, which lost information on asymmetric features in disks. To cope with these disadvantages, we developed Planet Gap neural Networks (PGNets) to infer the planet mass from 2D images. We first fit the gridded data in

Zhang et al. (2018) as a classification problem. Then, we quadrupled the data set by running additional simulations with near-randomly sampled parameters, and derived the planet mass and disk viscosity together as a regression problem. The classification approach can reach an accuracy of 92%, whereas the regression approach can reach 1σ as 0.16 dex for planet mass and 0.23 dex for disk viscosity. We can reproduce the degeneracy scaling $\alpha \propto M_p^3$ found in the linear fitting method, which means that the CNN method can even be used to find degeneracy relationship. The gradient-weighted class activation mapping effectively confirms that PGNets use proper disk features to constrain the planet mass. We provide programs for PGNets and the traditional fitting method from Zhang et al. (2018), and discuss each method's advantages and disadvantages.

4.2 Introduction

Detecting young planets in protoplanetary disks is essential to infer where and when planets form and how massive they are, putting stringent constraints on planet formation theory. Unfortunately, despite thousands of exoplanets having been discovered, only a few of them are around young stars within 10 million years old. There are even fewer young forming planets found in dusty protoplanetary disks. One notable example is PDS 70 system, where two young planets with several Jupiter mass have been discovered within the dusty cavity of 80 au (Keppler et al. 2018a; Müller et al. 2018b; Wagner et al. 2018b; Haffert et al. 2019b; Isella et al. 2019c; Christiaens et al. 2019b; Wang et al. 2020b; Hashimoto et al. 2020b). However, such firm detection seems to be rare (e.g., Zurlo et al. 2020), and we are not expecting to directly detect a planet whose mass is less than one Jupiter mass (Ruane et al. 2017). There are other promising methods to detect young planets in disks, such as using disk kinematic features influenced by the planet (Perez et al. 2015b; Teague

et al. 2018b; Pinte et al. 2018b; Rabago & Zhu 2021b; Izquierdo et al. 2021). However, all these methods can only detect planets that are more massive than Jupiter. The only method that can detect planets less massive than Jupiter is to use gaps in the dust continuum images (e.g., Zhang et al. 2018b). Since dust particles drift to the local pressure maximum, even small gas perturbations by a low mass planet can lead to observable dust gaps (Paardekooper & Mellema 2006; **?**; Rosotti et al. 2016a; **?**; Dong et al. 2018d).

Hydrodynamical simulations with dust particles have been carried out to infer the planet properties from radio observations. At early times when ALMA high resolution observations were scarce, numerical simulations were fine-tuned to fit one source at a time (e.g. Dong et al. 2015c; Dipierro et al. 2015b; Picogna & Kley 2015; Dipierro et al. 2018). However, when high angular-resolution surveys became available (e.g., Andrews et al. 2018a; Long et al. 2018b; Cieza et al. 2021b), it was impractical to run direct numerical simulations for each source. Thus, relationships between the gap and planet properties have been solved. For gaseous gaps, such relationships have been well characterized (Fung et al. 2014a; Kanagawa et al. 2015a; 2016a). However, the relationships are less clear for dusty gaps mainly because the gap width/depth can vary significantly with different sized particles in disks. Lodato et al. (2019b) assumed that the dusty gap width is scaled with the planet Hill radius to derive the masses of planets in the Taurus survey (Long et al. 2018b). Rosotti et al. (2016a) carried out simulations to derive the relationship between the planet mass and the distance between the planet and the pressure maximum at the outer gap edge. However, Rosotti et al. (2016a) did not consider the effects of particle size and disk viscosity, both of which can change the gap-planet relationship significantly. A detailed study was done by Zhang et al. (2018b), who carried out a large grid of planet-disk interaction simulations with dust particles, generated synthetic observations, and derived relationships between the planet mass, the disk scale

height, the disk viscosity, and the particle size in disks[1]. Such relationships have been used to derive the young planet population from the DSHARP survey (Andrews et al. 2018a; Zhang et al. 2018b).

However, the approach in Zhang et al. (2018b) still suffers several shortcomings. First, the procedures to derive the planet mass are relatively complicated. Disk viscosity, scale height, and particle size need to be constrained by other methods and specified beforehand. Based on these parameters, different fitting formulae need to be adopted. To make the method in Zhang et al. (2018b) easier to use, parallel to the method presented in this paper, we provide new PYTHON programs for the Zhang et al. (2018b) linear fitting method[2]., which can automatically find the planet mass after the parameters are specified. The second shortcoming, which is intrinsic to the method itself, is that the synthetic images generated from simulations were azimuthally averaged before deriving the relationship between the planet mass and gap widths/depths. Thus, all information from non-axisymmetric features was lost. These features have rich information on disk and planet properties. For example, an eccentric gap suggests a massive planet. A lopsided disk with a large intensity asymmetry indicates a low viscosity or large particles.

To directly extract information from 2D images, in this work, we adopted machine learning techniques. Machine learning techniques have been widely used across the astronomical community for decades, and here we briefly describe several works related to computer vision image tasks, using Convolutional Neural Networks (CNNs), specifically.

CNNs have been used widely in galactic and extra-galactic studies. Dieleman et al. (2015) is

[1]We use "the linear fitting method" to denote this method throughout this paper.

[2]The code is available at https://github.com/zhangsj96/DSHARPVII.git

one of the first works that use modern CNN networks. It originated from an international competition *Galaxy Challenge* that aimed to build automated tools for galaxy morphology classification based on annotated images from the Galaxy Zoo project. They applied CNNs to the morphological classification of crowd-sourcing annotated images and achieved $> 99\%$ accuracy, which would benefit analysis in future large galaxy surveys such as Vera C. Rubin Observatory. Hezaveh et al. (2017) used CNNs to automate analysis of strong gravitational lenses. The traditional method with maximum likelihood modeling requires human expertise and is time-consuming. The network can quantify image distortions caused by strong gravitational lensing and estimate these structures' corresponding matter distribution with comparable accuracy as the traditional method, but ten million times faster. Non-experts can quickly obtain lensing parameters for a large sample of data. Hassan et al. (2019) utilized CNNs to identify reionization sources from 21 cm maps. Active galactic nuclei and star-forming galaxies are two leading sources that reionized our Universe. CNNs were trained to distinguish the sources on the 21 cm images. The technique would aid power-spectrum observations and provide extra information to break degeneracies between a broad range of reionization models. The classification accuracy is between 92-100%, depending on the redshift and neutral fraction range.

CNNs have also been used in the Solar System study. Lieu et al. (2019) trained CNNs on simulated observations of an upcoming mission *Euclid* for Solar system objects identification. They used transfer learning (i.e., training on several established CNN architectures with some modifications) on a relatively small data set. Their best model correctly identified objects with a top accuracy of 94%, successfully separating solar system objects from other astronomical sources.

In the field of star formation, identifying signatures of stellar feedback in molecular clouds used to mainly rely on visual inspection. Van Oort et al. (2019) ran 3D MHD simulations with stellar

feedback and produced 2D synthetic CO continuum images. They trained CNNs on synthetic data and identified shells in real observations. Later they extended the work to 3D so that they could make full use of molecular line spectra datacube. They found stellar feedback bubbles and predicted feedback properties (Xu et al. 2020b), and identified 20 new outflows (Xu et al. 2020a) that were missed by previous visual inspections.

While CNNs have not been applied to the planet-disk interaction study, general machine learning techniques are receiving more attention in the field. Recently Auddy & Lin (2020b) used fully connected neural networks to fit the relationship between the planet mass and parameters such as gap width, aspect ratio, viscosity, dust-to-gas ratio, Stokes number, and density profile. Compared to previous fitting methods, the work is the first to fit the relationship non-linearly. Since a deep neural network is good at fitting problems that are intrinsically non-linear, their estimated planet mass follows closer to the simulation data given a multi-dimensional input. Nevertheless, users still need to provide inputs that are barely constrained from observations, and asymmetric information is still lost when 2D images are converted to 1D radial profiles. While we were modifying this paper after the first referee report, Auddy et al. (2021) published a CNN approach for the 2D images, which alleviated some of these shortcomings.

Our aim in this paper is to infer the planet mass from the 2D observational images directly [3]. In Section 4.3 we briefly introduce the background and the basic glossary of CNNs. In section 5.4 we describe the simulation setup, synthetic observation production, prepossessing, augmentation, and the neural network setup and training. In Section 8.4 we analyze the results, apply the networks to several gaps in DSHARP observations, and compare the derived planet masses to those from the previous method. After a short discussion in Section 8.5, we conclude our paper in Section 7.8.

[3]The code is available at https://github.com/zhangsj96/PGNets.git.

4.3.1 Regular Neural Network

The most common subset of deep learning is regular neural networks (or fully-connected neural networks). Neural networks receive a vector and transform it through a series of hidden layers. Each hidden layer is made up of a set of neurons, where each neuron is fully connected to all neurons in the previous layer. The last fully-connected layer is called the "output layer". For classification problems, it gives scores for different classes. For regression problems, it predicts continuous values.

Each neuron has some parameters to be tuned, which can be accomplished by training the model. The training is a process of minimizing the loss function and updating parameters through back-propagation. The data are separated as training, validation and testing sets. The training data are used to feed into the neural network. The validation data are not used in training the model but are used as a metric to monitor the training result at every epoch. The testing data are used to evaluate the model accuracy after the training is completed.

4.3.2 Convolutional Neural Network (CNN)

For regular neural networks, the input vector could be extremely large if the input is an image that is represented by either a flattened matrix (e.g., a gray-scale image) or a flattened tensor (e.g., an RGB-colored image). There are correlations between neighboring pixels and different color channels in an image, but a vector representation loses such correlations. Thus, regular neural networks are not ideal for training image data. The convolutional operation naturally takes the local connections into account. To that end, CNNs are powerful in fitting image data. As a variation of

regular neural networks, their primary unit of computation is the convolutional operation instead of simple matrix multiplication. A layer of a convolutional network has neurons arranged in three dimensions: width, height, and depth. A convolutional kernel will be operated on this 3D tensor, and the output becomes the next layer. Usually, the network's width and height become smaller for later layers, while the depth becomes deeper. The process of downsampling the feature map is called pooling. LeCun et al. (1998) introduced LeNet to recognize hand-written digit characters. It reached a very high performance and brought artificial neural networks into popularity.

4.3.3 Residual Neural Network

A residual neural network (ResNet) is a kind of CNNs that has connections even between skipping (non-neighboring) layers (He et al. 2016a). It has shortcuts to jump over some layers. Typical ResNet models are implemented with double or triple skips that contain ReLU and batch normalization (Ioffe & Szegedy 2015) in between. Skipping effectively simplifies the networks and reduces the parameters. It also avoids the problem of vanishing gradients so that the network can go deeper than traditional CNNs while still improving the performance.

4.4 Method

A schematic view of our method from input to output is summarized in Figure 4.1. We first introduce how we convert the simulations to synthetic observations (Section 4.4.1), and then discuss the prepossessing (Section 4.4.2) and augmentation (Section 4.4.3) steps to make the network robust. We layout the PGNet structures (VGG-like or ResNet classification; Section 4.4.4; regression; Section 4.4.5) and finally obtain the output prediction.

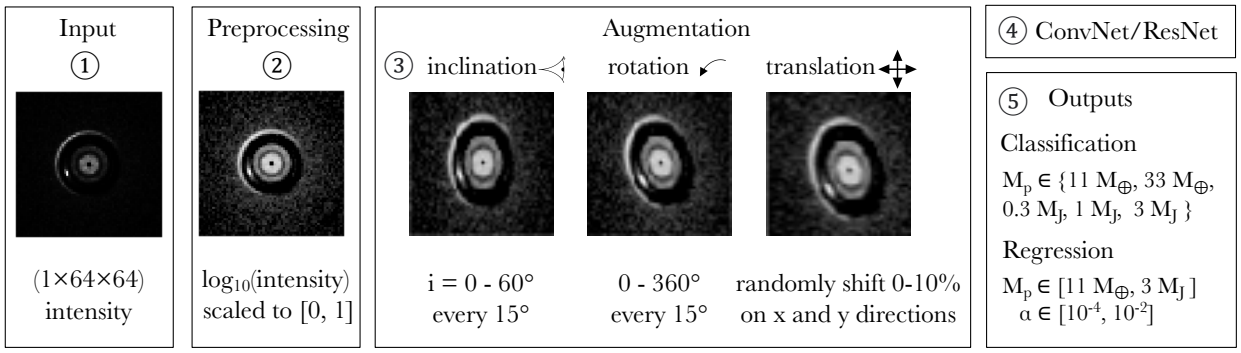

Figure 4.1: A schematic view of our work from input to output. There are five steps. First, we prepared the input from simulations or observations. Second, the image was prepossessed and normalized. Third, the image was augmented for different inclinations, rotations, and translational shifts. Then it flowed into the neural network. Finally, we obtained class scores and chose the label with the highest score for the classification problem. A planet mass, viscosity pair was returned for the regression problem.

At the output layer, we tried both classification and regression problems. At first, we treated the fitting of the planet mass as a classification problem, since the data set of Zhang et al. (2018b) are too sparse (only five discrete planet masses) to return continuous-valued predictions. They were used to demonstrate that CNNs can successfully predict planet masses on discrete grids. Then we ran additional 150 simulations to provide more sampling between these grids, and built regression model which predict continuous planet mass and disk viscosity at the same time. The samples were drawn using the Latin hypercube sampling (LHS) (McKay et al. 1979).

4.4.1 Simulations

For the classification problem, we used the results of the planet-disk interaction simulations in Zhang et al. (2018b) on the grddied parameter space (5 planet masses, M_p, 3 aspect ratios, h/r , and 3 disk viscosities, α). We denote a model with a $\{M_p, h/r, \alpha\}$ pair as a generic model, as this model can be used to generate models with different surface densities and maximum particle sizes.

For the regression problem, we added additional 150 simulations with near-randomly generated M_p, h/r, and α. We briefly summarize the simulations here. The simulations were carried out with 2D hydrodynamic code Fargo-ADSG (Baruteau & Masset 2008a;b; Baruteau & Zhu 2016). Dust grains were represented by 200,000 super-particles with different sizes. The Stokes number (St) of the particles at r_p ranged from 1.57 $\times 10^{-5}$ to 1.57. The simulations in the gridded parameter space covered three disk viscosities α=10^{-4}, 10^{-3} and 10^{-2}, three disk aspect ratios at r_p with h/r = 0.05, 0.07 and 0.1, and five planet masses with the planet-star mass ratios (q) of 3.3×10^{-5}, 10^{-4}, 3.3×10^{-4}, 10^{-3}, 3.3×10^{-3} (which are equivalent to the planet masses of 11 $M_\oplus$, 33 $M_\oplus$, 0.3 M_J, 1 M_J and 3 M_J if the central star is a solar mass star). The parameters for the LHS were drawn from $\alpha \in [10^{-4}, 10^{-2}]$, $h/r \in [0.05, 0.1]$, and $M_p \in [11\ M_\oplus, 3\ M_J]$. They were near-uniformly drawn in the interval of h/r, $\log(\alpha)$ and $\log(M_p)$.[4] We initialized the gas surface density as

$$\Sigma_g(r) = \Sigma_{g,0}(r/r_0)^{-1}\,, \tag{4.1}$$

where r_0 is the position of the planet and we set $r_0 = r_p = 1$. Our numerical grid extended from 0.1 r_0 to 10 r_0 in the radial direction and 0 to 2π in the θ direction. The data sets used in this paper are at 1000 planetary orbits. We assumed locally isothermal equation of state. The temperature at radius r follows $T(r) = T_0(r/r_0)^{-1/2}$.

To convert super-particle distributions to optical depth maps, we used a subset of particles and gave them different weights depending on their opacity, sizes, and surface density at their locations. We adopted DSHARP opacity (Birnstiel et al. 2018) and neglected scattering. These particles were

[4]We used `pyDOE` (https://github.com/tisimst/pyDOE) to generate parameters. The generated parameters can be found at https://github.com/zhangsj96/PGNets.git.

interpolated onto 1200 x 1200 regular grid with physical dimensions as 10 r_p $\times$ 10 r_p. Then we smoothed the gridded data with a Gaussian kernel similar to the resolution of ALMA. Gaussian σ = 2 pixels, which is 0.03 r_p. If the planet is at 20 au, this is the same as the resolution of a circular beam with FWHM = 1.4 au. Finally, we calculated the brightness temperature or intensity for each grid cell as

$$T_b(x,y) = T_d(r)(1 - e^{-\tau(x,y)}), \tag{4.2}$$

and we assumed that the midplane temperature follows

$$T_d(r) = T_d(r_0)\left(\frac{r}{r_0}\right)^{-0.5}. \tag{4.3}$$

For more details please see Zhang et al. (2018b).

In principle, the real synthetic image should be calculated with assumptions of detailed observational setups (e.g., antenna array configuration and integration time) and CLEAN methods. However, this is unrealistic since (a) they depend on specific observational setups and data reduction methods, which cannot be covered thoroughly, and (b) these time-consuming steps need to be applied on each augmented image (Section 4.4.3), which cannot be realized within our computational power. Instead, in Section 4.6.1 we will use one case to demonstrate that neglecting these steps does not affect the correctness of the prediction.

To generate synthetic radio continuum images of disks having various dust size distributions and disk surface densities, we chose 5 different maximum particle sizes a_{max} = 0.1 mm, 0.3 mm, 1 mm, 3 mm and 1 cm, and 7 different gas surface densities $\Sigma_{g,0}$ = 0.1 g/cm^2, 0.3 g/cm^2, 1 g/cm^2, 3 g/cm^2, 10 g/cm^2, 30 g/cm^2 and 100 g/cm^2. These combinations of a_{max} and $\Sigma_{g,0}$ correspond

to 9 different characteristic Stokes numbers (St $\propto a_{max}/\Sigma_{g,0}$). Figure 4.2 shows dust continuum intensity at 1.3 mm for a case with $M_p = M_J$, α= 10^{-3} and h/r=0.07, with all combinations of a_{max} and $\Sigma_{g,0}$. Note that for a_{max} = 3 mm (and 1 cm), the lowest (two) surface density case(s) exceed the upper limit of the particles' Stokes number in our simulation. In total, different a_{max} and $\Sigma_{g,0}$ lead to 32 combinations (7+7+7+6+5) for each generic model. Since no dust growth and back-reaction are included, the dust drift velocity only depends on the Stokes number. This is why the gaps look similar for a given Stokes number. They are still different in that (a) the opacity is dependent on the maximum particle size and (b) the dust surface density is different. Thus, the radial profile of the optical depth is different. When the disk changes from the optically thin to thick regime (from top to bottom panels), the intensity maps become smoother.

We explored different dust size distributions by choosing three different power-law indices (p; n(a)$\propto a^{-p}$) being 3.5, 3 and 2, but their intensity maps are very similar. This could lead to some duplication between training and testing sets. For this reason, we only used one power-law index p = 3.5.

An image with too many pixels takes a large amount of memory, does not help the training, and even leads to overfitting. Thus, we downgraded the image size and found that a 64 $\times$ 64 image is good enough to preserve features and help the training. Note that the real observation image will also be fed into the network using this resolution. To convert an observation to the input format, a simple linear interpolation suffices. For our models, we selected the central squared $3r_p$ $\times$ $3r_p$ region. Outside of this region, there is little emission from our simulations. The data are 2D (gray-color, 1$\times$64$\times$64) images of disk emission. There are 5 $\times$ 3 $\times$ 3 $\times$ 32 = 1440 models for the classification problem and (45+150) $\times$ 32 = 6240 models for the regression problem.

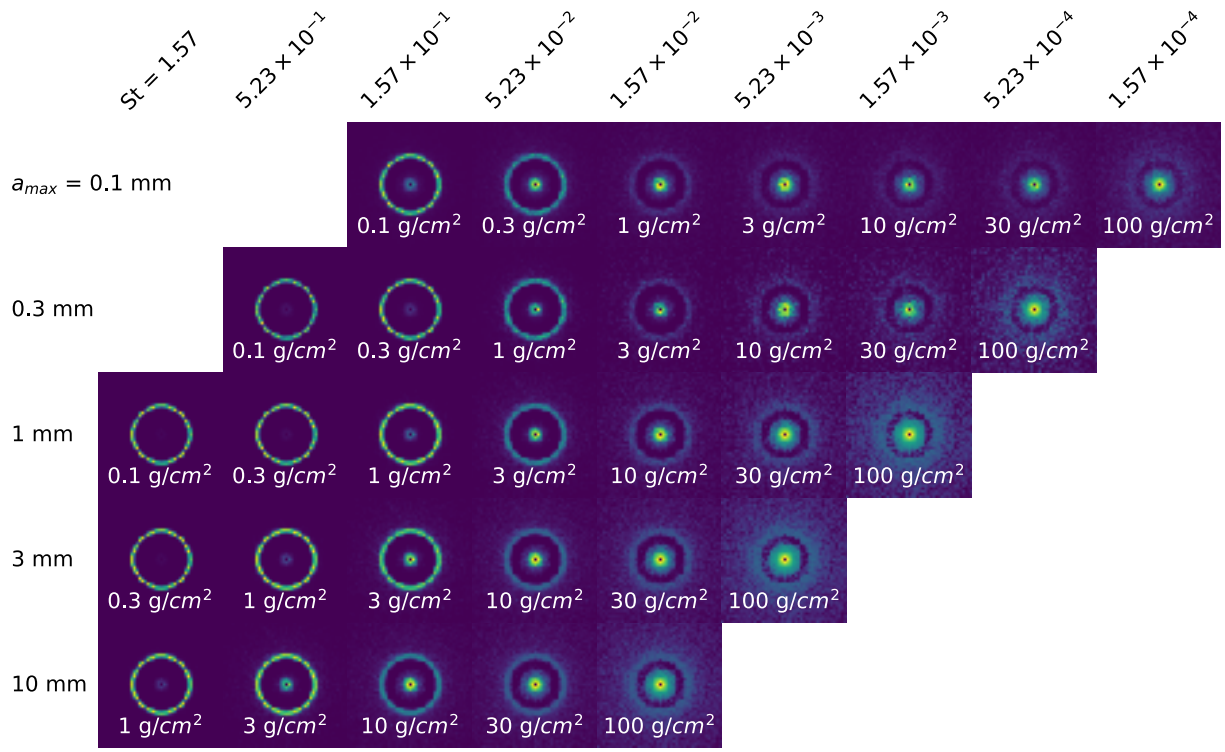

Figure 4.2: 1.3 mm dust continuum intensity maps for the M_p = 1 M_J, α= 10^{-3} and h/r=0.07 case with different a_{max} and $\Sigma_{g,0}$. In each row, the a_{max} is the same with increasing surface density from left to right. The Stokes number at the planet's location is the same at each column and decreasing from left to right.

4.4.2 Preprocessing

We found that adding some noise to images helped the training, so we added 10% RMS noise to each image. The initial value of the intensity in the image can be different by orders of magnitude. In neural networks, it is essential to normalize the input data. We found that taking the logarithm of the value works best for the training. We scaled the image values from 0 to 1. We also set an emission floor as 1% of the maximum emission intensity, so that values below that became zero. In expression,

$$\text{pixel value} = \begin{cases} \frac{\log_{10}(I)-\log_{10}(I_{max})+2}{2} \text{ if } \log_{10}(I) > \log_{10}(I_{max}-2), \\ 0 \qquad\qquad\qquad\qquad \text{elsewhere.} \end{cases} \tag{4.4}$$

This choice of the floor value can also be justified for observational data since the sensitivity limit for these high-resolution ALMA observations is usually between 1% to 0.1%. The gap region has low values, and the ring region has high values. Considering that previous studies used gap shapes to infer the planet mass, we reversed the value as (1-value) so that the gap had high values. It turned out that this procedure had little effect on the results. Since this procedure is well defined, it is also simple to apply it to the real observation and rapidly convert that to the network input. Note that our main focus is on the gap shape (width and depth, and asymmetric features). The normalization process we adopted removed the information of the absolute value of the emission. Ideally, the absolute value of the emission can provide extra information and can be considered in future works.

4.4.3 Data Augmentation

In real observations, disks are hardly to be exactly face-on (e.g., the configuration in Figure 4.2). As long as the gap is spatially resolved and the disk is not too edge-on, we should still obtain information from the image. Thus, we inclined the disk from the initial data from 0° to 60°, spacing every 15°. This was simply done by stretching the y-direction of the optical depth map, $\tau(x,y)$ while fixing the x-direction size. The optical depth is increased accordingly. This can be justified considering that mm dust is highly settled in protoplanetary disks (Pinte et al. 2016a). With this data augmentation, the observational data for disks with any inclinations can be directly used as an input for our networks.

To explore the rotational symmetry (Dieleman et al. 2015), we rotated the disk every 15°, from 0° to 360° (0° and 360° are only counted once). The degree of rotation is also called position angle. Note that the rotation and inclination variations were done on the original 1200 $\times$ 1200 (10 r_p $\times$10 r_p) data to avoid the sharp edges due to missing values, but whether including this step did not affect the results.

We also explored translational symmetry by randomly shifting the image in x and y directions from 0% to 10%. Even though CNNs should conserve translational symmetry by themselves, the fitting result was slightly improved. This is also helpful for the prepossessing of observational data since the disk does not need to be perfectly centered when they are fed into the networks.

Every one of the face-on images can generate thousands of augmented data. However, we still separated the training, validation, and testing sets with those original data. Otherwise, if we separate all the data after the augmentation, the fitting accuracy will actually increase since different augmented data generated from a single model can look very similar. However, this

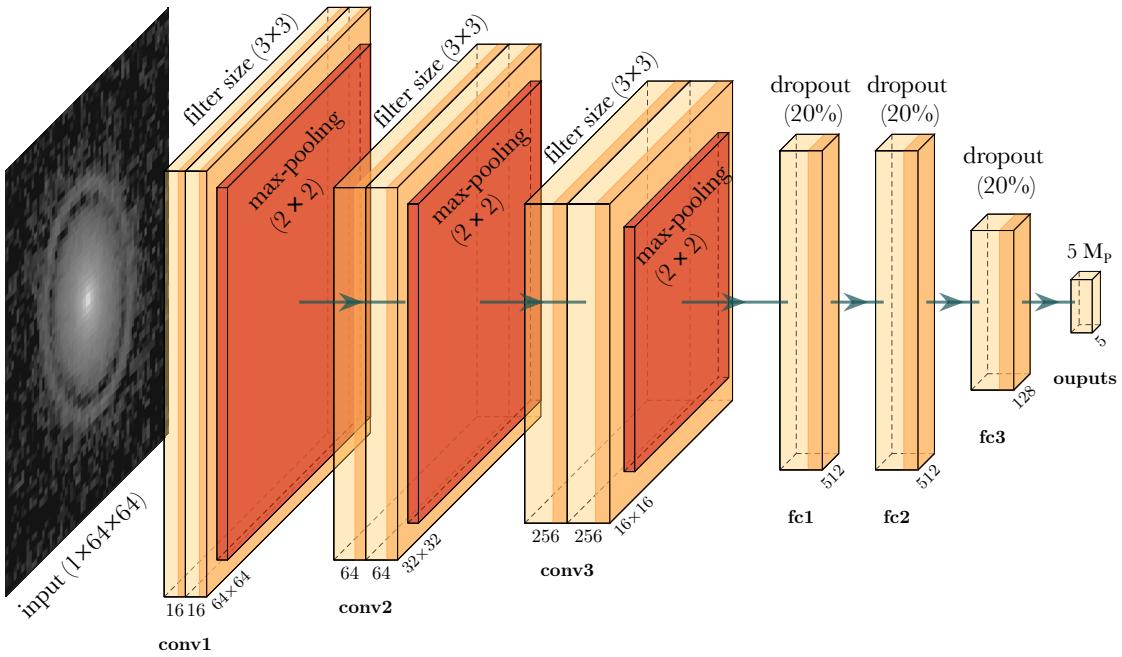

Figure 4.3: The architecture of VGG-like network. The image as an input is the $\log_{10}$ of the intensity, scaled between zero and one with only one channel. The example image is preprocessed image of GW Lup (Andrews et al. 2018a). Then there are six convolutional layers and three fully-connected layers.

increase of the accuracy is unreal due to the similar data in training, validation, and tests. Thus, we separated the data sets before the augmentation.

4.4.4 Classification Models

We first tested out CNN models as a classification problem on the gridded data set in Zhang et al. (2018b). We set up the network as a classification problem instead of a regression problem since our origional simulations only have five discrete planet masses. We built two neural networks for comparison, one architecture similar to VGG-16 (Simonyan & Zisserman 2014) and the other adapted from ResNet (He et al. 2016a). We chose not to use the original VGG-16 architecture since it introduced more parameters but did not improve the performance.

Figure 4.3 shows the architecture of VGG-like network. As mentioned in the previous section, the input data are gray-color images ($1\times 64 \times 64$), with values ranging from 0 to 1. Then it follows two convolutional layers with 16 channels (depth=16). In this specific neural network, the convolutional filter size is always 3×3 with 1 stride. The padding is on image edges so that the tensor keeps the same number of points (64) in both x and y directions. We also used ReLU (Rectification Linear Unit, i.e., max[0, x]), as the activation function for all layers. After a 2×2 max-pooling operation, the image dimension becomes 32×32. Then it follows two convolutional layers with 64 channels and another max-pooling. The last two convolutional layers have 256 channels before a max-pooling. Then it connects to 3 fully-connected layers, two with 512 nodes and one with 128 nodes. These fully-connected layers all have 20% dropout rates to avoid overfitting. Finally, the output layer has 5 nodes which stand for 5 different planet masses. There are 9,504,565 trainable parameters in total. We found that adding more layers did not increase the accuracy.

The learning rate is a hyper-parameter that controls the step size in an optimization process while it is minimizing the loss function. An analogy of it is the step size in solving differential equations. We adopted the initial learning rate as 0.001. We chose the sparse categorical cross-entropy as the loss function and `ADAM` as the optimizer (Kingma & Ba 2015). We defined accuracy of the method as

$$\text{accuracy} = \frac{\text{TP}+\text{TN}}{\text{TP}+\text{TN}+\text{FP}+\text{FN}}, \tag{4.5}$$

where TP, TN, FP and FN stand for true positive, true negative, false positive and false negative, respectively.

To balance the trade-off between rate of convergence and overshooting, we adopted an adaptive learning rate. The learning rate varying as the training epoch is a cosine function so that the

learning rate becomes much smaller at later training stages. The batch size is 128. The training, validation, and testing sets were split as 60%, 20%, and 20% of the 1440 models that were randomly shuffled. We also included different inclinations and rotations for the testing set, so there are total $1440 \times 0.2 \times 5 \times 24$ = 34560 testing images. The training was done on a single NVIDIA GPU GeForce RTX 2080 Ti 12GB. We used `Tensorflow v2` (Abadi et al. 2015) to build the network. The VGG-like network took less than an hour, while the ResNet model took two hours.

For the residual network, our network was adopted from ResNet v2 (He et al. 2016b) with three skips. It has a bottleneck layer with stacks of batch normalization, activation (ReLU) and convolutional layers. The batch normalization can make ANN faster and more stable. The first shortcut connection per layer is 1 x 1 convolution and the second and onward shortcut connection is identity. At the beginning of each stage, the feature map size is halved by a convolutional layer with 2 strides, while the number of filter maps is doubled. Within each stage, the layers have the same number of filters and the same filter map sizes. There are 22 convolutional layers in total, but with only 576,357 parameters, an order of magnitude smaller than the VGG-like model. The initial learning rate is 0.005. Other setups are the same as the VGG-like model.

4.4.5 Regression

After carrying out additional simulations with the randomly-generated parameters from the LHS, we were able to fit the planet mass in a continuous space. Thus, we fitted the combined data set as a regression problem. We used mean square error (MSE) as the loss function. We made the output layer as a M_p-α pair, as MSE can evaluate vectors (e.g., Alibert & Venturini 2019). In this way, the planet mass and disk viscosity can be predicted together. We made viscosity as an output since

a direct measurement of gas turbulence is difficult (e.g., Flaherty et al. 2018a). We adopted the ResNet architecture as mentioned in the previous subsection.

Slightly different from Section 4.4.4, we split 195 generic models into 175 and 20. The selection was random but can be reproduced in our repository. We then separated the first 175 models, together with their generated models with combinations of surface densities and maximum particle sizes into 60%, 20%, 20% splits as training, validation and test data. Finally, we used the rest 20 generic models as a "genuine test", as the input parameters of these models are completely outside the parameter space of $\{M_p, h/r, \alpha\}$ pairs in the training. This additional step can test if the overfitting happens in the $\{M_p, h/r, \alpha\}$ space. This is a more rigorous test than that in Section 4.4.4 since we separate the data even before generating the face-on images with different a_{max} and surface densities. We used callback function `ReduceLROnPlateau` to reduce learning rate when the loss had stopped improving. We kept other hyper-parameters the same as what were mentioned in previous subsections.

4.5 Results

4.5.1 Classification

The accuracy of VGG-like model reached a plateau after 10 training epochs but still slowly increased up to 40 epochs. The accuracy of the ResNet model reached a plateau after 90 epochs. The ResNet has slightly higher accuracy than the VGG-like model on the validation set. This is also the case for the testing set. The VGG-like model can reach an accuracy of 89%, and the ResNet model can reach an accuracy of 92%. Note that the accuracy reported is the micro accuracy (i.e., applying equation 4.5 for the whole sample, instead of calculating accuracies for each class

and averaging them, which is the macro accuracy). Even though each class (planet mass) has the same amount of sample in the whole data set, in each subsets (training, validation and testing sets), the data are slightly imbalanced due to the shuffling process to separate them. Nevertheless, macro and micro metrics are similar here.

Figure 4.4 shows the confusion matrix of planet mass prediction, and their ground truth for all testing data set applied to the ResNet network. The y-axis shows the true planet masses, whereas the x-axis shows the most likely planet masses predicted by the network. If the data point falls on the matrix diagonal, the prediction is correct. The accuracy is the sum of diagonal counts over the total counts. The planet mass is underestimated if it is on the left and overestimated if on the right. The upper number in each box shows the counts of a certain prediction given a ground truth. The lower percentage shows the fraction of it among all the images within that class. When the planet mass is small, i.e., the gap is narrow, the prediction accuracy is low. If the planet is 11 $M_{\oplus}$, only 87% of the samples account for correct predictions within that class. The planet mass is always overestimated given this setup. However, we caution that the planet mass can also be underestimated in reality, since this neural network cannot find planet with mass lower than this limit. The prediction accuracy increases with higher planet masses. If the planet mass is 3 M_J, 97% of the predictions within that class are correct. Likewise, 3 M_J is the upper mass limit in this network, so any real planet mass with higher value will be underestimated.

4.5.2 Regression

The loss of the regression model reached a floor after 70 training epochs. Figure 4.5 shows histograms for the deviation of the predicted planet masses and disk viscosities from the true values

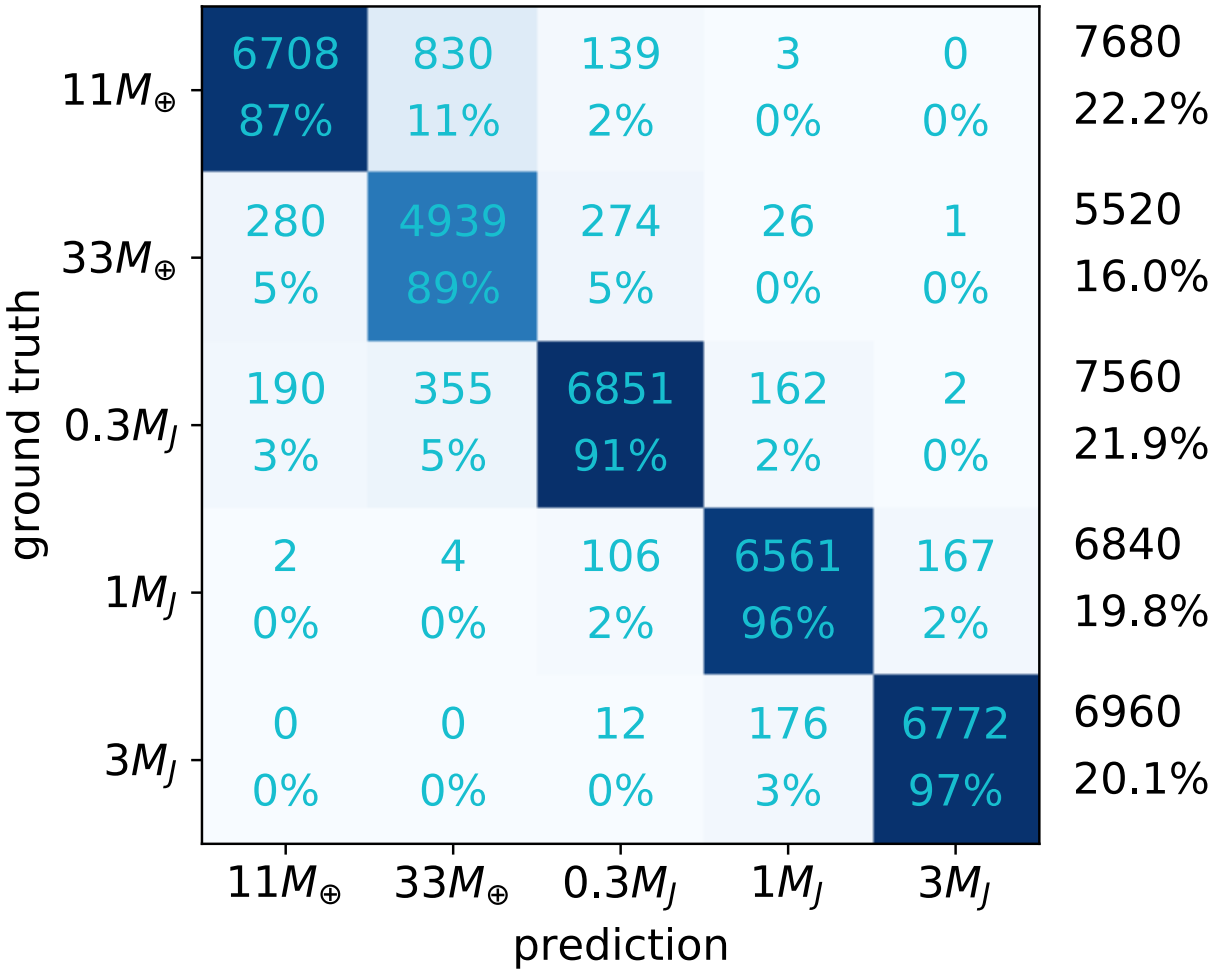

Figure 4.4: The confusion matrix for the ResNet model. The x-axis is the prediction from the neural network. The ground truth is on the y-axis. The upper number in a box shows the counts of planets with certain prediction and ground truth. The lower percentage shows the fraction of the prediction over the total number of the sample with certain ground truth (sum of a row). The rightmost numbers are total counts of testing data with certain class labels (sum of a given row) and the percentage among all testing data (sum of the rightmost column).

in dex. 2D histograms of the joint distribution between M_p and α are plotted at center, whereas the 1D distributions of the planet mass and viscosity differences are shown on the top and right. Panel (a) shows the result of the test set among the 175/195 generic models that were used in the training. The distributions of M_p and α are all centered close to zero, with uncertainties of 0.16 and 0.23 dex, respectively. They are symmetric with almost zero means. Planet masses and the disk viscosities tend to be over(under)-estimated at the same time and follow $\alpha \propto M_p^3$, which has also been found in Zhang et al. (2018b). Panel (b) shows the result of 20/195 generic models that are not used in the training. The overall distributions are similar to those in panel (a). The exception is that the deviation of α is skewed towards positive values (i.e., α tends to be over-predicted). This is because most of the viscosities among these randomly generated 20 generic models have low α (close to 10^{-4}), where it is more likely to be overestimated (see Figure 4.6). The similarity between panel (a) and (b) demonstrates that the fitting is robust and can also be applied to simulations not used in the training.

Figure 4.6 shows distributions of the difference of the prediction and ground truth in different mass and viscosity regimes. The data are from the test set of 175/195 generic models. The distributions are normalized to have the same height, and the inner box follows the convention of the box plot. The standard deviation of each distribution is listed on the right of each violin plot. The planet masses are divided into five bins in comparison with the classification problem (Figure 4.4). Similar to the classification problem, the error of the fitting becomes smaller as the planet mass increases. A small fraction of samples have large errors except at the highest mass bin. At the lower mass end, the planet mass is more likely to be overestimated. At the higher mass end, the uncertainty of the estimate can be as low as 0.1 dex (a factor of 1.3). The viscosity is divided into four bins. When α is less than $3\times\ 10^{-3}$, it tends to be overestimated. When it is large and close

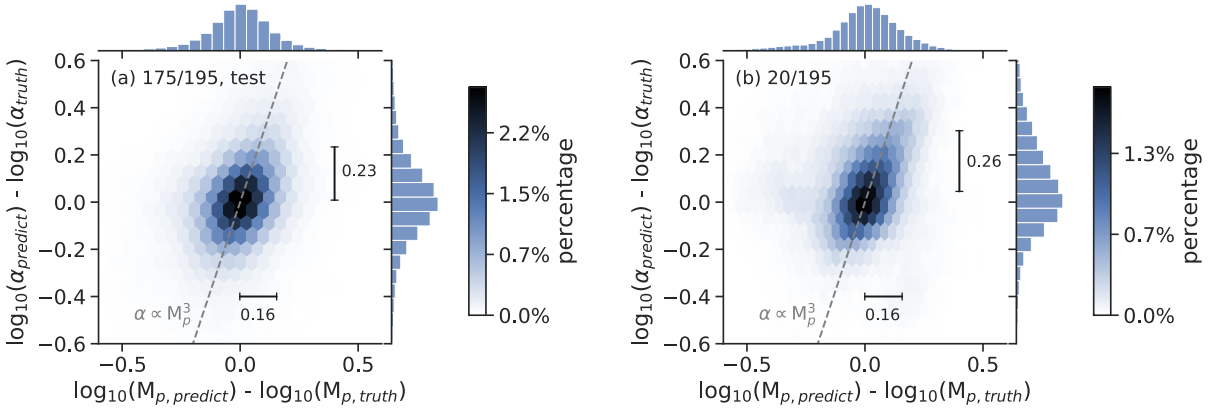

Figure 4.5: 1D and 2D histograms for the differences between predicted and true values of M_p (horizontal) and α (vertical). The 2D joint distributions are color-coded. (a) The test data set among 175/195 of the generic models. (b) The 20/195 data set that has not used in the training process. Most of the predictions have small deviations. The horizontal and vertical bars represent the standard deviation of each distributions. Dashed lines represent $\alpha \propto M_p^3$.

to 10^{-2}, it is more likely to be underestimated. In any viscosity regimes, a small fraction of the predictions would have large deviations from their true values.

4.5.3 Grad-CAM

While deep neural networks are difficult to interpret, some visualization tools help make sense of them. Gradient-weighted Class Activation Mapping (Grad-CAM; Selvaraju et al. 2017) is a technique for making CNN-based models more transparent by visualizing the regions of input that are important for predictions from these models. It uses the class-specific gradient information flowing into the final convolutional layer of a CNN to provide a coarse localization map of the important regions in the image. It is a generalization of the Class Activation Mapping (Zhou et al. 2016), but requires no re-training.

Figure 4.7 shows both images and the activation map derived from the Grad-CAM of the ResNet regression network. The disk is inclined and rotated. Here the true planet mass is 2.28

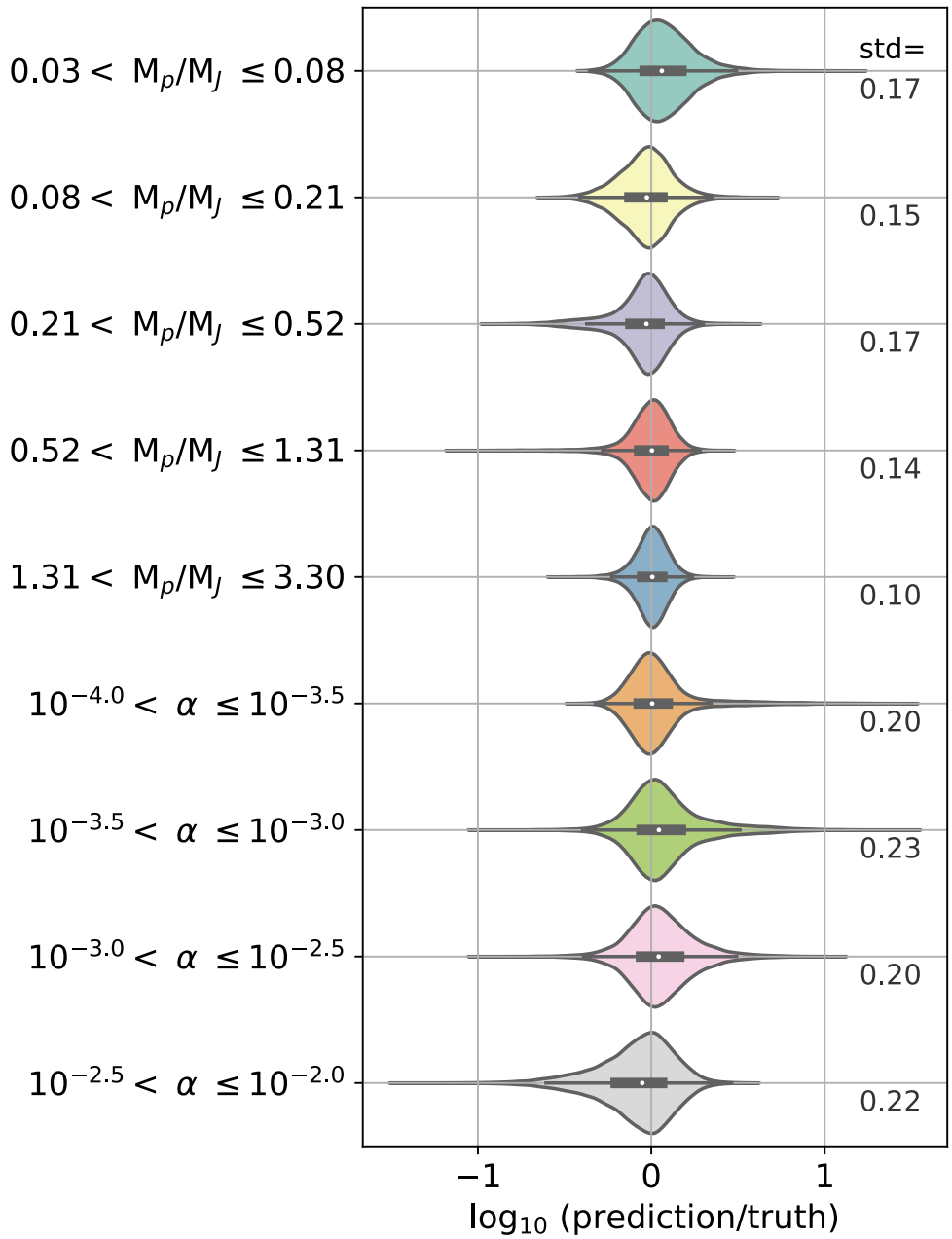

Figure 4.6: The violin plots of logarithmic-scaled deviation between predicted and true values of M_p and α in different mass and viscosity regimes. The data are from the test set of 175/195 generic models. The color-shaded regions show the distribution with normalized height, whereas the inner box follows the convention of a box-plot, which shows distribution's 25 percentile, 50 percentile (white dot), and 75 percentile. The decimals marked on the right are the standard deviation of each distribution.

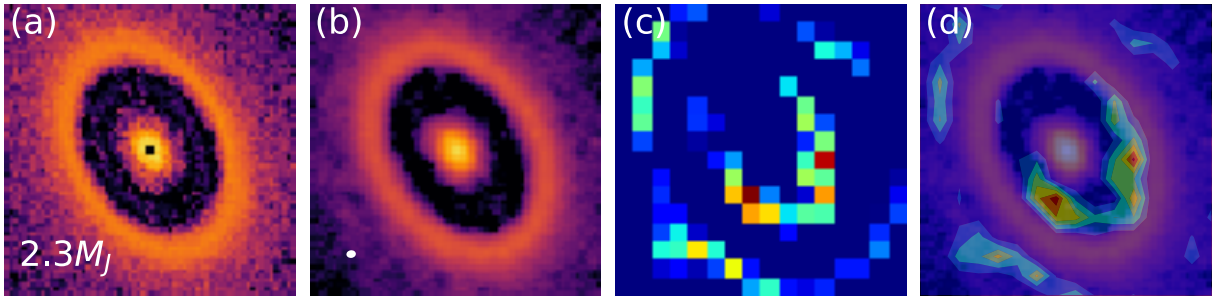

Figure 4.7: Grad-CAM for the ResNet regression problem. The image is among 20 generic models not in the training set. The true planet mass is 2.28 M_J and $\alpha = 1.4 \times 10^{-3}$. (a) log-scaled image without putting into CASA, (b) log-scaled synthetic image using CASA, (c) activation map of the synthetic image (b), (d) synthetic image overlaid by the activation map (filled contour). In this case, the activation map successfully focuses on the gap region. The beam size of panel (b) is shown as an ellipse in the bottom left.

M_J, and $\alpha = 1.4 \times 10^{-3}$. The gap region has high values in the activation map, which means that it is important in predicting the planet mass. This lends confidence to the network's reliability since the traditional method also focuses on the gap's properties. This is why we named these neural networks as Planet Gap neural networks (PGNets). One should be cautious that not every activation map of testing data shows such a good correspondence, and the activation map is a great tool if any result is in doubt.

4.5.4 Application to Observational Data

After testing against the synthetic observations, we applied our trained PGNets to real DSHARP observations (AS 209 Andrews et al. 2018a; Guzmán et al. 2018; Elias 24, GW Lup and Sz 114; Andrews et al. 2018a) to infer planet masses and compared them with what found in Zhang et al. (2018b). The designation follows Huang et al. (2018c), where the integer of gap location in au follows "D" (for dark gaps). There are several degeneracies if one wants to infer the planet mass. In the previous fitting of Zhang et al. (2018b), the gap width depends on not only the planet mass

but also the viscosity α and Stokes number St (or a_{max} and Σ_g). Thus, in comparison with Zhang et al. (2018b), we picked the median value as a reference point. The median value is the case with α=10^{-3} and a_{max}=1 mm. It is difficult to estimate the uncertainty in these models. For the linear fitting method, two known uncertainties come from α and a_{max}. A difference of 10 in α leads to around 0.33 dex change of M_p, whereas a change of 10 in a_{max} leads to around 0.2 dex change of M_p. For classification models, an error of reference can be 0.4 dex, since two neighbouring planet masses are spaced at that value. For the regression model, the uncertainty of M_p and α can be estimated as 0.16 dex and 0.23 dex, as shown in Figure 4.5, or read in specific regimes as shown in Figure 4.6. For AS 209 and Elias 24, fine-tuned planet masses are available from detailed case-by-case modelings. While the central stars of these disks have different masses, what matters is the planet-star mass ratio M_p/M_*. Thus, we will report M_p/M_* in units of the $M_J/M_\odot$ in the next paragraph. Notice that the radius of the semi-minor axis of the gap should be placed around one-sixth of the image size. However, the disk does not need to be centered nor scaled perfectly, since the images were randomly shifted during the training process.

AS 209 is a disk with many gaps. With the linear fitting method, the median value of AS 209 D99[5] is 0.45 $M_J/M_\odot$ (Zhang et al. 2018b). The detailed modeling infers 0.1 $M_J/M_\odot$. The VGG-like model predicts 0.1 $M_J/M_\odot$, whereas the ResNet classification model predicts 0.3 $M_J/M_\odot$. The regression model predicts 0.52 $M_J/M_\odot$ and $\alpha = 2 \times 10^{-4}$. With 64×64 resolution, gaps inside 40 au have been smoothed out. The secondary gap (a shallower gap inside the major gap) has already been considered since there are also many low-viscosity simulations with secondary gaps in our training data set.

[5]It is actually B99 ("B" stands for bright rings). However, that bright ring is just a shallow peak inside a wide gap.

With the traditional fitting method, Elias 24 D57 is 0.51 $M_J/M_\odot$. It is 0.2 $M_J/M_\odot$ using the fine-tuned model. Both VGG-like and ResNet classification model predicts 0.1 $M_J/M_\odot$. The regression model predicts M_p/M_* = 0.21 $M_J/M_\odot$, and $\alpha = 2 \times 10^{-4}$.

The inferred planet mass from the traditional fitting method for GW Lup D74 is 0.065 $M_J/M_\odot$. Both VGG-like and ResNet classification model predicts 0.03 $M_J/M_\odot$. The regression model predicts M_p/M_* = 0.05 $M_J/M_\odot$, and $\alpha = 1 \times 10^{-4}$.

Sz 114 is a disk with a very narrow gap. It is too narrow to use the linear fitting method. The mass was obtained by directly comparing with simulations (Zhang et al. 2018b). That value for Sz 114 D39 is 0.12 $M_J/M_\odot$. Both VGG-like and ResNet models predict 0.03 $M_J/M_\odot$. The regression model predicts M_p/M_* = 0.11 $M_J/M_\odot$, and $\alpha = 6 \times 10^{-4}$.

Overall, the VGG-like and ResNet classification models predict similar planet masses. The regression model predicts higher planet masses. It predicts lower viscosities for these disks.

There are many other gaps that can be compared between the linear fitting method and PGNets. Instead of doing extensive coverage of all available gaps, we made our code available online so that users can apply these methods to any new or archival data. With a super-resolution technique, Jennings et al. (2021) even found many more gaps inside 30 au for DSHARP observations. Those images and radial profiles can also be inputs for our models using either the PGNets or the linear fitting tools.

4.6.1 Synthetic Observation

To test if predictions from CNN models are affected by the way we produce synthetic observations, we picked the case in Figure 4.7 (a), put it into `CASA` (McMullin et al. 2007b) version 6.1.0, and used `simobserve` task to generate observations with angular resolutions and sensitivities comparable to those of the DSHARP observations. We assumed the planet is at 40 au, a_{max} = 1cm, $\Sigma_{g,0}$ = 30 g/cm^2, and L_* = 2 $L_\odot$. The synthetic observations consist of 12 minutes of on-source integration time with the Cycle 5 C43-5 antenna configuration, 35 minutes on-source in the C43-8 configuration, and 35 minutes on-source in the C43-9 configuration. A precipitable water vapor level of 1.0 mm was adopted. The synthetic visibility was imaged in the same manner as the DSHARP sources using `tclean` task, as described in Andrews et al. (2018a).

In Figure 4.7, panel (a) shows the intensity map converted from the simulation and panel (b) shows the intensity from the synthetic ALMA observation. The scales of them were normalized as discussed in Section 4.4.2. The angular resolution is $\sim$ 5 au in FWHM and is marked in the lower left corner of the panel. As shown in panel (c) and (d), the activated regions correctly focus on the gap. The predicted masses are 1.92 M_J and 2.39 M_J, with and without `CASA` operations, all comparable to the true value, 2.28 M_J. The predicted α viscosities are 1.3×10^{-3} and 1.2×10^{-3}, with and without `CASA` operations, also comparable to the true value, 1.4 $\times10^{-3}$. Thus, we conclude that our models can be used to predict real ALMA observations even though they were trained on the data without doing `simobserve` tasks.

4.6.2 Advantages

Compared to the traditional method, CNNs have many advantages. It is quick and convenient. The 2D images do not need to be converted to 1D profiles. Deriving 1D profiles seems to be a simple task but it takes time since one needs to run MCMC to find a disk's centroid, inclination, and position angle. Once the CNN model is trained, one can obtain a prediction within a second directly from the image plane. For this reason, it can be applied to a large disk sample. The training is one time and only takes an hour. Using a traditional method, one needs to search for the best fitting parameters. For instance, one parameter combining viscosity, h/r, and planet mass is enough to fit the gaseous gap depth and width (Kanagawa et al. 2015a; 2016a). However, if the dust is included, we also need to find several fitting formulae for different a_{max} and gas surface density (Zhang et al. 2018b). This is not the case for CNNs. With more data or new physics included, the network can be retrained quickly by providing more training data.

Asymmetric information is lost when a 2D image is converted to a 1D radial profile. CNNs can preserve this information. For instance, a low mass planet in an inviscid disk can have the same gap width as a high mass planet in a viscous disk. The traditional method cannot break this degeneracy. However, the viscosity of the disk can be inferred from a 2D image. If the disk looks more asymmetric, it should be more inviscid. The planet mass can be better constrained accordingly.

In a regression problem, the model can provide planet mass and disk viscosity at the same time. With the linear fitting method, one can only get a planet mass by assuming a disk viscosity, since both a higher planet mass and a more inviscid disk help open a wider gap. The CNN regression model partially breaks the degeneracy between them.

The CNN methods can handle very shallow or narrow gaps, which is of great difficulty for the traditional fitting method. In Zhang et al. (2018b), to make sure most of the data points fall onto the fitting line, narrow gaps with Δ below 0.15 were treated as outliers. One thus needs to compare with individual simulations to estimate a planet mass (e.g., inferring the potential planet in Sz 114's narrow gap), which is extremely time consuming.

4.6.3 Limitations

The first limitation of the CNN models is that training with the same data set but different architectures would lead to different predictions, even though their accuracy is similar statistically. Even given the same architecture, different random seeds or data augmentation would also result in different predictions. On the contrary, the traditional linear fitting method provides a definite planet mass as long as a gap width and other disk parameters are provided. Many details of fitting are empirical, but they are transparent to the user.

Compared to the linear fitting method, it is difficult to understand how CNN methods derive the results, even though the Grad-CAM can qualitatively inform us the important features the network uses. In the traditional fitting method, the gap width is proportional to some powers of planet mass, disk viscosity, and h/r at a given St. We can use some other ways to constrain some parameters and then narrow down the planet mass. In classification or single-output regression CNN models, we can only get a single prediction for these parameters when we apply them to observations. Deep neural networks are intrinsically highly non-linear. For an input image, these models are more of methods that help pick up an image in a training set with the most similar feature than methods of finding intrinsic relationships. The user can use their own knowledge to interpret why the planet

mass returned by a CNN model is as such (e.g., if the planet mass is low, the user can make sense of it by noticing the gap is narrow.), but the network itself cannot inform this to the user. Instead of using a linear fitting with many assumptions, it helps the user to find the most closed-match model for an input. In some sense, the classification and single-output regression models can be seen as another way to present all the simulations in Zhang et al. (2018b) by providing an automated tool to find a closed-match. Surprisingly, multi-output regression models can possibly solve this problem. For instance, the multi-output regression PGNets can help us find the exact relation of the degeneracy between planet mass and disk viscosity among simulations (Figure 4.5). There are hopes that we can learn valuable insights from CNN models.

Finally, compared to a detailed modelling, the prediction can only be as good as the physics included in the simulations. While our simulations span a large parameter space, they cannot cover every possible situation. For instance, we cannot predict planet masses below 11 $M_{\oplus}$ or above 3 M_J. A planet with a lower mass than 11 $M_{\oplus}$ can only be predicted as massive as that. Only one planet is put into the simulation, and its orbit is fixed. Thus, the model cannot be used to study multiple planets carving a common gap. However, if planets lead to several gaps and they do not influence each other, we can treat them as individual single gaps by masking others. Note that if we assume that one planet can carve two gaps (Dong et al. 2018d; Bae & Zhu 2018a;c) and the secondary gap is at 0.5 - 0.7 r_p, we can input all the gaps into CNN models since our CNN models have been trained with data which have these secondary gaps generated by a single planet. The model does not consider migration, which can lead to a different gap shape (Nazari et al. 2019; Kanagawa et al. 2020). The gap substructure can also change with time. The disks are at 1000 orbits, which is 1 Myr for a planet at 100 au or 0.1 Myr for a planet at 20 au. We used 2D simulations, but the situation in 3D might be different. We neglected the self-gravity of the disk

and the thermodynamic processes. These effects will also change the shape of the gap (Zhang & Zhu 2020; Miranda & Rafikov 2020b;a; Ziampras et al. 2020; Rowther et al. 2020). The dust in our simulations was treated as passive test particles. In reality, the dust's back-reaction onto the gas is important (Kanagawa et al. 2018; Yang & Zhu 2020; Huang et al. 2020b; Hsieh & Lin 2020). When producing the synthetic image, we neglected scattering, but it can affect the images when the disk is optically thick (Liu 2019a; Zhu et al. 2019). The dust was also assumed to be settled. Not to mention that it is very likely that some substructures can have non-planet origins (e.g., snowline and MHD effects). On the other hand, with more physical processes understood and included in simulations, CNNs can be used to make predictions.

4.6.4 Future Perspectives

This line of work can also be applied to infer the Stokes number St of particles in the disks. The Stokes number is highly correlated to the gap width and depth. Measuring St can help us understand the particle size and dust settling.

The gas component is more massive and has a larger radial and vertical extent than the dust in protoplanetary disks. The (sub)mm molecular line observations also contain velocity information at different disk positions, leading to a 3D datacube. One can infer planet mass from kinematic features in channel maps, such as the kink and the deviation from Keplerian velocity (Pinte et al. 2018b; Teague et al. 2018b). In star formation, CNN models have already been used on the whole 3D datacube (Xu et al. 2020b;a). This can possibly be applicable in protoplanetary disks as well.

4.7 Conclusions

Substructures are found to be ubiquitous in protoplanetary disks. If some of them are induced by planets, the increasing number of high-resolution protoplanetary disk observations is revealing the population of young forming planets.

The properties of these substructures (e.g., the width and depth of the gap) are related to the planet mass. Previous works used either fined-tuned models or linear fitting on a large parameter space to infer the planet mass. Instead, we used Convolutional Neural Networks to predict the planet mass directly from radio dust continuum images. To train the CNNs, we use data from synthetic observations in Zhang et al. (2018b) and some new simulations. We built both classification and regression models. The classification models can predict five planet masses ranging from 11 $M_\oplus$ to 3 M_J. The VGG-like model can reach 89% accuracy, whereas the ResNet model can reach 92% accuracy. The accuracies for less massive planets are lower. They are higher for more massive planets. The regression model can predict planet mass and disk viscosity at the same time. Similar to the classification model, it predicts more massive planets with higher accuracy. The standard deviation of the prediction is around 0.16 dex. The prediction of α has uncertainty around 0.23 dex, and can be used to constrain the disk turbulence.

CNN models cannot fully break the degeneracy between the planet mass and disk viscosity. It tends to over(under)-predict them at the same time. However, it is surprising that this degeneracy relationship can be easily found in CNNs without the need of theoretical knowledge (Kanagawa et al. 2016a) and detailed fitting and tuning (Zhang et al. 2018b). This shows the potential of CNNs as diagnostic tools.

Using Grad-CAM, we showed that the networks indeed catch the important feature, i.e., gaps,

in predicting the planet mass. We also applied the networks to several DSHARP gaps and found the predictions are reasonable compared with the traditional method in Zhang et al. (2018b). The code, along with that of the traditional method, is also provided.

The CNN methods are fast compared to fined-tuned models. It is more convenient than the linear fitting method since one can get a prediction instantaneously as long as an image is provided. The network can also be easily updated with more data or physical processes. It preserves the 2D information that should help break the degeneracy between planet mass and disk properties. The regression model can predict several quantities at the same time. Unlike the traditional method, predicting shallow and narrow gaps takes the same amount of effort using CNNs, even though the prediction still has higher uncertainty in this regime.

There are also several shortcomings for CNN models. Different architectures or training procedures might lead to different predictions. The CNNs are not transparent, and it is difficult to know how exactly the networks work. Lastly, in contrast to the detailed modelling, the robustness of our CNNs ultimately is limited by our training data (simulations), i.e., the physical processes included.

The methods are more suitable for a large disk sample to obtain statistical trends of a young planet population. For individual disk, we can use this method to narrow down the parameter space for detailed simulations. Overall, the traditional linear fitting method (e.g., Zhang et al. 2018b) still provides users more control on the input disk parameters, while the wide choice of tools in CNNs (e.g., classification and regression) and diagnostic tools (Grad-CAM) start to make CNNs more robust.

CHAPTER 5 The Effects of Disk Self-Gravity And Radiative Cooling on the Formation of Gaps And Spirals by Young Planets

Shangjia Zhang,[1] Zhaohuan Zhu[1]

[1]Department of Physics and Astronomy, University of Nevada, Las Vegas, 4505 S. Maryland Pkwy, Las Vegas, NV, 89154, USA

5.1 Abstract

We have carried out two-dimensional hydrodynamical simulations to study the effects of disk self-gravity and radiative cooling on the formation of gaps and spirals. (1) With disk self-gravity included, we find stronger, more tightly-wound spirals and deeper gaps in more massive disks. The deeper gaps are due to the larger Angular Momentum Flux (AMF) of the waves excited in more massive disks, as expected from the linear theory. The position of the secondary gap does not change, provided that the disk is not extremely massive ($Q \gtrsim 2$). (2) With radiative cooling included, the excited spirals become monotonically more open (less tightly-wound) as the disk's cooling timescale increases. On the other hand, the amplitude and strength of the spirals decrease when the cooling time increases from a small value to $\sim 1/\Omega$, but then the amplitude starts to increase again when the cooling time continues to increase. This indicates that radiative dissipation becomes important for waves with $T_{cool} \sim 1$. Consequently, the induced primary gap is narrower and the secondary gap becomes significantly shallower when the cooling time becomes $\sim 1/\Omega$.

When the secondary gap is present, the position of it moves to the inner disk from the fast cooling cases to the slow cooling cases. The dependence of gap properties on the cooling timescale (e.g., in AS 209) provides a new way to constrain the disk optical depth and thus disk surface density.

5.2 Introduction

Protoplanetary disks from ALMA observations reveal many substructures (e.g., gaps, rings, and spiral arms) in dust continuum emission (Andrews et al. 2018a; Long et al. 2018b; Pérez et al. 2016). Among them, the most common features are concentric gaps and rings (Huang et al. 2018c). There are many interpretations for these features, such as zonal flows (Flock et al. 2015), aggregate sintering (Okuzumi et al. 2016a), secular gravitational instabilities (Takahashi & Inutsuka 2014), self-induced dust pile-ups (Gonzalez et al. 2017), dust growth at snowlines (Zhang et al. 2015a; Pinilla et al. 2017b), planet-disk interactions (de Juan Ovelar et al. 2013; Dong et al. 2015c), and so on. Recent high-resolution observations for a relatively large sample of disks (Huang et al. 2018c; Long et al. 2018b; van der Marel et al. 2019) conclude that snowlines cannot consistently match the positions of these gap features, but it may still apply to individual objects.

Of all the exciting scenarios, this paper focuses on the interpretation of planet-disk interactions. Assuming these features are due to the planets, many authors infer the planet mass from the gap properties by comparing observations with hydrodynamical simulations. These properties include gap width and depth in dust emission (Zhang et al. 2018b), and sub/super keplerian rotational velocity in CO channel maps (Teague et al. 2018b; Zhang et al. 2018b; Gyeol Yun et al. 2019). Most past works associate each gap with a planet. Recent simulations show more promising results that one single planet can explain up to five gaps in ALMA observations (Bae et al. 2017a; Guzmán

et al. 2018; Zhang et al. 2018b). These multiple gaps that are induced by a single planet is due to the presence of multiple spirals, which results from constructive interference of the density waves at different m modes in the inner disk (Bae & Zhu 2018a;c; Miranda & Rafikov 2019b). The one-armed spiral opens the primary (major) gap at the position of the planet, and the secondary spiral opens the secondary gap in the inner disk and so on. The spacing of the gaps is also useful to constrain the gaseous disk scale height h/r since the ratio of the positions between the secondary gap and the primary gap mainly depends on the disk h/r (Dong et al. 2018d; Zhang et al. 2018b). If we can further constrain h/r using other observables like gap widths and depths, we can use the position of the secondary gap to even constrain the planet mass (Kanagawa et al. 2015a; 2016a; Bae et al. 2017a; Zhang et al. 2018b; Gyeol Yun et al. 2019).

However, most simulations that are used to infer the planet mass from the disk substructures neglect the (1) self-gravity from the disk and (2) radiative cooling. For the latter, they employ locally isothermal Equation of State (EoS) instead, which is equivalent to instant cooling. These two simplifications might not be valid to realistic disks. Consequently, the planet masses inferred from observations might be subject to systematic errors. Self-gravity and radiative cooling can play essential roles in some disks.

Several recent works suggest disks might be more massive than previously thought. Booth et al. (2019) measure the HD 163296 disk mass using $^{13}C^{17}O$ line, and find the gas mass is a factor of 2-6 higher than previously estimated using $C^{18}O$. Using the DSHARP opacity (Birnstiel et al. 2018) and optical-thin assumption, Zhang et al. (2018b) find that Toomre Q at the gap edges are $\lesssim 10$ for most of the disks (see Table 3 therein). Among the same series of papers, Dullemond et al. (2018) also find that most of the prominent rings are marginally gravitationally stable if the gas-to-dust ratio is 100 (see Figure 7 therein). Furthermore, Zhu et al. (2019) suggests that

these disks might be very optically thick, even though dust scattering makes these disks look like optically thin. Without the assumption of the dust opacity, Powell et al. (2019) analyze seven disks by measuring the locations of "dust lines"—the cutoff radii of continuum emission—at different wavelengths, and also find all of those disks have $Q \lesssim 10$, with several approaching unity. For these reasons, disk self-gravity can become quite important for the interactions between planets and disks.

The disk should also have orders of magnitude difference in cooling time at different radii (Zhu et al. 2015a; Miranda & Rafikov 2019c). Assuming the Minimum Mass Solar Nebula (MMSN), the cooling is faster at the outer disk and slower at the inner disk — 7 orders of magnitude of the cooling time between 1 au ($10^5/\Omega$) and 100 au ($10^{-2}/\Omega$) (Zhu et al. 2015a). The fast cooling resembles the locally isothermal disk, whereas the slow cooling represents the adiabatic disk. However, it is unclear how the disk might look like beyond these two extremes. Radiative cooling with different cooling timescales at different locations in disks might further change the disk substructures.

In this paper, we study spirals and gaps induced by planets in disks with non-negligible self-gravity and radiative cooling. In Section 5.3, we lay out the theoretical background of the linear theory and some basic quantities being used throughout the paper. In Section 5.4, we introduce the simulation setups. In Section 8.4, we present the results after adding these two physical processes separately, and also explore a situation that includes both self-gravity and radiative cooling. We also compare our simulation results with previous analytical results from Goldreich & Tremaine (1980) and Miranda & Rafikov (2019b). In Section 8.5, we quantify the change of AMF and discuss the observational implications in linear regime. Then, we take AS 209 disk as a test bed for these two processes, and address some limitations of our simulations. Finally, we conclude this

paper in Section 7.8.

5.3 Theoretical Background

Goldreich & Tremaine (1978; 1979; 1980) develop the linear theory for planet-disk interactions. This theory produces insightful analytical results which can be used to understand numerical simulations on planet migration and gap opening.

In order to study planet-disk interactions in the linear regime, the planet mass should be less than the thermal mass (Goodman & Rafikov 2001)

$$M_{th} = \left(\frac{h}{r}\right)_p^3 M_* = 1 M_J \left(\frac{(h/r)_p}{0.1}\right)^3 \frac{M_*}{M_\odot}, \tag{5.1}$$

where $(h/r)_p$ is the disk's aspect ratio at the planet's position. M_* is the mass of the central star. At the thermal mass, the gaseous disk scale height is comparable to both the Hill and Bondi radii of the planet, and the distance between the planet and spiral shock forming region is comparable to the planet's Bondi radius so that spiral shocks begin to affect planet accretion (Béthune & Rafikov 2019). If $M_p \gtrsim M_{th}$, the density wave excited by the planet starts from the non-linear regime, so that the spiral waves immediately become spiral shocks after the wave excitation. Below the thermal mass, the spiral shock region can be well separated from the wave launching area. Most of the simulations in this paper have $M_p \lesssim M_{th}$, but we also explore several cases in the high mass regime.

Angular momentum transport is one of the key aspects in the accretion theory. In the linear theory, the changing rate of the angular momentum in the disk enclosed within a radius r is equal

to the planet's torque Γ on that region minus the Angular Momentum Flux[1] (AMF) F_J that flows out of the region, that is

$$\frac{dL}{dt} = \Gamma(r) - F_J(r). \tag{5.2}$$

5.3.1 Torque

The first term on the right-hand side of Equation 5.2 is the planet's torque to the disk region within r,

$$\Gamma = -\int_{disk} \Sigma(\vec{r} \times \vec{F}) df = \int_r \frac{dT}{dr} dr, \tag{5.3}$$

as in Kley & Nelson (2012), where

$$\frac{dT}{dr}(r) = r \int_0^{2\pi} \Sigma(r,\phi) \frac{\partial \Phi_p}{\partial \phi} d\phi \tag{5.4}$$

is torque density and Φ_p is the planet's potential in the disk coordinate,

$$\Phi_p = -\frac{GM_p}{\left\{r_p^2 + r^2 - 2r_p r \cos(\phi - \phi_p) + s^2\right\}^{1/2}}, \tag{5.5}$$

where r_p, ϕ_p are planet's position in radial and azimuthal directions and s is the smoothing length used in simulations to avoid the singularity of the planetary potential. The planet feels the opposite torque, which leads to planet migration if the torque from the inner disk is not balanced by the torque from the outer disk.

[1]This is coined as angular momentum current in Binney & Tremaine (2008), denoted by capital "C".

Goldreich & Tremaine (1980) derive the one-sided torque as

$$F_{J0} = (M_p/M_*)^2 h_p^{-3} \Sigma_p r_p^4 \Omega_p^2 \tag{5.6}$$

where Ω_p is the angular frequency of the planet (all the "p" as a subscript in the paper refers to that quantity evaluated at the position of the planet). This value is commonly used to normalize the torque and AMF.

5.3.2 AMF

The second term on the right-hand side of Equation 5.2 is the AMF carried by the disturbance (e.g., spiral waves). The angular momentum carried by the spiral waves will be eventually deposited to the background disk to induce gaps in disks. In order to understand the gap properties, such as depth, width, and secondary gap positions, it is necessary to understand the AMF of the spiral waves. With disk self-gravity included in the analysis, AMF has two components, advective AMF, F_A, and gravitational AMF, F_G (Lynden-Bell & Kalnajs 1972; Goldreich & Tremaine 1979). The latter only occurs in self-gravitating disks. The total AMF is, $F_J = F_A + F_G$.

F_A is the advective transport of angular momentum due to the motion of the fluid and leads to a flow of angular momentum through circumference at radius r. It is also related to the Reynolds stress in turbulence studies. It can be calculated as,

$$F_A(r) = r^2 \Sigma(r) \oint u_r(r,\phi) u_\phi(r,\phi) d\phi, \tag{5.7}$$

where Σ is the gaseous disk surface density and u_r and u_ϕ are the velocity perturbations in the r

and ϕ directions.

F_G is due to the non-axisymmetric part of the disk potential. The spiral structure produces a spiral gravitational field, which exerts torque and transfers angular momentum from one part of the disk to another. It is non-zero in self-gravitating disks and becomes important when the following Tommre Q parameter is small,

$$Q = \frac{c_s \Omega}{\pi G \Sigma}, \tag{5.8}$$

where c_s is the sound speed and $c_s = (h/r)v_\phi$. Given fixed c_s and Ω, a smaller Q means a higher disk surface density. When $Q = 1$, the disk becomes gravitationally unstable. The value of F_G is the torque exerted to the inner disk,

$$F_G(r) = \int_0^r dr' r' \int_0^{2\pi} d\phi \Sigma \frac{\partial \Phi_{out}}{\partial \phi}, \tag{5.9}$$

where Φ_{out} is the disk potential at r (the formula is the same as Equation 5.4, except that Φ_p is replaced with Φ_{out}). For trailing spiral arms, the angular momentum is transferred from the inner to the outer disk, since the inner disk exerts positive gravitational torque on the outer disk (Lynden-Bell & Kalnajs 1972; Binney & Tremaine 2008).

Note that, in globally isothermal disks, the total AMF is conserved ($dF_J/dr = 0$) based on the linear theory (Goldreich & Tremaine 1979). However, as Miranda & Rafikov (2019c) point out, this is not the case in locally isothermal disks due to the torque applied onto the wave by the background shear flow (this is also reported in Lin & Papaloizou 2011; Lin 2015). In locally isothermal disks, $d(F_J/c_s^2)/dr = 0$ is conserved.

In the linear theory, all quantities can be further Fourier decomposed into individual m harmon-

ics,

$$\eta(r,\phi) = \sum_{m=-\infty}^{\infty} \eta_m(r) e^{im(\phi-\phi_p)} \tag{5.10}$$

where η can be u_r, u_ϕ, and Σ, and η_m is a complex number. Putting $u_r(r)$ and $u_\phi(r)$ in Equation 5.7,

$$\begin{aligned} F_A(r) &= 2\pi r^2 \Sigma(r) \sum_{m=-\infty}^{\infty} u_{r,m}(r) u^*_{\phi,m}(r) \\ &= 4\pi r^2 \Sigma(r) \sum_{m=0}^{\infty} \Re[u_{r,m}(r) u^*_{\phi,m}(r)]. \end{aligned} \tag{5.11}$$

The second equality holds because the Fourier transform of real signals is Hermitian. If F_A is expanded with positive integer harmonics (the $m = 0$ term is always zero),

$$F_A(r) = \sum_{m=1}^{\infty} F_{A,m}(r), \tag{5.12}$$

each m component of the advective AMF can be expressed as,

$$\begin{aligned} F_{A,m}(r) &= 4\pi r^2 \Sigma(r) \Re[u_{r,m}(r) u^*_{\phi,m}(r)] \\ &= 4\pi r^2 \Sigma(r) \Big(\Re[u_{r,m}(r)] \Re[u_{\phi,m}(r)] + \Im[u_{r,m}(r)] \Im[u_{\phi,m}(r)] \Big), \end{aligned} \tag{5.13}$$

which is identical to the result using continuous Fourier transform in the shearing sheet geometry (Dong et al. 2011b; Rafikov & Petrovich 2012). Likewise, the total AMF can be expanded as,

$$F_J(r) = \sum_{m=1}^{\infty} F_{J,m}(r). \tag{5.14}$$

The sum goes to infinity, but the normalized AMF ($F_{J,m}/F_{F_{J0}}$) reaches the maximum at $m \sim$

$(1/2)/(h/r)$ and becomes $\ll 1$ at several $1/(h/r)$. Thus, the sum can stop at some m (Goldreich & Tremaine 1980; Artymowicz 1993b;a; Ward 1997), which is known as the "torque cutoff".

Relative Importance Between F_A And F_G

Here we discuss the relative importance between F_A and F_G. We borrow the WKB solutions in the tightly-wound limit ($k \gg 1/R$) obtained by Goldreich & Tremaine (1979). Their analytical solution for the advective AMF is,

$$F_A = -\frac{\pi m r \Sigma k}{2\pi G\Sigma|k| - k^2 c_s^2}\Big(1 - \frac{c^2|k|}{2\pi G\Sigma}\Big)^2 \Phi(r)^2. \tag{5.15}$$

where $\Phi(r)$ is the amplitude of the perturbed disk gravitational potential in the form of WKB solution. The gravitational AMF is,

$$F_G = \mathrm{sgn}(k)\frac{mr\Phi^2(r)}{4G}. \tag{5.16}$$

Taking the ratio between the F_A and the F_G, and define the critical wave number k_{crit} (Binney & Tremaine 2008) as,

$$k_{crit} = \frac{\Omega^2}{2\pi G\Sigma} = \frac{Q}{2}\frac{\Omega}{c_s} = \frac{Q}{2h}, \tag{5.17}$$

we get,

$$\frac{F_A}{F_G} = 2\Big(\frac{Q^2}{4}\frac{|k|}{k_{crit}} - 1\Big) = 2\Big(\frac{|k|}{k_{cross}} - 1\Big), \tag{5.18}$$

where $k_{cross} = 4k_{crit}/Q^2 = 2/Qh$. When $|k| = (3/2)k_{cross}$, advective AMF and gravitational AMF have equal contribution, and we denote that $|k|$ as k_{eq}. $k_{eq} = (3/2)k_{cross} = 3/Qh$. When $|k|$ ¡ k_{eq},

F_G has larger contribution, whereas when $|k| > k_{eq}$, F_A contributes more. Hence, to compare the relative importance of F_A and F_G, we just need to compare the characteristic values of $|k|$ and k_{eq}.

Plugging Equations 5.8 and 5.17 into the dispersion relation,

$$\tilde{\omega}^2 = \Omega^2 - 2\pi G\Sigma|k| + c_s^2 k^2, \tag{5.19}$$

where $\tilde{\omega}(r) = m[\Omega_p - \Omega(r)]$ and $\Omega(r)$ is the angular velocity of the disk, we get the absolute value of the wave number in unit of k_{crit},

$$\frac{|k|}{k_{crit}} = \frac{2}{Q}\left\{m^2\left(1 - \frac{r^{3/2}}{r_p^{3/2}}\right)^2 - \left(1 - \frac{1}{Q^2}\right)\right\}^{1/2} + \frac{2}{Q^2}. \tag{5.20}$$

Here we choose the positive sign in front of the first term since it corresponds to the short wave that propagates beyond Lindblad resonances in disks (the negative sign solution corresponds to the long wave that is restrained inside Lindblad resonances and outside the forbidden region; see Figure 2 in Lovelace et al. 1997, Figure 6.14 in Binney & Tremaine 2008 and Equation 19 in Goldreich & Tremaine 1979 for details). Note that this equation reduces to the following (Ogilvie & Lubow 2002; Bae & Zhu 2018a) as $Q \to \infty$,

$$\frac{|k|}{m} = \frac{\Omega}{c_s}\left|\left(1 - \frac{r^{3/2}}{r_p^{3/2}}\right)^2 - \frac{1}{m^2}\right|^{1/2}. \tag{5.21}$$

With Equation 5.20, we evaluate the ratio of the $|k|$ and k_{eq} at the effective locations of Lindblad resonances. While both sound pressure and self-gravity shift the positions of the Lindblad resonances (Pierens & Huré 2005), we only account for the contribution from the pressure effect for

simplicity. The locations of the resonances become,

$$r = r_p \left\{ 1 \pm \frac{\left[1 + m^2 (h/r)^2\right]^{1/2}}{m} \right\}^{2/3}. \tag{5.22}$$

At these radii, the ratio reads,

$$\frac{|k|}{k_{eq}} = \frac{Q}{3} \left\{ m^2 (h/r)^2 + \frac{1}{Q^2} \right\}^{1/2} + \frac{1}{3}. \tag{5.23}$$

As $Q \to \infty$, the ratio $|k|/k_{eq} \to \infty$, which means that F_G has no contribution to the total AMF. However, when $Q = 5$ and we adopt $m = (1/2)/(h/r)$, $|k| \approx k_{eq}$. Hence, F_G contributes comparable amount of AMF as F_A. This simple calculation shows that as Q becomes smaller, the gravitational AMF becomes increasingly important and will exceed the contribution of the advective AMF at very low Q.

We caution that the detailed analysis on the relative importance of F_A and F_G requires numerically solving the linearized equations and is beyond the scope of this paper. In this paper, since we focus on disks with $Q \gtrsim 5$, we will only discuss F_A for simplicity. As shown in Section 5.6.4, we find that when $Q \sim 2$, the gap edge quickly becomes unstable even though the disk itself is gravitationally stable.

Calculation of the Total AMF

Here we summarize the calculation of the total AMF in the linear theory. In regions far from corotation ($|r - r_p|/r_p \to \infty$), advective AMF dominates ($F_A \gg F_G$, Goldreich & Tremaine 1980). Since F_J is conserved at different radii, F_J equals F_A far from corotation where WKB solutions

(of Equation 83 therein) are valid. The analytical solution can be obtained (Goldreich & Tremaine 1978) at the following condition (Goldreich & Tremaine 1980),

$$m(h/r) \ll \min\Big(\frac{Q^2-1}{3Q^2}, 1\Big). \tag{5.24}$$

The resulting AMF is given by,

$$F_J^{WKB}(m) = \frac{4}{3}\frac{m^2\Sigma}{\Omega^2}\Big(\frac{GM_p}{R}\Big)^2\{2K_0(2/3)+K_1(2/3)\}^2, \tag{5.25}$$

where the last term is around 6.35, and K_0 and K_1 are zeroth and first order modified Bessel function of the second kind. The value of $F_J^{WKB}(m)$ is approximately equal to 8.47 $m^2 F_{J0}$. However, the condition (5.24) is not always satisfied in the disk. The analytical solution deviates from the exact solution when $m \gtrsim 1/(h/r)$, or disk self-gravity is important ($m \gtrsim \frac{Q^2-1}{3Q^2}$). At this regime, Goldreich & Tremaine (1980) numerically integrate the WKB trial solutions for each m harmonic at given Q and obtain $F_J(m,Q)$, expressed in unit of $F_J^{WKB}(m)$ (see Figures 2 and 3 therein and Figures 5.3 and 5.4 in this paper). Summing up each m mode, the total AMF is given by,

$$F_J = f(Q)\frac{F_J^{WKB}(m)}{m^2} \approx 8.47 f(Q) F_{J0}, \tag{5.26}$$

where F_{J0} is expressed in Equation 5.6, and $f(Q)$ is a factor, which is a function of Q. From Goldreich & Tremaine (1980),

$$f(Q) = \frac{1}{3}\mu_{max}^3 = \int_0^\infty d\mu\,\mu^2 \frac{F_J(m,Q)}{F_J^{WKB}(m)}, \tag{5.27}$$

where $\mu = mc_s/\Omega r = m(h/r)$. The coefficient $F_J/F_{J0} \approx 0.93$ if $Q = \infty$ and $F_J/F_{J0} \approx 8.6$ if $Q = 2$, which means that more massive disks (with lower Toomre Q values) have higher AMF. We will compare this analytical solution with our simulation results in 5.5.1.

5.3.3 Pitch Angle

The pitch angle β is defined as the angle between the direction of the line tangent to the spiral arm and the azimuthal direction in the disk. If the spiral arms have m-fold rotational symmetry, and k is the radial wave number under the WKB approximation,

$$\beta = tan^{-1}(\frac{m}{kr}). \tag{5.28}$$

The dispersion relation for the spiral wave in the tightly wound limit (Equation 5.19) can also be used to derive the pitch angle. In the absence of disk self-gravity, the middle term on the right hand side of Equation 5.19 becomes zero. Thus, by manipulating Equation 5.21, the pitch angle for the m mode is,

$$tan(\beta) = \frac{m}{kr} = \frac{c_s}{\left\{|\Omega_p - \Omega|^2 - \frac{\Omega^2}{m^2}\right\}^{1/2}}. \tag{5.29}$$

If $m \gg 1$, different m modes have the same pitch angle and interfere with each other (Ogilvie & Lubow 2002), so that

$$tan(\beta) = \frac{m}{kr} = \frac{1}{r}\frac{c_s}{|\Omega_p - \Omega|}. \tag{5.30}$$

When the disk self-gravity is non-negligible, we can rewrite Equation 5.20 to derive the pitch angle

$$tan(\beta) = \frac{1}{r} \frac{c_s}{\left\{ |\Omega_p - \Omega|^2 - \frac{\Omega^2}{m^2}\left(1 - \frac{1}{Q^2}\right) \right\}^{1/2} + \frac{\Omega}{mQ}} . \tag{5.31}$$

Compared to Equation 5.29, two additional terms are $(\Omega/mQ)^2$ within the square root and Ω/mQ outside the square root. When $Q \gg 1$, Equation 5.31 reduces to Equation 5.29. Equation 5.31 also indicates that the pitch angle becomes smaller for higher disk masses (with smaller Q). However, this effect is not strong unless Q is very close to unity. For example, when $m \gg 1$, Equation 5.31 reduces to Equation 5.30 even in massive disks. Thus, different m modes should still have the same pitch angle and interfere with each other unless Q is close to one. The effect should be stronger in the inner disk than the outer disk since Ω decreases with r. We will confirm this pitch angle calculation using our simulations in Section 5.5.1.

5.3.4 Orbital Cooling

Miranda & Rafikov (2019c) carry out linear analysis on locally isothermal disks with temperature varying with the radius and run simulations to show that the spiral wave absorbs AMF from the background when it is propagating to hotter regions, resulting in higher AMF and higher density perturbation. The phenomenon is unique to locally isothermal disks. It would not happen even if the adiabatic disk is very close to locally isothermal (γ is very close to 1). They advocate that the inclusion of the energy equation would result in weaker density waves and shallower gaps. Thus, planet masses inferred from previous locally isothermal simulations might be systematically lower than their actual masses.

Besides running locally isothermal simulations, we further study this issue by carrying out

adiabatic simulations with a simple orbital cooling prescription. The adiabatic EoS is

$$P = (\gamma - 1)E. \tag{5.32}$$

where E is the internal energy per unit area and γ is the adiabatic index. We adopt $\gamma = 1.4$ in this study. Since the energy equation is solved in simulations with the adiabatic EoS, we can prescribe the effect of radiative cooling using the orbital cooling approach:

$$\frac{dE}{dt} = -\frac{E - c_v \Sigma T_{irr}}{t_{cool}}, \tag{5.33}$$

where Σ is the disk surface density. T_{irr} is the disk initial temperature, which is determined by the stellar irradiation in realistic disks. $c_v \equiv R/(\mu(\gamma-1))$ is the heat capacity per unit mass, $R \equiv k/m_H$ is the specific gas constant, k is the Boltzmann constant, μ is the mean molecular weight, m_H is the atomic unit mass, and t_{cool} is the cooling time. It is useful to define the dimensionless cooling time

$$T_{cool} = t_{cool}\Omega(r). \tag{5.34}$$

Thus, T_{cool} is t_{cool} in the unit of orbital time over 2π. This prescription is identical to Zhu et al. (2015a) and similar to the β-cooling in Gammie (2001). Small T_{cool} means fast cooling. Thus, the adiabatic disk with fast cooling should be closer to the isothermal disk, whereas large T_{cool} means slow cooling, and this disk is closer to the adiabatic disk without cooling. In the rest of the paper, we simply use adiabatic disks to refer to the adiabatic disks without cooling.

To estimate T_{cool} in realistic disks, we follow Zhu et al. (2015a) which use the radiative cooling

rate of

$$\frac{dE}{dt} = -\frac{16}{3}\sigma(T_{mid}^4 - T_{irr}^4)\frac{\tau}{1+\tau^2}, \tag{5.35}$$

where σ is the Stefan-Boltzmann constant, $\tau = (\Sigma/2)\kappa_R$ is the optical depth in the vertical direction, κ_R is the Rosseland mean opacity normalized to the gas surface density assuming dust-to-gas ratio is 1/100, $\kappa_R = \kappa_R(a_{max}, T)$, and T_{mid} is the midplane temperature. Assuming $E = c_v \Sigma T_{mid}$ and using Equations 5.33 and 5.35, we can derive

$$t_{cool} = \frac{3\Sigma c_v}{16\sigma(T_{mid}^2 + T_{irr}^2)(T_{mid} + T_{irr})}\frac{1+\tau^2}{\tau}. \tag{5.36}$$

Approximating $T_{mid} = T_{irr} = T_d$, where

$$T_d(r) = \begin{cases} \left(\frac{\phi L_*}{8\pi r^2 \sigma}\right)^{1/4} & r \leq r_{T_f} \\ T_f & r > r_{T_f} \end{cases} \tag{5.37}$$

where $\phi = 0.02$, representing flaring angle (Dullemond et al. 2018), and L_* is the stellar luminosity. We assume the disk temperature decreases as r and at a given radius it reaches a minimum floor temperature T_f, setting by the background heating processes (e.g., cosmic rays). This radius is

$$r_{T_f} = 39 \text{ au } \left(\frac{T_f}{20 \text{ K}}\right)^{-2}\left(\frac{L_*}{L_\odot}\right)^{1/2}\left(\frac{\phi}{0.02}\right)^{1/2}. \tag{5.38}$$

The dimensionless cooling time becomes,

$$T_{cool} = 0.015\left(\frac{f}{0.01}\right)^{-1}\left(\frac{\kappa_R(a_{max},T_d)}{1\ \mathrm{cm^2 g^{-1}}}\right)^{-1}\left(\frac{L_*}{L_\odot}\right)^{-3/4}\left(\frac{\phi}{0.02}\right)^{-3/4} \times\left(\frac{M_*}{M_\odot}\right)^{1/2}(1+\tau^2)\begin{cases}1 & r\le r_{T_f}\\ \left(\frac{r}{r_{T_f}}\right)^{-3/2} & r>r_{T_f}\end{cases}, \tag{5.39}$$

where f is the dust-to-gas mass ratio. For a given protoplanetary disk interior to r_{T_f}, and assuming constant f, T_{cool} only depends on the Rosseland mean opacity in the optically thin limit, whereas $T_{cool} \propto \tau^2/\kappa_R$ in the optically thick limit. Within r_{T_f}, it does not explicitly depend on r (the Rosseland mean opacity depends on the temperature which varies with the radius). Note that this optical depth is different from the optical depth in the dust continuum observation, since the Rosseland mean opacity is used for the cooling process. Aside from the optical depth effect, higher opacity, higher stellar radiation, larger flaring angle and smaller stellar mass would make T_{cool} smaller and vice versa. We also ignore energy diffusion in the radial direction (Goodman & Rafikov 2001), which might be important for very optically thick disks.

Here we provide several typical values of κ_R at different temperatures for references. Using the DSHARP opacity (Birnstiel et al. 2018), the Rosseland mean absorption opacity for the dust population with the maximum dust size a_{max} = 1 mm and the size distribution $n(a) \propto a^{-3.5}$ is $\kappa_R(20\ \mathrm{K}) = 0.21\ \mathrm{cm^2 g^{-1}}$, $\kappa_R(40\ \mathrm{K}) = 0.48\ \mathrm{cm^2 g^{-1}}$ and $\kappa_R(125\ \mathrm{K}) = 1.03\ \mathrm{cm^2 g^{-1}}$.

For a solar-type star, suppose $\Sigma = 100\ \mathrm{g\ cm^{-2}}$, $f = 0.01$ at 10 au and $T = 40$ K, $T_{cool} \sim 20$, which is approaching the adiabatic limit. Suppose $\Sigma = 1\ \mathrm{g\ cm^{-2}}$, $f = 0.01$ at 100 au, and $T = 20$ K, $T_{cool} \sim 0.02$, which is on the locally isothermal limit. Thus, the T_{cool} estimated from the gap substructures can help constrain the optical depth thus the surface density of the disk. We will use

this argument to constrain the surface density at ~ 100 au of the AS 209 disk in Section 5.6.3.

5.4 Method

To test the effects of disk self-gravity and radiative cooling on planet-disk interactions, we run four sets of 2D hydrodynamical simulations. We use FARGO-ADSG (Baruteau & Masset 2008a;b; Baruteau & Zhu 2016) in the first three sets and Athena++ (Stone et al. 2020, in prep) in the fourth set. For all the simulations, we fix the planet in circular orbits and do not consider planet migration. We apply the evanescent boundary condition to all the simulations. We choose not to include the indirect term for separating its effect from the effects studied in this paper. Our simulation setups are motivated and based on Bae & Zhu (2018a) and Bae et al. (2017a). We keep all the parameters the same but add disk self-gravity or/and radiative cooling. We denote them as `B18` (Set 1) and `B17` (Set 2), respectively. We denote simulations with adiabatic EoS and radiative cooling as `AD`, and simulations with self-gravity as `SG`. For example, a simulation that is built on Bae et al. (2017a) with both orbital cooling and self-gravity is written as `B17ADSG`. We also run a set of simulations `AS209` (Set 3) including radiative cooling and self-gravity with massive planets by adopting the parameters in the AS 209 α varying model in Zhang et al. (2018b) ($\{(h/r)_p,\ \alpha,\ M_p\} = \{0.05,\ 3\times10^{-4}(r/r_p)^2,\ 1\ M_{th}\}$). The `Athena++` (Stone et al., 2020 in prep) simulations (Set 4) have the same setup as `B17` and `B17AD` to verify the results. All the simulations that appear in this paper are summarized in Table 1 in (Zhang & Zhu 2020), and descriptions are detailed as follows.

(1) `B18` focuses on the linear regime of planet-disk interactions with very low mass planets. This setup is also adopted in Miranda & Rafikov (2019c). The planet mass $M_p = 0.01\ M_{th}$. The

aspect ratio at r_p is $(h/r)_p = 0.1$. The gas surface density is $\Sigma \propto r^{-1}$. The disk temperature is $T(r) \propto r^{-0.5}$ ($h/r \propto r^{0.25}$) with the locally isothermal EoS. The disk viscosity α is 0 (inviscid). The inner boundary is 0.05 r_p, whereas the outer boundary is 5.0 r_p. The damping regions are inside 0.06 r_p and outside 4.6 r_p. We run five simulations with $Q = \infty$ (non-selfgravitating), 100, 10, 5, and 2, where Q is evaluated at r_p. The self-gravity smoothing length is 0.3 h. Given the density and temperature profiles, Q is larger at the inner disk and smaller at the outer disk. $Q \propto r^{-4/3}$ and Q at the inner (outer) boundary is 9.5 times (0.30 times) the value at r_p. The resolution in (logarithmically spaced) r and ϕ directions is 4096 $\times$ 5580. There are $\sim$ 89 grid cells per scale height in the r direction. The planet potential is in the form of Equation 5.5 and the smoothing length s is 0.6 h. The implementation of the Poisson equation solver for self-gravity can be found in Baruteau & Masset (2008b). To study the AMF in simulations with adiabatic EoS and temperature varying with the radius, we also run three simulations (`B18AD`) with lower resolution (2048 $\times$ 2790) for $T_{cool} = 10^{-4}$, 10^{-3} and 0.01 cases.

(2) `B17` focuses on gap opening by more massive planets. These simulations start with globally isothermal disks. While one subset keeps the temperature constant, the other subset (`AD`) allows the disk to cool. The aspect ratio $(h/r)_p = 0.07$, with $h/r \propto r^{0.5}$ so that T is a constant. The disk viscosity $\alpha = 5 \times 10^{-5}$, and the gas surface density $\Sigma \propto r^{-1}$. The inner boundary is 0.2 r_p and the outer boundary is 2.0 r_p. The damping regions are inside 0.24 r_p and outside 1.6 r_p. The planet smoothing length s is 0.1 h. If the self-gravity is included, the self-gravity smoothing length is 0.3 h. $Q \propto r^{-1/2}$ and Q at the inner (outer) boundary is 2.2 times (0.71 times) the value at r_p. The resolution is 2048 (logarithmically spaced) $\times$ 5580 in the r and ϕ directions, so that dr:$d\phi \approx$ 1:1 for every grid in the domain. There are $\sim$ 62 grid cells per scale height in the r direction. The

planet mass grows with time as $M_p = M_{p,f} \sin^2(\frac{\pi}{2}\frac{t}{t_{grow}})$, and t_{grow} is 20 t_p for 0.1 M_{th}, 60 t_p for 0.3 M_{th} and 100 t_p for 1 and 3 M_{th}, where $t_p = 2\pi/\Omega$ is the orbital period of the planet. The planet grows to its full mass at t_{grow} and stays constant afterwards. We mainly use $M_p = 0.3\ M_{th}$ cases to study the gap opening, but some instability has developed for the $Q = 2$ disk before its planet grows to the full mass, complicating the analysis. Thus, we add four simulations ($M_p = 0.3\ M_{th}$, and Q = 100, 10, 5 and 2) with t_{grow} = 10 t_p. This set of simulations with a shortened planet growing time is almost identical to the previous one at the time step we choose to analyze, but now the planet grows to its full mass before the instability occurs. Overall, we have $Q = \infty$, 100, 10, 5 and 2 disks, with M_p = 0.1, 0.3, 1 and 3 M_{th}.

This set of simulations also includes dust, represented by 200, 000 dust super particles of different sizes. The Stokes numbers (St) of the particles at r_p ranges from 1.57 $\times 10^{-5}$ to 1.57. The setup for dust particles is identical to Zhang et al. (2018b). The Stokes number St for particles (also called particles' dimensionless stopping time) is

$$St = t_{stop}\Omega = \frac{\pi s \rho_p}{2\Sigma_{gas}} = 1.57 \times 10^{-3} \frac{\rho_p}{1\,\mathrm{g\,cm^{-3}}} \frac{s}{1\mathrm{mm}} \frac{100\,\mathrm{g\,cm^{-2}}}{\Sigma_g}. \tag{5.40}$$

where ρ_p is the density of the dust particle, s is the radius of the dust particle, and Σ_g is the gas surface density. We assume ρ_p=1 g cm^{-3} in our simulations. The Stokes number mentioned above is the Stokes number at the beginning of the simulations, St_0. As the disk evolves, the dust sizes are fixed, but as they can drift in the disk, the Stokes number can change.

For `B17AD` and `B17ADSG` disks, T_{cool} is constant everywhere in each simulation, but t_{cool} varies as radius since $\Omega_k \propto r^{-3/2}$. We explore T_{cool} = 0.01, 0.1, 1, 10 and 100, covering fast cooling to slow cooling. Note that for these simulations with cooling, the given h/r and the temperature

profiles above are just the initial values. Their values are subject to change as the simulations evolve. We also run a set of `B17ADSG` disks, which includes both radiative cooling and self-gravity. These disks have $Q = 5$ at the planet's position and T_{cool} = 0.01, 0.1, 1, 10 and 100.

(3) `AS209` is used to test the effects of radiative cooling in the massive planet regime ($\sim$ thermal mass). We run a set of varying α ($\alpha = 3 \times 10^{-4}(r/r_p)^2$) models (`AS209AD`) with T_{cool} = 0.01, 0.1, 1, 10 and 100. The $(h/r)_p$ is 0.05 and M_p is 1 M_{th} or 0.1 M_J if $M_* = M_\odot$. The resolution in the r and ϕ directions is 1024×2790. With lower resolution, we are able to run the simulations longer. We also add a set of simulations that also include self-gravity (`AS209ADSG`). Q is chosen to be 5 at r_p. The planet grows to its full mass at 20 t_p. Other parameters are the same as (2).

(4) `Athena++` simulations are used to verify the results. They include an isothermal simulation and a suite of adiabatic simulations, with the same setup as M_p = 0.1 M_{th}, `B17` and `B17AD` disks in (2), except for a shorter $t_{grow} = 5\ t_p$. To avoid a numerical artifact due to the small smoothing length, we use s = 0.2 h for $T_{cool} = 100$ (twice as large as what is used in the FARGO simulation).

5.5 Results

5.5.1 Self-Gravitating Disks

To study the effects of disk self-gravity in the linear regime, we first analyze `B18SG` disks with M_p = 0.01 M_{th}. Figure 5.1 shows the density perturbations with different disk masses in the polar coordinate. The planet is at $\phi = 180^\circ$ and r = 1 r_p. The density perturbation is

$$\delta\Sigma/\Sigma_0 = (\Sigma - \Sigma_0)/\Sigma_0, \tag{5.41}$$

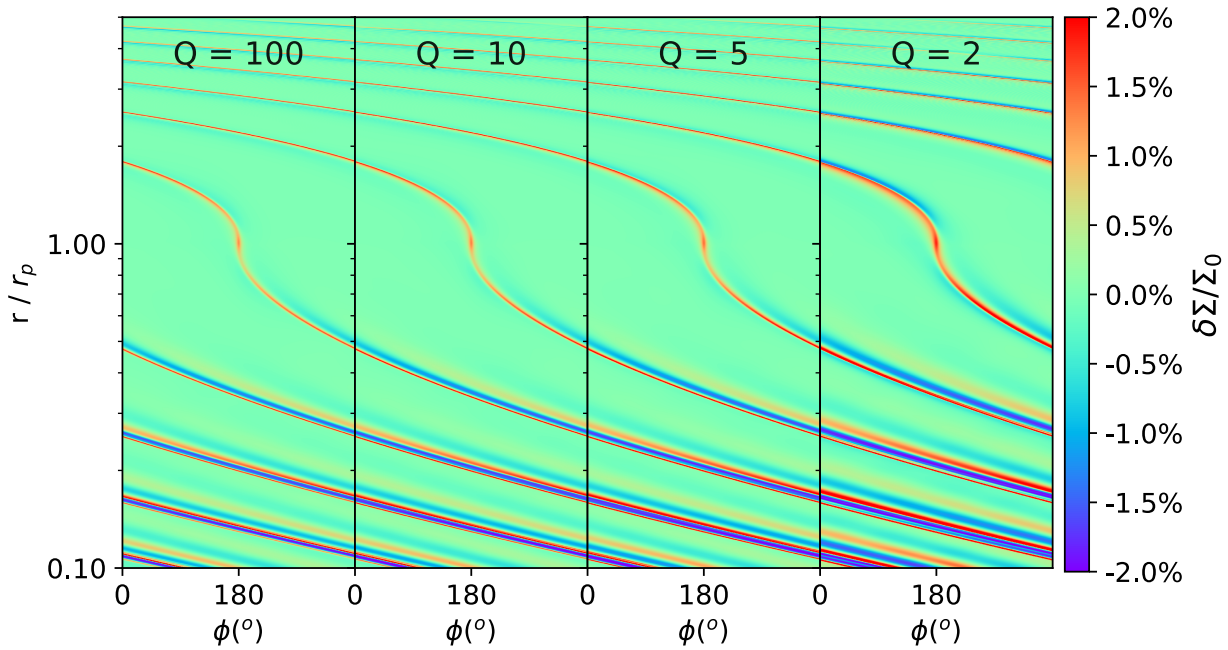

Figure 5.1: The gaseous density perturbations ($\delta\Sigma/\Sigma_0$) of the inviscid self-gravitating disks (B18SG) with a low mass planet M_p = 0.01 M_{th} at 10 orbits. The disk masses increase from left to right. At the position of the planet, the Toomre Q parameters are 100, 10, 5 and 2, respectively. Since the density profile goes as r^{-1}, Q is higher at the inner disk and lower at the outer disk. The spirals become stronger and tighter as the mass increases. This is the most evident in the $Q = 2$ disk.

where Σ_0 is the gaseous surface density at the initial condition, and Σ is the density at the time step (t = 10 t_p for this plot) that is analyzed. From left to right, the disk mass increases. The Toomre Q values at the $r = r_p$ are 100, 10, 5 and 2, respectively. As the disk mass increases, the spiral perturbations become stronger. This transition is the most evident from the $Q = 5$ to $Q = 2$ disk. The density perturbation changes slightly until $Q = 5$ and has a noticeable increase from the $Q = 5$ to $Q = 2$ disk. The underlying AMF that influences the density perturbation is shown Figure 5.2. The AMF increases as Q decreases. The AMF at $Q = 100$ (blue solid curve) is almost identical to the one in the non-selfgravitating disk (black curve) and identical to the result in Figure 1(a) in Miranda & Rafikov (2019c). As pointed out by Miranda & Rafikov (2019c), we can clearly

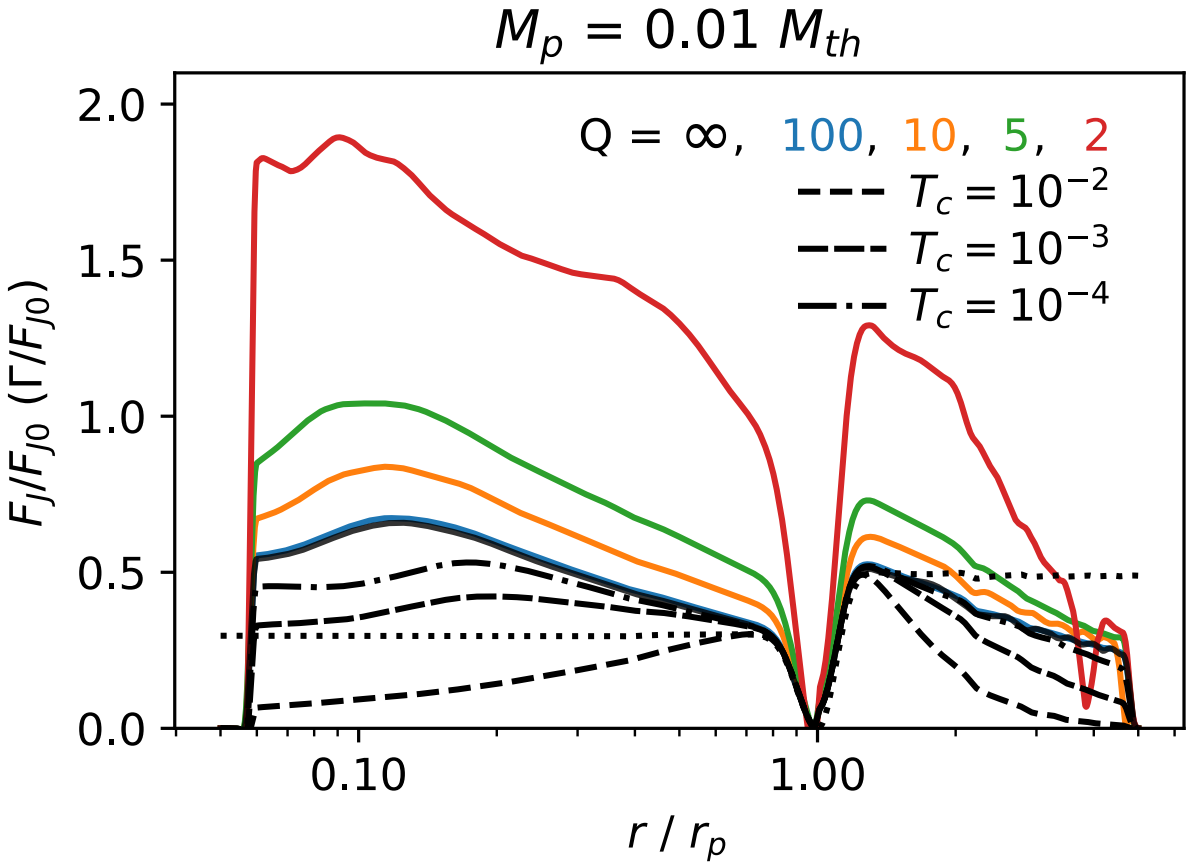

Figure 5.2: The Angular Momentum Flux (AMF) of the `B18`, `B18SG` and `B18AD` disks calculated from Equation 5.7 and normalized by Equation 5.6. The black curves represent the AMF (solid curve) and torque (dotted curve) of the non self-gravitating disk, which is almost identical to Figure 1(a) in Miranda & Rafikov (2019c). The AMF increases as the disk mass increases. The AMF of $Q = 2$ disk is ~ 3 times that of $Q = 100$ disk. This results in a stronger density perturbation. Short dashed, long dashed, and dashed-dotted curves in black represent `B18AD` with $T_{cool} = 0.01$, 10^{-3} and 10^{-4}, and with lower resolution (2048×2790). The $T_{cool} = 10^{-4}$ curve is similar to the case without cooling at such resolution.

see that the AMF increases towards the inner disk where the disk is hotter. However, it cannot be captured even with very small cooling time $T_{cool} = 0.01$ and 0.001, as shown by the short and long dashed curves. Different from the locally isothermal simulation, the spiral waves cannot pick up the AMF from the background disk when they propagate to hotter regions, even with a relatively short T_{cool}. Only extremely small cooling time ($T_{cool} = 10^{-4}$, shown by the dotted-dashed curve) can capture this increase of the AMF towards inner disk (the slightly lower values are due to the lower resolution). The jump of AMF is the largest from the $Q = 5$ to $Q = 2$ disk, where the AMF value of the latter almost doubles. The increase of the AMF with a smaller Q is consistent with the fact that the density perturbation becomes stronger with a smaller Q.

The spirals become more tightly wound as the disk mass increases. It is the most evident at the inner disk between the $Q = 5$ and $Q = 2$ disk. This effect is consistent with the prediction in Section 5.3 around Equation 5.31. Only when Q becomes very small, the two additional terms become important, which makes the pitch angle smaller. Note that Q is larger than Q_p in the inner disk, given the surface density profile we choose. The changes in pitch angle would be larger if Q is constant across the disk. This trend is also reported in Pohl et al. (2015), where their simulations lie in the non-linear regime with higher planet masses. Hence, the decrease of pitch angle with the disk mass applies to a large range of planet masses.

Yu et al. (2019) measure the pitch angles from 10 protoplanetary disks in near-infrared scattered-light images and three disks in ALMA millimeter dust continuum images. They find a tight relation between the spiral arm pitch angle and the disk mass—more massive disks have smaller pitch angles. While we find that the disk self-gravity cannot lead to such significant changes in pitch angles, spirals in scattered-light images might show more dramatic effects with disk self-gravity which needs to be studied in future. Without the consideration of the self-gravity, the different

pitch angles between scattered light and millimeter continuum images might be due to the vertical temperature gradient (Juhász & 2018; Rosotti et al. 2019). The near-infrared scattered-light observations probe higher atmosphere with higher temperature, thus the spirals have larger pitch angles than those in the midplane probed by ALMA.

Comparison to the Linear Theory

In this subsection, we provide a quantitative comparison with the linear theory. In Section 5.3, we briefly introduce the AMF in disks with and without self-gravity. The quantity we want to compare is $F_J(m,Q)/F_J^{WKB}(m)$ (ratio of the numerically integrated m harmonics of the AMF and the m mode AMF solved analytically; see Equation 5.27), which has been given in Figure 2 of Goldreich & Tremaine (1980). Similar comparisons have been performed before in non-selfgravitating shearing sheet simulations (Dong et al. 2011b). With our simulations, we measure the AMF at several h away from a low-mass planet ($M_p \ll M_{th}$) in the inner disk. Note that the spirals will shock at a certain distance away from the planet. This distance is l_{sh} (Goodman & Rafikov 2001), given by

$$l_{sh} \approx 0.8\Big(\frac{\gamma+1}{12/5}\frac{M_p}{M_{th}}\Big)^{-2/5}h. \tag{5.42}$$

The linear theory of wave propagation fails for $|r-r_p| > l_{sh}$, so the position that we measure the AMF cannot be too far from the planet. The position should also be chosen closer to the planet as the planet mass increases, as l_{sh} becomes shorter with higher mass planets.

We start the comparison with a very low planet mass, $M_p = 0.01\,M_{th}$ in `B18SG` disks. Figure 5.3 shows the AMF measured at $5h$, where we find the values match the linear theory the best. The blue curve shows the ratio of the non-selfgravitating disk, and the orange curve shows the ratio of the

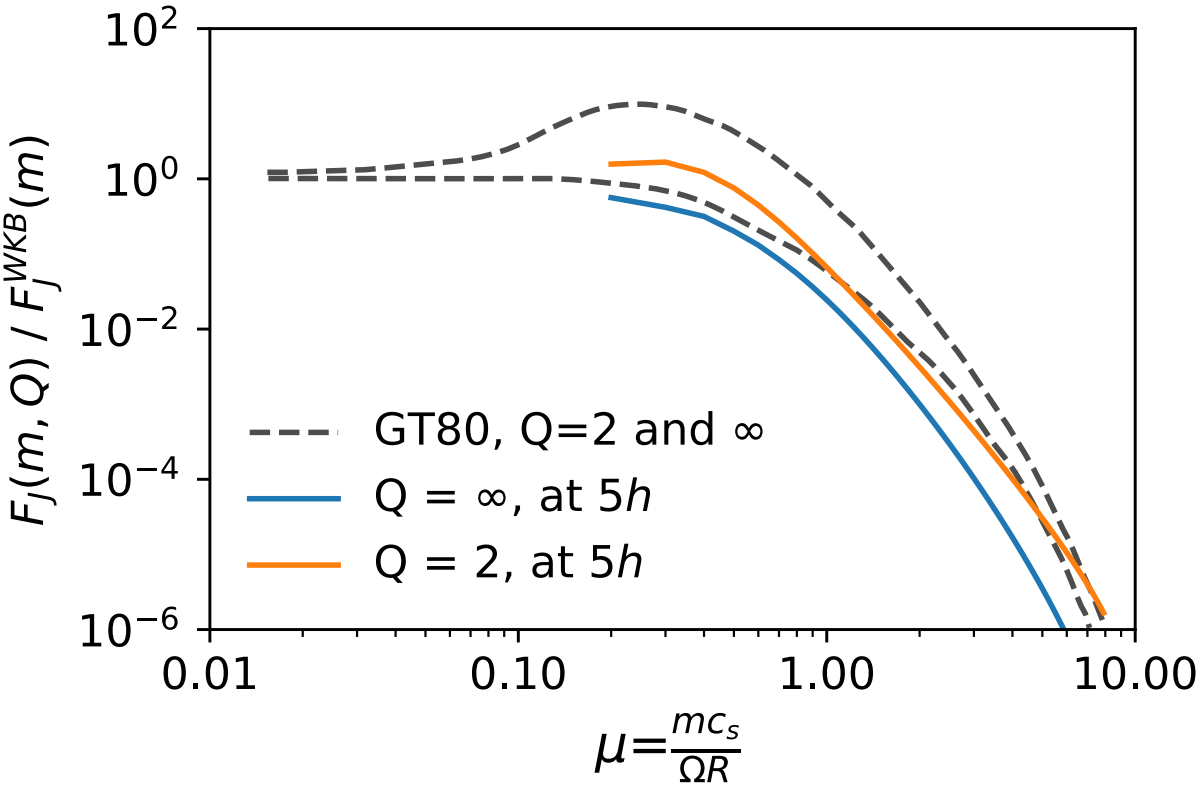

Figure 5.3: Comparison between $F_J(m,Q)/F_J^{WKB}(m)$ measured from simulations ($M_p = 0.01\ M_{th}$, `B18SG`) and calculated from the linear theory (Goldreich & Tremaine 1980). This ratio is measured at $5h$ (at $0.5\ r_p$) inside of the planet and is plotted on y-axis. The x-axis is $\mu = \frac{mc_s}{\Omega R}$ (or $m(h/r)$, where $(h/r)_p = 0.1$). The simulation results are shown in blue ($Q = \infty$) and orange ($Q = 2$) solid curves, whereas the analytical results are shown in dashed curves ($Q = 2$ curve is the higher).

$Q = 2$ disk. The ratios calculated from Goldreich & Tremaine (1980) are shown in dashed curves (the ratio of $Q = 2$, $F_J(m,2)/F_J^{WKB}(m)$ is shown above and that of $Q = \infty$, $F_J(m,\infty)/F_J^{WKB}(m)$ is shown below). The $Q = \infty$ curve matches the linear calculation relatively well, especially at $\mu \lesssim 1$. As for the differences, one of the reasons is that the temperature is assumed to be constant throughout the disk in the linear calculation, whereas $T \propto r^{-0.5}$ in the simulations. $F_J(m,Q)/F_J^{WKB}(m)$ of the self-gravitating disk is higher than that of $Q = \infty$ disk, which is consistent with the linear theory.

To make a more proper comparison with the analytical theory, we also present `B17SG` disks that are globally isothermal with M_p = 0.1 M_{th}. $F_J(m,Q)/F_J^{WKB}(m)$ at different distances from the planet are shown in Figure 5.4 (Top panel: $Q = 100$ disk, Bottom panel: $Q = 2$ disk). Similar to the results of isothermal shearing sheet simulations in Dong et al. (2011b), we also find a close agreement with the linear theory when $Q \to \infty$. However, the values in $Q = 2$ disk are still different from the linear theory expectation. They are lower by one order of magnitude when $\mu \lesssim 1$ and higher than the linear theory prediction at $\mu \sim 6$. The discrepancy in the high m (or high μ) is possibly due to the limited resolution in the azimuthal direction in simulations. We need very high resolutions to resolve the high m modes properly with a much smaller self-gravity smoothing kernel. As for the low m modes, it is actually not surprising to see discrepancy, since we only measure the advective AMF, and ignore the gravitational AMF (see Section 5.3.2). In $Q = 2$ disks, F_G should contribute a significant amount of AMF. It should be more important when Q is even smaller (close to 1). To match the analytical result of total AMF, one has to include F_G. On the other hand, we do see the increases of advective AMF as the Q becomes smaller. This indicates that as the disk becomes more massive, both F_A and F_G increase to contribute for the increase of total AMF, F_J. Being part of the AMF, F_A alone is enough to explain the change of the density

perturbations, i.e., the increases of F_A leads to the increases of the density perturbations. It is not necessary to add F_G when we want to explain the density perturbations qualitatively.

Gap Opening

In the linear theory, if the planet mass M_p is large enough (close to or higher than M_{th}), the planet can open gaps in the disk. However, the gap opening mass can be much lower, since the non-linear effects such as shock can occur even if the system starts in a linear regime (Goodman & Rafikov 2001; Rafikov 2002). The study of gap opening is very important since gaps are observable in both gaseous and dusty disks. They have been found ubiquitously in recent high-resolution ALMA observations (Huang et al. 2018c; Long et al. 2018b). Assuming these gaps are due to the planet, one might infer the planet mass from the gap width and depth (e.g., Zhang et al. 2018b). Now we use higher mass planets to demonstrate the effect of the self-gravity on gap opening.

We first show the results of `B17SG` disks with $M_p = 0.3\ M_{th}$, where the evolution starts in linear regime, marginally opening gap for non-selfgravitating disk at longer time evolution. Figures 5.5 and 5.6 show the density perturbations in 2D and 1D at $t = 20\ t_p$ (we use the models whose $t_{grow} = 10\ t_p$ here). As the Q decreases, the gap becomes deeper. Pohl et al. (2015); Li & Li (2016) also find this effect for higher mass planets. The transition is the most evident from $Q = 5$ to $Q = 2$ disks, where the gap depth becomes a factor of 3 stronger at the major gap where the planet is located. The major gap is separated by the horseshoe region, thus resembles "w" shape. The gap width changes only slightly comparing to the gap depth (see Section 5.6.2 for details). The secondary gap is around 0.5 to 0.6 r_p, the location of which does not change as the Q decreases.

To understand the density perturbations, we plot the AMF of each simulation in Figure 5.7. The left panel shows $M_p = 0.1\ M_{th}$ disks and right panel shows $M_p = 0.3\ M_{th}$ disks. Given the same

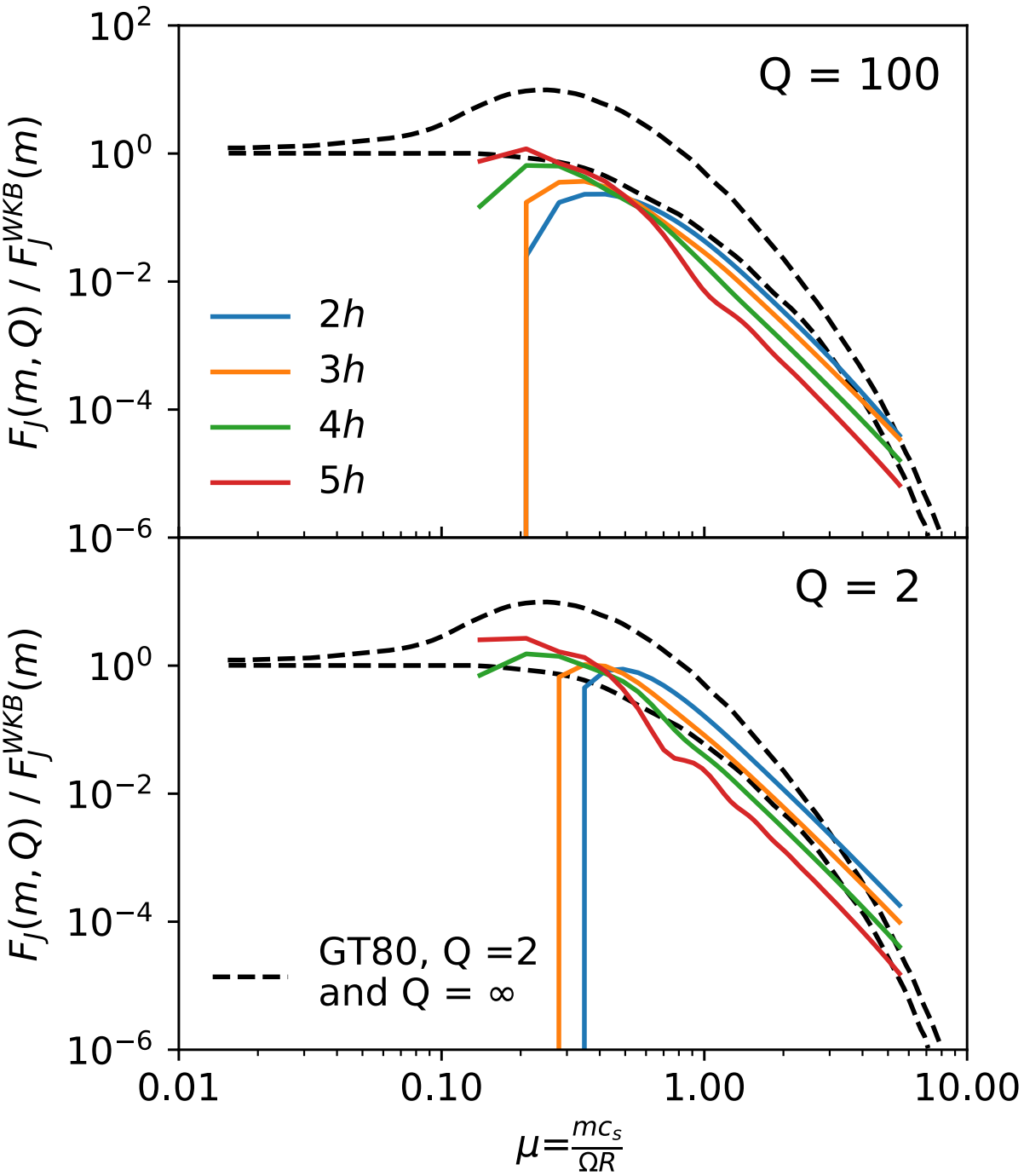

Figure 5.4: Similar to Figure 5.3, but for `B17SG`, $M_p = 0.1\ M_{th}$. This ratio is measured at $2h$ (blue), $3h$ (orange), $4h$ (green), and $5h$ (red) inside of the planet. The upper panel shows the results in $Q = 100$ disk, whereas the lower panel shows the results in $Q = 2$ disk. The dashed curves are the same as in Figure 5.3.

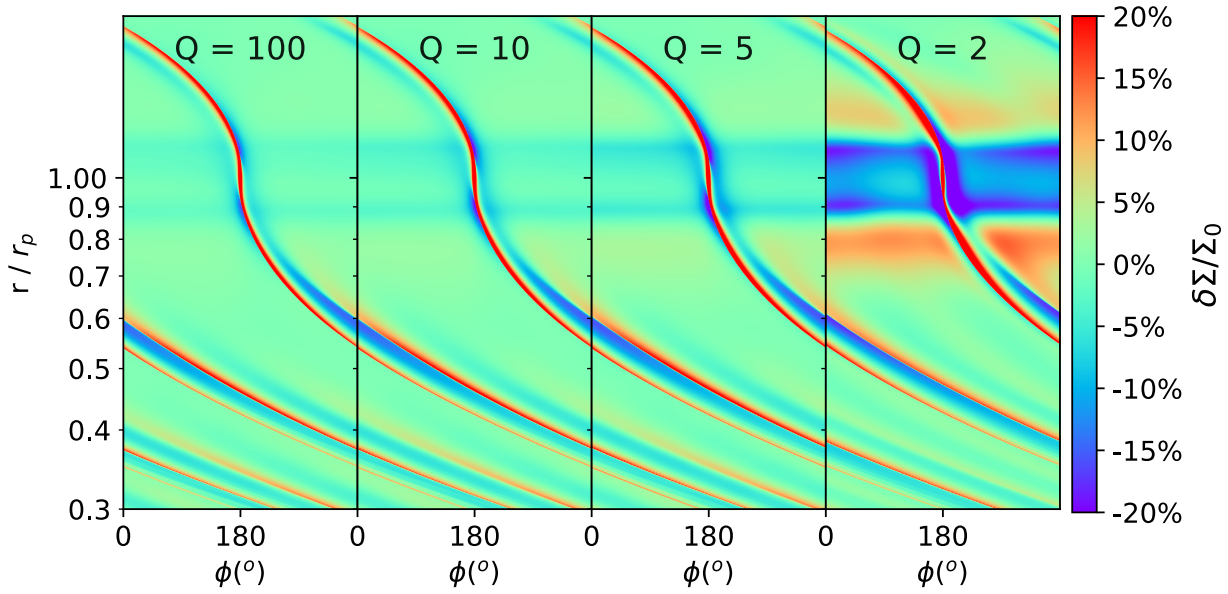

Figure 5.5: The gas density perturbations ($\delta\Sigma/\Sigma_0$) of the isothermal self-gravitating disks `B17SG` with a low mass planet $M_p = 0.3\ M_{th}$ at 20 orbits (with $t_{grow} = 10\ t_p$). Compared to Figure 5.1, higher planet mass can open deeper gap and even the secondary gap (see Figure 5.6). The depth of the primary gap becomes deeper with the decreases of Q. This is the most evident in $Q = 2$ disk.

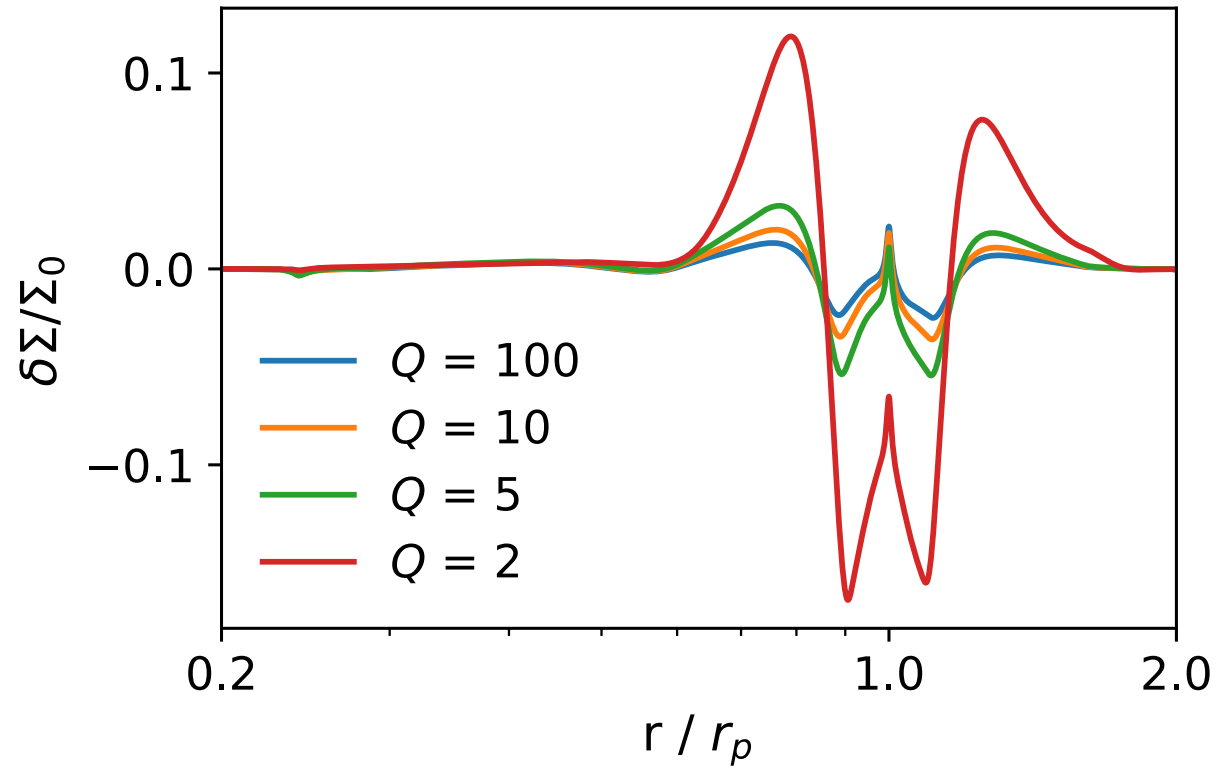

Figure 5.6: The azimutally averaged density perturbations of Figure 5.5. The blue, orange, green and red curves represent $Q = 100$, 10, 5 and 2 disks. As the disk mass increases, the perturbations become stronger and gaps become deeper, but the position of the secondary gap does not change significantly.

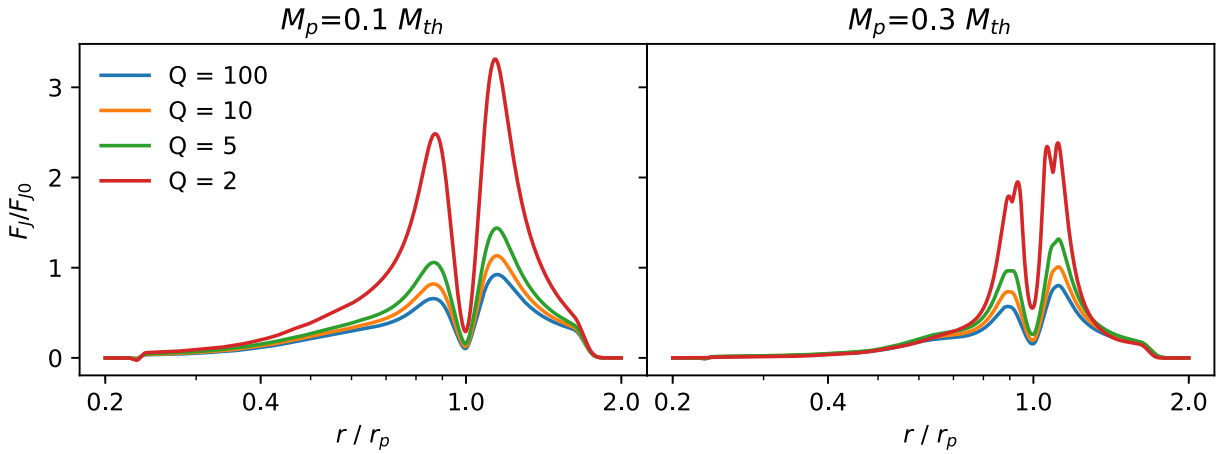

Figure 5.7: The AMF of the isothermal disks at 20 orbits with M_p = 0.1 and 0.3 M_{th}. Given the same disk mass, as the planet mass increases, the normalized AMF becomes lower at any disk with different Q, as shock forms earlier and closer to the planet with the increases of the planet mass.

Q, the normalized AMF decreases as the planet mass increases, which is due to the increasing non-linear shock dissipation. This is consistent with the result of non-selfgravitating disks in Miranda & Rafikov (2019c). The changes of the AMF at each Q has the same trend as the changes in density perturbations. From $Q = 5$ to $Q = 2$, the AMF doubles. We will quantify this trend in Section 5.6.1. Since the normalization factor $F_{J0} \propto Mp^2$, the absolute value of AMF is still higher in the disks with higher planet mass.

To study how disk self-gravity affects the dust continuum observations, we evolve simulations for a longer time scale (500 t_p) and plot the density perturbations of both gas and dust with different Stokes numbers in Figure 5.8. From top to bottom, it shows the $\delta\Sigma/\Sigma_0$ of gas, and dust with St = 0.001 (represented by St=[0.0005, 0.002]), 0.01 (represented by St=[0.005, 0.02]) and 0.1 (represented by St=[0.05, 0.2]). Notice that the St_0 is the Stokes number at the beginning of the simulations. As the simulations evolve, the particle sizes are fixed, so the dust grain might have different St after it drifts. From left to right, the planet masses are M_p = 0.1, 0.3 and 1.0 M_{th}. The

blue, orange and green curves represent Q = 100, 10, and 5 disks. As expected, the perturbations in the dust are stronger than those in gas, and dust with higher Stokes number has larger perturbations. This is because dust particles with higher St drift faster when $St \lesssim 1$. For M_p = 0.1 M_{th}, St = 0.1 disk, the dust particles have almost drifted to the inner disk. Similar to the trend in the gas, the gap becomes deeper, and the ring becomes higher as the Q becomes smaller, which are consistent with Li & Li (2016). The positions of the secondary gaps do not change. The overall shapes of the profiles do not change, except the gaps outside the planet become weaker for M_p = 0.3 and 1.0 M_{th} disks at St_0 = 0.001. The positions of them also shift outside. The region beyond $r = 1.6\ r_p$ should not be trusted as it is in the wave damping zone. For small Q and large M_p, some curves for disks with $Q = 5$ are missing since the disks have already become unstable at 500 t_p. We will discuss this phenomenon in Section 5.6.4.

5.5.2 Adiabatic Disks with Radiative Cooling

In this subsection, we study the effects of radiative cooling on planet-disk interactions, focusing on `B17AD`. The simulations presented in this section are globally isothermal, with $q = 0$. The absorption of AMF from the background occurs in locally isothermal disk (in Figures 5.1 and 5.2), but not in globally isothermal disks here. From left to right, Figure 5.9 shows the density perturbations for the M_p = 0.1 M_{th} isothermal disk, and adiabatic disks with cooling time T_{cool} = 0.01, 0.1, 1, 10 and 100. The top panels are results from FARGO-ADSG, whereas the bottom panels are results from Athena++. They are almost identical, except for the small difference for the corotation features in the $T_{cool} = 100$ cases. We analyze the simulations at $t = 40\ t_p$ for FARGO and 20 t_p for Athena++ due to a shorter t_{grow} adopted in Athena++ simulations. At these times, we find

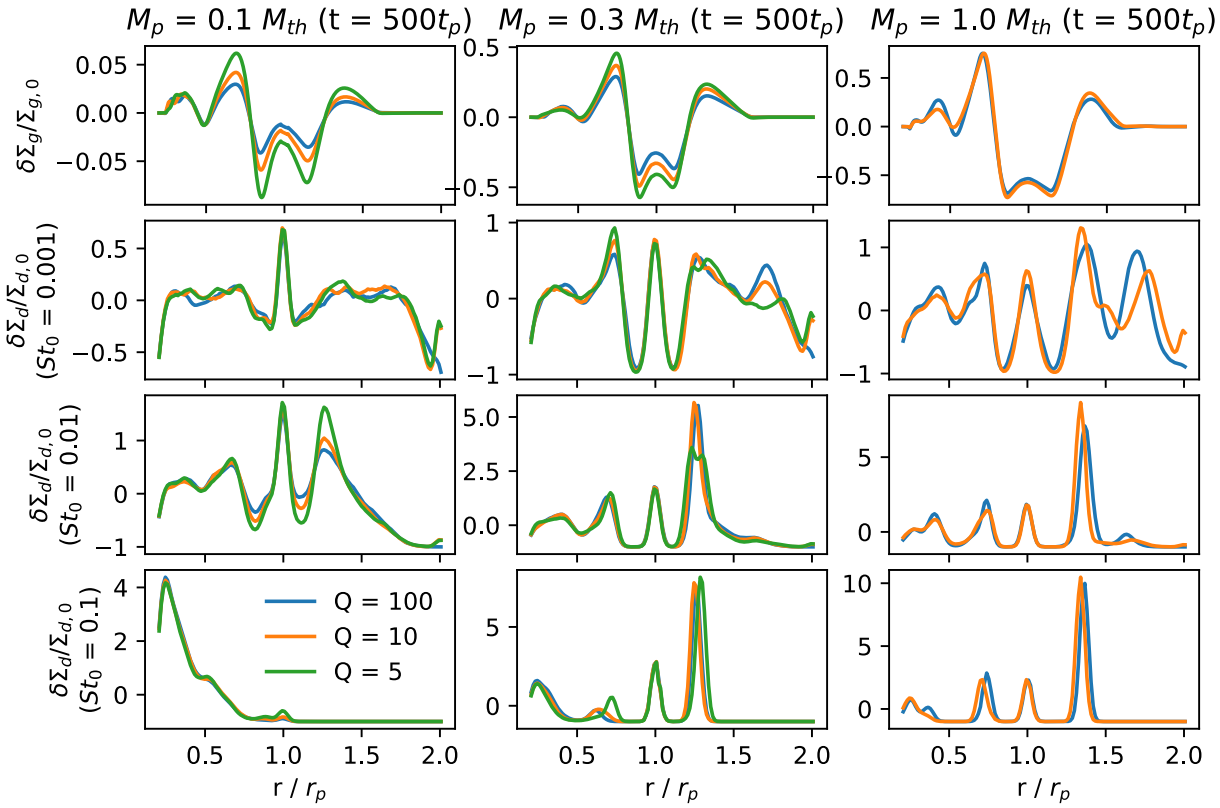

Figure 5.8: The density perturbations of the gas and dusts with different Stokes number ($St = 0.001$, 0.01, and 0.1) at t = 500 t_p in globally isothermal disk with M_p = 0.1, 0.3 and 1 M_{th} (from left to right). From top to bottom panels, there are density perturbations of the gas, $St = 0.001$, $St = 0.01$ and $St = 0.1$ sized dusts. Blue, orange and green curves represent $Q = 100$, 10, and 5 disks. Some curves for disks with $Q = 5$ are missing since the disk becomes unstable at this time steps in the simulations. Overall, the position of the secondary gap does not change with the increase of disk masses. The gap becomes deeper for lower Q values.

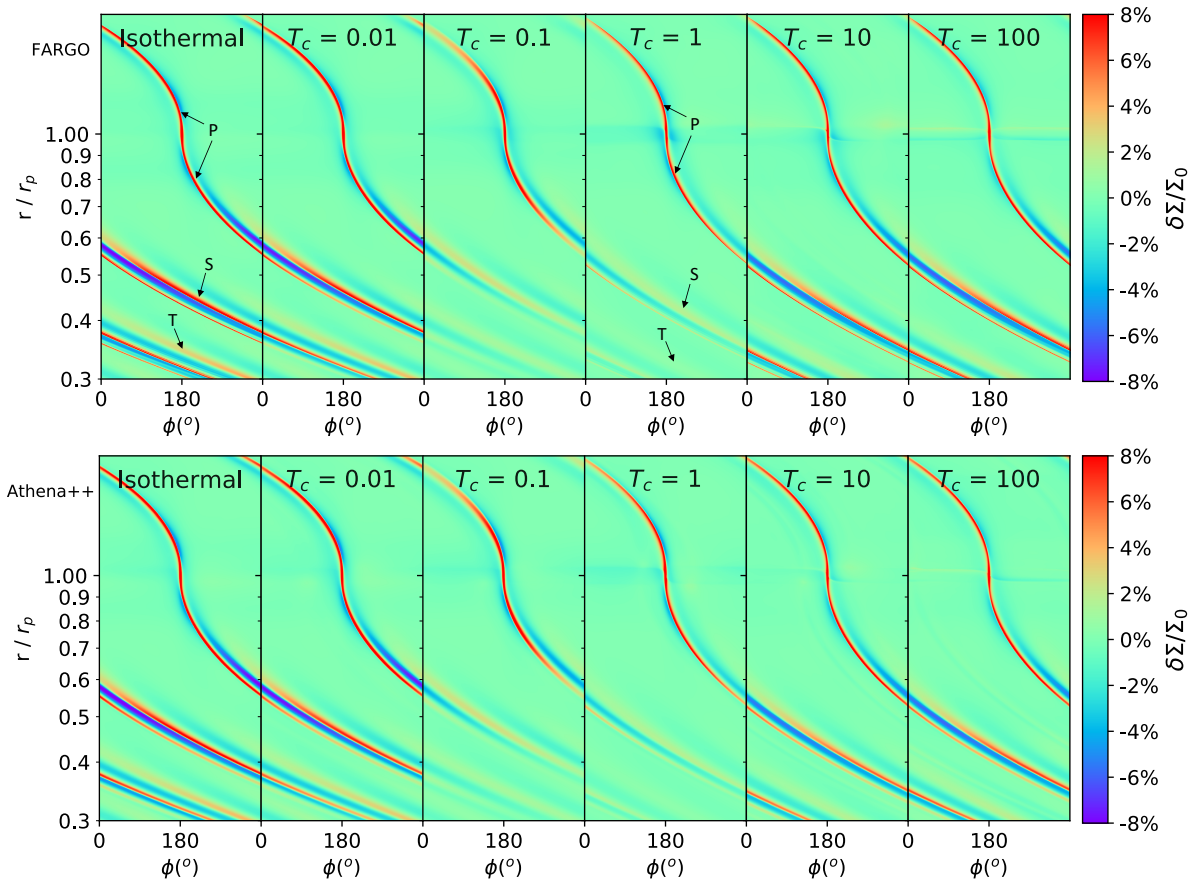

Figure 5.9: The density perturbations of the adiabatic simulations `B17AD` at 40 orbits (FARGO) and 20 orbits (Athena++) with $M_p = 0.1\ M_{th}$. From left to right, the disks represent fast to slow cooling. The isothermal disk is shown in the leftmost panel, then the dimensionless disk cooling parameters T_{cool} are 0.01, 0.1, 1, 10 and 100, respectively. The upper panels show results from FARGO-ADSG and the lower panels show results from Athena++. The primary spirals are marked as "P", the secondary spirals are marked as "S" and the tertiary spirals are marked as "T".

that all the disks are stable and have reached quasi-steady states. Disks with shorter dimensionless cooling times T_{cool} are more similar to isothermal disks, whereas disks with larger T_{cool} resemble adiabatic disks. The primary spirals are marked as "P", the secondary spirals are marked as "S" and the tertiary spirals are marked as "T" on the figure.

From the isothermal to the adiabatic limit (increasing T_{cool} from the left to the right panels), the spirals become weaker as the cooling timescale becomes longer until T_{cool} = 1 and then become stronger again as T_{cool} continues to increase. The secondary and tertiary spirals also become very weak at T_{cool} = 1 and stronger at T_{cool} = 10. Nevertheless, the secondary and tertiary spirals are still present at $T_{cool} = 1$ as indicated by the arrows.

The spirals become more open as the cooling time increases. This is due to the increases of the sound speed from $c_s = (RT/\mu)^{1/2}$ in the isothermal limit to $c_s = (\gamma RT/\mu)^{1/2}$ in the adiabatic limit. In other words, the effective γ in Equation 5.30 increases from 1 to 1.4 as T_{cool} becomes larger.

The change of the amplitude and position of the spiral arms with respect to the cooling time can be seen more clearly in 1D plots. Figure 5.10 (left panels) shows the density perturbations vs. azimuthal angle (ϕ) cut at $r = 0.45\ r_p$ and $r = 0.32\ r_p$. The density perturbations due to the primary spiral and the secondary spiral are marked as "P" and "S" on the figure. The one due to the tertiary spiral is also marked as "T" in the $r = 0.32\ r_p$ plot. The positions of the primary, secondary, and tertiary spirals in T_{cool} = 0.01 disks are similar to those in the isothermal disk. At $r = 0.45\ r_p$, the amplitude of the spiral in the T_{cool} = 0.01 disk is slightly lower than that in the isothermal disk.

There is a significant change of the spiral's amplitude when T_{cool} increases from $\lesssim 0.01$ to 0.1. The spiral's amplitude becomes much smaller at $T_{cool} = 0.1$ with a slight shift of the primary spiral position. The tertiary spiral almost disappears at $r = 0.32\ r_p$, but we can still see its presence with

a amplitude of $\sim 1\%$. But the biggest change of the spiral's position occurs when T_{cool} increases from 0.1 to 1. At $r = 0.45\ r_p$, the primary spiral shifts $\sim 45^o$ between $T_{cool} = 0.1$ to $T_{cool} = 1$ cases, although the amplitude does not change much. The tertiary spiral at $r = 0.32\ r_p$ is now the hump from 160° to 250° with a amplitude of $\sim 0.5\%$. At $T_{cool} = 10$, the amplitude of the spiral becomes much higher. The positions are very similar to those in $T_{cool} = 1$. The tertiary spiral also becomes stronger. But the spirals are still weaker than those in the isothermal disk. From $T_{cool} = 10$ to $T_{cool} = 100$ disks, the perturbations seem to converge to the limit of an adiabatic disk. Overall, from isothermal disks ($T_{cool} \lesssim 0.01$) to adiabatic disks ($T_{cool} \gtrsim 10$) the azimuthal angles of the spirals shift to smaller values by $\sim 50°$ at $r = 0.45\ r_p$. This is consistent with the finding in 2D plots that the spirals become less tightly wound as T_{cool} increases [2].

Since spirals are directly related to gap opening, we want to study how the properties of the induced gaps are related to radiative cooling. The top panel of Figure 5.11 shows the azimuathlly averaged density perturbations of disks with different cooling times. T_{cool} = 0.01 disk has a similar profile to the isothermal disk, but with smaller amplitudes. The secondary gap at T_{cool} = 0.1 and 1 disappears (the disappearance of the gap in gas does not necessarily lead to that in dust; see Section 5.6.3). It reappears at T_{cool} = 10, but the position changes from 0.5 r_p to 0.4 r_p and the amplitude becomes smaller. Since spirals carve gaps in disks, the inward shift of the secondary gap position is due to the more open secondary spiral for higher T_{cool}. On the other hand, the non-monotonically transition—the trend of high, low and high amplitudes of the secondary gap depth from the fast cooling to the slow cooling cases— is due to weaker spirals at intermediate

[2]Aside from the interesting behavior at $T_{cool} \sim 1$, we want to note that at two extremes, the spiral at the adiabatic limit is still weaker than that at the locally isothermal limit as expected. This is related to the increase of the effective sound speed with a longer cooling time. When the sound speed increases, the thermal mass increases and ratio between the planet mass and the thermal mass decreases so that the planet is less capable of exciting spiral waves.

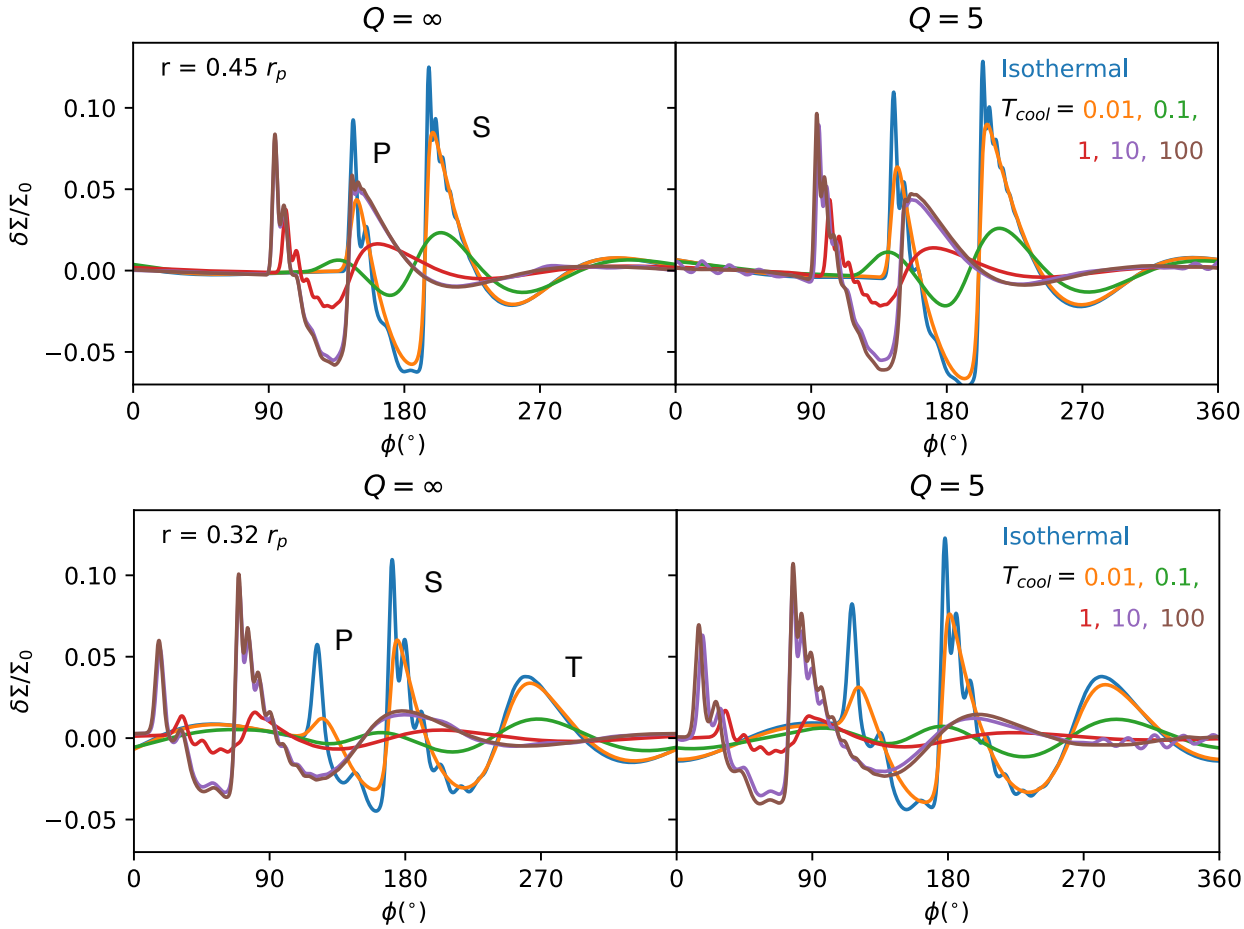

Figure 5.10: The density perturbations along $r = 0.45\ r_p$ (upper panels) and $r = 0.32\ r_p$ (lower panels) for `B17AD` (left panels) and `B17ADSG` (right panels) disks at t = 40 t_p. The positions of the primary, secondary and tertiary spirals for small T_{cool} are marked as "P", "S" and "T" on the left panels.

T_{cool}. Overall, for the intermediate massive planet ($M_p \sim 0.1\ M_{th}$), disks with $T_{cool} \lesssim 0.01$ can be treated as isothermal disks and disks with $T_{cool} \gtrsim 10$ can be seen as purely adiabatic disks, whereas the disks undergo a sharp transition between these limits, characterized by low amplitude spirals and shallow secondary gaps. Note that this $T_{cool} \lesssim 0.01$ criterion is more stringent with a low mass planet in the linear regime. As shown in Figure 5.2, only when $T_{cool} = 10^{-4}$ the AMF is close to the isothermal case with $M_p = 0.01\ M_{th}$. Both the temperature gradient ($\mathrm{T} \propto r^{-0.5}$) and the linear damping contribute to the AMF profile, but the linear damping is the dominant effect here.

Since such conditions with intermediate cooling times are very likely to occur in realistic protoplanetary disks (see Section 5.3), we are interested in whether these much shallower secondary gaps can still trap enough dust particles to be observable. Examining the previous models in Zhang et al. (2018b), we find the current set of simulations has very similar setup to the $h/r = 0.07$, $\alpha = 10^{-4}$, $M_p/M_* = 11 M_\oplus/M_\odot$ model in Zhang et al. (2018b) (the upper-left plots in 2D figures therein), despite the α is lower here. However, the secondary gap cannot be found in any dust configurations in that model, even though those simulations assume the locally isothermal EoS. Thus, we conclude that the models being analyzed in this subsection with such low planet mass is not suitable for testing the observability of the secondary gap. To that end, we run simulations with higher planet mass, 1 M_{th}, close to the setup of the AS 209 simulation, α varying model (Zhang et al. 2018b). We direct the discussion to Section 5.6.3.

We also plot the AMF (in solid curves) and the integrated torque (in dashed curves) of these disks in the lower panel of Figure 5.11. The torque is integrated from the planet's position towards either side of the disk. The AMF decreases monotonously close to the planet ($|r - r_p| \lesssim 0.1\ r_p$) due to the torque cutoff. The AMF far away from the planet (e.g., at r=0.3 r_p and 1.5 r_p) decreases to the lowest values at $T_{cool} = 0.1$ and 1 and increases back to the isothermal values at $T_{cool} = 10$ and 100. On the other hand, from the fast cooling (and isothermal) to the slow cooling cases, the torque first increases and reaches the maximum at T_{cool} = 1 and then decreases and reaches the minimum at T_{cool} = 100. The AMF and torque at several h away from the planet (e.g., at r = 0.85 r_p or 1.2 r_p) have similar values in both the very small (e.g., $T_{cool} = 0.01$) and very large (e.g., $T_{cool} = 100$) T_{cool} cases. However, the torque there is much higher than the AMF at T_{cool}= 0.1, 1 and 10. This indicates that, for intermediate cooling cases, the waves fail to launch or are damped right after they are launched, indicating radiative cooling is important for these cases. Note that

the normalization (characteristic value, F_{J0}) should have varied with different cooling times, since $F_{J0} \propto h_p^{-3}$. In adiabatic EoS, the sound speed, $c_s = \left(\gamma \frac{dp}{d\rho}\right)^{1/2}$ and the scale height $h \propto c_s \propto \gamma^{1/2}$. Thus, $F_J \propto \gamma^{-3/2}$. The effective normalization is 0.6 times the F_{J0} in Equation 5.6 at the slow cooling limit when $\gamma = 1.4$. This value should be in between 1 and 0.6 in transition from small to large T_{cool}. Nevertheless, we just use F_{J0} as Equation 5.6 and compare the absolute values of the AMF. We will have more detailed discussions in Section 5.6.1.

5.5.3 Disks with Both Self-Gravity and Radiative Cooling

We also explore a situation that both self-gravity and radiative cooling are included, even though we do not seek to carry out a parameter space study. The parameters we choose are $Q = 5$, `B17ADSG` disks with various T_{cool}. The density perturbations at two radii are shown in Figure 5.10's right panels. The profiles of the spirals are very similar to the non-selfgravitating ones on the left panels. All the trends found in Section 5.5.2 still apply. At the same cooling time, the perturbation amplitudes become stronger and the spirals become tighter if Q becomes smaller, which are consistent with the results in Section 5.5.1. This means that when both of these two physical processes (disk self-gravity and radiative cooling) are operating, they play similar roles as those that they play individually, at least for low mass planets. From the magnitudes of the changes due to these two processes, we can conclude that when the disk is not too massive ($Q \gtrsim 5$), the effects of the self-gravity on the disks are less important than those of the cooling.

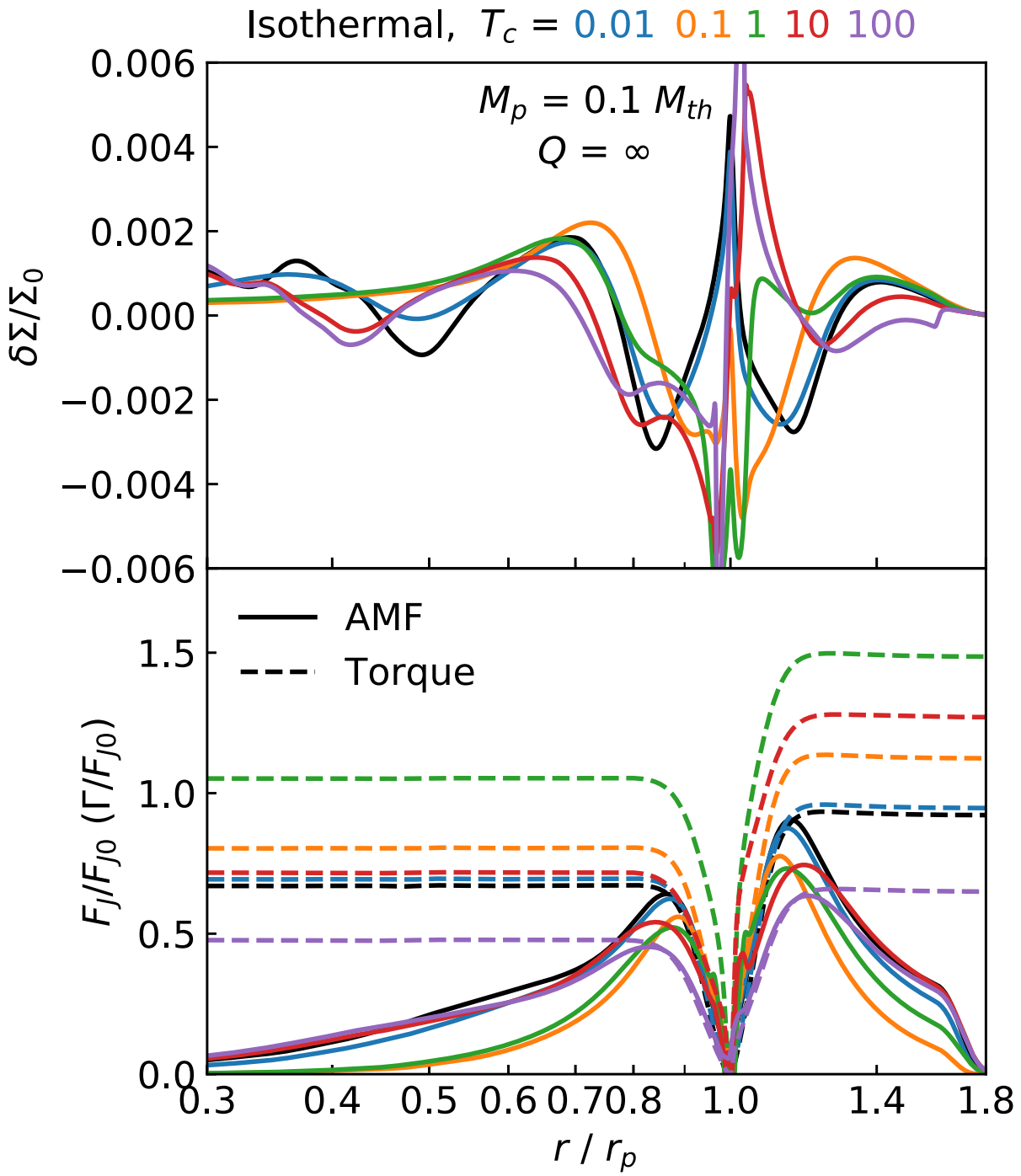

Figure 5.11: Top Panel: The azimuthally averaged density perturbations in Figure 5.9, upper panels. Bottom Panel: The normalized AMF (solid curves) and torque (dashed curves) for different cooling times, T_{cool}. The black curves represent isothermal disk, whereas blue, orange, green, red and purple curves represent adiabatic disks with T_{cool} = 0.01, 0.1, 1, 10 and 100, respectively. The changes of the AMF distribution should be responsible for the change of the density perturbations.

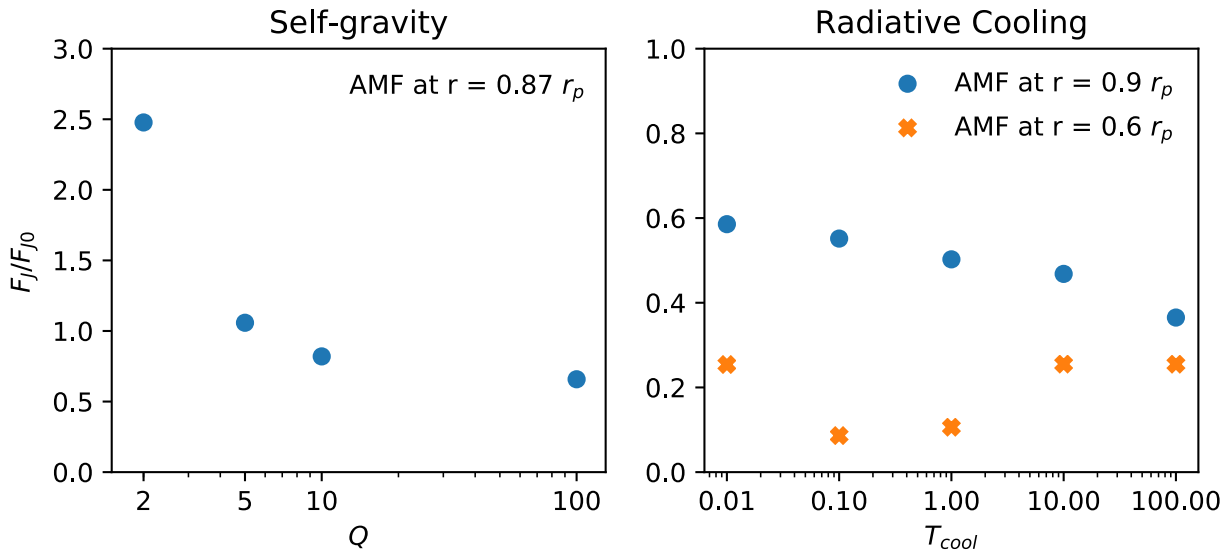

Figure 5.12: AMF vs. Q (left) and AMF vs. T_{cool} (right). The AMF is measured at $r = 0.87\ r_p$ for the `SG` runs and at $r = 0.6\ r_p$ (marked as "X"s) and $0.9\ r_p$ (marked as dots) for the `AD` runs.

5.6 Discussion

5.6.1 AMF vs. Q and T_{cool}

To quantify the relationships between AMF vs. Q and AMF vs. T_{cool}, we measure the AMF at given positions in Figure 5.7 and Figure 5.11 for `B17SG` and `B17AD` disks with $M_p = 0.1\ M_{th}$. We plot the AMF as a function of Q (the left panel) and T_{cool} (the right panel) in Figure 5.12. The AMF is measured at $0.87\ r_p$ for `B17SG` simulations, where it reaches the maximum at the inner disk. The AMF increases as the disk becomes more massive (with a smaller Q). This increase becomes quite fast when Q is approaching 2. The advective AMF in the $Q = 2$ simulation is almost 5 times the AMF in the $Q = 100$ simulation, which is roughly consistent with the analytical expectation (Equation 5.26).

As for the radiative cooling, we measure the AMF at $0.9\ r_p$ and $0.6\ r_p$. At the position very close to the planet (e.g., $0.9\ r_p$), the AMF decreases as the cooling time increases. As mentioned

in Section 5.5.2, this is most likely due to the transition of the effective γ (that enters the sound speed) from 1 to 1.4. The ratio between the AMF at $T_{cool} = 100$ and that at $T_{cool} = 0.01$ is ~ 0.6, which is very close to the expected change due to our definition of F_{J0}. However, if the AMF is measured farther away from the planet (e.g., 0.6 r_p), it first decreases and then increases as T_{cool} increases, reaching the minima at 0.1 and 1 T_{cool}. The decrease of the AMF with the distance away the planet is due to the wave damping as the wave propagates. When the wave propagates to 0.6 r_p, the damping is the strongest at $T_{cool} \sim 0.1 - 1$, implying that radiative cooling plays an important role on the wave damping/dissipation when $T_{cool} \lesssim 1$. We are expecting a stronger wave damping with a smaller T_{cool}. However, when T_{cool} becomes very small and approaches the isothermal limit, the temperature of the wave becomes the background disk temperature, and shock damping in this case behaves similar to the shock damping in the adiabatic limit (Goodman & Rafikov 2001; Dong et al. 2011a). At the position that the secondary spiral should form, the wave becomes already too weak to perturb the gas for the $T_{cool} = 0.1 - 1$ cases. Thus, the secondary gap can even disappear at these intermediate cooling times.

5.6.2 Implications for Observations

To quantify the properties of the primary gap, we measure the gap width and depth in the gas density perturbation maps for `B17SG` and `B17AD`, M_p = 0.1 M_{th}, using the definitions in Zhang et al. (2018b). Different from Zhang et al. (2018b), we only measure the gaps at $\sim$ 50 orbits and from the gas density perturbation profiles, because we do not run the simulations for very long time and the planet mass is still too small to open significant gaps in gas and dust. However, these measurements suffice to demonstrate the trend.

In the upper panels of Figure 5.13, the gap width - Q relation is shown on the left panel, whereas the depth - Q relation is shown on the right panel. Both the x and y axes are in logarithmic scales. Since the exponents in the gap depth relations are ~ 5 times larger than that of gap width relations (see Table 1 and 2 in Zhang et al. 2018b for details), the plotted y-axis range for the depth ($\delta - 1$) is 5 times of the range for the width (Δ). In this way the relative magnitude read on both y-axes is roughly proportional to the planet mass ratio. As Q changes to lower values, the gap depth has more significant changes than the width. The planet mass inferred from the gap depth without considering disk self-gravity will be overestimated. Adopting common exponents 0.25 and 1.25 for the width-M_p and depth-M_p relations (more precisely, width-K' and depth-K in Zhang et al. 2018b), the ratio of the inferred masses between $Q = 2$ and $Q = 100$ disks is 1.5 using the width-M_p relation, and 6 using the depth-M_p relation. Thus, if one wants to infer the planet mass, the gap width is a better observable than the gap depth since it is less sensitive to the disk mass.

The lower panels of Figure 5.13 show the width and depth as functions of the T_{cool}. The gap width and depth are not very well defined due to the irregular gap shape. We try to neglect the horseshoe region around r_p when we measure the gap width. It is better to use the gap depth as a proxy for the planet mass. If one uses the gap width to measure the planet mass in locally isothermal simulations, the planet mass will be underestimated if $T_{cool} \gtrsim 0.01$.

Note that these trends found in the low planet mass regime do not necessarily apply to the high planet mass regime, as we will discuss in the next subsection, where we find much less change in the gap shape for various cooling times.

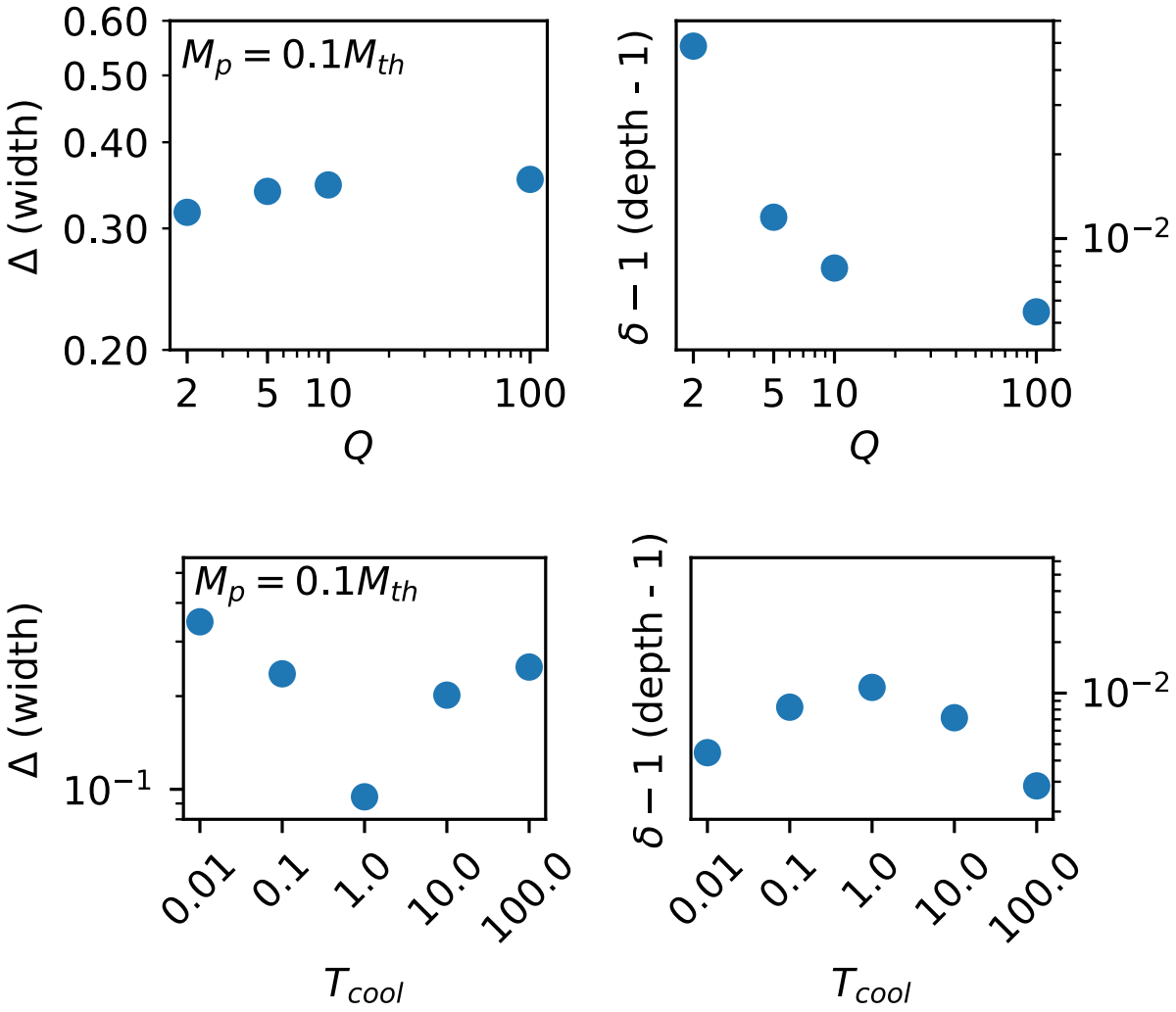

Figure 5.13: Gap width/depth vs. Q (top) and Gap width/depth vs. T_{cool} (bottom). Δ and δ - 1 are proportional to M_p. The range for the gap (depth - 1) is 5 times than that in the width. Under this factor, the y-axes on the left and right panels have approximately the same scaling to M_p. Thus, the y-axes of the left and right panels can be directly taken as the planet mass in an arbitrary unit.

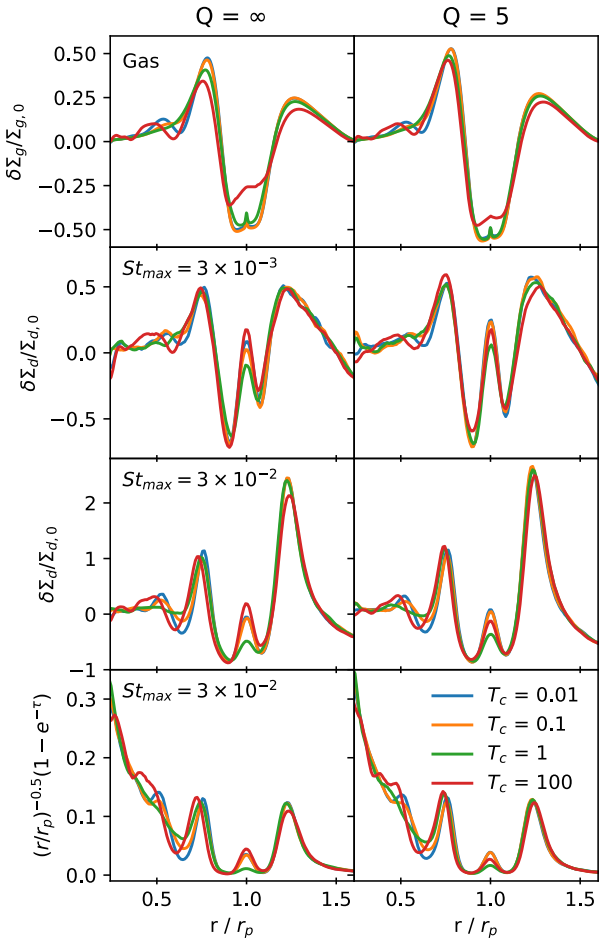

Figure 5.14: Azimuthally averaged density perturbations and brightness temperature of `AS209AD` and `AS209ADSG` at 400 t_p. From top to bottom, they are the density perturbations of the gas, dusts with $St_{max} = 3 \times 10^{-3}$ and $St_{max} = 3 \times 10^{-2}$. The bottom panels show the brightness temperature of the $St_{max} = 3 \times 10^{-2}$ ($a_{max} = 0.5$ mm) dust models. The left panels show the cases without self-gravity, whereas the right panels show the cases with $Q = 5$. Blue, orange, green and red curves represent T_{cool} = 0.01, 0.1, 1 and 100, respectively. The $T_{cool} = 0.01$ curves on the left panels are almost identical to the locally isothermal cases in Zhang et al. (2018b) (the slight difference is mainly due to the different setups in resolution, temperature profile, indirect term and smoothing length).

5.6.3 AS 209: Cooling in the High Planet Mass Regime

We have two goals in this subsection. One is to explore the effects of radiative cooling on the gap properties when the planet mass is relatively large reaching the thermal mass. Meanwhile, we decide to choose a model that resembles a realistic disk so that we are able to constrain its surface density via estimating its T_{cool}. Of all the DSHARP disks, AS 209 features many intricate gaps and rings (Guzmán et al. 2018). Using simple (without radiative cooling and self-gravity) hydrodynamical simulations, Zhang et al. (2018b) find an excellent match to the AS 209 disk with a model whose $(h/r)_p = 0.05$, $\alpha = 3 \times 10^{-4}(r/r_p)^2$ and $M_p/M_* = 10^{-4}$, or 1 M_{th}[3]. The dust size distribution is a power law $n(a) \propto a^{-3.5}$, a_{max} = 0.68 mm, and the gas surface density $\Sigma_{g,0} = 6.4$ g cm^{-1}. This model can explain up to five gaps in the disk, not only their locations, but also the intensity. Since we have found that self-gravity and radiative cooling have the potential to change the gap shape and the secondary gap position in the low planet mass regime, we would like to explore how the planet mass for AS 209 will change considering these two physical processes.

Figure 5.14 shows the azimuthally averaged density perturbation and brightness temperature of the `AS209` models with different cooling times (T_{cool} = 0.01, 0.1, 1 and 100) and different disk masses ($Q = \infty$ and 5) at 400 t_p. We choose not to show T_{cool} = 10 case to avoid crowdedness of the figure, but its feature is similar to the T_{cool} = 100 case with shallower gaps in dust. The left panels show the $Q = \infty$ cases, whereas the right panels show the $Q = 5$ cases. Blue, orange, green and red curves represent T_{cool} = 0.01, 1, 10, and 100 cases, respectively. From the top to bottom panels, it shows the density perturbations of the gas, the dust with $St_{max} = 3 \times 10^{-3}$, $St_{max} = 3 \times 10^{-2}$, and

[3]We also run simulations with constant α as the model (b) in Zhang et al. (2018b). Same as previous models, they reproduce AS 209's 1D profile, but are non-axisymmetric in 2D. We do not see more differences due to the viscosity profile.

the brightness temperature of the $St_{max} = 3 \times 10^{-2}$ models. We assume that the temperature in the disk is proportional to $r^{-0.5}$ in the last row and the procedure to obtain the optical depth is detailed in Zhang et al. (2018b). As the T_{cool} becomes larger, the perturbation at the major gap (where the planet locates) becomes shallower in gas. However, this is not the case in dust. The gap width and depth are almost the same across different cooling times. This result is different from that in the low planet mass regime, where the gap shapes are quite different across different cooling times. For dust profiles, the horseshoe region has the smallest density for T_{cool} = 1. The secondary gap disappears for $T_{cool} = 1$ in gas, but it is still noticeable in dust for $St_{max} = 3 \times 10^{-2}$, with a lower amplitude than T_{cool} = 0.01, 0.1, and 100 cases. This indicates that, due to the gaseous bump at the inner edge of the primary gap, dust particles can still be trapped there, forming the secondary gap in dust even if the secondary gap disappears in the $T_{cool} = 1$ case. The location of the secondary gap shifts from $\sim 0.65\ r_p$ to $\sim 0.6\ r_p$ when T_{cool} increases. The tertiary gap is also present in $T_{cool} = 0.01$ and 100 cases. It moves inwards from $\sim 0.43\ r_p$ to $\sim 0.37\ r_p$. Although the tertiary gap is not present in the $T_{cool} = 1$ case, a change of slope can been seen at $\sim 0.4\ r_p$ (this is more obvious in $Q = 5$ case). The $Q = 5$ disks are similar to the $Q = \infty$ disks but with slightly stronger perturbations. The differences between different T_{cool} curves are slightly smaller in $Q = 5$ disks than those in $Q = \infty$ disks.

Note that aside from the EoS, the simulation setups in this subsection are different from those in Zhang et al. (2018b) in several aspects (e.g., the resolution, domain size, temperature profile, indrect term, smoothing length, and planet growing time). Thus, the gap shape and position are expected to be slightly different from the simulations in Zhang et al. (2018b). Also, as time evolves, the position of the secondary and tertiary gaps will move slightly inwards. Thus, we do not try to compare these profiles with AS 209 observations. Instead, we use this example to demonstrate the

observable differences due to different cooling times.

We also want to emphasize that without the self-gravity, the location of the planet and the gaseous surface density from the simulation can be scaled to any value. However, when the disk self-gravity is included, the gas density and the location of the planet are related. The relation is $\Sigma_{g,0} = (M_*/r_p^2)(h/r)_p/(\pi Q_p)$. Taking M_* = 0.83 $M_\odot$, $r_p = 99$ au, $Q_p = 5$ and $(h/r)_p = 0.05$, we get $\Sigma_{g,0}$ = 2.4 g cm^{-2}. In Zhang et al. (2018b), the best fit model has $Q \approx 2$ at the planet's position in the initial condition.

Assuming the gaps at 24 au, 35 au, and 61 au in AS 209 are related to the planet at 99 au, we can use these gaps to constrain the AS 209 disk mass. Using Equation 5.39, and adopting the stellar luminosity as 1.4 $L_\odot$ and the mass as 0.87 $M_\odot$ from Andrews et al. (2018a), $\phi = 0.02$, $T_f = 20$ K, and $\kappa_R = 0.21$ cm^{2}g^{-1}, we have

$$T_{cool} = 0.02\left[1+0.01\left(\frac{\Sigma}{1\text{ g cm}^{-2}}\right)^2\right]\begin{cases} 2.5 & r \leq 46\text{ au} \\ \left(\frac{r}{99\text{ au}}\right)^{-3/2} & r > 46\text{ au} \end{cases}. \tag{5.43}$$

To produce an observable tertiary gap, we need low or high cooling times ($T_{cool} \lesssim 0.1$ or $T_{cool} \gtrsim 10$). However, $T_{cool} \gtrsim 10$ requires $\Sigma \gtrsim 200$ g cm^{-2}, which is impossible since Q would be $\ll 1$. If $T_{cool} \lesssim 0.1$, we can constrain $\Sigma \lesssim 20$ g cm^{-2}. While it is an independent constraint, this does not give tighter constraint on the density for this disk, since from gravitational instability criterion (Equation 5.8), the disk will become unstable if $\Sigma_{g,0} > 12$ g cm^{-2} at 99 au. Nevertheless, this constraint from the disk cooling is consistent with that from the disk instability.

The Q = 5 models with low T_{cool} might be plausible models for the AS 209 disk, since their density at 99 au is allowed given the constraints derived above. However, with the density $\Sigma_{g,0}$

= 2.4 g cm^{-2} from the $Q = 5$ disk, we cannot restore the intensity measured from the DSHARP observation. It is much lower than that from the observation. Only $\Sigma_{g,0} \gtrsim 6$ g cm^{-2} can explain the intensity. This means that either the actual opacity is higher than what we adopt (e.g., the dust-to-gas mass ratio is larger) or the disk has even lower Q. If the latter is true, the T_{cool} can be larger (but still < 1), since the low Q that is close to unity can produce much stronger perturbations, compensating for the weaker perturbations due to the larger value of the T_{cool}. Interestingly, Powell et al. (2019) estimate the gas surface density $\Sigma \approx 10$ g cm^{-2} at 100 au, using the "dust line" method. This high surface density is actually compatible and consistent with the constraints from disk self-gravity and radiative cooling for the AS 209 disk. If this is the case, it indicates that the outer disk of the AS 209 disk is marginally gravitational stable.

5.6.4 Long Time Evolution for Self-Gravitating Disks with Planets

On the other hand, in our long timescale simulations, we find that the self-gravitating disks with planets tend to become unstable at later times. This happens earlier if the Q is small or if the planet mass is high. Figure 5.15 shows the density perturbations of `B17SG` disks when M_p = 0.3 and 1.0 M_{th} (top and bottom) at $t = 100\ t_p$. $Q = 2$ disks have become unstable at this point. This is why low Q and high M_p curves are missing in Figure 5.8. The disk would become more stable if the radiative cooling is included. For instance, the `AS209ADSG` simulations discussed in Section 5.6.3 can evolve for very long time without any sign of instability even though their $Q = 5$ and $M_p = 1\ M_{th}$. Another interesting behavior in the lower panels is that as the disk becomes more massive, the number of vortices at the gap edge becomes larger. This is consistent with the simulation results in Lin (2012); Zhu & Baruteau (2016), as self-gravity can suppress large-scale

(small m) vortices produced by Rossby wave instability (Lovelace et al. 1999).

5.7 Conclusions

We run two dimensional hydrodynamical simulations to explore the effects of self-gravity and radiative cooling on the gap and spiral formation in protoplanetary disks. We explore these effects with different Toomre Q parameters and the dimensionless cooling times T_{cool} for low mass planets. As the disk becomes more massive (smaller Q), we find:

- The spirals become slightly more tightly-wound, especially when $Q \sim 2$, which is consistent with the linear theory.
- The spirals become stronger and the primary and secondary gaps become deeper. This is due to the higher AMF in more massive disks, which is consistent with the linear theory. The advective AMF in the $Q = 2$ disk is almost 5 times the AMF in the $Q = 100$ disk.
- If $Q \gtrsim 2$, the secondary gap's position does not change, despite gaps being deeper.

In disks with radiative cooling, we find:

- Even with a relatively short $T_{cool} = 0.01$, the spiral waves cannot pick up AMF from the background disk when they are propagating to hotter regions, different from locally isothermal disks.
- The spirals become less tightly-wound (more open) as the cooling time increases, due to the increase of the disk's effective sound speed. The spiral's openness changes dramatically from disks with $T_{cool} = 0.1$ to $T_{cool} = 1$.

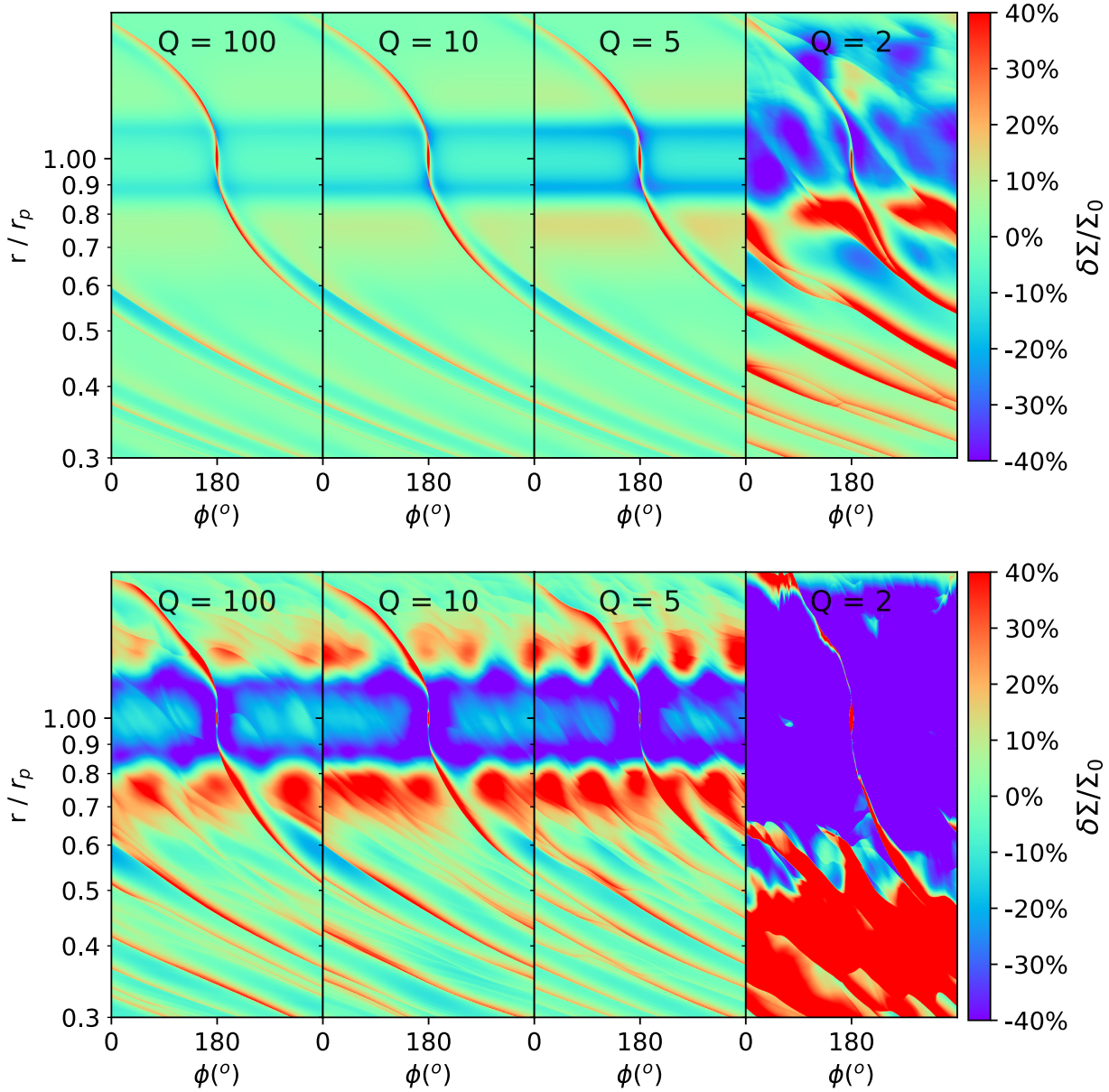

Figure 5.15: The density perturbations of `B17SG` disks with $M_p = 0.3$ and $1.0\ M_{th}$ (top and bottom) at $t = 100\ t_p$. The disk becomes unstable at $Q = 2$. The lower panel shows that self-gravity can suppress small m vortices, so that the number of the vortices increases as Q becomes smaller.

- The spirals become weaker as the cooling time increases from a small value to $1/\Omega$, and then start to become stronger as the cooling time increases. There is a significant change of the spiral's amplitude when T_{cool} increases from $\lesssim 0.01$ to 0.1.

- The AMF of the wave dissipates the fastest during its propagation when $T_{cool} \sim 0.1$ to 1, implying that radiative damping may be important.

- With weaker spirals, the secondary gaps due to low mass planets disappear when $T_{cool} = 0.1$ to 1.

- If the secondary gap is present, its position moves from $\sim 0.5\ r_p$ to $\sim 0.4\ r_p$ in a disk with $(h/r)_p = 0.07$ in transition from the isothermal limit to the adiabaitc limit.

- For $Q \gtrsim 5$ disks, the effect of radiative cooling is more critical than self-gravity.

Our simulations also have implications for the observations. We have run planet-disk simulations with massive planets ($\sim$ thermal mass):

- One might overestimate the planet mass using the simulation that neglects self-gravity. The gap width is less sensitive to the disk self-gravity than the gap depth. Thus, it is better to constrain the planet mass using the gap width when disk self-gravity is important.

- One might underestimate the planet mass using the simulation that neglects the radiative cooling. This is especially the case when $T_{cool} \sim 1$.

- For deep primary gaps in the high planet mass regime, their shapes are less affected by the cooling time, but the secondary gap's position and depth for the gas depend on the cooling time. On the other hand, the secondary gap in dust or brightness temperature is less sensitive

to the cooling time since dust drift fast to the primary gap edge forming secondary gaps. The tertiary gap becomes unnoticeable in both gas and dust when $T_{cool} = 1$.

- The dependence of the gap properties (e.g., gap depth, width, and secondary/tertiary gap's position and depth) on the cooling timescale provides a new way to constrain the gaseous disk surface density.

- Assuming the gaps at 24 au, 35 au, and 61 au in AS 209 are all associated with the planet at 99 au, the gas surface density at $\sim$100 au in AS 209 should be $\lesssim 20$ g cm^{-2} using the $T_{cool} \lesssim 0.1$ cooling constraints, which is consistent with the surface density constraint from $Q \gtrsim 1$.

CHAPTER 6 Self-Consistent Ring Model in Protoplanetary Disks: Temperature Dips and Substructure Formation

Shangjia Zhang,[1,2], Xiao Hu,[1,3], Zhaohuan Zhu,[1,2], and Jaehan Bae[4]

[1]Department of Physics and Astronomy, University of Nevada, Las Vegas, 4505 S. Maryland Pkwy, Las Vegas, NV, 89154, USA

[2]Nevada Center for Astrophysics, University of Nevada, Las Vegas, Las Vegas, NV 89154, USA

[3]Department of Astronomy, University of Virginia, 530 McCormick Road, Charlottesville, VA 22904, USA

[4]Earth and Planets Laboratory, Carnegie Institution for Science, 5241 Broad Branch Road NW, Washington, DC 20015, USA

6.1 Abstract

Rings and gaps are ubiquitous in protoplanetary disks. Larger dust grains will concentrate in gaseous rings more compactly due to stronger aerodynamic drag. However, the effects of dust concentration on the ring's thermal structure have not been explored. Using MCRT simulations, we self-consistently construct ring models by iterating the ring's thermal structure, hydrostatic equilibrium, and dust concentration. We set up rings with two dust populations having different settling and radial concentration due to their different sizes. We find two mechanisms that can lead to temperature dips around the ring. When the disk is optically thick, the temperature drops outside the ring, which is the shadowing effect found in previous works adopting a single-dust population

in the disk. When the disk is optically thin, a second mechanism due to excess cooling of big grains is found. Big grains cool more efficiently, which leads to a moderate temperature dip within the ring where big dust resides. This dip is close to the center of the ring. Such temperature dip within the ring can lead to particle pile-up outside the ring and feedback to the dust distribution and thermal structure. We couple the MCRT calculations with a 1D dust evolution model and show that the ring evolves to a different shape and may even separate to several rings. Overall, dust concentration within rings has moderate effects on the disk's thermal structure, and self-consistent model is crucial not only for protoplanetary disk observations but also for planetesimal and planet formation studies.

6.2 Introduction

Recent high angular resolution observations of protoplanetary disks have revealed many substructures. Andrews (2020) summarizes them into four categories: *rings/cavity* (which are "transition" disks with bright rings and depleted cavities, e.g., LkCa 15, J1610 Facchini et al. 2020, GM Aur Huang et al. 2020a, PDS 70 Keppler et al. 2019), *rings/gaps* (which are concentric, axisymmetric patterns of enhancing and depleting intensity, e.g., HL Tau ALMA Partnership et al. 2015a, TW Hya Andrews et al. 2012, RU Lup Andrews et al. 2018a, AS 209 Guzmán et al. 2018), *arcs* (which are non-axisymmetric substructures with a partial ring extending only a certain azimuthal angle, e.g., MWC 758 Dong et al. 2018e, HD 163296 Isella et al. 2018) and *spirals* (ranging from m=2 to asymmetrical spirals, e.g., IM Lup, Elias 27 Huang et al. 2018d). Among them, the first two kinds are observed most frequently. We call them *rings* hereafter.

Dozens of ring forming mechanisms have been proposed, including tidal interaction between

the planet and the disk (Lin & Papaloizou 1979; Goldreich & Tremaine 1980), disk dispersal with MHD-driven winds (Takahashi & Muto 2018) or photoevaprative flows (Ercolano & Pascucci 2017), zonal flows (Johansen et al. 2009a) in MHD disks, mass pile up at the boundary between magnetically active and dead zones (Flock et al. 2015), spontaneous ring formation due to reducing accretion by concentrated dust (Dullemond & Penzlin 2018; Hu et al. 2019), and condensation fronts at icelines (Zhang et al. 2015a).

All these mechanisms except icelines generate gaseous pressure bumps which trap dust grains. Intermediate-sized particles with Stokes number of about unity drift fastest responding to gaseous bumps. Small grains (St $\ll$ 1) are well-coupled to the gas, whereas very big grains (St $\gg$ 1) are fully decoupled. Under the protoplanetary disk condition at 100 au, cm particles have the most significant concentration within the gaseous bumps. There are indeed some tentative results from multi-wavelengths observations which indicate that grains are larger (towards cm size) at the ring and smaller (towards mm size) in the gap (Macías et al. 2019; Carrasco-González et al. 2019a; Huang et al. 2020a; Long et al. 2020b).

Different sized grains have different concentration on the vertical direction too. Very small grains ($<1\mu$m) have similar scale height as that of the gas, and are best probed by near-infrared scattered light observations. Bigger grains are settled to the midplane, and probed by (sub)mm/cm radio observations. The vertical extent of the settled grains depends on the strength of turbulence in the disk. The vertical settling of the grains is balanced by the turbulent diffusion that stirs up these grains (Youdin & Lithwick 2007). Stronger turbulence leads to thicker dusty layers. This vertical dust diffusion applies to the whole disk and also to rings.

These effects of dust concentration should also affect ring's thermal structure, since dust opacity is the primary source of opacity in the disk. The disk is heated by stellar radiation and viscous

heating, and cooled predominantly by dust thermal emission. The disk temperature is set when heating balances cooling. Studying disk temperature self-consistently is important for interpreting observations (e.g., the decrease of temperature in shadow can be misinterpreted as density depletion, Isella & Turner 2018), and understanding disk dynamics including the Vertical Shear Instability (Nelson et al. 2013a) and baroclinic instability (Klahr & Bodenheimer 2003). Furthermore, the temperature structure determines the radial pressure gradient (dP/dr) which directly affects dust trapping itself. This means that the thermal structure and dust concentration could have a feedback loop on each other: dust concentration changing the temperature structure while the temperature structure affecting the dust consternation. It is unclear if such feedback loop can result in a stable or unstable disk configuration. Thus, it is essential to consider dust distribution and disk thermal structure self-consistently.

In this work, we construct self-consistent models of rings by using two dust species with different density distributions. We iterate the ring's thermal structure, hydrostatic equilibrium and dust concentration with MCRT calculations. In Section 6.3, we use a toy model to demonstrate that the varying opacity in the ring can lead to moderate temperature variation, in addition to the previously studied shadowing effect. In Section 6.4, we present our setup for the systematic study of the shadowing and the opacity effects, using one and two populations of dust grains. In Section 6.5, we couple MCRT with a 1D dust evolution model, and demonstrate that the feedback loop can change the shape of the initial ring. In Section 8.5, we propose that the temperature gap in a recent observation can be more naturally explained by the opacity effect. We also discuss some other observational perspectives there. We conclude our work in Section 7.8.

6.3 A Toy Model for Excess Cooling

Due to dust trapping by a pressure bump, the dust inside and outside a gaseous ring have different size distributions, which leads to different opacities inside and outside the ring. Since the opacity affects the disk temperature (e.g., Calvet et al. 1991), it is very likely that the temperatures inside and outside the ring are different.

For an optically thin disk region which has only absorption opacity (κ_ν^{abs}), the heating Q_+ comes from the stellar irradiation at all wavelengths,

$$Q_+ = \int_0^\infty \kappa_{\rm abs} F_\nu^* d\nu. \tag{6.1}$$

If we assume that the star radiates as a black body, we have

$$F_\nu^* = \frac{4\pi R_*^2 \pi B_\nu(T_*)}{4\pi r^2}, \tag{6.2}$$

where R_* is the stellar radius and T_* is the stellar effective temperature.

The disk cools by its own radiation at the disk temperature (T_d) which is much lower than the stellar temperature. The cooling term is

$$Q_- = 4\pi \int_0^\infty \kappa_{\rm abs} B_\nu(T_d) d\nu. \tag{6.3}$$

When the disk is in thermal equilibrium, $Q_+ = Q_-$.

If we use the Planck mean opacity

$$\kappa_P^{abs}(T) \equiv \frac{\int_0^\infty \kappa_{\rm abs} B_\nu(T) d\nu}{\int_0^\infty B_\nu(T) d\nu}, \tag{6.4}$$

we can derive the disk temperature using $Q_+ = Q_-$ and express the disk temperature as

$$T_d = \left(\frac{R_*}{2r}\right)^{\frac{1}{2}} \frac{1}{\varepsilon^{1/4}} T_*, \tag{6.5}$$

where r is the distance to the star and

$$\varepsilon \equiv \frac{\kappa_P(T_d)}{\kappa_P(T_*)}, \tag{6.6}$$

is the thermal cooling coefficient. For the gray opacity whose κ_ν^{abs} is a constant with ν, ε is unity. This ε parameter is essential for determining the disk's vertical structure (Calvet et al. 1991; Chiang & Goldreich 1997). Considering that $B_\nu(T_d)$ peaks at mm wavelengths, we can approximate $\kappa_P(T_d)$ using the monochromatic opacity at 1 mm, $\kappa(\lambda = 1mm)$. For the same reason, we have $\kappa_P(T_*) \approx \kappa(\lambda = 1\mu m)$. Thus, we have $\varepsilon \approx \kappa(\lambda = 1\text{mm})/\kappa(\lambda = 1\mu\text{m})$.

For very big grains, the opacity is mostly gray, so $\varepsilon \approx 1$. For small grains, the opacity at μm is larger than the opacity at mm wavelengths, so $\varepsilon < 1$. Hence, the equilibrium temperature for the disk with mainly small grains is higher than the temperature for the disk mainly with big grains. Compared with small grains, big grains cool more efficiently with respect to the amount of energy they absorbed. Since there are much more big grains inside the ring than outside the ring, the temperature in the ring is expected to be lower.

To demonstrate this effect, we start with a power-law opacity ($\kappa_{\rm abs} \propto \nu^\beta$) in a disk. The disk

temperature can be solved as,

$$T_d = \left(\frac{R_*}{2r}\right)^{\frac{1}{2}\frac{1}{1+\beta/4}} T_*. \tag{6.7}$$

Thus, a disk with smaller grains (having a larger β) is hotter than a disk with bigger grains. When both small and big grains are present in one disk, the disk temperature at one radius will be determined by the dominant dust species at that radius.

We set up a ring and use the MCRT code RADMC-3D to calculate the temperature. For simplicity, we use a low density disk and only consider the absorption opacity. These simplifications highlight the opacity effect. (The more realistic setup will be given in the next section.)

The ring has two different dust species and their radial distributions are shown in Figure 7.1 (a). Both species have Gaussian surface density, and the big grains have larger peak surface density, but less radial and vertical extension due to radial trapping and vertical settling (Dullemond et al. 2018). The opacity for the small and big grains have slopes β = 0 and 1.5, respectively (Figure 7.1 b). The Orange curves in the rightmost panel are the temperatures from a disk which only has small grains, and the green curves are the temperatures from a disk which only has big grains. The temperatures from the MCRT calculations (solid orange and green curves) follow their analytical solutions (dashed lines) closely. The slight deviation of the temperature starting from the ring location indicates that the optically thin assumption is no longer valid. The blue curve is the temperature from a disk where both dust species are considered in the MCRT calculation. It approaches the small-grain-only temperature out of the ring and big-grain-only temperature within the ring (Figure 7.1 c). This is in a good agreement with the expectation that small grains dominate the opacity far away from the ring center while big grains dominate the opacity close to the ring center.

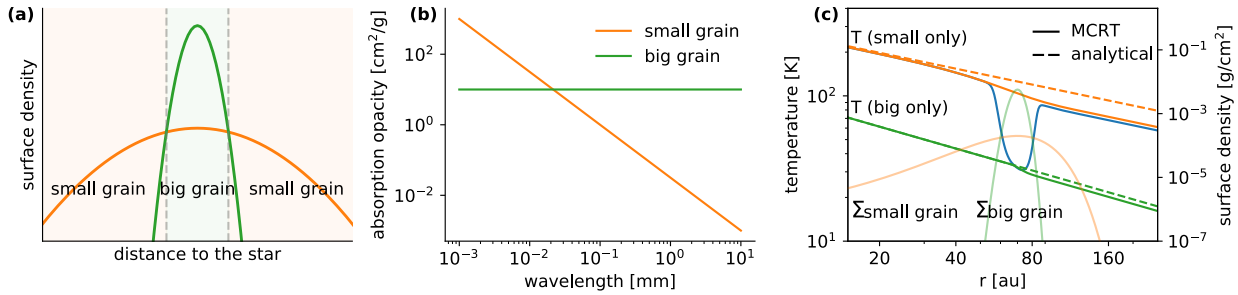

Figure 6.1: (a) The surface density of the toy model. The small (big) grain is represented by the orange (green) curve. The big grain has a narrower width and dominates inside the ring (green), whereas the small grain dominates outside the ring. (b) The absorption-only opacity used for the toy model. The big grain is represented by a constant opacity, whereas the small grain is represented by a opacity $\propto \nu^{1.5}$. (c) The temperature calculations. The orange (green) curves show temperature if the disk only has small (big) grains. The solid lines are calculations from RADMC-3D MCRT, and the dashed lines are analytical solution assuming optical thin. The small grain has a higher equilibrium temperature at the outer disk. The MCRT result when including both species is represented by the blue curve. The temperature approaches the small grain's outside the ring and approaches the big grain's inside the ring. Their respective surface density profiles are marked in transparent colors.

In the optically thin limit, the ratio between the temperature inside and outside the ring is the ratio between big-grain-only and small-grain-only equilibrium temperature, T_{big}/T_{small}. This ratio is $(\varepsilon_{small}/\varepsilon_{big})^{1/4}$ and can be calculated using Equation 6.6. We use single-sized DSHARP opacity (Birnstiel et al. 2018) and plot the temperature ratio for various pairs of small and big grains in Figure 6.2. Different disk temperatures have been explored. The ratio is smaller for a lower disk temperature (i.e., outer disk), since these parts of the disk emit at longer wavelengths leading to smaller ε_{small}. For disk temperature at 20 K, the ratio can be as low as 25% if the big grain is around hundreds of μm and the small grain is around 0.1 μm, which can be a realistic situation in protoplanetary disks. In a hotter disk (e.g., at the inner disk), the ratio can be as low as 50%. On the anti-diagonal lines, the ratio is unity when the big and small grains have the same size. To validate these analytical estimates, we calculate a smooth disk temperature using RADMC-3D. We adopt single sized opacities, with $a_{small} = 0.1\mu$m and various a_{big}. The temperature ratios measured in

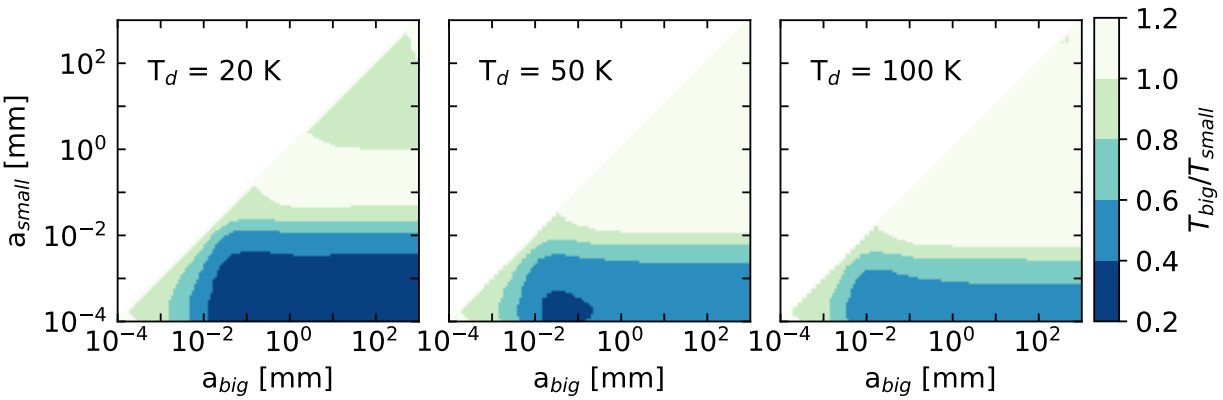

Figure 6.2: The equilibrium temperature ratio between the single-sized big species and the small species calculated using DSHARP opacity. The stellar temperature is 6000 K. From left to right, the disk temperatures T_d are 20, 50 and 100 K.

MCRT at 100 au are dotted in Figure 6.3 along with an analytical curve picked in Figure 6.2 with the T_d = 50 K, where T_{big} and T_{small} are measured from two different single-population simulations at 100 au. The analytical result predicts the Monte Carlo calculation closely.

Even though we only have two single-sized dust populations in Figure 6.2, these contours should still roughly apply to more realistic dust size distributions where the opacity is normally dominated by the biggest dust particles.

6.4 Ring Models

In this section, we explore the temperature structure with ring configurations in more realistic disk configurations. We adopt a more realistic opacity (Section 6.4.1), and iterate the dust and thermal structure of the disk (Section 6.4.2). We consider models with one-population (Section 6.4.3) or two-population (Section 6.4.4) dust species in the disks.

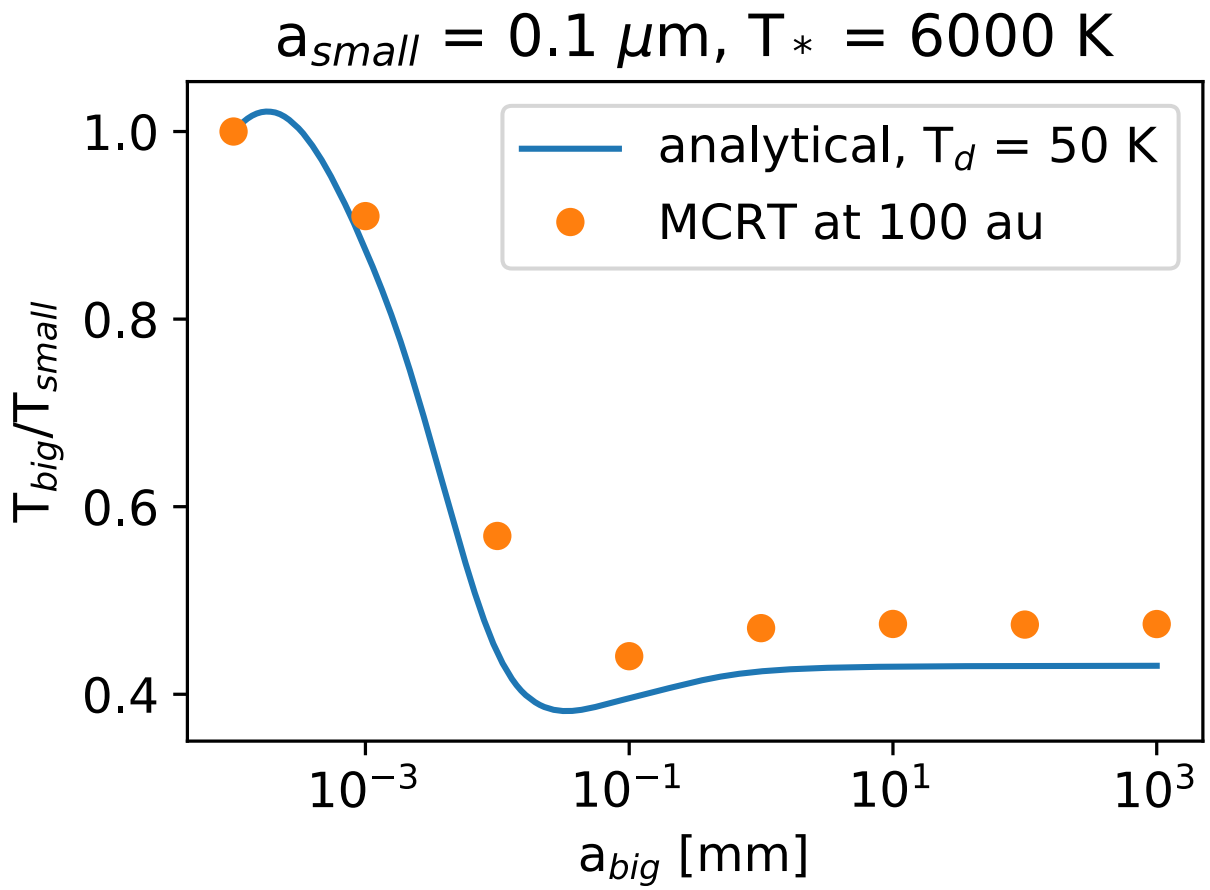

Figure 6.3: Comparison of analytical result in Figure 6.2 with MCRT at 100 au, in the optically thin limit.

6.4.1 Opacity

We assume a power-law dust size distribution with maximum particle size a_{max}, minimum particle size a_{min}, and power index q. The number density of particles follows,

$$n(a) \propto \begin{cases} a^{-q} & \text{for} \, a_{\min} \leq a \leq a_{\max} \\ 0 & \text{else.} \end{cases} \tag{6.8}$$

We fix $q = 3.5$ in this work, so the dust mass is top-heavy and proportional to $a^{0.5}$. The optical constants are taken from the DSHARP opacity in Birnstiel et al. (2018) (see also references therein). The opacity is calculated using the package `dsharp_opac` (Birnstiel 2018). For the one-population models and the small grain population in two-population models, we adopt a_{min} = 0.1 μm. For one-population setups, we use opacities with a_{max} = 1, 10, 100μm, 1mm and 1cm (see the top panel of Figure 6.4). For two-population setups, we use opacities from $\{a_{\rm min,small}$, $a_{\rm max,small}\}$ = $\{0.1\ \mu$m, 1 μm$\}$ to represent small grains and $\{a_{\rm min,big}$, $a_{\rm max,big}\}$ = $\{0.1$ mm, 10 mm$\}$ to represent big grains (see the bottom panel of Figure 6.4).

Note that in two-population models, the opacities used in small grain population and big grain population follow the power-law size distribution with $q = 3.5$, respectively. However, the combination of these two populations has a dust size distribution varying spatially, since the small and big grains have different scale heights and radial widths (see also in Section 6.4.4). In our configuration, we calibrate the surface density ratio between dust (including both populations) and gas as 1:100 only at the Gaussian ring's peak. Likewise, the surface density ratio between two populations only follows a power-law with $q = 3.5$ at the Gaussian ring's peak. This ratio is $(a^{0.5}_{\rm max,big} - a^{0.5}_{\rm min,big})/(a^{0.5}_{\rm max,small} - a^{0.5}_{\rm min,small})$=31.6[1]. Since the small grain population has a larger vertical scale height, the volume density does not follow this ratio even at the ring's peak. The surface density ratio between two populations is smaller than 31.6 away from ring's peak, since the small grain population has larger ring width. The dust to gas mass ratio is less than 1:100 away from the ring's peak.

[1] $a_{\rm max,small}$ used here is 10 μm instead of 1 μm. This gives the small-grain population a larger mass fraction. Otherwise, the ratio is around 132. We adopt the former ratio, but this does not affect results in this paper.

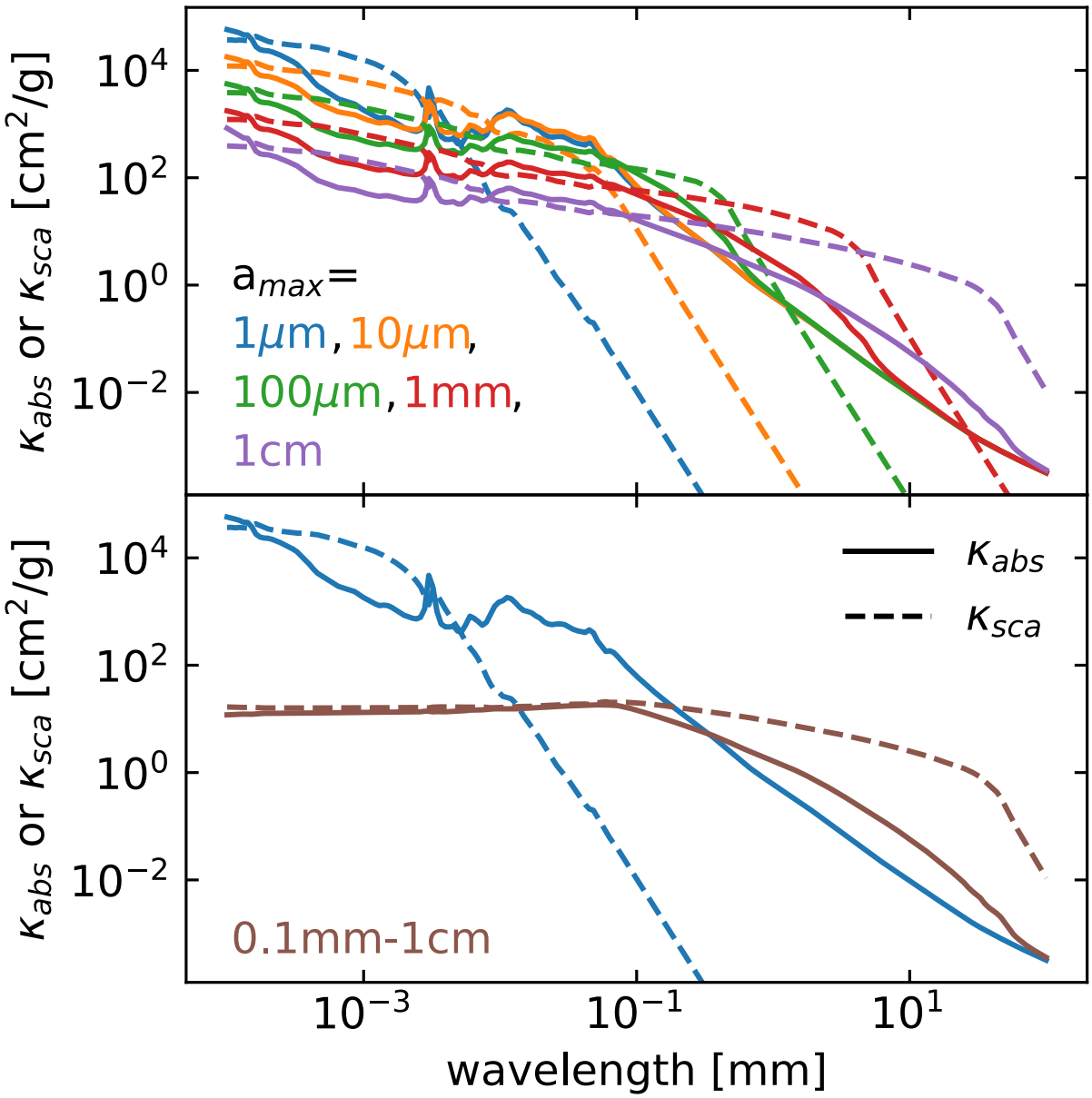

Figure 6.4: Top: The dust opacities used for the disk with a single dust population. Optical constants are from DSHARP (Birnstiel et al. 2018). The minimum grain size is 0.1 μm. At short wavelengths, the opacity decreases as the a_{max} increases. Blue, orange, green, red and purple denote a_{max} = 1 μm, 10 μ 100 μm, 1 mm and 1 cm cases, respectively. Solid curves represent absorption opacities ($\kappa_\nu^{abs,tot}$) and dashed curves represent scattering opacities ($\kappa_\nu^{sca,tot}$). Bottom: The opacities used for disks with two dust populations. The opacities between 0.1mm-1cm are marked in red-brown.

6.4.2 Self-Consistent Thermal Structure

We setup gas densities assuming vertical hydrostatic equilibrium. We distribute the dust based on the dust surface density and vertical scale height (see Section 6.4.3 and 6.4.4). Then, we calculate the temperature using MCRT code RADMC-3D. Initially, the gas, small and big grains are assumed to be at the same temperature. This is the case if small grains are coupled with the gas, and big and small grains reach thermal equilibrium through collisions. The new derived temperature from MCRT will be used to calculate a new vertical hydrostatic equilibrium structure. These processes are iterated until a converged solution has been reached.

In detail, to initialize the MCRT simulations, we assume that the disk is vertically isothermal and assign a Gaussian density profile in the vertical direction. The midplane temperature is set as

$$T_{irr}(r) = \left(\frac{fL_*}{4\pi R^2 \sigma_{SB}}\right)^{1/4}, \tag{6.9}$$

where f accounts for the flaring of the disk, and $f = 0.05$ in our initialization. L_* is the stellar luminosity. We adopt $L_* = 1.05\ L_\odot$ here. σ_{SB} is the Stefan-Boltzmann constant. This temperature is used to calculate the scale height $h = c_s/\Omega_K$ (we adpot $M_* = 1.25\ M_\odot$ for Ω_K). Then, we run RADMC-3D to get the $R-\theta$ temperature distribution for the first iteration. At this point, the new temperature is higher at the disk surface and is not vertically isothermal anymore. Thus, the vertical hydrostatic equilibrium solution needs to be adjusted. We use the hydrostatic equation in the vertical direction to calculate a new density profile,

$$-\frac{GM_* z}{(r^2+z^2)^{3/2}} - \frac{1}{\rho}\frac{\partial P}{\partial z} = 0, \tag{6.10}$$

where G is the gravitational constant, z is the height, ρ is the gas volume density. $P = \rho RT/\mu$ is the gas pressure. R and μ are the gas constant and mean molecular weight (we adopt μ=2.4). The vertically integrated surface density is constrained to be the profile we prescribe. Then we put this new density into RADMC-3D and iterate these steps for several times until the temperature is converged. We use five iterations in all of our models. The detail of temperature iteration can also be found in Bae et al. (2019) Appendix A.

For all runs, we use 10^8 photons and assume isotropic scattering. The calculation is in $R-\theta$ plane with mirroring boundary condition (in one quadrant of the meridian plane). The radial grid is 512 in logarithmic scale and vertical θ grid is 128 from 0 to 24° above the midplane. The inner boundary is 1 au and the outer boundary is 300 au. We assume the star as a point source, since our interests are at the outer disk midplane ($R_* \ll r$) where the size of the star is unimportant. The temperature of the star is 4500 K.

6.4.3 One-Population Models

As a first step and a baseline model for our two-population models, we run ring models with a single dust population. In these cases, the dust size distribution does not vary spatially. Nevertheless, shadowing effect can still affect the midplane temperature distribution. The mechanism can be understood as the following. The stellar radiation is intercepted by a puffed-up region in the disk. This region casts a shadow to the outer disk, so the temperature behind the puffed-up region drops. Since the disk flares, it comes out of the shadow at farther distance, and becomes brighter again. Thus, in the radial direction, the temperature first decreases and then increases. The idea of self-shadowing by a disk inner rim was first introduced to explain the observations of Herbig

Ae/Be stars (Dullemond & Dominik 2004). Later studies focus on the planet gap carved by planets (Jang-Condell & Turner 2012; 2013; Isella & Turner 2018). This effect can lead to a temperature contrast as high as $\sim$ 20%, depending on the planet mass (or the gap's shape). The contrast here refers to the deviation from a smooth temperature profile with a smooth surface density profile.

We carry out a systematic parameter study for the rings. We put a Gaussian ring at 70 au. The ring width σ = 5, 10 and 20 au. The dust surface density at the Gaussian peak Σ_{peak} = 0.02, 0.2 and 2 $\mathrm{g\,cm^{-2}}$. We put a density floor at the outer disk, so that the dust is not completely depleted. The floor density over the peak density $\Sigma_{floor}/\Sigma_{peak}$ = 0.1, 0.01, 10^{-3} and 10^{-4}. The radial profile can be described as the following,

$$\Sigma_d(r) = \begin{cases} \Sigma_{peak}\exp\left(-\frac{(r-70\text{ au})^2}{2\sigma^2}\right) \text{ if } \Sigma_d > \Sigma_{floor}, \\ \Sigma_{floor} \text{ if } \Sigma_d \leq \Sigma_{floor} \text{ and } r > r_{peak}. \end{cases} \tag{6.11}$$

These models are summarized in Table 6.1. We find that for this shadowing effect, the level of density floor matters, since it defines the sharpness of a ring. We will discuss this issue in Section 8.5. Here, we first study the effects from other parameters, using $\Sigma_{floor}/\Sigma_{peak}$ = 0.001. The midplane temperatures of models with different surface density profiles are shown in Figure 6.5. From top to bottom the density increases. The width of the ring decreases from left to right. In all models, the resulting temperature is not a power-law across the ring region. Instead, the temperature dip occurs at the outer edge of the ring. With the same density setup, the temperature profile depends on the opacity. In most of the cases, the temperature dip is stronger when $a_{\max}$ = 1 or 10 μm. The temperature variation respective to a smooth temperature profile can reaches $\sim$25%. These values are roughly consistent with previous works focusing on the temperature

profiles around the planetary gaps (Jang-Condell & Turner 2012; 2013; Isella & Turner 2018). The temperature profile is smoother for a_{max} = 1 cm cases, since grains with larger a_{max} have lower opacity at short wavelengths and higher opacity at long wavelengths. They emit more efficiently thus have lower equilibrium temperatures at the outer disk. These disks are less puffed-up. As the density increases or the ring becomes wider, the temperature becomes lower. This is also because the cooling is more efficient with more dust. A narrow ring also leads to a larger temperature gradient dT/dr.

The shadowing effect happens when the disk is optically thick. As the disk becomes more optically thick, the temperature dip becomes deeper. To quantify this, we calculate the Rosseland mean opacities of different dust size distributions. If the disk temperature T = 20K, the Rosseland mean absorption opacity $\kappa_{R,abs}$ = 9.27, 9.44, 16.8, 20.8, 8.40 $\mathrm{cm^2\,g^{-1}}$ for a_{max} = 1μm, 10μm, 100μm, 1mm and 1cm. τ=1 happens when the dust surface density at the peak $\Sigma_{peak} \approx 0.1\ \mathrm{g\,cm^{-2}}$ for a_{max} = 1μm, 10μm and 1cm and τ=1 happens when $\Sigma_d \approx 0.05\ \mathrm{g\,cm^{-2}}$ for a_{max} = 100μm and 1mm. This is corroborated in Figure 6.5 as the dips are very shallow when $\Sigma_{peak} = 0.02\ \mathrm{g\,cm^{-2}}$ and become much deeper when $\Sigma_{peak} = 0.2\ \mathrm{g\,cm^{-2}}$.

Parameters	Σ_{peak} [$\mathrm{g\,cm^{-2}}$]	σ [au]	$\Sigma_{\mathrm{floor}}/\Sigma_{\mathrm{peak}}$	a_{max}	α
one population	0.02, 0.2, 2	5, 10, 20	10^{-1}, 10^{-2}, 10^{-3}, 10^{-4}	1, 10, 100 μm, 1 mm, 1 cm	–
two population	0.0002, 0.002, 0.02, 0.2	5, 10, 20	10^{-1}, 10^{-2}, 10^{-3}, 10^{-4}	[0.1 μm to 1 μm] and [100 μm to 1 cm]	10^{-2}, 10^{-3}, 10^{-4}

Table 6.1: Model list.

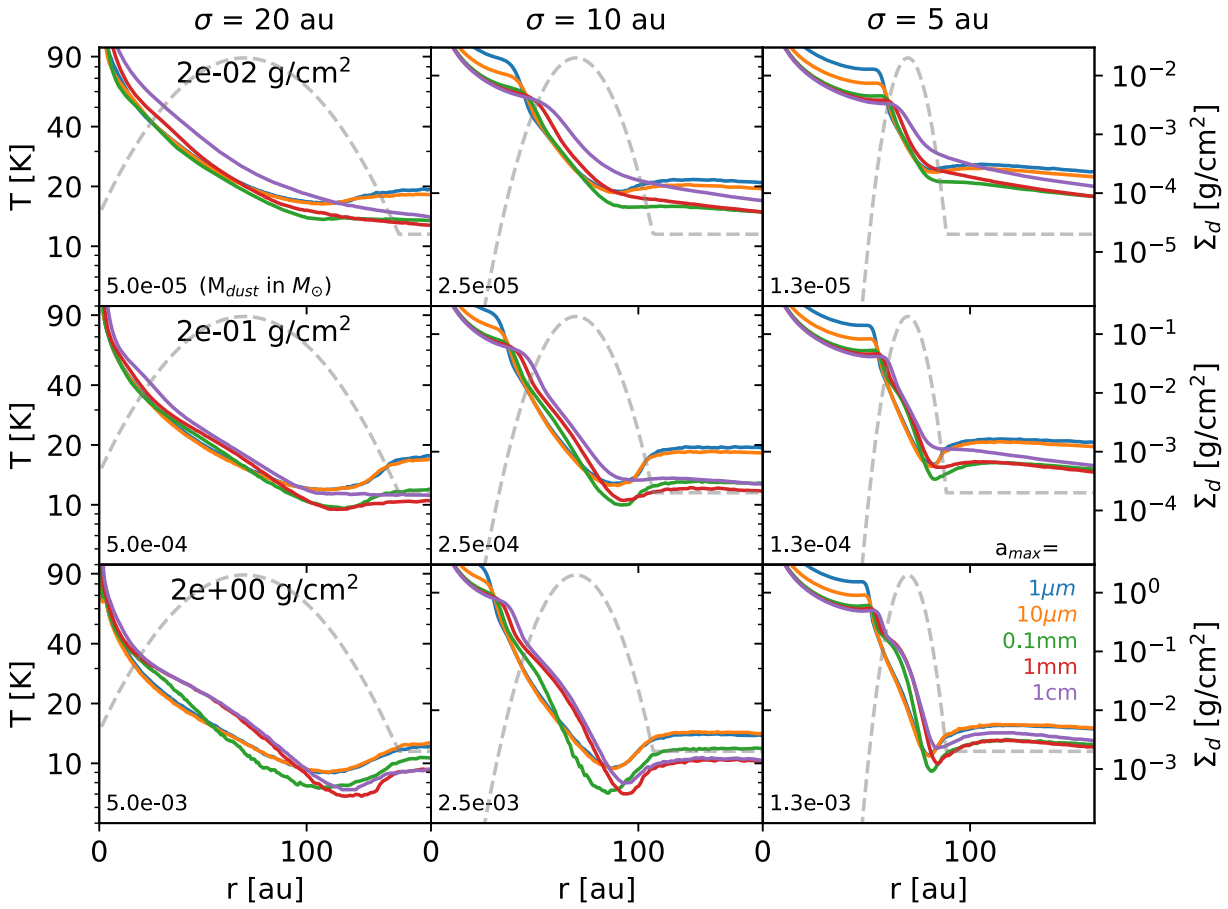

Figure 6.5: The midplane temperature of one population models with ring configurations. From top to bottom, the dust surface density at the Gaussian peak are 0.02, 0.2 and 2 $\mathrm{g\,cm^{-2}}$. From left to right, the Gaussian widths are 20, 10 and 5 au. a_{max} with increasing sizes are marked with blue, orange, green, red and magenta lines. The dashed lines are the dust surface density in logarithmic scale. The floor density over the peak density is 10^{-3}. The total dust mass is shown in the bottom left corner.

6.4.4 Two-Population Models

In two-population models, we add a second species, with different opacity and density distributions. The first population is still assumed to be small grains and coupled with the gas. The second population is assumed to be large grains, partially decoupled with the gas, and concentrated more to the midplane and the ring center. Its vertical density distribution is a Gaussian with the scale height determined by the midplane temperature calculated from MCRT and the coupling parameter

ψ (Dullemond et al. 2018, also in Zhu et al. 2012a). The coupling parameter ψ also determines the ring's width of the second species, and

$$\psi = \sqrt{\frac{\alpha}{St}}, \tag{6.12}$$

where α is the disk turbulence viscosity, and St is the Stokes number (or particle's dimensionless stopping time),

$$\begin{aligned} St &= t_{stop}\Omega = \frac{\pi a \rho_p}{2\Sigma_{gas}} \\ &= 1.57 \times 10^{-3} \frac{\rho_p}{1\mathrm{g\,cm^{-3}}} \frac{a}{1\mathrm{mm}} \frac{100\mathrm{g\,cm^{-2}}}{\Sigma_g}, \end{aligned} \tag{6.13}$$

where ρ_p is the density of the dust particle, a is the radius of the dust particle, and Σ_g is the gas surface density. We adopt ρ_p=1.675 g cm^{-3} as in the DSHARP opacity, and use a = 1 mm to represent big grains. Effectively, ψ is determined by the gas surface density Σ_g, the grain size a, and the disk viscosity α. To explore the parameter space, we vary α and Σ_g in the models. The width and scale height of big grains are (Dullemond et al. 2018),

$$\sigma_d = \sigma(1+\psi^{-2})^{-1/2}, \tag{6.14}$$

and

$$h_d = h_g(1+\psi^{-2})^{-1/2}. \tag{6.15}$$

The Gaussian peak is still centered at 70 au. At the Gaussian peak, we assume that the total dust to gas mass ratio ε = 1:100. At the Gaussian peak, the small and big grains' mass ratio is 1/31.6.

We assume that the small grains have the same distribution as the gas. Since the distributions of big and small grains have different widths and scale heights, the local ε and the mass ratio between big and small grains vary at the 2-D r-θ plane. Even though big grains contribute more mass inside the ring, the region outside the ring's midplane is still dominated by small grains, since small grains have a larger width and scale height.

For the two-population models, the second dust population is also involved in the iteration process in searching for the self-consistent thermal structure. In each iteration, besides adjusting the small grain and gas density, the big grains' scale height is changed due to the updated midplane temperature. Then the big dust density is adjusted vertically, but the surface density is always fixed. The convergence can also be reached after several iterations.

Our choices of α are 10^{-2}, 10^{-3}, and 10^{-4}. With weaker turbulence, the ring is radially narrower and vertically more settled. The peak surface density for small grains are Σ_{peak} = 0.0002, 0.002, 0.02 and 0.2 $\mathrm{g\,cm^{-2}}$. The peak surface density of the big grain population is 31.6 times higher. The total integrated dust mass of the big grain population is only around 10 times higher, since the small grain have wider radial distribution. The choices of widths and $\Sigma_{floor}/\Sigma_{peak}$ (the density floor ratio applies to both small and big grains) are the same as one-population models. The opacities for big and small grains are also fixed, as shown in bottom panel of Figure 6.4. These models are summarized in Table 6.1.

Figure 6.6 shows the midplane temperatures for $\Sigma_{floor}/\Sigma_{peak}$ = 0.001 cases after iterations. The layout is the same as Figure 6.5. From top to bottom, the peak surface density for the small grains are 0.002, 0.02 and 0.2 $\mathrm{g\,cm^{-2}}$. The peak densities of the big grains are larger by a factor of 31.6. The total dust masses are marked on the top-right corner of each panel and comparable to the respective panels in Figure 6.5. Blue, orange and green curves represent $\alpha = 10^{-4}$, 10^{-3},

10^{-2} cases. The surface densities of the small grains are marked in gray dashed lines, and those of the big grains are marked in colored dashed lines. If the optical depth is low (the surface density is low and the ring is narrow), the temperature has a dip exactly located at the ring's position. The temperature at the dip can be 30% lower than a smooth profile for the upper left cases. With a higher surface density and a wider ring, the dip moves towards the outer ring. When the surface density is high, the Stokes number becomes small and the big grains are more coupled to the gas. For the bottom panels, the temperature profiles are very similar to the one-population models (Figure 6.5). The temperature dips occur outside the ring. For reference, the Rosseland mean absorption opacity for the second species $k_{R,abs} = 8.13\ \mathrm{cm^2\,g^{-1}}$ at T=20 K. τ reaches unity when Σ_{peak} for the small-grain population is around $0.005\ \mathrm{g\,cm^{-2}}$ (with total surface density reaching $0.15\ \mathrm{g\,cm^{-2}}$). This explains why the shadowing effect dominates when $\Sigma_{peak} \gtrsim 0.02\ \mathrm{g\,cm^{-2}}$. In short, the underlying mechanism that affects the midplane temperature becomes the shadowing effect in the optically thick regime or the big grains are well-coupled to the small grains. A main difference between two mechanisms is the position of the temperature dip. If the excess cooling dominates, the dip is at the ring's peak, whereas if the shadowing effect dominates, the dip is far outside the ring's peak.

Figure 6.7 shows the brightness temperature profiles for these models. The most prominent trend is that as the optical depth becomes higher, the ring's center shifts to the left. This is because when the ring becomes more optically thick, the temperature instead of the density profile is dominant in determining the radial profile. The higher temperature in the inner disk makes the peak shift inwards. The absorption optical depths at the peak of rings are marked on left panels. As expected, the transition happens at $\Sigma_{peak} = 0.02\ \mathrm{g\,cm^{-2}}$, as τ_{abs} is around unity. It is also possible that the temperature dip at the peak's center reduces the intensity and split a single ring into

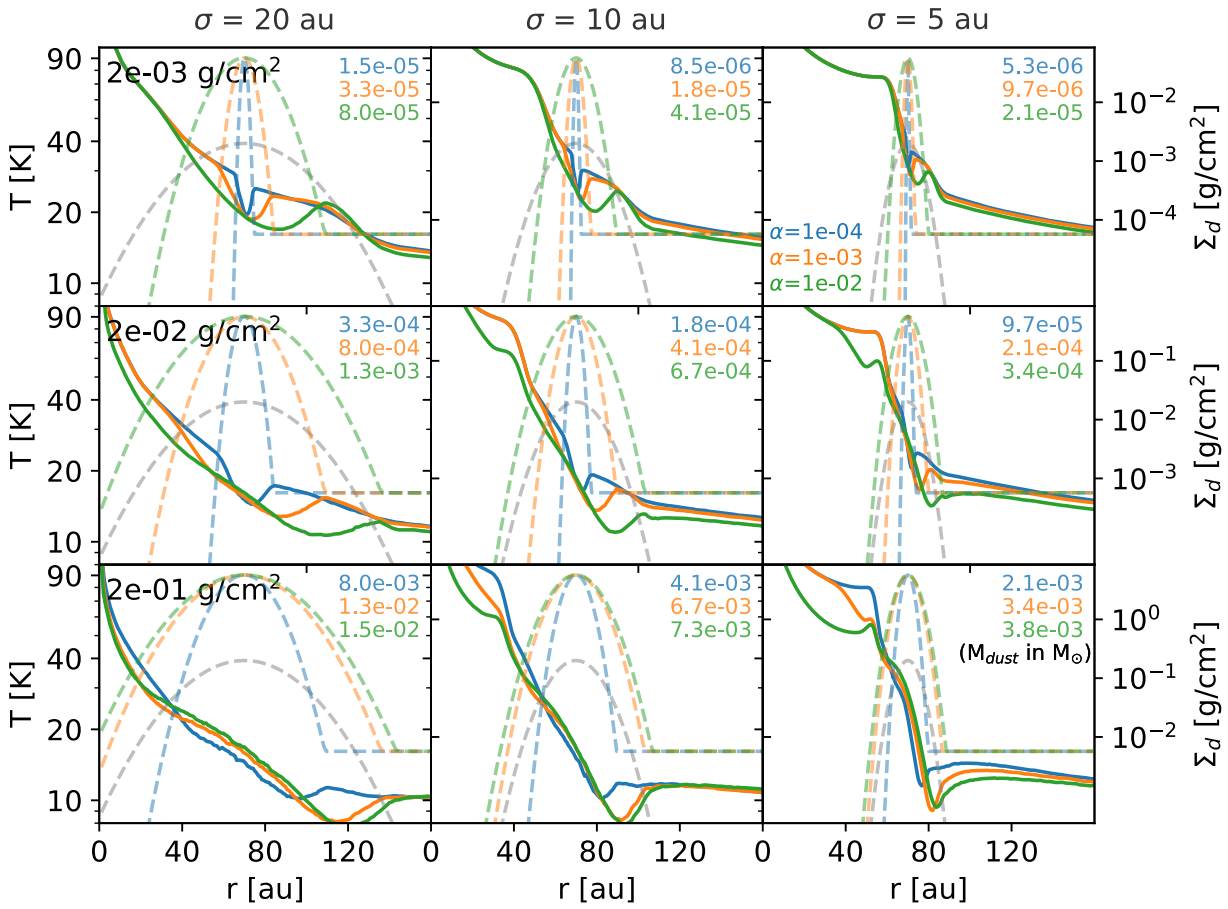

Figure 6.6: The midplane temperature of two population models with ring configurations. From top to bottom, the dust surface density for the small grains at the Gaussian peak are 0.002, 0.02 and 0.2 $\mathrm{g\,cm^{-2}}$ (the peak density of big grains are 31.6 times higher). From left to right, the Gaussian widths are 20, 10 and 5 au. Blue, orange and green curves represent α=10^{-4}, 10^{-3}, 10^{-2}. The gray dashed lines are surface density of small grains and colored dashed lines are those of big grains. The floor density over the peak density is 10^{-3}. The total dust masses are shown in the top right corner. In each panel, the dust mass depends on α. The total masses are comparable to what are shown in each panel of Figure 6.5.

ring-gap-ring shape, but we do not observe it in these models. A simple test shows that the temperature dip needs to be very deep (more than 50% decrease of temperature) to make it happen. The temperature decrease is at most 30% among these models.

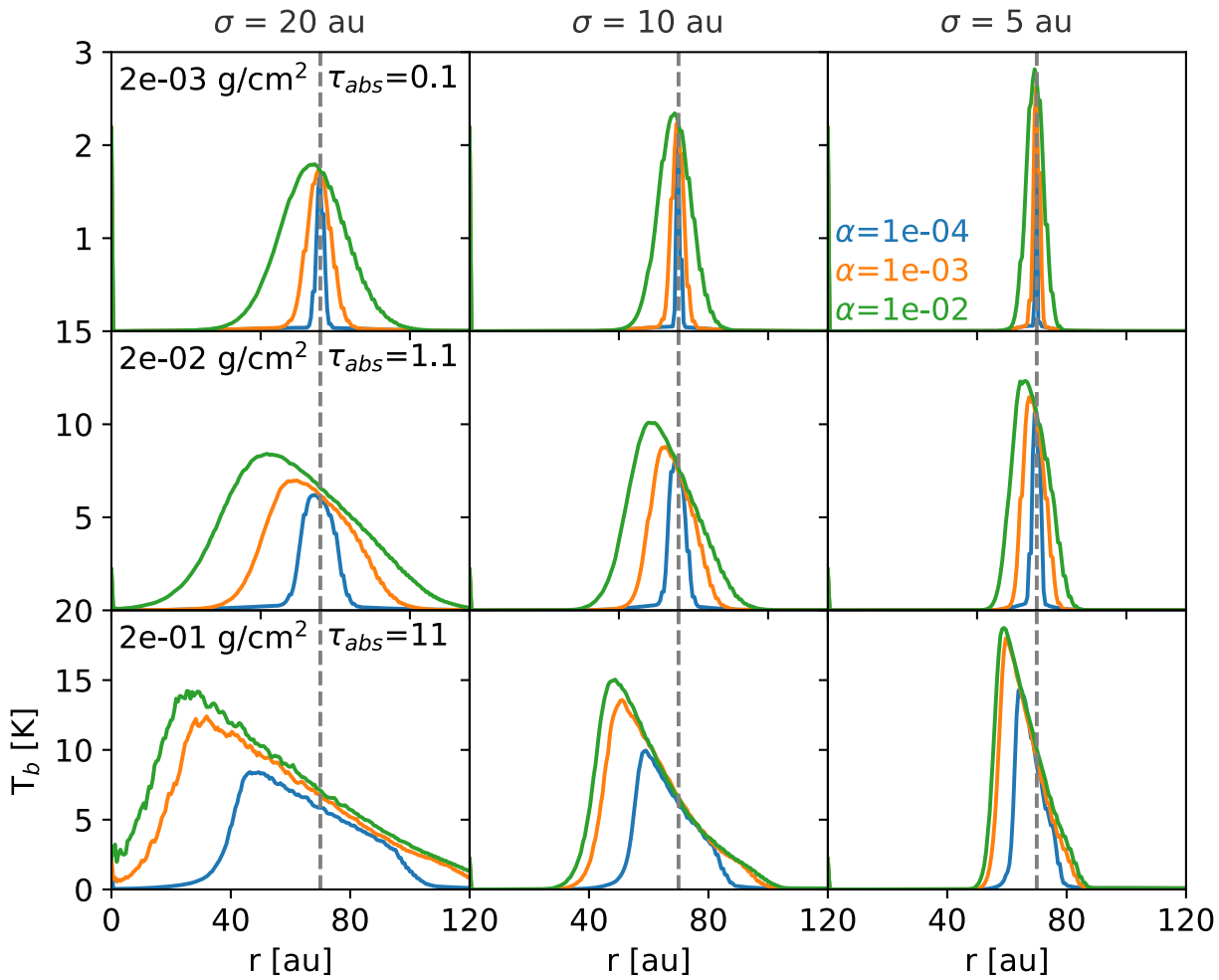

Figure 6.7: The radial profiles at 0.87 mm for two-population models in unit of brightness temperature as the same layout as Figure 6.6. Total absorption optical depths of Guassian's peaks (including both species) are marked on left panels. The ring's peaks at 70 au are marked as vertical dashed lines.

6.4.5 2D Thermal Structure

Besides the midplane temperature, we also study the vertical temperature structure, which can be probed by molecular line observations (e.g.,Pinte et al. 2018a). In Figure 6.8, we plot the $r-\theta$ distributions of a model in the optically thin limit. The peak surface density for the small grain is $\Sigma_{peak} = 2\times10^{-4}$ g cm^{-2} (that of big grains is 31.6 times higher), α=0.01, σ = 20 au and $\Sigma_{floor}/\Sigma_{peak} = 0.001$. The density and temperature maps are shown in the left panels. They have

been iterated to reach hydrostatic equilibrium. Big grains are concentrated at 70 au with significant settling. The temperature is lower at the ring. The lower-temperature region extends vertically to $\sim 2^\circ$ ($z/r \sim 0.034$), which is comparable to the local gas aspect ratio h/r. The positions of one scale height, $z = h(r)$ are marked as white curves. Note that for small grains, the vertical density distribution is not a Gaussian, since the temperature varies along the disk height. The scale height is then defined as z where

$$\left[-2\ln\left(\frac{\rho(r,z)}{\rho(r,0)}\right)\right]^{1/2} = 1. \tag{6.16}$$

The big grains' scale height is directly calculated from the midplane temperature and the coupling parameter ψ. At the ring, the scale heights of both species become lower due to the decrease of temperature there. For comparison, the upper-middle and upper-right panels show the density structures of the small-grain and big-grain components of the model, respectively. The lower-middle and lower-right panels are the temperatures of the disk if there is only small-grain or big-grain population. Note that their thermal structures are not self-consistently calculated, i.e., their temperatures are calculated using RADMC-3D without iterations and the density vertical structures are unchanged compared to the two-population case. Since the small-grain-only model's temperature structure is almost identical to the mixed model containing both species, it is clear that almost all the disk temperature structure is determined by the small grains. The exception is at the ring where big grains are concentrated. The temperature there is much lower. If the disk only has big grains, the radial temperature profiles at different scale heights are similar (except at the ring), i.e., the vertical temperature distribution is close to be isothermal.

We also run a case with 100 times higher surface density. The turbulent viscosity α is 10^{-4} so that the big grains' width is comparable to the previous one. The ring becomes optically thick, and

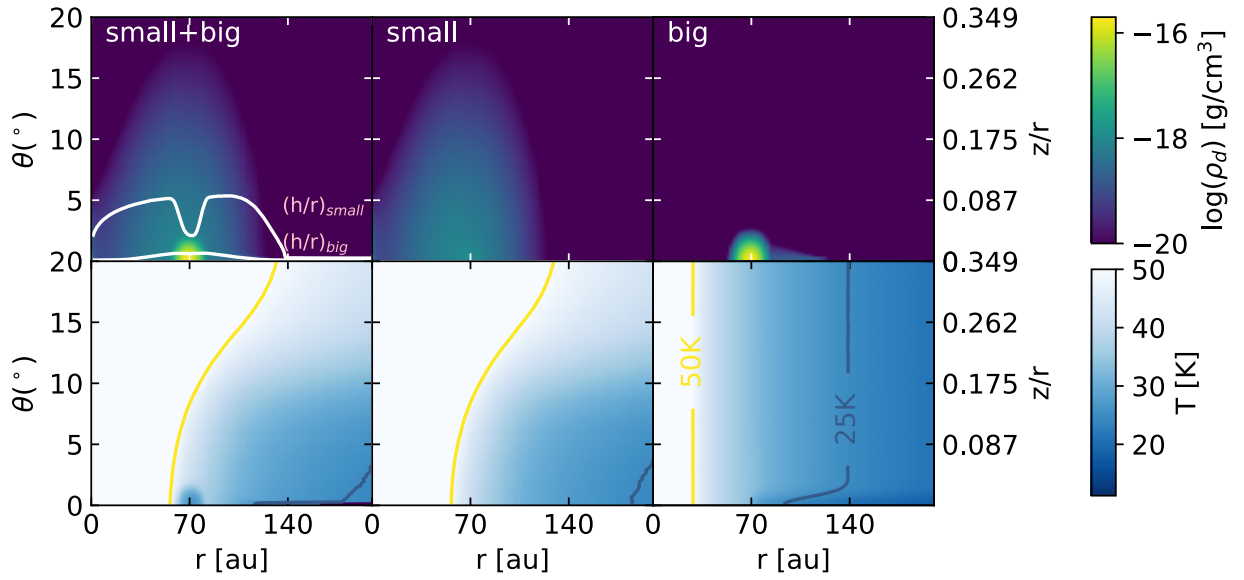

Figure 6.8: Left: 2D density (top) and temperature (bottom) distributions of model $\Sigma_{peak} = 2\times10^{-4}$ g cm^{-2}, α=0.01, σ = 20 au and $\Sigma_{floor}/\Sigma peak$ = 0.001. Middle: the density and temperature distributions with only small grains included. Right: with only big grains included. The white curves in top panels are the one scale-height contours of small (upper one) and big (lower one) grains.

has a different behavior in the disk atmosphere. Figure 6.9 shows the radial temperature profiles at different disk heights θ (or z/r) for these two models. The temperatures of low-mass disks are shown in the left panels and those of high-mass disks are shown in the right panels. The top four panels show the temperatures measured at the midplane, big grains' scale height, small grains' scale height (or gas scale height) and a location at a higher atmosphere. The temperature dips are obvious within the big grains' scale height for both low-mass and high-mass disks. This means that excess cooling is operating in both disks' midplane. At larger vertical heights, the temperature decreases smoothly with radius for the low-mass disk, whereas it has a dip outside the ring around 100 au for the high-mass disk. The latter is essentially a one-population scenario at these scale heights where small grains dominate. The small grains' ring is optically thick enough for the shadowing effect to operate. For reference, the small-grain-only and big-grain-only temperatures

using MCRT are marked as dashed and dotted-dashed curves. In the low-mass disk case, the small-grain-only temperature is higher than the big-grain-only temperature, while it is the opposite in the high-mass disk case. The bottom panels show the spectral indices for these models between ALMA band 6 and 7. Both models see the drop of spectral indices within the ring. The dip in the spectral index of the low-mass disk indicates that the ring is dominated by big grains, whereas the rest is dominated by small grains. For the high-mass disk, the spectral index α is even lower than two at the ring, which indicates that the ring is optically thick and dust scattering is substantial (Zhu et al. 2019; Liu 2019a). For these two configurations, the temperature dip due to excess cooling cannot be seen at one gas scale height for the two-population scenario. If the disk is optically thick, the temperature dip outside the ring can still be seen high above the midplane. At the big grain's scale height (z/r=0.008), the temperature profile even has two dips. One is at the ring position due to excess cooling from big grains, whereas the other is outside the ring due to the shadowing effect.

6.5 Disk Thermal Structure Coupled with a Dust Evolutionary Model

In both optically thin and thick cases, the disk temperature drops either at the ring or at the outer edge of the ring. In either cases, the temperature dip acts as a pressure trap, which can alter the shape of the ring. In this section we attempt to add dust growth and evolution in the feedback loop to test this scenario. The detail of the 1D dust evolution code is summarized in Appendix 6.8.

The gas surface density profile is set to resemble that of a transition disk, LkCa 15 (Facchini et al. 2020) with a depleted inner cavity,

$$\Sigma_g(r) = \Sigma_{g,c}\left(\frac{r}{65\mathrm{au}}\right)^p \arctan\left[\left(\frac{r}{65\mathrm{au}}\right)^{10}\right], \tag{6.17}$$

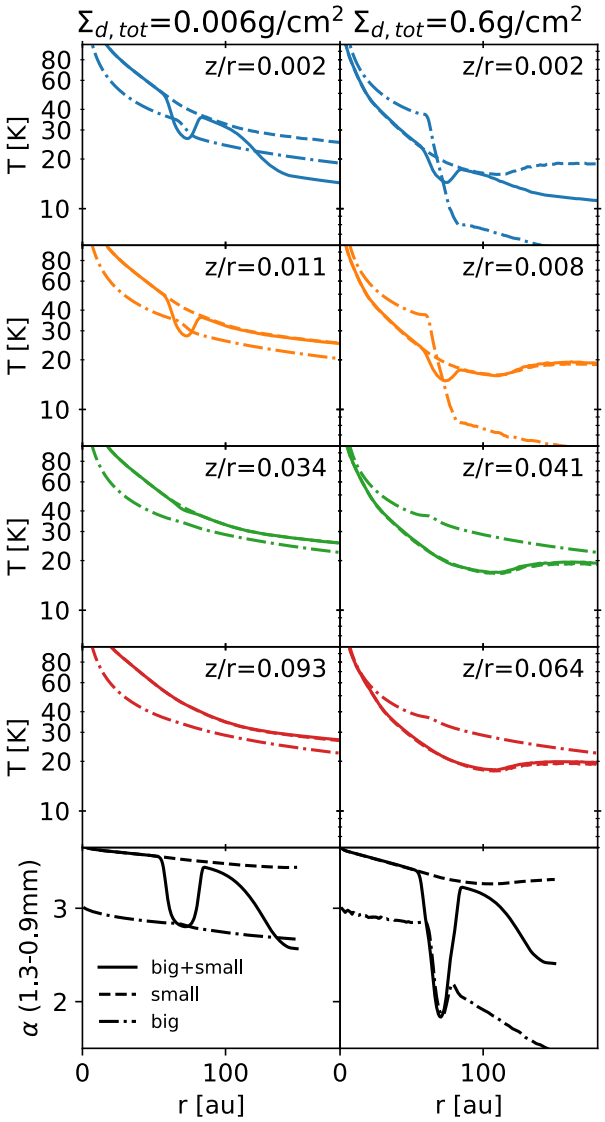

Figure 6.9: The radial temperature profiles at different heights for the setup of Figure 6.8 (left) and disks with 100× higher density (right), and $\alpha = 10^{-4}$. From top to bottom, the heights are picked at the disk's midplane, big grains' scale height, gaseous scale height and upper atmosphere. The bottom panels show the spectral index between 1.25 mm and 0.87 mm. Solid lines are the MCRT results with both big and small grains. Dashed lines are the temperatures profiles for MCRT with only small grains included. Dotted-dashed curves show big-grain-only cases.

where p is the slope of the surface density profile. We run dust evolution with a fixed temperature profile (T$\propto r^{-0.5}$) for 0.6 Myr. The gas surface density is fixed over time. At t=0.6 Myr, the dust has already piled up at the outer edge of the inner cavity and formed a Gaussian ring. The grain size

has grown to $\sim$ mm size at the ring. The evolving dust distribution should change the temperature profile, which in turn, alters the dust distribution. Starting from this point, the temperature is calculated using MCRT self-consistently as described in Section 6.4.4. The dust surface density in the dust evolution code is used as the big-grain population (with $\{a_{min}, a_{max}\}$=$\{0.1\text{mm}, 10\text{mm}\}$). When the coupling parameter ψ is involved, we assume all the big grains are 1 mm in the MCRT calculations. The small grain's density has the same profile as that of the gas. Their opacities are the same as mentioned in Section 6.4.4 and bottom of Figure 6.4. The surface density ratio between two populations is still calculated assuming power-law dust size distribution with a slope of 3.5 at the ring's peak. The derived midplane temperature is then used in the dust evolution code. The temperature is updated using MCRT every time interval dt_{MCRT}.

The convergence requires very high spatial and temporal resolutions. To resolve the dust evolution around the ring, we have 1024 radial bins uniformly spaced in $log(r)$ from 40 au to 300 au to make sure that each newly formed ring (if any) is resolved by at least 10 gird cells. The dt_{MCRT} needs to be small enough to capture particles' radial drift. The timescale for the disk to reach thermal equilibrium varies in several orders of magnitude across the disk. Bae et al. (2021) calculates the thermal relaxation timescale consisting of radiation, diffusion and gas-dust collisions. In their setup, the relaxation timescale at the midplane is comparable to the orbital timescale at 70 au, which is around 600 years. The particle's drift timescale is usually less than the orbital timescale (i.e., $St \lesssim 1$). The 2D MCRT calculation is much more numerically expensive than the 1D dust evolution.

In Figure 6.10, we present two models that evolve with dt_{MCRT} = 30 yr for 9 kyr starting from t=0.6 Myr. Both models have gas surface density $\Sigma_{g,c}$ = 4.1 $\text{g}\,\text{cm}^{-2}$, and p=0, so that the pressure gradient around the ring solely comes from the temperature profile. The surface density of big

grains is represented by colored curves, whereas small grain and gas components are represented by solid and dashed gray curves. Model (a) has α=2×10^{-3}. In this case, the turbulence is too strong to split a ring into more rings. Nevertheless, the initial Gaussian ring tilts towards the inner disk as the disk evolves. This skewed shape that deviates from a Gaussian profile is seen in HD 163296 B67 ring (Dullemond et al. 2018; Isella et al. 2018). Note that, even without considering the temperature feedback effect discussed here, any non-Gaussian shape of the pressure bump can also lead to this skewed profile of dust distribution. This skewed dust shape can also occur when the dust is drifting to the ring center before reaching the steady state. At the initial stage, the temperature dip is at the outer edge of the ring. This means that the mechanism for the temperature dip is due to the shadowing effect. This is not surprising since big grains always dominate in the area of interest. At a later stage, the temperature dip becomes shallower and smoother, which indicates a negative feedback. This negative feedback leads to a steady state where the radial pressure gradient gradually becomes zero.

To come up with a condition that excess cooling can operate in producing the temperature dip, we increase the small grains' surface density by a factor of 100 in model (b). Now big grains only dominate inside the ring, whereas small grains dominate outside the ring. In addition, we also lower the viscosity α to 7×10^{-4}, hoping to generate more substructures. After several thousand years, the initial ring evolves to several rings. With a larger optical depth, the temperature is thus much lower than the previous case. The initial temperature dip is close to the ring, which means that excess cooling is indeed operating. Due to the high computational cost of MCRT, the dust evolution is stopped after 3.5 kyr. At the end of simulations, neither of these two models reach steady states. We are expecting more dust will be trapped at the ring. On the other hand, this pile-up may last over the disk's lifetime and the disk may not reach any steady state eventually. To

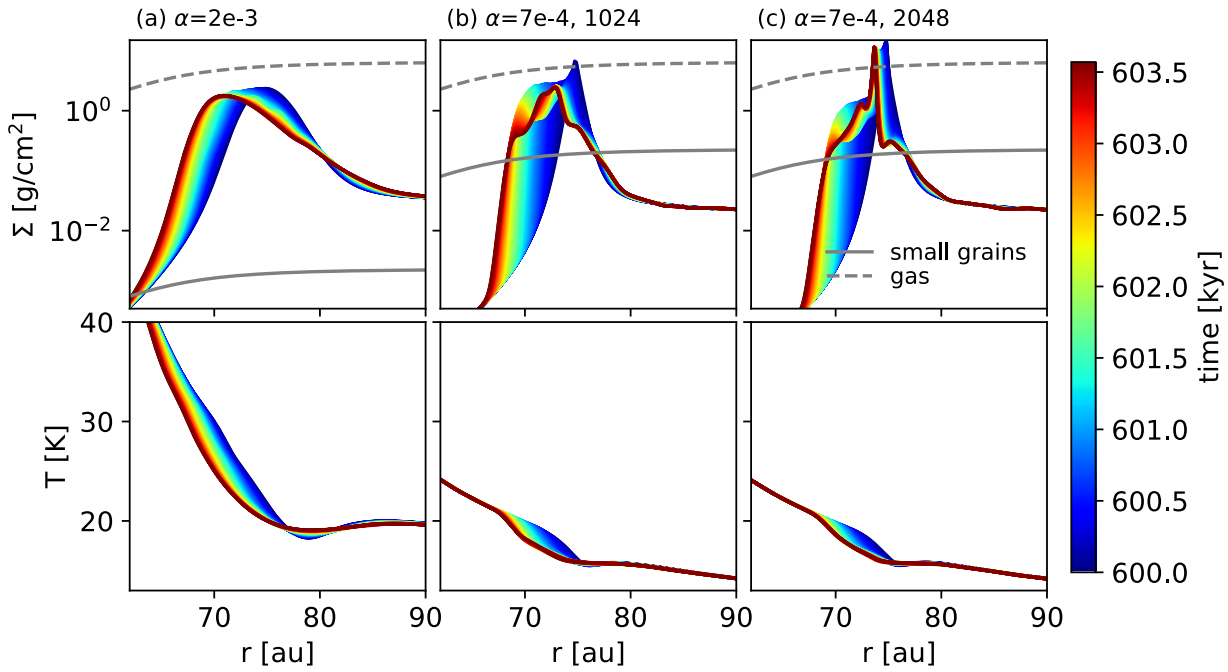

Figure 6.10: Dust surface density of the big-grain population (top panels) and midplane temperature (bottom panels). (a) Model with α=2×10^{-3}, Σ_g=4.1 g cm^{-2}, ε = 0.01 at the ring. (b, c) models with α=7×10^{-4} and with different radial resolutions. In these models small grains' surface density is 100× higher than that in model (a). The small grains' densities are marked by gray solid curves and gas surface densities are marked by gray dashed curves.

test the resolution effect, we increase the radial resolution to 2048 in panel (c). The substructure persists in the higher resolution run.

Finally, self-consistent ring structure model including both thermal effects and dust dynamics is important not only for protoplanetary disk observations but also for planetesimal and planet formation studies (Morbidelli 2020; Chambers 2021). The formation of skewed rings and even multiple rings will affect the mass and number of formed planetesimals. Converting dust into planetesimals can also affect the dust opacity and feedback to the ring's thermal structure. More work on this feedback loop on planetesimal formation needs to be studied in future.

6.6.1 Impact of Density Floor

We have studied how the density outside the Gaussian peak can affect the disk temperature. We assume that the dust density levels off at some distance away from the peak. We take $\Sigma_{floor}/\Sigma_{peak}$ = 10^{-3} as our fiducial model. This value affects the temperature gradient for the shadowing effect. We present other $\Sigma_{floor}/\Sigma_{peak}$ values for single population runs with Σ_{peak} = 0.2 $\mathrm{g\,cm^{-2}}$ in Figure 6.11. From top to bottom, the floor floor becomes lower. The temperature gradient becomes larger with lower density floor, but the change becomes insignificant when $\Sigma_{floor}/\Sigma_{peak} \leq 10^{-3}$. When the floor is higher, the temperature dip is shallower due to a less drastic change of the density profile. A higher density floor makes the density gradient smoother. This implies that if there are dust grains being constantly replenished in the outer disk, the temperature dip would be shallow.

6.6.2 Temperature Gap in CI Tau

During the preparation of this manuscript, a line emission gap in a continuum ring has been observed (Rosotti et al. 2021) in ^{13}CO emission of CI Tau disk. CI Tau is a disk that has been observed with substructures in dust continuum (Clarke et al. 2018). There are at least three rings at 23, 54 and 135 au. This temperature gap is located at the second continuum ring at 54 au (Rosotti et al. 2021). The authors exclude the possibility of reduction in surface density and explore the possibility of reduction in temperature. To reproduce a temperature gap, they multiply the small dust surface density at 20 au, with a Gaussian width σ = 10 au. It casts a shadow onto the outer disk, which has a lower temperature and is positioned around 54 au and thus explains the temperature gap. Their explanation falls into our one-population scenario. If this is the case, the location

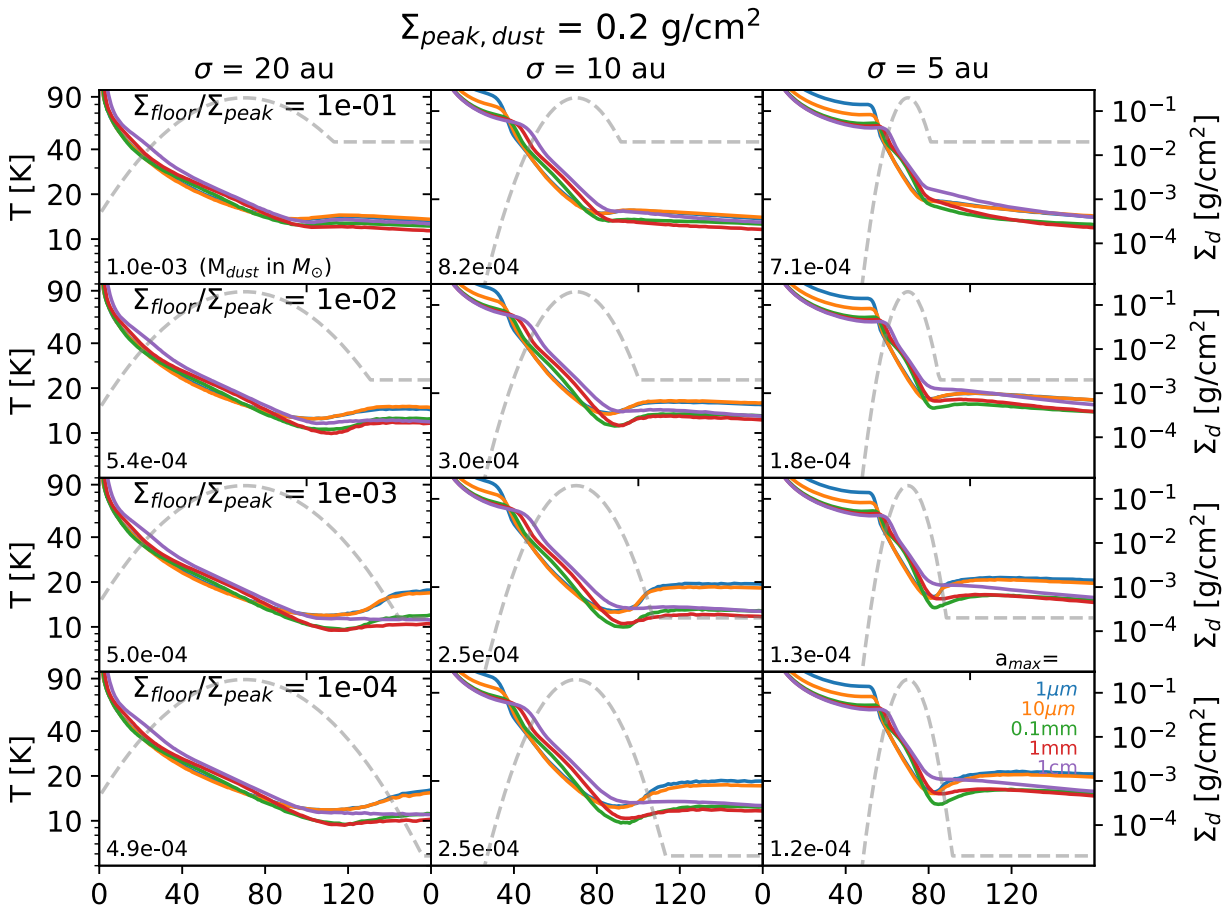

Figure 6.11: The effects of density floor on temperature profiles for one population. The dust peak surface density is 0.2 g cm^{-2}. From top to bottom, the density floors are 0.1, 0.01, 0.001 and 0001. The temperature dip becomes stronger with lower density floor.

of this temperature gap matches the second ring purely by chance. On the other hand, we propose that our two-population scenario can naturally explain why the temperature gap is exactly at the position of the ring. As mentioned in previous sections, big grains dominate in the ring and the cooling is more efficient. Thus, the temperature in the ring is lower. If this mechanism dominates, we predict that the temperature gap will disappear if one uses a more optically thick tracer to probe higher emission surfaces. On the other hand, if this is indeed due to the shadowing effect suggested by Rosotti et al. (2021), the temperature gap should still be able to be observed at several disk scale heights.

With more high-resolution line emission data available in future, we may be able to find more cases showing temperature gaps at or beyond a continuum ring, since both the shadowing effect and excess cooling can lead to a temperature gap.

6.7 Conclusion

We study the thermal structure of a dusty ring self-consistently by iterating the disk's dust distribution, thermal structure from MCRT, and vertical hydrostatic equilibrium. We find that two different effects can lead to a temperature dip in a ring. One is the shadowing effect and the other is excess cooling of big grains concentrated in rings. The latter effect is studied for the first time in this work.

We include two dust populations in our model: small and big grains. For each population, we adopt a Gaussian ring structure in the radial direction. Due to the dust trapping by the pressure bump, the small and big grains have different radial widths and scale heights, depending on their coupling to the gas. After several iterations, we find that temperature drops substantially inside the ring, which is due to the different equilibrium temperatures of small and big grains. With the higher opacity at submm/mm wavelengths, big grains have higher cooling efficiency, so that the temperature drops at the ring center where they are concentrated.

The temperature dip by the shadowing effect is important when the disk is optically thick. Its temperature dip exists in a large vertical region. On the other hand, the temperature dip by excess cooling of big grains is the strongest when the disk is optically thin, and it happens closer to the midplane. In reality, both mechanisms operate together to some degree. Both mechanisms can explain the temperature gap observed in CI Tau (Rosotti et al. 2021), but the excess cooling

effect does not need fine-tuning. The gap is located at the dust continuum ring, which is the exact prediction of this excess cooling mechanism, instead of a coincidence as in the shadowing mechanism.

Temperature dips by either of these two mechanisms can possibly lead to the formation of more rings beyond the initial dust ring. This is due to the feedback from the disk's thermal structure to the dust radial drift. The temperature bump can produce a pressure bump, given that the gas surface density does not vary abruptly. We demonstrate this possibility by combining the MCRT calculation with a 1D dust evolution code. If the drift timescale is long, the ring will not split into more rings. Instead, it will deviate from a Gaussian, with steeper inner edge and shallower outer edge. With a low viscosity and different dominant populations inside and outside of a ring, one ring can indeed evolve to more rings. The separation is around several au, which is within the observational limit of ALMA. We have already seen that with higher resolutions that previously observed wide single ring can be resolved into more rings (e.g., Facchini et al. 2020; Benisty et al. 2021). More systems with these closely packed rings may be found in future higher resolution observations. By constructing self-consistent ring models and comparing with observations, we may be able to constrain the dust size distribution, dust settling, and dust radial drift in rings of protoplanetary disks. These information can be used to constrain planetesimal and planet formation within rings.

6.8 1D Dust Evolution Model

We use a single size approximation for dust evolution calculation, similar to Sato et al. (2016). One of the motivations of this approach is that the mass-size distribution of dust is top heavy,

so the dust surface density can be well represented by its maximum sized species. In cylindrical coordinates, the advection-diffusion equation for dust surface density Σ_d is

$$\frac{\partial \Sigma_d}{\partial t} + \frac{1}{r}\frac{\partial}{\partial r}\left[r v_r \Sigma_d - \frac{\nu}{1+\mathrm{St}^2} r \Sigma_g \frac{\partial Z}{\partial r} \right] = 0, \tag{6.18}$$

where v_r is grain's radial velocity, ν is the turbulent viscosity, St is the dimensionless stopping time of the dust particles, and Z is the dust-to-gas surface density ratio. The exact value of v_r is governed by angular momentum loss by gas head wind (Weidenschilling 1977).

$$v_r = \frac{1}{\mathrm{St} + \mathrm{St}^{-1}} \eta v_K;\ \mathrm{St} = \frac{\pi}{2}\frac{\rho_d a}{\Sigma_g} \times \max\left[1, \frac{4a}{9\lambda}\right], \tag{6.19}$$

where v_K is the local Keplerian orbital velocity, ρ_d is mass density of individual particle, a is the dust particle radius, and λ is the mean free path of the gas. Stokes number St covers two drag regimes: Reynolds regime and the first Stokes regime. η is the parameter that reflects the gas disk's pressure gradient,

$$\eta = \frac{d\ln\left(c_s^2 \rho_g\right)}{d\ln r}\left(\frac{c_s}{v_K}\right)^2. \tag{6.20}$$

The core of the single sized approximation is the equation governing the size evolution of a representing particle,

$$\frac{\partial m_p}{\partial t} + v_r \frac{\partial m_p}{\partial r} = \Sigma_d \frac{2\sqrt{\pi} a_p^2 v_{pp}}{h_d}. \tag{6.21}$$

The source term on the right hand side is the growth kernel that defines how fast this particle

sweeps up mass. The particle-particle velocity, v_{pp} can be divided into five components,

$$v_{pp} = \sqrt{(\Delta v_B)^2 + (\Delta v_t)^2 + (\Delta v_r)^2 + (\Delta v_\phi)^2 + (\Delta v_z)^2}. \tag{6.22}$$

The first term is mutual velocity from Brownian motion. If the mass of the other particle is m'_p, then $\Delta v_B = \sqrt{8(m_p + m'_p)k_B T/(\pi m_p m'_p)}$. Since Δv_B does not diminish to zero when $m_p = m'_p$, we use $\Delta v_B = 4\sqrt{k_B T/(\pi m_p)}$ with m_p as the mass of the representing size in our single-sized model. The second term is velocity from turbulent mixing. For two particles with Stokes number St and St$'$ in a disk with α viscosity,

$$\Delta v_t = \begin{cases} \sqrt{\alpha} c_s \mathrm{Re_t}^{1/4} (\mathrm{St} - \mathrm{St}') & \text{if } \mathrm{St} \ll 1/\sqrt{Re_t}, \\ (1.4...1.7) \times \sqrt{\alpha} c_s \sqrt{\mathrm{St}} & \text{if } 1/\sqrt{\mathrm{Re_t}} \ll \mathrm{St} \ll 1, \\ \sqrt{\alpha} c_s \sqrt{\frac{1}{1+\mathrm{St}} + \frac{1}{1+\mathrm{St}'}} & \text{if } \mathrm{St} \gg 1, \end{cases} \tag{6.23}$$

where $\mathrm{Re_t} = 2\nu/v_{th}\lambda$ is the turbulent Reynolds number, and $v_{th} = \sqrt{8k_B T/\pi\mu}$ is the thermal velocity of the gas. Note that the first function diminishes to zero when $\mathrm{St} = \mathrm{St}'$. This is the same for $\Delta v_r, \Delta v_\phi, \Delta v_z$. When this happens one needs to use a second representing particle size to calculate St$'$, but does not need to evolve the second particle independently. Following Sato et al. (2016), this single sized model produces the best result when $\mathrm{St}'/\mathrm{St} = 0.5$ comparing with a full dust evolution model.

CHAPTER 7 Porous Dust Particles in Protoplanetary Disks: Application to the HL Tau Disk

Shangjia Zhang,[1,2], Zhaohuan Zhu,[1,2], Takahiro Ueda,[3,4], Akimasa Kataoka,[3], Anibal Sierra,[5], Carlos Carrasco-González,[6], and Enrique Macías[7]

[1]Department of Physics and Astronomy, University of Nevada, Las Vegas, 4505 S. Maryland Pkwy, Las Vegas, NV, 89154, USA

[2]Nevada Center for Astrophysics, University of Nevada, Las Vegas, Las Vegas, NV 89154, USA

[3]National Astronomical Observatory of Japan, Osawa 2-21-1, Mitaka, Tokyo 181-8588, Japan

[4]Max-Planck Institute for Astronomy (MPIA), Königstuhl 17, D-69117 Heidelberg, Germany

[5]Departamento de Astronomía, Universidad de Chile, Camino El Observatorio 1515, Las Condes, Santiago, Chile

[6]Instituto de Radioastronomía y Astrofísica (IRyA), Universidad Nacional Autónoma de México (UNAM), Mexico

[7]ESO Garching, Karl-Schwarzschild-Str. 2, 85748, Garching bei Munchen, Germany

7.1 Abstract

Dust particle sizes constrained from dust continuum and polarization observations by radio interferometry are inconsistent by at least an order of magnitude. Motivated by porous dust observed in small Solar System bodies (e.g., from the *Rosetta* mission), we explore how the dust particle's porosity affects the estimated particle sizes from these two methods. Porous particles have

lower refractive indices, which affect both opacity and polarization fraction. With weaker Mie interference patterns, the porous particles have lower opacity at mm wavelengths than the compact particles if the particle size exceeds several hundred microns. Consequently, the inferred dust mass using porous particles can be up to a factor of six higher. The most significant difference between compact and porous particles is their scattering properties. The porous particles have a wider range of particle sizes with high linear polarization from dust self-scattering, allowing mm-cm-sized particles to explain polarization observations. With a Bayesian approach, we use porous particles to fit HL Tau disk's multi-wavelength continuum and mm-polarization observations from ALMA and VLA. The moderately porous particles with sizes from 1 mm-1 m can explain both continuum and polarization observations, especially in the region between 20-60 au. If the particles in HL Tau are porous, the porosity should be from 70% to 97% from current polarization observations. We also predict that future observations of the self-scattering linear polarization at longer wavelengths (e.g., ALMA B1 and ngVLA) have the potential to further constrain the particle's porosity and size.

7.2 Introduction

Dust plays a fundamental role in the secular evolution of the protoplanetary disk by setting thermal structure and participating in dynamics as they aggregate and collapse to form planetesimals, eventually planets (Lesur et al. 2022). As dust particles are the primary source of opacity in protoplanetary disks, their presumed opacity is used to convert the radio continuum emissions to the disk dust mass. However, the opacity itself depends on the particle properties (such as composition, size, temperature, and distribution). Recently, ALMA continuum polarization observations

provide an independent constraint on dust particle properties. Both dust continuum observation and polarization observation should work in synergy, increasing our knowledge of dust properties (e.g., a review from Miotello et al. 2022).

7.2.1 Particle Size Problem

If the polarization is due to dust self-scattering, ALMA (sub)mm polarization observations can tightly constrain the particle size. In order to produce polarization with dust self-scattering, the radiation field needs to be anisotropic so that the polarization due to light from different directions does not cancel out. This condition makes inclined and substructured disks ideal for observing self-scattering polarization (Kataoka et al. 2015; 2016a; Yang et al. 2016). One of the best examples for protoplanetary disks are HL Tau (Stephens et al. 2014; 2017); HD 142527 (Kataoka et al. 2016b; Ohashi et al. 2018); IM Lup (Hull et al. 2018b); CW Tau, DG Tau (Bacciotti et al. 2018); AS 209 (Mori et al. 2019); and HD 163296 (Dent et al. 2019; Ohashi & Kataoka 2019). Among these disks, the dust continuum polarization fractions are detected as $\sim$1% at ALMA bands 6 and 7 ($\sim$1.3 mm, and 0.87 mm, respectively). Another condition requires strong dust scattering at mm wavelengths, and the scattered light needs to be polarized. For compact particles, the scattering albedo becomes substantial if the particle size $a \gtrsim \lambda/2\pi$, but the fraction of the polarized scattered light sharply drops to zero beyond that same particle size. These competing effects result in only a narrow range of particle sizes that can produce detectable polarization at a particular wavelength. In other words, the polarization fraction of the total intensity is very sensitive to the particle size. The inferred particle sizes are around 100 μm. particle sizes larger or smaller than this produce much lower linearly polarized emissions. However, this value is at least an order of magnitude less

than the particle size constrained from multi-wavelength continuum observations at radio bands (e.g., a review from Andrews 2020).

Traditionally, multi-wavelength dust continuum observations are used to constrain the particle size. If the disk is optically thin, the spectral index ($\alpha = d\ln I(\nu)/d\ln\nu$) between two wavelengths reveals the slope of dust absorption opacity ($\beta = d\ln\kappa_{\rm abs}(\nu)/d\ln\nu$). In the Rayleigh-Jeans limit, $\alpha = \beta$+2. With an assumption of dust composition, the particle size can be inferred from β. The typical β from diffuse clouds is $\sim$1.7 from far-infrared and submillimeter observations (Finkbeiner et al. 1999; Li & Draine 2001), whereas β from most of the protoplanetary disks at radio bands are significantly $\lesssim$1, indicating mm to cm sized particles (e.g., D'Alessio et al. 2001; Calvet et al. 2002; Draine 2006). Detailed radio observations that resolve the disk show that α increases with radius (Perez et al. 2015a; Tazzari et al. 2016) and within dark gaps (Huang et al. 2018a), suggesting particle sizes are smaller in the outer disk and the gaps if the emission is optically thin, consistent with the theoretical prediction of dust radial drift and dust trapping (e.g., Weidenschilling & Cuzzi 1993). Nevertheless, particles are still $\sim$1 mm even at these lower ends.

However, if the disk is optically thick, α will be $\sim$2 and cannot be used to constrain the particle size. Dust self-scattering can weaken the dust's thermal emission and affect the α value, even decreasing the α value below the blackbody value (Miyake & Nakagawa 1993; Liu 2019b; Zhu et al. 2019; Sierra & Lizano 2020). The scattering albedo affects the thermal emission, which makes the particle size constraint more difficult with just dual-wavelength observations (Huang et al. 2020a). In such a case, observations of three or more wavelengths are fit in tandem (Carrasco-González et al. 2019b; Ueda et al. 2020; Macías et al. 2021; Sierra et al. 2021; Ueda et al. 2021; 2022; Guidi et al. 2022). With scattering considered, the smallest particle sizes can be as low as several hundred microns in some regions, but mm-cm-sized particles are still valid solutions in

most of the disks (Ueda et al. 2020; 2021; 2022; Sierra et al. 2021; Guidi et al. 2022).

Modeling the disk in detail with both radio continuum SEDs (Spectral Energy Distributions) and polarization observations can give us more stringent constraints on the particle sizes and other disk properties. Lin et al. (2020) model HD 163296 with the spectral index between ALMA bands 6 and 7 and polarization at band 7 to show that purely 90 μm sized particles can explain both types of observations. Ueda et al. (2021) study the particle size in the HL Tau's inner disk ($\lesssim$20 au) by fitting SEDs from 4 ALMA/VLA bands and polarization measurements from 3 ALMA bands. They consider dust vertical settling with mm-sized particles concentrated in the midplane and 100 μm-sized particles in the disk atmosphere. They find that mm-sized particles can still be present in the disk as long as they are highly settled and hidden in the optically thick midplane. Small 100-μm-sized particles in the atmosphere contribute to the detectable polarization emissions (Ueda et al. 2021; Sierra & Lizano 2020; Brunngräber & Wolf 2021).

7.2.2 Consideration of Porosity

In this paper, we extend the work by Ueda et al. (2021) and study both the inner and outer regions of the HL Tau disk, focusing on the influence of particle porosity on SED and polarization fittings. This is inspired by recent small Solar System objects missions (e.g., the *Rosetta* mission). Cometary nuclei are considered to be the remnants of the planetesimals (Weissman et al. 2020) and are highly porous (Groussin et al. 2019). The km-sized cometary nucleus 67P/Churyumov–Gerasimenko has a porosity of 70%-85% constrained by measuring the dust's permittivity (Kofman et al. 2015; Herique et al. 2016) and the nucleus density (Jorda et al. 2016; Pätzold et al. 2016) from the *Rosetta* mission. In addition, porous particles are detected (Bentley et al. 2016; Mannel et al. 2016; 2019)

and account for more volume fractions than the compact particles among the collected samples (Merouane et al. 2016). While it is not clear whether the micro-porosity solely contributes to the total porosity, voids should be no larger than ~ 9 meters from radar measurements (Ciarletti et al. 2017), and models (Blum et al. 2017; Bürger et al. 2023) with a combination of particle porosity (micro-porosity; Weidling et al. 2009; Zsom et al. 2010) and random packing of the particles (Skorov & Blum 2012; Fulle & Blum 2017) can closely explain the observations from the *Rosetta* mission.[1]

Theory and experiments support the existence of porous particles in protoplanetary disks as micron-sized dust particles coagulate to form fluffy agglomerates (Ossenkopf 1993; Weidenschilling & Cuzzi 1993; Wurm & Blum 1998; Kempf et al. 1999; Krause & Blum 2004; Okuzumi et al. 2012; Kataoka et al. 2013; Krijt et al. 2015; Estrada et al. 2016; 2022; Estrada & Cuzzi 2022). Experiments reveal that the mm-cm-sized (pebble-sized) agglomerates that cannot surpass the bouncing barrier experience compression and eventually reach an equilibrium with porosity $\sim 64\%$ (Weidling et al. 2009; Zsom et al. 2010). Observationally, near-infrared scattered-light imaging starts to shed light on the small particle's porosity in protoplanetary disks. Recent analyses on the polarized scattered light phase functions observed by VLT/SPHERE reveal that micron-sized dust particles are porous in all 10 disks in their sample (Ginski et al. 2023). Particularly in IM Lup disk, particles are found to be fractal agglomerates with sizes $\sim 2\ \mu$m composed of ~ 200 nm monomers (Tazaki

[1]We declare nomenclature on dust particles following Güttler et al. (2019). We use *particle* for any unspecified dust particle; *grain* (or *monomer*) as the smallest solid particle with homogeneous composition (compact with zero porosity). A *dense aggregate* is an assemblage of rigidly joint grains, with porosity $<10\%$. A *porous agglomerate* is composed of grains or dense aggregates with porosities between 10%-99%. A *fluffy/fractal agglomerate* shows a fractal and dendritic nature with porosity $>99\%$. In this paper, we focus on *dense aggregates* and *porous agglomerates*. At a population level, we use *dust* to refer to the solid component in protoplanetary disks that contrasts the gas component.

et al. 2023).

For our problem, porous particles may help alleviate the size inconsistency in two ways. First, moderately porous particles (porous agglomerates) have a weaker size dependence of the self-scattering polarization fraction at mm wavelengths (Tazaki et al. 2019a; Brunngräber & Wolf 2021), so the particle size does not need to be precisely 100 μm to match the high polarization fraction in observations. Second, the absorption and scattering opacities of the compact particles have strong interference patterns when $2\pi a \gtrsim \lambda$. The absorption opacity of a single-sized particle oscillates with sizes and wavelengths in high amplitude due to the interference. These interference features are typically at mm-cm wavelengths for mm-cm-sized particles, providing a wide range of spectral index values at mm wavelengths. Thus, the favorable particle sizes from SED fittings often fall into mm-cm size regime. Porous particles have weaker interference features in the absorption opacity (Kataoka et al. 2014), making it more difficult to constrain the particle size in the mm-cm size range by fitting the spectral index. Allowing a non-zero porosity leaves more freedom in fitting SED and mm polarization observations in tandem. While we only focus on the impact of spherical porous particles in the current paper, we note that non-spherical compact particles (Kirchschlager & Bertrang 2020) and non-spherical porous particles (Kirchschlager et al. 2019) are also able to change the inferred opacity and polarization.

As the optical properties of dust particles are the key to understanding the fitting results, in Section 7.3, we give a holistic view of dust properties on wavelengths, sizes, and levels of porosity. In Section 7.4, we present the analytical fitting of SEDs considering different levels of porosity. In Section 7.5, we pick some best-fit models to run Monte Carlo Radiative Transfer (MCRT) to further compare with SEDs and polarization observations. In Section 7.6.1, we emphasize the significant impact of porous particles on dust mass estimation. In Section 7.6.2, we test whether

an even lower value of filling factor can reproduce two types of observations. In Section 7.6.3, we discuss the impact of a different particle size distribution. In Section 7.6.4, we use current polarization observations to constrain the possible range of the particle porosity in HL Tau. In Sections 7.6.5, we lay out the approach to testing the prediction in the future. We also compare our results with recent near-infrared scattered light observations and the *Rosetta* mission in Section 7.6.6. In Section 7.7, we use Table **??** and Figure 7.13 to summarize all possible solutions of particle sizes and porosities for HL Tau. Readers who prefer to skip the technical details can directly proceed to this section. We conclude our paper in Section 7.8.

7.3 Particle Optical Properties

Particle optical properties are generated by mixing different materials using the Effective Medium Approximation (EMA; see Appendix 7.9 for its validity). This process is essentially averaging the complex refractive indices of each component with certain rules to obtain a composite refractive index, $m(\lambda)$=$n(\lambda) + ik(\lambda)$. We adopt the DSHARP composition, which contain 20% water ice (Warren & Brandt 2008), 33% astronomical silicates (Draine 2003), 7% troilite (Henning & Stognienko 1996), and 40% refractory organics[2] (Henning & Stognienko 1996) in mass fractions (Birnstiel et al. 2018). To include porosity, we mix the DSHARP composition with vacuum using the Burggeman rule. The fraction of the vacuum is controlled by the porosity, $\mathscr{P}$, the volume fraction of the vacuum in the dust particle. Another widely used parameter is the filling factor, f, where f = 1-$\mathscr{P}$. Lastly, we calculate the particle optical properties using the Mie theory with the refractive index as an input.

[2]Including more absorptive carbonaceous materials can change the refractive index significantly and impact the polarization fraction (Yang & Zhu 2020). However, we only explore the composition with refractory organics in our paper.

We describe the behavior of four crucial particle optical properties generated by the Mie theory to predict the dust continuum emission and mm polarization for various levels of porosity. Understanding their behaviors helps fit and interpret observations in Sections 7.4 and 7.5. The four properties are absorption opacity ($\kappa_{\rm abs}$), effective scattering opacity ($\kappa_{\rm sca,eff}$) , effective albedo ($\omega_{\rm eff}$), and polarization fraction at 90° (P). The definition of these parameters can be found in Appendix 7.10. $\kappa_{\rm abs}$, $\kappa_{\rm sca,eff}$, and $\omega_{\rm eff}$, along with density and temperature, determine the continuum emission. The product of $\omega_{\rm eff}$ and P indicates the total linear polarization fraction (Kataoka et al. 2015).

On the particle size constraint from SEDs, the increase of the opacity due to Mie interference alters the opacity index (β), leading to different interpretations of the spectral index (α) based on compact and porous particle assumptions. The changing of $\kappa_{\rm sca,eff}$ and $\omega_{\rm eff}$ further complicates the interpretation when the disk is optically thick.

In the following, we use an example with af = 160 μm to introduce the behavior of $\kappa_{\rm abs}$ and $\kappa_{\rm sca,eff}$. We use af to characterize the particle size since a and f are fully degenerate for $\kappa_{\rm abs}$, except at the Mie interference regime.

7.3.1 Opacities at af = 160 μm

For absorption opacities $\kappa_{\rm abs}$, the values for various filling factors are similar, except at $a \sim \lambda/2\pi$, where only the compact particle has higher opacity due to the Mie interference. This is demonstrated in the upper left panel of Figure 7.1, where it shows single-sized DSHARP opacities for af = 160 μm along wavelengths for various filling factors. f = 1 is the compact particles (represented by blue lines), whereas f=0.3, 0.1, and 0.01 are porous agglomerates represented by orange, green,

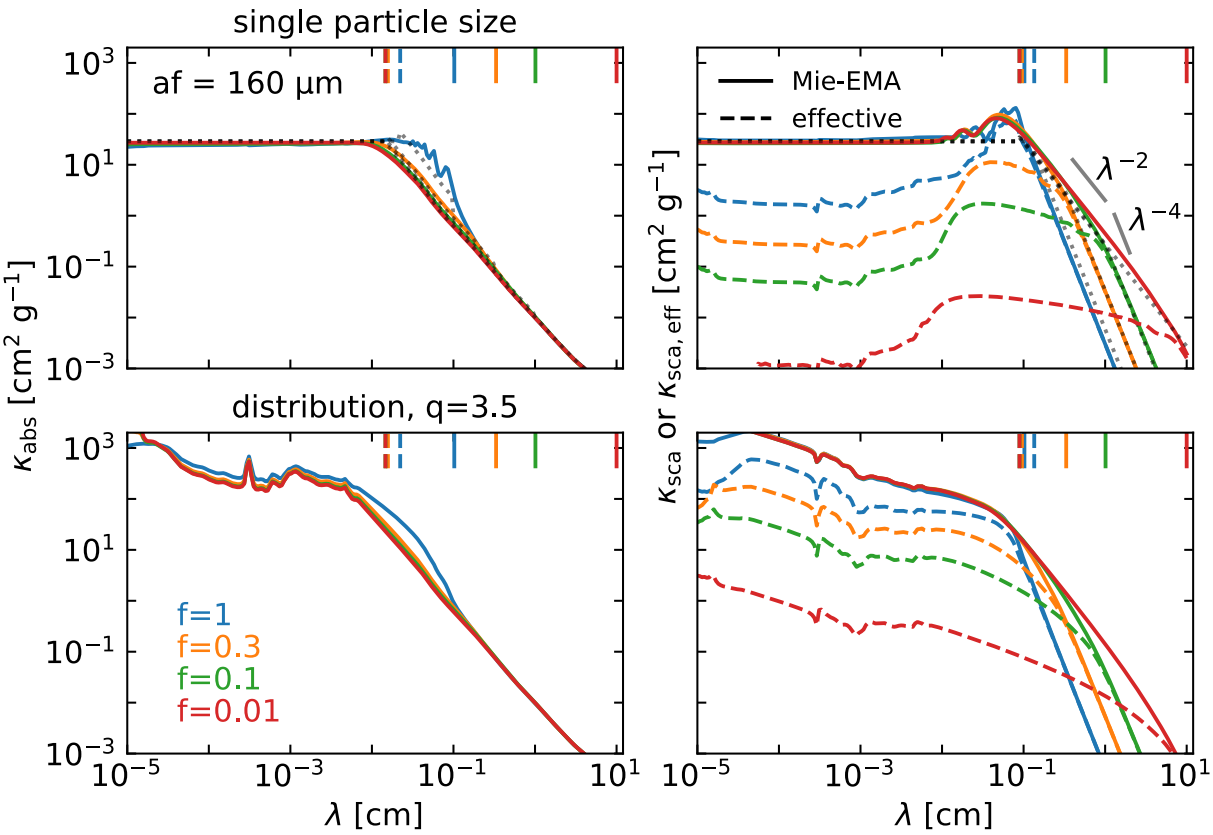

Figure 7.1: The wavelength dependence of the absorption opacity ($\kappa_{\rm abs}$), un-adjusted scattering opacity or effective scattering opacity ($\kappa_{\rm sca}$ or $\kappa_{\rm sca,eff}$) are shown from left to right. Top panels are single-particle-size values, whereas bottom panels are the values with particle size distribution $n(a) \propto a^{-3.5}$. Four filling factors are 1 (blue), 0.3 (orange), 0.1 (green) and 0.01 (red). Solid lines are the total scattering opacities calculated from the Mie theory ($\kappa_{\rm sca}$), whereas the dashed lines are scattering opacities with forward scattering truncated ($\kappa_{\rm sca,eff}$). The dotted lines are analytical approximations of $\kappa_{\rm abs}$ and $\kappa_{\rm sca}$ in Bohren & Huffman (1983); Kataoka et al. (2014). The vertical solid lines represent x=1, delineating Rayleigh and Mie regimes. The vertical dashed lines are locations where $kx = 3/8$ (for absorption) or $(n-1)x = 1$ (for scattering), delineating Mie's optically thin and thick regimes for the dust particles. x is the size parameter; $x = 2\pi a/\lambda$ or $2\pi a_{\rm max}/\lambda$; see Appendices 7.10, 7.11, and 7.12. The green vertical dashed line is almost at the same location as the red one.

and red lines, respectively.

The upper right panel of Figure 7.1 shows the un-adjusted scattering opacities, $\kappa_{\rm sca}$ (solid lines) and effective scattering opacities adjusted for the forward scattering, $\kappa_{\rm sca,eff}$ (dashed lines). We see that the effective scattering opacities have much lower values at shorter wavelengths com-

pared to $\kappa_{\rm sca}$. For $\kappa_{\rm sca}$, a and f are also degenerate for different filling factors at short wavelengths ($\lambda \lesssim 2\pi a$). However, the opacities are separated between various levels of porosity at longer wavelengths ($\lambda \gtrsim 2\pi a$). The effective scattering opacities, $\kappa_{\rm sca,eff}$, are well separated at all wavelengths since the dependence of forward scattering does not have degeneracy between a and f.

In reality, particles with a size distribution, rather than a single size, are a better approximation in protoplanetary disks. Thus, we generate opacity with a power-law size distribution, $n(a) \propto a^{-q}$, often used in the literature. We take the size distribution index q=3.5 as a typical ISM value (Mathis et al. 1977). The minimum particle size, $a_{\rm min}$, is 0.1 μm. At mm-cm wavelengths, $a_{\rm min}$ is not important in averaging the opacity if $a_{\rm min} \ll a_{\rm max}$ and $q < 4$ (the limit where the mass is dominated by the dust particles in the top-heavy mass distribution). The resulting absorption and scattering opacities are shown at the bottom panels of Figure 7.1. Since the small particles have higher opacities at shorter wavelengths, the resulting opacities are higher than the values shown on the top panel at short wavelengths. Other than the short wavelength regime, the overall trends of the opacity are similar to the single-sized opacity.

We note that the particle size distribution is not well-constrained from observations. While simple steady state solutions between coagulation and fragmentation lead to a power-law distribution with q=3.5 (Dohnanyi 1969; Tanaka et al. 1996), simulations with dust growth-fragmentation in disks give a complicated distribution, which cannot be described as a power-law (Birnstiel et al. 2011). We use q=3.5 as a fiducial model in this paper, and discuss the impact of q in Sections 7.6.3 and 7.6.4.

We also want to mention that absorption opacity ($\kappa_{\rm abs}$) alone strongly impacts the *dust mass* estimation from continuum observations. When $\lambda \sim 2\pi a$, the $\kappa_{\rm abs}$ for compact particles is around six times higher than that for porous particles (for f=0.1). This opacity increase is due to Mie in-

terference unique to the compact particles with a higher refractive index. Thus, with mm-cm-sized particles, adopting compact particles instead of porous particles can increase the dust continuum opacity at radio bands by a factor of six or more and decrease the mass estimate by the same factor. We will use Section 7.6.1 to emphasize its significance after discussing how it can alleviate the particle size problem.

In Appendices 7.11 to 7.14, we follow Kataoka et al. (2014) to develop a simple model to understand the particle opacity at various regimes. The simple model provides a clear physical picture obscured by the direct Mie calculations. These insights are general and not related to a specific dust composition mixture. The model is shown by the dotted lines in the upper panels of Figure 7.1. The vertical dashed lines also show three regimes for the model, delineated by the size parameter (x=$2\pi a/\lambda$), and the complex refractive index (see Appendices 7.10, 7.11, and 7.12). On the left of the vertical-dashed line, the particle is in *Mie's optically thick regime*. Between the vertical-dashed line and the vertical solid line, the particle is in *Mie's optically thin regime*[3]. On the right of the vertical-solid line, the particle is in *Rayleigh regime*. The analytical approximation fits the DSHARP opacities ($\kappa_{\rm abs}$, and $\kappa_{\rm sca}$) perfectly at short and long wavelengths except for $\lambda \sim 2\pi a$ in Mie's optically thin regime. A more detailed explanation on the analytical approximations can be found in Appendices 7.11 and 7.12.

7.3.2 More Particle Sizes and Polarization Fraction

We map out the optical properties for a wide range of $a_{\rm max}f$ with a particle size distribution $q = 3.5$. In the top rows of Figure 7.2, we show the wavelength dependence of the particle absorption

[3]We note that the optical depth here is referred to the optical depth *inside* a particle.

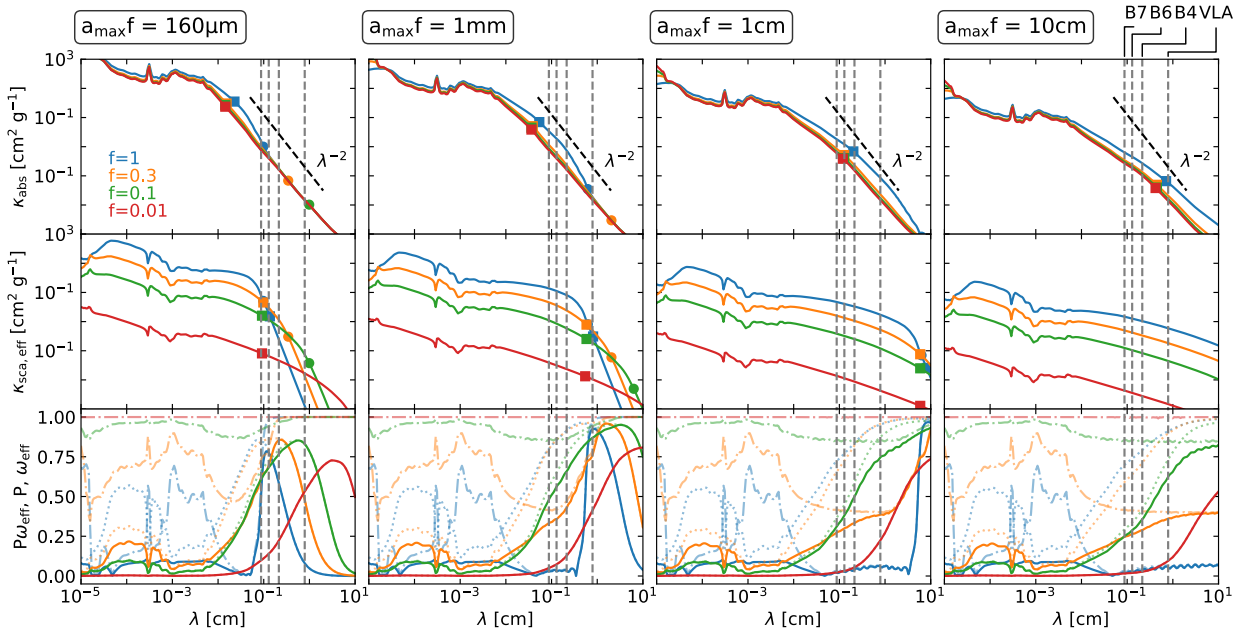

Figure 7.2: Wavelength dependence of the absorption opacity (top panels), effective scattering opacity (middle panels) and $P\omega_{\rm eff}$ (solid lines, bottom panels), P (dotted-dashed lines, bottom panels) and $\omega_{\rm eff}$ (dotted lines, bottom panels). From left to right, the maximum particle sizes $a_{\rm max}f$ are 160 μm, 1 mm, 1 cm and 10 cm. Four filling factors are 1 (blue), 0.3 (orange), 0.1 (green) and 0.01 (red). The circles (108) represent x=1, delineating Rayleigh and Mie regimes. The squares (110) are locations where $kx = 3/8$ (for absorption) or $(n-1)x = 1$ (for scattering), delineating Mie's optically thin and thick regimes for the dust particles. x is the size parameter; $x = 2\pi a_{\rm max}/\lambda$ (see Appendices 7.10, 7.11, and 7.12).

opacities, $\kappa_{\rm abs}$ for various $a_{\rm max}f$. From left to right, the maximum particle size $a_{\rm max}f$ increases from 160 μm to 10 cm. Additionally, four vertical lines indicate the observational wavelengths for ALMA bands 7 ($\sim$0.87 mm), 6 ($\sim$1.3 mm), 4 ($\sim$2.1 mm) and VLA Ka+Q band ($\sim$7.9 mm). Except for the small particles, $a_{\rm max}f$=160 μm (same as Figure 7.1), the compact particles have opacities several times higher than their porous counterparts at ALMA and VLA bands due to the interference pattern (Kataoka et al. 2014; Birnstiel et al. 2018). For these compact particles, the opacity index between different bands depends largely on the interference pattern and can vary far from λ^{-2} represented by the dashed line. For example, if $a_{\rm max}f$ = 1 mm, the opacity indices between ALMA bands are less than two, whereas that between ALMA band 4 ($\sim$2.1 mm) and VLA

band Ka+Q ($\sim$7.9 mm) can be much steeper than two. The feature disappears when the particle has a moderate porosity even if the filling factor f is as high as 0.3. For the porous particles, the opacity approaches to λ^{-2} at ALMA and VLA bands and its slope only starts to become shallower when $a_{\rm max}f \gtrsim 1$ cm. Compact and porous particles have such a significant difference at these wavelengths since they are within Mie's optically thin regime, where the boundaries between Rayleigh, Mie's optically thin, Mie's optically thick regimes are indicated by circles (108) and squares (110), respectively.

The second row of Figure 7.2 shows the effective scattering opacity $\kappa_{\rm sca,eff}$. The effective scattering opacity decreases with increasing $a_{\rm max}f$. Similar to Figure 7.1 ($a_{\rm max}$ = 160 μm), the effective scattering opacity at shorter wavelengths decreases as the particles become more porous. The more porous particles have higher effective scattering opacity at longer wavelengths ($\lambda > 2\pi a_{\rm max}$, i.e., the Rayleigh regime).

On the particle size constraint from polarization emission, both $\omega_{\rm eff}$ and P become more favorable in producing a higher polarization fraction with porous particles, as shown in the third row of Figure 7.2. $P\omega_{\rm eff}$, P, and $\omega_{\rm eff}$ are represented by solid, dotted-dashed, and dotted lines, respectively. For compact particles, $\omega_{\rm eff}$ is only high when $a \sim \lambda/2\pi$ at a given wavelength. The range of particle sizes with high polarization fraction is wider for porous particles[4]. P also becomes constantly high along all the wavelengths (Tazaki et al. 2019a), instead of a sharp drop-off when $a \gtrsim \lambda/2\pi$. Combining these two factors, we have a wider range of particle sizes to explain high polarization fractions observed in ALMA bands 6 and 7 (Tazaki et al. 2019a and see Appendix 7.13 for details). In other words, if particles are porous, an observed high polarization fraction at

[4]The range of particle sizes with high polarization fraction is also wider for non-spherical particles (Kirchschlager & Bertrang 2020), but with a different shape.

a certain wavelength can no longer translate to a tightly-constrained particle size, as it does for compact particles.

Take the $a_{\rm max}f = 160\ \mu$m case as an example, the compact particles only have high polarization fraction when $\lambda \sim 1$ mm. As the particles become more porous, the window for high polarization fraction becomes much wider. At f=0.1 (green curve), the $P\omega_{\rm eff}$ is above 0.5 for λ from sub-mm to several cm. However, when the particles are too porous (f=0.01), the polarization fraction becomes lower within ALMA bands (red curve) and can no longer explain observed high polarization fractions at bands 7 and 6, which is confirmed by MCRT calculations (see Figure 7.9 and Tazaki et al. 2019a; Brunngräber & Wolf 2021). For compact particles, as the maximum particle size increases, the narrow window for high polarization fraction shifts to longer wavelengths, so the high polarization fraction is expected to be observed only at longer wavelengths. In contrast, the window shift is less crucial for porous particle with f=0.1. For instance, the polarization fraction can still be high at ALMA band 7 even if $a_{\rm max}f = 1$ mm.

7.3.3 Spectral Indices and Polarization Fractions Predicted by $\kappa_{\rm abs}$, $\kappa_{\rm sca,eff}$, $\omega_{\rm eff}$, and P

Aside from predicting polarization fraction using $P\omega_{\rm eff}$, we can also predict the spectral index (α; $I_\nu \propto \nu^\alpha$) using $\kappa_{\rm abs}$, $\kappa_{\rm sca,eff}$, and $\omega_{\rm eff}$ with the help of the radiative solution of the plane parallel approximation considering scattering (Miyake & Nakagawa 1993; Zhu et al. 2019; Sierra et al.

2019; Carrasco-González et al. 2019b). The analytical expression[5] is

$$I_\nu = B_\nu(T)\Big\{1-\exp\Big(-\frac{\tau_\nu}{\mu}\Big)+\omega_\nu F(\tau_\nu,\omega_\nu)\Big\}, \tag{7.1}$$

where the third term in the curly braces is the correction due to scattering.

$$F(\tau_\nu,\omega_\nu)=\frac{f_1(\tau_\nu,\omega_\nu)+f_2(\tau_\nu,\omega_\nu)}{\exp(-\sqrt{3}\varepsilon_\nu\tau_\nu)(\varepsilon_\nu-1)-(\varepsilon_\nu+1)},$$
$$f_1(\tau_\nu,\omega_\nu)=\frac{1-\exp\{-(\sqrt{3}\varepsilon_\nu+1/\mu)\tau_\nu\}}{\sqrt{3}\varepsilon_\nu\mu+1},$$
$$f_2(\tau_\nu,\omega_\nu)=\frac{\exp(-\tau_\nu/\mu)-\exp(-\sqrt{3}\varepsilon_\nu\tau_\nu)}{\sqrt{3}\varepsilon_\nu\mu-1}, \tag{7.2}$$

where $\varepsilon_\nu = \sqrt{1-\omega_\nu}$. When the disk is very optically thick, $\omega_\nu F(\tau_\nu,\omega_\nu)$ is negative and contributes to the reduction of intensity below the blackbody radiation. To truncate forward scattering, we should use $\omega_{\rm eff}$ for ω_ν. Additionally, we should use $\kappa_{\rm sca,eff}$ to calculate the total optical depth, where

$$\tau_\nu \text{ or } \tau_{\rm tot} = (\kappa_{\rm abs}+\kappa_{\rm sca,eff})\Sigma_d, \tag{7.3}$$

where Σ_d is the dust surface density.

The general trend for the spectral indices is that they become less sensitive to particle sizes as the particles become more porous. In Figure 7.3, we demonstrate the predictions of spectral indices using Equation 7.1 in both optically thin (τ=0) and thick ($\tau\to\infty$) limits. All panels display the size dependence of particle optical properties with different filling factors (from left to right,

[5]We use the equation from Sierra et al. (2019), where the radiative transfer equation is integrated. The equation from Zhu et al. (2019) is similar but slightly different in that they use the Eddington approximation to find a solution to the emergent intensity.

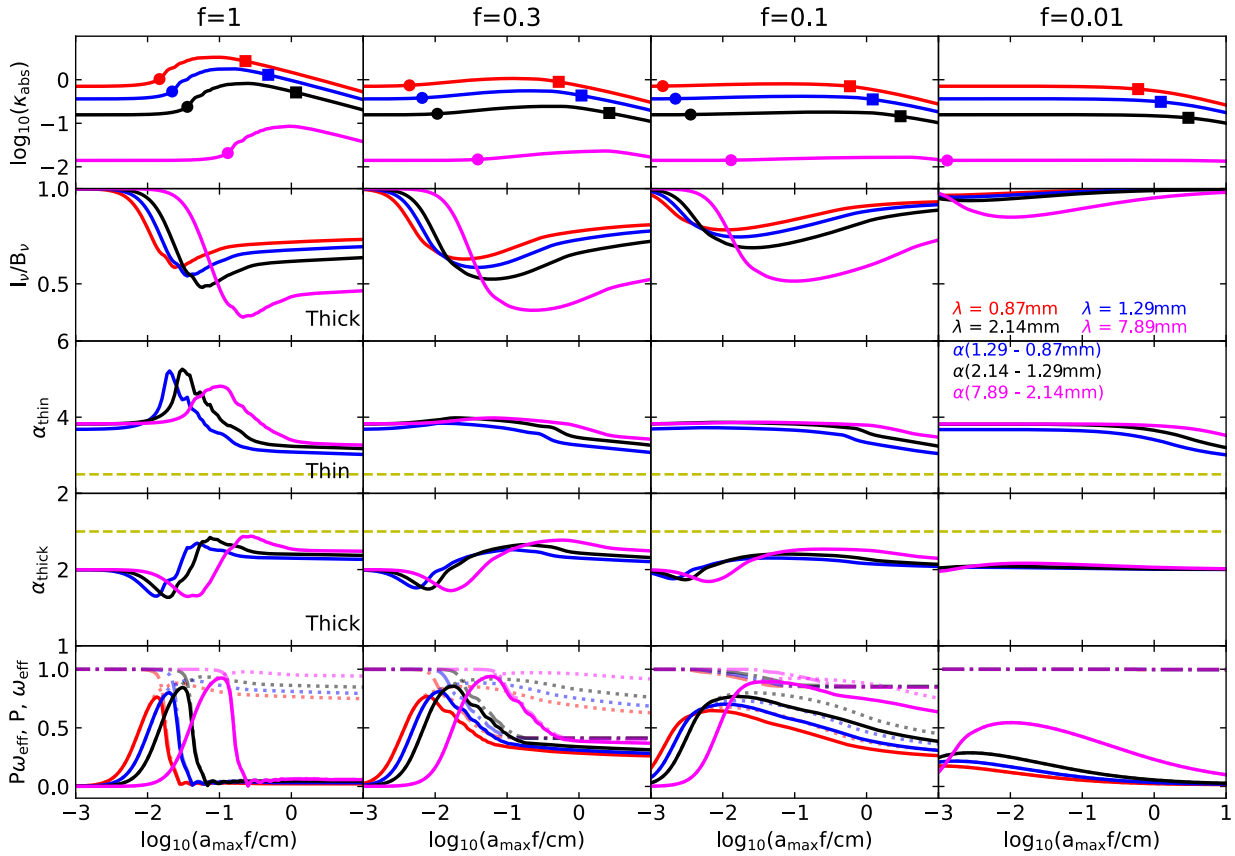

Figure 7.3: From top to bottom: the size ($a_{\rm max}f$) dependence of the $\kappa_{\rm abs}$ (absorption opacity), I_ν/B_ν (intensity reduction due to scattering compared to the blackbody radiation), $\alpha_{\rm thin}$, $\alpha_{\rm thick}$ (spectral indices at optically thin and thick regimes), and $P\omega_{\rm eff}$ (The product of the polarization fraction at 90°, P and the effective albedo, $\omega_{\rm eff}$). In the bottom panels, solid lines are $P\omega_{\rm eff}$, dotted lines are $\omega_{\rm eff}$, and dashed-dotted lines are P. From left to right, the filling factors are f=1, 0.3, 0.1, and 0.01. Red, blue, black, and magenta curves represent these quantities at 0.87 mm, 1.29 mm, 2.14 mm, and 7.89 mm. The circles (108) represent x=1, delineating Rayleigh and Mie regimes. The squares (110) are locations where $kx = 3/8$ (for absorption) delineating Mie's optically thin and thick regimes for the dust particles. Horizontal yellow dashed lines are α=2.5 as a reference point between $\alpha_{\rm thin}$ and $\alpha_{\rm thick}$.

the particles become more porous from f=1 to 0.01) and at different wavelengths (red: 0.87 mm; blue: 1.29 mm; black: 2.14 mm; magenta: 7.89 mm), corresponding to ALMA bands 7, 6, 4, and VLA Ka+Q bands.

The spectral indices in the optically thin limit where the scattering is negligible are shown in

the third row of Figure 7.3. The blackbody radiation is assumed to be at the Rayleigh-Jeans tail[6], so that α=β+2; $\kappa_{\rm abs}(\nu) \propto \nu^{\beta}$, where β is the opacity index. In this limit, the spectral index is only determined by the absorption opacity ($\kappa_{\rm abs}$) shown in the first row. For various porosities, the α changes from the ISM value ($\sim$ 3.7) at the small-particle end to lower values ($\sim$ 3.0) at the big-particle end. When the particle is compact, the spectral indices have peaks at $a_{\rm max} \sim \lambda/2\pi$ due to the interference feature in the absorption opacity. For ALMA bands, α can be as high as 5.0. Even with a moderate porosity, e.g., f=0.3, these peaks with very high values disappear. Instead, the spectral indices are similar (with a slight increase) to the ISM value until $a_{\rm max}f \sim$ several mm. After that, the spectral indices start to drop. This trend also happens in particles with smaller filling factors, but the drop of spectral indices is moving to larger particle sizes. The spectral index at the large particle extreme can be approximated using $\beta \approx (q-3)\beta_{\rm ISM}$ (Draine 2006), where q=3.5 and $\beta_{\rm ISM}$=1.7. An important implication for these trends is that with porosity, the particle size becomes difficult to infer from the spectral index since they are less sensitive to $a_{\rm max}f$. For example, the spectral indices observed similar to the ISM values can even be due to $a_{\rm max}f \sim$ mm particles.

The spectral indices at the optically thick regime mainly depend on the effective albedo, $\omega_{\rm eff}$, and can be taken as the ratio of the logarithmic intensity reduction between two wavelengths plus two ($\alpha_{\rm thick}$ = dln(I_ν/B_ν)/dlnν + 2). If there were no scattering, the spectral index should be exactly two in the Rayleigh-Jeans approximation.

We introduce the intensity reduction due to the dust scattering, I_ν/B_ν, shown in the second row of Figure 7.3. The reduction factor is what in the curly braces in Equation 7.1 and in the optically

[6]Note that in protoplanetary disks' midplane the temperature can be at several tens of Kelvin. At ALMA bands, $h\nu/k$T $\lesssim$ 1, but not much less than unity, so the blackbody spectrum is not completely in the Rayleigh-Jeans tail, i.e., the wavelength dependence is shallower than $B_\nu \propto \nu^2$. Nevertheless, the factor is highly temperature dependent and does not deviate from the two significantly.

thick limit with the assumption μ=1 (the disk is face-on)[7]. The reduction is stronger if the disk is inclined (Zhu et al. 2019; Sierra & Lizano 2020). For the compact particles, the intensity reduction starts at short wavelengths when $a_{\rm max}f < 100$ μm. When $a_{\rm max}f > 1$ mm, the intensity is reduced more at longer wavelengths. As the particles become more porous, the intensity is reduced less for a given $a_{\rm max}f$, and the particle size with the lowest reduction factor becomes smaller. However, the reduction is still substantial if $f \gtrsim 0.1$. The scattering is not crucial for f =0.01, expect for λ = 7.89 mm and $a_{\rm max}f < 1$ cm (with $I_\nu/B_\nu \sim 90\%$).

Now we are ready to present the spectral indices at the optically thick regime in the fourth row of Figure 7.3. For compact particles, the spectral indices are affected the most by the scattering. The spectral indices have a dip with the value $\sim$ 1.7 when $a_{\rm max}f$ is several 100 μm. As the particle size increases, the spectral indices increase and peak at 2.5 when $a_{\rm max}f$ is several mm. The trends at different wavelengths are similar. The peaks and dips are just shifted to larger sizes for longer wavelengths. As the particles become more porous, the dips shift to smaller particles, whereas the peaks shift to larger particles. In the meantime, the amplitudes of the varying spectral indices become smaller. For f= 0.01, the spectral indices for all particle sizes approach two for all wavelengths.

Overall, as the particle becomes more porous, the spectral index approaches ISM values at the optically thin limit and two at the optically thick limit in a vast parameter space.

To complete the prediction on polarization fraction, we show the proxy of polarization fraction, $P\omega_{\rm eff}$, in the bottom row of Figure 7.3. They are similar to the bottom row of Figure 7.2, but with

[7]Note that in some parameter space the intensity can be enhanced by scattering. If the disk is optically thin and its dust has a high albedo, the intensity with scattering can be higher than that without scattering at a face-on view (Sierra & Lizano 2020). This is because the scattering can remove the photons in the optically thick edge-on direction and put them into the optically thin face-on direction.

$a_{\rm max}f$ as the x-axis. The trend is similar to Figure 7.2–the more porous particles have a wider range of $a_{\rm max}f$ to produce high polarization fraction at a give wavelength. For the compact particles, at each wavelength, the polarization fraction has a sharp peak around a specific particle size. The peak is around $a_{\rm max} = \lambda/2\pi$. For 0.87 mm and 1.29 mm, $a_{\rm max}f$ is around 100 μm, which explains why mm polarization observations tend to constrain the particle size to be 100 μm (e.g., Kataoka et al. 2015; Yang et al. 2016). With porosity, however, the window for an $a_{\rm max}f$ that can reproduce a certain polarization fraction becomes wider.

While the wide window of $a_{\rm max}f$ to produce high polarization fraction makes it difficult to constrain the particle size at a particular wavelength, we can potentially probe whether the particles are porous through the wavelength dependence of the polarization fraction. For porous particles, as long as the particle size is larger than several 100 μm, the polarization fraction becomes larger for longer wavelengths. This contrasts with the 100 μm solution, in which the polarization fraction decreases with wavelengths and becomes negligible at VLA/ngVLA (Very Large Array/next-generation Very Large Array) bands ($\lambda \gtrsim$ several mm). With highly porous particles (f=0.01), the polarization fraction is too low to explain the observed polarization fraction (see Figure 7.9 and Tazaki et al. 2019a). This means that if particles are porous, we can constrain the porosity from current observations (see Section 7.6.4). Changing the slope of the particle size distribution can quantitatively change these relations, but the overall trend is the same as long as $q < 4$.

7.4 Analytical Fitting on Continuum

With a comprehensive understanding on the porous particles' optical properties in Section 7.3, we now fit the HL Tau continuum observations using a wide range of possible dust surface density,

temperature, and particle sizes for both compact and porous particles. These best-fit models will be used as inputs for the MCRT simulations in Section 7.5.

7.4.1 Observations

We use the radial profiles reduced in Carrasco-González et al. (2019b) for ALMA bands 7, 6, 4, and VLA Ka+Q bands (at $\sim$ 0.87, 1.3, 2.1, and 7.9 mm, respectively). All images have been convolved to the same angular resolution of $\sim$ 7.35 au (50 mas). Details of the observations and image reduction can be found therein.

7.4.2 Method

We use a Bayesian approach, i.e., P(model|data) = P(data|model)P(model)/P(data), to find the best parameters for the model. The best model is the combination of parameters that maximizes the posterior, P(model|data). To write it out explicitly,

$$\begin{aligned} &\mathrm{P}(T, \Sigma_d, a_{\max} f | I_{\mathrm{B7}}, I_{\mathrm{B6}}, I_{\mathrm{B4}}, I_{\mathrm{VLA}}) \\ &\propto \mathrm{P}(I_{\mathrm{B7}}, I_{\mathrm{B6}}, I_{\mathrm{B4}}, I_{\mathrm{VLA}} | T, \Sigma_d, a_{\max} f) \\ &\quad \times \mathrm{P}(T, \Sigma_d, a_{\max} f). \end{aligned} \tag{7.4}$$

The first term on the right-hand side,

$$\mathrm{P}(I_{\mathrm{B7}}, I_{\mathrm{B6}}, I_{\mathrm{B4}}, I_{\mathrm{VLA}} | T, \Sigma_d, a_{\max} f) \propto \exp(-\frac{\chi^2}{2}), \tag{7.5}$$

is the likelihood of the observations given a combination of parameters, where,

$$\chi^2 = \sum_i w_i \left(\frac{I_{\mathrm{obs},i} - I_{\mathrm{m},i}}{\sigma_i} \right)^2 . \tag{7.6}$$

The $I_{\mathrm{m,i}}$ is the modeled intensity at i band using Equation 7.1, with inclination being 46.72°. The $a_{\mathrm{max}}f$ enters the equation by determining the opacities and effective albedo (κ_{abs}, $\kappa_{\mathrm{sca,eff}}$, and ω_{eff}). Note that we only take q=3.5 as the size distribution in the current section, but we will also present a case with q=2.5 in Section 7.6.3. With the easy-to-use `dsharp_opac` package (Birnstiel 2018), the opacity with any composition and filling factors can be easily generated. Then they can be taken as the input for the analytical fitting. $I_{\mathrm{obs},i}$ and σ_i are the observed intensity and uncertainty at band i. The uncertainty is composed of the azimuthal variation $\Delta I_{\mathrm{obs},i}$ and calibration error $\delta I_{\mathrm{obs},i}$. The total uncertainty reads

$$\sigma_i^2 = (\Delta I_{\mathrm{obs},i})^2 + (\delta I_{\mathrm{obs},i})^2. \tag{7.7}$$

The calibration errors are set to be 10%, 10%, 5%, 5% for ALMA bands 7, 6, 4, and the VLA band. w_i is the weight for each wavelength. Since the VLA band is a combination of Ka and Q bands, we give the weight as 2, whereas all ALMA bands have weights as 1.

The second term on the right-hand side of Equation 7.4 is prior. In previous literature (Macías et al. 2021; Sierra et al. 2021; Ueda et al. 2022), the prior is assumed to be uniform (in logarithmic space) for $a_{\mathrm{max}}f$ and dust surface density within a certain range. We also set uniform priors for $a_{\mathrm{max}}f$ between 0.1 μm to 1 m, and dust surface density from $10^{-1.5}$ to $10^{1.5}$ g cm^{-2}. In addition to the whole particle population model, we also separate the particle population into big particles or

small particles to find the best model within these two populations, similar to Macías et al. (2021); Sierra et al. (2021); Ueda et al. (2022). This is motivated by the dependence of the spectral index on the particle size. As seen from the third row in Figure 7.4, two solutions can be found for a given spectral index[8]. The temperature prior ranges from 10 K to 300 K, but is not uniform, since for several regions in the disk, a uniform prior of temperature makes the temperature unconstrained. This is because temperature and surface density are correlated. The temperature can be fitted infinitely high while the surface density only decreases slightly. Hence, we assign a Gaussian prior with a large scattering to produce more smooth and reasonable temperature profiles. The prior temperature is centered on the following profile,

$$T_p(r) = 200 \text{ K} \times (r/\text{au})^{-0.4}, \tag{7.8}$$

with scattering also being $1 \times T_p(r)$,

$$\mathrm{P}(T, \Sigma_d, a_{\max} f) = \exp\left(-\frac{1}{2} \frac{(T - T_p(r))^2}{T_p(r)^2} \right). \tag{7.9}$$

In this way, the temperature is constrained in a reasonable range while the prior is still loose enough so that the temperature does not collapse onto the Gaussian prior center. A temperature prior is also used in Macías et al. (2021) in which the prior is based on the expected temperature profile for a passively irradiated disk. We fit the intensity profiles from 1 au to 100 au, spacing every 1 au, following Macías et al. (2021); Sierra et al. (2021); Ueda et al. (2022). We note that the neighboring radii are correlated due to the nature of radio images and the much larger beam size (7.35 au). The

[8]This is because the optically-thin spectral indices at ALMA bands have maxima when the particle size is sub-millimeter for compact particles.

temperature grid is spaced every 5 K; the ratio between the neighbouring particle sizes is 1.08; and the ratio between the neighbouring dust surface density is 1.04. We also emphasize that the main focus of this current paper is to explain the observations of the outer HL Tau disk ($\gtrsim$ 20 au) since the inner optically thick part can be substantially affected by dust vertical settling (Ueda et al. 2021). Nevertheless, we will discuss the fitting result at face value throughout the disk, including the inner part.

7.4.3 Results

f=1 (Compact Particles)

Figure 7.4 presents the continuum fitting results for compact particles. The left, middle and right panels are the results for the whole particle population, the small-particle-only ($a_{\rm max}f < 300$ μm) and the big-particle-only ($a_{\rm max}f > 300$ μm) priors. In the top panels, solid lines show the best-fit intensities, and the dashed lines with shaded areas are the observations with 1σ and 2σ uncertainties. The second row shows the best-fit total optical depth $\tau_{\rm tot}$, which is $(\kappa_{\rm abs} + \kappa_{\rm sca,eff})\Sigma_d$ (Equation 7.3). The third to fifth rows show the marginalized posterior for $a_{\rm max}f$, Σ_d and T, respectively. The posterior is normalized by the maximum value within the map. The yellow regions represent a higher probability. The hatched regions are not used in the fitting. The white lines are the best fit models among the 3-D parameter space. The dust masses in each model are also listed in the panels. The sixth row shows the spectral indices for models (solid lines) and observations (dashed lines with shaded areas). The last row shows the value of the posterior probability using the parameters of the best-fit model.

For the compact particles, the big-particle population fits better in the inner disk (<60 au),

whereas the small-particle population fits better in the outer disk (>60 au). The quality of the fitting can be indicated by the intensity profiles, spectral indices, and posterior probabilities. It is noticeable that no model can perfectly fit the VLA data beyond 60 au due to the low signal-to-noise ratio at that region. Considering only small particles, we cannot tightly constrain the particle sizes. They can be between 0.1 μm and 100 μm. For small particles, the fitting within 60 au is not good for three reasons. (a) The best $a_{\rm max}f$ is at the parameter boundary (0.1 μm); (b) spectral indices at two ALMA bands deviate from the observations up to $\Delta\alpha$=1 (also indicated by intensities); (c) the posterior probability is very low. So the small-particle model is not preferred within 60 au. The size can be better constrained with the big-particle population. Within 20 au, the $a_{\rm max}f$ exceeds 1 m; for 20 au $\lesssim r \lesssim$ 40 au, the $a_{\rm max}f$ is around 10 cm; for 40 au $\lesssim r \lesssim$ 60 au, the $a_{\rm max}f$ prefers 1 cm; beyond that the size becomes 1 mm or smaller. The exceedingly large particle sizes within 40 au can be due to a unique opacity feature for the particle size distribution q=3.5. If q=2.5, the particle size can be around several mm within 60 au (see Section 7.6.3, and Figures 7.10 and 7.17). The better constraint on $a_{\rm max}f$, closer matches on intensities and spectral indices, and a higher posterior probability indicate that big particles are better candidates within 60 au.

Big particles have higher opacities, so the inferred dust mass is much lower than using the small particles ($7.4\times10^{-3}\ M_\odot$ vs. $1.0\times10^{-3}\ M_\odot$ beyond 20 au). For the small-particle model, the optical depths for the ALMA bands are $\gtrsim 0.1$ across the disk, whereas the VLA band optical depth is two orders of magnitude lower. For the big-particle model, optical depths at four bands are all close to unity, except for regions beyond 60 au. For the small-particle model, if we assume the gas to dust mass ratio is 100:1, the gas disk mass is even comparable to the stellar mass, meaning that the disk is very gravitationally unstable. The temperature always has the opposite trend as the surface density, so the small-particle model prefers lower temperature. The incentive for separating small

and big particles can been seen on the probability plots for $a_{\rm max}f$ (the third row). Considering both populations, it is clear that the probability has a valley around $a_{\rm max}f$ =300 μm along all radii. Above and below this value, the probabilities are non-zero.

f=0.1 (Porous Particles)

For porous particles with f=0.1, the inner disk still prefers large particles; the outer disk still prefers small particles. The models are shown in Figure 7.5 with the same layout as Figure 7.4. For the small particles, the possible range of $a_{\rm max}f$ is still quite large, from 0.1 μm to 100 μm. The posterior probability is still low. For the big particles, the maximum particle sizes are higher than the compact counterparts. Within 20 au, the $a_{\rm max}f$ exceeds 1 m; for 20 au $\lesssim r \lesssim$ 40 au, the $a_{\rm max}f$ is around 1 m; for 40 au $\lesssim r \lesssim$ 60 au, the $a_{\rm max}f$ prefers 10 cm; beyond that the size becomes 1 mm or smaller. Again, the q=2.5 size distribution can bring the $a_{\rm max}f$ down to mm-cm (see Section 7.6.3, and Figures 7.10 and 7.17). Besides the size difference, small-particle and big-particle models predict similar surface density and temperature since the opacity for the big particles no longer has an interference pattern. The inferred masses for these two species are very high and similar to the small-particle model for compact particles. Keeping the particle size the same, using opacity of big porous particles can lead to a factor of 6.5 dust mass higher than their compact counterparts. Guidi et al. (2022) have a similar finding in HD 163296. Even though the particle size is still difficult to constrain by these observations, different particle sizes lead to similar constraints on the dust surface density and temperature.

Overall, the porous particles can also explain the continuum observations.

In Appendix 7.16, we extend SED fitting by examining additional cases with various combinations of filling factors and particle size distribution slopes. We also discuss more derived quantities,

such as gas-to-dust mass ratio and Stokes number from SED fitting.

7.5 MCRT Fitting and Polarization

We run Monte Carlo Radiative Transfer (MCRT) simulations with two goals. One is to test the 1D analytical fittings on continuum emissions (Section 7.4). In the 1D analytical approximation (Equation 7.1), $\kappa_{\rm sca,eff}$ is the same for any scattering angle (the total scattering opacity is scaled to an isotropic-equivalent value). In MCRT simulations, we use the angle-dependent scattering matrix to capture the anisotropic multiple scattering. Since many models predict marginally optically thick optical depths in HL Tau within $r \lesssim 60$ au, the full treatment of radiative transfer is necessary. The other is to generate linear self-scattering polarization maps to compare with current polarization data and make predictions at longer wavelengths. The metric for polarization fraction, $P\omega_{\rm eff}$ (introduced in Section 7.3) only approximates the case with isotropic single scattering, so the observed polarization fraction from multiple scattering needs to be calculated from a realistic 3D disk setup. Furthermore, even with the exact same particle size and composition, different optical depths and inclinations can lead to different polarization fractions.

7.5.1 MCRT Setup

Radiative transfer simulations are performed with the Monte Carlo radiative transfer code RADMC-3D (Dullemond et al. 2012). The detail of the method can be found in Ueda et al. (2021); Zhang et al. (2021b). Here we only provide a summary.

Vertical Settling. We use many particle species to simulate vertical settling. The particle size distribution is logarithmically divided into 15 particle size bins per decade. The vertical dust

density follows Gaussian profiles,

$$\rho_d(r,a) = \frac{\Sigma_d(r,a)}{\sqrt{2\pi}h_d(r,a)}\exp\left(-\frac{z^2}{2h_d(r,a)^2}\right), \tag{7.10}$$

where z is the vertical height, and h_d is the dust scale height. It is assumed to be in a mixing-settling equilibrium (Dubrulle et al. 1995; Youdin & Lithwick 2007),

$$h_d(r,a) = h_g(r)\left(1+\frac{\mathrm{St}}{\alpha_t}\frac{1+2\mathrm{St}}{1+\mathrm{St}}\right)^{-1/2}, \tag{7.11}$$

where h_g is the gas scale height given as $h_g(r) = c_s(r)/\Omega_K(r)$. c_s is the sound speed. Since we assume the temperature is constant on the vertical direction (i.e., a vertically isothermal disk), c_s is only dependent on r. The Stokes number, St=St(r, a), is

$$\mathrm{St} = \frac{\pi}{2}\frac{\rho a}{\Sigma_g(r)} = \frac{\pi}{2}\frac{\rho_{\rm int} af}{\Sigma_g(r)}. \tag{7.12}$$

This means that different particle species have different scale heights, which depend on the particle size af, particle internal density $\rho_{\rm int}$, local gas surface density Σ_g and turbulence[9] α_t. We adopt α_t = 10^{-4}, and Σ_g = 1000 (r/au)$^{-0.5}$ g cm^{-2}. This gas surface density profile is the same as the one in Ueda et al. (2021). We want to emphasize that the gas surface density here only affects the degree of settling through St. Since St/α_t determines the settling, for a fixed degree of settling (i.e., fixed St/α_t), a different Σ_g essentially means a different α_t. Hence, this adopted Σ_g does not prevent us from assuming different Σ_g in Section 7.6.4. While the vertical settling is crucial for the inner disk $\lesssim$ 20 au (Sierra & Lizano 2020; Ueda et al. 2021), it is not as important in the outer disk, where

[9]we use subscript 't' for the turbulence α to distinguish it from the spectral index α.

it is less optically thick. Thus, we only use one fiducial α_t, which is small enough to enable dust settling. Although dust settling has little effect on the SED and polarization of the outer disk, we include it to keep our models self-consistent. We can also capture the transition between optically thin and optically thick regions. For the DSHARP composition, the internal density, $\rho_{\rm int}$ = 1.675 g cm^{-3}. By definition of the Stokes number (Equation 7.12), we can see that af not only determines the opacity, but also St, therefore the vertical settling.

Radially Varying of $a_{\rm max}f$. To simulate the dust with a size distribution and varying $a_{\rm max}f$ at different radii, we give each dust species a certain weight at each radius, ensuring the particle size distribution still follows a power-law, $n(a) \propto a^{-q}$, with maximum particle size as $a_{\rm max}(r)$. The dust surface density for the i-th species reads,

$$\begin{aligned}
\Sigma_{d,i}(r,a_i) &= \Sigma_d(r)\frac{a_{i+1}^{-q+4}-a_i^{-q+4}}{a_{\rm max}^{-q+4}(r)-a_{\rm min}^{-q+4}}, \\
&\qquad \text{for } r \text{ where } a_{\rm max}(r) > a_{i+1}, \\
\Sigma_{d,i}(r,a_i) &= 0, \\
&\qquad \text{for } r \text{ where } a_{\rm max}(r) <= a_{i+1},
\end{aligned} \tag{7.13}$$

where the fraction after $\Sigma_d(r)$ is the mass fraction of the i-th species, and the sum of all species equals the total dust surface density.

We use the best-fit[10] radial profiles of $a_{\rm max}f$, $\Sigma_{\rm d}$, and T from Section 7.4 (Figures 7.4 and 7.5) as the inputs of MCRT calculations. There are six models in total. Namely, they are whole-population, small-particle-only and big-particle-only models with $f = 1$ and 0.1. These models

[10]"Best-fit" means the most-probable solution under some constraints. For example, the small-particle models can have lower posterior probabilities within 60 au for the continuum observations than the big-particle models.

have a fiducial size distribution q=3.5. Additionally, we also run several cases with $f = 0.01$ and $q = 2.5$, which will be presented in Sections 7.6.2 and 7.6.3.

To produce images, we incline and position the disk the same way as HL Tau. Since we find the best-fit parameters using the data with resolution as 7.35 au (Carrasco-González et al. 2019b), we compare the synthetic images directly with continuum images, without convolving them the second times. A more proper way is to deconvolve the observations, find the intrinsic parameters, use these intrinsic values as inputs to produce MCRT images, then convolve them with the observational resolution. While we have taken the beam effect into account, a different order from the proper way might lead to some error, but they should be less significant than completely ignoring the beam effect when deep gaps are present as discussed in Lin et al. (2020). To compare with polarization images, the MCRT images are smoothed with 30 au 2D Gaussian kernel, similar to the resolutions in observations (Kataoka et al. 2017; Stephens et al. 2017). We still use DSHARP opacity, but use `Optool` (Dominik et al. 2021) to generate opacity including scattering matrices thanks to its faster speed.

7.5.2 MCRT Results

Continuum Radial Profiles

Figure 7.6 shows radial profiles of MCRT models with six best-fit models in Figures 7.4 and 7.5 in ALMA bands 7, 6, 4 and VLA band Q+Ka (from top to bottom in each panel). They are generated by azimuthally averaging images produced by MCRT.

The first row shows the cases for compact particles (f=1). These radial profiles agree with the analytical results in Figure 7.4. From left to right, the dust includes the whole population,

small-particle population and big-particle population, with respect to solutions in Figure 7.4. The continuum emissions deviate from the observations within 60 au for the small-particle model. The small-particle model fits the outer disk ($\gtrsim$60 au) better, whereas the big-particle model fits the inner disk better. The whole population model combines the strengths of these two models.

As for the porous particles (f=0.1), the MCRT (Figure 7.6 lower panels) also agrees with the analytical results in Figure 7.5 largely, but the big-particle model fits the whole disk better. The small particle model under-predicts the emissions from several gaps and rings. Comparing the compact and porous models (top-left and bottom-left), the porous model fits the SEDs better. No models can predict VLA observations beyond 60 au accurately due to low signal-to-noise ratio for those observations in that region.

Integrated Polarization Fractions

Figure 7.7 presents the linear polarization fractions integrated in the central 20 au (blue '+') and within 100 au (orange '+'). The uncertainties of these models are taken to be 50%, as different MCRT codes show this level of variation for the polarization fraction (Kataoka et al. 2015). The observation values in the central 20 and 100 au with error bars (Kataoka et al. 2017; Stephens et al. 2017) are plotted in black. The observed polarization fractions within 100 au are very close[11] to those in the central 20 au. We just use one label to represent observed values from both regions. The polarization fraction is computed from the spatially integrated (within the region of interest) I, Q, and U emissions to average out the azimuthal polarization, focus on the component parallel to the minor axis, and boost the signal-to-noise ratio. A quick summary of observations is the

[11] 0.61% and 0.58% at B7; 0.53% and 0.50% at B6; and below the detection limit (0.1%) at B3 for integrated polarization fractions within 20 au and 100 au, respectively.

following. The polarization fractions are $\sim$ 0.5% at bands 7 and 6 ($\sim$0.87 and 1.3 mm). The linear polarization fraction at band 3 ($\sim$3.1 mm) is non-detection, with the upper limit as 0.1%. However, the self-scattering polarization fraction can still be as high as 0.4% indicated by '$\times$' since the polarization due to radiative alignment can cancel some of the self-scattering component (Mori & Kataoka 2021). Owing to this complication at band 3, we mainly focus on comparing with ALMA bands 7 and 6 observations.

Compact Particles. The upper panels of Figure 7.7 show models with compact particles (f=1). All three models (blue markers) fall short of polarization fractions to explain the bands 7 and 6 data in the inner disk by one order of magnitude. However, with a slight change of parameters, both small-particle and big-particle models can explain the polarization of the inner disk ($\lesssim$ 20 au).

For the small compact particle model ($\lesssim$20 au), the low polarization fraction is because the best-fit $a_{\rm max}f$ is around 0.1 μm in the inner disk, very far from $a_{\rm max}f \sim 100$ μm that can explain the high polarization fractions. Since 100-μm-sized particles are the preferred particle size in previous literature to explain band 7 polarization data (Kataoka et al. 2015; 2016a; Yang et al. 2016), we want to confirm they can produce enough polarization fractions in our setup. In the meantime, we want to test the quality of the SED fitting using 100-μm-sized particles compared to the small-particle model with $a_{\rm max}f$ around 0.1 μm. In Appendix 7.17 and Figure 7.18, we confirm that 100-μm-sized compact particles can explain the polarization fractions as previous studies, and the quality of the SED fitting is similar to that of the 0.1-μm-sized particles.

For the optically-thick inner region ($\lesssim$20 au), Ueda et al. (2021) has demonstrated that vertical settling can hide big particles in the midplane. The small particles on the surface can provide enough polarization. When the settling is very strong $\alpha_t \lesssim 10^{-5}$ (stronger than 10^{-4} adopted here), the $a_{\rm max}f$ = 1 mm case can still provide polarization fractions high enough at bands 7 and 6

at the inner disk (Ueda et al. 2021).

For the outer disk's integrated polarization fractions (< 100 au), the small compact particles (orange markers) can match the observed polarization fractions at bands 7 and 6, since the best solution of $a_{\rm max}f$ is around 100 μm in this region (see Figure 7.4 middle column). The compact-big-particle models cannot produce observed polarization fractions. Since the outer disk is most likely to be optically thin, the big particles cannot be hidden in the midplane. Thus, the compact-big-particle solution is ruled out.

Porous Particles. The lower panels of Figure 7.7 show cases with porous particles ($f = 0.1$). The polarization fractions of both inner and outer disk are much higher for big porous particles compared to big compact particles. Even for $a_{\rm max}f \sim 1$ m, the polarization fractions can match observations at bands 7 and 6. Note that these moderately porous particles (porous agglomerates) have similar properties to the large irregular particles, which can produce high polarization fractions even though their size is very large (Lin et al. 2023). All three models can match the polarization fractions across the disk. For all three models, the outer disks have similar but higher polarization fractions than the inner disks. We find that this is because the outer disk ($\gtrsim$20 au) has optical depths closer to unity, whereas the inner disk ($\lesssim$20 au) has $\tau_{\rm tot} \gg 1$ (see Figure 7.5 right column second row). The polarization is the strongest when the optical depth is around unity (Yang et al. 2017). Several more detailed tests show that the polarization fraction is high enough to match observations as long as $a_{\rm max}f \gtrsim 100$ μm. Overall, the prediction for porous big particles is that at longer wavelengths, the linear polarization fractions are higher than or comparable to bands 7 and 6 ($\sim 0.5\%$).

Polarization Fractions along Major and Minor Axes at ALMA B7

Figure 7.8 presents the linear polarization fraction at ALMA band 7 along major and minor axes as measured in Hull et al. (2018b). The layout for six models are the same as Figures 7.6 and 7.7. Now the polarization fraction is calculated at the sub-beam level as Figure 3 in Hull et al. (2018b). The dashed lines are observations (blue: major axis; orange: minor axis) and solid lines are models. The uncertainties of the observations are taken to be 0.1% as the receiver calibration errors. The model uncertainties are 50% of the central values due to the differences in various MCRT codes (Kataoka et al. 2015).

For compact particles, polarization fractions for big particles are too low to explain the observation. Since the outer disk ($r \gtrsim 30$ au) of HL Tau is optically thin, settling cannot explain the observed polarization fractions that are still high at bands 7, so the compact big particles solution can be ruled out in the outer disk. The small-particle model produces very low polarization in the inner disk and a strong linear polarization fraction at the outer disk. This is because the particle size for the small-particle model in the inner disk is ~ 0.1 μm but becomes ~ 100 μm in the outer disk (the same reason for explaining the difference of integrated polarization fractions between the inner and outer disk for the compact-small-particle model in Figure 7.7; see Appendix 7.17).

If the particle is porous, the parameter space of $a_{\rm max}f$ to explain the high linear polarization fraction becomes larger. Both big-particle and small-particle models can explain the high polarization fraction across the disk, as does their combination. Even though the models over-predict the polarization fraction at the outer disk, we treat them as good matches considering there are larger uncertainties at the outer disk, e.g., contamination from the outflow (Stephens et al. 2017). This means that with porosity, a wide parameter space of $a_{\rm max}f$ ($\gtrsim 100\mu$m) can explain the polarization

observations, which is already reflected in the analytical results of $P\omega_{\rm eff}$ in Figures 7.2 and 7.3.

7.6 Discussion

7.6.1 Dust Mass

Dust mass is one of the most crucial properties of the protoplanetary disks. While our paper focuses on reproducing continuum (SED) and polarization observations jointly with both particle's absorption and scattering features, we want to emphasize that the absorption opacity of the porous particles alone can have crucial impact on the dust mass estimation solely from single-band continuum observations.

Recent SED fitting on hundreds of (spatially-unresolved) protoplanetary disks from optical to mm-wavelengths (Ribas et al. 2020; Rilinger et al. 2023; Xin et al. 2023; Kaeufer et al. 2023) show that the dust masses are on average several times higher than those inferred from single-band (sub)mm fluxes (e.g., Andrews et al. 2013; Ansdell et al. 2016b; Pascucci et al. 2016a; Cieza et al. 2019b; Grant et al. 2021). This inconsistency is mainly attributed to the optically-thin assumption used in these mm single-band studies. With a more proper radiative transfer treatment of the optically thick disks (e.g., using Equation 7.1 or full MCRT), the inferred dust mass can be several times higher (Liu 2019b; Zhu et al. 2019; Liu et al. 2022).

However, perhaps not all protoplanetary disks are massive enough to be optically thick. If dust particles are porous in protoplanetary disks, the dust mass inferred from mm dust emissions can still be underestimated by using the compact particle's opacity at mm wavelengths even in the optically thin region. As indicated by Figures 7.4 and 7.5, the dust mass of HL Tau beyond 20 au inferred by porous-particle whole population model is three times higher than compact-particle

whole population model. If we compare the big-particle populations, the difference can be a factor of six. This is simply due to the Mie interference pattern of the absorption opacity when $\lambda \sim 2\pi a$. Since it is a common practice to presume the dust emissions observed at mm wavelengths are also produced by particles around mm, the opacities are always taken at or near the peak of the Mie interference pattern. This increase of the opacity can be around a factor of six, as shown by Figures 7.1, 7.2, and 7.3, which naturally explains why the dust mass is underestimated by that amount. The SED fitting across the whole spectrum does not suffer from this issue, since the opacities at other wavelengths (where $\lambda \ll a_{\rm max}$) do not show Mie interference pattern, so the compact and porous absorption opacities are almost identical (Figure 7.1 left panels). Even if these wide-wavelength-range SED fitting adopts the compact particles' opacity, only one or several fluxes at mm wavelengths are affected by the Mie interference pattern. This does not lead to a significant bias on the dust mass with the contribution of other tens to hundreds of data points spanning several orders of magnitudes of wavelengths.

7.6.2 More Porous Particles with f=0.01

We want to emphasize that we only study porous particles that belong to *dense aggregates* or *porous agglomerates* with fractal number $d_f \sim 3$ and $f \gtrsim 0.01$ (Güttler et al. 2019) in this paper. More porous particles ($f < 0.01$) are *fluffy agglomerates* that have fractal number $d_f \sim 2$ and different optical properties (e.g., Tazaki et al. 2016; Tazaki & Tanaka 2018). They are inefficient at producing mm dust self-scattering polarization (Tazaki et al. 2019a;b).

In this subsection, we test whether particles with f=0.01 (the lower bound of porous agglomerates' filling factor) can explain SED and polarization observations together. First, we try analytical

fitting of SEDs (see Figure 7.9 left column). The fitting is as good as the case with $f = 0.1$ (Figure 7.5 first column). For simplicity, we omit the temperature, spectral index, and posterior probability rows. The $a_{\rm max} f$ is $\sim$ 1 m for $r \lesssim 20$ au; 10 cm-1 m between 20-60 au; and $\sim$ 100 μm beyond 60 au. The dust mass beyond 20 au is 6.6×10^{-3} $M_\odot$, which is also similar to the case with $f = 0.1$.

Then we run a RADMC-3D (MCRT) simulation for the best-fit model from the analytical fitting and present the result in Figure 7.9 right column. The first row shows that the radial profiles of the intensities under-predict the observations by a small fraction. The second and third rows show that the model predicts non-detectable polarization fractions at ALMA bands 7 and 6. For this reason, it is not a valid solution in HL Tau disk. The very low values of the polarization fractions from the MCRT result can be predicted from $P\omega_{\rm eff}$ in Figures 7.2, 7.3, and 7.11 (also see Tazaki et al. 2019a; Brunngräber & Wolf 2021).

7.6.3 Impact on Different Particle Size Distribution Slope

The particle size distribution slope q is not well-constrained from observations. It may vary from the ISM value (or from the steady state solution between coagulation and fragmentation) of 3.5 or even does not follow a power-law due to the dust growth (Birnstiel et al. 2012). On the observational side, Macías et al. (2021) allow q as another fitting parameter and varying with radius to fit TW Hydrae disk. For that disk, the tightly constrained q value is larger than 3.5 beyond 20 au and can reach 4 at 50 au.

Here we try to study the impact of q by adopting a shallower slope q=2.5, which is more consistent with the dust growth model and SED constraints (D'Alessio et al. 2001). On the practical side, Sierra et al. (2021); Macías et al. (2021) have shown that with q=3.5, the optically thin spectral

indices are always greater than 3, so they cannot find a reasonable solution of $a_{\rm max}$ or otherwise the size is tremendously large. Adopting q=2.5 instead, the solution can be found around several mm (see Figure 4 in Sierra et al. 2021).

The left two columns of Figure 7.10 show the analytical fitting of continuum SEDs for f=1, q=2.5 and f=0.1, q=2.5. It is clear that both cases have much smaller particle sizes compared to their q=3.5 counterparts (Figures 7.4 and 7.5). This difference is due to the different opacity indices of two particle size distribution slopes as pointed out by Sierra et al. (2021); Macías et al. (2021). For the compact case (f=1), $a_{\rm max}f$ is 0.1-1 cm within 60 au, in contrast with 1 cm-1 m solution for q=3.5. Small particles ($\sim$100 μm) are preferred beyond 60 au. The total dust mass beyond 20 au stays almost the same (2.0×10^{-3} $M_\odot$ compared to 2.1×10^{-3} $M_\odot$ in Figure 7.4) when q changes from 3.5 to 2.5.

Similarly, for the porous case (f=0.1, q =2.5), $a_{\rm max}f$ is 100 μm-10 cm within 60 au. The inner 30 au seems to prefer both 100μm and 10 cm sized particles. Small particles ($\sim$100 μm) are also preferred beyond 60 au. Overall, the particle size decreases with increasing radius. The total dust mass beyond 20 au decreases slightly from 5.7×10^{-3} $M_\odot$ (in Figure 7.5) to 4.2×10^{-3} $M_\odot$.

The third column of Figure 7.10 shows the MCRT fitting results. The MCRT model over-predicts the intensities within 60 au and under-predicts them beyond 60 au. The polarization fractions are very similar to the case with q=3.5, f=0.1 (Figures 7.7 and 7.8). This model can match the observed polarization fractions at ALMA bands 7 and 6. We do not show the MCRT results for q=2.5, f=1 case, since they cannot produce enough polarization fractions and the fractions are very similar to the q=3.5, f=1 case (Figures 7.7, and 7.8).

Overall, the q=2.5, f=0.1 model can reproduce both SED and polarization observations. Admittedly, the SEDs from the MCRT do not fit the observations as good as the q=3.5, f=0.1 model

(Figure 7.6) without further tuning. It also predicts smaller particle sizes and slightly less dust masses.

7.6.4 Constraints on Filling Factor and Size Distribution Slope from Current Polarization Observations

With accurate MCRT models, we already know that f=0.1 cases can explain both SEDs and polarization fractions (Figures 7.6, 7.7, and 7.8). However, owing to the computational cost of MCRT calculations, we only generate discrete values of the filling factors (f = 1, 0.1, and 0.01). Using the proxy for polarization fraction, $P\omega_{\rm eff}$, we can further constrain the possible values of f in a continuous range from ALMA bands 7 and 6 polarization observations.

We caution that $P\omega_{\rm eff}$ can be only used as a reference, since the observed polarization fractions are always smaller than $P\omega_{\rm eff}$ due to complicated anisotropic multiple scattering. The exact ratio between the MCRT result and $P\omega_{\rm eff}$ depends on various parameters (e.g., $a_{\rm max}f$, q, dust surface density, disk inclination, etc.). We adopt the conversion factor C=2% (observed polarization fraction is $CP\omega_{\rm eff}$) from Kataoka et al. (2016a), which are calibrated for an HL Tau MCRT model with $a_{\rm max}f \sim 100$ μm, q=3.5, and f=1. This exact suite of parameters is different from our setups. Ideally, we should calibrate as many models as possible. However, this cannot be realized in our situation. As shown in the analytical fitting (Figure 7.17), $a_{\rm max}f$ is always changing with radius. Since the observational beams are large for current polarization observations ($\sim$ 30 au), the contribution of polarization from different particle sizes in different regions are highly mixed. Only an MCRT model with an observational setup can provide a definite value of the polarization fraction.

Figure 7.11 shows $P\omega_{\rm eff}$ for $a_{\rm max}f$ = 1 mm, q=3.5 against the filling factors at various wave-

lengths (red: 0.87 mm, blue: 1.29 mm,, black: 2.14 mm, and magenta: 7.89 mm). Except for λ= 7.89 mm, the polarization fraction has a peak around f=0.1 and drops to a low value when f is small or approaches unity. For ALMA B6 and B7 observations, the observational linear polarization fraction is around 0.5%. Converting to $P\omega_{\rm eff}$ with conversion factor C=2%, we find that $P\omega_{\rm eff}$ should be above 25% (the gray horizontal line). This means that the filling factor f should be from 0.03 to 0.3, or the porosity $\mathscr{P}$ should be 70-97%.

The slope of the particle size distribution also affects the polarization fraction. Typically, a smaller q produces weaker polarization fractions, since a smaller q means less contribution from the small particles that contribute to the high polarization. Fixing $a_{\rm max}f$ and f, we expect a larger q can fit the observed high polarization fractions better. Figure 7.12 shows $P\omega_{\rm eff}$ for two different particle size distribution slopes q (3.5 and 2.5) and various particle sizes $a_{\rm max}f$. For q=3.5 (top panels), when $a_{\rm max}f$ = 1 cm, filling factor $\sim$ 0.1 can still explain the high polarization fraction observed at band 6 and 7. When $a_{\rm max}f$ = 10 μm, only $f \lesssim 0.1$ can explain the observed polarization fraction. For $a_{\rm max}f$ = 100 μm, both q =3.5 (top-middle panel) and 2.5 (bottom-left panel) can explain the observed polarization fraction as long as $f \gtrsim 0.02$. For q=2.5 (bottom panels), $a_{\rm max}f$=1 mm can marginally match the observed polarization fraction only when $f \sim 0.1$. For $a_{\rm max}f$=1 cm, the polarization fractions are too low to explain the observations.

We note again that MCRT simulations are needed to compare with observations closely. As Figure 7.10 shown, the q=2.5, f=1 MCRT model has $a_{\rm max}f \gtrsim$ 1 cm between 30-60 au, so the polarization fractions in that region are expected to be low according to Figure 7.12 bottom right panel. However, the polarization fractions (within 20 au or 100 au) of the MCRT model can still match the observational polarization fractions at ALMA bands 7 and 6. This is because the polarization fractions are mixed with regions that can produce high polarization fractions for $r \lesssim$

30 au and $r \gtrsim 60$ au, where $a_{\rm max} f \sim 100$ μm.

7.6.5 Prediction for Future Observations

Higher resolution polarization observations at bands 7 and 6 can better constrain the particle properties. The current resolution for polarization observations is ~ 30 au. This blends the regions with different particle sizes together (perhaps also q and f). For example, as Section 7.6.4 mentioned, the $q = 2.5$ models should produce less polarization fractions than the $q = 3.5$ when $a_{\rm max} f$ = 1 cm. However, this distinction can be blended by the particles with 100 μm sizes that can produce higher polarization fractions in neighbouring regions. Higher resolution of the polarization observations at bands 7 and 6 can possibly separate the contributions from different parts of the disk.

Even with current angular resolution, we can still learn more on the porosity and particle size if we observe at longer wavelengths. Since only big porous particles can explain both SED and polarization observations between 20 to 60 au, the self-scattering polarization fractions for future longer wavelength observations (ALMA band 1 and ngVLA polarization observations) should be comparable to or higher than 0.5%. If not, one would need to come up with other mechanisms to explain the inconsistency between SED fittings and mm polarization observations.

Ideally, it is easy to test the prediction of the self-scattering polarization at longer wavelengths. The self-scattering polarization is either higher than 0.5% (pointing to large, porous particles) or non-detectable (pointing to small particles). However, the situation is complicated by the ever-stronger azimuthal polarization pattern due to the dust thermal polarization at longer wavelengths (Stephens et al. 2017; Kataoka et al. 2017). The self-scattering dominates at ALMA bands 7 and 6, whereas the dust thermal polarization dominates at band 3. The thermal polarization is thought to

come from the particle alignment, but the underlying mechanism is unclear. Fortunately, the elusive mechanism does not prevent the morphological studies of the observations. The polarization can be decomposed by self-scattering and particle alignment components under some assumptions. After subtracting the dust alignment component, even at band 3, a moderate amount of polarization ($\sim$0.4%) should come from the self-scattering to explain the observation (Yang et al. 2019; Mori & Kataoka 2021; Lin et al. 2022). In principle, we can follow these studies to probe the self-scattering component at longer wavelengths. If the self-scattering component is non-detected, the particle size should be small. Otherwise, it should be large and porous. However, one more complication comes from the assumption of small particle sizes in the Rayleigh regime ($a_{\rm max} \lesssim 100\mu$m) used in these previous studies on the particle alignment. While the patterns are easier to understand in the Rayleigh regime, the size for the big particle is in the Mie regime, where the polarization properties for particle alignment mechanisms are very different (Guillet et al. 2020). Under the large and porous particle scenario, one must carefully study the particle alignment polarization pattern before separating out the self-scattering component at longer wavelengths.

On the observational side, one needs to carefully characterize the free-free emission near the star and subtract its flux contribution before calculating the polarization in the inner disk (Carrasco-González et al. 2016; 2019b). For the outer disk where the emission is weaker, the challenge comes from the requirement of high signal-to-noise ratio (500 for 1% of polarization) and observations with high enough resolution to separate the free-free emission near the star.

7.6.6 Connection to the Near-Infrared Protoplanetary Disk Observations and the Comet 67P Measurements from the Rosetta Mission

Near-infrared scattered light observations are sensitive to micron-sized dust grains/aggregates/agglomerates in the upper atmosphere (several gas scale heights) of the protoplanetary disks. Recently, Ginski et al. (2023) reveal the porosity of the micron-sized particles among 10 disks observed by VLT/SPHERE by deriving the full polarizing scattering phase function of such particles at multiple wavelengths. Micron-sized particles are found to be porous in all the disks in the sample. From the shape of the phase function, they separate the disks into two categories. Category I is linked to fractal agglomerates, whereas Category II is consistent with moderately porous agglomerates with porosity $\sim 50\%$.

Since the mm-cm-sized particles observed in radio observations should have been formed from these micron-sized particles in the past, the mm-cm-sized particles have to grow with some levels of porosity in the beginning. If they formed a long time ago (fast particle growth), they may have formed from fractal agglomerates (Category I). If they formed recently (slow particle growth), they may have been formed from already processed particles with moderately porous agglomerates (Category II). In either cases, we should expect that the mm-cm-sized particles to form with some levels of porosity. This is in agreement with our finding that mm-cm-sized particles are porous in HL Tau (a relatively young protoplanetary disk). From mm self-scattering linear polarization, the level of porosity is roughly constrained to be 70%-97% using $P\omega_{\rm eff}$ (Figure 7.11). At face value, this level of porosity is lower than the Category I fractal agglomerates and higher than the Category II porous agglomerates. However, Category II micron-sized particles alone can be the constituents of the mm-cm-sized porous particles, since the inter micron-sized particles vacuum region can also

contribute to the bulk porosity.

Comets are originated from a population of kilometer-sized icy planetesimals that formed in the solar nebula beyond the snow line. A review by Blum et al. (2022) describes a plausible scenario to form comets as the following steps.

In protoplanetary disks (or the solar nebula, specifically), sub-μm sized particles mainly went through hit-and-stick processes to form up to mm-sized (or even larger) fractal agglomerates with $>95\%$ porosity (Okuzumi et al. 2012; Estrada et al. 2016; 2022; Estrada & Cuzzi 2022). As the fractal agglomerates grew larger and more massive, the increasing collision energy led to compaction of the fractal agglomerates with a higher fractal number and less porosity. Eventually, the growth met the bouncing barrier, where the dust could not grow further and mm-dm-sized pebbles with porosity $\sim 60\%$ formed (Güttler et al. 2010; Zsom et al. 2010; Lorek et al. 2018). Then, these pebbles could concentrate in eddies, vortices, pressure bumps (Johansen et al. 2014) and then by streaming instability (Youdin & Goodman 2005). Once the criterion for gravitational instability was met, the pebble cloud collapsed and planetesmials formed (Johansen et al. 2014). After the gas depletion, these planetesmials went through radiogenic heating (Mousis et al. 2017; Lichtenberg & Krijt 2021; Golabek & Jutzi 2021) and collisional evolution (Jutzi & Asphaug 2015; Jutzi & Benz 2017; Schwartz et al. 2018; Golabek & Jutzi 2021) and became comets. For low mass planetesimals (with radii $\lesssim 50$ km), the integrity of the pebbles can be preserved due to less collisions in the free-fall phase, surface impact during formation, and weaker hydrostatic pressures inside the planetesimals (Bukhari Syed et al. 2017; Wahlberg Jansson et al. 2017; Blum 2018).

The comet 67P/Churyumov–Gerasimenko is a km-sized comet and may well preserve the pristine pebbles through the dust growth. Various instruments on the *Rosetta* mission provide accurate measurements on the dust porosity (see a review by Güttler et al. 2019). Measurements on the bulk

density (Jorda et al. 2016; Pätzold et al. 2016) and the particle's permittivity (Kofman et al. 2015; Herique et al. 2016; Bürger et al. 2023) indicate the nucleus has porosity from 70%-85%. This is consistent with our constraint on the porosity in HL Tau from mm dust self-scattering polarization observations. However, macro-porosity (space between particles, pebbles, or boulders) might also contribute to the bulk porosity, even though the void should be no larger than 9 m (Ciarletti et al. 2017). Blum et al. (2017); Bürger et al. (2023) explain the bulk porosity as the combination of 60% micro-porosity as the result of compaction at the bouncing barrier (Weidling et al. 2009; Zsom et al. 2010) and 80% macro-porosity due to the random packing of these dust particles (Skorov & Blum 2012; Fulle & Blum 2017). If the porosity $\sim$ 60% due to compaction is applicable to the whole disk, the porosity of 70%-97% in HL Tau might indicate the dust is still growing and has not finished the compaction. On the other hand, the exact value of the porosity due to the compaction does depend on the location, dust-to-ice ratio, and the disk model. The quoted value is from the experiments that mimic the condition at 1 au with minimum mass solar nebula (Zsom et al. 2010). For larger radii to the star or increasing dust-to-ice ratio, the porosity due to the compaction can be larger (Lorek et al. 2018). Overall, we find a good agreement with the measurements on the porosity of comet 67P from the *Rosetta* mission.

7.7 Summary of the Constraints and Predictions

In Table **??**, we collect all the results in this paper and in Ueda et al. (2021) to provide a tabular summary of all the possible solutions of HL Tau's particle properties from both SED and polarization observations. We also provide the polarization fraction predictions at longer wavelengths (e.g., ALMA B1 and ngVLA) for these possible solutions. We divide the HL Tau disk into three

regions: within 20 au, where the disk is optically thick; 20-60 au, the major focus of our paper, where the disk has $\tau_{\rm tot} \lesssim 1$; and 60-100 au, where the signal-to-noise ratio for the VLA data is low. In Table **??**, each line presents a combination of porosity and particle size, following their viabilities of fitting current SED and polarization observations (marked by crosses or ticks), and predictions for polarization fractions at longer wavelengths. Only when two green ticks are on the same line, it is a viable solution.

7.7.1 1-20 au

Within 20 au, we find that big particles fit the SEDs better than small particles, regardless of the porosity (Figures 7.4, 7.5, and 7.6). For compact particles, small particles are needed to explain the high polarization fractions (Figures 7.7, and 7.8). For porous particles, both small and big particles with $f = 0.1$ can explain the high polarization fractions (Figures 7.7, and 7.8). For $f = 0.01$, neither small nor big particles can reproduce high polarization fractions (Figure 7.9). In summary, the only viable solution is big porous particles with f=0.1. We predict that polarization fractions are high ($\gtrsim 0.5\%$) at longer wavelengths (e.g., ALMA B1 and ngVLA). However, Ueda et al. (2021) show that vertical settling can make small compact particles a viable solution as well. Since the optical properties between small compact and small porous particles are similar, we believe small porous particle is also a viable solution (for this reason, we also list the prediction for this model, even though we mark a cross under the SED column). For these two small particle solutions, we expect non-detectable polarization fractions ($<0.1\%$) at longer wavelengths. Thus, future polarization observations at longer wavelengths can distinguish the big and small particle solutions.

7.7.2 20-60 au

Between 20-60 au, the situation is very similar to the case within 20 au. The only difference is that the optical depth becomes smaller in this region, so the particle vertical settling cannot hide big particles in the midplane. Thus, the only viable solution is $f = 0.1$ porous big particles, which is underlined in the table. With the help of $P\omega_{\rm eff}$ in Figure 7.11, we can optimistically loosen the possible f to be from 0.03-0.3.

Since the region between 20-60 au is of our primary focus, we use Figure 7.13 to visualize the process that eliminates other possible situations. The left two columns show compact cases with small and big particle models for f=1. The right two panels show porous cases for f=0.1. In the upper row, we take the spectral indices in Figures 7.4 and 7.5 to demonstrate the quality of SED fitting. In the lower row, we use the integrated polarization fractions within 100 au to demonstrate the quality of polarization fraction fitting, and also the predictions at longer wavelengths. If the model matches the observations, we mark the plot in green and labeled it as a green tick. If the model does not match the observations, we mark the plot in red and labeled it as a red cross. It is clear that only the $a_{\rm max}f > 100$ μm, f=0.1 model can explain both SED and polarization observations. At ALMA B1 and ngVLA wavelengths, the self-scattering linear polarization fraction should be high ($\gtrsim 0.5\%$).

7.7.3 60-100 au

The constraint is not strong between 60-100 au due to the poor signal-to-noise ratio of VLA data. Still, we describe the results at face value. In general, this region prefers small particles. For f=1, small particles can explain both SED and polarization observations (Figures 7.4, 7.6, 7.7, and 7.8).

This model predicts non-detectable polarization fraction at longer wavelengths. Big particles fail to explain both types of observations. For f=0.1, both small and big particles can explain both types of observations (Figures 7.5, 7.6, 7.7, and 7.8). Whether polarization fractions are high or not at longer wavelengths can distinguish the particle size. For f=0.01, both big and small particles can explain the SEDs, similar to the f=0.1 cases. However, both of the particle sizes fail to explain the polarization fractions at ALMA bands 7 and 6 (Figure 7.9).

7.8 Conclusion

We use porous particles to explain the inconsistency of the particle size constraints between the radio SEDs and mm polarization observations. We first explore the optical properties of particles with different porosities at different wavelengths. Then we test out our finding using the HL Tau disk. We use a Bayesian approach to fit the multi-wavelength continuum observations (SEDs) under different filling factors, taking the particle size, dust surface density, and temperature to be free parameters. With the obtained best solutions, we run Monte Carlo Radiative Transfer (MCRT) to make a closer comparison with SED (at ALMA bands 7, 6, 4, and VLA Q+Ka band) and polarization observations (at ALMA bands 7 and 6). Our main findings are as follows:

1. The porous particles have closer-to-unity refractive indices than compact particles. This makes the Mie interference pattern at mm wavelengths for mm-cm-sized particles disappear (Figures 7.1, 7.2, and 7.3).

2. The high opacity at mm wavelengths due to the Mie interference is unique to compact mm-cm-sized particles. This means that dust mass estimated using porous particles can be a factor of six or higher than compact particles (Figures 7.4, 7.5, and 7.17).

3. For compact particles, only 100-μm sized particles can provide enough polarization fractions at ALMA bands 7 and 6. For porous particles, the window for a high polarization fraction becomes much broader, leaving larger porous particles (f=0.03-0.3, $a_{\rm max}f \gtrsim 100\mu$m) a valid solution for the polarization observations (Figures 7.2, 7.3, 7.11, and 7.12).

4. We adopt a fiducial particle size distribution slope q=3.5. We find that the major impact on changing q from 3.5 to 2.5 is that the best solution's particle sizes can go down from 10 cm-1 m to 1 mm-10 cm. The estimated dust mass can also decrease slightly (Figures 7.5, 7.10, and 7.17).

5. Using MCRT, we demonstrate that f=0.01 cases cannot provide enough polarization fractions at ALMA B7 and B6, regardless of the particle size (Figure 7.9).

6. Combining SED and polarization fittings from analytical approximation and MCRT, we summarize the viable solutions of particle sizes and porosities in the table in Zhang et al. (2023b). In the table, we study the disk in three regions (1-20 au, 20-60 au, and 60-100 au), separated by small and big particle solutions, and three different filling factors (f = 1, 0.1, and 0.01).

7. In Table **??**, we also provide predictions for future polarization observations at longer wavelengths (e.g., ALMA B1 and ngVLA) that can distinguish the small and big particle solutions.

8. For radii between 20-60 au, we demonstrate that only f = 0.1, $a_{\rm max}f \gtrsim 100\mu$m MCRT model can explain both types of observations (Figure 7.13). With the help of $P\omega_{\rm eff}$ (an analytical proxy for polarization fraction), the allowable filling factors can be optimistically

relaxed to 0.03-0.3, which translates to porosities between 70%-97% (Figure 7.11).

9. We predict that we will observe higher linear self-scattering polarization fractions at ALMA B1 and ngVLA bands than ALMA B7 and B6 ($\sim$0.5%) when they are integrated within 100 au (Figure 7.13).

10. We find that the existence of porous particles in HL Tau disk and their levels of porosity are consistent with near-infrared scattered light observations of protoplanetary disks and characterization of the comet 67P from the *Rosetta* mission (Section 7.6.6).

7.9 Validity of the Effective Medium Approximation

In reality, dust particles can have different shapes and porosities, but it is unrealistic to measure the optical properties of each individual particle. Fortunately, the overall optical properties as an ensemble of heterogeneous particles can be well captured by the effective medium approximation (EMA) when $2\pi a_{\rm inc}/\lambda \ll 1$, where $a_{\rm inc}$ is the characteristic radius of the *inclusion*, rather than the dust particle's radius, a (Mishchenko et al. 2000). We choose the "Bruggeman" mixing rule to calculate all the optical properties throughout the paper, following Birnstiel et al. (2018). With this mixing rule, direct comparisons with experiments and direct dipole approximations (DDAs[12]) show that the error of angular dependent extinction property can be as low as 1% when $2\pi a_{\rm inc}/\lambda < 0.1$, and 10% even when $2\pi a_{\rm inc}/\lambda = 2$ (Mishchenko et al. 2000 and references therein). In our application, for $\lambda \sim 1$ mm, we need to assume the inclusions to be $\lesssim 200$ μm for the EMA to work, which should be a valid assumption as particles in the ISM have much smaller sizes ($< 1\mu$m). Recently, Tazaki et al. (2023) constrain the monomer sizes of the small particles on the

[12]a more accurate but more time-consuming method to calculate opacity.

atmosphere of IM Lup to be less than 0.4 μm. If we assume the big particles in the midplane are constituted of similar monomers, the EMA should be very accurate.

7.10 Key Parameters

The size parameter,

$$x = \frac{2\pi a}{\lambda}, \tag{7.14}$$

is a dimensionless parameter that characterizes the size of the particle, where a is the physical radius of the particle, and λ is the wavelength. We can separate the particle size into three regimes with the size parameter. When $x \ll 1$, the particle is small and in the Rayleigh regime. When $x \sim 1$, the particle is in the Mie regime. When $x \gg 1$, the particle is in the geometric regime. For spherical particles, the complex refractive index m fully determines the dust's optical properties, where

$$m(\lambda) = n(\lambda) + ik(\lambda), \tag{7.15}$$

where n is related to the scattering and k is associated with the absorption. However, both the reflective index's real and imaginary parts participate in calculating the dimensionless absorption and scattering properties, namely $Q_{\rm abs}$ and $Q_{\rm sca}$, the absorption and scattering efficiencies. They are the ratios between the absorption/scattering cross sections over the geometric cross-sections (e.g., πa^2, for a spherical particle).

These efficiencies can be converted to the mass opacity commonly used in observations,

$$\kappa_{\rm abs} \equiv \frac{\pi a^2}{\mathscr{M}} Q_{\rm abs} = \frac{3/4}{\rho_{\rm int} a f} Q_{\rm abs}, \tag{7.16}$$

and

$$\kappa_{\rm sca} \equiv \frac{\pi a^2}{\mathscr{M}} Q_{\rm sca} = \frac{3/4}{\rho_{\rm int} a f} Q_{\rm sca}, \tag{7.17}$$

where the $\mathscr{M}$ is the particle's mass, $\rho_{\rm int}$ is the internal density of the compact monomer that forms dust particles, and f is the filling factor (1-$\mathscr{P}$). It is worth noting that the scattering opacity in Equation 7.17 often needs to be adjusted with the forward-scattering parameter g (Ishimaru 1978; Bohren & Huffman 1983; Birnstiel et al. 2018). That is, we should use the effective scattering opacity, $\kappa_{\rm sca,eff} = (1\text{-}g)\kappa_{\rm sca}$. This is because the forward scattering becomes dominant when the size parameter $x > 1$. Since the forward scattering is effectively not scattering, this fraction must be adjusted in all the calculations related to scattering. The (effective) extinction opacity is the sum of the absorption and (effective) scattering opacity,

$$\kappa_{\rm ext} = \kappa_{\rm abs} + \kappa_{\rm sca}, \tag{7.18}$$

and

$$\kappa_{\rm ext,eff} = \kappa_{\rm abs} + \kappa_{\rm sca,eff}, \tag{7.19}$$

and the (effective) albedo is the fraction of (effective) scattered light among the total radiation,

$$\omega = \frac{\kappa_{\rm sca}}{\kappa_{\rm sca} + \kappa_{\rm abs}}, \tag{7.20}$$

and

$$\omega_{\rm eff} = \frac{\kappa_{\rm sca,eff}}{\kappa_{\rm sca,eff} + \kappa_{\rm abs}}. \tag{7.21}$$

The albedo is important in both modeling dust continuum when the disk is optically thick (e.g.,

Zhu et al. 2019) and the polarization. For the latter, it determines the fraction of the incident light that is scattered. Among the available scattered light, the fraction that produces polarized light is characterized by P, where P = -$Z_{12}(a,\theta)/Z_{11}(a,\theta)$ at θ = 90°[13]. θ is the scattering angle between the scattered light and the incident light. Z_{11} (relating to the total scattering by $\kappa_{\rm sca}(a) = \oint Z_{11}(a,\theta)\,{\rm d}\Omega$) and Z_{12} (the linear polarized scattering) are elements in the scattering matrix (or Mueller matrix, e.g., see the appendix of Kataoka et al. 2015). The product of P and $\omega_{\rm eff}$ indicates the total polarization fraction. Note that the $P\omega_{\rm eff}$ is typically much higher than the polarization fraction measured from MCRT synthetic images, so a conversion factor C is often used to convert the analytical prediction to the MCRT value. Thus, the MCRT value used to match observations is $CP\omega_{\rm eff}$, where C is normalized to be $\sim 2\%$ (Kataoka et al. 2016a) for 100-μm-sized particles in the HL Tau model.

7.11 Analytical Approximations

Suppose the refractive index of the compact particle mixture is m_c, the effective medium approximation (Maxwell-Garnett rule[14]) gives the refractive index of the porous particle as (Kataoka et al. 2014)

$$m_p^2 = \frac{1+2fF}{1-fF}, \tag{7.22}$$

[13]We follow the convention by taking the polarization fraction at 90°. In the Rayleigh regime, this is valid since polarization fraction peaks at 90°. As $x \gtrsim 1$, the polarization fraction no longer peaks at 90°, e.g., see Figure 2 in Kataoka et al. (2015). Still, the value at 90° can be a good indicator of the amplitude of the polarization fraction at the peak.

[14]Throughout the paper, we use the Bruggeman rule to calculate the refractive index as it is more accurate for our problems. Here we use Maxwell-Garnett rule to derive the analytical approximation following Kataoka et al. (2014), since it is a much simpler expression. It can also capture the overall behavior of the opacity.

where

$$F(\lambda) = \frac{m_c^2 - 1}{m_c^2 + 2}. \tag{7.23}$$

The squares in these equations are the multiplication of complex numbers, so m_p, m_c and F are all complex numbers. When $f < 1$, it can be shown that

$$n - 1 \approx \frac{3}{2} f \mathrm{Re}(F), \tag{7.24}$$

and

$$k \approx \frac{3}{2} f \mathrm{Im}(F), \tag{7.25}$$

so $n - 1 \propto f$, and $k \propto f$. For reference, the compact DSHARP mixture (Birnstiel et al. 2018) has the refractive index n=2.3 and k=0.02 at 1 mm. With increasing porosity, the real part of the refractive index n-1 at 1 mm are 1.3, 0.28, 9.0×10^{-2}, and 8.8 $\times10^{-3}$ for f=1, 0.3, 0.1 and 0.01 . The imaginary part k are 2.0×10^{-2}, 2.7×10^{-3}, 8.2×10^{-4}, 7.9×10^{-5}. Taking the ratio of the neighbouring refractive indices between two filling factors, we find that the refractive index ratio is closer to the filling factors' ratio (as expected from Equations 7.24 and 7.25) when the mixture is more porous. In other words, the approximation is better for smaller f. It is also worth noting that for radio wavelengths, n-1 $\gg k$.[15] A recent analysis on *Rosetta*/MIRO data constrains the refractive index of mm-cm-sized pebbles from sub-surface of comet 67P to be n = 1.074-1.256 and k = (2.580-7.431) $\times10^{-3}$ (Bürger et al. 2023) at 1.594 mm. This is similar to the DSHARP refractive index at 1 mm with $f \sim 0.1$.

[15]For further references, the refractive index of the DSHARP opacity can be found in Figure 2 in Birnstiel et al. (2018). Refractive indices across all the wavelengths can be seen in Figure A.1. in Kataoka et al. (2014). The dependence of refractive indices on wavelengths and levels of porosity can be reproduced using Birnstiel (2018) under `notebooks/porosity.ipynb`.

Three regimes for analytical approximations are the *Rayleigh* regime, the *Mie's optically thin* regime, and the *Mie's optically thick* regime. Note that the optical depth here refers to the optical depth inside a particle. The boundaries between these regimes are at $x = 1$ and $kx = 3/8$ (for absorption) or $(n-1)x = 1$ (for scattering). They are marked by solid vertical lines ($x = 1$) and dashed vertical lines ($kx = 3/8$ or $(n-1)x = 1$) in Figure 7.1, where the x-axes are the wavelengths. For compact particles, the Mie's optically thin regime can be very narrow or even does not exist. It is also worth noting that kx and $(n-1)x$ are all proportional to the product of particle size and filling factor, af (Equations 7.14, 7.24, 7.25). Thus, the location of the dashed lines is almost constant for different f with the same af, as long as f is small.

Combining three regimes, the approximation of the absorption efficiency is (Kataoka et al. 2014; Bohren & Huffman 1983)

$$\begin{aligned} Q_{\rm abs} &= \frac{24nkx}{(n^2+2)^2} \\ &\quad \text{for } x < 1; \\ &= \frac{8kx}{3n}\left(n^3 - (n^2-1)^{3/2}\right) \\ &\quad \text{for } x > 1 \text{ and } kx < 3/8; \\ &= 1 \\ &\quad \text{for } x > 1 \text{ and } kx > 3/8. \end{aligned} \tag{7.26}$$

Using Equations 7.24 and 7.25, the mass opacity can be written as,

$$\begin{aligned} \kappa_{\rm abs} &\propto \frac{{\rm Im}(F(\lambda))}{\lambda} \text{ for } x < 1 \text{ or } kx < 3/8; \\ &\propto \frac{1}{af} \quad \text{for } x > 1 \text{ and } kx > 3/8. \end{aligned} \tag{7.27}$$

The upper left panel of Figure 7.1 shows the single sized (af=160 μm) absorption opacity as a function of wavelength. Blue lines represent the compact particles, whereas orange, green and red lines represent porous particles with filling factors f= 0.3, 0.1 and 0.01. Dotted lines show the analytical approximation from Equations 7.26 or 7.27. The direct calculation and the analytical approximation are in excellent agreement.

In the Rayleigh regime ($x < 1$), the mass opacity does not depend on the particle size or porosity. To understand this, we can divide the dust particle into the smallest unit–atom or molecule (Moosmüller & Arnott 2009). We call them scatterers. Each scatterer has its own cross section, $\sigma_{\rm abs,i}$. The total cross section is proportional to the total number of the scatterers, $NV\sigma_{\rm abs,i}$, where N is the number density of the scatterers and V is the volume. N=$\rho/m_{\rm mol}$, where $m_{\rm mol}$ is the mass of the scatterer. On the other hand, the absorption mass opacity $\kappa_{\rm abs}$ is the total cross section divided by its mass, which is $NV\sigma_{\rm abs,i}/\rho V \propto \sigma_{\rm abs,i}/m_{\rm mol}$. This means that in the Rayleigh regime, the mass opacity is only dependent on the microscopic property of the particle along the wavelength, independent of the particle size and the filling factor. At long wavelengths, the opacity changes as $\lambda^{-1.7}$, and ${\rm Im}(F) \propto \lambda^{-0.7}$ (not shown here, but can be seen using the DSHARP refractive index m_c), in agreement with the approximation that $\kappa_{\rm abs} \propto {\rm Im}(F)/\lambda$ (Equation 7.27).

In the geometric regime (or Mie's optically thick regime), the opacity is inversely proportional to af, as the absorption cross section equals the geometric cross section ($Q_{\rm abs} = 1$). The opacity is independent of the wavelength in this regime.

In Mie's optically thin regime, a unique feature for compact particles is the interference feature, in which the opacity is much higher than its porous counterparts. This interference is partially captured by the analytical approximation (dotted lines). From the viewpoint of elementary optics, it is the interference between the incident and forward-scattered light at Mie's optically thin regime.

The amplitude of the absorption efficiency is proportional to m+1/m, and the separation between maxima is 1/2a(m-1) (Equations 4.63 and 4.64 in Bohren & Huffman 1983). Since $n-1 \gg k$, the amplitude ($\approx n+n^{-1}$) reaches a minimum when n approaches unity. The n of the more porous particles is closer to unity. The separation between peaks also becomes $1/f$ wider.

Overall, the analytical approximations closely match the single-sized absorption opacity. The opacity in all three regimes can be expressed in terms of af. For this reason, we use af to represent the particle size throughout the paper, as advocated by Kataoka et al. (2014).

7.12 Scattering Opacity

The scattering opacity is shown on the right panels of Figure 7.1. Similar to the absorption opacity, the scattering opacity can also be divided into three regimes, separated by $x = 1$ (solid vertical lines) and $(n-1)x = 1$ (dashed vertical lines). The analytical approximation fits the single-sized un-adjusted scattering opacity closely, except at $(n-1)x = 1$. Here, we emphasis the importance of adjustment for forward scattering by comparing dashed ($\kappa_{\rm sca,eff}$) and solid lines ($\kappa_{\rm sca}$). We can clearly see that the forward-scattering-adjusted scattering opacity has significantly lower values in the Mie regime ($x \gtrsim 1$). This is why we must use the effective scattering opacity when the particle size is comparable or larger than the observing wavelengths.

The scattering efficiency can also be approximated in the three regimes (Kataoka et al. 2014;

Bohren & Huffman 1983),

$$
\begin{aligned}
Q_{\rm sca} &= \frac{32}{27}x^4\left((n-1)^2+k^2\right) \\
&\quad \text{for } x<1; \\
&= \frac{32}{27}x^2\left((n-1)^2+k^2\right) \\
&\quad \text{for } x>1 \text{ and } x(n-1)<1; \\
&= 1 \\
&\quad \text{for } x>1 \text{ and } x(n-1)>1.
\end{aligned}
\tag{7.28}
$$

Using Equations 7.24 and 7.25, the mass opacity can be written as,

$$
\begin{aligned}
\kappa_{\rm sca} &\propto \frac{a^3 f}{\lambda^4}|F(\lambda)|^2 \text{ for } x<1; \\
&\propto \frac{af}{\lambda^2}|F(\lambda)|^2 \text{ for } x>1 \text{ and } x(n-1)<1; \\
&\propto \frac{1}{af} \qquad \text{for } x>1 \text{ and } x(n-1)>1.
\end{aligned}
\tag{7.29}
$$

The upper right panel of Figure 7.1 shows the analytical approximation against the DSHARP opacity at af =160μm for particles with various levels of porosity. These approximations also match the Mie calculations quite well, except around $(n-1)x$=1 due to the interference pattern.

In the Rayleigh regime, the scattering opacity is no longer proportional to the af (with $\lambda \gtrsim$ 0.1 cm in the right panels of Figure 7.1). Unlike the absorption light, the scattered light is due to individual scatterers radiating *in phase*. The scattered light energy is proportional to the square of the number of scatterers, $(NV)^2$. Thus, the mass opacity is $(NV)^2\sigma_{\rm sca,i}/\rho V \propto a^3 f \sigma_{\rm sca,i}\rho_{\rm int}/m_{\rm mol}^2$. The λ^{-4} dependence in Equation 7.29 can also be deduced by dimensional analysis (Moosmüller & Arnott 2009).

In the geometric regime (Mie's optically thick regime), the scattering efficiency approaches unity, so the mass opacity is inversely proportional to af. The opacity for different levels of porosity overlaps, given the same af. The opacity does not depend on the wavelength. However, forward scattering dominates in this regime, so the forward scattering parameter g is almost unity. After removing the forward scattering, the effective scattering opacity is nearly zero. The dashed lines show the effective scattering opacity. They are much lower than the unadjusted scattering opacity, with even lower values for more porous particles. Due to the forward scattering, the scattering opacity becomes wavelength-dependent.

In Mie's optically thin regime, the mass opacity is proportional to af and λ^{-2}. This regime is narrow for compact particles but wider for more porous particles. The forward scattering starts to dominate in this regime, so forward scattering adjustment is also necessary.

The analytical approximations also closely match the single-sized scattering opacity ($\kappa_{\rm sca}$, without adjustment). Aside from the Rayleigh scattering, the opacity in other regimes can be expressed in terms of af. However, the analytical approximations cannot capture the effective scattering opacity with the adjustment of the forward scattering, due to the g factor.

7.13 Polarization Fraction at 90°

While the albedo is just the scattering and extinction opacity ratio, the effective albedo, $\omega_{\rm eff}$, is difficult to characterize using analytical approximation. The same goes for the polarization fraction at 90°, P, which is also a scattering property. Nevertheless, we describe the behavior of albedo (left panels) and polarization fraction (right panels) in Figure 7.14 since they are crucial to predicting the observational polarization fraction. The values approach unity at Mie's optically

thin regime (between dashed and solid vertical lines) for un-adjusted scattering albedo. The albedo drops to zero at the Rayleigh regime (longer wavelengths). At the Mie's optically thick regime (shorter wavelengths), the albedo is 1/2, since the $Q_{\rm abs} = Q_{\rm sca} = 1$ (Equations 7.26, 7.28). After the adjustment of the forward scattering, the albedo in the whole Mie's regime drops to nearly zero, leaving only large values around $x = 1$. The situation is similar with a particle size distribution, albeit moderate values at shorter wavelengths contributed from small particles.

The polarization fraction P is shown on the right panels of Figure 7.14. The value can be either positive or negative. When the value is positive, the polarization direction is perpendicular to the incident direction of the radiation. When the value is negative, the polarization direction is parallel to the incident radiation, also called "polarization reversal" (e.g., Murakawa 2010; Kirchschlager & Wolf 2014; Kataoka et al. 2015; Yang et al. 2016; Brunngräber & Wolf 2019). The transparent lines on the top panel are the single-sized P. They have oscillating behavior between positive and negative values in the Mie regime. After averaging the values of the Z_{11} and Z_{12} in the 20 neighboring sizes, the polarization fraction becomes positive in most of the wavelengths but has zero or negative values around $(n-1)x = 1$. As the particle becomes more porous, this dip becomes narrower with higher values, which means that the available window for high polarization fraction becomes wider for more porous particles. For $f = 0.01$, the polarization fraction is unity across all the wavelengths. A particle size distribution makes the polarization fraction in the Mie's optically thick region (at shorter wavelengths) much lower, but it does not affect more porous particles. We restrain the discussion on why more porous particles have larger P in the Appendix 7.14.

For compact particle, the effective albedo peaks at $x(n-1) = 1$, and the polarization fraction drops sharply for $x > 1$. This leaves only a narrow range of wavelengths and sizes that can explain the high polarization fraction in ALMA observations. The sharp drop of P at $x(n-1) = 1$

narrows the range once again. Increasing the porosity does not widen the window of high-value effective albedo (the peak value even decreases for f=0.01). Instead, the significant difference for porous particle lies in constantly high values of P. Most of the scattered lights are polarized for more porous particles, so only the effective albedo determines the observational polarization fraction. This leaves a much broader window of particle sizes to explain high polarization fractions in observations (Tazaki et al. 2019a).

7.14 More on Polarization Fraction P

We use Figure 7.15 to show why more porous particles have constantly higher polarization fraction P. The scattering matrix elements Z_{11} (blue lines) and Z_{12} (green lines) at 90° are shown for various filling factors at λ= 1 mm. The single-sized values are represented in solid lines, whereas the values with particle size distributions are represented in dashed lines. Since P=-$(Z_{11}/Z_{12})|_{90^\circ}$, the P is unity as long as $Z_{11}|_{90^\circ}$ and $Z_{12}|_{90^\circ}$ are symmetric against zero. This is the case for $x < 1$ (on the left of the vertical dotted line). However, as $x > 1$, both values become very large and oscillate with ever smaller amplitudes. The P is very sensitive to the wavelength and particle size for single sized particles. On the other hand, the size distribution can average out this interference pattern, but the asymmetry between the two components is still strong for compact particles. At particular locations, $Z_{12}|_{90^\circ}$ can also be positive, so the polarization reversal occurs. As the particles become more porous, $Z_{12}|_{90^\circ}$ becomes more symmetric to the $Z_{11}|_{90^\circ}$. Thus, the polarization fraction becomes constantly high. An intuitive way to understand the polarization fraction is to make an analogy to the scattering between particles, where a single scattering produces polarized light, and multiple scattering depolarizes light. Similarly, within a particle, the Mie solution can

be thought of as a summation of the waves scattered by individual discrete dipole sub-elements in which the coherency comes into play to determine the net behavior of the single particle's polarization. As the size parameter becomes larger, the particle becomes more optically thick within the particle and the summation of individual waves become incoherent. This is why P is very low when $x > 1$ for compact particles. For porous particles, as $f \ll 1$, the refractive index is closer to that of the vacuum and becomes more optically thin, so it preserves the high polarization fraction for a large size parameter (Tazaki et al. 2019a).

7.15 Comparison to Carrasco-González et al.

In Carrasco-González et al. (2019b), the $a_{\rm max}$ from analytical fitting is around mm, but in this paper the $a_{\rm max} f$ can be as high as 1 m, under the same assumption of particle size distribution q=3.5. We demonstrate that this is due to the different fitting approaches in these papers. We first use the opacity in Carrasco-González et al. (2019b) to fit the disk, shown in the left panels of Figure 7.16. The result is very similar to the DSHARP in Figure 7.4 since the opacity used in the study originated in D'Alessio et al. (2001) is very similar to the DSHARP one, except for a higher water fraction. Hence, the difference in the results should be in the fitting method. In Carrasco-González et al. (2019b), the opacity and albedo are fitted with power laws, and then the radiative equations are solved iteratively using the observations from four bands. In their paper, the albedo is assumed to be constant, $\omega_{\rm eff} = 0.9$. However, the result of particle size is very sensitive to the albedo. A constant albedo might not be a good assumption since, for most of the particle sizes, the albedo varies with wavelengths drastically. A constant albedo might be valid only when $a_{\rm max}$ is ~ 1 mm. That is why their solution is around 1 mm. In the right column of Figure 7.16, we artificially

set the $\omega_{\rm eff}$ to be 0.9 for all wavelengths. The best-fit $a_{\rm max}$ becomes $\sim$ 1 mm, very close to the result in Carrasco-González et al. (2019b). Additionally, Carrasco-González et al. (2019b) does not consider the small particle population with $a_{\rm max} \lesssim 100$ μm. This work has no such assumption, and a more expansive parameter space has been explored. That is why the best-fit solution at the outer disk ($\gtrsim$ 60 au) are very small particles $\lesssim 100$ μm. Considering these factors, we do not find conflicting results between these papers.

7.16 More Constraints on Dust Properties from SED Fitting

We use analytical approximations to explore a larger parameter space of filling factors and particle size distributions to complement the observational constraints from MCRT models. The analytical approximations are less accurate than MCRT models, but they are less computational expensive. They can cover a broader and finer parameter space so we can have a better understanding on how different parameters are interconnected.

We describe the constraints on dust surface density, gas-to-dust mass ratio, maximum particle size, Stokes number in Figure 7.17 using current SED observations. Although the dust surface density and maximum particle size have been reported for individual models (Figures 7.4, 7.5, 7.9, and 7.10), now we collect them together since they are crucial to deriving other quantities.

7.16.1 Dust Surface Density

The first row of Figure 7.17 shows the dust surface densities in blue lines for various filling factors (f=1, 0.1, and 0.01, from left to right). They are obtained from the whole-population models (Figures 7.4, and 7.5 first columns, and Figures 7.9, and 7.10). More opaque colors are for q=3.5

and more transparent colors are for q=2.5. From compact to porous cases, the dust surface densities can increase several times within 60 au. Between f=0.1 and 0.01 cases, the dust surface densities are similar. For all three filling factors, the densities are similar beyond 60 au. The densities for q=2.5 cases are less than the q=3.5 cases by a small amount, but this difference is less significant than the change when we switch from compact particles to porous particles. The inner disk ($r \lesssim$ 20 au) for f=1 sees a factor of 5-10 difference between two size distribution slopes, and this is because the $q = 2.5$ solution picks up the small-particle population and the $q = 2.5$ solution falls into the big-particle population.

7.16.2 Gas-to-Dust Mass Ratio

With the obtained dust surface densities, we can estimate the maximum gas-to-dust mass ratio. This is done by calculating the maximum gas surface density when the disk becomes gravitationally unstable. This happens when $Q \lesssim 1$, where

$$Q = \frac{c_s \Omega_K}{\pi G \Sigma_g}. \tag{7.30}$$

c_s is the sound speed, and c_s=$(RT/\mu)^{1/2}$; R is the gas constant, μ is the mean molecular weight, G is the gravitational constant, and Ω_K is the Keplarian orbital frequency.

In Figure 7.17 we show the maximum gas surface densities (orange dashed curves) on the first row. The maximum gas surface densities for two different particle size distribution slopes are almost identical. The slight difference is due to their different temperatures.

The maximum gas-to-dust ratios are shown on the second row. For compact particles, the gas-to-dust mass ratio can be above 100, and even 1000 within 60 au where big particles dominate.

Beyond 60 au (where small particles dominate), the gas-to-dust mass ratio can only be as high as 100, since the small particles have lower opacities, leading to higher inferred dust mass. For porous particles (both f=0.1 and 0.01), the gas-to-dust mass ratios can also be very high within 20 au. Between 20 au to 60 au, they can only be as high as 20-80 (high metalicity) for q=3.5, since the dust surface densities are higher for porous cases. the gas-to-dust mass ratios can be 100-300 beyond 60 au. Overall, the $q = 2.5$ cases can have several times higher gas-to-dust mass ratios between 20-60 au.

7.16.3 Maximum Particle Size

The third row of Figure 7.17 shows the maximum particle size, $a_{\max} f$. Models of all three filling factors show decreasing $a_{\max} f$ with radius. For the $q = 3.5$ cases, $a_{\max} f$ can be as high as 1 m within 20 au, regardless of the filling factor. Between 20-60 au, $a_{\max} f$ is between 1-10 cm for f=1; and 10 cm-1 m for f=0.1 and 0.01. Beyond 60 au, small particles with $a_{\max} f \lesssim 100$ μm dominate. Models with q=2.5 predict much smaller $a_{\max} f$. They are 1 mm-1 cm for f=1; 1 mm-10 cm for f=0.1; and 1 cm-10 cm for f=0.01.

7.16.4 Stokes Number

The Stokes number (St) is another important parameter that determines the dynamical coupling between dust and gas (introduced in Equation 7.12). It is proportional to $a_{\max} f$ over the gas surface density. The dust-gas coupling is strong when St $\ll 1$, whereas when St ~ 1, the dust particle drifts the fastest in the gas radially. On the vertical direction, a larger St means the dust particles are more settled to the midplane (Equation 8.14, for a fixed turbulent α_t).

In the fourth row of Figure 7.17, we plot the St assuming either gas-to-dust mass ratio as 100:1 (blue curves) or maximum gas surface density in the first row (orange dashed curves, essentially the lower bound of St).

For all filling factors and size distribution slopes, the Stokes numbers are less than unity except for $r \sim 20$ au for compact particles q=3.5, where St can be as high as 10. This is where $a_{\max,f}$ is around 10 m. Overall, the q=2.5 cases have smaller St than the q=3.5 cases, since $a_{\max,f}$ (third row) is smaller. For most of the cases with q=2.5 size distribution, the St is less than 0.1 for the whole disk. The St is $\sim 10^{-4}$ beyond 60 au for all cases.

Current dust continuum observations show that the dust particles are highly settled into the disk midplane (e.g., Pinte et al. 2016c; Villenave et al. 2022), despite the expected vertical stirring that should be caused by the vertical shear instability (Stoll & Kley 2016; Lin 2019; Flock et al. 2020; Lehmann & Lin 2022). Dullemond et al. (2022) recently show that the only way to reconcile these razor-thin disks with the presence of the VSI is constraining St>1. If this condition is met, the dust particles would remain completely decoupled from the gas and hence unaffected by the VSI. Our constraint on HL Tau's Stokes numbers (whether compact or porous, q=3.5 or 2.5) are less than unity, which means that the VSI must be somehow quenched in order to reproduce the observed high levels of settling (Dullemond et al. 2022). However, when the gas-to-dust mass ratio is $\lesssim 10$, the St can be $\gtrsim 1$, consistent with the finding in Dullemond et al. (2022) that a high metalicity is required for St$\gtrsim 1$ so that the VSI can operate while the dust is settled in the midplane. On the other hand, St can be difficult to reach unity considering particle evolution without a pressure bump. When St approaches unity, the particles will drift very fast onto the star, in contrast with the large disk sizes we observed (Brauer et al. 2008; Birnstiel et al. 2009; Estrada et al. 2022). In summary, including porosity does not help explain the non-detection of the dust stir-up predicted

by VSI.

7.17 SED and Polarization Fraction Fitting with Compact 100 Micron-Sized Particles

While the small particles are less favorable solutions from the SED fitting compared to the big-particle model, the solution for 100-μm particles might have a similar quality to the 0.1-μm solution by examining Figure 7.4. Since the constraint on $a_{\rm max}f$ is weak (the marginalized posterior probability is constantly high from 0.1-50 μm), and the best-fit is found at the parameter boundary, $a_{\rm max}f$ = 100 μm might have a similar fitting score as 0.1-μm particles. To demonstrate this, we run another simulation with constant $a_{\rm max}f$ = 100 μm, using the small-particle model's best-fit surface density and temperature. The continuum and polarization fractions are shown in Figure 7.18. It is clear that the model has similar SEDs as the best-fit small-particle model (Figure 7.6) and can provide enough polarization fractions within 20 and 100 au at ALMA bands 7 and 6. If we neglect the poor quality of the SED fitting, the prediction for this solution is that the polarization fraction is negligible at longer wavelengths, e.g., ALMA bands 1 ($\sim$ 7 mm), 2 ($\sim$ 4 mm), or ngVLA bands (3 mm-2 m).

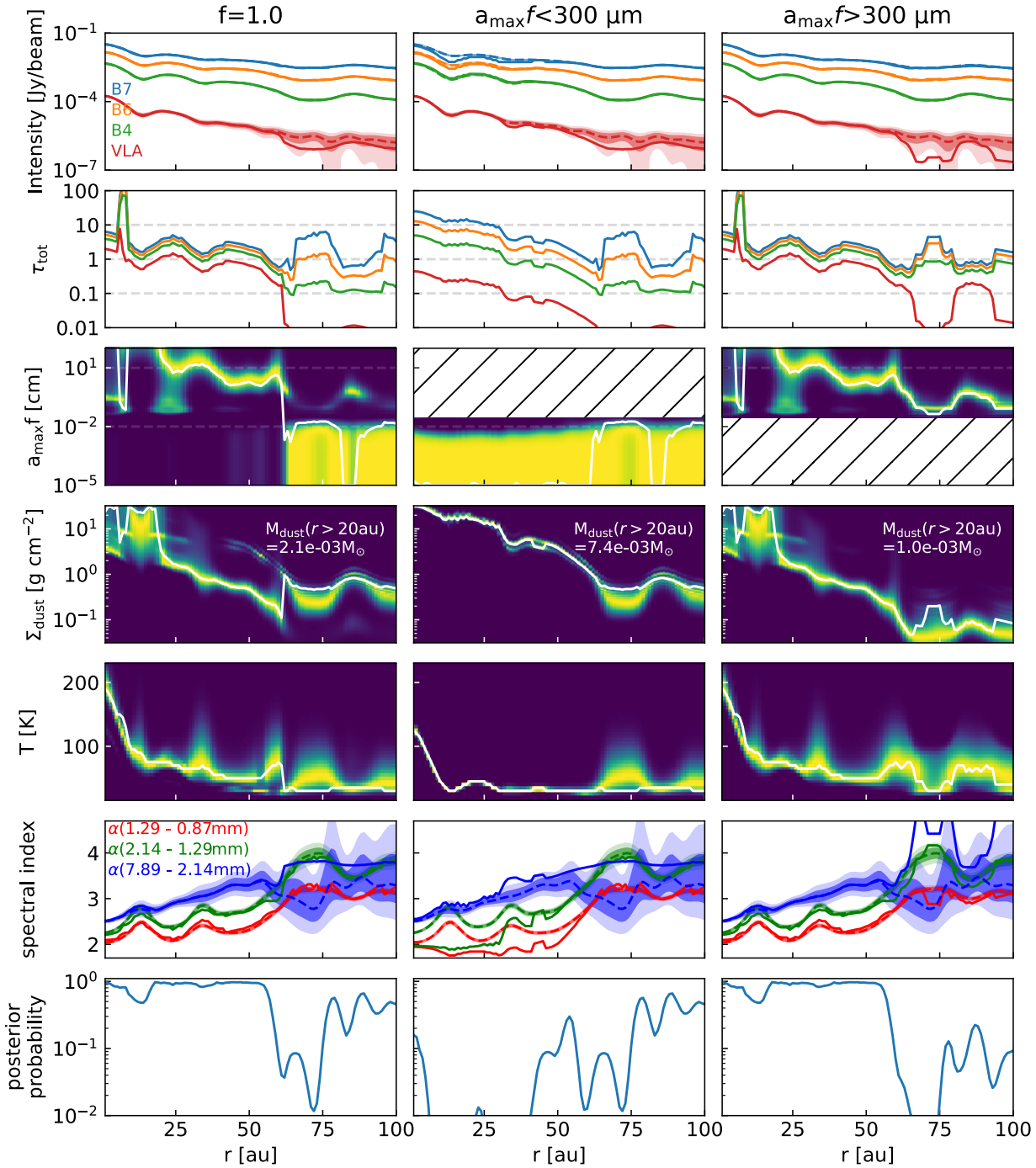

Figure 7.4: From left to right: best fit analytical models considering particles with all sizes, only small particles ($a_{\rm max}f < 300\mu$m) and only big particles ($a_{\rm max}f > 300\mu$m). From top to bottom: the intensity from the best model; total optical depths at different wavelengths; marginalized posterior probability of the maximum particle size $a_{\rm max}f$, dust surface density, and temperature; the spectral indices; and the posterior probability of the best fit. For the intensity and spectral index plots, observations are in dashed lines with the shaded area as 1 σ and 2 σ. For the total optical depth plots, horizontal dashed lines represent $\tau_{\rm tot}$ = 0.1, 1, and 10. For the $a_{\rm max}f$, Σ_d, and T, the best models are represented by white curves (the best models under three-dimensional parameter space). The dust mass beyond 20 au is listed on top of the surface density plots.

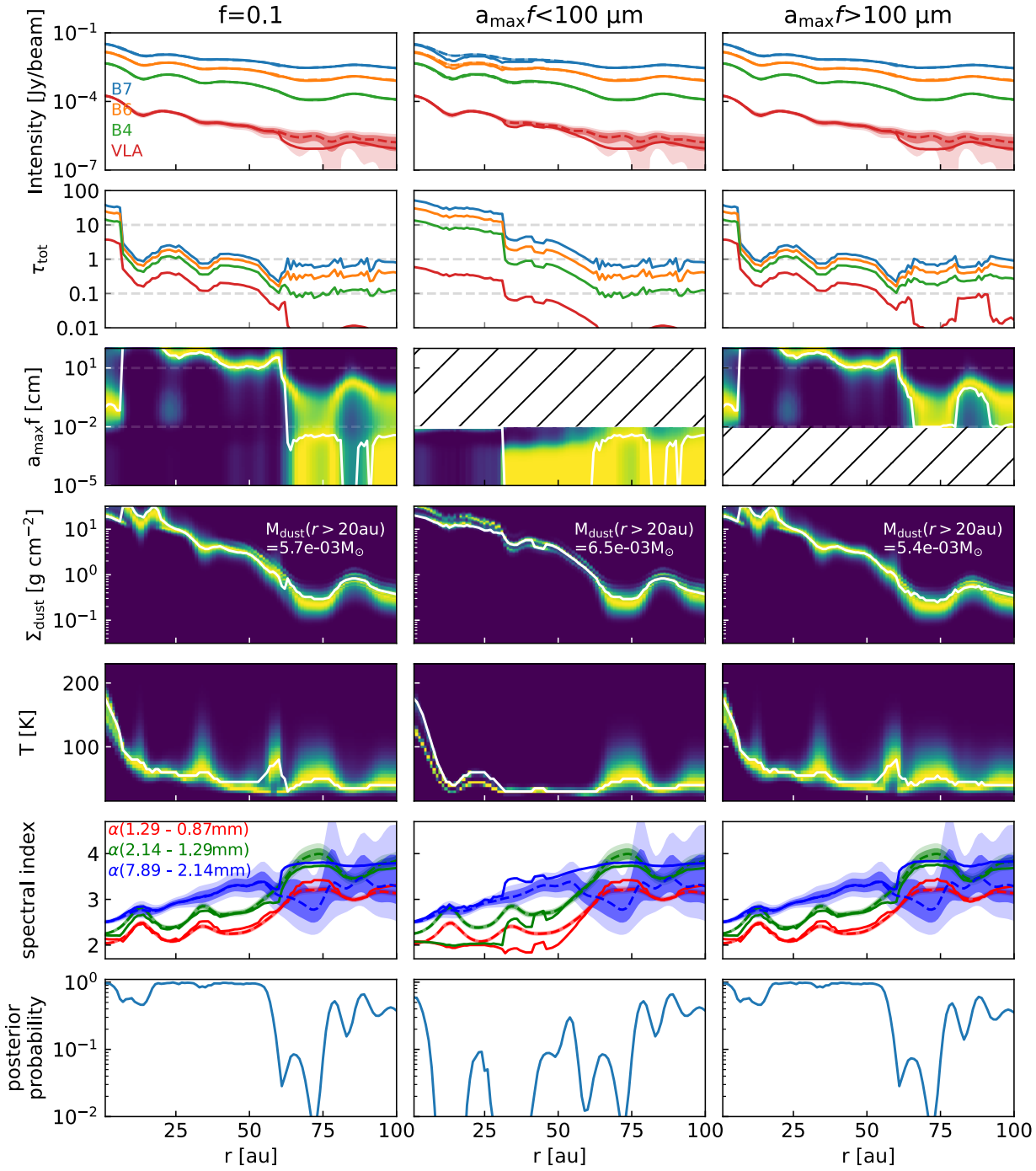

Figure 7.5: Same as Figure 7.4 but for porous particles with f=0.1. The particle size that separates big and small particles is $a_{\rm max}f$=100μm.

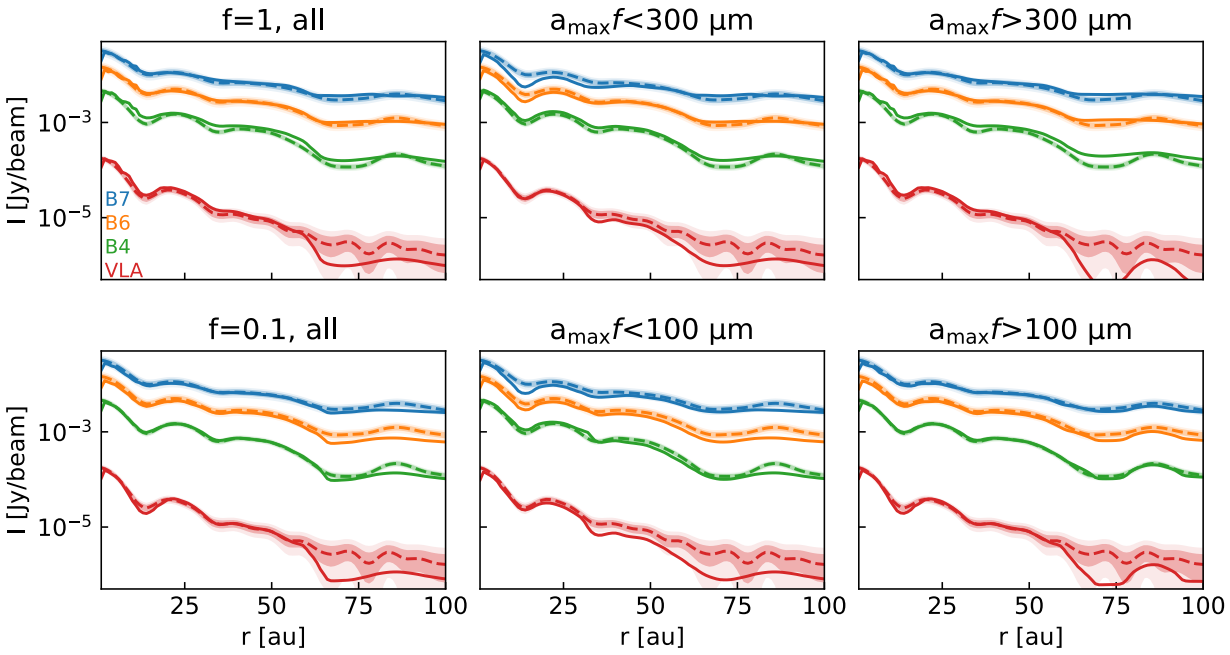

Figure 7.6: Intensities of RADMC-3D (MCRT) models with different levels of dust porosity and sizes. Top: compact particles considering the whole particle population, small-particle population ($a_{\max}f < 300$ μm) and big-particle population ($a_{\max}f > 300$ μm). Bottom: porous particles (f=0.1) considering the whole particle population, small-particle population ($a_{\max}f < 100\mu$m) and big-particle population ($a_{\max}f > 100\mu$m).

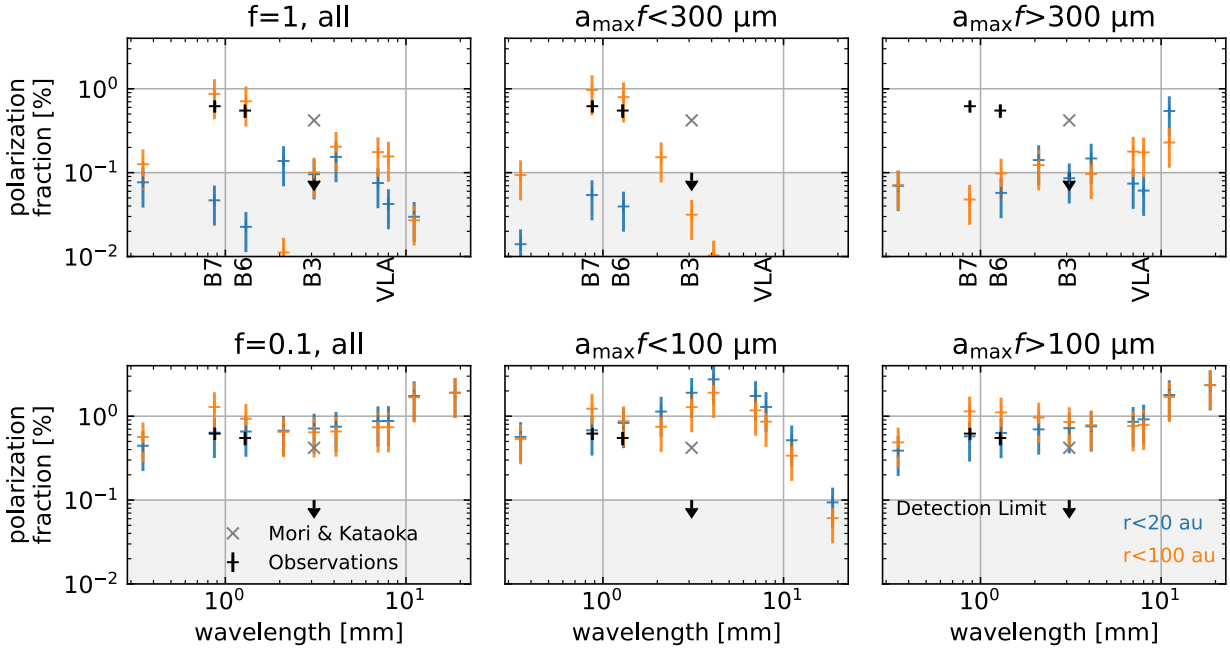

Figure 7.7: The wavelength dependence of the linear polarization fraction at the center 20 au (blue '+') and within 100 au (orange '+') from RADMC-3D (MCRT) models and ALMA observations. The uncertainties of these models are taken to be 50%, as different MCRT simulations show this level of variation (Kataoka et al. 2015). The existing observations are marked in black. The gray '×' indicates the self-scattering component of the linear polarization from Mori & Kataoka (2021). The layout is the same as Figure 7.6.

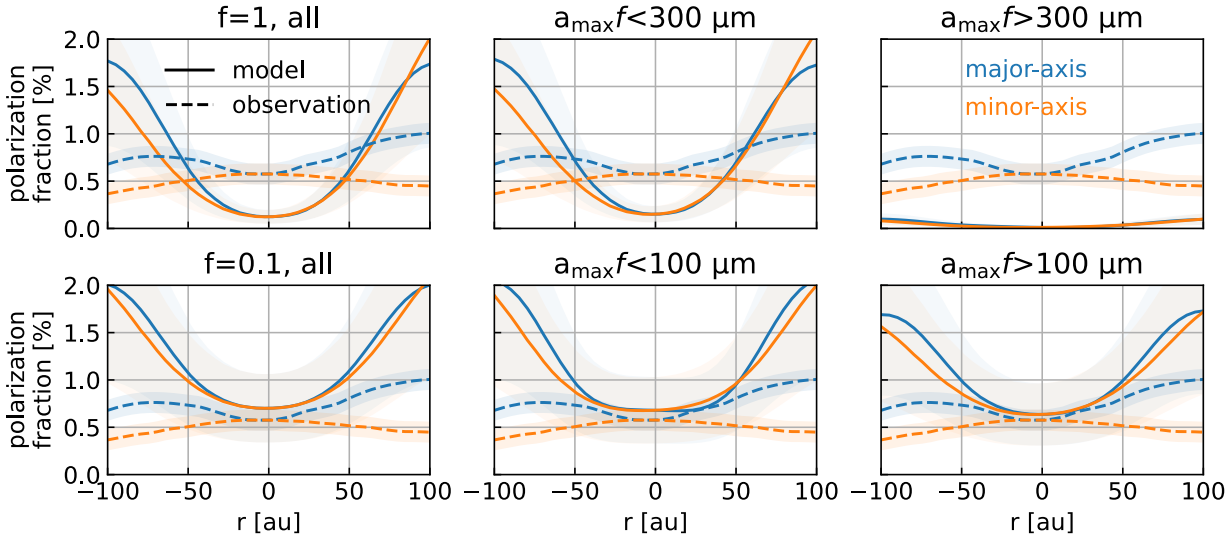

Figure 7.8: The polarization fraction along the major (blue) and minor (orange) axes at ALMA band 7 from RADMC-3D (MCRT) models and the ALMA observation. The solid curves are models and dashed curves are the observation. The layout is the same as Figures 7.6 and 7.7.

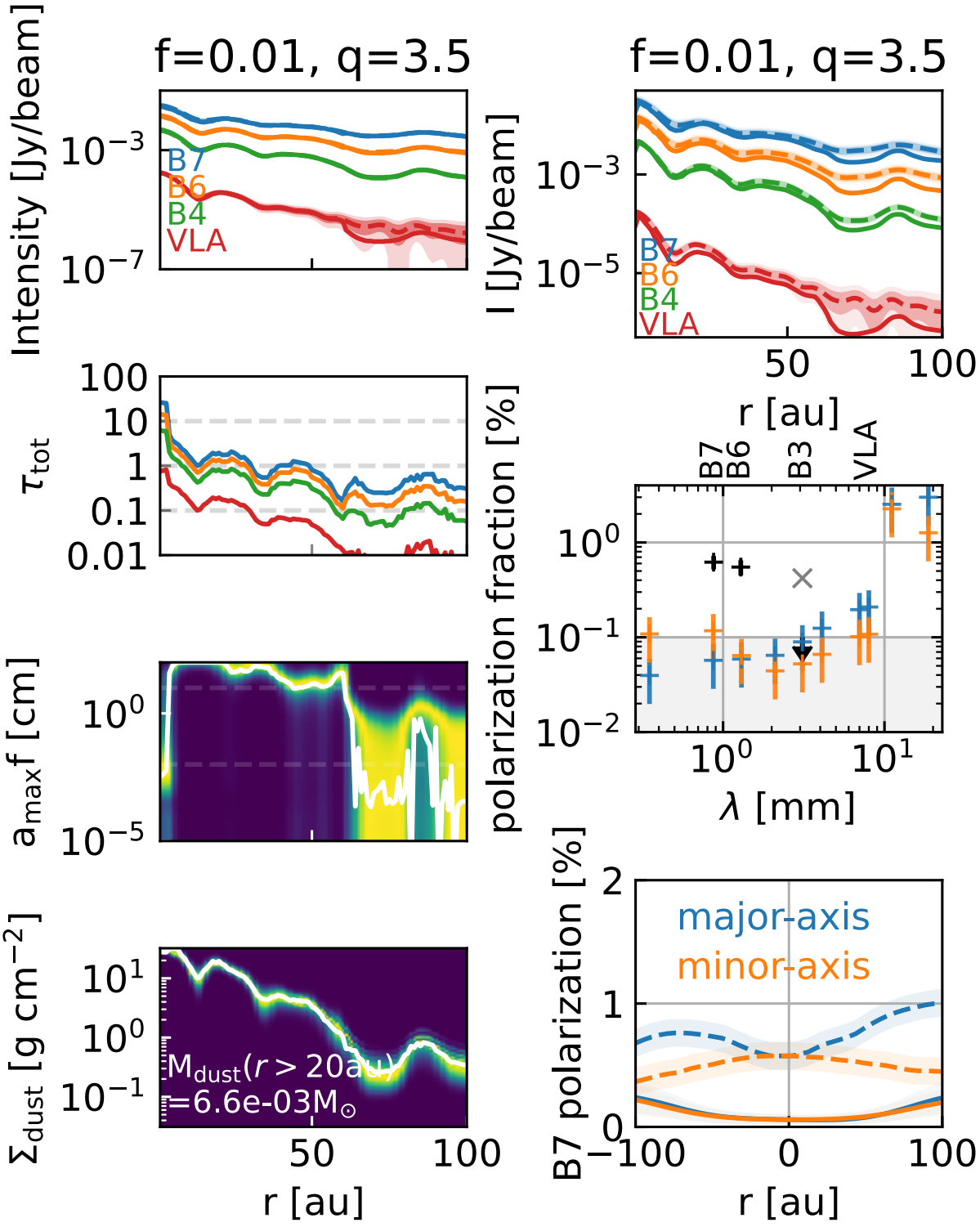

Figure 7.9: The analytical fitting of continuum SEDs (left) and the MCRT (right) results for f=0.01 case. From top to bottom, the analytical fittings are the intensities, total optical depths, $a_{\rm max}f$, and the dust surface densities. The MCRT results are the intensities, integrated polarization fractions at different wavelengths, and the major and minor axes cuts of the polarization fractions at ALMA band 7.

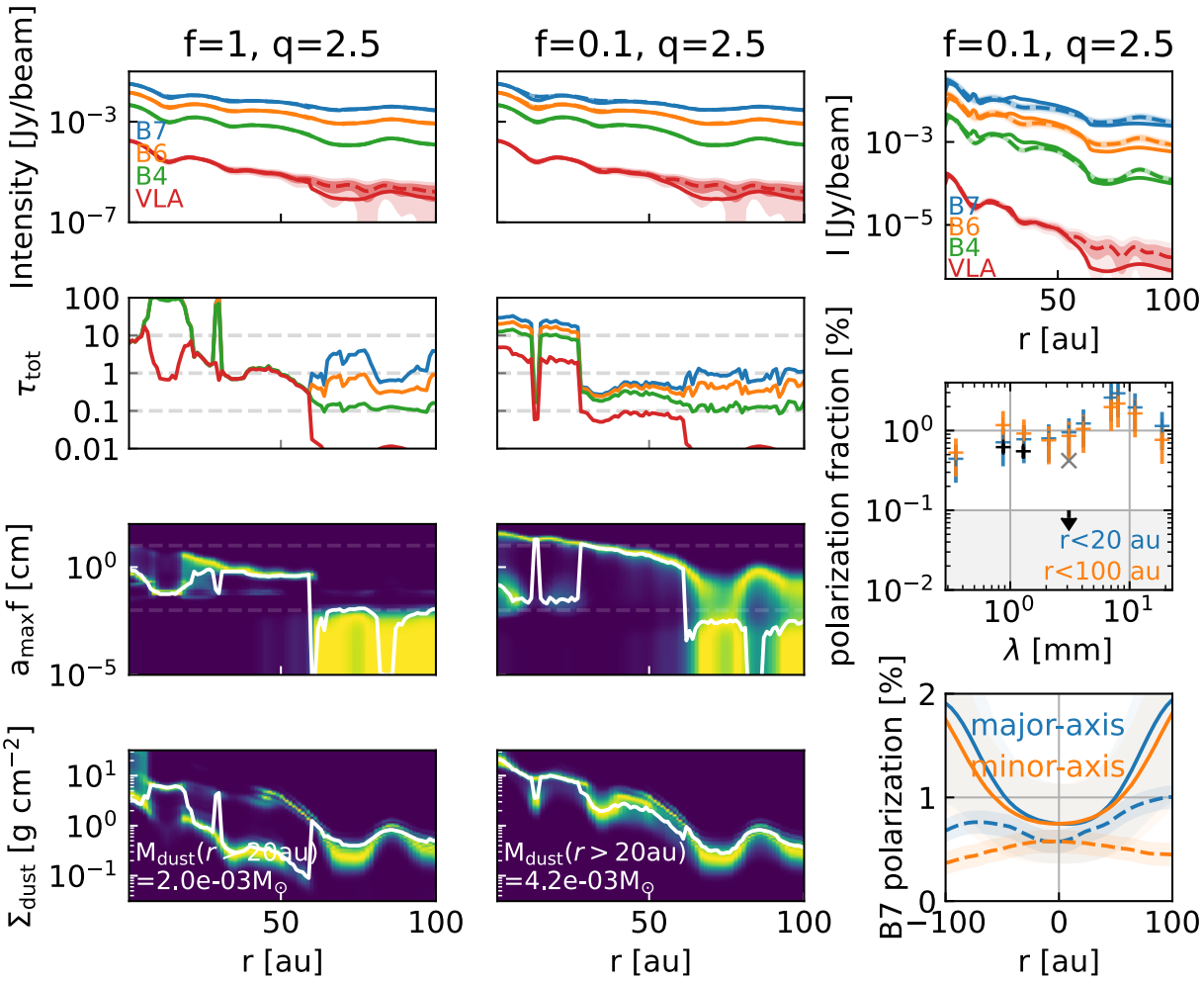

Figure 7.10: The SED fitting of q=2.5, f=1 and q=2.5, f=0.1 cases, and the MCRT fitting of the q=2.5, f=0.1 case. The layout is similar to Figure 7.9.

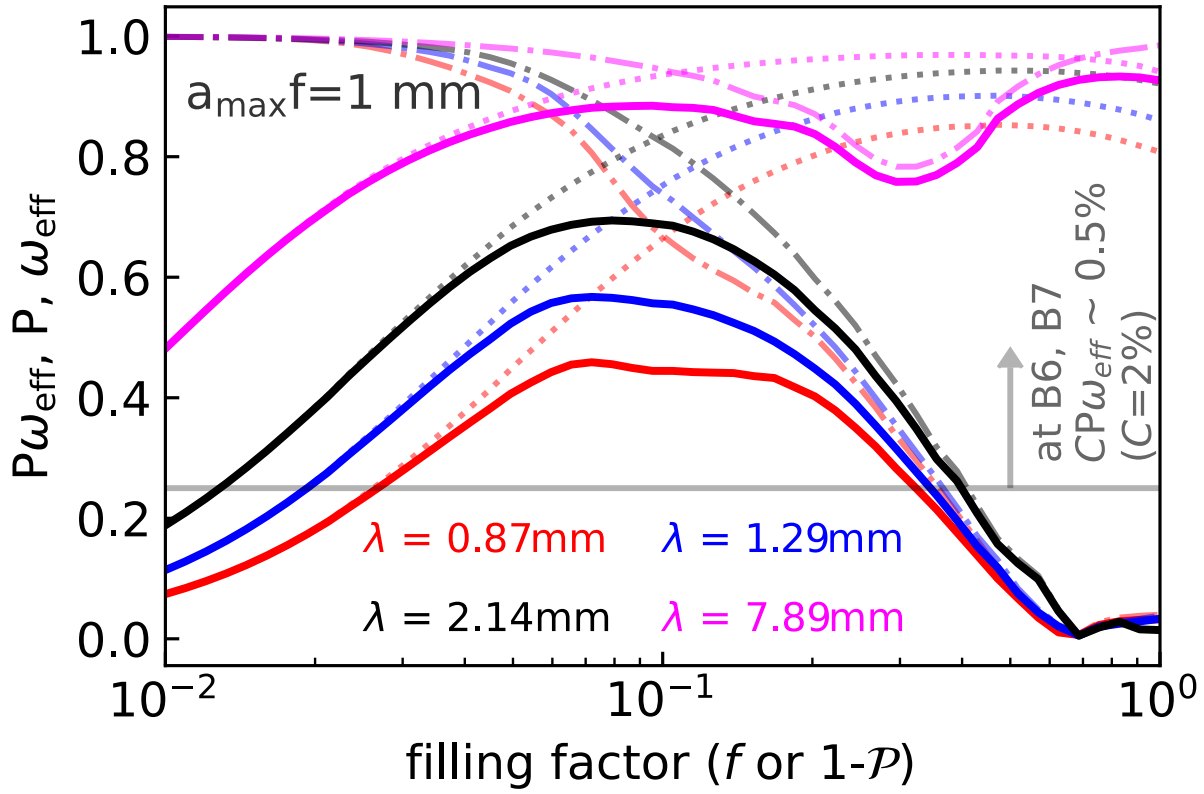

Figure 7.11: $P\omega_{\rm eff}$ of the particles against different filling factors for af = 1 mm, in a similar manner as Figure 7.3. Red, blue, black, and magenta curves represent these quantities at 0.87 mm, 1.29 mm, 2.14 mm, and 7.89 mm. Solid lines are $P\omega_{\rm eff}$, dotted lines are $\omega_{\rm eff}$, and dashed-dotted lines are P. The shallow horizontal gray line indicates the observational linear polarization values at ALMA B6, B7 transferred to $P\omega_{\rm eff}$ with a normalization constant $C = 2\%$ (e.g., Kataoka et al. 2016a). Other combinations of af and q can be found in Figure 7.12.

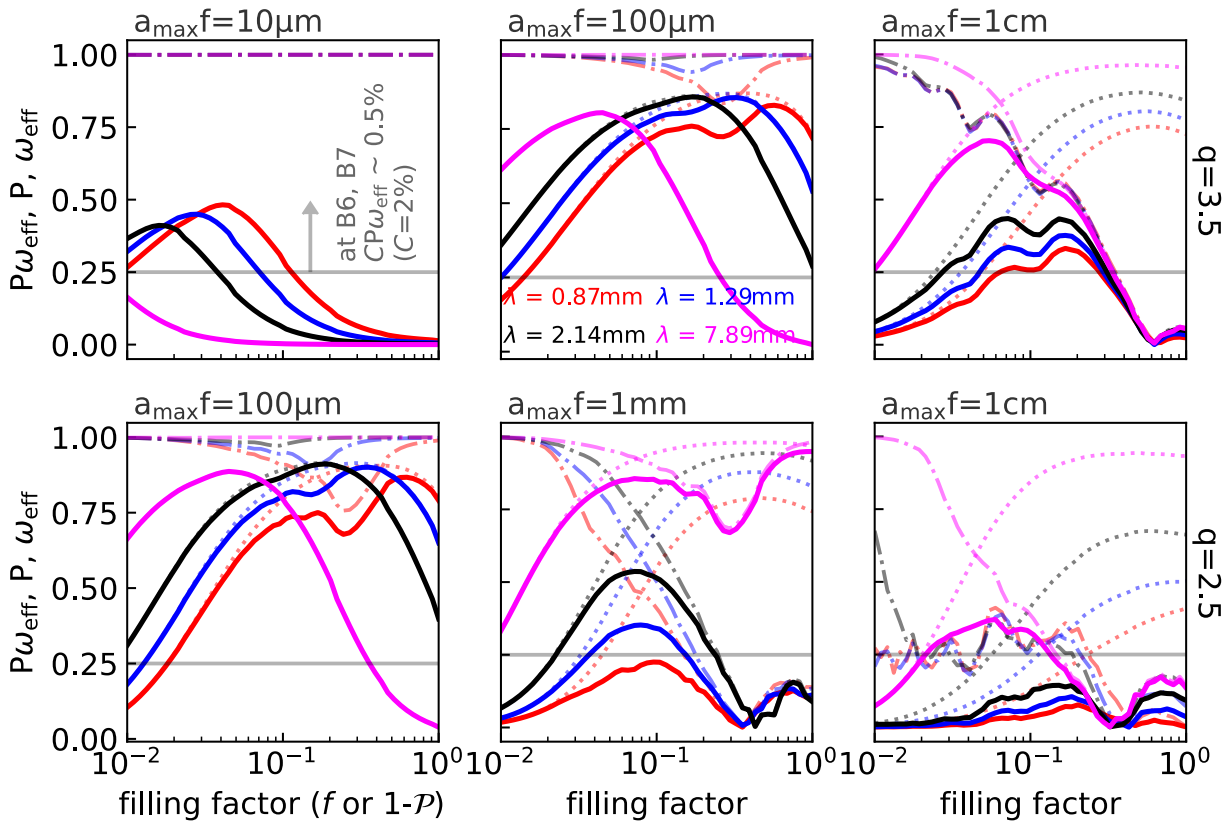

Figure 7.12: $P\omega_{\rm eff}$ of the particles against different filling factors for different af, and size distributions q that complements Figure 7.11. The top panels are with q=3.5 and af=10 μm, 100 μm, and 1 cm. The bottom panels are with q=2.5 and af=100 μm, 1 mm, and 1 cm.

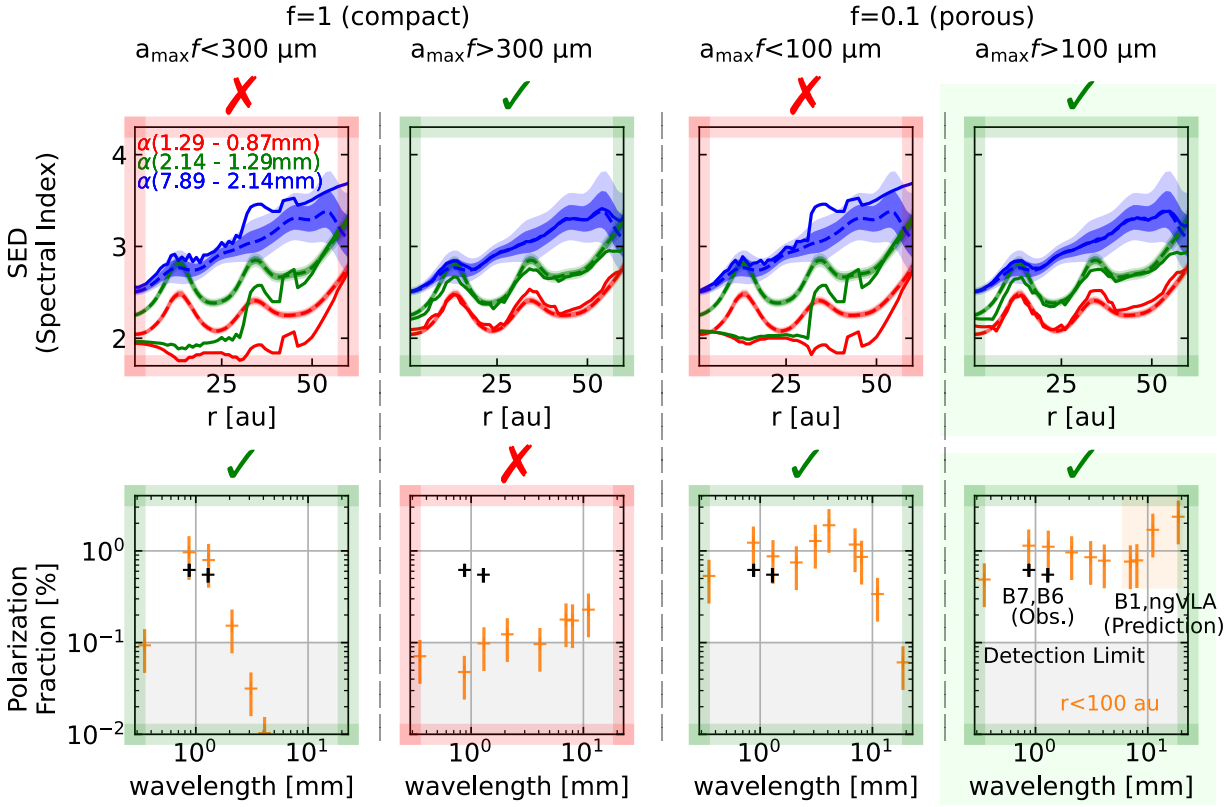

Figure 7.13: A summary of the constraints on the porosity and particle size from SED and polarization observations. Top row shows the spectral indices (from Figures 7.4 and 7.5) and the bottom row shows the integrated polarization fractions within 100 au at different wavelengths (from Figure 7.7). '51' means allowable solution, and '55' means a poor fitting.

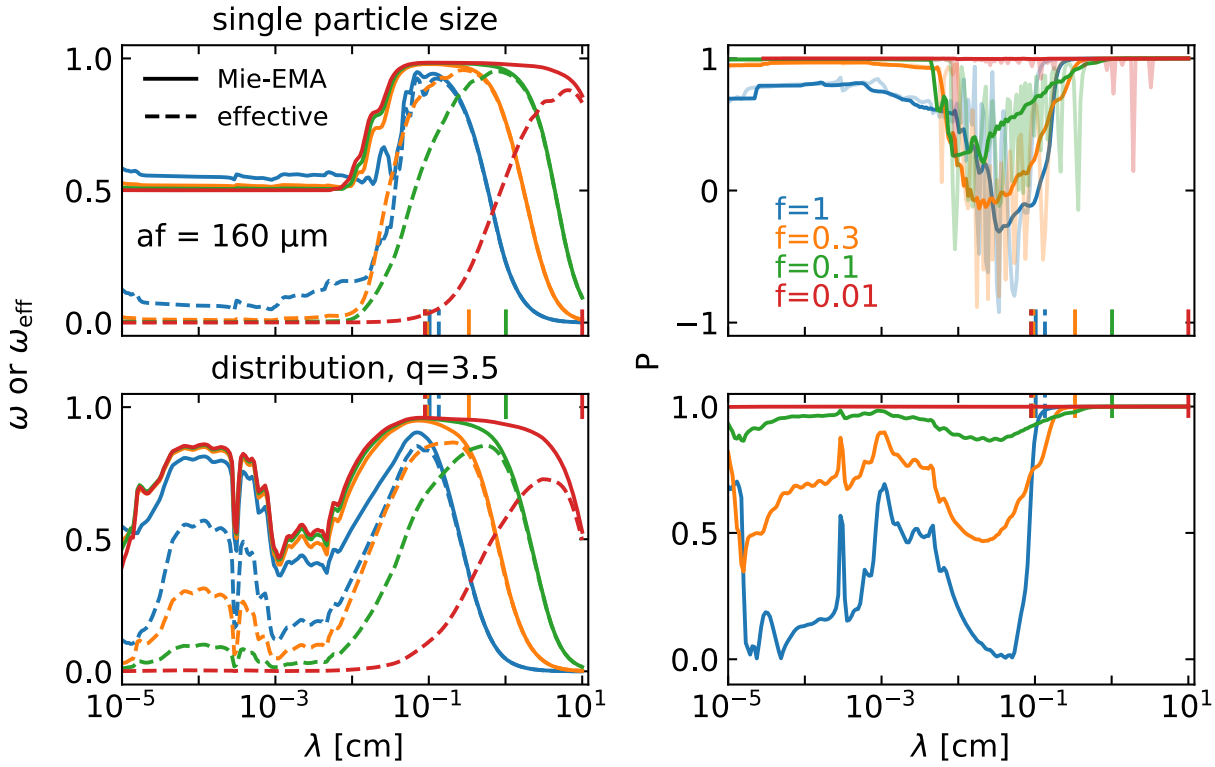

Figure 7.14: The albedo ω or $\omega_{\rm eff}$ (left panels) and polarization fraction P (right panels) for single-sized particles (top panels) and particles with size distribution q=3.5 (bottom panels). The dashed lines on the left panels are the effective albedo adjusted for the forward scattering. The more transparent lines for P are the single-sized values. The more opaque lines are the values averaging 20 neighboring particle sizes to smooth out the interference feature.

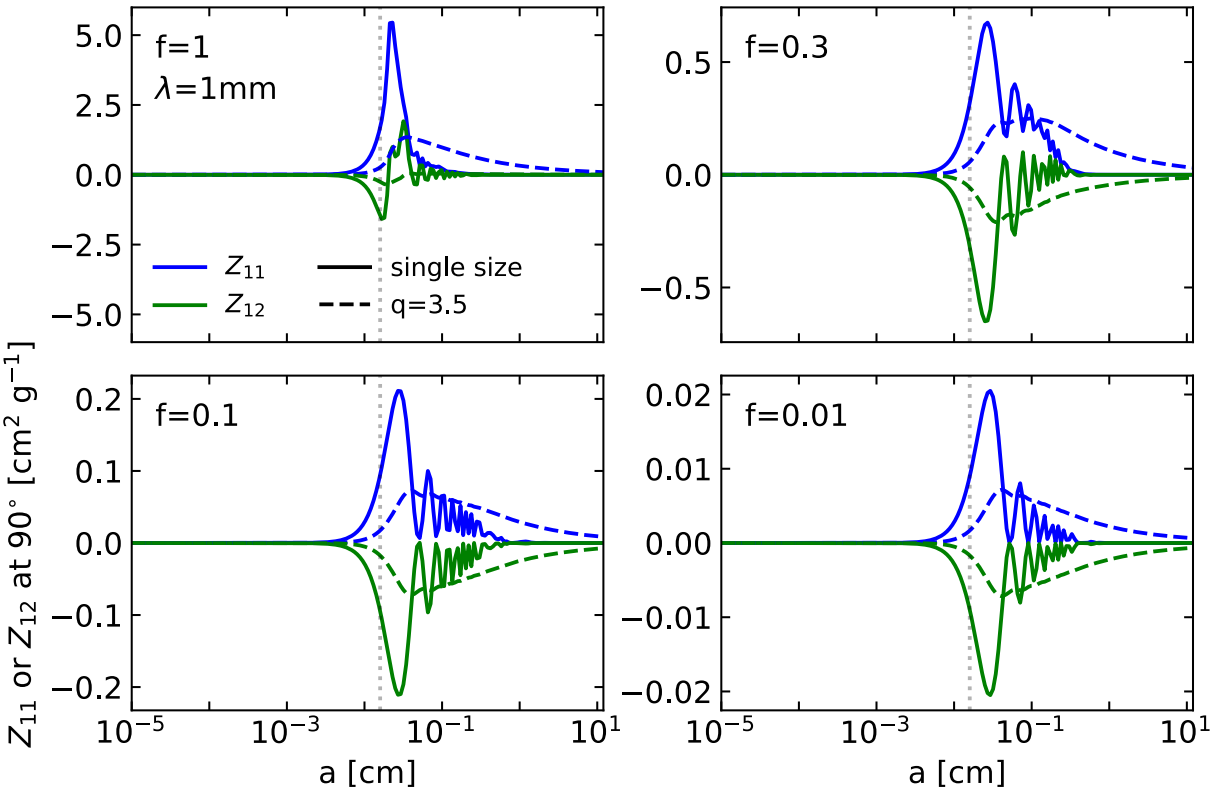

Figure 7.15: $Z_{11}|_{90^\circ}$ (blue curves) and $Z_{12}|_{90^\circ}$ (green curves) components of the scattering matrix against particle size a at 1 mm wavelength for $f = 1$, 0.3, 0.1 and 0.01. The solid lines show the single-sized values, whereas the dashed lines show the values with particle size distribution q=3.5. The vertical dotted lines are $x = 1$.

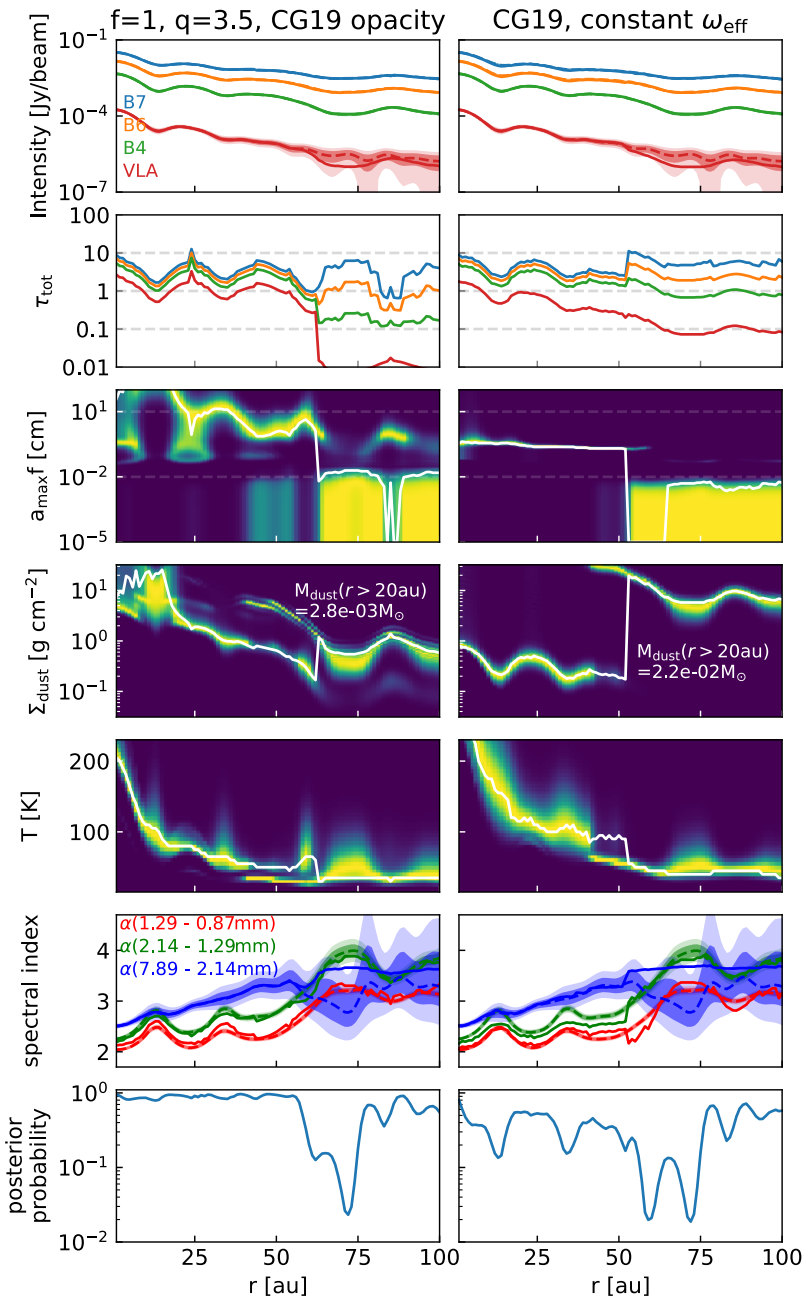

Figure 7.16: Analytical fitting of SEDs for the opacity used in Carrasco-González et al. (2019b) (left), the opacity used in Carrasco-González et al. (2019b) but with constant $\omega_{\rm eff}$(=0.9) (right). The layout is similar to Figures 7.4 and 7.5.

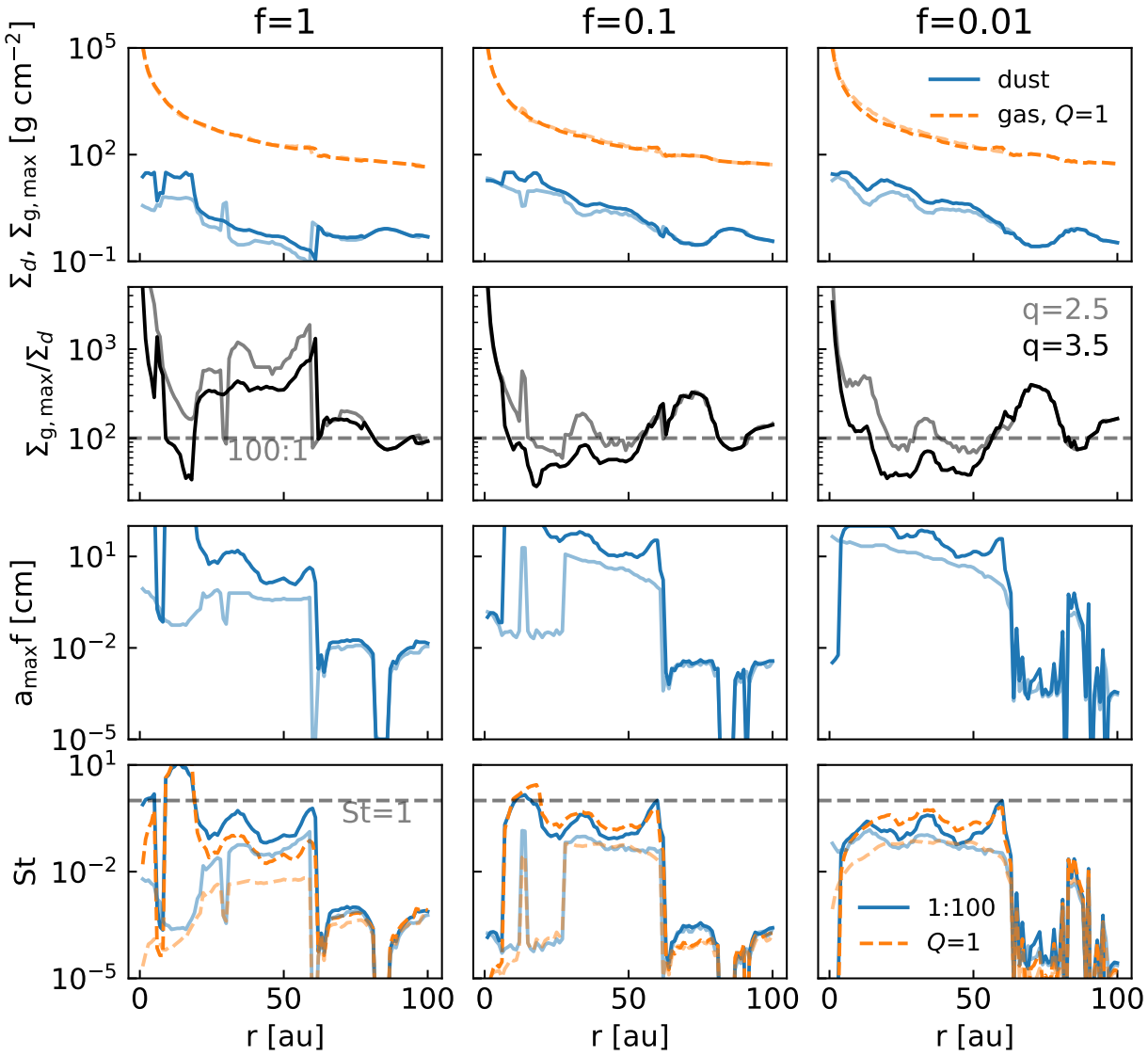

Figure 7.17: Gas and dust surface densities (first row), maximally allowed gas-to-dust mass ratios (second row), maximum particle sizes (third row), and Stokes numbers (fourth row) for f=1 (left column), 0.1 (middle column), and 0.01 (right column) cases. Cases with a particle size distribution $q = 3.5$ are shown in opaque colors, whereas the $q = 2.5$ cases are shown in more transparent colors. First row: dust surface densities constrained from analytical fittings (blue solid lines, Figures 7.4, 7.5, 7.9, and 7.10) and the maximally allowed (Q=1) gas surface densities (orange dashed lines). Bottom row: the Stokes numbers of the dust particles assuming gas-to-dust mass ratio as 100 (blue solid lines), and the Stokes numbers assuming the gas has the maximal surface density (orange dashed lines). The latter is also the minimal Stokes number a particle can have.

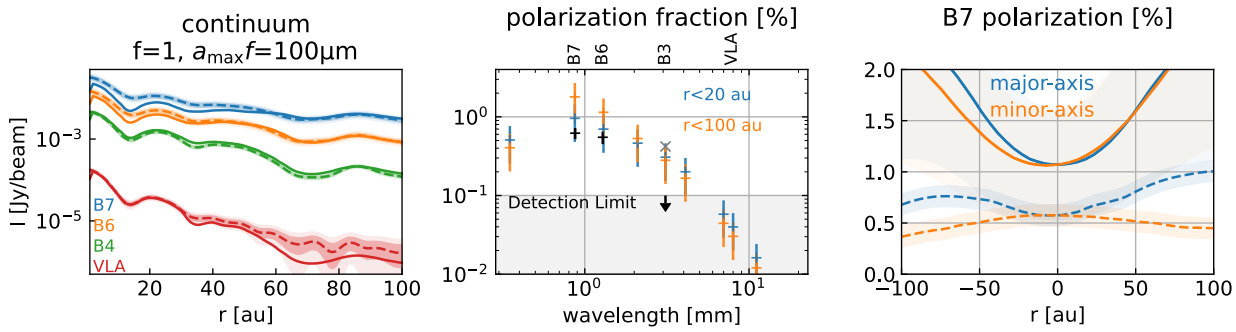

Figure 7.18: The RADMC-3D (MCRT) model with constant $a_{\rm max}f$ = 100 μm for compact particles. The left panel is the continuum emissions at ALMA bands 7, 6, 4, and VLA K+Qa band. The middle panel shows the linear polarization fractions within 20 au and 100 au at various wavelengths. The right panel shows the linear polarization fractions along major and minor axes (blue: major axis; orange: minor axis; dashed lines: observation; solid lines: models).

CHAPTER 8 Thermal Structure Determines Kinematics: Vertical Shear Instability in Stellar Irradiated Protoplanetary Disks

Shangjia Zhang,[1,2] Zhaohuan Zhu ,[1,2] and Yan-Fei Jiang[3]

[1]Department of Physics and Astronomy, University of Nevada, Las Vegas, 4505 S. Maryland Pkwy, Las Vegas, NV, 89154, USA

[2]Nevada Center for Astrophysics, University of Nevada, Las Vegas, Las Vegas, NV 89154, USA

[3]Center for Computational Astrophysics, Flatiron Institute, New York, NY 10010, USA

8.1 Abstract

Turbulence is crucial for protoplanetary disk dynamics, and Vertical Shear Instability (VSI) is a promising mechanism in outer disk regions to generate turbulence. We use Athena++ radiation module to study VSI in full and transition disks, accounting for radiation transport and stellar irradiation. We find that the thermal structure and cooling timescale significantly influence VSI behavior. The inner rim location and radial optical depth affect disk kinematics. Compared with previous vertically-isothermal simulations, our full disk and transition disks with small cavities have a superheated atmosphere and cool midplane with long cooling timescales, which suppresses the corrugation mode and the associated meridional circulation. This temperature structure also produces a strong vertical shear at $\tau_* = 1$, producing an outgoing flow layer at $\tau_* < 1$ on top of an ingoing flow layer at $\tau_* \sim 1$. The midplane becomes less turbulent, while the surface becomes more

turbulent with effective α reaching $\sim 10^{-2}$ at $\tau_* \lesssim 1$. This large surface stress drives significant surface accretion, producing substructures. Using temperature and cooling time measured/estimated from radiation-hydro simulations, we demonstrate that less computationally-intensive simulations incorporating simple orbital cooling can almost reproduce radiation-hydro results. By generating synthetic images, we find that substructures are more pronounced in disks with larger cavities. The higher velocity dispersion at the gap edge could also slow particle settling. Both properties are consistent with recent Near-IR and ALMA observations. Our simulations predict that regions with significant temperature changes are accompanied by significant velocity changes, which can be tested by ALMA kinematics/chemistry observations.

8.2 Introduction

Turbulence in protoplanetary disks plays significant roles in planet formation, such as determining mass accretion, angular momentum transport, and dust dynamics. In the disk midplane beyond 0.1 au, where the magnetorotational instability (MRI) is suppressed due to low ionization rates, turbulence can be generated by hydrodynamic instabilities (Turner et al. 2014; Armitage 2020; Lesur et al. 2022). One promising candidate among these instabilities is the vertical shear instability (VSI) (Nelson et al. 2013b; Stoll & Kley 2014; Barker & Latter 2015; Umurhan et al. 2016; Lesur et al. 2022). The VSI is driven by the vertical differential rotation of the disk ($dv_\phi/dZ \neq 0$). It occurs in baroclinic disks, characterized by non-parallel density and pressure gradients (Lesur et al. 2022; Klahr et al. 2023). Such a configuration is often satisfied in stellar irradiated protoplanetary disks, where the temperature decreases away from the central star in the radial direction. Most studies on the VSI assume a vertically constant temperature, which is thought to be

a valid assumption near the disk midplane (e.g., Calvet et al. 1991; Chiang & Goldreich 1997).

A distinctive feature of the VSI is the presence of the corrugation mode in the meridional plane, which involves large-scale gas circulations in the vertical direction, while remaining confined in the radial direction (Nelson et al. 2013b; Lyra & Umurhan 2019). As a result, anisotropic turbulence arises in the Z-ϕ and R-ϕ stresses, with the former typically reaching magnitudes of 10^{-2} and the latter ranging from 10^{-4} to 10^{-3} (Stoll & Kley 2014; 2016; Stoll et al. 2017; Flock et al. 2017; Manger & Klahr 2018; Manger et al. 2020; 2021; Pfeil & Klahr 2021). The amplitude of turbulence increases with the aspect ratio (i.e., temperature) of the disk (Manger et al. 2020; 2021). Simulations with mm-sized dust particles show that they can be stirred up very high above the midplane due to the strong turbulence in the vertical direction (Stoll et al. 2017; Flock et al. 2017; 2020; Blanco et al. 2021; Dullemond et al. 2022). High resolution simulations show that strong shears between neighbouring bands of these meridional circulations can generate vortices in the R-Z plane (Flores-Rivera et al. 2020; Klahr et al. 2023; Melon Fuksman et al. 2023b). Three-dimensional simulations also demonstrate they can generate vortices and zonal flows in the R-ϕ plane due to the Kelvin-Helmholtz instability (Flock et al. 2017; Manger & Klahr 2018; Flock et al. 2020; Blanco et al. 2021; Pfeil & Klahr 2021). These zonal flows can possibly explain some of the ubiquitous substructures observed by ALMA dust continuum observations (e.g., Andrews et al. 2018d; Long et al. 2018b; van der Marel et al. 2019; Cieza et al. 2021c; Blanco et al. 2021; Andrews 2020; Bae et al. 2023).

The role of thermodynamics is crucial in determining whether the vertical shear instability (VSI) can occur (Lin & Youdin 2015; Lyra & Umurhan 2019; Lesur et al. 2022). Specifically, the global mode of VSI requires a fast cooling timescale, where the cooling time normalized to the

orbital time should be less than a threshold (Lin & Youdin 2015),

$$\beta < \beta_c \equiv \Omega_K^{-1}(h/r)|q|/(\gamma_g - 1), \tag{8.1}$$

where Ω_K is the Keplerian frequency, h/r is the disk aspect ratio, q is the radial temperature power-law index, and γ_g is the adiabatic index. Analytical studies considering dust-gas coupling and dust evolution have identified regions where the VSI can operate (Malygin et al. 2017; Pfeil & Klahr 2019; Fukuhara et al. 2021). Disks with globally uniform cooling times larger than this critical cooling time do not develop VSI (Manger et al. 2021). However, short length-scale perturbations may still grow after evolving for a very long time (Klahr et al. 2023; Pfeil et al. 2023). In cases where the midplane has a long cooling timescale, yet the atmosphere has a short cooling time, studies using vertically isothermal simulations demonstrate the persistence of the VSI in the disk atmosphere (Pfeil & Klahr 2021; Fukuhara et al. 2023). The VSI in the unstable disk atmosphere can even penetrate the stable midplane, as long as the VSI-stable layer is less than two gas scale heights and the VSI-unstable layer is thicker than two gas scale heights (Fukuhara et al. 2023). Additionally, with equivalent short cooling times, radiation hydrodynamic simulations produce similar results to vertically isothermal simulations (Stoll & Kley 2014; Flock et al. 2017).

While VSI aligns with certain observational facets, such as a low level of R-ϕ turbulence, it also has tensions with some other facets.

- *A possible mechanism for substructures.* The (sub-)mm dust continuum emission traces $\sim$0.1-10 mm dust particles residing in the disk midplane, where substructures have been detected in a majority of observed disks when sufficient resolution is achieved (Bae et al. 2023). These substructures predominantly manifest as gaps and rings, although occasional

arcs and spirals have been observed as well. VSI can generate density perturbations and vortices owing to the zonal flow led by the corrugation mode. However, these perturbation are typically small and requires very high resolution and sensitivity to detect them (Blanco et al. 2021).

- *Consistent weak turbulence* $\alpha_{\rm R}$. The VSI generates a low level of turbulence in the R-ϕ plane ($\alpha_{\rm R} \sim 10^{-5}$ - 10^{-3}, Nelson et al. 2013b; Stoll & Kley 2014; Flock et al. 2017; Lesur et al. 2022). This is consistent with planet-disk interactions models with ad hoc turbulent viscosity to explain the observed multiple gaps and rings (Dong et al. 2017c; Bae et al. 2017c; Zhang et al. 2018b; Paardekooper et al. 2023). A low level of viscosity (10^{-4} - 10^{-3}) is also needed to match the disk dispersal timescale ($\sim$ Myrs) in disk evolution models (Mulders et al. 2017; Lodato et al. 2017; Tabone et al. 2022; Manara et al. 2022).

- *Overpredicted turbulence* $\alpha_{\rm Z}$. In the disk's vertical direction, edge-on and inclined disks exhibit remarkably thin dust emission layers, which can be translated to a low value of α_Z/St ($< 10^{-2}$, Pinte et al. 2016c; Doi & Kataoka 2021; Villenave et al. 2020; 2022; Sierra & Lizano 2020; Ueda et al. 2020; 2021), where α_Z is the turbulence in the Z-ϕ plane, and St is the Stokes number that characterizes the gas-dust coupling. An exception is that the inner ring of HD 163296, which has $\alpha_Z/{\rm St} > 1$ (Doi & Kataoka 2021). Adopting a typical Stokes number, the α_Z is estimated to be $\lesssim 10^{-4}$ in most cases. However, VSI generates very strong turbulence in the vertical direction ($\sim 10^{-2}$, e.g., Stoll & Kley 2014), with the correlation at neighbouring radii, which conflicts with many observations (Dullemond et al. 2022).

- *Yet-to-be-detected VSI corrugation mode.* Gas line emission observations demand higher sensitivities, yet data have been accumulating from recent and ongoing ALMA large pro-

grams such as, MAPS (Öberg et al. 2021). With the aid of channel maps derived from these observations, we can measure the 3D velocity and temperature structure of the disk for a large sample of disks (e.g., Miotello et al. 2022; Pinte et al. 2023). Barraza-Alfaro et al. (2021) predicts that the alternating blueshifted-redshifted corrugation mode can be observed in the CO channel maps given very high spectral resolution (50 m s^{-1} at ALMA band 6). However, there is no firm detection of this pattern so far.

While disk thermodynamics plays a key role in VSI, most previous studies focused on simple thermodynamics such as locally isothermal or orbital cooling treatments. The vertical thermal structure is also underexplored. With a more self-consistent treatment, we can provide a more robust model and improve connections between observations and theory.

To that end, we employ a self-consistent radiation-hydrodynamics approach with temperature-dependent DSHARP opacity (Birnstiel et al. 2018). Unlike previous simulations that utilized locally isothermal equations of state or flux-limited diffusion approximation with constant opacity, we utilize the Athena++ (Stone et al. 2020) implicit radiation module (Jiang et al. 2014; Jiang & Ormel 2021). This module incorporates angle-dependent radiative transfer equations with implicit solvers to accurately model the disk radiation transport. The module can capture both optically thin and thick regimes and shadowing and beam crossing accurately. Additionally, we incorporate stellar irradiation using long-characteristic ray tracing as a heating source.

Recently, Melon Fuksman et al. (2023a;b) independently study VSI in irradiated protoplanetary disks using M1 method (Melon Fuksman et al. 2021). While we focus on the outer disk beyond 20 au and they focus on 4-7 au in the inner disk, the results for our fiducial model are consistent with their dust depleted disk models, which show quiescent midplane and turbulent atmosphere.

The paper layout is the following. In Section 8.3, we discuss the numerical setup of the simulations. In Section 8.4, we present results of radiation hydrodynamic simulations, accompanied with a series of pure hydro simulations. In Section 8.5, we discuss the formation of substructures, and observational/modeling prospect. Finally, we conclude the paper in Section 8.6.

8.3 Methods

8.3.1 Disk Model Setup

In our study, we explored both full disks and transition disks with varying inner disk truncation radii or cavity sizes, denoted as r_{cav}. Our simulations were performed in spherical polar coordinates r, θ, ϕ, while most of the disk structure was set up in cylindrical coordinates R, Z, ϕ.

The gas surface density profile follows a power-law with an exponential cutoff, consistent with viscous evolution models (Lynden-Bell & Pringle 1974; Hartmann et al. 1998) and observational constraints (e.g., Miotello et al. 2022). The gas surface density is given by:

$$\Sigma_g = \Sigma_{g,0}(R/1\ \mathrm{au})^{-1} \exp(-R/100\ \mathrm{au}), \tag{8.2}$$

where $\Sigma_{g,0}$ is the gas surface density at a reference radius of 1 au. In our fiducial models, $\Sigma_{g,0}$ is set to 178 g cm^{-2}, following Zhu et al. (2012a).

Regarding the initial temperature structure, we assumed a radial power-law profile as the initial condition:

$$T(R,Z) = T(R_0)\left(\frac{R}{R_0}\right)^q, \tag{8.3}$$

where q is set to -0.5. The reference temperature $T(R_0)$ is given by:

$$T(R_0) = \left(\frac{fL_*}{4\pi R_0^2 \sigma_b}\right)^{1/4}. \tag{8.4}$$

Here, f accounts for the flaring of the disk, and we used a value of $f = 0.1$ in our initial conditions. The stellar luminosity L_* is assumed to be 1 $L_\odot$, and σ_b represents the Stefan-Boltzmann constant.

Then the hydrostatic equilibrium in the $R-Z$ plane requires the initial density profile at the disk midplane to be (e.g., Nelson et al. 2013b)

$$\begin{aligned} &\rho_0(R, Z=0) \\ &= \rho_0(R=R_0, Z=0)\left(\frac{R}{R_0}\right)^p \exp\left((\mathrm{R_0}-\mathrm{R})/100\ \mathrm{au}\right), \end{aligned} \tag{8.5}$$

where at the initial condition, the gas surface density and the volume density is related by $\rho_0(\mathrm{R}, \mathrm{Z}=0) = (2\pi)^{-1/2}\Sigma_\mathrm{g}(\mathrm{R})h(\mathrm{R})^{-1}$. The midplane radial density profile power-law index p can be related to the surface density power-law index r ($\Sigma_g \propto R^r$) and temperature power-law index q, by $p = r - q/2 - 3/2$. Since we adopted $q = -0.5$ and $r = -1$, p = -2.25. The temperature is used to calculate the gas scale height $h = c_s/\Omega_K$, where $c_s = (P/\rho)^{1/2}$ is the isothermal sound speed, and $\Omega_K = (GM_*/R^3)^{1/2}$ is the Keplarian orbital frequency. We adopt M_* = 1 $M_\odot$.

In the vertical direction

$$\rho_0(R,Z) = \rho_0(R,Z=0)\exp\left[\frac{GM}{c_s^2}\left(\frac{1}{\sqrt{R^2+Z^2}} - \frac{1}{R}\right)\right], \tag{8.6}$$

and

$$\mathrm{v}_\phi(R,Z) = \mathrm{v}_K \left[(p+q) \left(\frac{c_s}{\mathrm{v}_K} \right)^2 + 1 + q - \frac{qR}{\sqrt{R^2+Z^2}} \right]^{1/2}, \tag{8.7}$$

where $\mathrm{v}_K = \Omega_K R = \sqrt{GM_*/R}$. We can see that the vertical shear rate $d\mathrm{v}_\phi/dZ$ is non-zero as long as $q \neq 0$. The other two velocity components v_R and v_Z are set to be zero at the initial condition. We do not consider the self-gravity of the disk in this paper, which should be a valid assumption for most of the Class II disks (Miotello et al. 2022).

In the initial condition (Equation 8.3), we also assumed the temperature to be vertically isothermal. This assumption is valid near the midplane. However, we will demonstrate that the quasi-steady state of our simulations exhibits a cool midplane and a superheated atmosphere which is consistent with classical analytical calculations (Calvet et al. 1991; Chiang & Goldreich 1997; D'Alessio et al. 1998), Monte Carlo radiative transfer calculations (Pascucci et al. 2004; Pinte et al. 2009), previous radiation hydrodynamic simulations (Flock et al. 2013; 2017; 2020; Kuiper et al. 2010; Kuiper & Klessen 2013), and recent ALMA CO observations (Law et al. 2022; 2023). We will also show that this vertical temperature gradient, together with the varying local orbital cooling time, is crucial for the gas kinematics.

The full disk corresponds to a value of $\mathrm{r_{cav}}$ equal to 3 solar radii (`3r`$_\odot$`-rad`), which represents the magnetic spherical accretion truncation radius (e.g., Hartmann et al. 2016). The total gas mass is approximately 0.01 solar masses. The transition disks have $\mathrm{r_{cav}}$ values of 18 au (`18au-rad`, fiducial model) and 54 au (`54au-rad`). Additionally, we considered a case where the gas surface density is reduced to 1% of the fiducial value, i.e., $\Sigma_{\mathrm{g},0}$ is set to 1.78 g cm^{-2} (`18au-lowdens-rad`). In this low-density disk scenario, the total gas mass is approximately 10^{-4} solar masses. For transition disk with $\mathrm{r_{cav}}$ = 54 au, we used a `tanh` profile to make a smooth

transition at the inner gap so that it satisfies the Rayleigh criterion (e.g., Yang & Menou 2010) at the initial condition. We summarize all our models in Table 1 in Zhang et al. (2024).

Limited by the computational cost, the inner boundary of the disk cannot be too small. Thus, we set the inner boundary at 21.6 au. For $r_{\rm cav}$ = 3 $r_\odot$, and 18 au disks, the simulation inner boundaries are beyond the cavity sizes. To mimic the optical depth effect of these disks, we artificially added optical depth between 3 $r_\odot$/18 au and the simulation's inner boundary at 21.6 au (see Equation 8.21 in Appendix 8.7). However, this preset optical depth cannot adjust its vertical structure self-consistently and can lead to discontinuities at the simulation's inner boundary. The direct irradiation on disk inner cavity is also related to the shadowing effect in Dullemond et al. (2001); Jang-Condell & Turner (2012; 2013); Siebenmorgen & Heymann (2012); Zhang et al. (2021b). Therefore, what occurs near the inner boundary might not be reliable.

8.3.2 Radiation Hydrodynamics

We introduce the numerical setup for the radiation hydrodynamic simulations using the frequency-integrated (gray) radiation module (Jiang & Ormel 2021). We detail the implementation of the stellar irradiation and unit conversion in Appendix 8.7.

We adopted the Courant–Friedrichs–Lewy (CFL) number to be 0.4, and used second order Van Leer time integrator (vl2), second order spatial reconstruction, and HLLC Riemann Solver. We adopted adiabatic index γ_g = 1.4. We discretized the radial direction into 1568 cells, logarithmically spaced from 0.54 to 8 times the reference radius (r_0 = 40 au, so 21.6 au to 320 au from inner and outer boundaries). The polar direction was divided into 1536 cells, covering a range from 0.383 to 2.76 radians (68° above and below the midplane). For our fiducial model, this amounts to 45 cells

per scale height at r_0 (40 au). For the hydro boundary conditions, we used outflow at the inner boundary, and copied initial conditions for outer, upper and lower boundaries. As for radiation boundary conditions, light beams can freely transport out of the domain. If the beam points inward the computational domain, the radiation is assumed to have the background temperature (10 K = 1.63×10^{-3} T_0, where T_0 is the temperature in code unit), which is a typical temperature of molecular clouds. We adopted periodic boundary condition in the azimuthal ϕ-direction.

The radiation transport uses discrete ordinate, where rays are discretized into different angles. We used the discretization better suited for curvilinear coordinates (`angle_flag` = 1) and set `nzeta` = 2, `npsi` = 2, where `nzeta` represents angles from 0 to $\pi/2$ in θ direction and `npsi` represents 0 to π in ϕ direction. There are 16 angles in total. To test the convergence of the temperature calculated by different numbers of rays, we froze the hydrodynamics (assuming a static disk) and tried `nzeta` = 4, `npsi` = 4, and `nzeta` = 8, `npsi` = 8. We found convergence when `nzeta` = 4 and `npsi` = 4. Since the temperature difference is already small between `nzeta` = `npsi` = 2 and `nzeta` = `npsi` = 4, we adopted the former to save computational time.

We ran simulations with `cfl_rad` = 0.3 (`cfl_rad` is an additional factor multiplied in front of the CFL number to help convergence for implicit method), reduced speed of light $\mathbb{R} = 4 \times 10^{-3}$ (Zhang et al. 2018a; Zhu et al. 2020), and `error_limit` = 10^{-3} for the first 10 orbits (P_{in}, the orbital period of the inner boundary at 0.54 r_0 or 21.6 au) to approach the quasi-steady state. Otherwise the iteration times or errors were extremely large. Then we restarted the simulation and changed `cfl_rad` and $\mathbb{R}$ back to 1. Thus, we do not use reduced speed of light for the longer time evolution for our simulations. We also changed the `error_limit` to 10^{-5} after the restart. We note that after the restart it only took one iteration to reach the error limit and the typical error was only 10^{-7}-10^{-6} .

Dust Opacity Setup

While the radiation module can treat isotropic scattering properly, we neglected dust scattering and only considered absorption opacity in this paper to better compare with previous isothermal simulations. We also used the frequency-integrated (gray) radiation transport, but we note that multi-group radiation module is also available (Jiang 2022). Both dust scattering and multi-frequency radiative transfer will be considered in a future publication.

We used the DSHARP composition (Birnstiel et al. 2018) and a power law MRN dust size distribution ($n(a) \propto a^{-3.5}$, Mathis et al. 1977). The minimum grain size $a_{\rm min} = 0.1$ μm and maximum grain size $a_{\rm max} = 1$ mm. In our fiducial models, we assumed that only small grains determine the temperature distribution due to their high opacity at the peak of the stellar spectrum; therefore, we considered grains sized between 0.1 and 1 μm, which account for f_s=0.02184 of the total dust mass. The mass ratio between all the dust and gas was assumed to be 1/100. Then we calculated the Planck and Rosseland mean opacities normalized to the total dust mass ($\kappa_{P,d}$, and $\kappa_{R,d}$) at various disk temperatures and fitted by univariate spline functions labeled as solid and dashed curves, respectively in Figure 8.1. We also calculated the stellar Rosseland mean opacity normalized to the total dust mass ($\kappa_{*,d} = 3995$ cm^{2}g^{-1}) at the solar temperature labeled as the star legend. These opacities can be simply converted to the ones normalized to gas ($\kappa_{P,g}$, $\kappa_{R,g}$, and $\kappa_{*,g}$) by multiplying the dust to gas mass ratio, which is 0.01 for all models. Disk opacities are inputs for the radiation module, whereas the stellar opacity is used in the stellar irradiation as an extra heating source term (see Appendix 8.7).

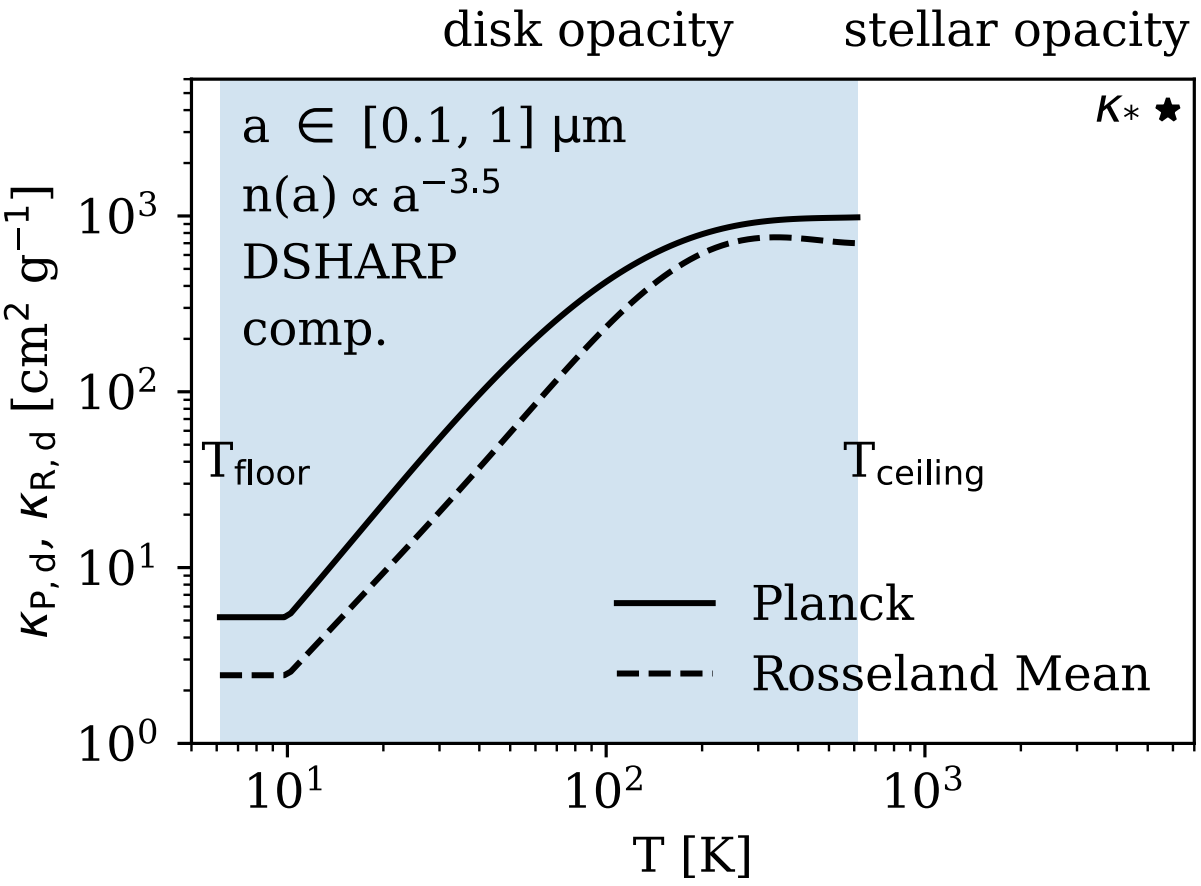

Figure 8.1: The temperature-dependent dust opacities adopted for all the radiation-hydro models. The solid line indicates the Planck opacity of the disk, whereas the dashed line indicates the Rosseland mean opacity of the disk. The wavelength-dependent DSHARP opacity (Birnstiel et al. 2018) is convolved at different temperatures to obtain temperature-dependent mean opacities. The stellar temperature is assumed to be 1 $T_{\odot}$. Its Planck opacity and Rosseland mean opacity are assumed be the same and marked by the star.

Comparison with RADMC-3D

We froze the hydrodynamics and used the initial conditions of full and transition disk models to test the temperature calculation of our irradiation implementation. Then we compared the results with Monte Carlo radiative transfer code RADMC-3D (Dullemond et al. 2012) using the same density structure. In RADMC-3D, we also used the same DSHARP opacity with the same dust properties and dust scattering turned off. When the disk is mostly optically thin to the stellar irradiation, the difference is at most $\sim$7%, such as in the transition disk with $r_{\rm cav}$ = 54 au (shown in Figure 8.2).

The difference comes from the frequency integrated radiative transfer in Athena++ module and the more accurate multi-frequency treatment in RADMC-3D. This difference has been extensively studied in Kuiper et al. (2010); Kuiper & Klessen (2013), where they found that the temperature calculated by the gray radiation transfer can be underestimated in the optically thick regime and overestimated in the optically thin regime for the stellar irradiation, which is consistent with our results. This is because the region near the midplane is optically thick to the stellar irradiation, so the heating comes from the $\tau_* = 1$ (τ_* is the stellar optical depth integrated in the radial direction, see Equation 8.21) surface in the atmosphere (Calvet et al. 1991; Chiang & Goldreich 1997). However, even though the stellar spectrum peaks at optical to UV wavelengths, the continuum stellar spectrum still has a set of $\tau_* = 1$ surfaces for each frequency instead of a single one. The $\tau_* = 1$ surfaces at longer wavelengths can penetrate deeper and transport more energy to the midplane, thus increasing the temperature at the optically thick region (Kuiper et al. 2010). They also demonstrated that even within the single frequency radiation-hydro framework, the temperature calculation can be as accurate as the multi-frequency one by integrating the multi-frequency stellar irradiation to mimic continuous $\tau_* = 1$ surfaces ("hybrid method" therein). This treatment has also

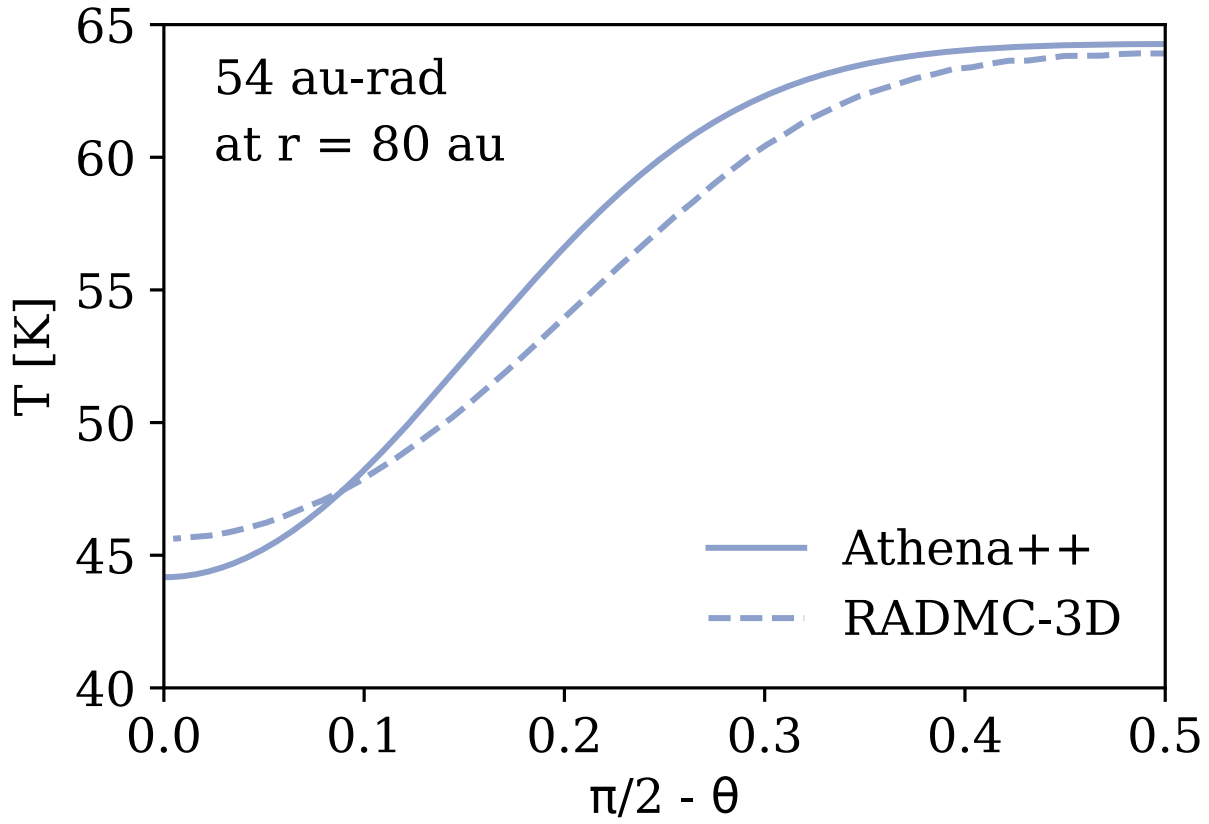

Figure 8.2: Temperature comparison between Athena++ and RADMC-3D for the transition disk model (`54au-rad`) at r = 80 au in the vertical direction. The solid and dashed curves show the temperatures in θ direction for Athena++ and RADMC-3D, respectively.

been implemented and tested for our problem and can be used in our future projects. For the full disk model ($r_{\rm cav} = 3 r_\odot$) in the current paper, the temperature at the midplane can be underestimated by 40%, due to the very high optical depth. Therefore, processes that are sensitive to the absolute temperature values (e.g., chemistry) need the hybrid method (Kuiper et al. 2010; Kuiper & Klessen 2013) or the multi-band radiation module (Jiang 2022) in the optically thick regime.

8.3.3 Pure Hydro Simulations with Different Levels of Simplifications

Since most of the understanding on VSI was from previous vertically isothermal simulations and linear theory, we also ran various pure hydro simulations with different levels of simplifications to compare with our rad-hydro simulations. Namely, they are (a) vertically isothermal simulations with adiabatic EoS and instant cooling ($\beta = 10^{-6}$), (b) vertically varying background temperature with adiabatic EoS and instant cooling, and (c) varying background temperature with adiabatic EoS and local orbital cooling. Their model names are also listed in Table 1 in Zhang et al. (2024).

(a) Vertically Isothermal Simulations. We tried to compare the vertically isothermal simulations using the same disk aspect ratio (h/r) as the rad-hydro simulations, as the Reynolds stress is dependent on h/r (Manger et al. 2020) and also temperature power-law index q (Manger et al. 2021). Since radiation hydro simulation will adjust the temperature to reach hydrostatic equilibrium from the initial condition, the disk scale height can change from initial condition depending on the radial optical depth of the star. The midplane and atmosphere also have different temperatures. Thus, we measured the midplane temperature and surface density at r_0 (40 au), and radial power-law density and temperature indices (p and q) of the rad-hydro simulations and put them as initial conditions for these vertically isothermal simulations. The midplane temperatures for four radiation hydro simulations are shown in Figure 8.3, along with their initial condition (dashed line).

(b) Background Temperature with Isothermal EoS. We used the R-Z two dimensional background temperature averaged between t = 1000-1200 P_{in} (500-700 P_{in} for r_{cav} = 54 au) from rad-hydro simulations and fixed them throughout the simulation. The gas density will adjust according to the temperature profile after the simulation begins.

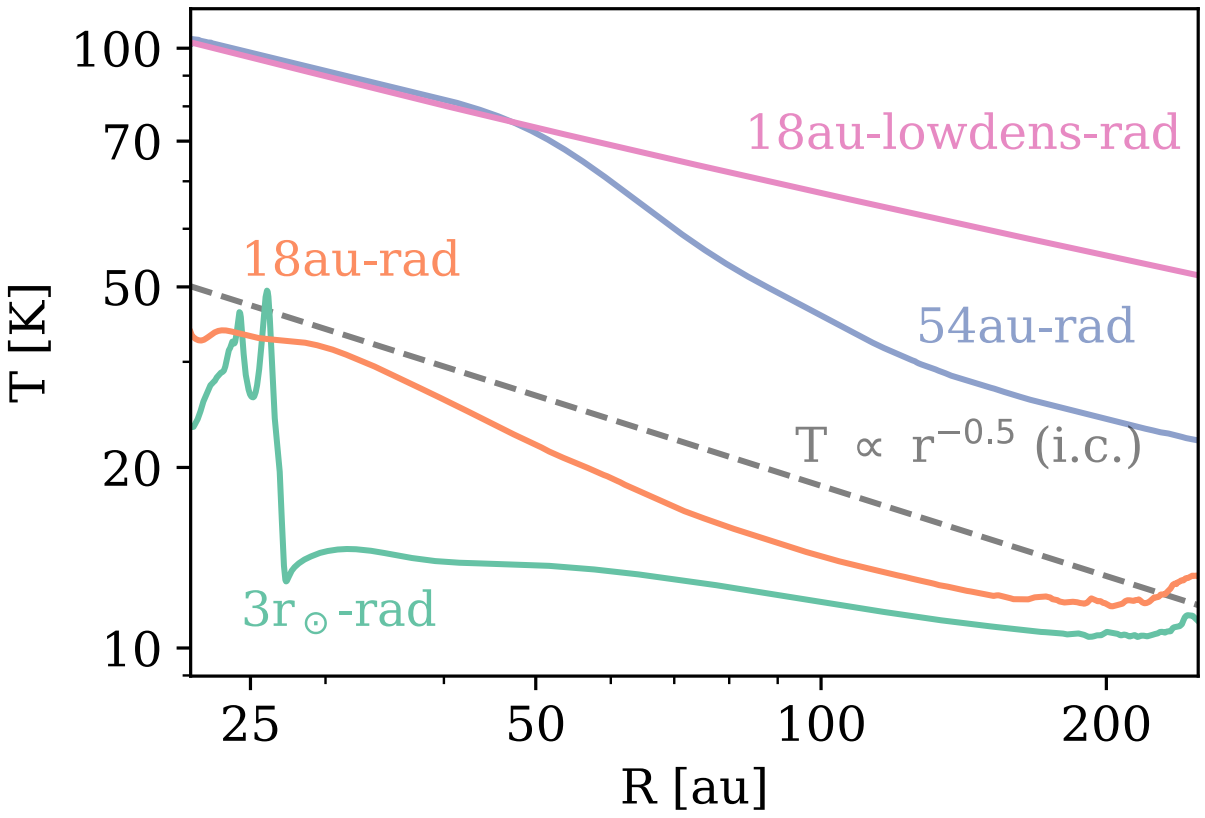

Figure 8.3: The midplane temperature profiles for four radiation-hydro models (time-averaged from t = 1000-1200 P_{in}, and t = 500-700 P_{in} for `54au-rad`). Models for `3r⊙-rad`, `18au-rad`, `54au-rad`, `18au-lowdens-rad` are shown in green, orange, purple, and magenta lines, respectively. The dashed line indicates the initial condition of the temperature, which is proportional to $R^{-0.5}$.

(c) Background Temperature with Local Oribital Cooling. For these simulations, we used the R-Z background temperature as (b), but used adiabatic EoS with local orbital cooling, where the cooling means that the temperature will be relaxed to the background temperature in a dimensionless cooling time β (the cooling time normalized by the Keplerian orbital frequency). We used the simple optically thin and thick cooling times (Flock et al. 2017),

$$\beta = \beta_{\rm thin} + \beta_{\rm thick} = \frac{c_v \Omega_K}{16\sigma_b T^3}\left(\kappa_{P,g}^{-1}(T) + 3(h/\hat{k})^2 \rho^2 \kappa_{R,g}(T)\right), \tag{8.8}$$

where $c_v = (\gamma_g - 1)^{-1} k_b/\mu m_H$ is the specific heat capacity at constant volume. We estimated the disk scale height by,

$$h = h_0 (r/r_0)^{1.5+q/2} \tag{8.9}$$

where q is the midplane temperature power-law slope in the radial direction shown in Table 1 in Zhang et al. (2024). We assumed $\hat{k}$ = 10 as h/10 is a typical length scale measured in Lin & Youdin (2015). However, since the optically thin term ($\beta_{\rm thin}$) dominates in most of the region, this adoption of h and $\hat{k}$ is not critical. By combining realistic vertical temperatures and location dependent cooling times, these simulations should have the closest thermodynamical properties compared with rad-hydro simulations, as we will demonstrate in the next section.

8.4 Results

8.4.1 Overview

The significant difference between the rad-hydro simulation (top panel) and classical vertically isothermal simulation (bottom panel) can be demonstrated in Figure 8.4, where we show the line in-

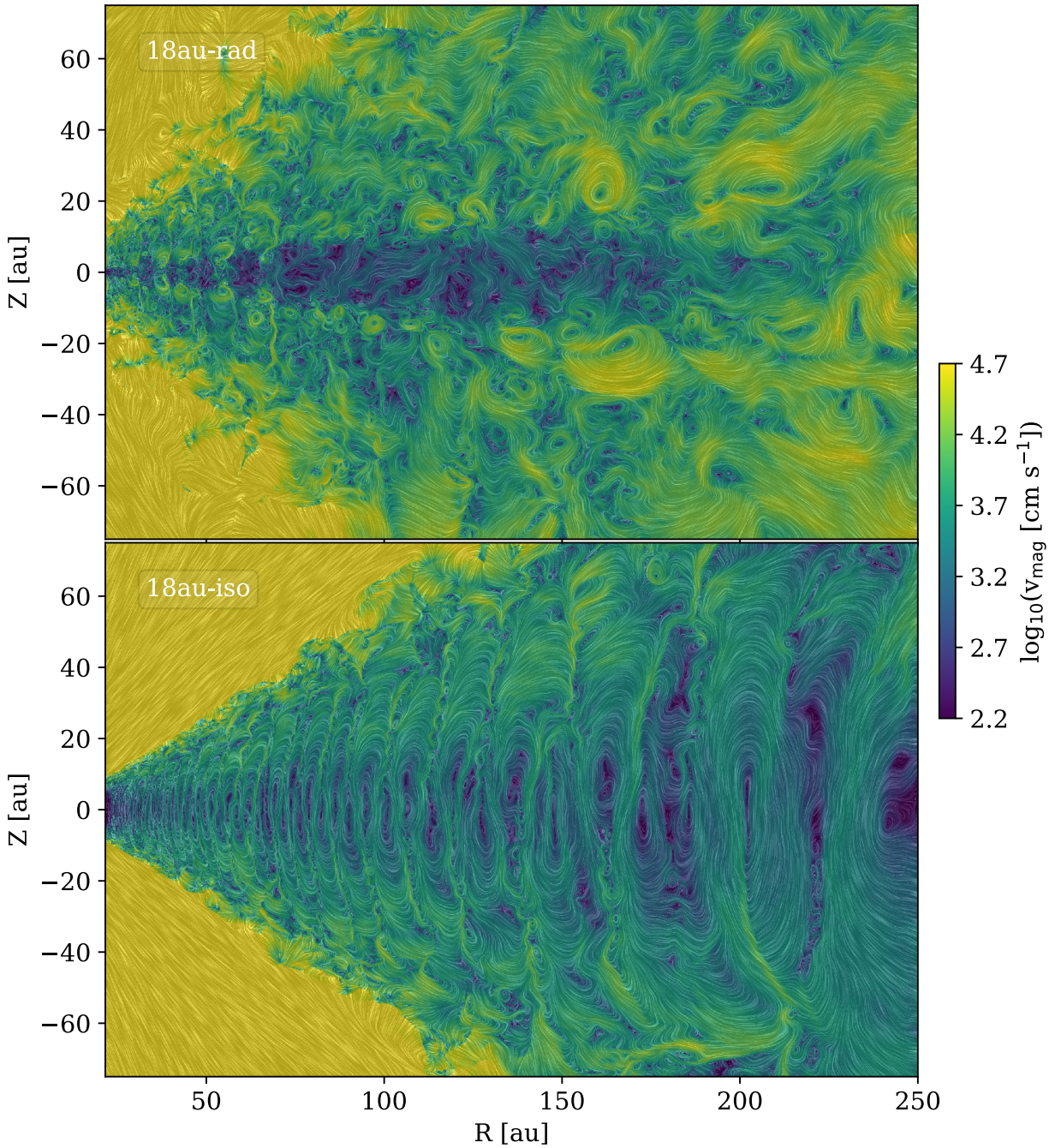

Figure 8.4: The line integral convolution (LIC) of the velocity field in the meridional plane, (v_R, v_Z), color-coded by its magnitude, v_{mag} for fiducial (r_{cav} = 18 au) radiaiton-hydro (top, `18au-rad`) and vertically isothermal (bottom, `18au-iso`) models. The flow pattern in the bottom panel is very similar to Figure 7 in Flores-Rivera et al. (2020).

tegral convolution[1] (LIC, similar to Flores-Rivera et al. 2020) of our fiducial models (r_{cav} = 18 au), `18au-rad` and `18au-iso` at t = 1000 P_{in}, color-coded by the meridional velocity, $\left(v_R^2+v_Z^2\right)^{1/2}$. In the vertically and locally isothermal simulation (bottom panel), the classical corrugation mode (the radially narrow, vertically extended circulation pattern) is clear. In the rad-hydro simulation (top panel), the disk is separated in two parts, the cool midplane and the superheated atmosphere. In the cool midplane, the velocity and turbulence levels are low, whereas the superheated atmosphere is more turbulent. The boundary between the cool midplane and superheated atmosphere exists a strong shear that leads to many small-scale vortices. The global circulation pattern that can be easily identified in locally and vertically isothermal simulation is replaced by turbulence on smaller scales.

Next, we analyze all of our radiation models in detail accompanied by pure-hydro simulations with various levels of simplifications. These quantities are taken either at t = 1000 P_{in} or time-averaged values between 1000-1200 P_{in}. In the case of the r_{cav} = 54 au transition disk, the flow at the cavity edge will reach the critical condition for the Rayleigh stability criterion and become unstable. A giant vortex develops at $\sim$ 800 orbits, which should break into smaller vortices in realistic 3D disks. Therefore, we analyze this particular model from 500 to 700 P_{in} (t=500 P_{in} for the snapshot) to avoid this unphysical feature in 2D.

8.4.2 Thermal Structure Determines Kinematics

We will use four rad-hydro simulations to demonstrate that $\tau_* = 1$ surface (τ_*: radial stellar optical depth, see Equation 8.21) sets disk temperature and equivalent local orbital cooling structures.

[1] We used python package `lic` (https://gitlab.com/szs/lic).

Subsequently, these two structures determine the disk kinematics.

The 2D (R-Z) snapshots of gas density (left panels), temperature (middle panels), and the vertical velocity (right panels) for four models are shown in Figure 8.5. The gas density does not deviate significantly from the initial conditions. Gas scale heights are represented by the white contours overlaid on gas densities, calculated by assuming that vertical density follows a Gaussian profile (see Equation 8.6) and that the temperature is taken at the midplane. In cases where r_{cav} = 3$r_\odot$ and 18 au (`3r⊙-rad` and `18au-rad`), the midplane temperature is lower than the initial condition, whereas the atmosphere temperature is higher, resulting in smaller effective gas scale heights in the midplane (see Table 1 in Zhang et al. (2024) and Figure 8.3) and larger effective gas scale heights in the atmosphere. In contrast, for r_{cav} = 54 au and 18 au, low-density cases (`54au-rad` and `18au-lowdens-rad`), temperatures are higher than the initial condition, leading to larger effective gas scale heights (see Table 1 in Zhang et al. (2024)). The black contours represent $\tau_* = 1$ surfaces where stellar irradiation intercepts the disk, setting the two temperature structure of the disk (cool midplane and superheated atmosphere). Note that the low density model (`18au-lowdens-rad`) lacks this surface, meaning that the entire disk is optically thin to stellar irradiation.

The locations of the $\tau_* = 1$ surfaces are shown in the temperature panels (middle panels) in Figure 8.5. We observe sharp decreases in temperature below these surfaces for the first three models. The low-density model (`18au-lowdens-rad`) is nearly vertically isothermal because the entire disk is optically thin to stellar irradiation. The white contours on top of the temperature maps indicate where the cooling time, estimated using Equation 8.8, equals the critical cooling time from Equation 8.1, denoted as β_c in each panel. The radial temperature gradient q is estimated by fitting a power-law to the midplane temperature profile (see Table 1 in Zhang et al. (2024) and

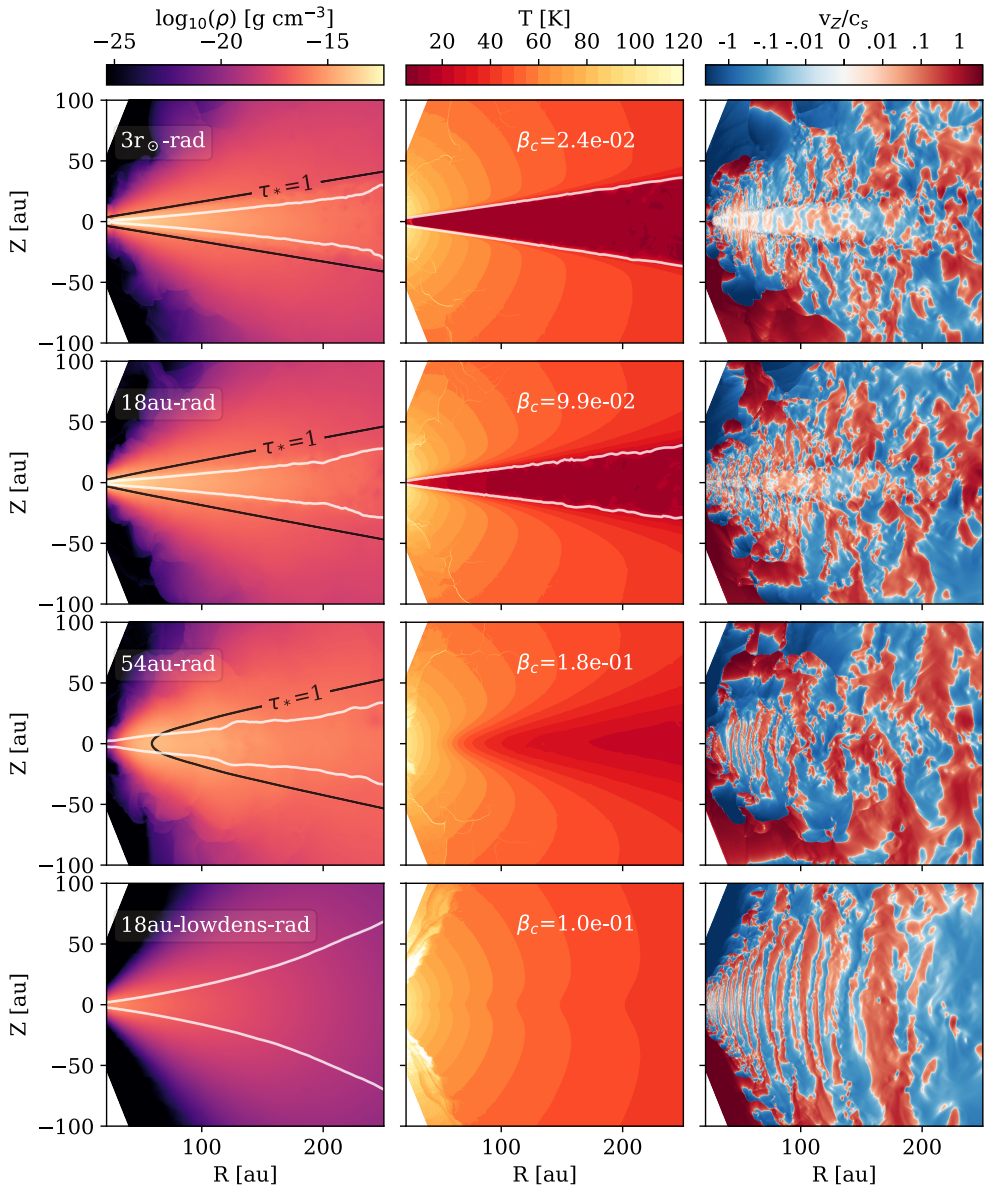

Figure 8.5: From left to right: the gas density (ρ), temperature (T), and vertical velocity (v_Z) of four radiation-hydro models at t = 1000 P_{in} (at t =500 P_{in} for r_{cav} = 54 au, `54au-rad`) in the meridional (R-Z) plane. From top to bottom: the full disk model with r_{cav} = 3 $r_\odot$ (`3r⊙-rad`), the transition disks with r_{cav} = 18 au (`18au-rad`), r_{cav} = 54 au (`54au-rad`), and 1% of the fiducial density (`18au-lowdens-rad`). The white contours on the density maps mark the one gas scale height. The black contours are the locations where the stellar optical depth in the radial direction reaches unity (the last model, `18au-lowdens-rad`, has $\tau_* < 1$ for the whole disk). The β_c on the temperature maps is the critical cooling time for VSI, represented by the white contours. The region enclosed by the contour near the midplane has $\beta > \beta_c$, so the VSI should not be operating according to linear analysis. The last two models, `54au-rad` and `18au-lowdens-rad`, have $\beta < \beta_c$ for the whole domain.

Figure 8.3). The r_{cav} = 3 $r_\odot$ and 18 au models exhibit cooling times exceeding the critical cooling time in the cool midplane indicating stability, while the superheated atmosphere has cooling times less the critical cooling time, indicating that the region is unstable to the VSI. The r_{cav} = 54 au and low-density models do not have cooling times exceeding β_c, indicating instability throughout the domain.

The vertical velocity (v_Z/c_s) structure in the right panels of Figure 8.5 also reflects temperature and cooling time structures. For the r_{cav} = 3$r_\odot$ and 18 au models, the vertical velocity is below 1% of the local sound speed in the cool midplane and above 10% of the local sound speed in the superheated atmosphere. The separation occurs around a gas scale height and slightly below the τ_* = 1 surface. In the atmosphere, the vertical velocity is still vertically extended and radially narrow, similar to the n=1 corrugation mode, but the upper and lower disk vertical velocities tend to have opposite signs, differing from the classical corrugation mode. We show in Appendix 8.10 (Figure 8.22) that these velocities tend to be anti-correlated. The classical n=1 corrugation mode only dominates when the disk has a vertically constant temperature and a short cooling time ($\beta < \beta_c$), which is the case inside the inner cavity of the r_{cav} = 54 au model and throughout the low-density model.

For the full disk model (r_{cav} = 3 $r_\odot$), we observe strong density and velocity perturbations near the inner boundary. This is a simulation artifact because our simulation domain cannot extend to 3 $r_\odot$ due to the computational cost associated with the very large dynamical range (see the end of Section 8.3.1).

To quantify the vertical structure of the disk in these radiative-hydrodynamic models, we present time-averaged vertical profiles of gas density, temperature, the radially integrated stellar optical depth (τ_*), vertically integrated disk optical depth ($\tau_{P,d}$), and cooling time (β) at $r = 80$

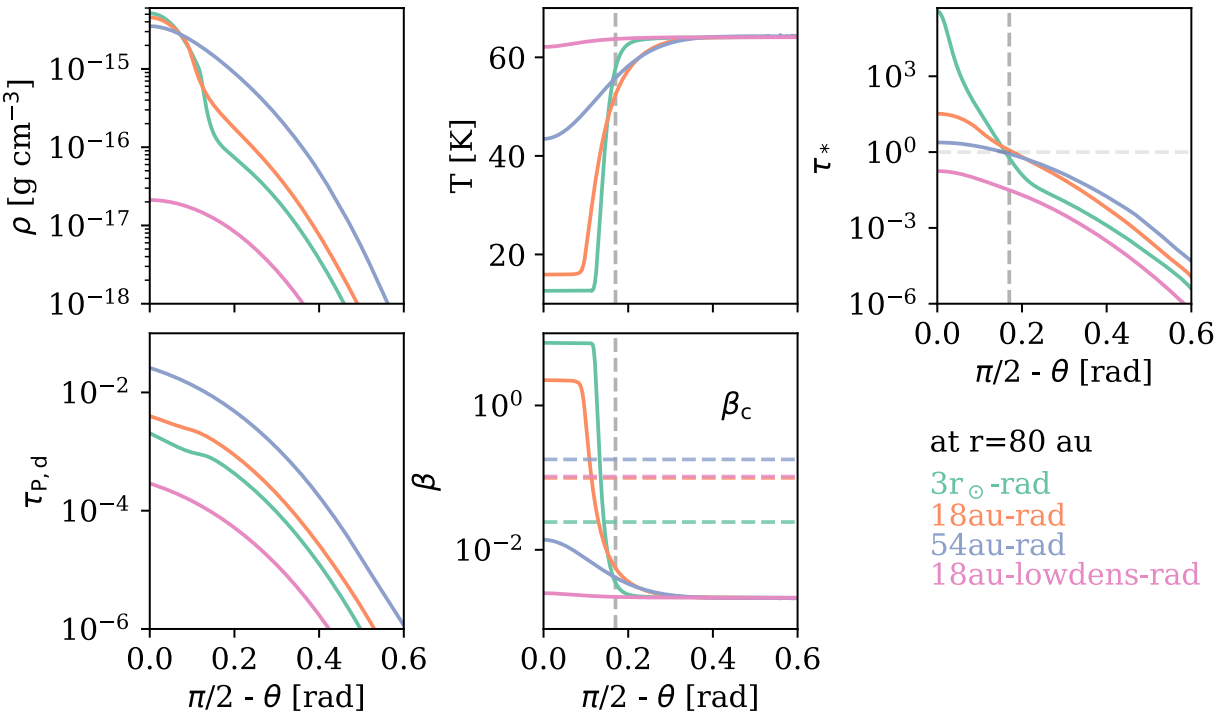

Figure 8.6: Time-averaged (t = 1000-1200 P_{in} and 500-700 P_{in} for r_{cav} = 54 au, `54au-rad` model) gas density, temperature, stellar optical depth in the radial direction (τ_*), disk optical depth in the vertical direction ($\tau_{P,d}$), and the cooling time (β_c) for four radiation-hydro models cut at r = 80 au in the vertical direction. Models for `3r⊙-rad`, `18au-rad`, `54au-rad`, `18au-lowdens-rad` are shown in green, orange, purple, and magenta lines, respectively. The horizontal dashed lines in the last panel indicate the critical cooling time, β_c. The vertical dashed lines indicate the τ_* = 1 surface for the first three models.

au in Figure 8.6. The densities of the $r_{cav} = 3\ r_\odot$ and 18 au models (`3r⊙-rad` and `18au-rad`) exhibit two Gaussian distributions, one concentrated at the midplane and the other more extended in the atmosphere. These correspond to the cool midplane and the warmer atmosphere, as shown in the temperature profiles. The temperatures remain almost constant in these two regions, with the transition occurring between 0.1 to 0.3 radians, roughly equivalent to 2-4 gas scale heights. For the $r_{cav} = 54$ au and low-density models (`54au-rad` and `18au-lowdens-rad`), two-Gaussian profiles are not as clear, given their smoother temperature transition. The low-density model is nearly vertically isothermal, with a slight temperature drop at the midplane. The transition between optically thin and thick stellar irradiation occurs at approximately 0.17 radians for all three models at 80 au (indicated by the vertical dashed lines). The low-density case is optically thin to stellar irradiation. This model only contains 10^{-4} $M_\odot$, which falls at the lower end of protoplanetary disk masses. Another way to achieve a very optically thin disk is to modify our assumptions regarding the fiducial small grain fraction and the dust-to-gas mass ratio. If the disk is entirely depleted of small particles or has an extremely low dust-to-gas mass ratio, it can become optically thin to stellar irradiation. The $\tau_{P,d}$ panel indicates that all models are optically thin to the disk's emission. The dimensionless cooling times for these models range from 10^{-3} to 10. Their critical cooling times, denoted by the horizontal dashed lines, differ due to variations in gas scale heights and radial temperature gradients. For the $r_{cav} = 3\ r_\odot$ and 18 au models, the transition between the VSI unstable atmosphere and the VSI stable midplane occurs around 0.15 radians, approximately 2-3 gas scale heights. The $r_{cav} = 54$ au and low-density models have cooling times smaller than the critical cooling times throughout their vertical extent, suggesting that the VSI should operate along the entire vertical extent.

To indicate locations where VSI is active or inactive in the R-Z plane, we present R-ϕ ($T_{R,\phi}$,

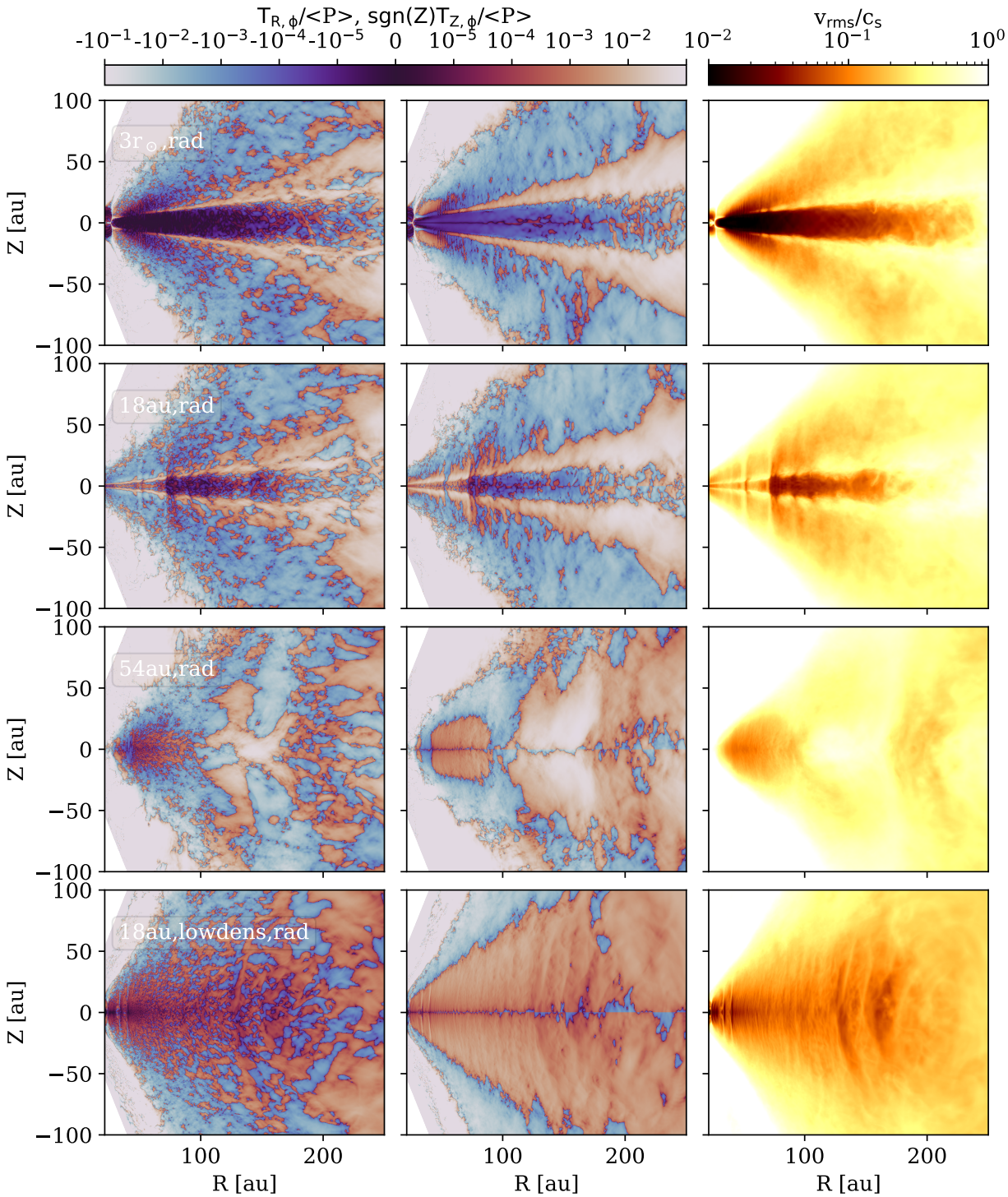

Figure 8.7: From left to right: the turbulence stresses for Z-ϕ and R-ϕ components normalized by the averaged gas pressure, and the root mean square velocity normalized by the local sound speed. The values are calculated between t = 1000-1200 P_{in}, (at t =500-700 P_{in} for r_{cav} = 54 au, `54au-rad`). Other layouts are similar to Figure 8.5.

left panels) and Z-ϕ ($T_{\mathrm{Z},\phi}$, middle panels) Reynolds stresses, normalized by the time-averaged pressure, along with root mean square velocity normalized by the local sound speed (right panels) for four radiation models in Figure 8.7. We define $\alpha_R \equiv T_{\mathrm{R},\phi}/\langle P \rangle_{\mathrm{t}}$ and $\alpha_Z \equiv T_{\mathrm{Z},\phi}/\langle P \rangle_{\mathrm{t}}$, where $T_{\mathrm{R},\phi} \equiv \langle \rho \mathrm{v_R} \mathrm{v}_\phi \rangle_{\mathrm{t}} - \langle \mathrm{v}_\phi \rangle_{\mathrm{t}} \langle \rho \mathrm{v_R} \rangle_{\mathrm{t}}$, and $T_{\mathrm{Z},\phi} \equiv \langle \rho \mathrm{v_Z} \mathrm{v}_\phi \rangle_{\mathrm{t}} - \langle \mathrm{v}_\phi \rangle_{\mathrm{t}} \langle \rho \mathrm{v_Z} \rangle_{\mathrm{t}}$ (Nelson et al. 2013b; Stoll & Kley 2014; Flock et al. 2017). The values are calculated between t = 1000-1200 $\mathrm{P_{in}}$, except for the `54au-rad` simulation which was taken between t = 500-700 $\mathrm{P_{in}}$. In all three columns, brighter colors indicate higher turbulence values. In the two stress columns, red colors denote positive values, while blue colors indicate negative values. The `3r`$_\odot$`-rad` model shows low levels of α_R ($\lesssim 10^{-5}$) and α_Z ($\lesssim 10^{-4}$) in the midplane, but they increase from the inner to the outer disk. The stress becomes much larger around the $\tau_* = 1$ surface and approaches 10^{-2} before reversing sign to negative values. Overall, α_Z is larger than α_R near the midplane. The root mean square velocity is at the percent level of the sound speed near the midplane, approaching a fraction of the sound speed in the atmosphere, with the strongest values at the transition region (see Section 8.4.3). The `18au-rad` model exhibits similar behavior. Its midplane turbulence becomes slightly higher and the low turbulence region is more confined to the midplane. The `54au-rad` model shows VSI-like anisotropic turbulence between α_R and α_Z (similar to `18au-lowdens-rad`) in the cavity and at the ring until ~ 90 au, where α_R is $\sim 10^{-4}$ and α_Z is $\sim 10^{-2}$. At the outer disk, turbulence levels become much higher ($\gtrsim 10^{-2}$) in both stress components, which are much stronger than all other models. This suggests that the gap edge in transition disks can be highly turbulent due to direct stellar irradiation. For the `18au-lowdens-rad` model, the turbulence structures are very similar to those of vertically and locally isothermal VSI simulations. The α_R is $\sim 10^{-4}$ and α_Z is $\sim 10^{-2}$ throughout the disk, while the root mean square velocity is at the percent level of the local sound speed globally, yet still higher than the midplane values for `3r`$_\odot$`-rad` and `18au-rad`

models.

8.4.3 Accretion, Zonal Flow, and Vertical Shear Rate

The stress structure determines the disk's accretion structure. We can reveal this relation by averaging the angular momentum equation in the azimuthal direction (e.g., Turner et al. 2014; Lesur 2021; Rabago & Zhu 2021a; Zhu et al. 2023) and obtain

$$R\frac{\partial\langle\rho\delta v_\phi\rangle}{\partial t} = -\langle\rho v_R\rangle\frac{\partial}{\partial R}\big(R\langle v_\phi\rangle\big) - \langle\rho v_Z\rangle R\frac{\partial\langle v_\phi\rangle}{\partial Z} - \frac{1}{R}\frac{\partial}{\partial R}\Big(R^2 T_{R,\phi}\Big) - R\frac{\partial}{\partial Z}T_{Z,\phi}\ , \tag{8.10}$$

where $\delta v_\phi = v_\phi$ - $\langle v_\phi\rangle$, $T_{\mathrm{R},\phi} = \langle\rho \mathrm{v_R} \mathrm{v}_\phi\rangle - \langle \mathrm{v}_\phi\rangle\langle\rho \mathrm{v_R}\rangle$, and $T_{\mathrm{Z},\phi} = \langle\rho \mathrm{v_Z} \mathrm{v}_\phi\rangle - \langle \mathrm{v}_\phi\rangle\langle\rho \mathrm{v_Z}\rangle$. Since our simulations are in 2D, we calculate time averaged instead of azimuthally averaged quantities. If we adopt a smooth disk structure (Equation 8.7), the change of $\langle v_\phi\rangle$ is small in Z direction, so the second term in the first line can be neglected. We note that in our rad hydro models, the shear at the transition region between the atmosphere and midplane can be large, but since $\langle\rho v_Z\rangle$ is still small compared to $\langle\rho v_R\rangle$, the second term is still less than the first term. If we also assume the disk reaches a steady state (left hand side is zero), the accretion structure is only determined by the derivatives of the stresses. That is[2],

$$\langle\rho v_R\rangle\frac{\partial}{\partial R}\big(R\langle v_\phi\rangle\big) = -\frac{1}{R}\frac{\partial}{\partial R}\Big(R^2 T_{R,\phi}\Big) - R\frac{\partial}{\partial Z}T_{Z,\phi}\ . \tag{8.11}$$

[2]Besides angular momentum, we also briefly discuss the energy budget in Figure 8.18 in the Appendix.

Then we can use Figure 8.7 and Equation 8.11 to explain the time-averaged radial velocity (v_R/c_s) in Figure 8.8 shown on the left panels. Since in all our models the vertical gradient of the stress is greater than the radial gradient among the transition region between midplane and atmosphere, and $T_{Z,\phi}$ is greater than $T_{R,\phi}$, we can just use the second term on the right hand side of Equation 8.11 and the center column of Figure 8.7 to understand the accretion structure. The radial velocity in the midplane is very small for both $r_{cav} = 3\ r_\odot$ and 18 au models due to the small stress and stress gradient there. At the boundary between the cool midplane and superheated atmosphere, an outgoing flow is on top of an ingoing flow, resembling layered accretion. In Figure 8.7, the region of the ingoing flow is aligned with the sharp transition of negative stress to positive stress above the midplane, whereas the region of the outgoing flow is aligned with the transition of positive stress to negative stress in the upper atmosphere. The sign and magnitude of $\langle \rho v_R \rangle$ can be perfectly calculated from Equation 8.11. These regions also align with the regions that have the strongest shear (right panels). In contrast, the midplane shear rate is at least an order of magnitude smaller. The $r_{cav} = 54$ au and low-density models have ingoing flow in the midplane, and outgoing flow in the atmosphere, which is consistent with previous analytical studies on VSI operating isothermal disks–much strong anistropic turbulence between $R-\phi$ and $Z-\phi$ directions (Stoll et al. 2017; Rabago & Zhu 2021a). These vertical shear rates for these two models are more uniformly distributed in the vertical direction, due to their more vertically uniform stress profiles which result from smoother temperature profiles. Compared to $r_{cav} = 3\ r_\odot$ and 18 au models, the shear rates in these two models are larger in the midplane.

The direction of the radial velocity and shear rate can be intuitively understood by examining the azimuthal velocity shown in the middle panels of Figure 8.8 (azimuthal velocity subtracted by the local Keplerian velocity). For the first two models that have temperature stratification, the mid-

plane has faster rotational velocity than the atmosphere. At the transition region near the midplane, the gas loses its angular momentum due to the shear, thus moving inward, whereas the gas near the atmosphere gains its angular momentum and moves outward. In the bottom two models, which lack a strong vertical temperature structure, the azimuthal velocity has less vertical dependence, resulting in significantly smaller shear and radial velocity. Additionally, all four models exhibit zonal flows with perturbations to the azimuthal velocity. The $r_{cav} = 3\ r_{\odot}$ and 18 au models have relatively smaller scale perturbations on several au, whereas the 54 au model has zonal flows on tens of au. The low density model's azimuthal velocity perturbation is small and follows the corrugation pattern for vertical velocity. These zonal flows are associated with substructures in gas (see Section 8.5.1) and can be observed in near-infrared scattered light (see Section 8.5.2).

To be more quantitative, we present vertical profiles of various time-averaged velocity fields at $r = 80$ au in Figure 8.9. Regarding radial velocity, the outgoing and ingoing flows for the $r_{cav} = 3\ r_{\odot}$ and 18 au models are approximately 5% of the local sound speed, with the outgoing flow having a higher magnitude than the ingoing flow. The $r_{cav} = 54$ au model shows ingoing flow in the midplane and outgoing flow above the midplane, both at around 2% of the sound speed. In contrast, the low-density model displays ingoing flow in the midplane at less than 1% of the sound speed, and outgoing flow above the midplane, which gradually increases to 4% of the sound speed at 0.5 radians. The time-averaged vertical velocities in the first three models are at the level of 1-2% of the sound speed, while the low-density model has negligible velocity. As for azimuthal velocity, all models show sub-Keplerian motion due to the radial pressure gradient. The $r_{cav} = 3r_{\odot}$ and 18 au models exhibit a sharp transition in azimuthal velocity around 0.2 radians, attributed to the steep vertical temperature gradient between the cool midplane and the superheated atmosphere. In the same region, there is a smooth transition in azimuthal velocity for the $r_{cav} = 54$ au model.

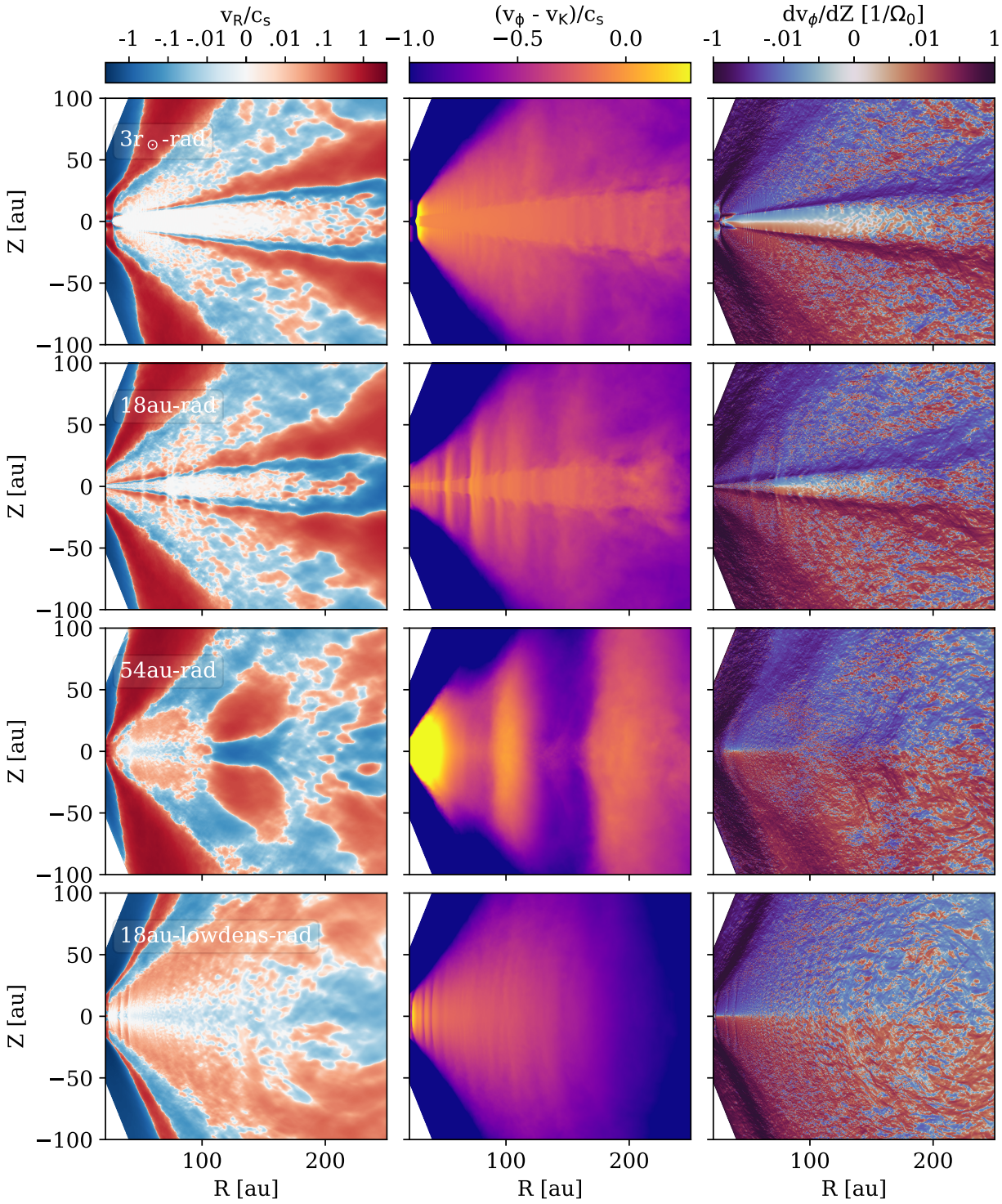

Figure 8.8: From left to right: the time-averaged (t = 1000-1200 P_{in} and 500-700 P_{in} for r_{cav} = 54 au, `54au-rad` model) values of the radial velocity (v_R), azimuthal velocity subtracted by Keplerian velocity (v_ϕ - v_K), and the vertical shear rate dv_ϕ/dZ for four radiation-hydro models in the meridional (R-Z) plane in the same layout as Figure 8.5.

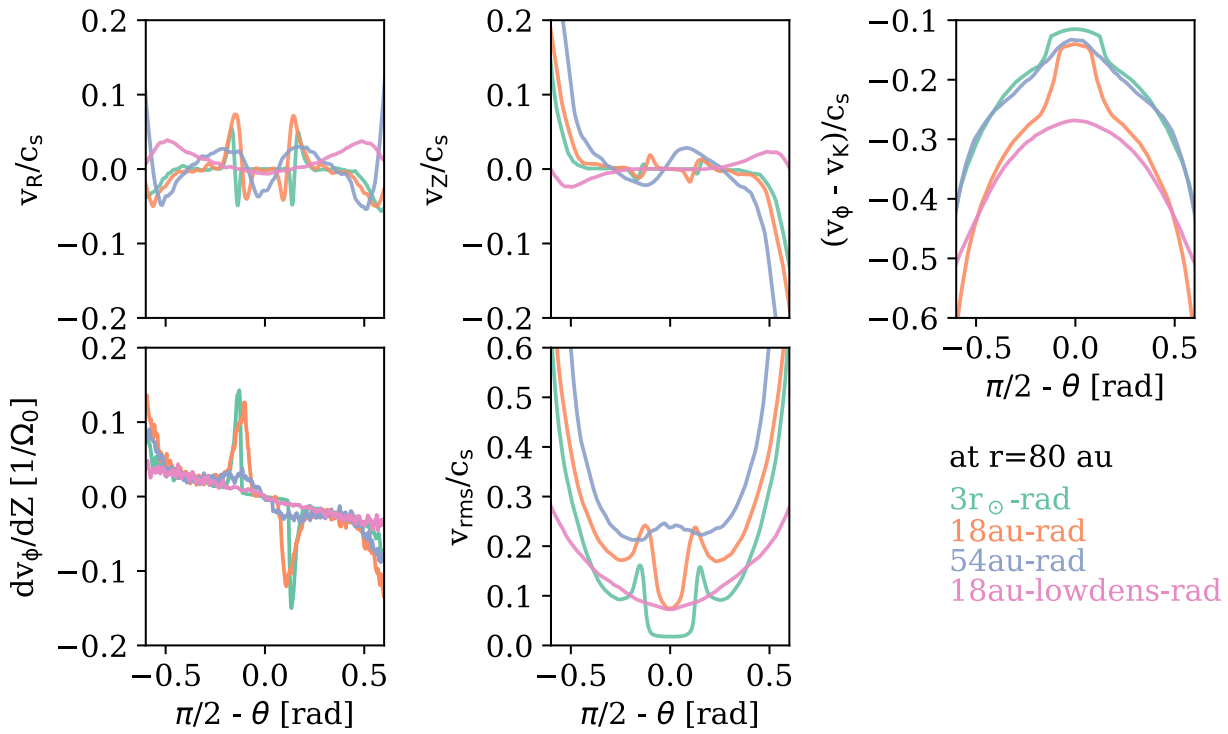

Figure 8.9: The vertical slices of the time-averaged (from 1000-1200 P_{in} and 500-700 P_{in} for r_{cav} = 54 au, `54au-rad` model) radial velocity (v_R), vertical velocity (v_Z), azimuthal velocity subtracted by Keplerian velocity (v_ϕ - v_K), vertical shear rate (dv_ϕ/dZ), and the root mean square velocity (v_{rms}) of four radiation-hydro models at r = 80 au.

The shear rate for the $r_{cav} = 3$ $r_\odot$ and 18 au models peaks at 0.2 radians, reaching 0.15 $\Omega_{K,0}^{-1}$, where $\Omega_{K,0}^{-1}$ is the time unit, or the inverse of Keplerian orbital frequency at unit radius r_0 = 40 au. The $r_{cav} = 54$ au model also exhibits a slight increase in the same region. In contrast, the low-density model displays a linear increase in vertical shear above and below the midplane. The root mean square of the full velocity is also highest around 0.2 radians for the two models. At the midplane, the $r_{cav} = 3$ $r_\odot$ model is relatively quiet, with velocities at approximately 2% of the sound speed. The 18 au model and the low-density model exhibit similar values at the midplane, approximately 1% of the sound speed. In contrast, the 54 au model is much more turbulent, with velocities exceeding 20% of the sound speed even at the midplane.

We also integrated $\langle \rho v_R \rangle$ along the vertical direction to obtain (time-averaged and radially-averaged) radial mass accretion rates ($\dot{M}_{acc} = 2\pi R \int \langle \rho v_R \rangle dZ$) as functions of R and show them in Figure 8.10 (upper panel). We also show the vertically integrated α_R parameter in the lower panel, defined as

$$\alpha_{int} = \frac{\int T_{R,\phi} dZ}{\int \langle P \rangle dZ}. \tag{8.12}$$

$\dot{M}_{acc}$ is associated with the radial gradient of α_{int}, since if we integrate Equation 8.11 along Z and assume that $\langle v_\phi \rangle$ equals to the midplane Keplerian speed v_K and does not change with Z, Equation 8.11 can be written as

$$\dot{M}_{acc} = -\frac{2\pi}{\partial R v_K / \partial R} \times \left(\frac{\partial}{\partial R} \left(R^2 \alpha_{int} \int \langle P \rangle dZ \right) + R^2 T_{Z,\phi} \Big|_{Z_{min}}^{Z_{max}} \right), \tag{8.13}$$

where the $T_{Z,\phi}$ is typically small at the boundaries due to the small densities at the disk surface.

The fluctuation is strong in the radial direction with the accretion rate frequently changing signs on au scale (Figure 8.10 upper panel), whereas the integrated α_{int} has a lower variability (Figure 8.10 lower panel). For $r_{cav} = 3$ $r_\odot$ model, the accretion rate is negative (ingoing) in the inner disk until 35 au, then it changes signs rapidly until reaching positive (outgoing) 10^{-9} $M_\odot$ yr^{-1} in the outer disk. Except near the inner boundary, the α_{int} increases from $\lesssim 10^{-6}$ at 50 au to $\sim 10^{-2}$ beyond 200 au. The $r_{cav} = 18$ au model has positive (outgoing) 10^{-9} $M_\odot$ yr^{-1} inside 25 au, but it can be affected by the setup for inner boundary. Then the accretion rate becomes negative until 100 au, and becomes positive in the outer disk. The α_{int} increases from $\sim 10^{-4}$ to $\sim 10^{-2}$ from inner to outer disk. The $r_{cav} = 54$ au model has the highest magnitude of accretion rate, reaching

positive 10^{-8} $M_\odot$ yr^{-1} around 100 au and positive 10^{-8} $M_\odot$ yr^{-1} around 200 au. The low density model has almost zero accretion rate ($< 10^{-11}$ $M_\odot$ yr^{-1}; the M_{acc} for the low density model is multiplied by 100 to show its value) and α_{int} between 10^{-5}-10^{-4} throughout the disk. We want to emphasize that even though the fiducial `18au-rad` model has lower stress values than the equivalent vertically isothermal model `18au-rad-lowdens` at the midplane, the integrated α_{int} can be still larger due to the layered accretion at the disk surface.

We quantify the stress levels in Figure 8.11. These stresses exhibit fluctuations with respect to time, radius, and θ, thus we compute the average of these quantities between 60-100 au to represent the stress at 80 au. The time average spans 200 P_{in}, consistent with previous figures. We present the stresses for three rad-hydro simulations ($r_{cav} = 3$ $r_\odot$, 18 au, and 54 au models in panels a, b and d), alongside three pure-hydro simulations with various assumptions (panels c, e, and f, which we will discuss more in the next section, Section 8.4.4). Solid lines represent α_Z, while dashed lines represent α_R.

For the full disk model (`3r`$_\odot$`-rad`), both α_R and α_Z peak around 0.2 radians, coinciding with the location of the strongest shear and reaching values on the order of 10^{-2}. In the midplane, α_R remains less than 10^{-6}, whereas α_Z is around 10^{-4}. The `18au-rad` model exhibits similar behavior, with α_Z and α_R both reaching values of approximately 10^{-2} at the transition region between the midplane and the atmosphere. For both components, α remains around 10^{-4} to 10^{-3} in the midplane. In the case of the `54au-rad` model, vertical turbulence α_Z consistently remains at a higher level, around 10^{-3} to 0.4 radians, whereas α_R can be lower by an order of magnitude, approximately 10^{-3}. For classical locally-isothermal and vertically isothermal VSI (`18au-iso`), the anisotropy between these two components are more pronounced, with α_Z ($\sim 10^{-2}$) exceeding α_R ($\sim 10^{-4}$) by two orders of magnitude, consistent with previous studies (e.g., Stoll et al. 2017).

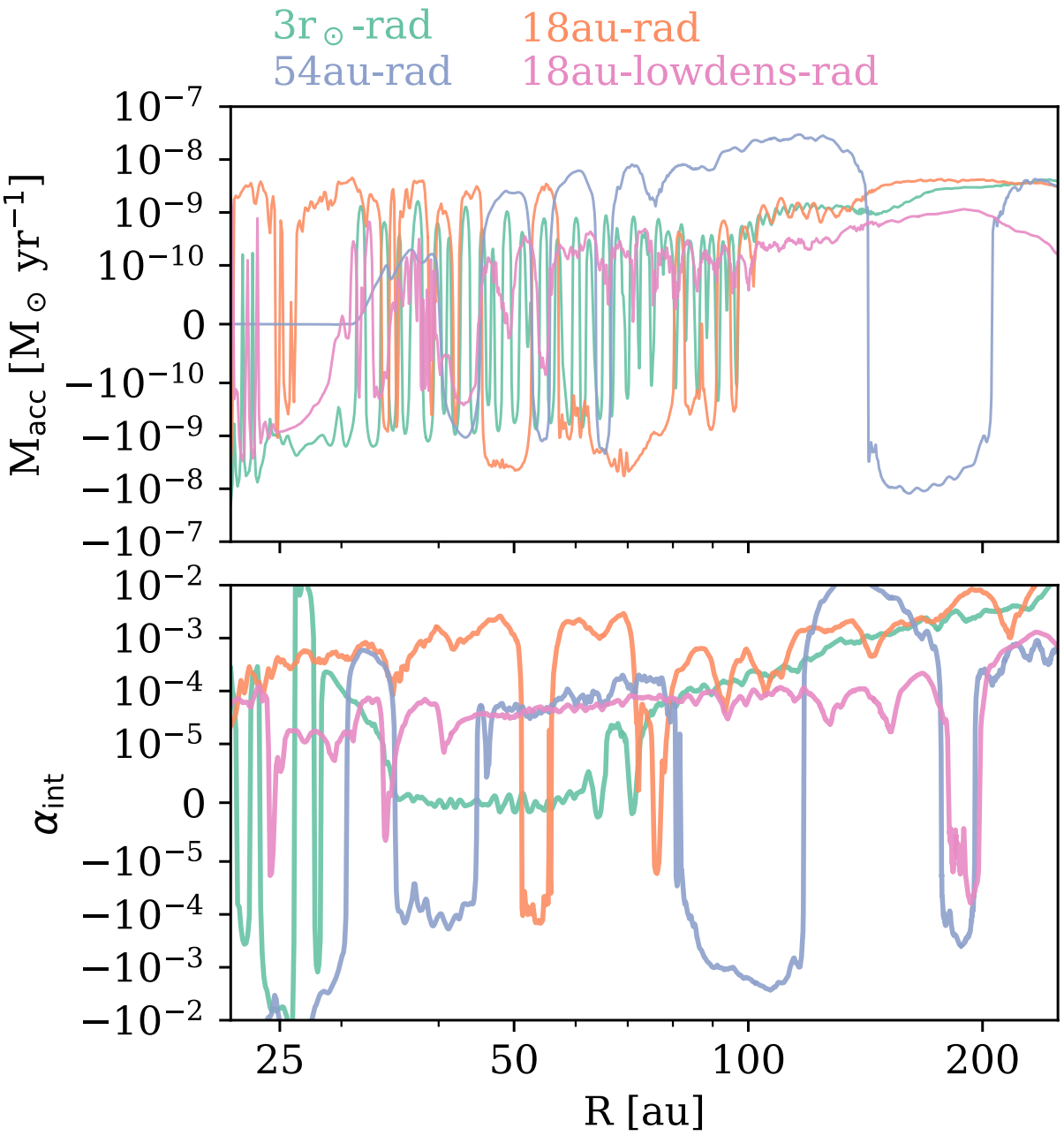

Figure 8.10: The time-averaged accretion rate in the radial direction (integrated in the vertical direction), and α_{int} (vertically integrated α_R) for four radiation-hydro models. The $M_\odot$ yr^{-1} for the low density model is multiplied by 100 to show its value. The color representations are the same as previous figures.

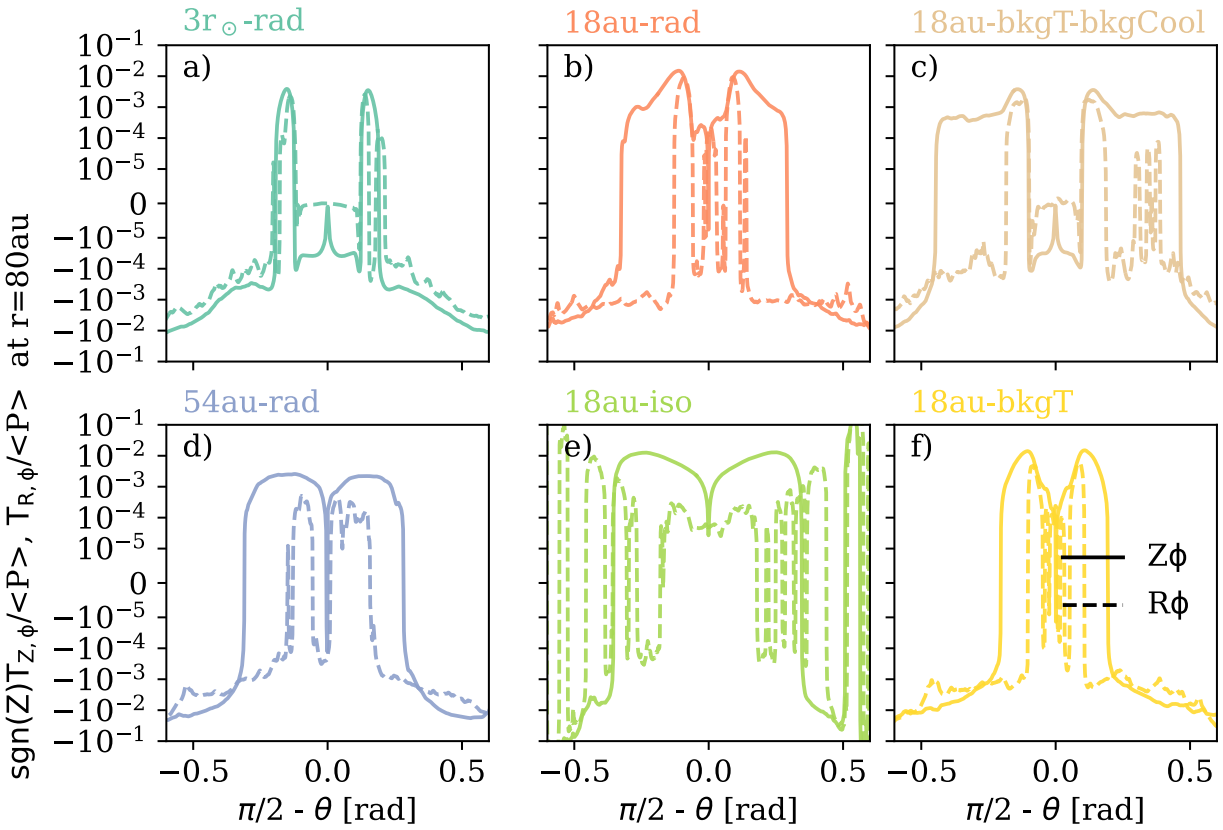

Figure 8.11: The turbulence stresses for Z-ϕ and (solid lines) R-ϕ (dashed lines) components normalized by the averaged gas pressure at 80 au along the vertical direction. The values are calculated between t = 1000-1200 P_{in}, and averaged from r = 60-100 au. From left to right, they are `3r⊙-rad`, `18au-rad`, `18au-bkgT-bkgCool`, `54au-rad`, `18au-iso`, and `18au-bkgT` models, respectively.

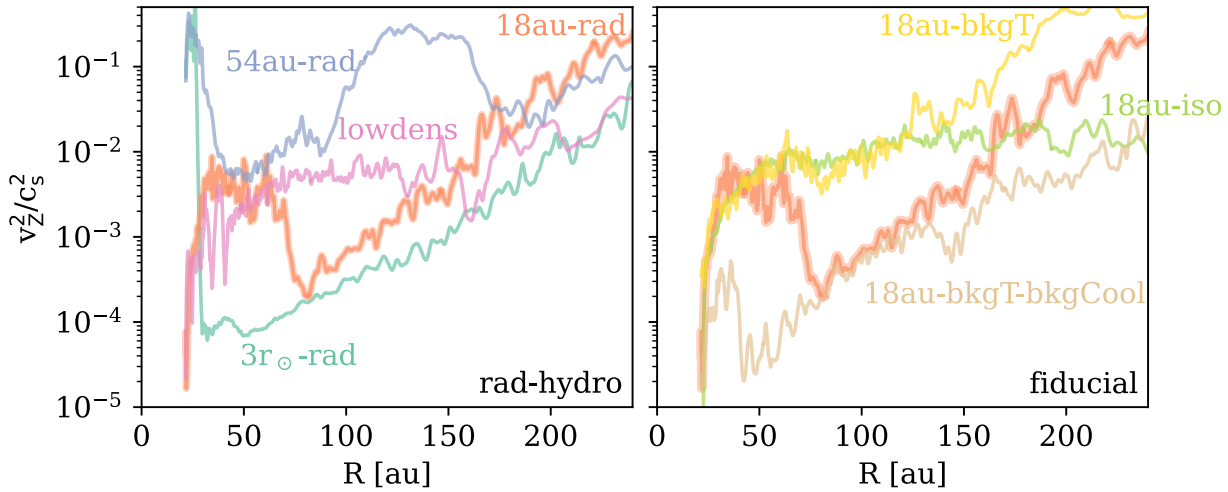

Figure 8.12: Time-averaged v_Z^2/c_s^2 that represents the turbulence level in the midplane for rad hydro models (`3r⊙-rad`, `18au-rad`,`54au-rad`, and `18au-lowdens-rad`) on the left panel and fiducial models (`18au-rad`, `18au-iso`, `18au-bkgT`, and `18au-bkgT-bkgCool`) on the right panel.

In the radial direction, not only the integrated turbulence α_{int} increases with radius as shown in Figure 8.10, but also the midplane turbulence. This can be seen in 2D velocity maps such as Figures 8.4 and 8.5, and turbulence map in Figure 8.7. We quantify this by plotting the time-averaged v_Z^2 in Figure 8.12. On the left panel we show four rad-hydro models. For `3r`$_\odot$`-rad` and `18au-rad`, the vertical velocities are low in the inner disk $\sim 1\%$ of the local sound speed at ~ 50 au and increases to more than 10% of the sound speed in the outer disk at ~ 200 au. For the `54au-rad` model, the turbulence level is high across the disk ($\gtrsim 10\%$ of the sound speed), where the perturbation is aligned with the zonal flow. The trend can be explained by the fact that as the effective scale height becomes larger in the outer disk, the density contrast between the midplane and atmosphere becomes smaller. At ~ 200 au, the turbulent flow at the atmosphere already has enough energy to disturb the quiet midplane. For the `18au-lowdens-rad` model, the turbulence is almost constant across the disk, on the order of 10% of the sound speed, since there is no thermal stratification.

In a recent paper by Melon Fuksman et al. (2023a), their $f_{\rm dg} = 10^{-4}$ model ($f_{\rm dg}$ is the dust to gas mass ratio) also has a similar temperature and cooling time stratification to our fiducial model, which leads to a quiet midplane and turbulent atmosphere. We find consistent results except a higher level of turblence in the midplane. Their midplane turbulence is below 10^{-7} whereas ours is between 10^{-5}-10^{-4}. This difference might be explained by multiple factors. First, their inner disk has a lower h/r, and a lower h/r leads to a lower turbulence (Manger et al. 2020; 2021). In Figure 8.12, we also show that the turbulence increases with R since the energy contrast between the midplane and atmosphere becomes lower, which points to a lower turbulence value for the inner disk. They also have 200 cells per scale height resolution which can better resolve lower turbulence levels.

8.4.4 Good Approximation: Background Temperature with Local Orbital Cooling

As rad-hydro simulations differ significantly from classical VSI shown in vertically and locally isothermal simulations, we attempt to use pure-hydro simulations with varying levels of assumptions for comparison with rad-hydro simulations. We use Figure 8.13 to illustrate that pure hydro simulations with background temperature and local orbital cooling provide a good approximation for rad-hydro simulations.

Figure 8.13 displays (from left to right) vertical velocity snapshots, time-averaged radial velocity, azimuthal velocity subtracted from Keplerian velocity, and vertical shear rate. From top to bottom panels, we have the rad-hydro fiducial model (`18au-rad`), the vertically and locally isothermal model (`18au-iso`), the locally isothermal and background temperature model (`18au-bkgT`), and the orbital cooling and background temperature model (`18au-bkgT-bkgCool`). The rad-hydro model has been introduced in Figures 8.5 and 8.8; we retain them since these panels can be directly compared with the isothermal model in the second row, representing a classical VSI picture. The isothermal model (`18au-iso`) also resembles the low-density rad-hydro model. We note that the radial temperature gradient and h/r in `18au-iso` model are measured in the midplane of rad-hydro simulations for a close comparison. In the pure-hydro simulation that incorporates the background temperature of the rad-hydro simulation (third row, `18au-bkgT`), we observe the disruption of the delicate n=1 corrugation mode. Layered accretion and strong shear in the temperature transition region become evident, but the midplane vertical velocity remains higher than in rad-hydro simulations, as this region is still VSI unstable due to the almost zero cooling time ($\beta = 10^{-6}$). The zonal flow in the azimuthal velocity also differs from the rad-hydro

simulation.

By incorporating the estimated cooling time from the rad-hydro simulation in the bottom panels (`18au-bkgT-bkgCool`), all four fields closely resemble the rad-hydro simulations. Therefore, we demonstrate that computationally inexpensive pure-hydro simulations can capture crucial features of rad-hydro simulations.

It is important to note that they are not identical; an apparent difference is that the zonal flow in the pure-hydro model has narrower length scales than in the rad-hydro simulations. This discrepancy could be attributed to the static temperature and estimated cooling profiles in pure-hydro simulations, while rad-hydro simulations undergo secular evolution of temperature and cooling times. Additionally, the cooling is no longer local, since the radiative cooling can be affected by other parts of the disk. Their Reynolds stresses are similar but not identical.

In Figure 8.11, the `18au-bkgT-bkgCool` and `18au-bkgT` models exhibit shapes more similar to the rad-hydro model (`18au-rad`) but still display some differences. Their α_Z and α_R exhibit similar magnitudes, indicating that the turbulence becomes much more isotropic than in the isothermal model (`18au-iso`). However, `18au-bkgT-bkgCool` shows lower turbulence levels, and the sign of Z-ϕ stress differs from `18au-rad` beyond 0.3 radians and within 0.1 radians. Additionally, α_R is smaller in the midplane. The α_Z of the `18au-bkgT` model has a different sign than `18au-rad` between 0.2-0.3 radians. Overall, values from rad-hydro models and those pure-hydro models that adopted the rad-hydro thermal structures have smaller than 10^{-3} α_Z in the midplane, except in the case of a large cavity (54 au). They also exhibit more isotropic turbulence than the isothermal one. The low-density case is not presented here, but its stress profile is similar to that of an isothermal simulation with a larger h/r than the `18au-iso` model due to its almost isothermal profiles and low equivalent cooling time (Figures 8.5 to Figure 8.8).

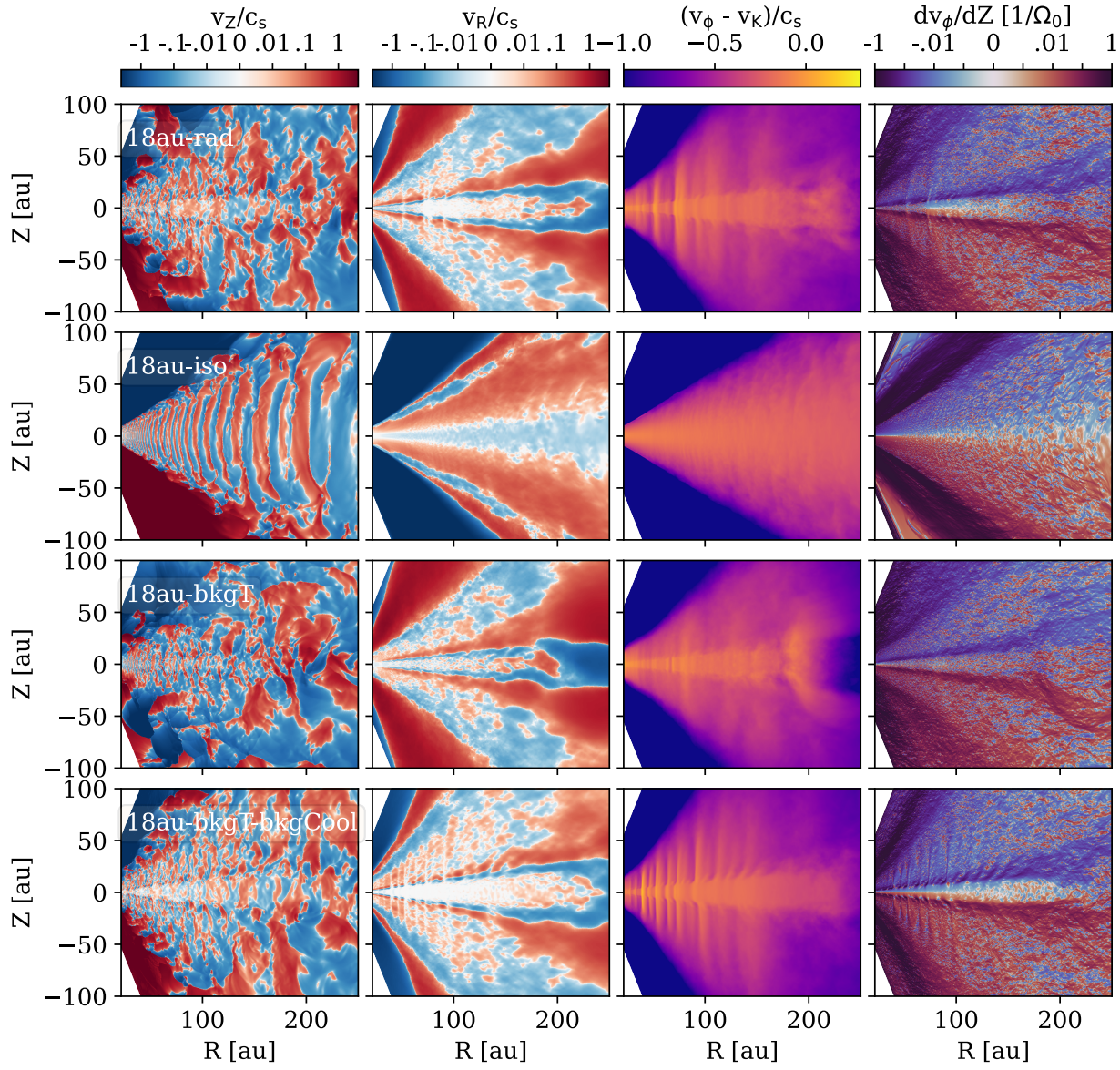

Figure 8.13: Comparison of the velocity fields between rad-hydro (first panel), isothermal (second panel), background temperature (third panel), and background temperature with cooling (fourth panel) models. From left to right: vertical velocity (v_Z) snapshot, time-averaged radial velocity (v_R), azimuthal velocity subtracted by Keplerian velocity (v_ϕ - v_K), and vertical shear rate (dv_ϕ/dZ).

In the radial direction, the turbulence levels between the pure hydro and rad-hydro simulations are similar but not identical. On the right panel of Figure 8.12, we show pure hydro models along with the fiducial rad-hydro model. `18au-bkgT` and `18au-bkgT-bkgCool` models follow the fiducial model's trend, but the former overestimates the turbulence whereas the latter underestimate the turbulence. The local orbital cooling prescription strongly under-predict the turbulence level within 70 au. The vertically isothermal model has almost constant turbulence level around the disk similar to that of the low density rad-hydro model.

8.5 Discussion

8.5.1 Gas Substructures

Related to the zonal flows shown in Figure 8.13, gas substructures can also develop depending on the inner cavity size as shown in Figure 8.14. The full disk model (`3r`$_\odot$`-rad`) preserves the initial condition except at the inner disk due to the boundary effect. The `18au-rad` model has perturbation on several au scale, whereas the `54au-rad` model has perturbation on tens of au scale. `18au-bkgT-bkgCool` and `18au-bkgT` models have similar perturbations as the `18au-rad`, whereas the isothermal model `18au-iso` keeps the initial condition.

Figure 8.15 shows the time evolution of the surface density. The full disk model (`3r`$_\odot$`-rad`) and the isothermal model (`18au-iso`) do not show evident substructures. For the rest of the models, substructures can form and propagate to the outer disk. for r_{cav} = 18 au models, some of these rings form at the inner boundary, but other rings can form in the middle of the disk and move to the outer disk at a lower speed. The time evolutions between `18au-rad`, `18au-bkgT`, and `18au-bkgT-bkgCool` are not identical. The rings in `18au-bkgT-bkgCool` model move at

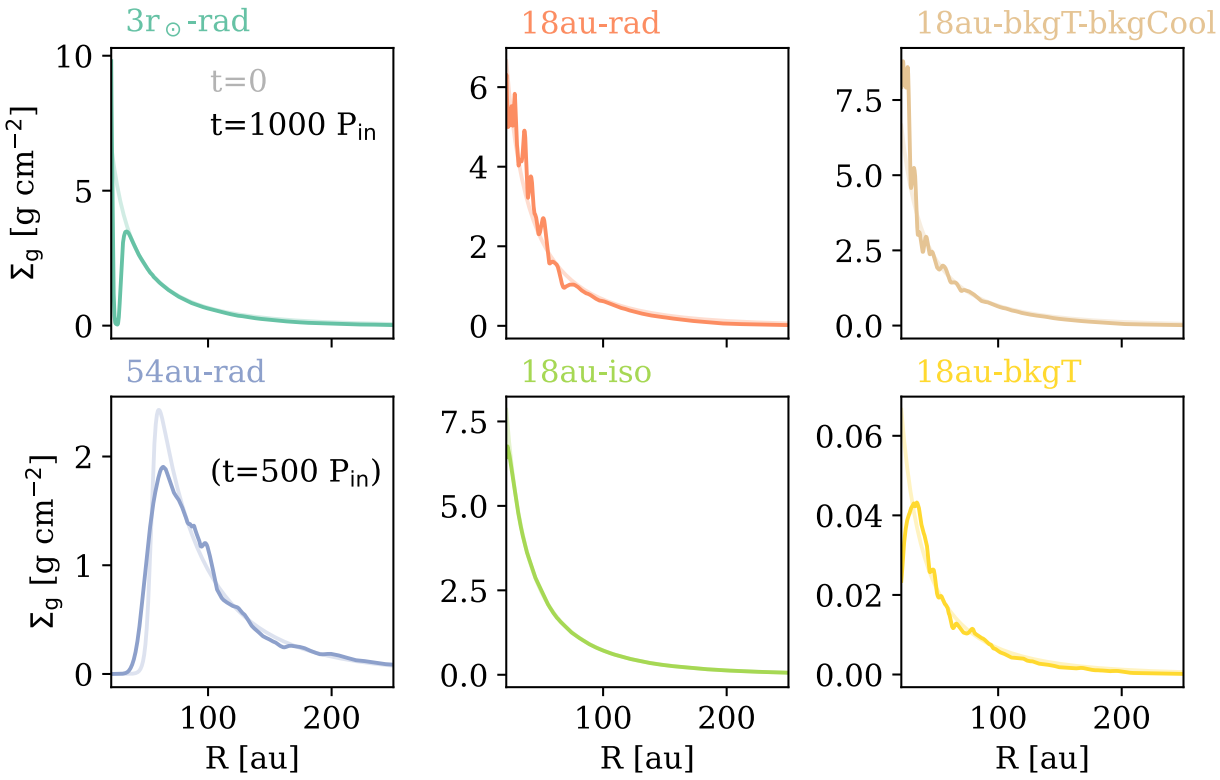

Figure 8.14: The gas surface density profiles in the radial direction at t = 1000 P_{in} or 500 P_{in} for `54au-rad` (more opaque lines) and at the initial condition (more transparent lines). The layout is the same as Figure 8.11.

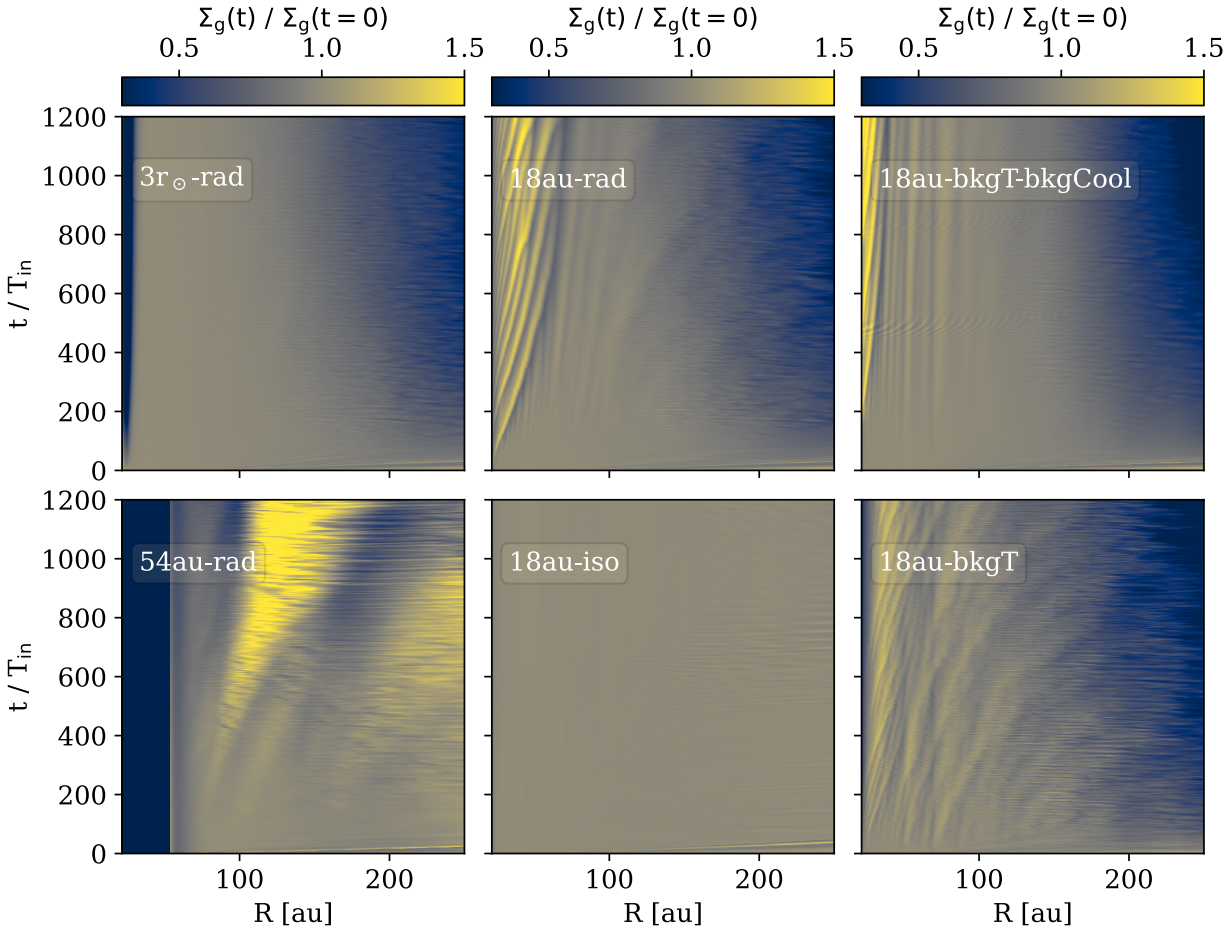

Figure 8.15: The gas surface density normalized by the initial condition as a time evolution from t = 0-1200 P_{in}. Brown colors mean that the surface density is almost unchanged. Yellow colors indicate the increase of density, whereas blue colors indicate the decrease of density. The layout is the same as Figure 8.11.

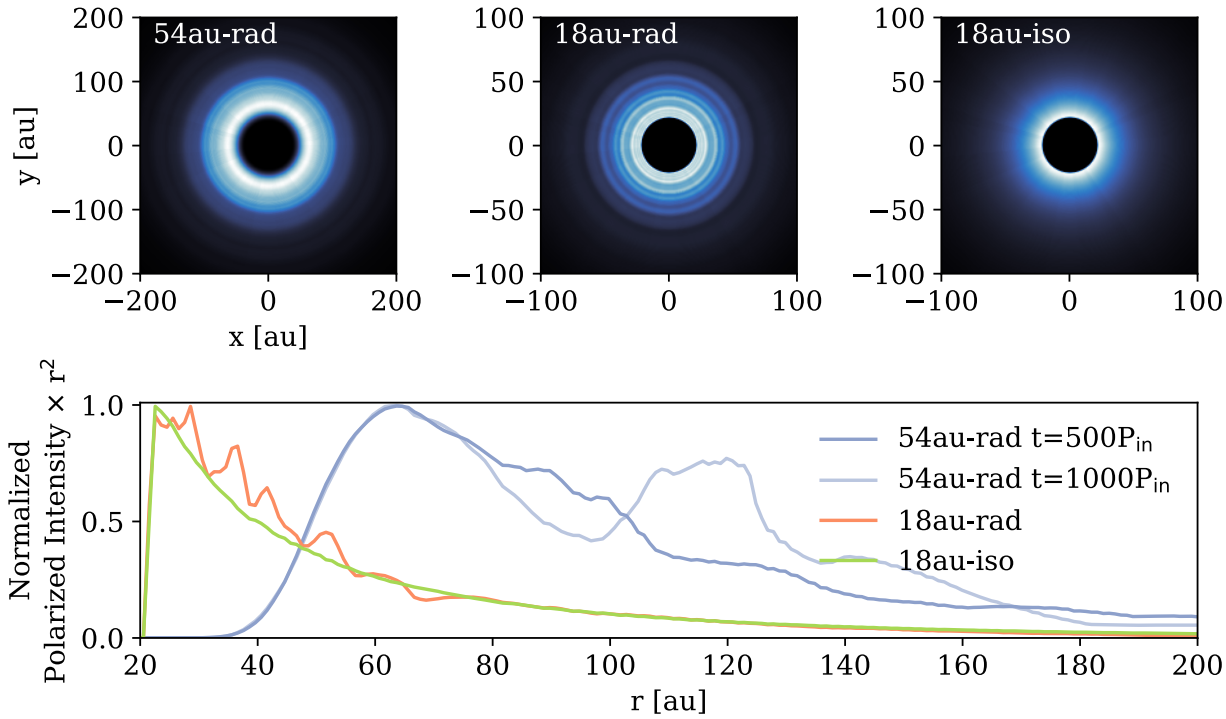

Figure 8.16: Near infrared scattered light images (polarized intensity) at H-band (1.63 μm) for `54au-rad`, `18au-rad`, and `18au-iso` models.

a lower speed than those in `18au-rad`. For the `54au-rad` model, the perturbation becomes much stronger after 700 orbits due to the vortex formation around 100 au, which may only happen in 2D (r-ϕ) simulations. Future 3D studies will unveil a more realistic structure of this model. These gas substructures can also possibly lead to dust substructures, but this needs to be tested in future studies that includes dust particles. Overall, our limited sample of rad-hydro models shows a tentative trend that transition disks with larger cavity sizes are more prone to develop zonal flows and substructures.

8.5.2 Observational and Modeling Prospect

While we focus on 2D modeling, the thermal structure is calculated self-consistently so we can make some predictions for axis-symmetric disks. In Figure 8.16 we show the near-infrared scattered light polarized intensity at λ=1.63 μm (H-band) using RADMC-3D for face-on `54au-rad`, `18au-rad`, and `18au-iso` models in linear scale from 0 to maximum value. We used the same DSHARP opacity (Figure 8.1), assuming that the dust to gas ratio is 0.01 and small grains (0.1-1 μm) account for 0.02184 of the total dust mass. The temperature is directly taken from rad-hydro simulations. For the isothermal model (`18au-iso`), we run thermal Monte Carlo (`radmc3d mctherm`) to calculate temperature in the $r-\theta$ plane. The RADMC-3D calculated the full Stokes image using the scattering matrix. The polarized intensity is $(Q^2+U^2)^{1/2}$. For the large cavity transition disk model `54au-rad` (taken at t = 500 P_{in}), we can clearly observe the inner rim and rings at around 100 au. If we take the snapshot at a later time, the ring structure becomes more evident, consistent with the surface density perturbation in Figure 8.15. However, we need to test whether this perturbation is still large in 3D simulations in future. For `18au-rad` model, several rings can also be seen close to the inner rim, resembling Figure 8.14, but the length scale is smaller than the disk with a larger cavity, making their substructures more difficult to be observed. In contrast, we can only see the inner rim of the vertically and locally isothermal model (`18au-iso`), meaning that the outer disk is in the shadow (i.e., this is a self-shadowed disk as defined in Garufi et al. 2018b; 2022). While we only have limited numbers of rad-hydro models with varying cavity sizes, we find the tendency that disks with larger cavity sizes can produce wider rings and can be easier to be observed in near-infrared scattered light images. This is consistent with the finding in current scattered light disk demographics which shows that ring structures are predominantly

found in disks with weak Near-IR excess (Benisty et al. 2023), where weak Near-IR excess is often interpreted as no inner disk.

As shown in Figure 8.12, the turbulence level appears to be strong in the region where the disk is directly exposed to stellar irradiation, suggesting that dust turbulent diffusion could be also strong at the cavity edge. In HD 163296, Rosotti et al. (2020); Doi & Kataoka (2021; 2023) have found that the α/St value is higher for the inner ring at 68 au, which is more exposed to stellar irradiation than the outer ring at 101 au. This finding aligns with our results, assuming that the Stokes number (St) does not vary significantly between these two rings. To validate the impact of direct stellar irradiation on dust diffusion, it will be crucial to measure dust settling at the cavity edges through ALMA observations and incorporate dust particles into 3D hydro simulations. Furthermore, in Figure 8.12, for full disks or transition disks with small cavities, midplane turbulence values increase with radius, a trend that can be readily examined through ALMA observations.

Different molecular lines from the ALMA MAPS Large Program (Öberg et al. 2021) and other high-resolution, high-sensitivity datasets are used to map the temperature structure in protoplanetary disks (Zhang et al. 2021a; Law et al. 2021; 2022; 2023; 2024). Conversely, these data can also reveal the velocity vectors at line emission surfaces, as indicated in numerous studies (see a review by Pinte et al. 2023). Specifically, Teague et al. (2019); Yu et al. (2021); Galloway-Sprietsma et al. (2023) identify disk winds and meridional flows attributed to embedded planets. Currently, we anticipate a substantial increase in sample size from the ALMA Large Program exoALMA. Aligning with the theme of the current paper–where temperature structure influences kinematics–we use Figure 8.17 to illustrate our ability to establish correspondence between the temperature structure and kinematic features. The figure shows temperature contours overlaid by meridional velocity vectors for the `18au-rad`, `54au-rad`, and `18au-lowdens-rad` models.

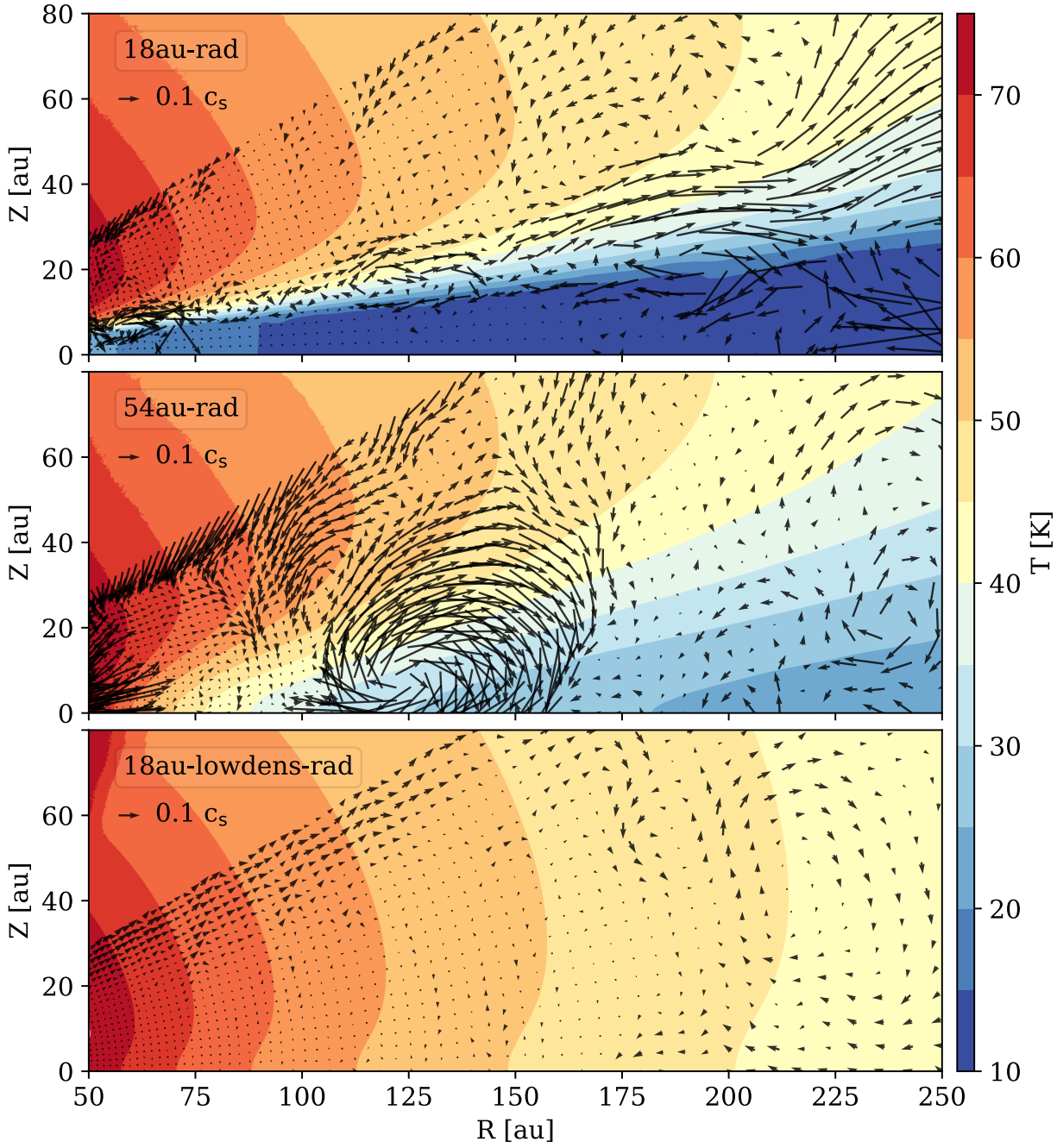

Figure 8.17: Time-averaged temperature and meridional velocity vectors for `18au-rad`, `54au-rad`, and `18au-lowdens-rad` models. 10% of the local sound speed is shown on the upper left of each panel.

In our fiducial `18au-rad` model, the temperature is 10-20 K in the midplane, and the velocity remains low within 200 au. At the transition region from the midplane to the atmosphere, the gas flows inward, reaching 10% of the sound speed. At higher altitudes, the gas flows outward with increasing velocity towards the outer disk. In contrast, for the low-density model, since the temperature has no vertical dependence, the gas velocity remains low throughout the disk. The change of the flow structure in response to the temperature structure can be identified in observations. However, the emission surface does not necessarily parallel the streamline. This implies that the changing direction of the velocity measured along the emission surface in observations can be attributed to the multiple crossings of the streamlines. A recent study by Martire et al. (2024) has demonstrated that the difference in inferred rotational velocities from ^{12}CO and ^{13}CO can be attributed to vertical thermal stratification (see middle panels of Figure 8.8), with the midplane (traced by ^{13}CO) exhibiting a higher rotational velocity than the atmosphere (traced by the more optically thick ^{12}CO). By accounting for thermal stratification, they can retrieve properties such as disk mass and stellar mass more accurately. In our current paper, we want to highlight that considering thermal structure can lead to further consequences, including spatially varying radial velocity, vertical velocity, and zonal flow.

The middle panel of Figure 8.17 shows the temperature and flow structure of the transition disk `54au-rad`. In this case, the temperature varies both vertically and radially. A giant clockwise rotating vortex is also present. While the strength of the vortex needs testing in 3D simulations, it could result from the radial and vertical variation of the temperature, as a similar feature was found in a pure-hydro simulation, `54au-bkgT-bkgCool`. We note that the temperature variation across the transition disk cavity has been identified from observations (Leemker et al. 2022) and can shape the variety of transition disk gas substructures (Wölfer et al. 2023), meaning that

the correspondence between the temperature structure and the kinematic features in transition disk can also be probed with current observations.

It has been well-known that temperature structure strongly shapes disk chemistry, but we also aim to use Figure 8.17 to demonstrate that the thermal structure can influence disk chemistry by shaping disk kinematics, thereby affecting material transport. While static disk models cover more complete chemical networks, studies considering dynamical effects (e.g., Aikawa & Herbst 1999; Semenov & Wiebe 2011; Furuya et al. 2013; Furuya & Aikawa 2014; Price et al. 2020; Bergner & Ciesla 2021; Van Clepper et al. 2022) by incorporating radial and/or vertical gas/dust mixing often reveal different chemical distributions compared to static models. These dynamic models may provide a better explanation for observations (see reviews by Krijt et al. 2022; Öberg et al. 2023; and references therein). We anticipate that, by accounting for advection and turbulent diffusion due to a specific thermal structure, the chemical distribution can be more accurately predicted. For instance, the layered accretion in our fiducial model `18au-rad`, where an outgoing flow is atop an ingoing flow, can transport material inward in the colder layer and outward in the hotter layer, which may also have implications on solid transport in our solar system (Ciesla 2009). The turbulence level measured at both the midplane and the atmosphere in our fiducial model has some similarities to layered accretion models featuring an MRI-active atmosphere and a dead zone in the midplane (Gammie 1996; Simon et al. 2011; 2013; Bai 2015; Xu et al. 2017; Simon et al. 2018). On the other hand, the high turbulence values in the upper layer are only measured in a few of protoplanetary disks (Flaherty et al. 2020; Paneque-Carreño et al. 2023) (see a recent review by Rosotti 2023). Our objective is to conduct 3D simulations to predict unique channel map features, following previous studies by Hall et al. (2020); Barraza-Alfaro et al. (2021). As demonstrated in Section 8.4.4 (Figure 8.13), background temperature and local orbital cooling profiles prove

to be effective approximations for rad-hydro simulations. This sets the groundwork for using 3D simulations in our future work to make ALMA and near-infrared scattered light observational predictions.

8.6 Conclusions

Vertical shear instability (VSI) is a promising candidate to generate turbulence in the outer region of protoplanetary disks. It can be crucial for gas and dust transport in protoplanetary disks. We studied VSI using the Athena++ radiation module with stellar irradiation, which self-consistently captured the thermal structure and hydrodynamics. We studied disks with different inner cavity sizes, accompanied by pure hydro simulations with various assumptions. We find that temperature structure strongly influences disk kinematics. Our main findings are as follows:

1. The radial optical depth of the star determines the disk's thermal structure. For realistic disk setups ($M_d = 10^{-2}$ $M_\odot$, cavity size < 54 au), the disk can be separated into the cool midplane and super-heated atmosphere, delineated by the $\tau_* = 1$ surface (Figure 8.5). If the disk is optically thin to the stellar irradiation (low mass disk with $M_d = 10^{-4}$ $M_\odot$), the temperature is almost vertically isothermal.

2. The thermal structure determines disk's kinematics. The temperature and cooling time (β) stratification suppresses the classical n = 1 corrugation mode that leads to meridional circulations found in isothermal simulations (Figure 8.4). Instead, the turbulence becomes more isotropic on a more local scale, in contrast to very large vertical-azimuthal Reynolds stress α_Z ($\sim 10^{-2}$) and weak radial-azimuthal Reynolds stress α_R ($\sim 10^{-4}$) found in isothermal simulations (Figure 8.11). The low mass disk has vertically isothermal profiles, so it closely

resembles all features in isothermal simulations.

3. The strongest vertical shear occurs at the transition region between the cool midplane and superheated atmosphere where many vortices form. At this transition region, layered accretion happens with an outgoing flow on top of an ingoing flow (Figure 8.8). This layered accretion can be perfectly explained by the vertical variation of the stress structure (Figure 8.7) using Equation 8.11.

4. Pure hydro simulations with measured temperature structures and estimated orbital cooling profiles can be good approximations for rad-hydro simulations (Figure 8.13).

5. Zonal flows and gas substructures can develop, and a disk with a larger cavity size has perturbations with a longer length scale and stronger magnitude (Figures 8.8 and 8.14). At the cavity edge, the gas has stronger turbulence, which could slow dust settling. Using MCRT simulations, we confirm that transition disks tend to have rings, and the disks with larger cavities tend to have more prominent rings, which are easier to be observed in near-infrared scattered light images (Figure 8.16), consistent with the fact that rings in scattered light images are predominantly found in disks with weak Near-IR excess.

6. The correspondence between the temperature structure and kinematic features can be tested by current ALMA observations (Figure 8.17). The temperature structure can also influence chemistry through shaping the disk kinematics. It can be tested by current ALMA chemistry observations and considering both disk dynamics and chemistry.

8.7 Implementation of Stellar Irradiation and Unit Conversion

We employ the Athena++ frequency-integrated implicit radiation module (Jiang & Ormel 2021) to solve the following set of equations: three hydrodynamic equations and one radiation transfer equation. Additionally, in the energy equation, we incorporate stellar irradiation as a source term (- $\nabla \cdot F_*$), similar to Flock et al. (2017).

The set of equations is

$$\begin{aligned}
\frac{\partial \rho}{\partial t} + \nabla \cdot (\rho v) &= 0, \\
\frac{\partial (\rho v)}{\partial t} + \nabla \cdot (\rho v v + P\mathbf{I}) &= -\boldsymbol{S_r}(P) + \rho \mathbf{a}_{\rm grav}, \\
\frac{\partial E}{\partial t} + \nabla \cdot [(E+P)v] &= -S_r(E) - \nabla \cdot F_* + \rho \mathbf{a}_{\rm grav} \cdot v, \\
\frac{\partial I}{\partial t} + cn \cdot \nabla I &= cS_I,
\end{aligned} \tag{8.14}$$

Here, ρ represents the gas density, v is the flow velocity, P denotes the gas pressure, $\mathbf{I}$ is the unit tensor, E is the total energy, I represents the lab-frame specific intensity of photons emitted by the disk locally, c is the speed of light, and n is the angle in the lab frame. The terms $\boldsymbol{S_r}(P)$ and $S_r(E)$ represent the disk's radiation source terms in the momentum and energy equations. They are moments of the source term S_I in the radiation transfer equation, given by:

$$
\begin{aligned}
S_I \equiv \Gamma^{-3} \, [\, & \rho \, (\kappa_s + \kappa_a) \, (J_0 - I_0) \\
& + \rho \, \kappa_P \left(\frac{a_r T^4}{4\pi} - J_0 \right)] \, , \\
S_r(E) & \equiv 4\pi c \int S_I d\Omega, \\
\boldsymbol{S_r}(P) & \equiv 4\pi \int n S_I d\Omega,
\end{aligned}
\tag{8.15}
$$

where κ_a, κ_s, and κ_P are the Rosseland mean opacity, scattering opacity, and Planck mean opacity, respectively. These opacities are all normalized to the gas. The intensity I in the lab frame is related to the intensity in the co-moving frame I_0 through a Lorentz transformation:

$$
I_0(n') = \gamma^4 \, (1 - n \cdot v/c)^4 \, I(n) \equiv \Gamma^4(n, v) I(n), \tag{8.16}
$$

where $\gamma \equiv 1/\sqrt{1 - v^2/c^2}$ is the Lorentz factor, $\Gamma(n, v) \equiv \gamma(1 - n \cdot v/c)$, and n' is the angle in the co-moving frame given by:

$$
n' = \frac{1}{\gamma(1 - n \cdot v/c)} \left[n - \gamma \frac{v}{c} \left(1 - \frac{\gamma}{\gamma + 1} \frac{n \cdot v}{c} \right) \right]. \tag{8.17}
$$

The angular-averaged mean intensity in the co-moving frame J_0 is defined as:

$$J_0 \equiv \frac{1}{4\pi} \int I_0 d\Omega_0, \tag{8.18}$$

where Ω_0 represents the angular element in the co-moving frame.

The total gas energy density E is given by:

$$E = E_g + \frac{1}{2}\rho v^2, \tag{8.19}$$

where E_g represents the gas internal energy. Assuming an ideal gas equation of state (EoS), the internal energy is related to the gas pressure P through the adiabatic index γ_g as $E_g = P/(\gamma_g - 1)$ for $\gamma_g \neq 1$. The gas temperature T is calculated using $T = \mu P/(R_{\rm ideal}\rho)$, where $R_{\rm ideal}$ is the ideal gas constant and μ is the mean molecular weight. We adopted γ_g = 1.4 and μ = 2.3 in this paper.

We adopted temperature, density and length units to be T_0, ρ_0, r_0 respectively. The time unit is given by $\Omega_{K,0}^{-1} = (GM_* r_0^{-3})^{-1/2}$. The velocity unit v_0 is then the Keplerian velocity at r_0. These parameters are used to calculate two key parameters in the radiation module $\mathbb{P} \equiv a_r T_0^4/(\rho_0 R_{\rm ideal} T_0/\mu)$ and $\mathbb{C} \equiv c/a_0$ (Jiang et al. 2012). a_0 is the characteristic isothermal sound speed, $\left(R_{\rm ideal} T_0/\mu\right)^{1/2}$. The values for our fiducial model are T_0 = 6.14 $\times$ 10^3 K; ρ_0 = 4.28 $\times$ 10^{-14} g cm^{-3}; r_0 = 40 au; hence $\mathbb{P}$ = 1.13 $\times$ 10^3; and $\mathbb{C}$ = 6.36 $\times$ 10^4. $\mathbb{P}$ represents the ratio between the radiation pressure and gas pressure at these unit quantities, whereas $\mathbb{C}$ represents the ratio between speed of light and characteristic sound speed a_0. The $\mathbb{P}$ is larger than unity since we adopt a very large value of T_0. We adopt this exact value of T_0 since $v_0 = a_0$ so we do not need to distinguish between the unit

velocity and the characteristic sound speed. For typical values of density ($\sim \rho_0$) and temperature (tens of Kelvins) at the midplane, the radiation pressure is much less than the gas pressure. Similarly, the typical ratio between the speed of light and local sound speed is $\gg \mathbb{C}$, as T_0 is much greater than a typical disk temperature. We set density floor to be 10^{-12} and pressure floor to be 10^{-15} in code units. We also set a temperature floor to be 0.001 T_0 (6.14 K) and a temperature ceiling to be 0.1 T_0 (614 K) to avoid numerical hotspots.

To account for stellar irradiation, we include a heating source term in the energy equation. This source term is necessary for frequency-integrated radiation transport (e.g., Flock et al. 2017) as the stellar irradiation is at significantly higher temperatures (thousands of Kelvins) compared to the thermal emission from the disk (tens to hundreds of Kelvins). In a future work (Baronett et al., in prep) that uses a multi-group radiation module (Jiang 2022), this source term is not required, and it can better capture the multi-frequency nature of radiation transport both for the stellar irradiation and disk emission.

The stellar irradiation heating flux $\mathbf{F}_*(r)$ is given by:

$$\mathbf{F}_*(\mathrm{r}) = \left(\frac{\mathrm{R}_*}{\mathrm{r}}\right)^2 \sigma_\mathrm{b} \mathrm{T}_*^4 \mathrm{e}^{-\tau} \hat{\mathbf{r}}, \tag{8.20}$$

where T_* and R_* represent the stellar surface temperature and radius, respectively. Here, σ_b denotes the Stefan-Boltzmann constant, which is related to the radiation constant a_r as $\sigma_b = a_r c/4$.

The radial optical depth for the star at each θ is given by:

$$\begin{aligned}\tau_*(\mathrm{r},\theta) &= \int_{\mathrm{R}_*}^{\mathrm{r}} \kappa(\mathrm{T}_*,\theta)\rho_{\mathrm{dust}}(\mathrm{r},\theta)\mathrm{dr} \\ &= \tau_{*,\mathrm{bc}}(\mathrm{r},\theta) + \tau_{*,\mathrm{domain}}(\mathrm{r},\theta) \\ = \int_{\mathrm{R}_*}^{\mathrm{r_{in}}} \kappa(\mathrm{T}_*,\theta)\rho_{\mathrm{dust}}(\mathrm{r},\theta)\mathrm{dr} &+ \int_{\mathrm{r_{in}}}^{\mathrm{r}} \kappa(\mathrm{T}_*,\theta)\rho_{\mathrm{dust}}(\mathrm{r},\theta)\mathrm{dr}\,, \end{aligned} \tag{8.21}$$

where r_{in} represents the inner radius of the computational domain. The first term in the second line of Equation 8.21 refers to the optical depth within the region interior to the computational domain. These values are not evolved with time but depend on the density and opacity setup of the global disk. Namely, they depend on the inner cavities' radii, gas scale height, and surface density.

To ensure compatibility with MPI (Message Passing Interface), where the ray-tracing needs to cross all the grids in the radial direction and a ray can enter different `MeshBlocks` located on different CPUs, we adopted the following procedure. First, we calculated the optical depth within each `MeshBlock`. Then, we declared a user-defined `Mesh` data array to store all the τ_* values at the outer boundaries of each `MeshBlock`. These values represent the local optical depths integrated from the inner boundary ($\mathrm{r_{mb,in}}$) to the outer boundary ($\mathrm{r_{mb,out}}$) of each `MeshBlock`. For the zeroth column, it stores values of $\tau_{*,\mathrm{bc}}$. In the middle of each timestep, we cumulatively sum the the user defined `Mesh` data in the radial direction. Then an `MPI_Allreduce` operation is performed to update all the user-defined `Mesh` data array in all the CPUs so that the inner boundary optical depths of each `MeshBlock` has their correct global values. Finally, the optical depth τ_* within each `MeshBlock` can be calculated by adding up its current `MeshBlock`'s inner boundary value and its local integrated value. Specifically, within each `MeshBlock`, the optical

depth is given by:

$$\tau_*(\mathrm{r},\theta) = \tau_*(\mathrm{r_{mb,in}},\theta) + \int_{\mathrm{r_{mb,in}}}^{\mathrm{r}} \kappa(\mathrm{T}_*,\theta)\rho_{\mathrm{dust}}(\mathrm{r},\theta)\mathrm{dr}, \tag{8.22}$$

where $\tau_*(\mathrm{r_{mb,in}},\theta)$ is the global optical depth at the `MeshBlock`'s inner boundary stored in the user-defined `Mesh` data array.

8.8 Energy Budget

We use the energy equation in Equation 8.14 and refer to Figure 8.18 to illustrate the energy budget in our fiducial model, `18au-rad`, where each term is time-averaged between t=1000-1200 $\mathrm{P_{in}}$. Assuming a steady state ($\partial E/\partial t$=0), the energy flux divergence term on the left-hand side ($\nabla\cdot[(E+P)v]$) should be balanced by three terms on the right-hand side: cooling from the disk radiation (-$Sr(E)$), heating from the stellar irradiation (-$\nabla\cdot F*$), and the work done by the stellar gravity ($\rho\mathbf{a}_{\mathrm{grav}}\cdot v$). We can move the gravity term to the left-hand side and incorporate it into the energy flux divergence, considering it as the flux divergence of gravitational potential energy.

Figure 8.18 compares the disk cooling (left panel), stellar heating (middle panel), and the energy flux divergence (right panel). In the atmosphere, stellar heating is prominent, and most of the energy is radiated away by disk cooling, as both -$\nabla\cdot F_*$ and $Sr(E)$ exhibit similar values. However, in the midplane, stellar heating is nearly negligible, given our implementation of single-frequency stellar irradiation (Equation 8.20), where few photons can penetrate below the $\tau_* = 1$ surface. Interestingly, while disk cooling values are relatively small in the midplane, they still surpass stellar heating significantly. This additional disk cooling is offset by the negative energy flux divergence shown in the right panel.

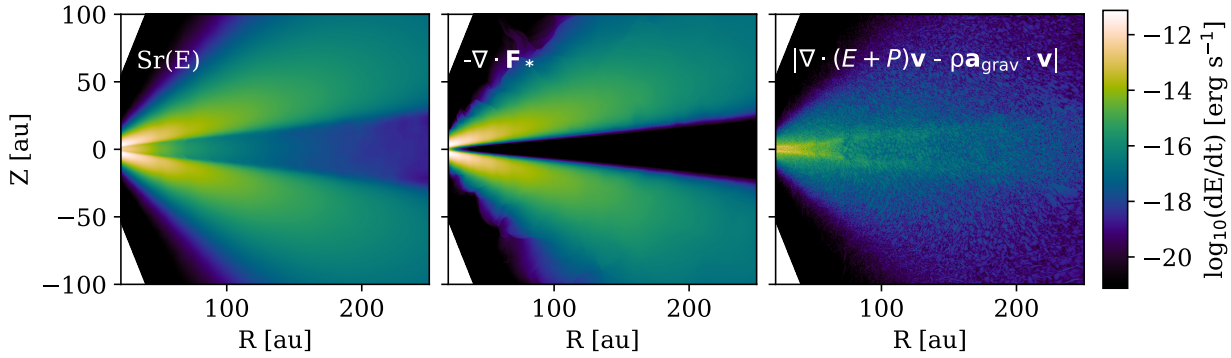

Figure 8.18: Time averaged (t=1000-1200 P_{in}) source terms and energy flux divergence in the energy equation (Equation 8.14) for the fiducial model `18au-rad`. Left panel: disk's radiation source term ($Sr(E)$); middle panel: stellar irradiation heating source term ($-\nabla \cdot F_*$); right panel: energy flux divergence including gravitational energy.

Upon closer examination of each flux component, we find that the negative divergence arises from the advection of energy from the upper and lower atmospheres to the midplane. When we deactivate advection by freezing the hydrodynamics and solely conduct radiative transfer, the midplane temperature experiences a slight decrease by a few percent, indicating that energy advection can increase the temperature of the cold midplane by a few percent. We expect that when we include multi-wavelength stellar irradiation, the midplane can receive more stellar heating so that the influence of advection on the midplane temperature can be weaker.

8.9 Disruption of the Inertial Wave

Linear theory has unveiled the global model of VSI as an overstability, a destabilized inertial wave (Barker & Latter 2015). Recently, Svanberg et al. (2022) (also see Stoll & Kley 2014) used locally and vertically isothermal simulations to investigate the inertial wave patterns of VSI. A significant finding is that inertial waves associated with the corrugation mode could be identified in several radial wave zones separated at Lindblad resonances, each characterized by different

frequencies. These wave zones also exhibit slightly different turbulence values.

However, when considering a self-consistent thermal structure that takes into account stellar irradiation, the inertial wave patterns become less distinct. Figure 8.19 illustrates the time evolution of the vertical velocity at the midplane, while the accompanying frequency and wavelength analyses are presented in Figures 8.20 and 8.21. In the isothermal simulation `18au-iso`, we observe the classical corrugation model pattern as found in Stoll & Kley (2014) and Svanberg et al. (2022), characterized by alternating peaks and troughs moving radially. These patterns represent group velocity and phase velocities propagating in opposite directions (Figure 3 in Svanberg et al. 2022). In contrast, the remaining simulations do not exhibit this evident wave feature, except for `54au-rad` between 30-60 au, within the cavity and at the ring location. This is consistent with our observations in Figure 8.5, where the corrugation mode is identified in v_Z for `54au-rad` near the cavity. Similarly, the `18au-lowdens-rad` model (not displayed here) exhibits a wave pattern similar to the isothermal simulation. For the other models, we can still observe certain wave patterns, albeit different from the inertial wave patterns identified in the isothermal model. The pronounced velocity in $3r_\odot$`-rad` is likely an inner boundary effect due to the disk surface's (h/r) discontinuity. A comprehensive understanding of these wave patterns still needs ongoing studies.

In summary, the classical VSI inertial wave pattern only manifests when the disk is optically thin to stellar irradiation so that the disk is close to vertically isothermal and has a short cooling time. This can occur when the disk has low dust opacity (`18au-rad,lowdens`) or when the disk possesses a wide inner cavity (`54au-rad`).

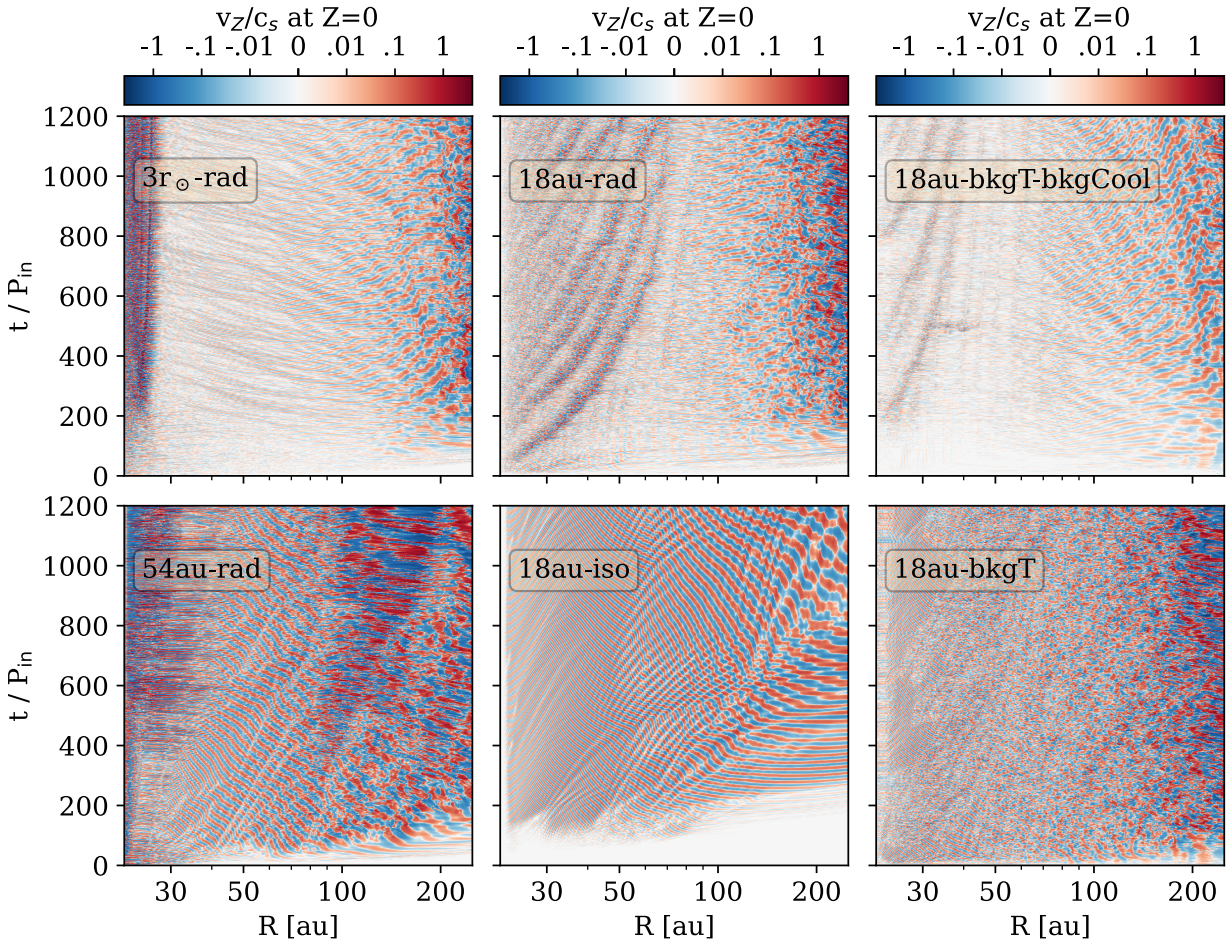

Figure 8.19: The time evolution of the vertical velocity (v_Z) in the midplane from 0-1200 P_{in} for various models in the same layout as previous figures.

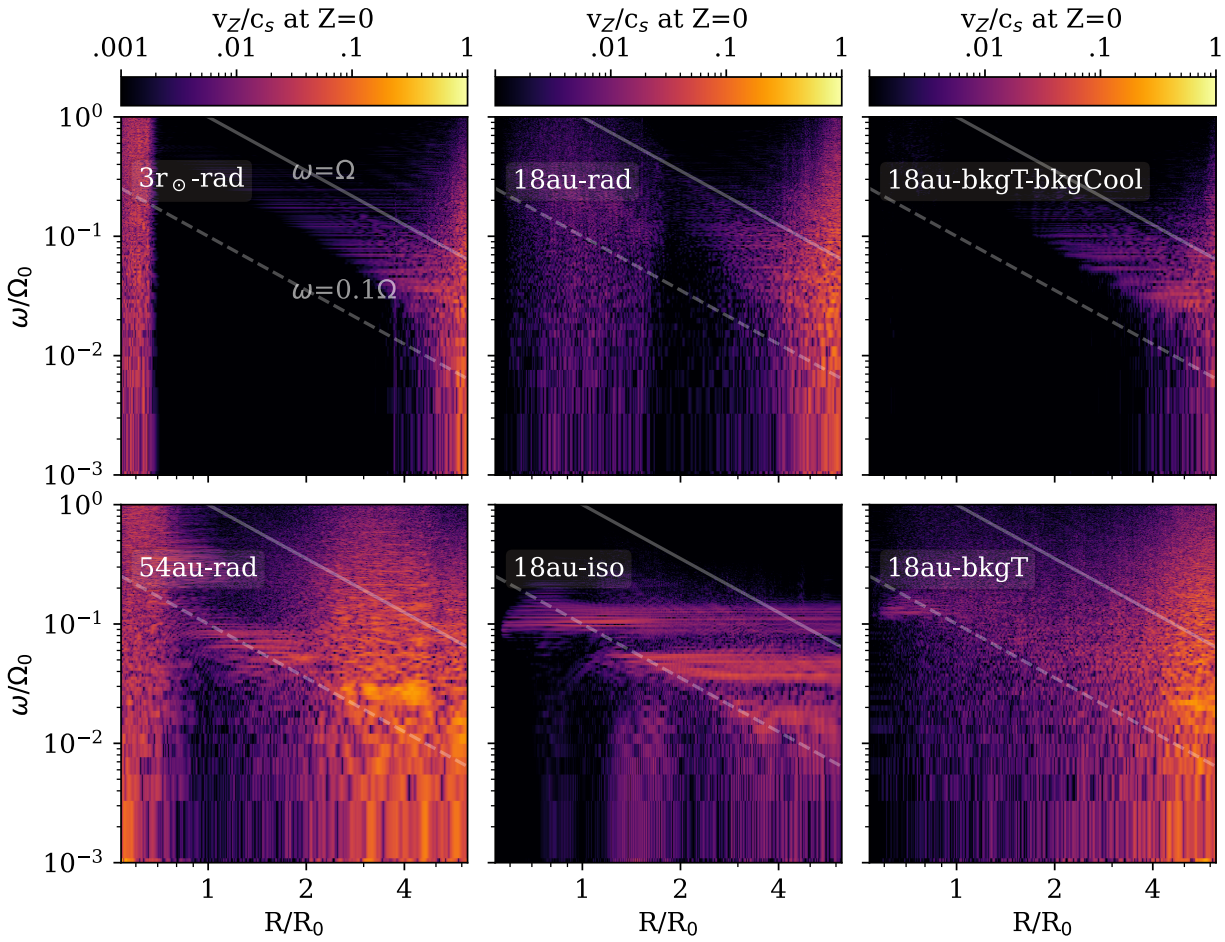

Figure 8.20: The Fourier transform of the time evolution of the vertical velocity in the midplane (Figure 8.19). The frequency (ω) is in unit of $1/\Omega_{K,0}$, where $\Omega_{K,0}$ is the Keplerian frequency at 40 au. R is also normalized by $R_0 = 40$ au. The diagonal solid line indicates $\omega = \Omega = \Omega_{K,0}(R/R_0)^{-1.5}$, and the dashed line indicates $\omega = 0.1\Omega$. The layout is the same as previous figures.

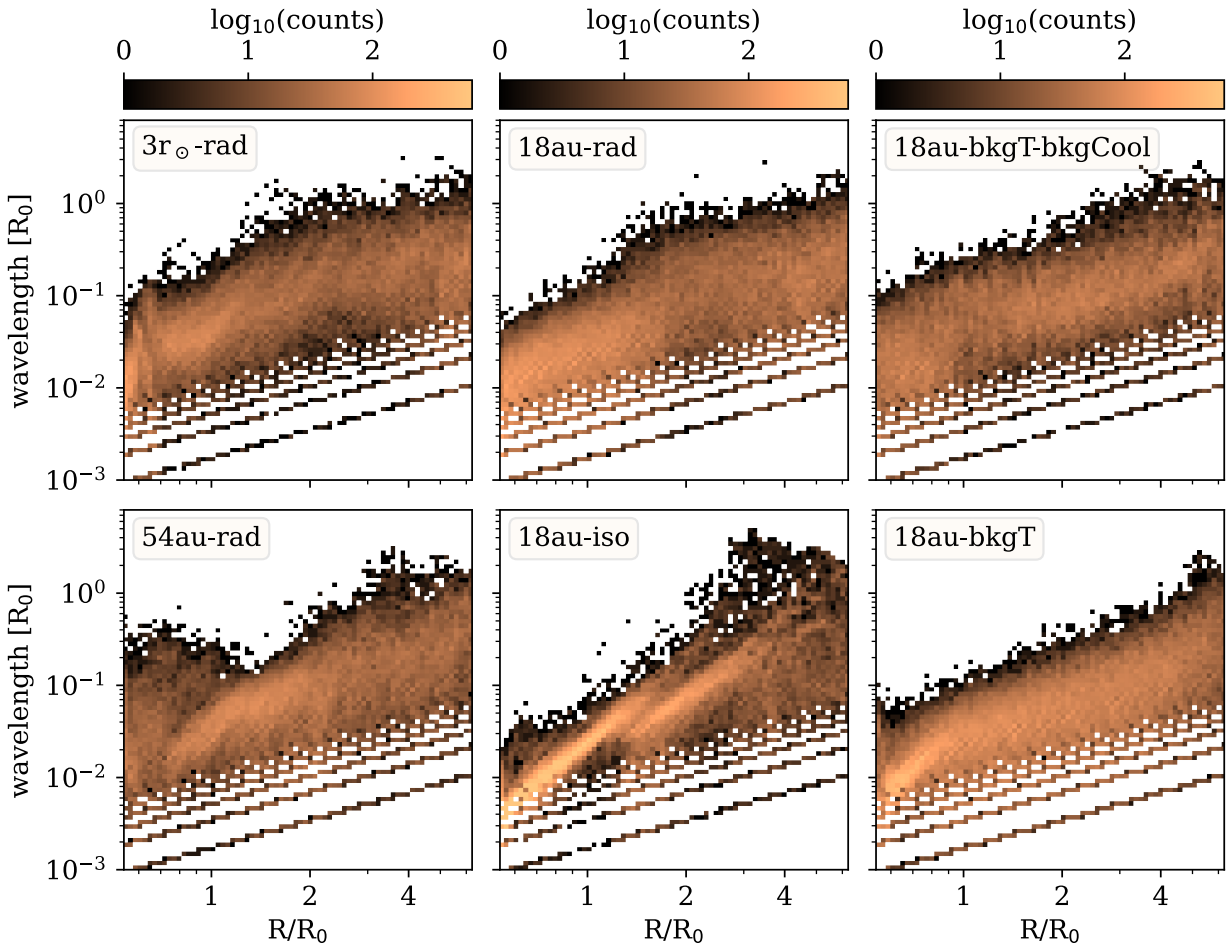

Figure 8.21: The wavelength occurrence of the vertical velocity (v_Z) in the midplane measured from every snapshot from t = 0-1200 P_{in}, with 1 P_{in} as the interval. The wavelength is measured as the distance of the neighbouring zero crossing points. The brighter colors represent higher counts. The layout is the same as previous figures.

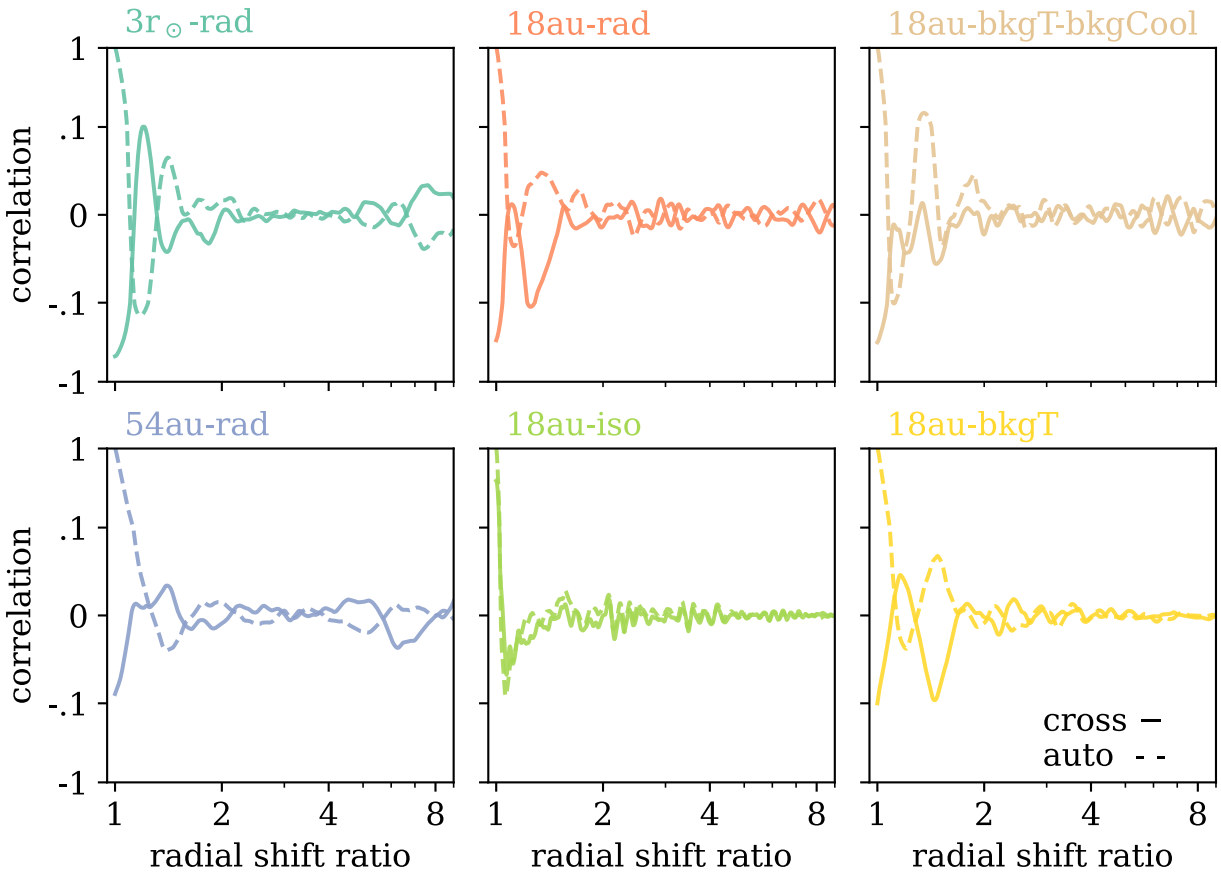

Figure 8.22: The cross-correlation functions of the v_Z between the upper and lower atmosphere shifted in the radial (r) direction with varying shift ratios, averaged between 0.2-0.25 radians above and below the midplane for t = 1000-1200 P_{in} (t = 500-700 P_{in} for `54au-rad`). The values are normalized by the auto-correlation functions in the upper atmosphere without a shift (shift ratio = 1). If the upper and lower atmosphere has the same v_Z, i.e., $v_Z(r, \theta) = v_Z(r, \pi - \theta)$, the correlation should be unity at shift ratio = 1.

8.10 Asymmetry Above and Below the Midplane

While we have demonstrated that the inertial wave pattern associated with the corrugation mode in classical VSI becomes less apparent in rad-hydro simulations or pure hydro simulations with self-consistent thermal structures, we can still observe some elongated stripes in the vertical direction for v_Z, as depicted in Figures 8.5 and 8.13. In contrast to isothermal simulations, the gas parcels above and below the midplane do not appear to move consistently in the same direction. The vertical velocity in Melon Fuksman et al. (2023a) also shows anti-symmetry when the disk midplane is VSI-inactive ($f_{\rm dg}$=10^{-4} therein), whereas corrugation mode only occurs when the VSI is active in the whole domain ($f_{\rm dg}$=10^{-3} therein).

In Figure 8.22, we attempt to quantify these trends by measuring the autocorrelation function (dashed lines) for a horizontal cut within the range of 0.2-0.25 radians in the radial direction and a cross-correlation function (solid lines) between this cut and the one on the other side of the disk ($\pi - \theta$) at a specific snapshot and then averaging over 200 $\rm P_{in}$. Their values are normalized by the autocorrelation value with no radial shift (radial shift ratio = 1). Absolute values between 0.1 to 1 are presented in a log-scale, while absolute values between 0 and 0.1 are shown in a linear scale. The cross-correlation of the isothermal model (`18au-iso`) closely aligns with the autocorrelation function, suggesting that the upper and lower disks move in the same direction, echoing the n=1 corrugation model in Figure 8.13. In contrast, the remaining models exhibit trends where auto-correlation and cross-correlation functions have the opposite signs during the first few turnovers, indicating that the upper and lower disks are more likely to move in opposite directions. This anti-correlation between upper and lower surfaces resembles that of the n=2 breathing mode found in the initial growing phase of VSI (e.g., Nelson et al. 2013b; Barker & Latter 2015). However, this

anti-correlation is not as strong as those in the linear growth phase, indicating that more than one modes are operating in this highly non-linear regime. A possible explanation is that the n=1 corrugation mode requires communication between the upper and lower disk. However, in our fiducial radiation models, the communication between two surfaces are disturbed by the temperature and cooling time stratification so that n=2 and other modes take over.

8.11 Parameter List

Symbol	Description
r, θ, ϕ	spherical polar coordinate
R, Z, ϕ	cylindrical coordinate
$\pi/2$ - θ	this value is 0 at the midplane
Ω	orbital frequency
$\Omega_{\rm K}$	Keplerian velocity
$\rm r_\odot$	$\approx$ 0.0047 au, solar radius
$\rm r_0$	= 40 au = 1 code unit of length
$\rm r_{cav}$	cavity size
$\Omega_{\rm K,0}^{-1}$	= 1 code unit of time $\approx$ 40 yr
p	midplane density power-law index
q	temperature power-law index
r	surface density power-law index
γ_g	= $\rm c_p/c_V$ = 1.4, adiabatic index
$R_{\rm ideal} = k_b/m_p$	ideal gas constant
μ	= 2.3 mean molecular weight
c_s	= $(R{\rm T}/\mu)^{1/2}$, isothermal sound speed
P	gas pressure
ρ	gas density
$\Sigma_{\rm g}$	gas surface density
$\Sigma_{\rm g}/\Sigma_{\rm d}$	gas-to-dust mass radio
$\rm v_{rms}$	= root mean square velocity (e.g., Flock et al. 2020)
$\rm v_{mag}$	magnitude of the meridoinal velocity
$\rm v_0$	unit velocity
$\rm a_0$	characteristic sound speed
T	temperature, assume $\rm T_{gas}$=$\rm T_{dust}$
$\rm T_0$	= 1 code unit of temperature = 6.14×10^3 K
$\rm T_{floor}$	= 6.14 K, temperature floor
$\rm T_{ceiling}$	= 614 K, temperature ceiling
$\rm T_\odot$	solar temperature
$\rm r_{in}$	= 21.6 au, inner boundary
$\rm P_{in}$	$\approx$ 100 yr, orbital period at $\rm r_{in}$
β	dimensionless cooling time
$\beta_{\rm c}$	critical cooling time for VSI
$\rm f_s$	mass fraction of the small dust
h	gas vertical scale height
τ_*	stellar optical depth in the radial direction
$\kappa_{\rm P,d}$, $\kappa_{\rm R,d}$	Planck and Rosseland mean opacities (to dust)
$\kappa_{\rm P,g}$, $\kappa_{\rm R,g}$	Planck and Rosseland mean opacities (to gas)
$\tau_{\rm P,d}$, $\tau_{\rm R,d}$	disk optical depth in the vertical direction
$M_{\rm acc}$	mass accretion rate
$\alpha_{\rm int}$	vertically integrated $\alpha_{R,\phi}$

Table 8.1: Parameters used in the paper.

CHAPTER 9 Conclusion

In this dissertation, I first used planet-disk interaction simulations to explain the ubiquitous substructures observed among protoplanetary disks and inferred young planet populations, calculated their occurrence rates, and compared them with exoplanet statistics (Chapters 2 and 3). These young planets are located between 10-100 au, with most of them having Neptune masses. In Chapter 4, I developed a machine learning technique to infer young planet mass and disk viscosity directly from the disk images.

The rest of the dissertation is dedicated to the self-consistent treatment of thermal structure and dust properties in protoplanetary disks. In Chapter 5, I explored the effects of disk self-gravity and radiative cooling on the formation of gaps, spirals, and young planets. I found that when the cooling time is similar to the orbital time, the spirals are dampened, and the gaps become narrower and shallower. Consequently, the planet mass would be underestimated if we still use locally isothermal simulations to fit planet mass. In Chapter 6, I considered two populations of dust species and calculated the temperature structure around Gaussian rings when the disk reaches hydrostatic equilibrium. I identified two mechanisms that can lead to temperature differences across the ring. The first is the shadowing effect, where the region behind the ring is in shadow and has a lower temperature. The second is the excess cooling of the big grains. Since big grains are trapped more efficiently in the ring and they have higher opacity at longer wavelengths, the equilibrium temperature is lower at the ring. We predict that the temperature drop can be observed by ALMA CO line emission and can even lead to possible dynamic effects. In Chapter 7, we tried to explain

the SED and dust self-scattering polarization of HL Tau disk together by using porous dust particles. When porosity is considered, we found that the inconsistency of the dust size constrained from these two methods disappeared, and we can even constrain the mm-cm sized dust grains to have porosity from 70%-97%. In Chapter 8, I made the thermal structure and hydrodynamics fully coupled by using radiation-hydrodynamics to study a promising hydrodynamic instability, the vertical shear instability (VSI). I found that the thermal structure and cooling timescale significantly influence VSI behavior. The inner rim location and radial optical depth affect disk kinematics. Compared with previous vertically-isothermal simulations, our full disk and transition disks with small cavities have a superheated atmosphere and cool midplane with long cooling timescales, which suppress the corrugation mode and the associated meridional circulation. This temperature structure also produces a strong vertical shear at $\tau_* = 1$, producing an outgoing flow layer at $\tau_* < 1$ on top of an ingoing flow layer at $\tau_* \sim 1$. The midplane becomes less turbulent, while the surface becomes more turbulent, with effective α reaching $\sim 10^{-2}$ at $\tau_* \lesssim 1$. This large surface stress drives significant surface accretion, producing substructures.

In the future, I aim to continue exploring the influence of thermodynamics in protoplanetary disks and try to answer, "What role does radiation play in shaping disk kinematics and morphology?". My immediate goal is to distinguish between substructures that originate from planets and those that have non-planetary origins and establish a quantitative link between planet properties and kinematic/morphological features. My ultimate goal is to probe young planet populations and constrain planet formation mechanisms.

REFERENCES

Abadi, M., Agarwal, A., Barham, P., Brevdo, E., Chen, Z., Citro, C., Corrado, G. S., Davis, A., Dean, J., Devin, M., Ghemawat, S., Goodfellow, I., Harp, A., Irving, G., Isard, M., Jia, Y., Jozefowicz, R., Kaiser, L., Kudlur, M., Levenberg, J., Mané, D., Monga, R., Moore, S., Murray, D., Olah, C., Schuster, M., Shlens, J., Steiner, B., Sutskever, I., Talwar, K., Tucker, P., Vanhoucke, V., Vasudevan, V., Viégas, F., Vinyals, O., Warden, P., Wattenberg, M., Wicke, M., Yu, Y., & Zheng, X. 2015, TensorFlow: Large-Scale Machine Learning on Heterogeneous Systems, software available from tensorflow.org

Aikawa, Y. & Herbst, E. 1999, A&A, 351, 233

Alexander, R., Pascucci, I., Andrews, S., Armitage, P., & Cieza, L. 2014, in Protostars and Planets VI, ed. H. Beuther, R. S. Klessen, C. P. Dullemond, & T. Henning, 475

Alibert, Y. & Venturini, J. 2019, A&A, 626, A21

ALMA Partnership, Brogan, C. L., Pérez, L. M., Hunter, T. R., Dent, W. R. F., Hales, A. S., Hills, R. E., Corder, S., Fomalont, E. B., Vlahakis, C., Asaki, Y., Barkats, D., Hirota, A., Hodge, J. A., Impellizzeri, C. M. V., Kneissl, R., Liuzzo, E., Lucas, R., Marcelino, N., Matsushita, S., Nakanishi, K., Phillips, N., Richards, A. M. S., Toledo, I., Aladro, R., Broguiere, D., Cortes, J. R., Cortes, P. C., Espada, D., Galarza, F., Garcia-Appadoo, D., Guzman-Ramirez, L., Humphreys, E. M., Jung, T., Kameno, S., Laing, R. A., Leon, S., Marconi, G., Mignano, A., Nikolic, B., Nyman, L.-A., Radiszcz, M., Remijan, A., Rodón, J. A., Sawada, T., Takahashi, S., Tilanus, R. P. J., Vila Vilaro, B., Watson, L. C., Wiklind, T., Akiyama, E., Chapillon, E., de Gregorio-Monsalvo,

I., Di Francesco, J., Gueth, F., Kawamura, A., Lee, C.-F., Nguyen Luong, Q., Mangum, J., Pietu, V., Sanhueza, P., Saigo, K., Takakuwa, S., Ubach, C., van Kempen, T., Wootten, A., Castro-Carrizo, A., Francke, H., Gallardo, J., Garcia, J., Gonzalez, S., Hill, T., Kaminski, T., Kurono, Y., Liu, H.-Y., Lopez, C., Morales, F., Plarre, K., Schieven, G., Testi, L., Videla, L., Villard, E., Andreani, P., Hibbard, J. E., & Tatematsu, K. 2015a, ApJ, 808, L3

ALMA Partnership, Brogan, C. L., Pérez, L. M., Hunter, T. R., Dent, W. R. F., Hales, A. S., Hills, R. E., Corder, S., Fomalont, E. B., Vlahakis, C., Asaki, Y., Barkats, D., Hirota, A., Hodge, J. A., Impellizzeri, C. M. V., Kneissl, R., Liuzzo, E., Lucas, R., Marcelino, N., Matsushita, S., Nakanishi, K., Phillips, N., Richards, A. M. S., Toledo, I., Aladro, R., Broguiere, D., Cortes, J. R., Cortes, P. C., Espada, D., Galarza, F., Garcia-Appadoo, D., Guzman-Ramirez, L., Humphreys, E. M., Jung, T., Kameno, S., Laing, R. A., Leon, S., Marconi, G., Mignano, A., Nikolic, B., Nyman, L. A., Radiszcz, M., Remijan, A., Rodón, J. A., Sawada, T., Takahashi, S., Tilanus, R. P. J., Vila Vilaro, B., Watson, L. C., Wiklind, T., Akiyama, E., Chapillon, E., de Gregorio-Monsalvo, I., Di Francesco, J., Gueth, F., Kawamura, A., Lee, C. F., Nguyen Luong, Q., Mangum, J., Pietu, V., Sanhueza, P., Saigo, K., Takakuwa, S., Ubach, C., van Kempen, T., Wootten, A., Castro-Carrizo, A., Francke, H., Gallardo, J., Garcia, J., Gonzalez, S., Hill, T., Kaminski, T., Kurono, Y., Liu, H. Y., Lopez, C., Morales, F., Plarre, K., Schieven, G., Testi, L., Videla, L., Villard, E., Andreani, P., Hibbard, J. E., & Tatematsu, K. 2015b, ApJ, 808, L3

Andrews, S. M. 2020, ARA&A, 58, 483

Andrews, S. M. 2020, Annual Review of Astronomy and Astrophysics, 58, 483

Andrews, S. M., Huang, J., & et al. 2018a, ApJ

Andrews, S. M., Huang, J., Pérez, L. M., Isella, A., Dullemond, C. P., Kurtovic, N. T., Guzmán, V. V., Carpenter, J. M., Wilner, D. J., Zhang, S., Zhu, Z., Birnstiel, T., Bai, X.-N., Benisty, M.,

Hughes, A. M., Öberg, K. I., & Ricci, L. 2018b, ApJ, 869, L41

Andrews, S. M., Rosenfeld, K. A., Kraus, A. L., & Wilner, D. J. 2013, ApJ, 771, 129

Andrews, S. M., Terrell, M., Tripathi, A., Ansdell, M., Williams, J. P., & Wilner, D. J. 2018c, ApJ, 865, 157

Andrews, S. M., Wilner, D. J., Hughes, A. M., Qi, C., Rosenfeld, K. A., Öberg, K. I., Birnstiel, T., Espaillat, C., Cieza, L. A., Williams, J. P., Lin, S.-Y., & Ho, P. T. P. 2012, ApJ, 744, 162

Andrews, S. M., Wilner, D. J., Zhu, Z., Birnstiel, T., Carpenter, J. M., Pérez, L. M., Bai, X.-N., Öberg, K. I., Hughes, A. M., Isella, A., & Ricci, L. 2016a, ApJ, 820, L40

—. 2016b, ApJ, 820, L40

—. 2018d, ApJ, 820, L40

Ansdell, M., Williams, J. P., Trapman, L., van Terwisga, S. E., Facchini, S., Manara, C. F., van der Marel, N., Miotello, A., Tazzari, M., Hogerheijde, M., Guidi, G., Testi, L., & van Dishoeck, E. F. 2018, ApJ, 859, 21

Ansdell, M., Williams, J. P., van der Marel, N., Carpenter, J. M., Guidi, G., Hogerheijde, M., Mathews, G. S., Manara, C. F., Miotello, A., Natta, A., Oliveira, I., Tazzari, M., Testi, L., van Dishoeck, E. F., & van Terwisga, S. E. 2016a, ApJ, 828, 46

—. 2016b, ApJ, 828, 46

Armitage, P. J. 2020, Astrophysics of Planet Formation, 2nd edn. (Cambridge University Press)

Artymowicz, P. 1993a, ApJ, 419, 166

—. 1993b, ApJ, 419, 155

Asensio-Torres, R., Henning, T., Cantalloube, F., Pinilla, P., Mesa, D., Garufi, A., Jorquera, S., Gratton, R., Chauvin, G., Szulágyi, J., van Boekel, R., Dong, R., Marleau, G. D., Benisty, M., Villenave, M., Bergez-Casalou, C., Desgrange, C., Janson, M., Keppler, M., Langlois, M.,

Ménard, F., Rickman, E., Stolker, T., Feldt, M., Fusco, T., Gluck, L., Pavlov, A., & Ramos, J. 2021, A&A, 652, A101

Ataiee, S., Pinilla, P., Zsom, A., Dullemond, C. P., Dominik, C., & Ghanbari, J. 2013, A&A, 553, L3

Auddy, S., Dey, R., Lin, M.-K., & Hall, C. 2021, ApJ, 920, 3

Auddy, S. & Lin, M.-K. 2020a, ApJ, 900, 62

—. 2020b, ApJ, 900, 62

Avenhaus, H., Quanz, S. P., Garufi, A., Perez, S., Casassus, S., Pinte, C., Bertrang, G. H.-M., Caceres, C., Benisty, M., & Dominik, C. 2018a, ApJ, 863, 44

Avenhaus, H., Quanz, S. P., Garufi, A., Perez, S., Casassus, S., Pinte, C., Bertrang, G. H. M., Caceres, C., Benisty, M., & Dominik, C. 2018b, ApJ, 863, 44

Bacciotti, F., Girart, J. M., Padovani, M., Podio, L., Paladino, R., Testi, L., Bianchi, E., Galli, D., Codella, C., Coffey, D., Favre, C., & Fedele, D. 2018, ApJ, 865, L12

Bae, J., Isella, A., Zhu, Z., Martin, R., Okuzumi, S., & Suriano, S. 2023, in Astronomical Society of the Pacific Conference Series, Vol. 534, Protostars and Planets VII, ed. S. Inutsuka, Y. Aikawa, T. Muto, K. Tomida, & M. Tamura, 423

Bae, J., Pinilla, P., & Birnstiel, T. 2018, ApJ, 864, L26

Bae, J., Teague, R., & Zhu, Z. 2021, ApJ, 912, 56

Bae, J. & Zhu, Z. 2018a, ApJ, 859, 118

—. 2018b, ApJ, 859, 118

—. 2018c, ApJ, 859, 119

—. 2018d, ApJ, 859, 119

Bae, J., Zhu, Z., Baruteau, C., Benisty, M., Dullemond, C. P., Facchini, S., Isella, A., Keppler, M.,

Pérez, L. M., & Teague, R. 2019, ApJ, 884, L41

Bae, J., Zhu, Z., & Hartmann, L. 2016, ApJ, 819, 134

—. 2017a, ApJ, 850, 201

—. 2017b, ApJ, 850, 201

—. 2017c, ApJ, 850, 201

Bai, X.-N. 2015, ApJ, 798, 84

—. 2017, ApJ, 845, 75

Bai, X.-N. & Stone, J. M. 2014, ApJ, 796, 31

Barker, A. J. & Latter, H. N. 2015, MNRAS, 450, 21

Barraza-Alfaro, M., Flock, M., Marino, S., & Pérez, S. 2021, A&A, 653, A113

Baruteau, C., Crida, A., Paardekooper, S.-J., Masset, F., Guilet, J., Bitsch, B., Nelson, R., Kley, W., & Papaloizou, J. 2014, Protostars and Planets VI, 667

Baruteau, C. & Masset, F. 2008a, ApJ, 672, 1054

—. 2008b, ApJ, 678, 483

Baruteau, C. & Zhu, Z. 2016, MNRAS, 458, 3927

Benisty, M., Bae, J., Facchini, S., Keppler, M., Teague, R., Isella, A., Kurtovic, N. T., Pérez, L. M., Sierra, A., Andrews, S. M., Carpenter, J., Czekala, I., Dominik, C., Henning, T., Menard, F., Pinilla, P., & Zurlo, A. 2021, ApJ, 916, L2

Benisty, M., Dominik, C., Follette, K., Garufi, A., Ginski, C., Hashimoto, J., Keppler, M., Kley, W., & Monnier, J. 2023, in Astronomical Society of the Pacific Conference Series, Vol. 534, Protostars and Planets VII, ed. S. Inutsuka, Y. Aikawa, T. Muto, K. Tomida, & M. Tamura, 605

Benisty, M., Juhasz, A., Facchini, S., Pinilla, P., de Boer, J., Perez, L. M., Keppler, M., Muro-Arena, G., Villenave, M., Andrews, S., Dominik, C., Dullemond, C. P., Gallenne, A., Garufi, A.,

Ginski, C., & Isella, A. 2018, ArXiv e-prints

Bentley, M. S., Schmied, R., Mannel, T., Torkar, K., Jeszenszky, H., Romstedt, J., Levasseur-Regourd, A.-C., Weber, I., Jessberger, E. K., Ehrenfreund, P., Koeberl, C., & Havnes, O. 2016, Nature, 537, 73

Bergner, J. B. & Ciesla, F. 2021, ApJ, 919, 45

Béthune, W. & Rafikov, R. R. 2019, MNRAS, 487, 2319

Binney, J. & Tremaine, S. 2008, Galactic Dynamics: Second Edition (Princeton University Press)

Birnstiel, T. 2018, birnstiel/dsharp_opac: revised release of package, Zenodo

Birnstiel, T. 2018, dsharp_opac: The DSHARP Mie-Opacity Library

Birnstiel, T., Dullemond, C. P., & Brauer, F. 2009, A&A, 503, L5

Birnstiel, T., Klahr, H., & Ercolano, B. 2012, A&A, 539, A148

Birnstiel, T., Ormel, C. W., & Dullemond, C. P. 2011, A&A, 525, A11

Birnstiel et al., T. 2018, ApJ

Blanco, D., Ricci, L., Flock, M., & Turner, N. 2021, ApJ, 920, 70

Blum, J. 2018, Space Sci. Rev., 214, 52

Blum, J., Bischoff, D., & Gundlach, B. 2022, Universe, 8, 381

Blum, J., Gundlach, B., Krause, M., Fulle, M., Johansen, A., Agarwal, J., von Borstel, I., Shi, X., Hu, X., Bentley, M. S., Capaccioni, F., Colangeli, L., Della Corte, V., Fougere, N., Green, S. F., Ivanovski, S., Mannel, T., Merouane, S., Migliorini, A., Rotundi, A., Schmied, R., & Snodgrass, C. 2017, MNRAS, 469, S755

Bohren, C. F. & Huffman, D. R. 1983, Absorption and scattering of light by small particles

Bollati, F., Lodato, G., Price, D. J., & Pinte, C. 2021, MNRAS, 504, 5444

Booth, A. S., Walsh, C., Ilee, J. D., Notsu, S., Qi, C., Nomura, H., & Akiyama, E. 2019, ApJ, 882,

L31

Bowler, B. P. & Nielsen, E. L. 2018a, ArXiv e-prints

—. 2018b, in Handbook of Exoplanets, ed. H. J. Deeg & J. A. Belmonte (Springer International Publishing), 155

Brauer, F., Dullemond, C. P., & Henning, T. 2008, A&A, 480, 859

Brunngräber, R. & Wolf, S. 2019, A&A, 627, L10

—. 2021, A&A, 648, A87

Bukhari Syed, M., Blum, J., Wahlberg Jansson, K., & Johansen, A. 2017, ApJ, 834, 145

Bürger, J., Glißmann, T., Lethuillier, A., Bischoff, D., Gundlach, B., Mutschke, H., Höfer, S., Wolf, S., & Blum, J. 2023, MNRAS, 519, 641

Calvet, N., D'Alessio, P., Hartmann, L., Wilner, D., Walsh, A., & Sitko, M. 2002, ApJ, 568, 1008

Calvet, N., Patino, A., Magris, G. C., & D'Alessio, P. 1991, ApJ, 380, 617

Carrasco-González, C., Henning, T., Chandler, C. J., Linz, H., Pérez, L., Rodríguez, L. F., Galván-Madrid, R., Anglada, G., Birnstiel, T., van Boekel, R., Flock, M., Klahr, H., Macias, E., Menten, K., Osorio, M., Testi, L., Torrelles, J. M., & Zhu, Z. 2016, ApJ, 821, L16

Carrasco-González, C., Sierra, A., Flock, M., Zhu, Z., Henning, T., Chandler, C., Galván-Madrid, R., Macías, E., Anglada, G., Linz, H., Osorio, M., Rodríguez, L. F., Testi, L., Torrelles, J. M., Pérez, L., & Liu, Y. 2019a, arXiv e-prints, arXiv:1908.07140

—. 2019b, ApJ, 883, 71

Casassus, S., van der Plas, G., M, S. P., Dent, W. R. F., Fomalont, E., Hagelberg, J., Hales, A., Jordán, A., Mawet, D., Ménard, F., Wootten, A., Wilner, D., Hughes, A. M., Schreiber, M. R., Girard, J. H., Ercolano, B., Canovas, H., Román, P. E., & Salinas, V. 2013, Nature, 493, 191

Chabrier, G., Johansen, A., Janson, M., & Rafikov, R. 2014, Protostars and Planets VI, 619

Chambers, J. 2021, ApJ, 914, 102

Charnoz, S., Fouchet, L., Aleon, J., & Moreira, M. 2011, ApJ, 737, 33

Chiang, E. I. & Goldreich, P. 1997, ApJ, 490, 368

Christiaens, V., Casassus, S., Absil, O., Cantalloube, F., Gomez Gonzalez, C., Girard, J., Ramírez, R., Pairet, B., Salinas, V., Price, D. J., Pinte, C., Quanz, S. P., Jordán, A., Mawet, D., & Wahhaj, Z. 2019a, MNRAS, 486, 5819

—. 2019b, MNRAS, 486, 5819

Ciarletti, V., Herique, A., Lasue, J., Levasseur-Regourd, A.-C., Plettemeier, D., Lemmonier, F., Guiffaut, C., Pasquero, P., & Kofman, W. 2017, MNRAS, 469, S805

Ciesla, F. J. 2009, Icarus, 200, 655

Cieza, L. A., Casassus, S., Pérez, S., Hales, A., Cárcamo, M., Ansdell, M., Avenhaus, H., Bayo, A., Bertrang, G. H.-M., Cánovas, H., Christiaens, V., Dent, W., Ferrero, G., Gamen, R., Olofsson, J., Orcajo, S., Osses, A., Peña-Ramirez, K., Principe, D., Ruíz-Rodríguez, D., Schreiber, M. R., van der Plas, G., Williams, J. P., & Zurlo, A. 2017, ApJ, 851, L23

Cieza, L. A., González-Ruilova, C., Hales, A. S., Pinilla, P., Ruíz-Rodríguez, D., Zurlo, A., Casassus, S., Pérez, S., Cánovas, H., Arce-Tord, C., Flock, M., Kurtovic, N., Marino, S., Nogueira, P. H., Perez, L., Price, D. J., Principe, D. A., & Williams, J. P. 2021a, MNRAS, 501, 2934

—. 2021b, MNRAS, 501, 2934

—. 2021c, MNRAS, 501, 2934

Cieza, L. A., Ruíz-Rodríguez, D., Hales, A., Casassus, S., Pérez, S., Gonzalez-Ruilova, C., Cánovas, H., Williams, J. P., Zurlo, A., Ansdell, M., Avenhaus, H., Bayo, A., Bertrang, G. H. M., Christiaens, V., Dent, W., Ferrero, G., Gamen, R., Olofsson, J., Orcajo, S., Peña Ramírez, K., Principe, D., Schreiber, M. R., & van der Plas, G. 2019a, MNRAS, 482, 698

—. 2019b, MNRAS, 482, 698

Clanton, C. & Gaudi, B. S. 2014, ApJ, 791, 91

Clarke, C. J., Tazzari, M., Juhasz, A., Rosotti, G., Booth, R., Facchini, S., Ilee, J. D., Johns-Krull, C. M., Kama, M., Meru, F., & Prato, L. 2018, ApJ, 866, L6

Crnkovic-Rubsamen, I., Zhu, Z., & Stone, J. M. 2015, MNRAS, 450, 4285

Cugno, G., Pearce, T. D., Launhardt, R., Bonse, M. J., Ma, J., Henning, T., Quirrenbach, A., Ségransan, D., Matthews, E. C., Quanz, S. P., Kennedy, G. M., Müller, A., Reffert, S., & Rickman, E. L. 2023, A&A, 669, A145

D'Alessio, P., Calvet, N., & Hartmann, L. 2001, ApJ, 553, 321

D'Alessio, P., Canto, J., Calvet, N., & Lizano, S. 1998, ApJ, 500, 411

D'Antona, F. & Mazzitelli, I. 1994, ApJS, 90, 467

Davies, M. B., Adams, F. C., Armitage, P., Chambers, J., Ford, E., Morbidelli, A., Raymond, S. N., & Veras, D. 2014, Protostars and Planets VI, 787

de Juan Ovelar, M., Min, M., Dominik, C., Thalmann, C., Pinilla, P., Benisty, M., & Birnstiel, T. 2013, A&A, 560, A111

Dent, W. R. F., Pinte, C., Cortes, P. C., Ménard, F., Hales, A., Fomalont, E., & de Gregorio-Monsalvo, I. 2019, MNRAS, 482, L29

Dieleman, S., Willett, K. W., & Dambre, J. 2015, MNRAS, 450, 1441

Dipierro, G., Pinilla, P., Lodato, G., & Testi, L. 2015a, ArXiv e-prints

Dipierro, G., Price, D., Laibe, G., Hirsh, K., Cerioli, A., & Lodato, G. 2015b, MNRAS, 453, L73

Dipierro, G., Ricci, L., Pérez, L., Lodato, G., Alexander, R. D., Laibe, G., Andrews, S., Carpenter, J. M., Chandler, C. J., Greaves, J. A., Hall, C., Henning, T., Kwon, W., Linz, H., Mundy, L., Sargent, A., Tazzari, M., Testi, L., & Wilner, D. 2018, MNRAS, 475, 5296

Disk Dynamics Collaboration, Armitage, P. J., Bae, J., Benisty, M., Bergin, E. A., Casassus, S., Czekala, I., Facchini, S., Fung, J., Hall, C., Ilee, J. D., Keppler, M., Kuznetsova, A., Le Gal, R., Loomis, R. A., Lyra, W., Manger, N., Perez, S., Pinte, C., Price, D. J., Rosotti, G., Szulagyi, J., Schwarz, K., Simon, J. B., Teague, R., & Zhang, K. 2020, arXiv e-prints, arXiv:2009.04345

Dodson-Robinson, S. E. & Salyk, C. 2011, ApJ, 738, 131

Dohnanyi, J. S. 1969, J. Geophys. Res., 74, 2531

Doi, K. & Kataoka, A. 2021, ApJ, 912, 164

—. 2023, ApJ, 957, 11

Dominik, C., Min, M., & Tazaki, R. 2021, OpTool: Command-line driven tool for creating complex dust opacities, Astrophysics Source Code Library, record ascl:2104.010

Donati, J. F., Moutou, C., Malo, L., Baruteau, C., Yu, L., Hébrard, E., Hussain, G., Alencar, S., Ménard, F., Bouvier, J., Petit, P., Takami, M., Doyon, R., & Cameron, A. C. 2016, Nature, 534, 662

Dong, R. & Fung, J. 2017, ApJ, 835, 146

Dong, R., Li, S., Chiang, E., & Li, H. 2017a, ApJ, 843, 127

—. 2017b, ApJ, 843, 127

—. 2017c, ApJ, 843, 127

—. 2018a, ArXiv e-prints

—. 2018b, ArXiv e-prints

—. 2018c, ApJ, 866, 110

—. 2018d, ApJ, 866, 110

Dong, R., Liu, S.-y., Eisner, J., Andrews, S., Fung, J., Zhu, Z., Chiang, E., Hashimoto, J., Liu, H. B., Casassus, S., Esposito, T., Hasegawa, Y., Muto, T., Pavlyuchenkov, Y., Wilner, D.,

Akiyama, E., Tamura, M., & Wisniewski, J. 2018e, ApJ, 860, 124

Dong, R., Rafikov, R. R., & Stone, J. M. 2011a, ApJ, 741, 57

Dong, R., Rafikov, R. R., Stone, J. M., & Petrovich, C. 2011b, ApJ, 741, 56

Dong, R., Zhu, Z., Rafikov, R. R., & Stone, J. M. 2015a, ApJ, 809, L5

Dong, R., Zhu, Z., & Whitney, B. 2015b, ApJ, 809, 93

—. 2015c, ApJ, 809, 93

Draine, B. T. 2003, ARA&A, 41, 241

—. 2006, ApJ, 636, 1114

Dubrulle, B., Morfill, G., & Sterzik, M. 1995, Icarus, 114, 237

Duffell, P. C. & MacFadyen, A. I. 2012, ApJ, 755, 7

Dullemond, C. P. & Dominik, C. 2004, A&A, 417, 159

Dullemond, C. P., Dominik, C., & Natta, A. 2001, ApJ, 560, 957

Dullemond, C. P., Juhasz, A., Pohl, A., Sereshti, F., Shetty, R., Peters, T., Commercon, B., & Flock, M. 2012, RADMC-3D: A multi-purpose radiative transfer tool

Dullemond, C. P. & Penzlin, A. B. T. 2018, A&A, 609, A50

Dullemond, C. P., Ziampras, A., Ostertag, D., & Dominik, C. 2022, A&A, 668, A105

Dullemond et al., C. P. 2018, ApJ

Ercolano, B. & Pascucci, I. 2017, Royal Society Open Science, 4, 170114

Espaillat, C., Muzerolle, J., Najita, J., Andrews, S., Zhu, Z., Calvet, N., Kraus, S., Hashimoto, J., Kraus, A., & D'Alessio, P. 2014, Protostars and Planets VI, 497

Estrada, P. R. & Cuzzi, J. N. 2022, ApJ, 936, 40

Estrada, P. R., Cuzzi, J. N., & Morgan, D. A. 2016, ApJ, 818, 200

Estrada, P. R., Cuzzi, J. N., & Umurhan, O. M. 2022, ApJ, 936, 42

Facchini, S., Benisty, M., Bae, J., Loomis, R., Perez, L., Ansdell, M., Mayama, S., Pinilla, P., Teague, R., Isella, A., & Mann, A. 2020, A&A, 639, A121

Fedele, D., Tazzari, M., Booth, R., Testi, L., Clarke, C. J., Pascucci, I., Kospal, A., Semenov, D., Bruderer, S., Henning, T., & Teague, R. 2018, A&A, 610, A24

Fernandes, R. B., Mulders, G. D., Pascucci, I., Mordasini, C., & Emsenhuber, A. 2019, ApJ, 874, 81

Finkbeiner, D. P., Davis, M., & Schlegel, D. J. 1999, ApJ, 524, 867

Flaherty, K., Hughes, A. M., Simon, J. B., Qi, C., Bai, X.-N., Bulatek, A., Andrews, S. M., Wilner, D. J., & Kóspál, Á. 2020, ApJ, 895, 109

Flaherty, K. M., Hughes, A. M., Teague, R., Simon, J. B., Andrews, S. M., & Wilner, D. J. 2018a, ApJ, 856, 117

—. 2018b, ApJ, 856, 117

Flock, M., Fromang, S., González, M., & Commerçon, B. 2013, A&A, 560, A43

Flock, M., Nelson, R. P., Turner, N. J., Bertrang, G. H. M., Carrasco-González, C., Henning, T., Lyra, W., & Teague, R. 2017, ApJ, 850, 131

Flock, M., Ruge, J. P., Dzyurkevich, N., Henning, T., Klahr, H., & Wolf, S. 2015, A&A, 574, A68

Flock, M., Turner, N. J., Nelson, R. P., Lyra, W., Manger, N., & Klahr, H. 2020, ApJ, 897, 155

Flores-Rivera, L., Flock, M., & Nakatani, R. 2020, A&A, 644, A50

Fu, W., Li, H., Lubow, S., Li, S., & Liang, E. 2014, ApJ, 795, L39

Fuente, A., Baruteau, C., Neri, R., Carmona, A., Agúndez, M., Goicoechea, J. R., Bachiller, R., Cernicharo, J., & Berné, O. 2017, ApJ, 846, L3

Fukuhara, Y., Okuzumi, S., & Ono, T. 2021, ApJ, 914, 132

—. 2023, PASJ, 75, 233

Fulle, M. & Blum, J. 2017, MNRAS, 469, S39

Fulton, B. J., Rosenthal, L. J., Hirsch, L. A., Isaacson, H., Howard, A. W., Dedrick, C. M., Sherstyuk, I. A., Blunt, S. C., Petigura, E. A., Knutson, H. A., Behmard, A., Chontos, A., Crepp, J. R., Crossfield, I. J. M., Dalba, P. A., Fischer, D. A., Henry, G. W., Kane, S. R., Kosiarek, M., Marcy, G. W., Rubenzahl, R. A., Weiss, L. M., & Wright, J. T. 2021, ApJS, 255, 14

Fung, J. & Dong, R. 2015, ApJ, 815, L21

Fung, J., Shi, J.-M., & Chiang, E. 2014a, ApJ, 782, 88

—. 2014b, ApJ, 782, 88

Furuya, K. & Aikawa, Y. 2014, ApJ, 790, 97

Furuya, K., Aikawa, Y., Nomura, H., Hersant, F., & Wakelam, V. 2013, ApJ, 779, 11

Gaia Collaboration, Brown, A. G. A., Vallenari, A., Prusti, T., de Bruijne, J. H. J., Babusiaux, C., Bailer-Jones, C. A. L., Biermann, M., Evans, D. W., Eyer, L., Jansen, F., Jordi, C., Klioner, S. A., Lammers, U., Lindegren, L., Luri, X., Mignard, F., Panem, C., Pourbaix, D., Randich, S., Sartoretti, P., Siddiqui, H. I., Soubiran, C., van Leeuwen, F., Walton, N. A., Arenou, F., Bastian, U., Cropper, M., Drimmel, R., Katz, D., Lattanzi, M. G., Bakker, J., Cacciari, C., Castañeda, J., Chaoul, L., Cheek, N., De Angeli, F., Fabricius, C., Guerra, R., Holl, B., Masana, E., Messineo, R., Mowlavi, N., Nienartowicz, K., Panuzzo, P., Portell, J., Riello, M., Seabroke, G. M., Tanga, P., Thévenin, F., Gracia-Abril, G., Comoretto, G., Garcia-Reinaldos, M., Teyssier, D., Altmann, M., Andrae, R., Audard, M., Bellas-Velidis, I., Benson, K., Berthier, J., Blomme, R., Burgess, P., Busso, G., Carry, B., Cellino, A., Clementini, G., Clotet, M., Creevey, O., Davidson, M., De Ridder, J., Delchambre, L., Dell'Oro, A., Ducourant, C., Fernández-Hernández, J., Fouesneau, M., Frémat, Y., Galluccio, L., García-Torres, M., González-Núñez, J., González-Vidal, J. J., Gosset, E., Guy, L. P., Halbwachs, J. L., Hambly, N. C., Harrison, D. L., Hernández, J., Hestrof-

fer, D., Hodgkin, S. T., Hutton, A., Jasniewicz, G., Jean-Antoine-Piccolo, A., Jordan, S., Korn, A. J., Krone-Martins, A., Lanzafame, A. C., Lebzelter, T., Löffler, W., Manteiga, M., Marrese, P. M., Martín-Fleitas, J. M., Moitinho, A., Mora, A., Muinonen, K., Osinde, J., Pancino, E., Pauwels, T., Petit, J. M., Recio-Blanco, A., Richards, P. J., Rimoldini, L., Robin, A. C., Sarro, L. M., Siopis, C., Smith, M., Sozzetti, A., Süveges, M., Torra, J., van Reeven, W., Abbas, U., Abreu Aramburu, A., Accart, S., Aerts, C., Altavilla, G., Álvarez, M. A., Alvarez, R., Alves, J., Anderson, R. I., Andrei, A. H., Anglada Varela, E., Antiche, E., Antoja, T., Arcay, B., Astraatmadja, T. L., Bach, N., Baker, S. G., Balaguer-Núñez, L., Balm, P., Barache, C., Barata, C., Barbato, D., Barblan, F., Barklem, P. S., Barrado, D., Barros, M., Barstow, M. A., Bartholomé Muñoz, S., Bassilana, J. L., Becciani, U., Bellazzini, M., Berihuete, A., Bertone, S., Bianchi, L., Bienaymé, O., Blanco-Cuaresma, S., Boch, T., Boeche, C., Bombrun, A., Borrachero, R., Bossini, D., Bouquillon, S., Bourda, G., Bragaglia, A., Bramante, L., Breddels, M. A., Bressan, A., Brouillet, N., Brüsemeister, T., Brugaletta, E., Bucciarelli, B., Burlacu, A., Busonero, D., Butkevich, A. G., Buzzi, R., Caffau, E., Cancelliere, R., Cannizzaro, G., Cantat-Gaudin, T., Carballo, R., Carlucci, T., Carrasco, J. M., Casamiquela, L., Castellani, M., Castro-Ginard, A., Charlot, P., Chemin, L., Chiavassa, A., Cocozza, G., Costigan, G., Cowell, S., Crifo, F., Crosta, M., Crowley, C., Cuypers, J., Dafonte, C., Damerdji, Y., Dapergolas, A., David, P., David, M., de Laverny, P., De Luise, F., De March, R., de Martino, D., de Souza, R., de Torres, A., Debosscher, J., del Pozo, E., Delbo, M., Delgado, A., Delgado, H. E., Di Matteo, P., Diakite, S., Diener, C., Distefano, E., Dolding, C., Drazinos, P., Durán, J., Edvardsson, B., Enke, H., Eriksson, K., Esquej, P., Eynard Bontemps, G., Fabre, C., Fabrizio, M., Faigler, S., Falcão, A. J., Farràs Casas, M., Federici, L., Fedorets, G., Fernique, P., Figueras, F., Filippi, F., Findeisen, K., Fonti, A., Fraile, E., Fraser, M., Frézouls, B., Gai, M., Galleti, S., Garabato, D., García-

Sedano, F., Garofalo, A., Garralda, N., Gavel, A., Gavras, P., Gerssen, J., Geyer, R., Giacobbe, P., Gilmore, G., Girona, S., Giuffrida, G., Glass, F., Gomes, M., Granvik, M., Gueguen, A., Guerrier, A., Guiraud, J., Gutiérrez-Sánchez, R., Haigron, R., Hatzidimitriou, D., Hauser, M., Haywood, M., Heiter, U., Helmi, A., Heu, J., Hilger, T., Hobbs, D., Hofmann, W., Holland, G., Huckle, H. E., Hypki, A., Icardi, V., Janßen, K., Jevardat de Fombelle, G., Jonker, P. G., Juhász, Á. L., Julbe, F., Karampelas, A., Kewley, A., Klar, J., Kochoska, A., Kohley, R., Kolenberg, K., Kontizas, M., Kontizas, E., Koposov, S. E., Kordopatis, G., Kostrzewa-Rutkowska, Z., Koubsky, P., Lambert, S., Lanza, A. F., Lasne, Y., Lavigne, J. B., Le Fustec, Y., Le Poncin-Lafitte, C., Lebreton, Y., Leccia, S., Leclerc, N., Lecoeur-Taibi, I., Lenhardt, H., Leroux, F., Liao, S., Licata, E., Lindstrøm, H. E. P., Lister, T. A., Livanou, E., Lobel, A., López, M., Managau, S., Mann, R. G., Mantelet, G., Marchal, O., Marchant, J. M., Marconi, M., Marinoni, S., Marschalkó, G., Marshall, D. J., Martino, M., Marton, G., Mary, N., Massari, D., Matijevič, G., Mazeh, T., McMillan, P. J., Messina, S., Michalik, D., Millar, N. R., Molina, D., Molinaro, R., Molnár, L., Montegriffo, P., Mor, R., Morbidelli, R., Morel, T., Morris, D., Mulone, A. F., Muraveva, T., Musella, I., Nelemans, G., Nicastro, L., Noval, L., O'Mullane, W., Ordénovic, C., Ordóñez-Blanco, D., Osborne, P., Pagani, C., Pagano, I., Pailler, F., Palacin, H., Palaversa, L., Panahi, A., Pawlak, M., Piersimoni, A. M., Pineau, F. X., Plachy, E., Plum, G., Poggio, E., Poujoulet, E., Prša, A., Pulone, L., Racero, E., Ragaini, S., Rambaux, N., Ramos-Lerate, M., Regibo, S., Reylé, C., Riclet, F., Ripepi, V., Riva, A., Rivard, A., Rixon, G., Roegiers, T., Roelens, M., Romero-Gómez, M., Rowell, N., Royer, F., Ruiz-Dern, L., Sadowski, G., Sagristà Sellés, T., Sahlmann, J., Salgado, J., Salguero, E., Sanna, N., Santana-Ros, T., Sarasso, M., Savietto, H., Schultheis, M., Sciacca, E., Segol, M., Segovia, J. C., Ségransan, D., Shih, I. C., Siltala, L., Silva, A. F., Smart, R. L., Smith, K. W., Solano, E., Solitro, F., Sordo, R., Soria Nieto, S.,

Souchay, J., Spagna, A., Spoto, F., Stampa, U., Steele, I. A., Steidelmüller, H., Stephenson, C. A., Stoev, H., Suess, F. F., Surdej, J., Szabados, L., Szegedi-Elek, E., Tapiador, D., Taris, F., Tauran, G., Taylor, M. B., Teixeira, R., Terrett, D., Teyssandier, P., Thuillot, W., Titarenko, A., Torra Clotet, F., Turon, C., Ulla, A., Utrilla, E., Uzzi, S., Vaillant, M., Valentini, G., Valette, V., van Elteren, A., Van Hemelryck, E., van Leeuwen, M., Vaschetto, M., Vecchiato, A., Veljanoski, J., Viala, Y., Vicente, D., Vogt, S., von Essen, C., Voss, H., Votruba, V., Voutsinas, S., Walmsley, G., Weiler, M., Wertz, O., Wevers, T., Wyrzykowski, Ł., Yoldas, A., Žerjal, M., Ziaeepour, H., Zorec, J., Zschocke, S., Zucker, S., Zurbach, C., & Zwitter, T. 2018, A&A, 616, A1

Gaia Collaboration, Prusti, T., de Bruijne, J. H. J., Brown, A. G. A., Vallenari, A., Babusiaux, C., Bailer-Jones, C. A. L., Bastian, U., Biermann, M., Evans, D. W., Eyer, L., Jansen, F., Jordi, C., Klioner, S. A., Lammers, U., Lindegren, L., Luri, X., Mignard, F., Milligan, D. J., Panem, C., Poinsignon, V., Pourbaix, D., Randich, S., Sarri, G., Sartoretti, P., Siddiqui, H. I., Soubiran, C., Valette, V., van Leeuwen, F., Walton, N. A., Aerts, C., Arenou, F., Cropper, M., Drimmel, R., Høg, E., Katz, D., Lattanzi, M. G., O'Mullane, W., Grebel, E. K., Holland, A. D., Huc, C., Passot, X., Bramante, L., Cacciari, C., Castañeda, J., Chaoul, L., Cheek, N., De Angeli, F., Fabricius, C., Guerra, R., Hernández, J., Jean-Antoine-Piccolo, A., Masana, E., Messineo, R., Mowlavi, N., Nienartowicz, K., Ordóñez-Blanco, D., Panuzzo, P., Portell, J., Richards, P. J., Riello, M., Seabroke, G. M., Tanga, P., Thévenin, F., Torra, J., Els, S. G., Gracia-Abril, G., Comoretto, G., Garcia-Reinaldos, M., Lock, T., Mercier, E., Altmann, M., Andrae, R., Astraatmadja, T. L., Bellas-Velidis, I., Benson, K., Berthier, J., Blomme, R., Busso, G., Carry, B., Cellino, A., Clementini, G., Cowell, S., Creevey, O., Cuypers, J., Davidson, M., De Ridder, J., de Torres, A., Delchambre, L., Dell'Oro, A., Ducourant, C., Frémat, Y., García-Torres, M., Gosset, E., Halbwachs, J. L., Hambly, N. C., Harrison, D. L., Hauser, M., Hestroffer, D., Hodgkin,

S. T., Huckle, H. E., Hutton, A., Jasniewicz, G., Jordan, S., Kontizas, M., Korn, A. J., Lanzafame, A. C., Manteiga, M., Moitinho, A., Muinonen, K., Osinde, J., Pancino, E., Pauwels, T., Petit, J. M., Recio-Blanco, A., Robin, A. C., Sarro, L. M., Siopis, C., Smith, M., Smith, K. W., Sozzetti, A., Thuillot, W., van Reeven, W., Viala, Y., Abbas, U., Abreu Aramburu, A., Accart, S., Aguado, J. J., Allan, P. M., Allasia, W., Altavilla, G., Álvarez, M. A., Alves, J., Anderson, R. I., Andrei, A. H., Anglada Varela, E., Antiche, E., Antoja, T., Antón, S., Arcay, B., Atzei, A., Ayache, L., Bach, N., Baker, S. G., Balaguer-Núñez, L., Barache, C., Barata, C., Barbier, A., Barblan, F., Baroni, M., Barrado y Navascués, D., Barros, M., Barstow, M. A., Becciani, U., Bellazzini, M., Bellei, G., Bello García, A., Belokurov, V., Bendjoya, P., Berihuete, A., Bianchi, L., Bienaymé, O., Billebaud, F., Blagorodnova, N., Blanco-Cuaresma, S., Boch, T., Bombrun, A., Borrachero, R., Bouquillon, S., Bourda, G., Bouy, H., Bragaglia, A., Breddels, M. A., Brouillet, N., Brüsemeister, T., Bucciarelli, B., Budnik, F., Burgess, P., Burgon, R., Burlacu, A., Busonero, D., Buzzi, R., Caffau, E., Cambras, J., Campbell, H., Cancelliere, R., Cantat-Gaudin, T., Carlucci, T., Carrasco, J. M., Castellani, M., Charlot, P., Charnas, J., Charvet, P., Chassat, F., Chiavassa, A., Clotet, M., Cocozza, G., Collins, R. S., Collins, P., Costigan, G., Crifo, F., Cross, N. J. G., Crosta, M., Crowley, C., Dafonte, C., Damerdji, Y., Dapergolas, A., David, P., David, M., De Cat, P., de Felice, F., de Laverny, P., De Luise, F., De March, R., de Martino, D., de Souza, R., Debosscher, J., del Pozo, E., Delbo, M., Delgado, A., Delgado, H. E., di Marco, F., Di Matteo, P., Diakite, S., Distefano, E., Dolding, C., Dos Anjos, S., Drazinos, P., Durán, J., Dzigan, Y., Ecale, E., Edvardsson, B., Enke, H., Erdmann, M., Escolar, D., Espina, M., Evans, N. W., Eynard Bontemps, G., Fabre, C., Fabrizio, M., Faigler, S., Falcão, A. J., Farràs Casas, M., Faye, F., Federici, L., Fedorets, G., Fernández-Hernández, J., Fernique, P., Fienga, A., Figueras, F., Filippi, F., Findeisen, K., Fonti, A., Fouesneau, M., Fraile, E., Fraser, M., Fuchs, J., Furnell,

R., Gai, M., Galleti, S., Galluccio, L., Garabato, D., García-Sedano, F., Garé, P., Garofalo, A., Garralda, N., Gavras, P., Gerssen, J., Geyer, R., Gilmore, G., Girona, S., Giuffrida, G., Gomes, M., González-Marcos, A., González-Núñez, J., González-Vidal, J. J., Granvik, M., Guerrier, A., Guillout, P., Guiraud, J., Gúrpide, A., Gutiérrez-Sánchez, R., Guy, L. P., Haigron, R., Hatzidimitriou, D., Haywood, M., Heiter, U., Helmi, A., Hobbs, D., Hofmann, W., Holl, B., Holland, G., Hunt, J. A. S., Hypki, A., Icardi, V., Irwin, M., Jevardat de Fombelle, G., Jofré, P., Jonker, P. G., Jorissen, A., Julbe, F., Karampelas, A., Kochoska, A., Kohley, R., Kolenberg, K., Kontizas, E., Koposov, S. E., Kordopatis, G., Koubsky, P., Kowalczyk, A., Krone-Martins, A., Kudryashova, M., Kull, I., Bachchan, R. K., Lacoste-Seris, F., Lanza, A. F., Lavigne, J. B., Le Poncin-Lafitte, C., Lebreton, Y., Lebzelter, T., Leccia, S., Leclerc, N., Lecoeur-Taibi, I., Lemaitre, V., Lenhardt, H., Leroux, F., Liao, S., Licata, E., Lindstrøm, H. E. P., Lister, T. A., Livanou, E., Lobel, A., Löffler, W., López, M., Lopez-Lozano, A., Lorenz, D., Loureiro, T., MacDonald, I., Magalhães Fernandes, T., Managau, S., Mann, R. G., Mantelet, G., Marchal, O., Marchant, J. M., Marconi, M., Marie, J., Marinoni, S., Marrese, P. M., Marschalkó, G., Marshall, D. J., Martín-Fleitas, J. M., Martino, M., Mary, N., Matijevič, G., Mazeh, T., McMillan, P. J., Messina, S., Mestre, A., Michalik, D., Millar, N. R., Miranda, B. M. H., Molina, D., Molinaro, R., Molinaro, M., Molnár, L., Moniez, M., Montegriffo, P., Monteiro, D., Mor, R., Mora, A., Morbidelli, R., Morel, T., Morgenthaler, S., Morley, T., Morris, D., Mulone, A. F., Muraveva, T., Musella, I., Narbonne, J., Nelemans, G., Nicastro, L., Noval, L., Ordénovic, C., Ordieres-Meré, J., Osborne, P., Pagani, C., Pagano, I., Pailler, F., Palacin, H., Palaversa, L., Parsons, P., Paulsen, T., Pecoraro, M., Pedrosa, R., Pentikäinen, H., Pereira, J., Pichon, B., Piersimoni, A. M., Pineau, F. X., Plachy, E., Plum, G., Poujoulet, E., Prša, A., Pulone, L., Ragaini, S., Rago, S., Rambaux, N., Ramos-Lerate, M., Ranalli, P., Rauw, G., Read, A., Regibo, S., Renk, F., Reylé, C., Ribeiro,

R. A., Rimoldini, L., Ripepi, V., Riva, A., Rixon, G., Roelens, M., Romero-Gómez, M., Rowell, N., Royer, F., Rudolph, A., Ruiz-Dern, L., Sadowski, G., Sagristà Sellés, T., Sahlmann, J., Salgado, J., Salguero, E., Sarasso, M., Savietto, H., Schnorhk, A., Schultheis, M., Sciacca, E., Segol, M., Segovia, J. C., Segransan, D., Serpell, E., Shih, I. C., Smareglia, R., Smart, R. L., Smith, C., Solano, E., Solitro, F., Sordo, R., Soria Nieto, S., Souchay, J., Spagna, A., Spoto, F., Stampa, U., Steele, I. A., Steidelmüller, H., Stephenson, C. A., Stoev, H., Suess, F. F., Süveges, M., Surdej, J., Szabados, L., Szegedi-Elek, E., Tapiador, D., Taris, F., Tauran, G., Taylor, M. B., Teixeira, R., Terrett, D., Tingley, B., Trager, S. C., Turon, C., Ulla, A., Utrilla, E., Valentini, G., van Elteren, A., Van Hemelryck, E., van Leeuwen, M., Varadi, M., Vecchiato, A., Veljanoski, J., Via, T., Vicente, D., Vogt, S., Voss, H., Votruba, V., Voutsinas, S., Walmsley, G., Weiler, M., Weingrill, K., Werner, D., Wevers, T., Whitehead, G., Wyrzykowski, Ł., Yoldas, A., Žerjal, M., Zucker, S., Zurbach, C., Zwitter, T., Alecu, A., Allen, M., Allende Prieto, C., Amorim, A., Anglada-Escudé, G., Arsenijevic, V., Azaz, S., Balm, P., Beck, M., Bernstein, H. H., Bigot, L., Bijaoui, A., Blasco, C., Bonfigli, M., Bono, G., Boudreault, S., Bressan, A., Brown, S., Brunet, P. M., Bunclark, P., Buonanno, R., Butkevich, A. G., Carret, C., Carrion, C., Chemin, L., Chéreau, F., Corcione, L., Darmigny, E., de Boer, K. S., de Teodoro, P., de Zeeuw, P. T., Delle Luche, C., Domingues, C. D., Dubath, P., Fodor, F., Frézouls, B., Fries, A., Fustes, D., Fyfe, D., Gallardo, E., Gallegos, J., Gardiol, D., Gebran, M., Gomboc, A., Gómez, A., Grux, E., Gueguen, A., Heyrovsky, A., Hoar, J., Iannicola, G., Isasi Parache, Y., Janotto, A. M., Joliet, E., Jonckheere, A., Keil, R., Kim, D. W., Klagyivik, P., Klar, J., Knude, J., Kochukhov, O., Kolka, I., Kos, J., Kutka, A., Lainey, V., LeBouquin, D., Liu, C., Loreggia, D., Makarov, V. V., Marseille, M. G., Martayan, C., Martinez-Rubi, O., Massart, B., Meynadier, F., Mignot, S., Munari, U., Nguyen, A. T., Nordlander, T., Ocvirk, P., O'Flaherty, K. S., Olias Sanz, A., Ortiz, P.,

Osorio, J., Oszkiewicz, D., Ouzounis, A., Palmer, M., Park, P., Pasquato, E., Peltzer, C., Peralta, J., Péturaud, F., Pieniluoma, T., Pigozzi, E., Poels, J., Prat, G., Prod'homme, T., Raison, F., Rebordao, J. M., Risquez, D., Rocca-Volmerange, B., Rosen, S., Ruiz-Fuertes, M. I., Russo, F., Sembay, S., Serraller Vizcaino, I., Short, A., Siebert, A., Silva, H., Sinachopoulos, D., Slezak, E., Soffel, M., Sosnowska, D., Straižys, V., ter Linden, M., Terrell, D., Theil, S., Tiede, C., Troisi, L., Tsalmantza, P., Tur, D., Vaccari, M., Vachier, F., Valles, P., Van Hamme, W., Veltz, L., Virtanen, J., Wallut, J. M., Wichmann, R., Wilkinson, M. I., Ziaeepour, H., & Zschocke, S. 2016, A&A, 595, A1

Gaidos, E., Mann, A. W., Kraus, A. L., & Ireland, M. 2016, MNRAS, 457, 2877

Galloway-Sprietsma, M., Bae, J., Teague, R., Benisty, M., Facchini, S., Aikawa, Y., Alarcón, F., Andrews, S. M., Bergin, E., Cataldi, G., Cleeves, L. I., Czekala, I., Guzmán, V. V., Huang, J., Law, C. J., Le Gal, R., Liu, Y., Long, F., Ménard, F., Öberg, K. I., Walsh, C., & Wilner, D. J. 2023, ApJ, 950, 147

Gammie, C. F. 1996, ApJ, 457, 355

—. 2001, ApJ, 553, 174

Garufi, A., Benisty, M., Pinilla, P., Tazzari, M., Dominik, C., Ginski, C., Henning, T., Kral, Q., Langlois, M., Ménard, F., Stolker, T., Szulagyi, J., Villenave, M., & van der Plas, G. 2018a, A&A, 620, A94

—. 2018b, A&A, 620, A94

Garufi, A., Benisty, M., Stolker, T., Avenhaus, H., de Boer, J. ., Pohl, A., Quanz, S. P., Dominik, C., Ginski, C., Thalmann, C., van Boekel, R., Boccaletti, A., Henning, T., Janson, M., Salter, G., Schmid, H. M., Sissa, E., Langlois, M., Beuzit, J.-L., Chauvin, G., Mouillet, D., Augereau, J.-C., Bazzon, A., Biller, B., Bonnefoy, M., Buenzli, E., Cheetham, A., Daemgen, S., Desidera, S.,

Engler, N., Feldt, M., Girard, J., Gratton, R., Hagelberg, J., Keller, C., Keppler, M., Kenworthy, M., Kral, Q., Lopez, B., Maire, A.-L., Menard, F., Mesa, D., Messina, S., Meyer, M. R., Milli, J., Min, M., Muller, A., Olofsson, J., Pawellek, N., Pinte, C., Szulagyi, J., Vigan, A., Wahhaj, Z., Waters, R., & Zurlo, A. 2017, The Messenger, 169, 32

Garufi, A., Dominik, C., Ginski, C., Benisty, M., van Holstein, R. G., Henning, T., Pawellek, N., Pinte, C., Avenhaus, H., Facchini, S., Galicher, R., Gratton, R., Ménard, F., Muro-Arena, G., Milli, J., Stolker, T., Vigan, A., Villenave, M., Moulin, T., Origne, A., Rigal, F., Sauvage, J. F., & Weber, L. 2022, A&A, 658, A137

Ghezzi, L., Montet, B. T., & Johnson, J. A. 2018, ApJ, 860, 109

Ginski, C., Facchini, S., Huang, J., Benisty, M., Vaendel, D., Stapper, L., Dominik, C., Bae, J., Ménard, F., Muro-Arena, G., Hogerheijde, M. R., McClure, M., van Holstein, R. G., Birnstiel, T., Boehler, Y., Bohn, A., Flock, M., Mamajek, E. E., Manara, C. F., Pinilla, P., Pinte, C., & Ribas, Á. 2021, ApJ, 908, L25

Ginski, C., Tazaki, R., Dominik, C., & Stolker, T. 2023, arXiv e-prints, arXiv:2301.04617

Golabek, G. J. & Jutzi, M. 2021, Icarus, 363, 114437

Goldreich, P. & Tremaine, S. 1978, ApJ, 222, 850

—. 1979, ApJ, 233, 857

—. 1980, ApJ, 241, 425

Gonzalez, J.-F., Laibe, G., & Maddison, S. T. 2017, MNRAS, 467, 1984

Gonzalez, J.-F., Pinte, C., Maddison, S. T., Ménard, F., & Fouchet, L. 2012, A&A, 547, A58

González-Ruilova, C., Cieza, L. A., Hales, A. S., Pérez, S., Zurlo, A., Arce-Tord, C., Casassus, S., Cánovas, H., Flock, M., Herczeg, G. J., Pinilla, P., Price, D. J., Principe, D. A., Ruíz-Rodríguez, D., & Williams, J. P. 2020, ApJ, 902, L33

Goodman, J. & Rafikov, R. R. 2001, ApJ, 552, 793

Grant, S. L., Espaillat, C. C., Wendeborn, J., Tobin, J. J., Macías, E., Rilinger, A., Ribas, Á., Megeath, S. T., Fischer, W. J., Calvet, N., & Hee Kim, K. 2021, ApJ, 913, 123

Groussin, O., Attree, N., Brouet, Y., Ciarletti, V., Davidsson, B., Filacchione, G., Fischer, H. H., Gundlach, B., Knapmeyer, M., Knollenberg, J., Kokotanekova, R., Kührt, E., Leyrat, C., Marshall, D., Pelivan, I., Skorov, Y., Snodgrass, C., Spohn, T., & Tosi, F. 2019, Space Sci. Rev., 215, 29

Guidi, G., Isella, A., Testi, L., Chandler, C. J., Liu, H. B., Schmid, H. M., Rosotti, G., Meng, C., Jennings, J., Williams, J. P., Carpenter, J. M., de Gregorio-Monsalvo, I., Li, H., Liu, S. F., Ortolani, S., Quanz, S. P., Ricci, L., & Tazzari, M. 2022, A&A, 664, A137

Guillet, V., Girart, J. M., Maury, A. J., & Alves, F. O. 2020, A&A, 634, L15

Güttler, C., Blum, J., Zsom, A., Ormel, C. W., & Dullemond, C. P. 2010, A&A, 513, A56

Güttler, C., Mannel, T., Rotundi, A., Merouane, S., Fulle, M., Bockelée-Morvan, D., Lasue, J., Levasseur-Regourd, A. C., Blum, J., Naletto, G., Sierks, H., Hilchenbach, M., Tubiana, C., Capaccioni, F., Paquette, J. A., Flandes, A., Moreno, F., Agarwal, J., Bodewits, D., Bertini, I., Tozzi, G. P., Hornung, K., Langevin, Y., Krüger, H., Longobardo, A., Della Corte, V., Tóth, I., Filacchione, G., Ivanovski, S. L., Mottola, S., & Rinaldi, G. 2019, A&A, 630, A24

Guzmán, V. V., Huang, J., Andrews, S. M., Isella, A., Pérez, L. M., Carpenter, J. M., Dullemond, C. P., Ricci, L., Birnstiel, T., Zhang, S., Zhu, Z., Bai, X.-N., Benisty, M., Öberg, K. I., & Wilner, D. J. 2018, ApJ, 869, L48

Guzmán et al., V. V. 2018, ApJ

Gyeol Yun, H., Kim, W.-T., Bae, J., & Han, C. 2019, arXiv e-prints, arXiv:1908.11065

Haffert, S. Y., Bohn, A. J., de Boer, J., Snellen, I. A. G., Brinchmann, J., Girard, J. H., Keller,

C. U., & Bacon, R. 2019a, Nature Astronomy, 3, 749

—. 2019b, Nature Astronomy, 3, 749

Hall, C., Dong, R., Teague, R., Terry, J., Pinte, C., Paneque-Carreño, T., Veronesi, B., Alexander, R. D., & Lodato, G. 2020, ApJ, 904, 148

Hammer, M., Kratter, K. M., & Lin, M.-K. 2017, MNRAS, 466, 3533

Hartmann, L., Calvet, N., Gullbring, E., & D'Alessio, P. 1998, ApJ, 495, 385

Hartmann, L., Herczeg, G., & Calvet, N. 2016, ARA&A, 54, 135

Hashimoto, J., Aoyama, Y., Konishi, M., Uyama, T., Takasao, S., Ikoma, M., & Tanigawa, T. 2020a, AJ, 159, 222

—. 2020b, AJ, 159, 222

Hassan, S., Liu, A., Kohn, S., & La Plante, P. 2019, MNRAS, 483, 2524

He, K., Zhang, X., Ren, S., & Sun, J. 2016a, Proceedings of the IEEE Computer Society Conference on Computer Vision and Pattern Recognition, 2016-December, 770

He, K., Zhang, X., Ren, S., & Sun, J. 2016b, in Computer Vision – ECCV 2016, ed. B. Leibe, J. Matas, N. Sebe, & M. Welling (Cham: Springer International Publishing), 630–645

Henning, T. & Stognienko, R. 1996, A&A, 311, 291

Herique, A., Kofman, W., Beck, P., Bonal, L., Buttarazzi, I., Heggy, E., Lasue, J., Levasseur-Regourd, A. C., Quirico, E., & Zine, S. 2016, MNRAS, 462, S516

Hezaveh, Y. D., Perreault Levasseur, L., & Marshall, P. J. 2017, Nature, 548, 555

Howard, A. W., Marcy, G. W., Bryson, S. T., Jenkins, J. M., Rowe, J. F., Batalha, N. M., Borucki, W. J., Koch, D. G., Dunham, E. W., Gautier, Thomas N., I., Van Cleve, J., Cochran, W. D., Latham, D. W., Lissauer, J. J., Torres, G., Brown, T. M., Gilliland, R. L., Buchhave, L. A., Caldwell, D. A., Christensen-Dalsgaard, J., Ciardi, D., Fressin, F., Haas, M. R., Howell, S. B.,

Kjeldsen, H., Seager, S., Rogers, L., Sasselov, D. D., Steffen, J. H., Basri, G. S., Charbonneau, D., Christiansen, J., Clarke, B., Dupree, A., Fabrycky, D. C., Fischer, D. A., Ford, E. B., Fortney, J. J., Tarter, J., Girouard, F. R., Holman, M. J., Johnson, J. A., Klaus, T. C., Machalek, P., Moorhead, A. V., Morehead, R. C., Ragozzine, D., Tenenbaum, P., Twicken, J. D., Quinn, S. N., Isaacson, H., Shporer, A., Lucas, P. W., Walkowicz, L. M., Welsh, W. F., Boss, A., Devore, E., Gould, A., Smith, J. C., Morris, R. L., Prsa, A., Morton, T. D., Still, M., Thompson, S. E., Mullally, F., Endl, M., & MacQueen, P. J. 2012, ApJS, 201, 15

Hsieh, H.-F. & Lin, M.-K. 2020, MNRAS, 497, 2425

Hu, X., Zhu, Z., Okuzumi, S., Bai, X.-N., Wang, L., Tomida, K., & Stone, J. M. 2019, ApJ, 885, 36

Huang, J., Andrews, S. M., Cleeves, L. I., Öberg, K. I., Wilner, D. J., Bai, X., Birnstiel, T., Carpenter, J., Hughes, A. M., Isella, A., Pérez, L. M., Ricci, L., & Zhu, Z. 2018a, ApJ, 852, 122

Huang, J., Andrews, S. M., Dullemond, C. P., Isella, A., Pérez, L. M., Guzmán, V. V., Öberg, K. I., Zhu, Z., Zhang, S., Bai, X.-N., Benisty, M., Birnstiel, T., Carpenter, J. M., Hughes, A. M., Ricci, L., Weaver, E., & Wilner, D. J. 2018b, ApJ, 869, L42

Huang, J., Andrews, S. M., Dullemond, C. P., Öberg, K. I., Qi, C., Zhu, Z., Birnstiel, T., Carpenter, J. M., Isella, A., Macías, E., McClure, M. K., Pérez, L. M., Teague, R., Wilner, D. J., & Zhang, S. 2020a, ApJ, 891, 48

Huang, J., Andrews, S. M., & et al. 2018c, ApJ

—. 2018d, ApJ

Huang, P., Li, H., Isella, A., Miranda, R., Li, S., & Ji, J. 2020b, ApJ, 893, 89

Hubeny, I. 1990, ApJ, 351, 632

Huber, D., Zinn, J., Bojsen-Hansen, M., Pinsonneault, M., Sahlholdt, C., Serenelli, A., Silva

Aguirre, V., Stassun, K., Stello, D., Tayar, J., Bastien, F., Bedding, T. R., Buchhave, L. A., Chaplin, W. J., Davies, G. R., García, R. A., Latham, D. W., Mathur, S., Mosser, B., & Sharma, S. 2017, ApJ, 844, 102

Hull, C. L. H., Yang, H., Li, Z.-Y., Kataoka, A., Stephens, I. W., Andrews, S., Bai, X., Cleeves, L. I., Hughes, A. M., Looney, L., Pérez, L. M., & Wilner, D. 2018a, ApJ, 860, 82

Hull, C. L. H., Yang, H., Li, Z.-Y., Kataoka, A., Stephens, I. W., Andrews, S., Bai, X., Cleeves, L. I., Hughes, A. M., Looney, L., Pérez, L. M., & Wilner, D. 2018b, ApJ, 860, 82

Ilee, J. D., Walsh, C., Jennings, J., Booth, R. A., Rosotti, G. P., Teague, R., Tsukagoshi, T., & Nomura, H. 2022, arXiv e-prints, arXiv:2205.01396

Ioffe, S. & Szegedy, C. 2015, in ICML, 448–456

Isella, A., Benisty, M., Teague, R., Bae, J., Keppler, M., Facchini, S., & Pérez, L. 2019a, ApJ, 879, L25

—. 2019b, ApJ, 879, L25

—. 2019c, ApJ, 879, L25

Isella, A., Guidi, G., Testi, L., Liu, S., Li, H., Li, S., Weaver, E., Boehler, Y., Carpenter, J. M., de Gregorio-Monsalvo, I., Manara, C., Natta, A., Pérez, L. M., Ricci, L., Sargent, A., Tazzari, M., & Turner, N. 2016, Phys. Rev. Lett., 117, 251101

Isella, A. & Turner, N. J. 2018, ApJ, 860, 27

Isella et al., A. 2018, ApJ

Ishimaru, A. 1978, Wave propagation and scattering in random media. Volume 1 - Single scattering and transport theory, Vol. 1

Izquierdo, A. F., Testi, L., Facchini, S., Rosotti, G. P., & van Dishoeck, E. F. 2021, A&A, 650, A179

Jang-Condell, H. & Turner, N. J. 2012, ApJ, 749, 153

—. 2013, ApJ, 772, 34

Jennings, J., Booth, R. A., Tazzari, M., Clarke, C. J., & Rosotti, G. P. 2021, arXiv e-prints, arXiv:2103.02392

—. 2022a, MNRAS, 509, 2780

Jennings, J., Booth, R. A., Tazzari, M., Rosotti, G. P., & Clarke, C. J. 2020, MNRAS, 495, 3209

Jennings, J., Tazzari, M., Clarke, C. J., Booth, R. A., & Rosotti, G. P. 2022b, MNRAS, 514, 6053

Jiang, H. & Ormel, C. W. 2021, MNRAS

Jiang, Y.-F. 2022, ApJS, 263, 4

Jiang, Y.-F., Stone, J. M., & Davis, S. W. 2012, ApJS, 199, 14

—. 2014, ApJS, 213, 7

Jin, S., Li, S., Isella, A., Li, H., & Ji, J. 2016, ApJ, 818, 76

Johansen, A., Blum, J., Tanaka, H., Ormel, C., Bizzarro, M., & Rickman, H. 2014, in Protostars & Planets VI, eds. H. Beuther, R. Klessen, C. Dullemond, & Th. Henning (Univ. Arizona Press: Tucson), in press

Johansen, A., Youdin, A., & Klahr, H. 2009a, ApJ, 697, 1269

—. 2009b, ApJ, 697, 1269

Johns-Krull, C. M., McLane, J. N., Prato, L., Crockett, C. J., Jaffe, D. T., Hartigan, P. M., Beichman, C. A., Mahmud, N. I., Chen, W., Skiff, B. A., Cauley, P. W., Jones, J. A., & Mace, G. N. 2016, ApJ, 826, 206

Johnson, J. A., Aller, K. M., Howard, A. W., & Crepp, J. R. 2010, PASP, 122, 905

Jones, E., Oliphant, T., Peterson, P., et al. 2001–, SciPy: Open source scientific tools for Python, [Online; accessed ¡today¿]

Jorda, L., Gaskell, R., Capanna, C., Hviid, S., Lamy, P., Ďurech, J., Faury, G., Groussin, O., Gutiérrez, P., Jackman, C., Keihm, S. J., Keller, H. U., Knollenberg, J., Kührt, E., Marchi, S., Mottola, S., Palmer, E., Schloerb, F. P., Sierks, H., Vincent, J. B., A'Hearn, M. F., Barbieri, C., Rodrigo, R., Koschny, D., Rickman, H., Barucci, M. A., Bertaux, J. L., Bertini, I., Cremonese, G., Da Deppo, V., Davidsson, B., Debei, S., De Cecco, M., Fornasier, S., Fulle, M., Güttler, C., Ip, W. H., Kramm, J. R., Küppers, M., Lara, L. M., Lazzarin, M., Lopez Moreno, J. J., Marzari, F., Naletto, G., Oklay, N., Thomas, N., Tubiana, C., & Wenzel, K. P. 2016, Icarus, 277, 257

Juhász, A. & , G. P. 2018, MNRAS, 474, L32

Jutzi, M. & Asphaug, E. 2015, Science, 348, 1355

Jutzi, M. & Benz, W. 2017, A&A, 597, A62

Kaeufer, T., Woitke, P., Min, M., Kamp, I., & Pinte, C. 2023, A&A, 672, A30

Kanagawa, K. D., Muto, T., Okuzumi, S., Tanigawa, T., Taki, T., & Shibaike, Y. 2018, ApJ, 868, 48

Kanagawa, K. D., Muto, T., Tanaka, H., Tanigawa, T., Takeuchi, T., Tsukagoshi, T., & Momose, M. 2015a, ApJ, 806, L15

—. 2015b, ApJ, 806, L15

—. 2016a, PASJ, 68, 43

—. 2016b, PASJ, 68, 43

Kanagawa, K. D., Nomura, H., Tsukagoshi, T., Muto, T., & Kawabe, R. 2020, ApJ, 892, 83

Kataoka, A., Muto, T., Momose, M., Tsukagoshi, T., & Dullemond, C. P. 2016a, ApJ, 820, 54

Kataoka, A., Muto, T., Momose, M., Tsukagoshi, T., Fukagawa, M., Shibai, H., Hanawa, T., Murakawa, K., & Dullemond, C. P. 2015, ApJ, 809, 78

Kataoka, A., Okuzumi, S., Tanaka, H., & Nomura, H. 2014, A&A, 568, A42

Kataoka, A., Tanaka, H., Okuzumi, S., & Wada, K. 2013, A&A, 557, L4

Kataoka, A., Tsukagoshi, T., Momose, M., Nagai, H., Muto, T., Dullemond, C. P., Pohl, A., Fukagawa, M., Shibai, H., Hanawa, T., & Murakawa, K. 2016b, ApJ, 831, L12

Kataoka, A., Tsukagoshi, T., Pohl, A., Muto, T., Nagai, H., Stephens, I. W., Tomisaka, K., & Momose, M. 2017, ApJ, 844, L5

Kempf, S., Pfalzner, S., & Henning, T. K. 1999, Icarus, 141, 388

Keppler, M., Benisty, M., Müller, A., Henning, T., van Boekel, R., Cantalloube, F., Ginski, C., van Holstein, R. G., Maire, A.-L., Pohl, A., Samland, M., Avenhaus, H., Baudino, J.-L., Boccaletti, A., de Boer, J., Bonnefoy, M., Chauvin, G., Desidera, S., Langlois, M., Lazzoni, C., Marleau, G.-D., Mordasini, C., Pawellek, N., Stolker, T., Vigan, A., Zurlo, A., Birnstiel, T., Brandner, W., Feldt, M., Flock, M., Girard, J., Gratton, R., Hagelberg, J., Isella, A., Janson, M., Juhasz, A., Kemmer, J., Kral, Q., Lagrange, A.-M., Launhardt, R., Matter, A., Ménard, F., Milli, J., Mollière, P., Olofsson, J., Pérez, L., Pinilla, P., Pinte, C., Quanz, S. P., Schmidt, T., Udry, S., Wahhaj, Z., Williams, J. P., Buenzli, E., Cudel, M., Dominik, C., Galicher, R., Kasper, M., Lannier, J., Mesa, D., Mouillet, D., Peretti, S., Perrot, C., Salter, G., Sissa, E., Wildi, F., Abe, L., Antichi, J., Augereau, J.-C., Baruffolo, A., Baudoz, P., Bazzon, A., Beuzit, J.-L., Blanchard, P., Brems, S. S., Buey, T., De Caprio, V., Carbillet, M., Carle, M., Cascone, E., Cheetham, A., Claudi, R., Costille, A., Delboulbé, A., Dohlen, K., Fantinel, D., Feautrier, P., Fusco, T., Giro, E., Gluck, L., Gry, C., Hubin, N., Hugot, E., Jaquet, M., Le Mignant, D., Llored, M., Madec, F., Magnard, Y., Martinez, P., Maurel, D., Meyer, M., Möller-Nilsson, O., Moulin, T., Mugnier, L., Origné, A., Pavlov, A., Perret, D., Petit, C., Pragt, J., Puget, P., Rabou, P., Ramos, J., Rigal, F., Rochat, S., Roelfsema, R., Rousset, G., Roux, A., Salasnich, B., Sauvage, J.-F., Sevin, A., Soenke, C., Stadler, E., Suarez, M., Turatto, M., & Weber, L. 2018a, A&A, 617, A44

Keppler, M., Benisty, M., Müller, A., Henning, T., van Boekel, R., Cantalloube, F., Ginski, C., van Holstein, R. G., Maire, A. L., Pohl, A., Samland, M., Avenhaus, H., Baudino, J. L., Boccaletti, A., de Boer, J., Bonnefoy, M., Chauvin, G., Desidera, S., Langlois, M., Lazzoni, C., Marleau, G. D., Mordasini, C., Pawellek, N., Stolker, T., Vigan, A., Zurlo, A., Birnstiel, T., Brandner, W., Feldt, M., Flock, M., Girard, J., Gratton, R., Hagelberg, J., Isella, A., Janson, M., Juhasz, A., Kemmer, J., Kral, Q., Lagrange, A. M., Launhardt, R., Matter, A., Ménard, F., Milli, J., Mollière, P., Olofsson, J., Pérez, L., Pinilla, P., Pinte, C., Quanz, S. P., Schmidt, T., Udry, S., Wahhaj, Z., Williams, J. P., Buenzli, E., Cudel, M., Dominik, C., Galicher, R., Kasper, M., Lannier, J., Mesa, D., Mouillet, D., Peretti, S., Perrot, C., Salter, G., Sissa, E., Wildi, F., Abe, L., Antichi, J., Augereau, J. C., Baruffolo, A., Baudoz, P., Bazzon, A., Beuzit, J. L., Blanchard, P., Brems, S. S., Buey, T., De Caprio, V., Carbillet, M., Carle, M., Cascone, E., Cheetham, A., Claudi, R., Costille, A., Delboulbé, A., Dohlen, K., Fantinel, D., Feautrier, P., Fusco, T., Giro, E., Gluck, L., Gry, C., Hubin, N., Hugot, E., Jaquet, M., Le Mignant, D., Llored, M., Madec, F., Magnard, Y., Martinez, P., Maurel, D., Meyer, M., Möller-Nilsson, O., Moulin, T., Mugnier, L., Origné, A., Pavlov, A., Perret, D., Petit, C., Pragt, J., Puget, P., Rabou, P., Ramos, J., Rigal, F., Rochat, S., Roelfsema, R., Rousset, G., Roux, A., Salasnich, B., Sauvage, J. F., Sevin, A., Soenke, C., Stadler, E., Suarez, M., Turatto, M., & Weber, L. 2018b, A&A, 617, A44

Keppler, M., Teague, R., Bae, J., Benisty, M., Henning, T., van Boekel, R., Chapillon, E., Pinilla, P., Williams, J. P., Bertrang, G. H. M., Facchini, S., Flock, M., Ginski, C., Juhasz, A., Klahr, H., Liu, Y., Müller, A., Pérez, L. M., Pohl, A., Rosotti, G., Samland, M., & Semenov, D. 2019, A&A, 625, A118

Kingma, D. P. & Ba, J. 2015, in 3rd International Conference on Learning Representations, ICLR 2015, San Diego, CA, USA, May 7-9, 2015, Conference Track Proceedings, ed. Y. Bengio &

Y. LeCun

Kirchschlager, F. & Bertrang, G. H. M. 2020, A&A, 638, A116

Kirchschlager, F., Bertrang, G. H. M., & Flock, M. 2019, MNRAS, 488, 1211

Kirchschlager, F. & Wolf, S. 2014, A&A, 568, A103

Klahr, H., Baehr, H., & Melon Fuksman, J. D. 2023, arXiv e-prints, arXiv:2305.08165

Klahr, H. H. & Bodenheimer, P. 2003, ApJ, 582, 869

Kley, W. & Dirksen, G. 2006, A&A, 447, 369

Kley, W. & Nelson, R. P. 2012, ARA&A, 50, 211

Kofman, W., Herique, A., Barbin, Y., Barriot, J.-P., Ciarletti, V., Clifford, S., Edenhofer, P., Elachi, C., Eyraud, C., Goutail, J.-P., Heggy, E., Jorda, L., Lasue, J., Levasseur-Regourd, A.-C., Nielsen, E., Pasquero, P., Preusker, F., Puget, P., Plettemeier, D., Rogez, Y., Sierks, H., Statz, C., Svedhem, H., Williams, I., Zine, S., & Van Zyl, J. 2015, Science, 349, 2.639

Krause, M. & Blum, J. 2004, Phys. Rev. Lett., 93, 021103

Krijt, S., Kama, M., McClure, M., Teske, J., Bergin, E. A., Shorttle, O., Walsh, K. J., & Raymond, S. N. 2022, arXiv e-prints, arXiv:2203.10056

Krijt, S., Ormel, C. W., Dominik, C., & Tielens, A. G. G. M. 2015, A&A, 574, A83

Kuiper, R., Klahr, H., Dullemond, C., Kley, W., & Henning, T. 2010, A&A, 511, A81

Kuiper, R. & Klessen, R. S. 2013, A&A, 555, A7

Kurtovic, N., Pérez, L. M., & et al. 2018, ApJ

Kurtovic, N. T., Pinilla, P., Long, F., Benisty, M., Manara, C. F., Natta, A., Pascucci, I., Ricci, L., Scholz, A., & Testi, L. 2021, A&A, 645, A139

Kuznetsova, A., Bae, J., Hartmann, L., & Low, M.-M. M. 2022, ApJ, 928, 92

Law, C. J., Benisty, M., Facchini, S., Teague, R., Bae, J., Isella, A., Kamp, I., Öberg, K. I., Portilla-

Revelo, B., & Rampinelli, L. 2024, arXiv e-prints, arXiv:2401.03018

Law, C. J., Crystian, S., Teague, R., Öberg, K. I., Rich, E. A., Andrews, S. M., Bae, J., Flaherty, K., Guzmán, V. V., Huang, J., Ilee, J. D., Kastner, J. H., Loomis, R. A., Long, F., Pérez, L. M., Pérez, S., Qi, C., Rosotti, G. P., Ruíz-Rodríguez, D., Tsukagoshi, T., & Wilner, D. J. 2022, ApJ, 932, 114

Law, C. J., Teague, R., Loomis, R. A., Bae, J., Öberg, K. I., Czekala, I., Andrews, S. M., Aikawa, Y., Alarcón, F., Bergin, E. A., Bergner, J. B., Booth, A. S., Bosman, A. D., Calahan, J. K., Cataldi, G., Cleeves, L. I., Furuya, K., Guzmán, V. V., Huang, J., Ilee, J. D., Le Gal, R., Liu, Y., Long, F., Ménard, F., Nomura, H., Pérez, L. M., Qi, C., Schwarz, K. R., Soto, D., Tsukagoshi, T., Yamato, Y., van't Hoff, M. L. R., Walsh, C., Wilner, D. J., & Zhang, K. 2021, ApJS, 257, 4

Law, C. J., Teague, R., Öberg, K. I., Rich, E. A., Andrews, S. M., Bae, J., Benisty, M., Facchini, S., Flaherty, K., Isella, A., Jin, S., Hashimoto, J., Huang, J., Loomis, R. A., Long, F., Muñoz-Romero, C. E., Paneque-Carreño, T., Pérez, L. M., Qi, C., Schwarz, K. R., Stadler, J., Tsukagoshi, T., Wilner, D. J., & van der Plas, G. 2023, ApJ, 948, 60

LeCun, Y., Bottou, L., Bengio, Y., & Haffner, P. 1998, Proceedings of the IEEE, 86, 2278

Leemker, M., Booth, A. S., van Dishoeck, E. F., Pérez-Sánchez, A. F., Szulágyi, J., Bosman, A. D., Bruderer, S., Facchini, S., Hogerheijde, M. R., Paneque-Carreño, T., & Sturm, J. A. 2022, A&A, 663, A23

Lehmann, M. & Lin, M. K. 2022, A&A, 658, A156

Lesur, G. 2021, Journal of Plasma Physics, 87, 205870101

Lesur, G., Ercolano, B., Flock, M., Lin, M. K., Yang, C. C., Barranco, J. A., Benitez-Llambay, P., Goodman, J., Johansen, A., Klahr, H., Laibe, G., Lyra, W., Marcus, P., Nelson, R. P., Squire, J., Simon, J. B., Turner, N., Umurhan, O. M., & Youdin, A. N. 2022, arXiv e-prints,

arXiv:2203.09821

Lesur, G., Hennebelle, P., & Fromang, S. 2015, A&A, 582, L9

Li, A. & Draine, B. T. 2001, ApJ, 554, 778

Li, S. & Li, H. 2016, Journal of Physics: Conference Series, 719, 012007

Lichtenberg, T. & Krijt, S. 2021, ApJ, 913, L20

Lieu, M., Conversi, L., Altieri, B., & Carry, B. 2019, MNRAS, 485, 5831

Lin, D. N. C. & Papaloizou, J. 1979, MNRAS, 186, 799

Lin, M.-K. 2012, MNRAS, 426, 3211

—. 2015, MNRAS, 448, 3806

—. 2019, MNRAS, 485, 5221

Lin, M.-K. & Papaloizou, J. C. B. 2011, MNRAS, 415, 1445

Lin, M.-K. & Youdin, A. N. 2015, ApJ, 811, 17

Lin, Z.-Y. D., Li, Z.-Y., Yang, H., Looney, L., Stephens, I., & Hull, C. L. H. 2020, MNRAS, 496, 169

Lin, Z.-Y. D., Li, Z.-Y., Yang, H., Muñoz, O., Looney, L., Stephens, I., Hull, C. L. H., Fernández-López, M., & Harrison, R. 2023, MNRAS, 520, 1210

Lin, Z.-Y. D., Li, Z.-Y., Yang, H., Stephens, I., Looney, L., Harrison, R., & Fernández-López, M. 2022, MNRAS, 512, 3922

Liu, H. B. 2019a, ApJ, 877, L22

—. 2019b, ApJ, 877, L22

Liu, S.-F., Jin, S., Li, S., Isella, A., & Li, H. 2018, ApJ, 857, 87

Liu, Y., Linz, H., Fang, M., Henning, T., Wolf, S., Flock, M., Rosotti, G. P., Wang, H., & Li, D. 2022, A&A, 668, A175

Lodato, G., Dipierro, G., Ragusa, E., Long, F., Herczeg, G. J., Pascucci, I., Pinilla, P., Manara, C. F., Tazzari, M., Liu, Y., Mulders, G. D., Harsono, D., Boehler, Y., Ménard, F., Johnstone, D., Salyk, C., van der Plas, G., Cabrit, S., Edwards, S., Fischer, W. J., Hendler, N., Nisini, B., Rigliaco, E., Avenhaus, H., Banzatti, A., & Gully-Santiago, M. 2019a, MNRAS, 486, 453

—. 2019b, MNRAS, 486, 453

Lodato, G., Scardoni, C. E., Manara, C. F., & Testi, L. 2017, MNRAS, 472, 4700

Long, D. E., Zhang, K., Teague, R., & Bergin, E. A. 2020a, ApJ, 895, L46

Long, F., Herczeg, G. J., Harsono, D., Pinilla, P., Tazzari, M., Manara, C. F., Pascucci, I., Cabrit, S., Nisini, B., Johnstone, D., Edwards, S., Salyk, C., Menard, F., Lodato, G., Boehler, Y., Mace, G. N., Liu, Y., Mulders, G. D., Hendler, N., Ragusa, E., Fischer, W. J., Banzatti, A., Rigliaco, E., van de Plas, G., Dipierro, G., Gully-Santiago, M., & Lopez-Valdivia, R. 2019, ApJ, 882, 49

Long, F., Pinilla, P., Herczeg, G. J., Andrews, S. M., Harsono, D., Johnstone, D., Ragusa, E., Pascucci, I., Wilner, D. J., Hendler, N., Jennings, J., Liu, Y., Lodato, G., Menard, F., van de Plas, G., & Dipierro, G. 2020b, ApJ, 898, 36

Long, F., Pinilla, P., Herczeg, G. J., Harsono, D., Dipierro, G., Pascucci, I., Hendler, N., Tazzari, M., Ragusa, E., Salyk, C., Edwards, S., Lodato, G., van de Plas, G., Johnstone, D., Liu, Y., Boehler, Y., Cabrit, S., Manara, C. F., Menard, F., Mulders, G. D., Nisini, B., Fischer, W. J., Rigliaco, E., Banzatti, A., Avenhaus, H., & Gully-Santiago, M. 2018a, ApJ, 869, 17

—. 2018b, The Astrophysical Journal, 869, 17

Lorek, S., Lacerda, P., & Blum, J. 2018, A&A, 611, A18

Lovelace, R. V. E., Jore, K. P., & Haynes, M. P. 1997, ApJ, 475, 83

Lovelace, R. V. E., Li, H., Colgate, S. A., & Nelson, A. F. 1999, ApJ, 513, 805

Lubow, S. H. 1991a, ApJ, 381, 259

—. 1991b, ApJ, 381, 268

Lynden-Bell, D. & Kalnajs, A. J. 1972, MNRAS, 157, 1

Lynden-Bell, D. & Pringle, J. E. 1974, MNRAS, 168, 603

Lyra, W., Johansen, A., Klahr, H., & Piskunov, N. 2009, A&A, 493, 1125

Lyra, W. & Lin, M.-K. 2013, ApJ, 775, 17

Lyra, W. & Umurhan, O. M. 2019, PASP, 131, 072001

Macías, E., Espaillat, C. C., Osorio, M., Anglada, G., Torrelles, J. M., Carrasco-González, C., Flock, M., Linz, H., Bertrang, G. H. M., Henning, T., Gómez, J. F., Calvet, N., & Dent, W. R. F. 2019, ApJ, 881, 159

Macías, E., Guerra-Alvarado, O., Carrasco-González, C., Ribas, Á., Espaillat, C. C., Huang, J., & Andrews, S. M. 2021, A&A, 648, A33

Macintosh, B., Graham, J. R., Barman, T., De Rosa, R. J., Konopacky, Q., Marley, M. S., Marois, C., Nielsen, E. L., Pueyo, L., Rajan, A., Rameau, J., Saumon, D., Wang, J. J., Patience, J., Ammons, M., Arriaga, P., Artigau, E., Beckwith, S., Brewster, J., Bruzzone, S., Bulger, J., Burningham, B., Burrows, A. S., Chen, C., Chiang, E., Chilcote, J. K., Dawson, R. I., Dong, R., Doyon, R., Draper, Z. H., Duchêne, G., Esposito, T. M., Fabrycky, D., Fitzgerald, M. P., Follette, K. B., Fortney, J. J., Gerard, B., Goodsell, S., Greenbaum, A. Z., Hibon, P., Hinkley, S., Cotten, T. H., Hung, L. W., Ingraham, P., Johnson-Groh, M., Kalas, P., Lafreniere, D., Larkin, J. E., Lee, J., Line, M., Long, D., Maire, J., Marchis, F., Matthews, B. C., Max, C. E., Metchev, S., Millar-Blanchaer, M. A., Mittal, T., Morley, C. V., Morzinski, K. M., Murray-Clay, R., Oppenheimer, R., Palmer, D. W., Patel, R., Perrin, M. D., Poyneer, L. A., Rafikov, R. R., Rantakyrö, F. T., Rice, E. L., Rojo, P., Rudy, A. R., Ruffio, J. B., Ruiz, M. T., Sadakuni, N., Saddlemyer, L., Salama, M., Savransky, D., Schneider, A. C., Sivaramakrishnan, A., Song, I., Soummer, R., Thomas, S.,

Vasisht, G., Wallace, J. K., Ward-Duong, K., Wiktorowicz, S. J., Wolff, S. G., & Zuckerman, B. 2015, Science, 350, 64

Malygin, M. G., Klahr, H., Semenov, D., Henning, T., & Dullemond, C. P. 2017, A&A, 605, A30

Manara, C. F., Ansdell, M., Rosotti, G. P., Hughes, A. M., Armitage, P. J., Lodato, G., & Williams, J. P. 2022, arXiv e-prints, arXiv:2203.09930

Manger, N. & Klahr, H. 2018, MNRAS, 480, 2125

Manger, N., Klahr, H., Kley, W., & Flock, M. 2020, MNRAS, 499, 1841

Manger, N., Pfeil, T., & Klahr, H. 2021, MNRAS, 508, 5402

Mannel, T., Bentley, M. S., Boakes, P. D., Jeszenszky, H., Ehrenfreund, P., Engrand, C., Koeberl, C., Levasseur-Regourd, A. C., Romstedt, J., Schmied, R., Torkar, K., & Weber, I. 2019, A&A, 630, A26

Mannel, T., Bentley, M. S., Schmied, R., Jeszenszky, H., Levasseur-Regourd, A. C., Romstedt, J., & Torkar, K. 2016, MNRAS, 462, S304

Markwardt, C. B. 2009, in Astronomical Society of the Pacific Conference Series, Vol. 411, Astronomical Data Analysis Software and Systems XVIII, ed. D. A. Bohlender, D. Durand, & P. Dowler, 251

Marois, C., Zuckerman, B., Konopacky, Q. M., Macintosh, B., & Barman, T. 2010, Nature, 468, 1080

Martire, P., Longarini, C., Lodato, G., Rosotti, G. P., Winter, A., Facchini, S., Hardiman, C., Benisty, M., Stadler, J., Izquierdo, A. F., & Testi, L. 2024, arXiv e-prints, arXiv:2402.12236

Masset, F. 2000, A&AS, 141, 165

Masset, F. S. 2002, A&A, 387, 605

Mathis, J. S., Rumpl, W., & Nordsieck, K. H. 1977, ApJ, 217, 425

Mayor, M., Marmier, M., Lovis, C., Udry, S., Ségransan, D., Pepe, F., Benz, W., Bertaux, J. L., Bouchy, F., Dumusque, X., Lo Curto, G., Mordasini, C., Queloz, D., & Santos, N. C. 2011, arXiv e-prints, arXiv:1109.2497

McKay, M. D., Beckman, R. J., & Conover, W. J. 1979, Technometrics, 21, 239

McMullin, J. P., Waters, B., Schiebel, D., Young, W., & Golap, K. 2007a, in Astronomical Society of the Pacific Conference Series, Vol. 376, Astronomical Data Analysis Software and Systems XVI, ed. R. A. Shaw, F. Hill, & D. J. Bell, 127

McMullin, J. P., Waters, B., Schiebel, D., Young, W., & Golap, K. 2007b, in Astronomical Society of the Pacific Conference Series, Vol. 376, Astronomical Data Analysis Software and Systems XVI, ed. R. A. Shaw, F. Hill, & D. J. Bell, 127

Melon Fuksman, J. D., Flock, M., & Klahr, H. 2023a, arXiv e-prints, arXiv:2312.06882

—. 2023b, arXiv e-prints, arXiv:2312.06890

Melon Fuksman, J. D., Klahr, H., Flock, M., & Mignone, A. 2021, ApJ, 906, 78

Merouane, S., Zaprudin, B., Stenzel, O., Langevin, Y., Altobelli, N., Della Corte, V., Fischer, H., Fulle, M., Hornung, K., Silén, J., Ligier, N., Rotundi, A., Ryno, J., Schulz, R., Hilchenbach, M., Kissel, J., & COSIMA Team. 2016, A&A, 596, A87

Meru, F., Juhász, A., Ilee, J. D., Clarke, C. J., Rosotti, G. P., & Booth, R. A. 2017, ApJ, 839, L24

Meshkat, T., Mawet, D., Bryan, M. L., Hinkley, S., Bowler, B. P., Stapelfeldt, K. R., Batygin, K., Padgett, D., Morales, F. Y., Serabyn, E., Christiaens, V., Brandt, T. D., & Wahhaj, Z. 2017a, AJ, 154, 245

—. 2017b, AJ, 154, 245

Miotello, A., Kamp, I., Birnstiel, T., Cleeves, L. I., & Kataoka, A. 2022, arXiv e-prints, arXiv:2203.09818

Miranda, R. & Rafikov, R. R. 2019a, ApJ, 875, 37

—. 2019b, ApJ, 875, 37

—. 2019c, ApJ, 878, L9

—. 2020a, ApJ, 904, 121

—. 2020b, ApJ, 892, 65

Mishchenko, M. I., Hovenier, J. W., & Travis, L. D. 2000, Light scattering by nonspherical particles : theory, measurements, and applications

Miyake, K. & Nakagawa, Y. 1993, Icarus, 106, 20

Montesinos, M., Cuello, N., Olofsson, J., Cuadra, J., Bayo, A., Bertrang, G. H. M., & Perrot, C. 2021, ApJ, 910, 31

Moosmüller, H. & Arnott, W. P. 2009, Journal of the Air & Waste Management Association, 59, 1028

Morbidelli, A. 2020, A&A, 638, A1

Mori, T. & Kataoka, A. 2021, ApJ, 908, 153

Mori, T., Kataoka, A., Ohashi, S., Momose, M., Muto, T., Nagai, H., & Tsukagoshi, T. 2019, ApJ, 883, 16

Mousis, O., Drouard, A., Vernazza, P., Lunine, J. I., Monnereau, M., Maggiolo, R., Altwegg, K., Balsiger, H., Berthelier, J. J., Cessateur, G., De Keyser, J., Fuselier, S. A., Gasc, S., Korth, A., Le Deun, T., Mall, U., Marty, B., Rème, H., Rubin, M., Tzou, C. Y., Waite, J. H., & Wurz, P. 2017, ApJ, 839, L4

Mulders, G. D. 2018, in Handbook of Exoplanets, ed. H. J. Deeg & J. A. Belmonte (Springer International Publishing), 153

Mulders, G. D., Pascucci, I., & Apai, D. 2015, ApJ, 814, 130

Mulders, G. D., Pascucci, I., Ciesla, F. J., & Fernandes, R. B. 2021, ApJ, 920, 66

Mulders, G. D., Pascucci, I., Manara, C. F., Testi, L., Herczeg, G. J., Henning, T., Mohanty, S., & Lodato, G. 2017, ApJ, 847, 31

Müller, A., Keppler, M., Henning, T., Samland, M., Chauvin, G., Beust, H., Maire, A. L., Molaverdikhani, K., van Boekel, R., Benisty, M., Boccaletti, A., Bonnefoy, M., Cantalloube, F., Charnay, B., Baudino, J. L., Gennaro, M., Long, Z. C., Cheetham, A., Desidera, S., Feldt, M., Fusco, T., Girard, J., Gratton, R., Hagelberg, J., Janson, M., Lagrange, A. M., Langlois, M., Lazzoni, C., Ligi, R., Ménard, F., Mesa, D., Meyer, M., Mollière, P., Mordasini, C., Moulin, T., Pavlov, A., Pawellek, N., Quanz, S. P., Ramos, J., Rouan, D., Sissa, E., Stadler, E., Vigan, A., Wahhaj, Z., Weber, L., & Zurlo, A. 2018a, A&A, 617, L2

—. 2018b, A&A, 617, L2

Müller, T. W. A., Kley, W., & Meru, F. 2012, A&A, 541, A123

Murakawa, K. 2010, A&A, 518, A63

Muto, T., Suzuki, T. K., & Inutsuka, S.-i. 2010, ApJ, 724, 448

NASA Exoplanet Archive. 2022, Planetary Systems

Nayakshin, S., Elbakyan, V., & Rosotti, G. 2022, MNRAS, 512, 6038

Nazari, P., Booth, R. A., Clarke, C. J., Rosotti, G. P., Tazzari, M., Juhasz, A., & Meru, F. 2019, MNRAS, 485, 5914

Nelson, R. P., Gressel, O., & Umurhan, O. M. 2013a, MNRAS, 435, 2610

—. 2013b, MNRAS, 435, 2610

Nielsen, E. L., De Rosa, R. J., Macintosh, B., Wang, J. J., Ruffio, J.-B., Chiang, E., Marley, M. S., Saumon, D., Savransky, D., Ammons, S. M., Bailey, V. P., Barman, T., Blain, C., Bulger, J., Burrows, A., Chilcote, J., Cotten, T., Czekala, I., Doyon, R., Duchêne, G., Esposito, T. M.,

Fabrycky, D., Fitzgerald, M. P., Follette, K. B., Fortney, J. J., Gerard, B. L., Goodsell, S. J., Graham, J. R., Greenbaum, A. Z., Hibon, P., Hinkley, S., Hirsch, L. A., Hom, J., Hung, L.-W., Dawson, R. I., Ingraham, P., Kalas, P., Konopacky, Q., Larkin, J. E., Lee, E. J., Lin, J. W., Maire, J., Marchis, F., Marois, C., Metchev, S., Millar-Blanchaer, M. A., Morzinski, K. M., Oppenheimer, R., Palmer, D., Patience, J., Perrin, M., Poyneer, L., Pueyo, L., Rafikov, R. R., Rajan, A., Rameau, J., Rantakyrö, F. T., Ren, B., Schneider, A. C., Sivaramakrishnan, A., Song, I., Soummer, R., Tallis, M., Thomas, S., Ward-Duong, K., & Wolff, S. 2019, AJ, 158, 13

Öberg, K. I., Facchini, S., & Anderson, D. E. 2023, ARA&A, 61, 287

Öberg, K. I., Guzmán, V. V., Walsh, C., Aikawa, Y., Bergin, E. A., Law, C. J., Loomis, R. A., Alarcón, F., Andrews, S. M., Bae, J., Bergner, J. B., Boehler, Y., Booth, A. S., Bosman, A. D., Calahan, J. K., Cataldi, G., Cleeves, L. I., Czekala, I., Furuya, K., Huang, J., Ilee, J. D., Kurtovic, N. T., Le Gal, R., Liu, Y., Long, F., Ménard, F., Nomura, H., Pérez, L. M., Qi, C., Schwarz, K. R., Sierra, A., Teague, R., Tsukagoshi, T., Yamato, Y., van't Hoff, M. L. R., Waggoner, A. R., Wilner, D. J., & Zhang, K. 2021, ApJS, 257, 1

Ogilvie, G. I. & Lubow, S. H. 2002, MNRAS, 330, 950

Ohashi, N., Tobin, J. J., Jørgensen, J. K., Takakuwa, S., Sheehan, P., Aikawa, Y., Li, Z.-Y., Looney, L. W., Williams, J. P., Aso, Y., Sharma, R., Sai, J. I. C., Yamato, Y., Lee, J.-E., Tomida, K., Yen, H.-W., Encalada, F. J., Flores, C., Gavino, S., Kido, M., Han, I., Lin, Z.-Y. D., Narayanan, S., Phuong, N. T., Santamaría-Miranda, A., Thieme, T. J., van't Hoff, M. L. R., de Gregorio-Monsalvo, I., Koch, P. M., Kwon, W., Lai, S.-P., Lee, C. W., Plunkett, A., Saigo, K., Hirano, S., Lam, K. H., & Mori, S. 2023, ApJ, 951, 8

Ohashi, S. & Kataoka, A. 2019, ApJ, 886, 103

Ohashi, S., Kataoka, A., Nagai, H., Momose, M., Muto, T., Hanawa, T., Fukagawa, M., Tsuk-

agoshi, T., Murakawa, K., & Shibai, H. 2018, ApJ, 864, 81

Okuzumi, S., Momose, M., Sirono, S.-i., Kobayashi, H., & Tanaka, H. 2016a, ApJ, 821, 82

—. 2016b, ApJ, 821, 82

Okuzumi, S., Tanaka, H., Kobayashi, H., & Wada, K. 2012, ApJ, 752, 106

Ossenkopf, V. 1993, A&A, 280, 617

Paardekooper, S., Dong, R., Duffell, P., Fung, J., Masset, F. S., Ogilvie, G., & Tanaka, H. 2023, in Astronomical Society of the Pacific Conference Series, Vol. 534, Protostars and Planets VII, ed. S. Inutsuka, Y. Aikawa, T. Muto, K. Tomida, & M. Tamura, 685

Paardekooper, S.-J. & Mellema, G. 2006, A&A, 453, 1129

Paneque-Carreño, T., Izquierdo, A. F., Teague, R., Miotello, A., Bergin, E. A., Loomis, R., & van Dishoeck, E. F. 2023, arXiv e-prints, arXiv:2312.04618

Pascucci, I., Testi, L., Herczeg, G. J., Long, F., Manara, C. F., Hendler, N., Mulders, G. D., Krijt, S., Ciesla, F., Henning, T., Mohanty, S., Drabek-Maunder, E., Apai, D., Szűcs, L., Sacco, G., & Olofsson, J. 2016a, ApJ, 831, 125

Pascucci, I., Testi, L., Herczeg, G. J., Long, F., Manara, C. F., Hendler, N., Mulders, G. D., Krijt, S., Ciesla, F., Henning, T., Mohanty, S., Drabek-Maunder, E., Apai, D., Szűcs, L., Sacco, G., & Olofsson, J. 2016b, ApJ, 831, 125

Pascucci, I., Wolf, S., Steinacker, J., Dullemond, C. P., Henning, T., Niccolini, G., Woitke, P., & Lopez, B. 2004, A&A, 417, 793

Pätzold, M., Andert, T., Hahn, M., Asmar, S. W., Barriot, J. P., Bird, M. K., Häusler, B., Peter, K., Tellmann, S., Grün, E., Weissman, P. R., Sierks, H., Jorda, L., Gaskell, R., Preusker, F., & Scholten, F. 2016, Nature, 530, 63

Pearson, T. J. 1999, in Astronomical Society of the Pacific Conference Series, Vol. 180, Synthesis

Imaging in Radio Astronomy II, ed. G. B. Taylor, C. L. Carilli, & R. A. Perley, 335

Pérez, L. M., Carpenter, J. M., Andrews, S. M., Ricci, L., Isella, A., Linz, H., Sargent, A. I., Wilner, D. J., Henning, T., Deller, A. T., Chandler, C. J., Dullemond, C. P., Lazio, J., Menten, K. M., Corder, S. A., Storm, S., Testi, L., Tazzari, M., Kwon, W., Calvet, N., Greaves, J. S., Harris, R. J., & Mundy, L. G. 2016, Science, 353, 1519

Pérez, L. M., Chandler, C. J., Isella, A., Carpenter, J. M., Andrews, S. M., Calvet, N., Corder, S. A., Deller, A. T., Dullemond, C. P., Greaves, J. S., Harris, R. J., Henning, T., Kwon, W., Lazio, J., Linz, H., Mundy, L. G., Ricci, L., Sargent, A. I., Storm, S., Tazzari, M., Testi, L., & Wilner, D. J. 2015, ApJ, 813, 41

Perez, S., Casassus, S., Ménard, F., Roman, P., van der Plas, G., Cieza, L., Pinte, C., Christiaens, V., & Hales, A. S. 2015a, ApJ, 798, 85

Perez, S., Dunhill, A., Casassus, S., Roman, P., Szulágyi, J., Flores, C., Marino, S., & Montesinos, M. 2015b, ApJ, 811, L5

Pérez et al., L. 2018, ApJ

Pfeil, T., Birnstiel, T., & Klahr, H. 2023, arXiv e-prints, arXiv:2310.07332

Pfeil, T. & Klahr, H. 2019, ApJ, 871, 150

—. 2021, ApJ, 915, 130

Picogna, G. & Kley, W. 2015, A&A, 584, A110

Pierens, A. & Huré, J.-M. 2005, A&A, 433, L37

Pinilla, P., Birnstiel, T., Ricci, L., Dullemond, C. P., Uribe, A. L., Testi, L., & Natta, A. 2012, A&A, 538, A114

Pinilla, P., Flock, M., Ovelar, M. d. J., & Birnstiel, T. 2016, A&A, 596, A81

Pinilla, P., Pohl, A., Stammler, S. M., & Birnstiel, T. 2017a, ApJ, 845, 68

—. 2017b, ApJ, 845, 68

Pinte, C., Dent, W. R. F., Ménard, F., Hales, A., Hill, T., Cortes, P., & de Gregorio-Monsalvo, I. 2016a, ApJ, 816, 25

—. 2016b, ApJ, 816, 25

—. 2016c, ApJ, 816, 25

Pinte, C., Harries, T. J., Min, M., Watson, A. M., Dullemond, C. P., Woitke, P., Ménard, F., & Durán-Rojas, M. C. 2009, A&A, 498, 967

Pinte, C., Ménard, F., Duchêne, G., Hill, T., Dent, W. R. F., Woitke, P., Maret, S., van der Plas, G., Hales, A., Kamp, I., Thi, W. F., de Gregorio-Monsalvo, I., Rab, C., Quanz, S. P., Avenhaus, H., Carmona, A., & Casassus, S. 2018a, A&A, 609, A47

Pinte, C., Price, D. J., Ménard, F., Duchêne, G., Dent, W. R. F., Hill, T., de Gregorio-Monsalvo, I., Hales, A., & Mentiplay, D. 2018b, ApJ, 860, L13

Pinte, C., Teague, R., Flaherty, K., Hall, C., Facchini, S., & Casassus, S. 2023, in Astronomical Society of the Pacific Conference Series, Vol. 534, Protostars and Planets VII, ed. S. Inutsuka, Y. Aikawa, T. Muto, K. Tomida, & M. Tamura, 645

Pohl, A., Pinilla, P., Benisty, M., Ataiee, S., Juhász, A., Dullemond, C. P., Van Boekel, R., & Henning, T. 2015, MNRAS, 453, 1768

Poleski, R., Skowron, J., Mróz, P., Udalski, A., Szymański, M. K., Pietrukowicz, P., Ulaczyk, K., Rybicki, K., Iwanek, P., Wrona, M., & Gromadzki, M. 2021, , 71, 1

Powell, D., Murray-Clay, R., Pérez, L. M., Schlichting, H. E., & Rosenthal, M. 2019, ApJ, 878, 116

Price, E. M., Cleeves, L. I., & Öberg, K. I. 2020, ApJ, 890, 154

Rabago, I. & Zhu, Z. 2021a, MNRAS, 502, 5325

—. 2021b, MNRAS

Rafikov, R. R. 2002, ApJ, 572, 566

—. 2017, ApJ, 837, 163

Rafikov, R. R. & Petrovich, C. 2012, ApJ, 747, 24

Ragusa, E., Rosotti, G., Teyssandier, J., Booth, R., Clarke, C. J., & Lodato, G. 2018, MNRAS, 474, 4460

Raymond, S. N., Kokubo, E., Morbidelli, A., Morishima, R., & Walsh, K. J. 2014, Protostars and Planets VI, 595

Ribas, Á., Espaillat, C. C., Macías, E., & Sarro, L. M. 2020, A&A, 642, A171

Ribas, Á., Merín, B., Bouy, H., & Maud, L. T. 2014, A&A, 561, A54

Ricci, L., Liu, S.-F., Isella, A., & Li, H. 2018, ApJ, 853, 110

Ricci, L., Testi, L., Natta, A., & Brooks, K. J. 2010a, A&A, 521, A66

Ricci, L., Testi, L., Natta, A., Neri, R., Cabrit, S., & Herczeg, G. J. 2010b, A&A, 512, A15

Rice, W. K. M., Armitage, P. J., Wood, K., & Lodato, G. 2006, MNRAS, 373, 1619

Rilinger, A. M., Espaillat, C. C., Xin, Z., Ribas, Á., Macías, E., & Luettgen, S. 2023, ApJ, 944, 66

Rosotti, G. P. 2023, New Astronomy Reviews, 96, 101674

Rosotti, G. P., Benisty, M., Juhász, A., Teague, R., Clarke, C., Dominik, C., Dullemond, C. P., Klaassen, P. D., Matra, L., & Stolker, T. 2019, MNRAS, 2689

Rosotti, G. P., Ilee, J. D., Facchini, S., Tazzari, M., Booth, R. A., Clarke, C., & Kama, M. 2021, MNRAS, 501, 3427

Rosotti, G. P., Juhasz, A., Booth, R. A., & Clarke, C. J. 2016a, MNRAS, 459, 2790

—. 2016b, MNRAS, 459, 2790

Rosotti, G. P., Teague, R., Dullemond, C., Booth, R. A., & Clarke, C. J. 2020, MNRAS, 495, 173

Rowther, S., Meru, F., Kennedy, G. M., Nealon, R., & Pinte, C. 2020, ApJ, 904, L18

Ruane, G., Mawet, D., Kastner, J., Meshkat, T., Bottom, M., Femenía Castellá, B., Absil, O., Gomez Gonzalez, C., Huby, E., Zhu, Z., Jensen-Clem, R., Choquet, É., & Serabyn, E. 2017, AJ, 154, 73

Ruge, J. P., Flock, M., Wolf, S., Dzyurkevich, N., Fromang, S., Henning, T., Klahr, H., & Meheut, H. 2016, A&A, 590, A17

Sallum, S., Follette, K. B., Eisner, J. A., Close, L. M., Hinz, P., Kratter, K., Males, J., Skemer, A., Macintosh, B., Tuthill, P., Bailey, V., Defrère, D., Morzinski, K., Rodigas, T., Spalding, E., Vaz, A., & Weinberger, A. J. 2015, Nature, 527, 342

Sato, T., Okuzumi, S., & Ida, S. 2016, A&A, 589, A15

Schwartz, S. R., Michel, P., Jutzi, M., Marchi, S., Zhang, Y., & Richardson, D. C. 2018, Nature Astronomy, 2, 379

Selvaraju, R. R., Cogswell, M., Das, A., Vedantam, R., Parikh, D., & Batra, D. 2017, in 2017 IEEE International Conference on Computer Vision (ICCV), 618–626

Semenov, D. & Wiebe, D. 2011, ApJS, 196, 25

Siebenmorgen, R. & Heymann, F. 2012, A&A, 539, A20

Sierra, A. & Lizano, S. 2020, ApJ, 892, 136

Sierra, A., Lizano, S., Macías, E., Carrasco-González, C., Osorio, M., & Flock, M. 2019, ApJ, 876, 7

Sierra, A., Pérez, L. M., Zhang, K., Law, C. J., Guzmán, V. V., Qi, C., Bosman, A. D., Öberg, K. I., Andrews, S. M., Long, F., Teague, R., Booth, A. S., Walsh, C., Wilner, D. J., Ménard, F., Cataldi, G., Czekala, I., Bae, J., Huang, J., Bergner, J. B., Ilee, J. D., Benisty, M., Le Gal, R., Loomis, R. A., Tsukagoshi, T., Liu, Y., Yamato, Y., & Aikawa, Y. 2021, ApJS, 257, 14

Simon, J. B., Armitage, P. J., & Beckwith, K. 2011, ApJ, 743, 17

Simon, J. B., Bai, X.-N., Armitage, P. J., Stone, J. M., & Beckwith, K. 2013, ApJ, 775, 73

Simon, J. B., Bai, X.-N., Flaherty, K. M., & Hughes, A. M. 2018, ApJ, 865, 10

Simonyan, K. & Zisserman, A. 2014, arXiv e-prints, arXiv:1409.1556

Sinclair, C. A., Rosotti, G. P., Juhasz, A., & Clarke, C. J. 2020, MNRAS, 493, 3535

Skorov, Y. & Blum, J. 2012, Icarus, 221, 1

Stephens, I. W., Looney, L. W., Kwon, W., Fernández-López, M., Hughes, A. M., Mundy, L. G., Crutcher, R. M., Li, Z.-Y., & Rao, R. 2014, Nature, 514, 597

Stephens, I. W., Yang, H., Li, Z.-Y., Looney, L. W., Kataoka, A., Kwon, W., Fernández-López, M., Hull, C. L. H., Hughes, M., Segura-Cox, D., Mundy, L., Crutcher, R., & Rao, R. 2017, ApJ, 851, 55

Stoll, M. H. R. & Kley, W. 2014, A&A, 572, A77

—. 2016, A&A, 594, A57

Stoll, M. H. R., Kley, W., & Picogna, G. 2017, A&A, 599, L6

Stone, J. M. & Norman, M. L. 1992, ApJS, 80, 753

Stone, J. M., Tomida, K., White, C. J., & Felker, K. G. 2020, ApJS, 249, 4

Suriano, S. S., Li, Z.-Y., Krasnopolsky, R., & Shang, H. 2017, MNRAS, 468, 3850

—. 2018, MNRAS, 477, 1239

Suzuki, D., Bennett, D. P., Sumi, T., Bond, I. A., Rogers, L. A., Abe, F., Asakura, Y., Bhattacharya, A., Donachie, M., Freeman, M., Fukui, A., Hirao, Y., Itow, Y., Koshimoto, N., Li, M. C. A., Ling, C. H., Masuda, K., Matsubara, Y., Muraki, Y., Nagakane, M., Onishi, K., Oyokawa, H., Rattenbury, N., Saito, T., Sharan, A., Shibai, H., Sullivan, D. J., Tristram, P. J., Yonehara, A., & MOA Collaboration. 2016a, ApJ, 833, 145

Suzuki, T. K., Ogihara, M., Morbidelli, A., Crida, A., & Guillot, T. 2016b, A&A, 596, A74

Svanberg, E., Cui, C., & Latter, H. N. 2022, MNRAS, 514, 4581

Szulágyi, J., Binkert, F., & Surville, C. 2022, ApJ, 924, 1

Tabone, B., Rosotti, G. P., Cridland, A. J., Armitage, P. J., & Lodato, G. 2022, MNRAS, 512, 2290

Takahashi, S. Z. & Inutsuka, S.-i. 2014, ApJ, 794, 55

Takahashi, S. Z. & Muto, T. 2018, ApJ, 865, 102

Takeuchi, T. & Lin, D. N. C. 2002, ApJ, 581, 1344

—. 2005, ApJ, 623, 482

Tanaka, H., Inaba, S., & Nakazawa, K. 1996, Icarus, 123, 450

Tanaka, H., Takeuchi, T., & Ward, W. R. 2002, ApJ, 565, 1257

Tazaki, R., Ginski, C., & Dominik, C. 2023, ApJ, 944, L43

Tazaki, R. & Tanaka, H. 2018, ApJ, 860, 79

Tazaki, R., Tanaka, H., Kataoka, A., Okuzumi, S., & Muto, T. 2019a, ApJ, 885, 52

Tazaki, R., Tanaka, H., Muto, T., Kataoka, A., & Okuzumi, S. 2019b, MNRAS, 485, 4951

Tazaki, R., Tanaka, H., Okuzumi, S., Kataoka, A., & Nomura, H. 2016, ApJ, 823, 70

Tazzari, M., Testi, L., Ercolano, B., Natta, A., Isella, A., Chandler, C. J., Pérez, L. M., Andrews, S., Wilner, D. J., Ricci, L., Henning, T., Linz, H., Kwon, W., Corder, S. A., Dullemond, C. P., Carpenter, J. M., Sargent, A. I., Mundy, L., Storm, S., Calvet, N., Greaves, J. A., Lazio, J., & Deller, A. T. 2016, A&A, 588, A53

Teague, R., Bae, J., & Bergin, E. A. 2019, Nature, 574, 378

Teague, R., Bae, J., Bergin, E. A., Birnstiel, T., & Foreman-Mackey, D. 2018a, ApJ, 860, L12

—. 2018b, ApJ, 860, L12

Teague, R., Bae, J., Birnstiel, T., & Bergin, E. 2018c, ArXiv e-prints

Teyssandier, J. & Ogilvie, G. I. 2017, MNRAS, 467, 4577

Thompson, S. E., Coughlin, J. L., Hoffman, K., Mullally, F., Christiansen, J. L., Burke, C. J., Bryson, S., Batalha, N., Haas, M. R., Catanzarite, J., Rowe, J. F., Barentsen, G., Caldwell, D. A., Clarke, B. D., Jenkins, J. M., Li, J., Latham, D. W., Lissauer, J. J., Mathur, S., Morris, R. L., Seader, S. E., Smith, J. C., Klaus, T. C., Twicken, J. D., Van Cleve, J. E., Wohler, B., Akeson, R., Ciardi, D. R., Cochran, W. D., Henze, C. E., Howell, S. B., Huber, D., Prša, A., Ramírez, S. V., Morton, T. D., Barclay, T., Campbell, J. R., Chaplin, W. J., Charbonneau, D., Christensen-Dalsgaard, J., Dotson, J. L., Doyle, L., Dunham, E. W., Dupree, A. K., Ford, E. B., Geary, J. C., Girouard, F. R., Isaacson, H., Kjeldsen, H., Quintana, E. V., Ragozzine, D., Shabram, M., Shporer, A., Silva Aguirre, V., Steffen, J. H., Still, M., Tenenbaum, P., Welsh, W. F., Wolfgang, A., Zamudio, K. A., Koch, D. G., & Borucki, W. J. 2018, ApJS, 235, 38

Trapman, L., Rosotti, G., Bosman, A. D., Hogerheijde, M. R., & van Dishoeck, E. F. 2020, A&A, 640, A5

Turner, N. J., Fromang, S., Gammie, C., Klahr, H., Lesur, G., Wardle, M., & Bai, X.-N. 2014, Protostars and Planets VI, 411

Ueda, T., Flock, M., & Birnstiel, T. 2021, arXiv e-prints, arXiv:2105.13852

Ueda, T., Kataoka, A., & Tsukagoshi, T. 2020, ApJ, 893, 125

—. 2022, ApJ, 930, 56

Umurhan, O. M., Nelson, R. P., & Gressel, O. 2016, A&A, 586, A33

van Boekel, R., Henning, T., Menu, J., de Boer, J., Langlois, M., Müller, A., Avenhaus, H., Boccaletti, A., Schmid, H. M., Thalmann, C., Benisty, M., Dominik, C., Ginski, C., Girard, J. H., Gisler, D., Lobo Gomes, A., Menard, F., Min, M., Pavlov, A., Pohl, A., Quanz, S. P., Rabou, P., Roelfsema, R., Sauvage, J. F., Teague, R., Wildi, F., & Zurlo, A. 2017, ApJ, 837, 132

Van Clepper, E., Bergner, J. B., Bosman, A. D., Bergin, E., & Ciesla, F. J. 2022, ApJ, 927, 206

van der Marel, N., Dong, R., di Francesco, J., Williams, J. P., & Tobin, J. 2019, ApJ, 872, 112

van der Marel, N. & Mulders, G. D. 2021, AJ, 162, 28

van der Marel, N., van Dishoeck, E. F., Bruderer, S., Birnstiel, T., Pinilla, P., Dullemond, C. P., van Kempen, T. A., Schmalzl, M., Brown, J. M., Herczeg, G. J., Mathews, G. S., & Geers, V. 2013, Science, 340, 1199

Van Oort, C. M., Xu, D., Offner, S. S. R., & Gutermuth, R. A. 2019, ApJ, 880, 83

Vigan, A., Bonavita, M., Biller, B., Forgan, D., Rice, K., Chauvin, G., Desidera, S., Meunier, J.-C., Delorme, P., Schlieder, J. E., Bonnefoy, M., Carson, J., Covino, E., Hagelberg, J., Henning, T., Janson, M., Lagrange, A.-M., Quanz, S. P., Zurlo, A., Beuzit, J.-L., Boccaletti, A., Buenzli, E., Feldt, M., Girard, J. H. V., Gratton, R., Kasper, M., Le Coroller, H., Mesa, D., Messina, S., Meyer, M., Montagnier, G., Mordasini, C., Mouillet, D., Moutou, C., Reggiani, M., Segransan, D., & Thalmann, C. 2017a, A&A, 603, A3

—. 2017b, A&A, 603, A3

Vigan, A., Fontanive, C., Meyer, M., Biller, B., Bonavita, M., Feldt, M., Desidera, S., Marleau, G. D., Emsenhuber, A., Galicher, R., Rice, K., Forgan, D., Mordasini, C., Gratton, R., Le Coroller, H., Maire, A. L., Cantalloube, F., Chauvin, G., Cheetham, A., Hagelberg, J., Lagrange, A. M., Langlois, M., Bonnefoy, M., Beuzit, J. L., Boccaletti, A., D'Orazi, V., Delorme, P., Dominik, C., Henning, T., Janson, M., Lagadec, E., Lazzoni, C., Ligi, R., Menard, F., Mesa, D., Messina, S., Moutou, C., Müller, A., Perrot, C., Samland, M., Schmid, H. M., Schmidt, T., Sissa, E., Turatto, M., Udry, S., Zurlo, A., Abe, L., Antichi, J., Asensio-Torres, R., Baruffolo, A., Baudoz, P., Baudrand, J., Bazzon, A., Blanchard, P., Bohn, A. J., Brown Sevilla, S., Carbillet, M., Carle, M., Cascone, E., Charton, J., Claudi, R., Costille, A., De Caprio, V., Delboulbé, A.,

Dohlen, K., Engler, N., Fantinel, D., Feautrier, P., Fusco, T., Gigan, P., Girard, J. H., Giro, E., Gisler, D., Gluck, L., Gry, C., Hubin, N., Hugot, E., Jaquet, M., Kasper, M., Le Mignant, D., Llored, M., Madec, F., Magnard, Y., Martinez, P., Maurel, D., Möller-Nilsson, O., Mouillet, D., Moulin, T., Origné, A., Pavlov, A., Perret, D., Petit, C., Pragt, J., Puget, P., Rabou, P., Ramos, J., Rickman, E. L., Rigal, F., Rochat, S., Roelfsema, R., Rousset, G., Roux, A., Salasnich, B., Sauvage, J. F., Sevin, A., Soenke, C., Stadler, E., Suarez, M., Wahhaj, Z., Weber, L., & Wildi, F. 2021, A&A, 651, A72

Villenave, M., Ménard, F., Dent, W. R. F., Duchêne, G., Stapelfeldt, K. R., Benisty, M., Boehler, Y., van der Plas, G., Pinte, C., Telkamp, Z., Wolff, S., Flores, C., Lesur, G., Louvet, F., Riols, A., Dougados, C., Williams, H., & Padgett, D. 2020, A&A, 642, A164

Villenave, M., Stapelfeldt, K. R., Duchêne, G., Ménard, F., Lambrechts, M., Sierra, A., Flores, C., Dent, W. R. F., Wolff, S., Ribas, Á., Benisty, M., Cuello, N., & Pinte, C. 2022, ApJ, 930, 11

Wagner, K., Follette, K. B., Close, L. M., Apai, D., Gibbs, A., Keppler, M., Müller, A., Henning, T., Kasper, M., Wu, Y.-L., Long, J., Males, J., Morzinski, K., & McClure, M. 2018a, ApJ, 863, L8

—. 2018b, ApJ, 863, L8

Wahlberg Jansson, K., Johansen, A., Bukhari Syed, M., & Blum, J. 2017, ApJ, 835, 109

Wang, J. J., Ginzburg, S., Ren, B., Wallack, N., Gao, P., Mawet, D., Bond, C. Z., Cetre, S., Wizinowich, P., De Rosa, R. J., Ruane, G., Liu, M. C., Absil, O., Alvarez, C., Baranec, C., Choquet, É., Chun, M., Defrère, D., Delorme, J.-R., Duchêne, G., Forsberg, P., Ghez, A., Guyon, O., Hall, D. N. B., Huby, E., Jolivet, A., Jensen-Clem, R., Jovanovic, N., Karlsson, M., Lilley, S., Matthews, K., Ménard, F., Meshkat, T., Millar-Blanchaer, M., Ngo, H., Orban de Xivry, G., Pinte, C., Ragland, S., Serabyn, E., Catalán, E. V., Wang, J., Wetherell, E., Williams, J. P.,

Ygouf, M., & Zuckerman, B. 2020a, AJ, 159, 263

—. 2020b, AJ, 159, 263

Wang, S., Kanagawa, K. D., & Suto, Y. 2022, arXiv e-prints, arXiv:2204.08826

Ward, W. R. 1997, Icarus, 126, 261

Warren, S. G. & Brandt, R. E. 2008, Journal of Geophysical Research (Atmospheres), 113, D14220

Weidenschilling, S. J. 1977, MNRAS, 180, 57

—. 1997, Icarus, 127, 290

Weidenschilling, S. J. & Cuzzi, J. N. 1993, in Protostars and Planets III, ed. E. H. Levy & J. I. Lunine, 1031

Weidling, R., Güttler, C., Blum, J., & Brauer, F. 2009, ApJ, 696, 2036

Weissman, P., Morbidelli, A., Davidsson, B., & Blum, J. 2020, Space Sci. Rev., 216, 6

Whipple, F. L. 1972, in From Plasma to Planet, ed. A. Elvius, 211

Williams, J. P., Cieza, L., Hales, A., Ansdell, M., Ruiz-Rodriguez, D., Casassus, S., Perez, S., & Zurlo, A. 2019, ApJ, 875, L9

Wolf, S. & D'Angelo, G. 2005, ApJ, 619, 1114

Wölfer, L., Facchini, S., van der Marel, N., van Dishoeck, E. F., Benisty, M., Bohn, A. J., Francis, L., Izquierdo, A. F., & Teague, R. D. 2023, A&A, 670, A154

Wurm, G. & Blum, J. 1998, Icarus, 132, 125

Xin, Z., Espaillat, C. C., Rilinger, A. M., Ribas, Á., & Macías, E. 2023, ApJ, 942, 4

Xu, D., Offner, S. S. R., Gutermuth, R., & Oort, C. V. 2020a, ApJ, 905, 172

—. 2020b, ApJ, 890, 64

Xu, R., Bai, X.-N., & Öberg, K. 2017, ApJ, 835, 162

Yang, C.-C., Mac Low, M.-M., & Johansen, A. 2018, ApJ, 868, 27

Yang, C.-C. & Menou, K. 2010, MNRAS, 402, 2436

Yang, C.-C. & Zhu, Z. 2020, MNRAS, 491, 4702

Yang, H., Li, Z.-Y., Looney, L., & Stephens, I. 2016, MNRAS, 456, 2794

Yang, H., Li, Z.-Y., Looney, L. W., Girart, J. M., & Stephens, I. W. 2017, MNRAS, 472, 373

Yang, H., Li, Z.-Y., Stephens, I. W., Kataoka, A., & Looney, L. 2019, MNRAS, 483, 2371

Youdin, A. N. & Goodman, J. 2005, ApJ, 620, 459

Youdin, A. N. & Lithwick, Y. 2007, Icarus, 192, 588

Yu, H., Teague, R., Bae, J., & Öberg, K. 2021, ApJ, 920, L33

Yu, L., Donati, J.-F., Hébrard, E. M., Moutou, C., Malo, L., Grankin, K., Hussain, G., Collier Cameron, A., Vidotto, A. A., Baruteau, C., Alencar, S. H. P., Bouvier, J., Petit, P., Takami, M., Herczeg, G., Gregory, S. G., Jardine, M., Morin, J., Ménard, F., & Matysse Collaboration. 2017, MNRAS, 467, 1342

Yu, S.-Y., Ho, L. C., & Zhu, Z. 2019, ApJ, 877, 100

Zhang, D., Davis, S. W., Jiang, Y.-F., & Stone, J. M. 2018a, ApJ, 854, 110

Zhang, K., Bergin, E. A., Blake, G. A., Cleeves, L. I., Hogerheijde, M., Salinas, V., & Schwarz, K. R. 2016, ApJ, 818, L16

Zhang, K., Blake, G. A., & Bergin, E. A. 2015a, ApJ, 806, L7

—. 2015b, ApJ, 806, L7

Zhang, K., Booth, A. S., Law, C. J., Bosman, A. D., Schwarz, K. R., Bergin, E. A., Öberg, K. I., Andrews, S. M., Guzmán, V. V., Walsh, C., Qi, C., van't Hoff, M. L. R., Long, F., Wilner, D. J., Huang, J., Czekala, I., Ilee, J. D., Cataldi, G., Bergner, J. B., Aikawa, Y., Teague, R., Bae, J., Loomis, R. A., Calahan, J. K., Alarcón, F., Ménard, F., Le Gal, R., Sierra, A., Yamato, Y., Nomura, H., Tsukagoshi, T., Pérez, L. M., Trapman, L., Liu, Y., & Furuya, K. 2021a, ApJS,

257, 5

Zhang, S., Hu, X., Zhu, Z., & Bae, J. 2021b, ApJ, 923, 70

Zhang, S., Kalscheur, M., Long, F., Zhang, K., Long, D. E., Bergin, E. A., Zhu, Z., & Trapman, L. 2023a, ApJ, 952, 108

Zhang, S. & Zhu, Z. 2020, MNRAS, 493, 2287

Zhang, S., Zhu, Z., & et al. 2018b, ApJ

Zhang, S., Zhu, Z., Huang, J., Guzmán, V. V., Andrews, S. M., Birnstiel, T., Dullemond, C. P., Carpenter, J. M., Isella, A., Pérez, L. M., Benisty, M., Wilner, D. J., Baruteau, C., Bai, X.-N., & Ricci, L. 2018c, ApJ, 869, L47

Zhang, S., Zhu, Z., & Jiang, Y.-F. 2024, arXiv e-prints, arXiv:2404.05608

Zhang, S., Zhu, Z., & Kang, M. 2022, MNRAS, 510, 4473

Zhang, S., Zhu, Z., Ueda, T., Kataoka, A., Sierra, A., Carrasco-González, C., & Macías, E. 2023b, ApJ, 953, 96

Zhou, B., Khosla, A., Lapedriza, A., Oliva, A., & Torralba, A. 2016, in 2016 IEEE Conference on Computer Vision and Pattern Recognition (CVPR), 2921–2929

Zhu, Z., Andrews, S. M., & Isella, A. 2018, MNRAS, 479, 1850

Zhu, Z. & Baruteau, C. 2016, MNRAS, 458, 3918

Zhu, Z., Dong, R., Stone, J. M., & Rafikov, R. R. 2015a, ApJ, 813, 88

Zhu, Z., Jiang, Y.-F., & Stone, J. M. 2020, MNRAS, 495, 3494

Zhu, Z., Nelson, R. P., Dong, R., Espaillat, C., & Hartmann, L. 2012a, ApJ, 755, 6

—. 2012b, ApJ, 755, 6

Zhu, Z., Nelson, R. P., Hartmann, L., Espaillat, C., & Calvet, N. 2011, ApJ, 729, 47

Zhu, Z., Stone, J. M., & Bai, X.-N. 2015b, ApJ, 801, 81

Zhu, Z., Stone, J. M., & Calvet, N. 2023, MNRAS

Zhu, Z., Stone, J. M., & Rafikov, R. R. 2013, ApJ, 768, 143

Zhu, Z., Stone, J. M., Rafikov, R. R., & Bai, X.-n. 2014a, ApJ, 785, 122

—. 2014b, ApJ, 785, 122

Zhu, Z., Zhang, S., Jiang, Y.-F., Kataoka, A., Birnstiel, T., Dullemond, C. P., Andrews, S. M., Huang, J., Pérez, L. M., Carpenter, J. M., Bai, X.-N., Wilner, D. J., & Ricci, L. 2019, ApJ, 877, L18

Ziampras, A., Kley, W., & Dullemond, C. P. 2020, A&A, 637, A50

Zsom, A., Ormel, C. W., Güttler, C., Blum, J., & Dullemond, C. P. 2010, A&A, 513, A57

Zurlo, A., Cugno, G., Montesinos, M., Perez, S., Canovas, H., Casassus, S., Christiaens, V., Cieza, L., & Huelamo, N. 2020, A&A, 633, A119

CURRICULUM VITAE

Name: Shangjia Zhang
E-mail: shangjiazhang24@gmail.com

EDUCATION

University of Nevada, Las Vegas
Ph.D. in Astronomy, Advisor: Prof. Zhaohuan Zhu, 2018–2024
University of Michigan, Ann Arbor
B.S. in Astronomy and Physics, Advisor: Prof. Lee Hartmann, 2016–2018

PUBLICATIONS

- Zhang, Shangjia and Zhu, Zhaohuan and Jiang, Yan-Fei, Thermal Structure Determines Kinematics: Vertical Shear Instability in Stellar Irradiated Protoplanetary Disks. ApJ, in press
- Zhang, S., Kalscheur, M., Long, F., et al. Substructures in Compact Disks of the Taurus Star-forming Region. ApJ 952, 108. (Aug. 2023)
- Zhang, S., Zhu, Z., Ueda, T., et al. Porous Dust Particles in Protoplanetary Disks: Application to the HL Tau Disk. ApJ 953, 96. (Aug. 2023)
- Zhang, S., Zhu, Z. & Kang, M. PGNets: planet mass prediction using convolutional neural networks for radio continuum observations of protoplanetary discs. MNRAS 510, 4473–4484. (Mar. 2022)
- Zhang, S., Hu, X., Zhu, Z., et al. Self-consistent Ring Model in Protoplanetary Disks: Temperature Dips and Substructure Formation. ApJ 923, 70. (Dec. 2021)
- Zhang, S. & Zhu, Z. The effects of disc self-gravity and radiative cooling on the formation of gaps and spirals by young planets. MNRAS 493, 2287–2305. (Apr. 2020)
- Zhu, Z., Zhang, S., Jiang, Y.-F., et al. One Solution to the Mass Budget Problem for Planet Formation: Optically Thick Disks with Dust Scattering. ApJL 877, L18. (June 2019)
- Zhang, S., Zhu, Z., Huang, J., et al. The Disk Substructures at High Angular Resolution Project (DSHARP). VII. The Planet-Disk Interactions Interpretation. ApJL 869, L47. (Dec. 2018)
- Zhang, S., Hartmann, L., Zamora-Avilés, M., et al. On estimating angular momenta of infalling protostellar cores from observations. MNRAS 480, 5495–5503. (Nov. 2018)

Contributing Publications

- Wallack, N. L., Ruffio, J.-B., Ruane, G., et al. A Survey of Protoplanetary Disks Using the Keck/NIRC2 Vortex Coronagraph. *ApJ*, in press (2023).

- Long, F., Andrews, S. M., Zhang, S., et al. ALMA Detection of Dust Trapping around Lagrangian Points in the LkCa 15 Disk. *ApJL* 937, L1. arXiv: 2209.05535 [astro-ph.EP] (Sept. 2022).

- Burrill, B. P., Ricci, L., Harter, S. K., et al. Investigating the Future Potential of an Upgraded ALMA to Image Planet-forming Disks at Sub-astronomical-unit Scales. *ApJ* 928, 40. arXiv: 2202.08348 [astro-ph.EP] (Mar. 2022).

- Andrews, S. M., Elder, W., Zhang, S., et al. Limits on Millimeter Continuum Emission from Circumplanetary Material in the DSHARP Disks. *ApJ* 916, 51. arXiv: 2105.08821 [astro-ph.EP] (July 2021).

- Ueda, T., Kataoka, A., Zhang, S., et al. Impact of Differential Dust Settling on the SED and Polarization: Application to the Inner Region of the HL Tau Disk. *ApJ* 913, 117. arXiv: 2104.05927 [astro-ph.EP] (June 2021).

- Jorquera, S., Pérez, L. M., Chauvin, G., et al. A Search for Companions via Direct Imaging in the DSHARP Planet-forming Disks. *AJ* 161, 146. arXiv: 2012.10464 [astro-ph.EP] (Mar. 2021).

- Harter, S. K., Ricci, L., Zhang, S., et al. Imaging the Dusty Substructures due to Terrestrial Planets in Planet-forming Disks with ALMA and the Next-generation Very Large Array. *ApJ* 905, 24. arXiv: 2011.08279 [astro-ph.EP] (Dec. 2020).

- Huang, J., Andrews, S. M., Dullemond, C. P., et al. A Multifrequency ALMA Characterization of Substructures in the GM Aur Protoplanetary Disk. *ApJ* 891, 48. arXiv: 2001.11040 [astro-ph.EP] (Mar. 2020).

- Isella, A., Huang, J., Andrews, S. M., et al. The Disk Substructures at High Angular Resolution Project (DSHARP). IX. A High-definition Study of the HD 163296 Planet-forming Disk. *ApJL* 869, L49. arXiv: 1812.04047 [astro-ph.SR] (Dec. 2018).

- Dullemond, C. P., Birnstiel, T., Huang, J., et al. The Disk Substructures at High Angular Resolution Project (DSHARP). VI. Dust Trapping in Thin-ringed Protoplanetary Disks. *ApJL* 869, L46. arXiv: 1812.04044 [astro-ph.EP] (Dec. 2018).

- Pérez, L. M., Benisty, M., Andrews, S. M., et al. The Disk Substructures at High Angular Resolution Project (DSHARP). X. Multiple Rings, a Misaligned Inner Disk, and a Bright Arc in the Disk around the T Tauri star HD 143006. *ApJL* 869, L50. arXiv: 1812.04049 [astro-ph.SR] (Dec. 2018).

- Kurtovic, N. T., Pérez, L. M., Benisty, M., et al. The Disk Substructures at High Angular Resolution Project (DSHARP). IV. Characterizing Substructures and Interactions in Disks around Multiple Star Systems. *ApJL* 869, L44. arXiv: 1812.04536 [astro-ph.SR] (Dec. 2018).

- Guzmán, V. V., Huang, J., Andrews, S. M., et al. The Disk Substructures at High Angular Resolution Program (DSHARP). VIII. The Rich Ringed Substructures in the AS 209 Disk. *ApJL* 869, L48. arXiv: 1812.04046 [astro-ph.SR] (Dec. 2018).
- Andrews, S. M., Huang, J., Pérez, L. M., et al. The Disk Substructures at High Angular Resolution Project (DSHARP). I. Motivation, Sample, Calibration, and Overview. *ApJL* 869, L41. arXiv: 1812.04040 [astro-ph.SR] (Dec. 2018).
- Huang, J., Andrews, S. M., Dullemond, C. P., et al. The Disk Substructures at High Angular Resolution Project (DSHARP). II. Characteristics of Annular Substructures. *ApJL* 869, L42. arXiv: 1812.04041 [astro-ph.EP] (Dec. 2018).
- Huang, J., Andrews, S. M., Pérez, L. M., et al. The Disk Substructures at High Angular Resolution Project (DSHARP). III. Spiral Structures in the Millimeter Continuum of the Elias 27, IM Lup, and WaOph 6 Disks. *ApJL* 869, L43. arXiv: 1812.04193 [astro-ph.SR] (Dec. 2018).
- Birnstiel, T., Dullemond, C. P., Zhu, Z., et al. The Disk Substructures at High Angular Resolution Project (DSHARP). V. Interpreting ALMA Maps of Protoplanetary Disks in Terms of a Dust Model. *ApJL* 869, L45. arXiv: 1812.04043 [astro-ph.SR] (Dec. 2018).
- Li, J.-T., Bregman, J. N., Wang, Q. D., et al. The Circum-Galactic Medium of Massive Spirals. II. Probing the Nature of Hot Gaseous Halo around the Most Massive Isolated Spiral Galaxies. *ApJS* 233, 20. arXiv: 1710.07355 [astro-ph.GA] (Dec. 2017).

SELECTED TALKS

- U. Chicago Geo. Sci. Seminar (Dec 2023)
- TCAN Meeting, Tuscon, AZ (Nov 2023)
- Princeton Thunch, Princeton, NJ (Oct 2023)
- NRAO TUNA Talk, Charlottesville, VA (Oct 2023)
- UW-Madison Monday Science Seminar, Madison, WI (Oct 2023)
- U. of Hawaii SPLAT Talk, Honolulu, HI (Sep 2023)
- CfA SMA Seminars, Cambridge, MA (Sep 2023)
- Harvard ITC Luncheon, Cambridge, MA (Sep 2023)
- Origins Seminars, Tuscon, AZ (Sep 2023)
- Emerging Researchers in Exoplanet Science (ERES), New Haven, CT (Jun 2023)
- Athena++ workshop, New York, NY (May 2023)
- Planet Formation Group Meeting, Flatiron Institute (online) (Jan 2023)

- Planet Formation Group Meeting, U. Victoria (online) (Feb 2022)
- Star and Planet Formation Seminar, UMich (online) (Feb 2022)
- Caltech Direct Imaging Group, Caltech (online) (Dec 2021)
- New paradigms for radiatively efficient accretion disks, New York, NY (Dec 2021)
- Star Formation: From Clouds to Discs, Malahide, Ireland (Oct 2021)
- Five years after HL Tau: a new era in planet formation (online) (Dec 2020)
- New Horizons in Planetary Systems, Victoria, BC, Canada (May 2019)
- 233rd AAS Meeting, Seattle, WA (Jan 2019)
- Peking U. KIAA SPF Group Meeting, Beijing, China (Dec 2018)

SELECTED POSTERS

- GRC and GRS Origins of Solar Systems, South Hadley, MA, Jun 2023

Selected Grants and Awards

- NASA Hubble Fellowship Program (NHFP) Sagan Fellow
- Future Investigators in NASA Earth and Space Science and Technology (FINESST)
- UNLV Russell L. and Brenda Frank Scholarship (7,000 USD)
- UNLV Barrick Graduate Fellowship
- AAS International Travel Grant
- UNLV GPSA Travel Fund
- OISS Distinguished Contribution Award

SELECTED SERVICE AND OUTREACH

- Referee of ApJL, ApJ, MNRAS, and PASJ
- Co-founder, Speaker, and Webmaster, Astronomy on Tap, Las Vegas (1/season) (2018–Current)
- Judge of Beal Bank Science Fair (2021–2024)
- Sole Organizer UNLV Astro Coffee and Astro Journal Club (2023)
- Presenter UNLV Art in Science Exhibition (2023)

- AAS Astronomy Ambassador Program (2019–Current)
- Sole Organizer Lunar Eclipse on the Strip, Las Vegas (2013)

TEACHING

- Lecturer & Grader Astro 105: Introductory Astronomy Laboratory

STUDENT ADVISING

- Sarah Harter (Undergraduate student at CSUN, now graduate student at U. Rochester) Project: Imaging the Dusty Substructures due to Terrestrial Planets in Planet-forming Disks with ALMA and the Next-generation Very Large Array.

SKILLS

- General: (Radiation)-Hydrodynamics, Monte Carlo Radiative Transfer, Deep Neural Networks